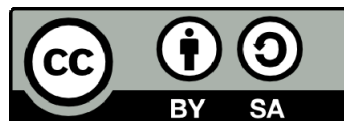




UNIVERSITAT<sub>DE</sub>  
BARCELONA

# Transformations and pathways of Southern Ocean waters into the South Atlantic Ocean

Anna Olivé Abelló



Aquesta tesi doctoral està subjecta a la llicència **Reconeixement- Compartiqual 4.0. Espanya de Creative Commons.**

Esta tesis doctoral está sujeta a la licencia **Reconocimiento - Compartiqual 4.0. España de Creative Commons.**

This doctoral thesis is licensed under the **Creative Commons Attribution-ShareAlike 4.0. Spain License.**

# TRANSFORMATIONS AND PATHWAYS OF THE SOUTHERN OCEAN WATERS INTO THE SOUTH ATLANTIC OCEAN

Anna Olivé Abelló

TESI DOCTORAL

INSTITUT DE CIÈNCIES DEL MAR - CSIC

2022



TESI DOCTORAL

# TRANSFORMATIONS AND PATHWAYS OF SOUTHERN OCEAN WATERS INTO THE SOUTH ATLANTIC OCEAN

**Anna Olivé Abelló**

**INSTITUT DE CIÈNCIES DEL MAR (ICM – CSIC)**

Tesi doctoral presentada per a optar al grau de Doctora per la Universitat de Barcelona.  
Programa de Doctorat de Ciències del Mar.

|                     |                        |                       |                        |
|---------------------|------------------------|-----------------------|------------------------|
| <b>Anna</b>         | <b>Josep Lluís</b>     | <b>Francisco</b>      | <b>Montserrat</b>      |
| <b>Olivé Abelló</b> | <b>Pelegrí Llopart</b> | <b>Machín Jiménez</b> | <b>Vidal Barcelona</b> |
| PhD student         | PhD supervisor         | PhD supervisor        | PhD tutor              |

Barcelona, desembre de 2022



*El poder de la marea  
está en cada ola.*



## PREFACE

This dissertation, entitled **Transformations and pathways of Southern Ocean waters into the South Atlantic Ocean**, is presented to obtain the Doctoral degree from the Universitat de Barcelona. This investigation is the compilation of 5 studies aimed at describing how the incorporation of Antarctic waters into the South Atlantic Ocean takes place in terms of circulation, variability, and water mass transformations. The research presented here has been conducted between 2018 and 2022 at Institut de Ciències del Mar – Consejo Superior de Investigaciones Científicas, under the guidance of Dr. Josep Lluís Pelegrí Llopart and Dr. Francisco Machín Jiménez, supported by the Spanish Government through an FPU predoctoral grant (FPU17/03796). It has been developed in the frame of the projects VA-DE-RETRO, reference CTM2014-56987-P, and SAGA, reference RTI2018-100844-B-C33. This dissertation is also part of the research carried out within the Unidad Océano y Clima of the Universidad de Las Palmas de Gran Canaria, an R+D+I CSIC associate unit. We recognize the institutional support of the Spanish Government through the Severo Ochoa Center of Excellence accreditation (CEX2019-000928-S).

This doctoral dissertation is structured into an Introduction, Methodology, Results, General Discussion and Conclusions, constituting the dissertation's core the five chapters inside the Results section. Two of them (**Chapters 3.1** and **3.3**) have already been published or are in the final steps of the publishing process, while the other three (**Chapters 3.2**, **3.4** and **3.5**) are still in preparation and should therefore be considered as preliminary drafts. The thesis concludes with the exposition of the main results and comments on the potential future lines of research. Despite the COVID-19 pandemic and its derived difficulties, three collaborative research short-stays were done at the University of Las Palmas de Gran Canaria under the guidance of Dr. Francisco Machín, at the University of Sorbonne under the guidance of Dra. Christine Provost and Dra. Camila Artana, and at the CSIRO Ocean & Atmosphere under the guidance of Dr. Steve Rintoul. Two of them were funded through travel grants awarded by the Universitat de Barcelona and the Ministry of Universities (EST21/00374). The derived works are shown in **Chapters 3.2** and **3.5**, respectively. During this period, the author of this thesis has contributed to eight congresses/symposiums and has participated in two oceanographic cruises, RETRO-ERZ and SAGA-10W, on board of two Spanish research vessels, the BIO Hespérides and the B/O Sarmiento de Gamboa.





# CONTENTS

|  |           |
|--|-----------|
| <b>PREFACE</b> .....   | <b>7</b>  |
| <b>CONTENTS</b> .....  | <b>9</b>  |
| <b>ACKNOWLEDGMENTS – AGRADECIMIENTOS – AGRAÏMENTS</b> .....  | <b>13</b> |
| <b>SUMMARY – RESUMEN – RESUM</b> .....   | <b>15</b> |
| <b>ACRONYMS LIST</b> .....   | <b>23</b> |
| <b>I. INTRODUCTION</b> .....   | <b>25</b> |
| 1.1. The Global and Meridional Overturning Circulation.....  | 26        |
| 1.1.1. The Atlantic Meridional Overturning Circulation .....   | 28        |
| 1.1.2. The Southern Ocean circulation.....   | 30        |
| 1.1.3. Main Southern Ocean water masses.....   | 33        |
| 1.2. The Southern Ocean waters transfer to the South Atlantic Ocean.....                               | 38        |
| 1.2.1. The South Atlantic Ocean circulation.....   | 39        |
| 1.2.2. Warm and cold contributions to the returning AMOC into the South Atlantic Ocean .....           | 40        |
| 1.3. Objectives and outline of this thesis .....   | 43        |
| <b>II. METHODOLOGY</b> .....   | <b>47</b> |
| 2.1. From Argo floats to model products .....  | 48        |
| 2.1.1. <i>In situ</i> observations: floats, satellites, marine mammals and oceanographic cruises ..... | 49        |
| 2.1.2. Numerical model products.....   | 52        |
| 2.2. Inverse model .....   | 53        |
| 2.2.1. Geostrophic velocity and transport .....  | 53        |
| 2.2.2. Inverse model formulation .....   | 55        |
| 2.2.3. The full matrix system .....  | 63        |
| 2.3. Lagrangian analysis .....   | 64        |
| 2.3.1. Evolution of the Lagrangian approach .....  | 64        |
| 2.3.2. Advection and diffusion algorithms .....  | 66        |
| 2.3.3. Computing Lagrangian simulations.....   | 67        |
| 2.4. Horizontal diffusion coefficients.....  | 70        |
| 2.4.1. One major ocean dynamic challenge.....  | 70        |
| 2.4.2. Basic diffusive concepts.....   | 71        |
| 2.4.3. Radial offset by diffusion method .....   | 72        |

|  |            |
|--|------------|
| <b>III. RESULTS .....</b>  | <b>75</b>  |
| <b>3.1. The transfer of Antarctic Circumpolar waters to the western South Atlantic Ocean .....</b> | <b>77</b>  |
| 3.1.1. Context and objectives .....  | 78         |
| 3.1.2. Material and methods .....  | 80         |
| 3.1.2.1. Study area.....   | 80         |
| 3.1.2.2. Argo floats.....  | 80         |
| 3.1.2.3. Data processing .....   | 81         |
| 3.1.3. Results .....   | 86         |
| 3.1.3.1. Reference velocities.....   | 86         |
| 3.1.3.2. Vertical sections.....  | 89         |
| 3.1.4. Discussion.....   | 91         |
| 3.1.4.1. Water transports.....   | 91         |
| 3.1.4.2. Cross-frontal exchange.....   | 94         |
| 3.1.4.3. Interannual variability.....  | 97         |
| 3.1.4.4. Seasonal variability .....  | 100        |
| 3.1.4.5. Comparison with previous estimates.....   | 102        |
| 3.1.5. Concluding remarks.....   | 105        |
| <b>3.2. Mass and biogeochemical fluxes in the Scotia Sea .....</b>                                 | <b>111</b> |
| 3.2.1. Context and objectives .....  | 112        |
| 3.2.2. Materials and methods .....   | 115        |
| 3.2.2.1. Domain and datasets .....   | 115        |
| 3.2.2.2. Inverse model setup.....  | 121        |
| 3.2.2.3. Sensitivity study .....   | 127        |
| 3.2.2.4. Biogeochemical approach .....   | 128        |
| 3.2.3. Results .....   | 129        |
| 3.2.3.1. Vertical boundary sections .....  | 129        |
| 3.2.3.2. Water velocities and biogeochemical fluxes.....   | 133        |
| 3.2.4. Discussion.....   | 137        |
| 3.2.4.1. Water, salt and heat transports .....   | 137        |
| 3.2.4.2. Transport of biogeochemical properties .....  | 141        |
| 3.2.4.3. Biogeochemical processes and anthropogenic DIC storage.....                               | 144        |
| 3.2.4.4. Comparison with SOSE and B-SOSE.....  | 147        |
| 3.2.5. Final remarks.....  | 153        |

---

|   |            |
|---|------------|
| <b>3.3. Spatial variability of horizontal diffusivity in the southwestern South Atlantic Ocean.....</b> | <b>157</b> |
| 3.3.1. Context and objectives.....  | 158        |
| 3.3.2. Data .....   | 160        |
| 3.3.2.1. Case-study area.....   | 160        |
| 3.3.2.2. Global Drifter Program data .....  | 161        |
| 3.3.2.3. RAFOS floats .....   | 161        |
| 3.3.2.4. Argo floats.....   | 162        |
| 3.3.2.5. GLORYS12v1 reanalysis .....  | 162        |
| 3.3.3. Methods.....   | 163        |
| 3.3.3.1. Comparing the field and numerical positions.....   | 163        |
| 3.3.3.2. Radial diffusion model.....  | 169        |
| 3.3.3.3. Comparing the experimental and theoretical particle distributions.....                         | 170        |
| 3.3.4. Results.....   | 173        |
| 3.3.4.1. Variability with depth.....  | 173        |
| 3.3.4.2. Variability per frontal regions.....   | 175        |
| 3.3.5. Discussion.....  | 177        |
| 3.3.5.1. Limitations and advantages of the method .....   | 177        |
| 3.3.5.2. Comparison with other observations for the study area .....                                    | 179        |
| 3.3.6. Final remarks .....  | 182        |
| <b>3.4. Direct pathways from the Drake Passage to the South Atlantic subtropical gyre.....</b>          | <b>185</b> |
| 3.4.1. Context and objectives.....  | 186        |
| 3.4.2. Materials and methods.....   | 187        |
| 3.4.2.1. GLORYS12v1 reanalysis .....  | 187        |
| 3.4.2.2. Lagrangian experiments .....   | 188        |
| 3.4.2.3. Lagrangian streamfunctions.....  | 190        |
| 3.4.2.4. Loss/gain of heat and salt transport .....   | 190        |
| 3.4.3. Results.....   | 191        |
| 3.4.3.1. Transport contribution to the South Atlantic Ocean .....                                       | 191        |
| 3.4.3.2. Heat and freshwater transfer .....   | 199        |
| 3.4.3.3. Water mass transformation.....   | 203        |
| 3.4.4. Discussion.....  | 205        |
| 3.4.4.1. Net horizontal diffusion effect .....  | 205        |
| 3.4.4.2. Recirculation in the subtropical gyre .....  | 207        |
| 3.4.4.3. Seasonal variability.....  | 209        |

|   |            |
|---|------------|
| 3.4.4.4. Comparison with other studies.....   | 211        |
| 3.4.5. Summary and conclusions .....  | 214        |
| <b>3.5. The cold and warm intermediate contributions to the South Atlantic subtropical gyre .....</b> | <b>217</b> |
| 3.5.1. Context and objectives.....  | 218        |
| 3.5.2. Methodology .....  | 220        |
| 3.5.2.1. Area of study, reference sections and intermediate water masses.                             | 220        |
| 3.5.2.2. Lagrangian simulations.....  | 220        |
| 3.5.3. Results .....  | 223        |
| 3.5.3.1. Warm and cold pathways and transit times .....   | 223        |
| 3.5.3.2. Thermohaline properties.....   | 228        |
| 3.5.3.3. Density variations and water mass transformations .....                                      | 232        |
| 3.5.4. Discussion.....  | 236        |
| 3.5.4.1. Cold and warm contribution through the Agulhas Current .....                                 | 236        |
| 3.5.4.2. Interannual variability.....   | 238        |
| 3.5.4.3. Comparison with previous estimates.....  | 242        |
| 3.5.5. Preliminary conclusion .....   | 244        |
| <b>IV. GENERAL DISCUSSION .....</b>   | <b>247</b> |
| 4.1. Advantages and limitations of the methodologies used.....  | 248        |
| 4.2. Integrated vision of the Southern Ocean – South Atlantic Ocean connection .....                  | 252        |
| <b>V. CONCLUSIONS .....</b>   | <b>265</b> |
| 5.1. Main scientific contributions.....   | 267        |
| 5.2. Future lines of research.....  | 271        |
| <b>PUBLICATIONS.....</b>  | <b>273</b> |
| <b>LIST OF FIGURES.....</b>   | <b>275</b> |
| <b>LIST OF TABLES.....</b>  | <b>295</b> |
| <b>REFERENCES.....</b>  | <b>299</b> |

## ACKNOWLEDGMENTS – AGRADECIMIENTOS – AGRAÏMENTS

Debo confesar que me fascina leer los agradecimientos de las tesis doctorales, ya que, a diferencia del resto de contenido, es realmente donde se puede conocer al autor. Esos párrafos no van a ser editados o reescritos por nadie y van a reflejar qué ha supuesto realmente este desarrollo de cuatro o más años, qué le ha nutrido, inspirado y quienes fielmente le han acompañado. Así que aquí van los míos.

La família sempre primer. Començo pels que m'han deixat en aquests quatre anys, la meva àvia Nuri i els meus avis Jordi i Josep. Sé que éreu els que més ganes teníeu de que acabés aquesta tesi i tornés a casa, ja que segons vosaltres com a casa enlloc i cada vegada que marxava lluny teníeu por per si no tornava, ja fos Barcelona, Canàries o Punta Arenas. Al final qui no ha tornat a la meva vida heu sigut vosaltres. Agrair també a la meva padrina Pilar que s'ha encarregat personalment de què en els anys de pandèmia estigués ben alimentada, a la meva mare que és una lluitadora i no ha tingut cap problema en seure al meu costat i ajudar-me a resoldre les equacions geostròfiques, al meu pare que no ha dubtat en portar-me en cotxe amunt, avall, a l'aeroport i on fos necessari, i a la meva tata Judit que sempre m'anima a marxar encara més lluny. Gràcies per tot l'amor incondicional que sempre m'heu donat, us estimo.

Después, por orden cronológico y por su capacidad de ser omnipresentes en mi día a día, aunque puedan pasar meses e incluso años sin vernos, agradecer a María y a Markel por haberse cruzado en mi vida. Dos de las personas más brillantes, capaces, inteligentes, zurdas, constantes, vegetarianas y nacidos para la ciencia que he conocido. Gracias por ser referentes y ayudarme, ya sea en la carrera, máster o en la tesis. Sé que llegaréis donde queráis.

Agradecer también a mi familia oceanográfica del ICM: a Nina que fue la primera que me acogió cuando aún no tenía claro si meterme de lleno en esta aventura, y a Dorleta y a Ignasi, por hacerme ver que depositar la tesis, ya seas súper trabajadora o pasota, es posible. A mis, en algún momento, compañeros de despacho B36: Seb, Marta y Julia por no dejar que muera en el intento, hacerme reír, por enseñarme a meterle morro a la vida, escucharme y a criticar a quien monopoliza Gaia constantemente. A Ana y Federica, quienes, entre cafés, cenas, dramas, palabras inventadas y raquetas de nieve, habéis sido mis dos pilares en este doctorado y me habéis dado risas, salseo y las ganas de vivir que tanto necesitaba, siempre os querré, por muy lejos que estéis. A Karen, por hacer las mejores arepas del mundo.

De los del ICM, tampoco me puedo olvidar de mi Marta y Manu. ¡Qué descubrimiento! Sin vosotros no hubieran nacido mis ganas de cantar en la coral ni dar docencia en la UB. Sois

luz, gracias por haber sacado la loca/leona que hay en mí. Y porqué no, también al resto de ICMYR.

A mis Garraputas favoritas, Laura, María y Paula. Que suplicio convivir con vosotras y cuanto me habéis hecho reír y sentir parte de una familia a pesar de llegar la última.

A los que habéis hecho que mis estancias y campañas oceanográficas, lejos de todo, sean más amenas y merezcan la pena. A Nadia, porque sin conocernos, siempre nos hemos apoyado en los momentos difíciles. A Vicky, por pasarnos las noches de campaña despiertas ya fuese contando estrellas fugaces o mil historias. A mis niñas Lea y Camila, quienes han conseguido que quiera ir y sobre todo volver a París, a la vez que montar una campaña clandestina y low-cost a la Antártida. A Laura y Bea por cuidarme en Hobart. A Mikhail y a Joel, por siempre tenerme en cuenta y tener cientos de historias que contar. Gracias.

A mis directores de tesis, Josep Lluís y Francis, por apostar por mí, tener paciencia, corregirme infinitas veces los manuscritos, apoyarme psicológicamente y permitirme adentrarme en el mundo de la oceanografía física. Por intentar innumerables veces que me fuera a la Antártida y por abrirme siempre las puertas de Canarias. A mi tutora Montse, por haberme permitido ser profesora de tropecientos futuros científicos marinos en un entorno tan mágico como el delta de l'Ebre. A Jorge Sarmiento, Alex y Graeme, por sus aportaciones y haber intentado que fuese a Princeton aunque la pandemia tenía otros planes para mí. Finalmente, a mis supervisores de estancias Christine y Steve, por haber compartido vuestro país y cultura conmigo, haciéndome sentir como en casa. *Merci beaucoup and thank you so much.*

No puedo olvidarme de mis Hitos de Ruta: Alicia, Ola, Dan, Merche y Edu. Con vosotros subiría las montañas más altas y me pasaría los días haciendo jabones sin pensarlo. Habéis sido mis planes de puente, fin de semana e incluso cumpleaños. Me habéis hecho ver que no todo en la tesis es investigar.

Y por último agradecer a quien sin quererlo ha sido parte de todo lo anterior. Quien ha tirado de mí para que saliese adelante, quien ha conseguido que corriese una media maratón, que mi pasión fuera organizar limpiezas de playa en Barcelona, que me plantease escalar y hacer vías ferratas, y me ha acompañado a explorar otros países. Con quien desgraciadamente nos ha tocado sufrir en nuestros seres queridos la peor enfermedad de estos días. Quien siempre ha estado al otro lado de la pantalla y no ha tenido ningún problema en programar conmigo hasta altas horas de la madrugada. *Gràcies Carlos.*

# SUMMARY – RESUMEN – RESUM

## Summary

The returning limb of Atlantic Meridional Overturning Circulation (AMOC), a key component of the regional and global Earth's climate system, is mainly supplied by the northward transport of lighter upper-ocean waters from the South Atlantic Ocean back into high latitudes. Part of the primary sources of this South Atlantic upper limb is formed by the cold-fresh waters that enter from the Pacific Ocean through the Drake Passage. Its existence permits the inflow of the Antarctic Circumpolar Current (ACC) waters cross the western South Atlantic Ocean up to the subtropical gyre eluding a series of topographic and dynamic obstacles. This PhD dissertation focuses precisely on understanding how this incorporation takes place in terms of circulation, variability, and water mass transformations in one of the most remote, isolated, and least studied regions of our planet.

In **Chapter 3.1** we focus on the initial stage of this cold returning limb: the Scotia Sea. In this relatively small basin, the ACC fronts are constrained latitudinally and its waters are forced to outcrop and flow northward through the relatively narrow and shallow passages of the North Scotia Ridge, hence controlling the ACC interocean exchange. The geostrophic transports and temporal variability, calculated using the Argo profiles and positions, and analyzed from the point of view of fronts and water masses, have revealed that the transports are substantially greater than previously calculated. Up to the isoneutral  $28.00 \text{ kg m}^{-3}$ , the mean water inflow through the Drake Passage is  $140.8 \pm 7.4 \text{ Sv}$  and the outflow through the Northern Passages is  $115.9 \pm 8.3 \text{ Sv}$ . Below this isoneutral reference and down to 2000 m, an additional  $23.4 \text{ Sv}$  enters through the Drake Passage. The mean barotropic contribution always represents over half the total transports, with substantial seasonal and moderate interannual variability in the size and composition of the water transports, associated with changes in water exchange across the frontal systems. The water mean-residence time in the Scotia Sea is estimated to be about 6 - 8 months.

Combining the Argo floats data with other observational measurements from oceanographic cruises and marine mammals, we apply a climatological high-resolution inverse model over the Scotia Sea boundaries to define the ACC inflow and outflow, balancing mass, heat, salt and biogeochemical properties in the upper-ocean layers up to the  $28.00 \text{ kg m}^{-3}$  isoneutral (**Chapter 3.2**). We find that the main circulation pattern consists of inputs from the western and southern passages – the Drake, Philip and South Scotia Ridge passages – while the outputs are through the north – across the North Scotia Ridge and Georgia Passages.



Hence, the ACC enters  $136.7 \pm 1.0$  Sv through the Drake Passage and exits  $137.9 \pm 1.0$  Sv through the northern boundary, with the difference responding to the South Scotia Ridge and Philip Passages contributions, resulting in a net volume imbalance of only 0.03 Sv. The distribution of the integrated transports responds largely to the reference velocities, suggesting a high barotropic component. Along its northward path, the ACC waters lose heat but gain freshwater transport. Within the Scotia Sea, the surface-mode and surface-intermediate waters (SASW/SAMW and AASW/AAIW) experience production in all biogeochemical variables, as expected from the remineralization of relatively young waters. Finally, regarding anthropogenic DIC, the Scotia Sea stores carbon in the surface-mode and surface-intermediate waters and utilizes carbon further deep, resulting in a net reservoir of the order of  $0.123 \text{ Pg C yr}^{-1}$ , which remarks the importance of this basin in the global carbon cycle.

In **Chapter 3.3**, we present the radial offset by diffusion method (ROD), a new simple and robust methodological approach aimed at estimating the effective eddy horizontal diffusivities. The method is a simple model-dependent approach which compares actual drifters (Argo, GDP and RAFOS) displacements with numerical trajectory predictions. The observed-predicted differences in final positions, isotropic radial offsets, respond to diffusive motions not captured by the numerical models and are reproduced with a one-dimensional radial-diffusive solution to select the best diffusion coefficient properly. The ROD method is applied in the western South Atlantic Ocean leading to maximum diffusivities of  $4630 - 4980 \text{ m}^2 \text{ s}^{-1}$  in the upper 200 m of the water column, and minimum values of  $1080 - 1270 \text{ m}^2 \text{ s}^{-1}$  below the 1400 m, presenting an inverse relationship with depth. The diffusivities near the surface are fairly constant in latitude but the diffusion coefficients at 1000 m decrease considerably south of the Southern Boundary.

With the horizontal diffusion coefficients obtained in the previous chapter, we use the Lagrangian technique to determine the fraction of the upper-ocean transport that remains in the ACC flow as it crosses the South Atlantic Ocean and the fraction that contributes to the South Atlantic subtropical gyre (**Chapter 3.4**). The mean results reveal that 94.8 Sv remain in the ACC after crossing the South Atlantic Ocean, whereas a total of 15.1 Sv contributes directly to the AMOC as part of the cold-water route with slight seasonal variability. This AMOC transport takes a median of 14.3 years to arrive to the Brazilian Current from the Drake Passage. Furthermore, 78.1% of the particles that recirculate in the subtropical gyre perform one recirculation, 18.5% travel two complete gyres and the remaining 3.4% revolve three times. The results confirm that the water masses entering the subtropical gyre through its eastern edge warm up substantially during their eastward flow. Most upper-ocean waters that are incorporated into the subtropical gyre lose density, partly transformed to surface waters, while

those water masses that remain in the ACC are largely transferred to both the surface and deep layers.

In the final **Chapter 3.5**, we compare the contributions at the eastern edge of the South Atlantic subtropical gyre of the warm-water route, via the Agulhas Current, and the cold-water route, proceeding from the Drake Passage. For this purpose, we perform numerical simulations of Lagrangian trajectories to identify the multiple direct and indirect pathways of intermediate waters. The total cold-route contribution of intermediate waters to the reference section represents between 17.9 and 18.9%, substantially higher than the 7.1 to 12.3% warm-route contribution. These percentages confirm that the cold-water route has a greater transport contribution than previously stated, being essential for the upper limb of the returning branch of the AMOC. Several individual pathways form both routes, but the direct path to the eastern part of the subtropical gyre is the preferential pathway followed by 83.6 to 87.2% of the water parcels in austral winter. In terms of transformations of water masses, as the intermediate waters cross some key regions (Brazilian Current, south Madagascar and Cape Basin), they warm and become more saline, also experiencing large changes in depth, either rising or subducting. The direct cold route is the one that undergoes a greater transformation of its water masses, followed by the indirect warm pathway that recirculates along the western edge of the South Atlantic subtropical gyre. Finally, it is confirmed that the cold route also directly feeds the Agulhas Current, contributing to a similar transport to that coming from the Indonesian Throughflow.

## **Resumen**

La rama de retorno de la circulación meridional del Atlántico (AMOC), componente clave del sistema climático de la Tierra tanto a nivel regional como global, es principalmente sustentada por el transporte hacia el norte de aguas oceánicas ligeras procedentes del océano Atlántico Sur en su regreso a latitudes polares. Dicha rama superior del Atlántico Sur está formada, en parte, por las aguas frías y frescas que proceden del océano Pacífico a través del pasaje de Drake. Su existencia permite la entrada de las aguas de la Corriente Circumpolar Antártica (ACC) a través del Atlántico Sur occidental y llegar hasta el giro subtropical sorteando una serie de obstáculos topográficos y dinámicos. Esta tesis doctoral se centra precisamente en comprender cómo se produce esta incorporación en términos de circulación, variabilidad y transformaciones de masa de agua en una de las regiones más remotas, aisladas y menos estudiadas de nuestro planeta.

En el **Capítulo 3.1** nos centramos en la etapa inicial de esta rama fría de retorno: el mar de Scotia. En esta cuenca relativamente pequeña, los frentes de la ACC están restringidos latitudinalmente y sus aguas están obligadas a emerger y fluir hacia el norte a través de los pasajes relativamente estrechos y someros de la cresta submarina del Norte de Scotia; por lo que controla el intercambio interoceánico de la ACC. Los transportes geostróficos y la variabilidad temporal, calculados mediante las posiciones y perfiles Argo y analizados desde el punto de vista de los frentes y masas de agua, han revelado que los transportes son sustancialmente mayores a los previamente estimados. Hasta la isoneutra de  $28.00 \text{ kg m}^{-3}$ , la entrada media de agua a través del paso de Drake es de  $140.8 \pm 7.4 \text{ Sv}$  mientras que la salida a través de los pasos del Norte corresponde a  $115.9 \pm 8.3 \text{ Sv}$ . Por debajo de esta referencia y hasta los 2000 m, entran  $23.4 \text{ Sv}$  adicionales a través del paso de Drake. Su componente barotrópica media siempre representa más de la mitad de los transportes totales, con una variabilidad interanual moderada y estacional considerable en el tamaño y la composición de los transportes de agua asociada con el intercambio de agua a través de los sistemas frontales. El tiempo medio estimado de residencia de las aguas antárticas en el mar de Scotia es de unos 6 - 8 meses.

Combinando los datos de boyas Argo con otras mediciones observacionales procedentes de campañas oceanográficas y mamíferos marinos, aplicamos un modelo inverso climatológico de alta resolución en los límites del mar de Scotia con el fin de definir el flujo de entrada y salida de la ACC, balanceando masa, calor, sal y las propiedades biogeoquímicas en las capas superiores del océano hasta la isoneutra de  $28.00 \text{ kg m}^{-3}$  (**Capítulo 3.2**). Encontramos que el patrón principal de circulación oceánica consiste en agua que entra de los pasajes localizados al oeste y sur – pasos de Drake, Philip y los de la cordillera de Scotia del Sur – mientras que las salidas son a través del norte – pasos de Georgia y de la cordillera de Scotia del Norte. Así pues,  $136.7 \pm 1.0 \text{ Sv}$  de la ACC entran por el paso de Drake y salen  $137.9 \pm 1.0 \text{ Sv}$  por el límite norte, con la diferencia perteneciente a las contribuciones de la dorsal de Scotia del Sur y el paso de Philip, lo que da lugar a un desequilibrio neto de volumen de solamente  $0.03 \text{ Sv}$ . La distribución de los transportes integrados responde en gran medida a las velocidades de referencia, lo que sugiere una elevada componente barotrópica. A lo largo de su trayectoria hacia el norte, las aguas de la ACC pierden calor pero ganan transporte de agua dulce. Dentro del mar de Scotia, las aguas superficiales-modales y superficiales-intermedias (SASW/SAMW y AASW/AAIW) experimentan producción en todas las variables biogeoquímicas, como se espera de la remineralización de aguas relativamente jóvenes. Finalmente, en cuanto al DIC antropogénico, el mar de Scotia almacena carbono en aguas superficiales-modales y superficiales-intermedias y utiliza carbono en profundidad, lo que da

lugar a un reservorio neto de  $0.123 \text{ Pg C año}^{-1}$ , lo que remarca la importancia de esta cuenca en el ciclo global del carbono.

En el **Capítulo 3.3**, presentamos el método de la distancia radial por difusión (ROD), un nuevo enfoque metodológico simple y robusto, con el objetivo de estimar la difusión horizontal efectiva. El método es un enfoque simple dependiente del modelo usado, que compara los desplazamientos reales de los derivadores (Argo, GDP y RAFOS) con las trayectorias de las partículas simuladas en modelos numéricos. Las diferencias observadas-predichas en las posiciones finales, distancias radiales isotrópicas, responden a movimientos difusivos no capturados por los modelos numéricos y las reproducimos con una solución radial-difusiva unidimensional para compararlas y seleccionar adecuadamente el mejor coeficiente de difusión. El método ROD es aplicado en el Atlántico Sur occidental obteniendo difusiones máximas de  $4630 - 4980 \text{ m}^2 \text{ s}^{-1}$  en los primeros 200 m de la columna de agua, y coeficientes mínimos de  $1080 - 1270 \text{ m}^2 \text{ s}^{-1}$  por debajo de los 1400 m, presentando así, una relación inversa con la profundidad. Cerca de la superficie, los coeficientes de difusión son bastante constantes en latitud, sin embargo a 1000 m los coeficientes disminuyen considerablemente al sur del frente Límite Sur.

Con los coeficientes de difusión horizontal obtenidos en el capítulo anterior, realizamos simulaciones Lagrangianas para determinar qué fracción del transporte de las aguas superiores del océano permanece en la ACC cuando cruza el océano Atlántico Sur y qué cantidad de transporte se desvía al norte para alimentar el giro subtropical del Atlántico Sur (**Capítulo 3.4**). Los resultados medios revelan que  $94.8 \text{ Sv}$  permanecen en la ACC, mientras que un total de  $15.1 \text{ Sv}$  contribuyen directamente a la AMOC como parte de la ruta de agua fría mostrando una ligera variabilidad estacional. Este transporte que se incorpora a la AMOC tarda una mediana de 14.3 años en llegar a la corriente de Brasil desde el paso de Drake. Además, el 78.1% de las partículas que recirculan en giro subtropical del Atlántico Sur realizan una vuelta, el 18.5% realiza dos vueltas completas y el 3.4% restante gira tres veces. Los resultados confirman que las masas de agua que entran al giro subtropical a través del borde oriental se calientan sustancialmente durante su flujo hacia el este. La mayoría de aguas oceánicas superiores que se incorporan al giro subtropical pierden densidad, parcialmente transformadas en aguas superficiales, mientras que las masas de agua que permanecen en la ACC se transfieren en gran medida hacia capas superficiales y profundas.

En el último **Capítulo 3.5**, comparamos las contribuciones de la ruta cálida, via la corriente de Agulhas, y la ruta fría, procedente del paso de Drake, en el margen oriental del giro subtropical del Atlántico Sur. Con ese fin, realizamos simulaciones numéricas para identificar las múltiples vías directas e indirectas de las aguas intermedias. La contribución total de las aguas intermedias a la sección de referencia por parte de la ruta fría representa

entre un 17.9 y 18.9 %, siendo sustancialmente mayor que el 7.1 y 12.3 % de la contribución de la ruta cálida. Estos porcentajes confirmarían que la ruta de agua fría contribuye con un mayor transporte del que se ha afirmado hasta ahora, siendo esencial en la rama de retorno superior de la AMOC. Ambas rutas están formadas por múltiples vías individuales pero la vía directa hacia la parte oriental del giro subtropical es la vía preferente seguida por el 83.6 – 87.2% de las parcelas de agua en el invierno austral. En cuanto a las transformaciones de masas de agua, a medida que las aguas intermedias atraviesan algunas regiones clave (corriente de Brasil, el sur de Madagascar y la cuenca del Cabo), se calientan y se vuelven más salinas, experimentando también grandes cambios de profundidad, aflorando o subduciendo. La ruta fría directa es la que sufre una mayor transformación de sus aguas, seguida por la ruta cálida indirecta que recircula a lo largo del borde occidental del giro subtropical del Atlántico Sur. Finalmente, se confirma que la ruta fría también alimenta directamente la corriente de Agulhas, contribuyendo con un transporte similar al procedente del trasvase Indonésico.

## Resum

La branca de retorn de la circulació meridional de l'Atlàntic (AMOC), component clau del sistema climàtic de la Terra tant a nivell regional com global, és principalment sustentada pel transport cap al nord d'aigües oceàniques lleugeres procedents de l'oceà Atlàntic Sud en el seu retorn a latituds polars. Aquesta branca superior de l'Atlàntic Sud està formada, en part, per les aigües fredes i fresques que procedeixen de l'oceà Pacífic a través del passatge de Drake. La seva existència permet l'entrada de les aigües del corrent Circumpolar Antàrtic (ACC) a través de l'Atlàntic Sud occidental fins al gir subtropical superant una sèrie d'obstacles topogràfics i dinàmics. Aquesta tesi doctoral se centra precisament en comprendre com es produeix aquesta incorporació en termes de circulació, variabilitat i transformacions de massa d'aigua en una de les regions més remotes, aïllades i menys estudiades del nostre planeta.

En el **Capítol 3.1**, ens centrem en l'etapa inicial d'aquesta branca freda de retorn: el mar de Scotia. En aquesta conca relativament petita, els fronts del ACC estan restringits latitudinalment i les seves aigües obligades a emergir i fluir cap al nord a través dels passatges relativament estrets i poc profunds de la cresta submarina del Nord de Scotia; pel que controla l'intercanvi interoceànic del ACC. Els transports geostrofics i la variabilitat temporal, calculats mitjançant les posicions i perfils Argo i analitzats des del punt de vista dels fronts i masses d'aigua, han revelat que els transports són substancialment majors als prèviament estimats. Fins a la isoneutra de  $28.00 \text{ kg m}^{-3}$ , l'entrada d'aigua mitja a través del pas de Drake és de  $140.8 \pm 7.4 \text{ Sv}$  mentre que la sortida a través dels passos del Nord correspon a  $115.9 \pm 8.3 \text{ Sv}$ . Per sota d'aquesta referència i fins als 2000 m, entren  $23.4 \text{ Sv}$  addicionals a través de la zona del Drake.

La seva component barotròpica mitjana sempre representa més de la meitat dels transports totals, amb una variació interanual moderada i estacional considerable en la grandària i composició dels transports d'aigua associada amb l'intercanvi d'aigua a través dels sistemes frontals. El temps mig estimat de residència de les aigües antàrtiques en el mar de Scotia és d'uns 6 - 8 mesos.

Combinant les dades de boies Argo amb altres mesures observacionals procedents de campanyes oceanogràfiques i mamífers marins, apliquem un model invers climatològic d'alta resolució en els límits de el mar de Scotia amb la finalitat de definir el flux d'entrada i sortida del ACC, balancejant massa, calor, sal i les propietats biogeoquímiques en les capes superiors de l'oceà fins a la isoneutra de  $28.00 \text{ kg m}^{-3}$  (**Capítol 3.2**). Trobem que el patró principal de circulació oceànica consisteix en aigua que entra dels passatges localitzats a l'oest i sud – passos de Drake, Philip i els de la serralada de Scotia del Sud– mentre que les sortides són a través del nord – passos de Geòrgia i de la serralada de Scotia del Nord. Així doncs,  $136.7 \pm 1.0 \text{ Sv}$  del ACC entren pel pas de Drake i surten  $137.9 \pm 1.0 \text{ Sv}$  pel límit nord, amb la diferència pertanyent a les contribucions de la dorsal de Scotia del Sud i el pas de Philip, la qual cosa dona lloc a un desequilibri net de volum de només  $0.03 \text{ Sv}$ . La distribució dels transports integrats respon en gran manera a les velocitats de referència, la qual cosa suggereix una elevada component barotròpica. Al llarg de la seva trajectòria cap al nord, les aigües del ACC perden calor però guanyen transport d'aigua dolça. Dins del mar de Scotia, les aigües superficials-modals i les superficials-intermèdies (SASW/SAMW i AASW/AAIW) experimenten producció en totes les variables biogeoquímiques, com s'espera de la remineralització d'aigües relativament joves. Finalment, en quant al DIC antropogènic, el mar de Scotia emagatzema carboni en aigües superficials-modals i superficials-intermèdies, i utilitza carboni en profunditat, donant lloc a un reservori net de  $0.123 \text{ Pg C any}^{-1}$ , la qual cosa remarca la importància d'aquesta conca en el cicle global del carboni.

En el **Capítol 3.3**, presentem el mètode de distància radial per difusió (ROD), un nou enfocament metodològic simple i robust amb l'objectiu d'estimar la difusió horitzontal efectiva. El mètode és un enfocament simple, dependent del model usat, que compara els desplaçaments reals dels derivadors (Argo, GDP i RAFOS) amb les trajectòries de les partícules simulades en models numèrics. Les diferències observades-predites en les posicions finals, distàncies radials isotròpiques, responen a moviments difusius no capturats pels models numèrics i les reproduïm amb una solució radial-difusiva unidimensional per a comparar-les i seleccionar adequadament el millor coeficient de difusió. El mètode ROD és aplicat a l'Atlàntic Sud occidental obtenint difusions màximes de  $4630 - 4980 \text{ m}^2 \text{ s}^{-1}$  en els primers 200 m de la columna d'aigua, i coeficients mínims de  $1080 - 1270 \text{ m}^2 \text{ s}^{-1}$  per sota dels 1400 m, presentant així, una relació inversa amb la profunditat. Prop de la superfície, els coeficients de

difusió són bastant constants en latitud, no obstant això a 1000 m els coeficients disminueixen considerablement al sud del front Límit Sud.

Amb els coeficients de difusió horitzontal obtinguts en el capítol anterior, realitzem simulacions Lagrangianes per a determinar quina fracció de transport roman en el ACC quan creua l'oceà Atlàntic Sud i quina quantitat de transport es desvia al nord per a alimentar el gir subtropical de l'Atlàntic Sud (**Capítol 3.4**). Els resultats mitjans revelen que 94.8 Sv romanen en el ACC, mentre que un total de 15.1 Sv contribueixen directament a la AMOC com a part de la ruta d'aigües fredes mostrant una lleugera variabilitat estacional. Aquest transport que s'incorpora a la AMOC triga una mediana de 14.3 anys en arribar al corrent del Brasil des del pas de Drake. A més, el 78.1% de les partícules que recirculen en el gir subtropical de l'Atlàntic Sud realitzen una volta, el 18.5% realitza dues voltes completes i el 3,4% restant gira tres vegades. Els resultats confirmen que les masses d'aigua que entren al gir subtropical per la vora oriental s'escalfen substancialment durant el seu flux cap a l'est. La majoria de les aigües de l'oceà superior que s'incorporen al gir subtropical perden densitat, parcialment transformades en aigües superficials, mentre que les masses d'aigua que romanen al ACC es transfereixen en gran mesura a les capes superficials i profundes.

En l'últim **Capítol 3.5**, comparem les contribucions de la ruta càlida, via el corrent de Agulhas, i la ruta freda, procedent del pas de Drake, en el marge oriental del gir subtropical de l'Atlàntic Sud. Amb aquesta fi, realitzem simulacions numèriques per a identificar les múltiples vies directes i indirectes de les aigües intermèdies. La contribució total de les aigües intermèdies a la secció de referència per part de la ruta freda representa entre un 17.9 i 18.9%, sent substancialment major que el 7.1 i 12.3% de la contribució per part de la ruta càlida. Totes dues rutes estan formades per múltiples vies individuals però la via directa cap a la part oriental del gir subtropical és la via preferent seguida pel 83.6 – 87.2% de les parcel·les d'aigua a l'hivern austral. En quant a transformacions de masses d'aigua, a mesura que les aigües intermèdies creuen algunes regions clau (corrent del Brasil, el sud de Madagascar i la conca del Cap), és quan s'escalfen i es tornen més salines, experimentant també grans canvis de profunditat, aflorant o subduint. La ruta freda directa és la que sofreix una major transformació de les seves aigües, seguida per la ruta càlida indirecta que recircula al llarg de la vora occidental del gir subtropical de l'Atlàntic Sud. Finalment, es confirma que la ruta freda també alimenta directament el corrent de Agulhas, contribuint amb un transport similar al procedent del transvasament Indonèsic.

## ACRONYMS LIST

**AABW** Antarctic Bottom Water

**AAIW** Antarctic Intermediate Water

**AASW** Antarctic Surface Water

**AC** Agulhas Current

**ACC** Antarctic Circumpolar Current

**AMOC** Atlantic Meridional Overturning  
Circulation

**ANDRO** Argo New Displacements  
Rannou and Ollitrault

**AP** Antarctic Peninsula

**BC** Brazil Current

**BGC-IM** Biogeochemical Inverse Model

**B-SOSE** Biogeochemical Southern Ocean  
State Estimate

**CMEMS** Copernicus Marine  
Environment Monitoring Service

**CTD** Conductivity-Temperature-  
Depth

**DIC** Dissolved Inorganic Carbon

**DIVA** Data-Interpolating Variational  
Analysis

**DO** Dissolved Oxygen

**DP** Drake Passage

**DWBC** Deep Western Boundary Current

**ECMWF** European Centre for Medium-  
Range Weather Forecasts

**ERA5** ECMWF Reanalysis v5

**ESA** European Space Agency

**GDP** Global Drifter Program

**GLODAPv2** Global Ocean Data  
Analysis Project Version 2

**GOC** Global Overturning Circulation

**GP** Georgia Passage

**IM** Inverse Model

**ITF** Indonesian Throughflow

**LCDW** Lower Circumpolar Deep Water

**MC** Malvinas Current

**MEOP** Marine Mammals Exploring the  
Oceans Pole to Pole

**MOC** Meridional Overturning  
Circulation

**NADW** North Atlantic Deep Water

**NBC** North Brazil Current

**NCEI** National Centers for  
Environmental Information

**NOAA** National Oceanic and  
Atmospheric Administration

**NEMO** Nucleus for European Modelling  
of the Ocean

**NOCS** National Oceanography Centre  
Southampton

**NSR** North Scotia Ridge

**OGCMs** Ocean General Circulation  
Models

**PF** Polar Front

**PW** PetaWatt ( $10^{15}$  W)

**RAFOS** SOFAR spelled backwards

**ROD** Radial Offset by Diffusion



---

|  |   |
|--|---|
| <b>SA</b> South America  | <b>SOCCOM</b> Southern Ocean Carbon and Climate Observations and Modeling |
| <b>SAC</b> South Atlantic Current                              | <b>SODB</b> Southern Ocean Data Base                                      |
| <b>SACCF</b> Southern Antarctic Circumpolar Current Front      | <b>SOFAR</b> Sound Fixing And Ranging                                     |
| <b>SADCP</b> Shipboard Acoustic Doppler Current Profiler       | <b>SOSE</b> Southern Ocean State Estimate                                 |
| <b>SAF</b> Subantarctic Front                                  | <b>SRP</b> Shag Rocks Passage   |
| <b>SAMW</b> Subantarctic Mode Water                            | <b>SSH</b> Sea Surface Height   |
| <b>SASW</b> Subantarctic Surface Water                         | <b>STF</b> Subtropical Front  |
| <b>SB</b> Southern Boundary                                    | <b>Sv</b> Sverdrup ( $10^6 \text{ m}^3 \text{ s}^{-1}$ )                  |
| <b>SD</b> Standard deviation                                   | <b>UCDW</b> Upper Circumpolar Deep Water                                  |
| <b>SEaOS</b> Southern Elephant seals as Oceanographic Samplers | <b>USGODAE</b> U.S. Global Ocean Data Assimilation Experiment             |
| <b>SMRU</b> Sea Mammal Research Unit                           | <b>WOA</b> World Ocean Database   |
| <b>SOCAT</b> Surface Ocean CO <sub>2</sub> Atlas Database      | <b>WOCE</b> World Ocean Circulation Experiment                            |
|  | <b>WSDW</b> Weddell Sea Deep Water  |

# I. INTRODUCTION

## 1.1. The Global and Meridional Overturning Circulation

The Global Overturning Circulation (GOC) is formed by a complex three-dimensional large-scale circulation with upwelling and downwelling branches, ocean-atmosphere exchanges, interbasin connections, and tracer redistribution between the Pacific, Indian, and Atlantic Oceans (Figure 1.1). The earliest circulation schematics and theories appeared at the end of the last century through the work of Henry Stommel and Wallace Broecker, establishing the bases of our modern conceptualization of the ocean's large-scale overturning and emphasizing its climatic importance (Stommel, 1958; Broecker, 1987). While Stommel's work pointed out the overturning spatial structure revealing that the equatorward transport of deep water masses was confined to the basin's western boundaries, Broecker's provided a temporal context highlighting the role of the GOC as a critical climate agent on the abrupt global warming (Lozier, 2010). After decades, the mechanisms responsible for driving the ocean circulation are mainly summarized in the near-surface wind-driven and the deep-ocean thermohaline components, among other mesoscale and small-scale motions needed to sustain the GOC.

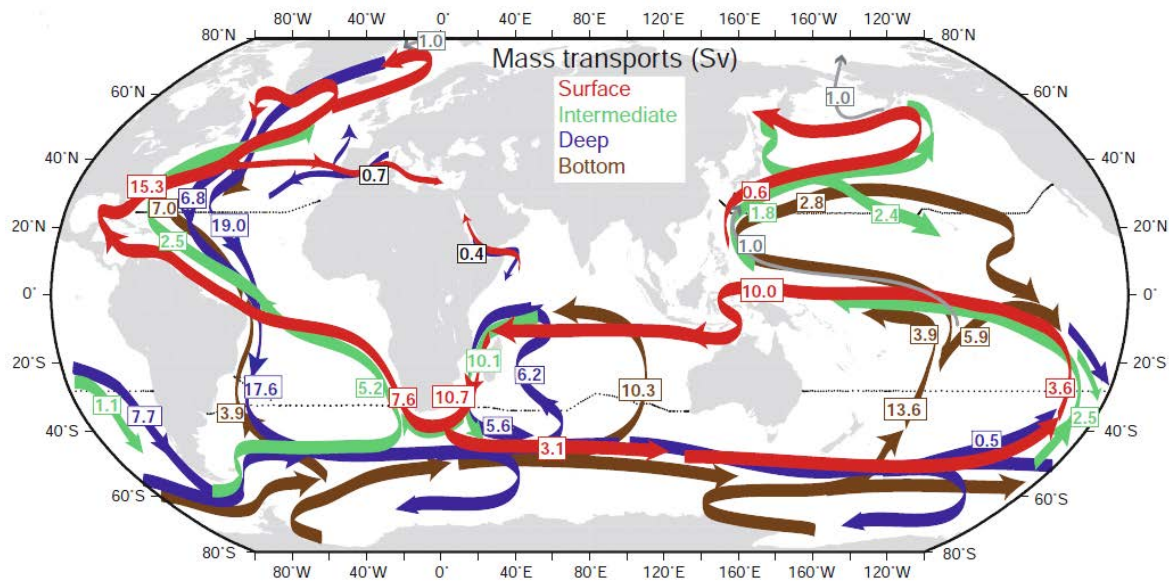


**Figure 1.1.** Simplified scheme of the Global Overturning Circulation and net transports (Sv) in different water strata across the selected hydrographic sections. Ribbons indicate flow direction and overturn locations schematically. Source: Talley (2008).

The GOC can be grossly divided into two major global connected cells: the North Atlantic Deep Water (NADW) cell, with deep-water formation around the North Atlantic, previously referred to as the Global Ocean Conveyor (Gordon, 1986; Broecker, 1987), and the Antarctic Bottom Water (AABW) cell featured by the dense water formed around Antarctica

(Gordon, [1991](#); Schmitz, [1995](#)). A third weak overturning cell is also found in the North Pacific, forming a small amount of intermediate water (NPIW) that remains largely unconnected to the previous two cells (Talley, [2011](#)). In general terms, the NADW cell consists of the returning upwelled waters into the northern North Atlantic from the Indian, via the Agulhas Current, and from the Pacific Oceans, through the Drake Passage. Regarding the AABW cell, it begins when recently formed and dense Antarctic waters escape northward across the topography into the main three ocean basins, upwelling in each of them as NADW, Indian Deep Water (IDW) or Pacific Deep Water (PDW), constituting an essential step in the GOC (Gordon, [1986](#), [1991](#); Schmitz, [1995](#); Lumpkin & Speer, [2007](#); Talley, [2008](#)).

The dense and cold waters transfer and redistribute heat and salt within and between the ocean basins. Salinity controls the overturning circulation through the freshwater transports, conditioning the strength of the ocean circulation and the locations of dense water formation through brine rejection during sea ice formation. While the surface waters of the Atlantic and Indian Oceans are highly saline, the Southern Ocean and Arctic are fresher than the intermediate layers (Talley, [2008](#)). The magnitude of the salinity differences between oceans depends on the mass transports, and at the same time, the transports depend on the salinity differences, leading to a complex system with numerous feedbacks (Stommel, [1961](#); Talley, [2008](#)). The freshwater transport in the ocean flows from regions of net precipitation and runoff (fresher) to regions of net evaporation (saltier): from the Pacific to the Atlantic, through the Bering Strait and the Drake Passage, and also to the Indian Ocean through the Indonesian Throughflow (Piola & Gordon, [1984](#); Aagaard & Carmack, [1989](#); Rintoul, [1991](#)). This also occurs with the freshwater transport from the Arctic Ocean to the Atlantic Ocean, and from the Southern Ocean to the Pacific, Atlantic and Indian Oceans.

Regarding heat, the ocean stores large amounts of the heat energy received from the Sun due to the very high density and heat capacity of water, having incorporated approximately 90% of the anthropogenic heat associated with global warming. This heat is carried by ocean currents, exported or imported to different basins. Specifically, the Pacific and Indian Oceans move heat poleward. The Atlantic Ocean is an exception, transporting heat always northward because of the deep-water formation at high latitudes of the North Atlantic Ocean. Thus, while the physical return of the deep waters to the sea surface is largely controlled by the Southern Ocean westerly winds, the properties and especially the heat content of the upwelled waters strongly depend on both diffusion at low latitudes and the pathway of abyssal and deep waters through the Indian and Pacific Oceans (Talley, [2011](#)).

In contrast to the GOC, the Meridional Overturning Circulation (MOC) includes only the latitudinal overturning circulation, where mass transport is zonally integrated, producing a redistribution of heat and freshwater and controlling the cycle and storage of biogeochemical

species such as carbon dioxide throughout the oceans (Jeffreys, [1925](#); Kuhlbrodt et al., [2007](#)). Heat is transported meridionally from the tropics, a domain with maximum heat input, to higher latitudes. In particular, the shallow tropical cells carry heat from the tropics to the subtropics, and then the subtropical gyres carry the heat toward the enhanced heat-loss regions of their western boundary currents. Heat also controls ocean stratification, setting the natural propagating subsurface pathways for the different water masses (Talley, [2003](#)).

### 1.1.1. The Atlantic Meridional Overturning Circulation

The Earth's climate is largely conditioned by the strength of the Atlantic Meridional Overturning Circulation (AMOC), the Atlantic branch of the global MOC. It extends from the Southern Ocean to the northern North Atlantic, involving the interaction between surface currents, deep currents, eddy-driven circulation, and even large water mass transformation (Figure [1.2](#); Buckley & Marshall, [2016](#)). The AMOC is responsible for the Northern Hemisphere being slightly warmer than the Southern Hemisphere, carrying northward 0.5 PW of heat flux across the equator. During the last decades, its interannual variability has been directly related to abrupt climate alterations in Europe and North America, African rainfall, Atlantic hurricane activity, Arctic sea-ice coverage, and even atmospheric carbon sequestration (Buckley & Marshall, [2016](#); Trenberth & Caron, [2001](#); Lozier et al., [2017](#)). Many evidences confirm that the subpolar gyre of the North Atlantic has slowed notably during the last decade, which, together with 20% less of deep waters overflowing from Greenland, has contributed to the reduction of more than 30% in the strength of the MOC (Häkkinen & Rhines, [2004](#); Bryden et al., [2005](#)), revealing the fragility of the climate system.

The main AMOC circulation consists of two overturning cells: the upper ventilates about the first 2000 m of the ocean and the lower contributes to maintaining cold the abyssal ocean (Carter et al., [2008](#)). Both cells are defined by the formation of deep water masses. The cold NADW formed in the North Atlantic Ocean constitutes the upper cell which flows southward and is exported from convective regions through the Deep Western Boundary Current (DWBC). Meanwhile, the deep cell is dominated by the densest AABW formed around the Antarctic continental shelf, which flows northward following the topography (Talley, [2013](#)). The formation and sinking of NADW and AABW are promoted during the winter of each hemisphere in the high latitudes, NADW due to buoyancy and heat loss to the atmosphere and AABW formed by brine rejection, together with intense mixing and vertical convection processes. The total production rate of AABW is roughly twice that of NADW, confirming the major role of the Southern Ocean in the deep overturning circulation (Gordon, [1975](#)).

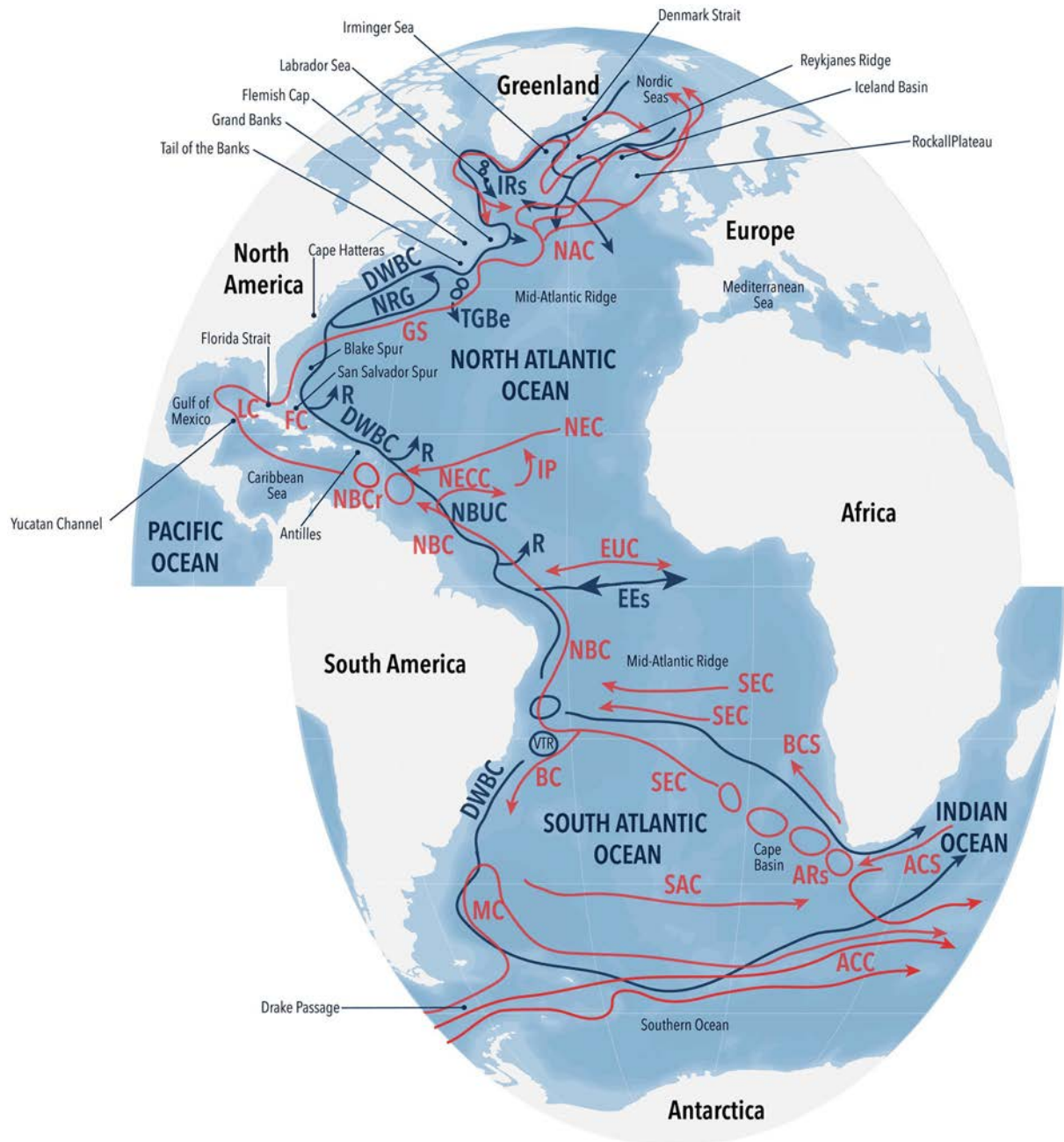


**Figure 1.2.** Overview of the upper (red) and lower (blue) limbs of the Atlantic Meridional Overturning Circulation in the South Atlantic Ocean. Bathymetry is shaded at 1000 m intervals. In alphabetical order: ACC, Antarctic Circumpolar Current; ACS, Agulhas Current System; ARs, Agulhas Rings; BC, Brazil Current; BCS, Benguela Current System; DWBC, Deep Western Boundary Current; EEs, Equatorial Excursions; EUC, Equatorial Undercurrent; FC, Florida Current; GS, Gulf Stream; IP, Interior Pathways; IRs, Irminger Rings; LC, Loop Current; MAR, mid-Atlantic Ridge; MC, Malvinas Current; NAC, North Atlantic Current; NBC, North Brazil Current; NBCr, North Brazil Current Rings; NBUC, North Brazil Undercurrent; NEC, North Equatorial Current; NECC, North Equatorial Counter Current; NRG, Northern Recirculation Gyre; R, Recirculation; SAC, South Atlantic Current; SEC, South Equatorial Current, TGBe, Tail of the Grand Bank Eddies. Source: Bower et al. (2019).

The AMOC circulation, which takes hundreds of years, transfers large amounts of heat and carbon dioxide into the deep ocean and returns inorganic nutrients and carbon-rich deep waters to the ocean surface sustaining high rates of primary production. The upwelling of these dense deep waters along isopycnals in the Southern Ocean is essential to maintain the AMOC (Wunsch, [2002](#); Wunsch & Ferrari, [2004](#)), which results from the combination of turbulent mixing in the deep ocean and northward wind-driven upwelling. The first mechanism is driven by the energy cascading from mesoscale to submesoscale internal waves and small-scale motions that diffuse heat and lighten the dense waters (Munk & Wunsch, [1998](#); Nikurashin & Vallis, [2011](#); Orúe-Echevarría, [2019](#)). The second mechanism is driven by the strong westerly winds blowing around the Southern Ocean that induce equatorward water transport, also resulting in a poleward upwelling supplied by southward geostrophic flow at depth (Kuhlbrodt et al., [2007](#)). In summary, whereas the deep-water return to the Antarctic continent is relatively simple, the return to the high latitudes of the North Atlantic Ocean in order to sustain the AMOC is much more complex. Eventually, part of the Southern waters is incorporated into the subtropical gyre of the South Atlantic Ocean, crossing large series of topographic and dynamic obstacles. Hence, the AMOC and the global ocean circulation are connected and sustained through the Southern Ocean.

### 1.1.2. The Southern Ocean circulation

The Southern Ocean encircles and partly isolates the Antarctic continent from the warmer subtropical waters, storing and transporting key physical and biogeochemical properties to the different ocean basins, with a profound influence on climate. The Southern Ocean is estimated to be responsible for about 75% of the anthropogenic heat uptake since the preindustrial period and also responsible for over 40% of the intake of anthropogenic carbon dioxide by the global ocean (1 Pg C year<sup>-1</sup>), becoming a major efficient global-warming regulator (Frölicher et al., [2015](#); Khatiwala et al., [2013](#)). Furthermore, the extension of the Antarctic ice sheet influences the Earth's surface albedo, exhibiting one of the largest albedo variations on Earth, associated with the seasonal expansion and contraction of sea ice. Its reduction would drive a decrease in albedo, so the Southern Ocean will take up more solar radiation, increasing the temperature of the surface waters and diminishing their capacity to absorb carbon dioxide (Rintoul et al., [2010](#)).

The lack of meridional boundaries and the intense westerly winds causes the southward outcrop of the deep overturning cell, with two main effects. On the one hand, it leads to the eastward Antarctic Circumpolar Current (ACC), the planet's most intense, largest, and deepest current, which connects the three major ocean basins contributing to the establishment of the GOC (Figure [1.3](#)) (Rintoul et al., [2001](#)). On the other hand, it permits the

direct interaction between the atmosphere and the deep waters, regulating the exchange of mass, heat, salt, carbon, oxygen and other properties between the lower and upper layers of the global ocean. The sinking of dense waters, together with the wind-induced upwelling of subsurface waters, leads to the formation of the lower and upper subantarctic vertical cells. The upwelling branch of both cells raises the old deep waters between 30°S and the Drake Passage – depleted in oxygen and enriched in dissolved inorganic carbon and macronutrients – to the upper ocean. In turn, the downwelling branches deliver heat, oxygen, anthropogenic carbon and other properties into the deep ocean interior.

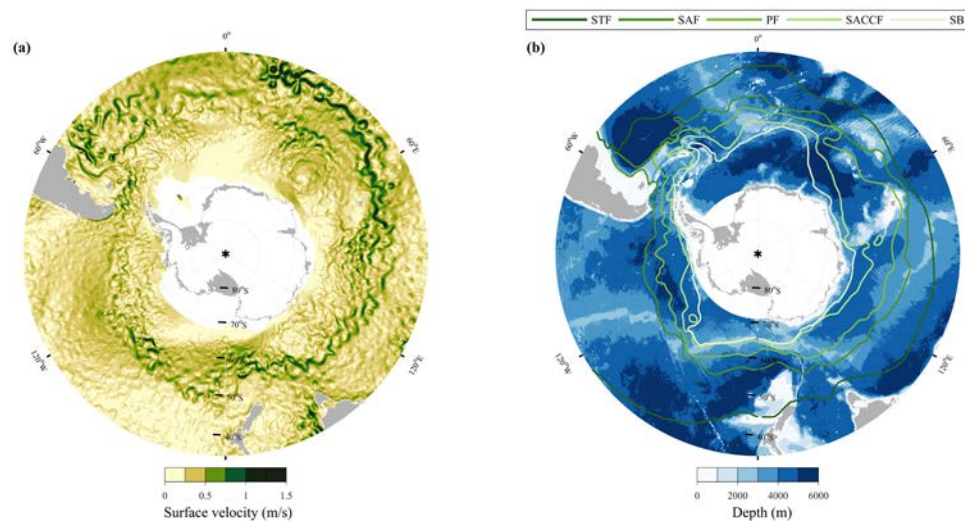


**Figure 1.3.** (a) Daily snapshot (30 May 2020) of the sea-surface eddy-rich structure in the Southern Ocean, as deduced from a 0.25° resolution dataset that combines satellite data with numerical model products. (b) Bathymetry and position of the ACC fronts as determined by Orsi et al. (1995), from north to south: Subtropical Front (STF), Subantarctic Front (SAF), Polar Front (PF), Southern ACC Front (SACCF), and Southern Boundary (SB) Front.

The eastward wind-driven ACC dominates the Southern Ocean circulation, connecting the Pacific, Atlantic, and Indian Oceans. It consists of four circumpolar fronts separating five broad zones associated with strongly sloping isopycnals, water mass boundaries and the core of deep-reaching eastward jets (Orsi et al., 1995). Its flow and position around the Antarctic continent are strongly conditioned by bathymetry, with the Drake Passage being the most restrictive topographic element. These fronts, from north to south, are the Subantarctic Front (SAF), the Polar Front (PF), the Southern ACC Front (SACCF) and the Southern Boundary of the ACC (SB), although this last is not considered a dynamical front (Rintoul & Naveira Garabato, 2013). While the SAF can be identified through the 4 or 5 °C isotherms at 200 m depth (Sievers & Emery, 1978), reaching its farthest north location between 39°S - 40°S in the western South Atlantic Ocean, the PF is identified with the 2 °C isotherm surrounding the



temperature minimum layer (Botnikov, [1963](#); Joyce et al., [1978](#)). These fronts are composed of multiple branches or filaments, which merge and diverge along the circumpolar trajectory, being the SACCF and SB fronts not always distinct (Sokolov & Rintoul, [2007](#)). The flow is near-quiet in the zones between the fronts, usually dominated by eddies. These zones can be summarized as the Subantarctic Zone (SAZ; north of the SAF), Polar Frontal Zone (PFZ; between the SAF and the PF), Antarctic Zone (AZ; between the PF and SACCF), the Southern Zone (SZ; between the SACCF and SB), and the Subpolar Region (south of the SB; Orsi et al., [1995](#); see Figure [1.4](#) for more detail). The wind also contributes to a northward Ekman surface current, which is an important part of the meridional overturning of the Southern Ocean. Below this wind-driven surface layer, the density structure is in near-geostrophic balance with the circulation. South of the ACC, the circulation is organized in cyclonic gyres in the Weddell and Ross Seas (Talley, [2011](#)).

The Scotia Sea, located east of the Drake Passage in the southwestern Atlantic Basin of the Southern Ocean, is surrounded by a shallow ridge system constituted in the north by the 2000 km long North Scotia Ridge and in the south and east by the South Scotia Ridge and the South Sandwich Island Arc. This north submarine ridge, where strong zonal pressure gradients are generated, represents a major obstacle to the deep water flow of the ACC (Smith et al., [2010](#)), forcing the ACC to flow through the relatively narrow passages (Naveira Garabato et al., [2002](#); Thorpe et al., [2002](#); Artana et al., [2016](#)). Hence, our contribution in **Chapter 3.1** has been to study the ACC waters – the upper water mass transport, cross-frontal exchange and temporal variability – as they flow over the deep topographic passages in the western and northern Scotia Sea boundaries, in what represents the first stage of their pathway through the western South Atlantic Ocean.

Within the Scotia Sea topography, the ACC waters undergo an intense modification (Naveira Garabato et al., [2003](#)). The most voluminous among these water masses is the Circumpolar Deep Water (divided into upper, UCDW, and lower, LCDW), which experiences a net poleward transport and upwelling in the Southern Ocean. When the UCDW reaches the upper layers, it becomes the Antarctic Surface Water (AASW), which subducts near the Polar Front (PF), contributing to the formation of the Antarctic Intermediate Water (AAIW) that later emerges to the north of the SAF. Overlying AAIW north of this last front, Subantarctic Mode Water (SAMW) is produced by the winter deepening of the upper-ocean mixed layer (Talley, [1996](#)), playing an essential role in AAIW formation. The remaining upwelled deep waters, LCDW, are transformed into the densest bottom waters and transported northward to fill the global abyssal ocean (see subsection [1.1.3](#) for further details and the origin of water masses). Inside the Scotia Sea, the ACC also finds the contribution of dense Weddell Gyre waters, resulting in the Weddell–Scotia Confluence (Gordon, [1967](#)). Consequently, the Scotia Sea hosts

the initial stage of the ACC inside the South Atlantic basin and has a crucial role in ACC interocean exchange. To quantify all these water mass modifications, how the region is physically and biogeochemically balanced and how the southern boundaries are affected by the Weddell–Scotia Confluence, we applied an inverse box model in **Chapter 3.2**.

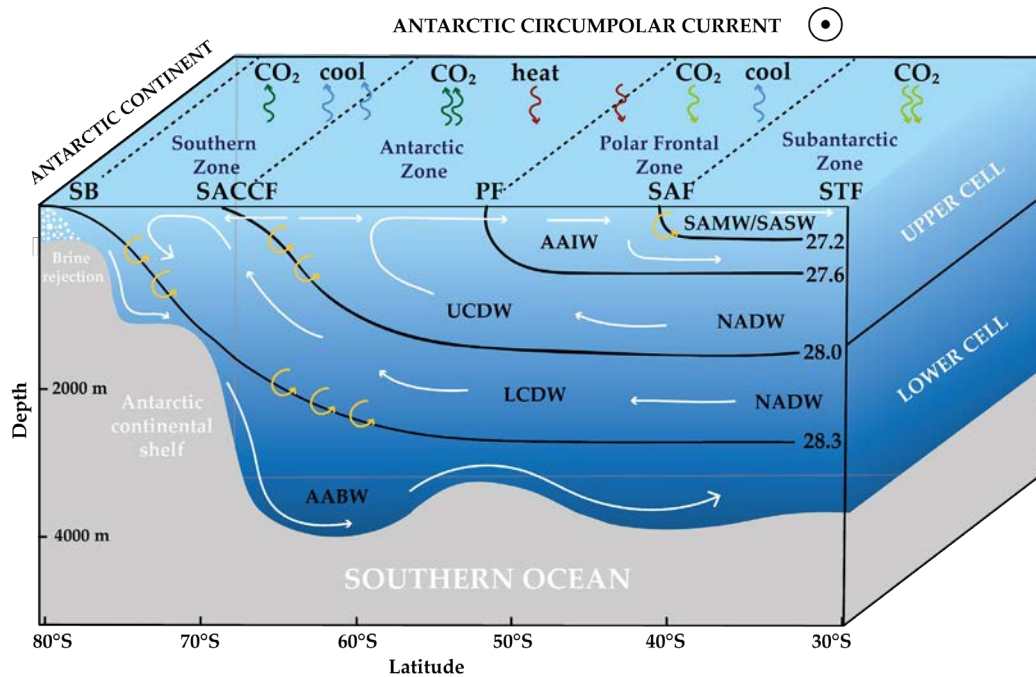


**Figure 1.4.** Schematic meridional section in the Southern Ocean showing the water masses according to their neutral density ( $\text{kg m}^{-3}$ ), the meridional-vertical cells, and the main carbon dioxide and heat release/uptake zones relative to the circumpolar fronts. The water masses are Subantarctic Mode Water (SAMW), Subantarctic Surface Water (SASW), Antarctic Intermediate Water (AAIW), Upper Circumpolar Deep Water (UCDW), Lower Circumpolar Deep Water (LCDW), Antarctic Bottom Water (AABW) and North Atlantic Deep Water (NADW). Following Orsi et al. (1995) and Whitworth III et al. (1985).

### 1.1.3. Main Southern Ocean water masses

The concept of water mass refers to a body of water having a particular origin and, consequently, identifiable physical and biogeochemical characteristics. Most water masses are formed at the sea surface by ocean-atmosphere interaction and depending on where and how the interaction occurs, the water mass is formed with a distinct characteristic or another. Some water masses flow along the different world basins turning nearly global in extent, while others are confined to a small region. In this way, the vertical structure of the ocean can be described in terms of water masses that are related to the source region where they were formed, hence allowing to trace oceanic circulation.

This subsection briefly describes the source and the ocean process that creates the principal water masses found in the Southern Ocean and the resulting specific characteristic. Most of the water masses found in the South Atlantic Ocean are connected with the cold and fresh waters of the returning branch of the AMOC. The water masses have been divided according to the ocean layer where they are typically found and schematically summarized in Table [1.1](#).

### 1.1.3.1 Surface waters

As the name indicates, surface water masses are those in contact with the atmosphere having the lower density in the water column. The water masses found at the Southern Ocean surface are the Subantarctic Surface Water, the Subantarctic Mode Water and the Antarctic Surface Water.

The **Subantarctic Surface Water** (SASW) extends from 150 to 450 m and is characterized by a shallow subsurface salinity maximum caused by the excess precipitation over evaporation at these mid-latitudes (Ansorge & Lutjeharms, [2002](#)). This high salinity layer ranges from 33.9 to 34.3 g kg<sup>-1</sup> and is located north of the SAF. Generally, its temperature ranges from 4 to 12 °C, although it can reach up to 14 °C in summer (Talley, [2011](#)). The lowest temperatures and salinities are found in the Pacific sector, while the highest are in the Atlantic sector, and both increase sharply toward the north (changes of 4 - 5 °C and 0.5 g kg<sup>-1</sup>), being the STF its northern limit (Deacon, [1982](#)). The SASW salinities and temperatures are largely altered by mixing and ocean-atmospheric interactions along its circumpolar path, especially in the Indian sector (Ansorge & Lutjeharms, [2002](#)).

North of the SAF in the southeast and central Pacific, the winter cooling and mixing of the surface waters form a very thick and deep mixed layer known as **Subantarctic Mode Water** (SAMW) (McCartney, [1977](#); McCartney & Talley, [1982](#); Morris et al., [2001](#)). The deep convection imprints its characteristic properties: a vertically well-mixed, ventilated and voluminous water mass subducts northwards to about 500 m depth with relatively warm temperatures (> 14 °C) east of South America (Rintoul et al., [2001](#)). Because of this, it is identified by its high oxygen content. SAMW is characterized to have a potential density of  $26.85 < \sigma_{\theta} < 27.1$  kg m<sup>-3</sup>, potential vorticity less than  $30 \times 10^{-12}$  m<sup>-1</sup> s<sup>-1</sup>, absolute salinities of 34.4 – 35.6 g kg<sup>-1</sup>, and conservative temperatures that range from 4 to 15 °C (Cerovečki et al., [2019](#); Li et al., [2021](#)). Its water properties are vertically as well as horizontally homogenized.

The cold and fresh surface layer from the Antarctic continental shelf to the PF is called **Antarctic Surface Water** (AASW) and extends to the base of the mixed layer in winter. It is characterized by a subsurface temperature minimum associated with the remnants of Winter Water (Belkin & Gordon, [1996](#)). In this way, the surface mixed layer and the remnant of the

previous winter mixed layer capped by seasonal warming and freshening (Winter Water) constitute the AASW in summer (Park et al., [1998](#)). This water mass is seasonally variable, its temperature being controlled by the sea-ice formation and melting processes varying between less than 0 and 4 °C. It consists of a 50 to 250-m thick surface layer, depending on the season, with salinities from 33 to 34.5 g kg<sup>-1</sup>. South of the SACCF, the AASW is a true surface layer, located at about 50 m in all longitudes (Talley, [2011](#)). One way to differentiate the AASW from the underlying Circumpolar Deep Water is the high oxygen concentration of AASW, more than 7 ml l<sup>-1</sup> (Park et al., [1998](#)).

### 1.1.3.2 *Intermediate waters*

Intermediate water masses are located immediately below the surface waters. The water mass found at intermediate depths in the Southern Ocean, which flows and expands to the vast majority of basins, is the **Antarctic Intermediate Water** (AAIW).

The AAIW is formed by vertical convection processes in the Antarctic region of the Pacific Ocean. However, its origin remains unclear. The traditional view defends that it comes from the sinking of cold AASW; however, the opposite view suggests it evolves in part from dense SAMW (McCartney, [1977](#)). It is located under SAMW and can reach a maximum depth of 1400 m. The AAIW is identified by the coldest and freshest salinity minimum (34.3 - 34.5 g kg<sup>-1</sup>) and temperatures of 3 - 7 °C. The AAIW has a relatively high oxygen content of 250 - 300 mmol kg<sup>-1</sup> because it recently left the sea surface. After subducting in the Drake Passage, it first travels northward and later is advected eastwards through the Malvinas loop east of South America, carried by the South Atlantic Current, before its incorporation into the South Atlantic's subtropical gyre (Suga & Talley, [1995](#)). The AAIW circulates in the anticyclonic subtropical gyre and even extends north towards the equator before returning south, transported by western boundary currents (Rintoul et al., [2001](#); Ridgway & Dunn, [2007](#); Machín & Pelegrí, [2009](#)).

### 1.1.3.3 *Deep waters*

Deep waters include the most abundant and spread water masses in the Southern Ocean: the Circumpolar Deep Waters (Upper for the lighter part and Lower for the denser), the Antarctic Bottom Water and Weddell Sea Deep Water.

The **Circumpolar Deep Water** (CDW) lies beneath the AASW or AAIW (depending on whether they are south or north of the SAF) and consists of a thick layer extending down to the densest bottom waters created on the Antarctic shelves. These Circumpolar Deep Waters are advected at depth around the Southern Ocean and originated partly from NADW, PDW,

and IDW, depending on the Deep Water of each ocean basin. The CDW is divided into Upper CDW (UCDW) characterized by an oxygen minimum layer (oxygen < 180  $\mu\text{mol kg}^{-1}$ ) and Lower CDW (LCDW) visible as a salinity maximum layer (34.70 - 34.75  $\text{g kg}^{-1}$ ) (Whitworth III et al., 1985; Orsi et al., 1999; Rintoul et al., 2001). The UCDW is truly circumpolar and extends between 200 and 2000 m, it includes a temperature maximum layer at 1.5 to 2.5  $^{\circ}\text{C}$  and has a potential density of about 27.6  $\text{kg m}^{-3}$ . In the Antarctic Zone, the minimum oxygen layer matches the maximum temperature. Furthermore, the UCDW is characterized to have high nutrient concentrations, supplying nutrients to the surface layer through upwelling.

Instead, the **Lower Circumpolar Deep Water** (LCDW) includes the vertical salinity maximum that comes from NADW (Reid & Lynn, 1971; Reid, 1994). Its neutral density varies from 28.00 to 28.26  $\text{kg m}^{-3}$ , its lower boundary coinciding with the top of the AABW (at 0  $^{\circ}\text{C}$ ). The tilted LCDW isopycnals are found from 400 to 3000 m in the Atlantic sector but reach the ocean bottom in most of the Pacific and Indian Oceans. Its core potential temperature is 1.3 - 1.8  $^{\circ}\text{C}$ , and its salinity maximum is highest in the Atlantic sector, around 34.8 to 34.9  $\text{g kg}^{-1}$ . Furthermore, the LCDW can also be produced from AABW that is transported northward off the continental slope and circulates in the abyssal gyres mixing with the overlying water (Sloyan, 2006). At the same time, the LCDW can also generate AABW when it rises through the continental Antarctic slope and mixes with cold shelf water (Foster & Carmack, 1976; Jacobs et al., 1985; Orsi et al., 1999), turning into a less dense UCDW (Rintoul et al., 2001).

The **Weddell Sea Deep Water** (WSDW) is defined as the deep water with a potential temperature between 0 and -0.7  $^{\circ}\text{C}$  (Fahrbach et al., 1995). It constitutes a very thick water mass that occupies depths of about 1500 to 4000 m, with no particular characteristic maximum/minimum values but yet relatively high salinity and low oxygen values (Gordon et al., 2001; Talley, 2011). It is formed within the Weddell Sea through the mixing of different water masses such as AASW, UCDW and shelf water that descend into the deep ocean (Gordon et al., 1993). Its ventilated version (VWSDW) originates in the southwest Weddell Sea due to the influx of lower-salinity shelf water descending along the continental slope in the Antarctic Peninsula (Gordon et al., 2001). The Weddell Sea overflows into the Scotia Sea and passes through the deep passage east of South Georgia Island into the western South Atlantic (Locarnini et al., 1993).

The **Antarctic Bottom Water** (AABW) is the coldest and densest water mass in the Southern Ocean, just warmer than the freezing point (Orsi et al., 1999; Whitworth III et al., 1985). It is formed through mixing between deep water and shelf water in specific areas of the Antarctic shelf (Jacobs, 1986), later sinking to abyssal depths and finally being exported around the Antarctic continental margins (Jacobs et al., 1970, 1985; Gordon et al., 2004). With neutral densities higher than 28.27  $\text{kg m}^{-3}$ , it covers the ocean bottom of the entire ACC region and

extends northward in the western South Atlantic and into two basins in the western Indian Ocean. The AABW formed in the Weddell Sea is the freshest and coldest, while that originated in the Ross Sea is the warmest and saltiest (Rintoul, 1985). Volumetrically, most AABW is of Weddell Sea origin (66%), and the Ross Sea has the smallest amount (7%). Only AABW from the Weddell Sea can escape northward from the Antarctic region through a deep gap in the South Scotia Ridge (Talley, 2011). This AABW enters the Scotia Sea, flows westward to the Drake Passage, and then eastward with the ACC, crossing the Scotia Sea and spreading northward into the western South Atlantic Ocean, being able to reach the eastern coast of Brazil.

**Table 1.1** Principal water masses found/originated in the Southern Ocean. Adapted from Talley (2011).

| Water mass                   | Acronym | Characteristics  | Layer / Depth                | Formation origin                                 |
|------------------------------|---------|--|------------------------------|--|
| Subantarctic Surface Water   | SASW    | Warm, salty  | Surface<br>150 - 450 m       | Local  |
| Subantarctic Mode Water      | SAMW    | Potential vorticity minimum and oxygen maximum in subtropical South Atlantic | Surface<br>0 - 600 m         | Subducted thick winter mixed layers north of SAF |
| Antarctic Surface Water      | AASW    | Fresh and temperature minimum  | Surface<br>100 - 250 m       | From surface mixed layer and Winter Water        |
| Antarctic Intermediate Water | AAIW    | Vertical salinity minimum  | Intermediate<br>500 - 1200 m | Advection fresh surface water north of the SAF   |
| Upper Circumpolar Deep Water | UCDW    | Low oxygen   | Deep<br>1000 - 3000 m        | Mixture of IDW, PDW, and deep waters             |
| Lower Circumpolar Deep Water | LCDW    | Salinity maximum core  | Deep<br>200 - 4000 m         | From NADW  |
| Weddell Sea Deep Water       | WSDW    | Cold, dense, thick layer from the CDW to the seafloor                        | Deep<br>1500 - 4000 m        | Brine rejection and convection                   |
| Antarctic Bottom Water       | AABW    | Deep salinity and oxygen maxima, nutrient minima                             | Bottom<br>> 3000 m           | Brine rejection and mixed with NADW, PDW and IDW |

## 1.2. The Southern Ocean waters transfer to the South Atlantic Ocean

After crossing the Scotia Sea, the ACC flow veers northward, diverting towards the North Scotia Ridge and South Georgia Island latitudes. The discontinuities in the North Scotia Ridge – mainly the Shag Rocks Passage with 3100 m depth – and the Georgia Passage – between the South Georgia Island and the South Sandwich Island Arc – turn out to be the pathways for the deep waters, influencing the location of the SAF, PF and SACCF fronts (Smith et al., [2010](#)). In particular, the presence of the 54-54 Passage (western passage of the North Scotia Ridge) allows the entrance of the SAF, with its load of UCDW waters, as a western boundary current flowing north along the continental slope of South America into the western South Atlantic basin, finally converted into the Malvinas Current (MC) (Artana et al., [2016](#)). This intense, largely barotropic and relatively narrow Malvinas Current is formed by multiple fronts, bound nearshore by a Shelf Break Front (SBF) located roughly along the 200 m isobath; further, two additional fronts are located on both sides of the SBF (onshore and offshore; Franco et al., [2008](#)).

The MC penetrates northward into the Argentine Basin east of the Malvinas Islands (Lumpkin & Johnson, [2013](#)) and then flows northward following the 1000 - 2000 m isobaths (Piola et al., [2013](#)) up to 38°S where it encounters the southward flowing Brazil Current (BC). The confluence of these two western boundary currents with opposite directions and properties (warm salty subtropical water versus cold fresh subantarctic water) leads to possibly one of the highest intense thermohaline frontal systems in the open ocean with numerous high-energy eddies and strong variability called Brazil-Malvinas Confluence (BMC). After the BMC, part of it sharply turns south describing a sharp cyclonic loop and flows southeast at about 45°S (Peterson & Whitworth III, [1989](#); Orúe-Echevarría et al., [2019](#), [2021](#)). Then, the flow continues eastward at about 40°S as the South Atlantic Current (SAC), roughly in parallel to the PF that follows an eastward path along 50°S to also feed the SAC. The South Atlantic Current constitutes the southern limb of the South Atlantic subtropical gyre and remains separated from the ACC by the STF. Its surface velocities and volume transports are high in the Argentine Basin and decrease, losing strength as it crosses the Mid-Atlantic Ridge towards the Cape Basin (see Figure [1.5](#) in subsection [1.2.1](#); Peterson & Stramma, [1991](#)). Finally, both contributions, one coming initially from the SAF and the other from the PF, are incorporated into the SAC and then into the subtropical gyre circulation (Speich et al., [2001](#)). These cold-fresh water incorporations following the main ACC fronts to the SAC have been assessed through surface drifters and Argo floats combined with off-line Lagrangian particles in **Chapter 3.3**. In particular, we explore the horizontal eddy-diffusivities in the western South

Atlantic Ocean up to 10°W, which are responsible for the differences in trajectories between the real drifters and the numerical particles.

### 1.2.1. The South Atlantic Ocean circulation

The South Atlantic anticyclonic subtropical gyre is the largest circulation feature of the South Atlantic Ocean, bound by the cyclonic tropical gyre to the north and the circumpolar current system to the south. Its anticyclonic subtropical gyre is driven at south by the high-latitude westerlies and at north by the low-latitude south-easterlies (Talley, [2011](#)). This wind system drives Ekman convergence, raising the sea surface high and lowering the isopycnals in the centre of the gyre, causing the subduction of surface waters (Peterson & Stramma, [1991](#); Stramma & England, [1999](#)). In contrast, the South Atlantic tropical gyre is cyclonic and much shallower, with important zonal flows. Both circulation systems meet in the South Equatorial Current (SEC), a westward flow which connects the eastern and western boundaries of the South Atlantic. Furthermore, the South Atlantic subtropical gyre has its prominent front, the STF, and its own surface water masses as the Subtropical Shelf Water (STSW), Subtropical Mode Water (STMW), South Atlantic Central Water (SACW), among others (Tsuchiya et al., [1994](#); Provost et al., [1999](#)). The STSW is formed as a mixture of river and BC waters, the STMW is formed within the subtropical gyre, with its light variety located around 35°S over the BC, and a high-salinity variety of SACW is made in the BMC zone (Provost et al., [1995](#); Stramma & England, [1999](#)).

The South Atlantic Ocean is a key region where the upper and lower AMOC limbs are connected to the Indian and Pacific Oceans and are entangled in the GOC system (e.g., Gordon, [1986](#); Broecker, [2010](#); Schmitz, [1995](#); Richardson, [2008](#); Talley, [2013](#)). The export of NADW to the other ocean basins is compensated by a net northward flow through the South Atlantic Ocean, being the main pathway of surface, central and intermediate waters to maintain mass balance (Broecker, [2010](#); Schmitz, [1995](#)). In particular, this compensating northward flow is a mixture of warm and salty surface and central waters, and cooler and fresher intermediate waters. While the surface water is formed in the tropics/subtropics and subducted between 12°S and 15°S (Tomczak & Godfrey, [1994](#)), the mode and intermediate waters (SAMW and AAIW) are commonly subducted into the thermocline at the southern extreme of the South Atlantic subtropical gyre (Campos et al., [1999](#); Garzoli & Matano, [2011](#)). These cold and fresh intermediate waters, which are exported northward from the southwestern South Atlantic, constitute the first step of the returning path of the AMOC.

The South Atlantic, however, is not just a passive conduit of remotely formed water masses, but its internal dynamics also influence the AMOC and actively participate in its



transformations. Across the South Atlantic basin, water masses experience important alterations due to the air-sea interactions, diapycnal mixing (Bianchi et al., 1993; Sloyan & Rintoul, 2001a; R  hs et al., 2019), eddy-induced isopycnal mixing, subduction and advection processes (Garzoli & Matano, 2011). These alterations occur across the entire basin but are strongly influenced in regions of high energy and mesoscale variability, particularly at the BMC and the Agulhas Retroflection region. These two regions are connected through the SAC, which crosses the South Atlantic to feed the eastern-boundary Benguela Current (Stramma & Peterson, 1990). As the weakened SAC flows east, it enters the eddy-filled region of the Agulhas Current Retroflection (ACR) and turns north into the Benguela Current, closing the southeastern edge of the South Atlantic subtropical gyre (Figure 1.5; Peterson & Stramma, 1991).

These pathways and connections are addressed in **Chapter 3.4**, where we explore the cold waters' subduction and advection processes, thermohaline variations and water mass transformations across the South Atlantic Basin, starting in the Drake Passage and finishing at the 21  S section in the western coast.

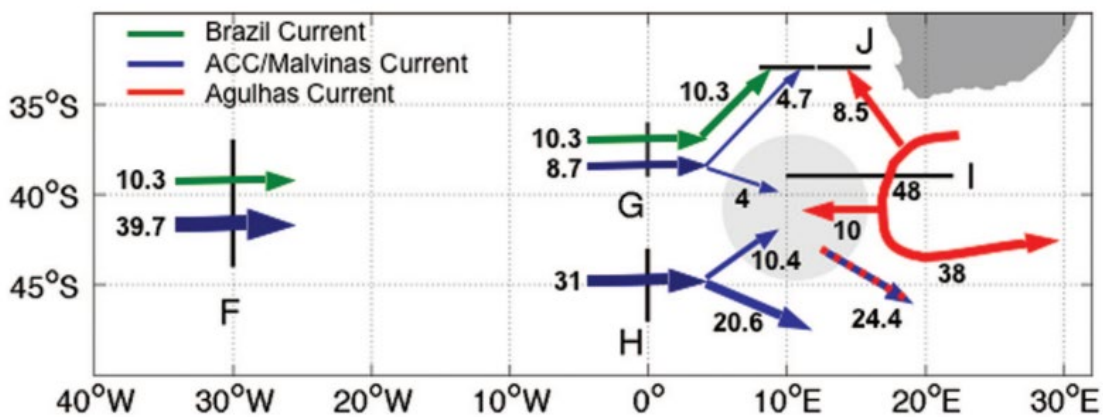


**Figure 1.5.** Schematic illustration of the volume transports (Sv) down to 1000 dbar. The inputs to the Cape Basin are 19.1 Sv (4.7 + 4 + 10.4 Sv) from the Pacific Ocean via the ACC and 18.5 Sv (8.5 + 10 Sv) from the Indian Ocean. The arrows represent the transports, coloured according to the origin. The grey-shaded area represents the region where waters from both Pacific and Indian Oceans interact. Source: Rodrigues et al. (2010).

### 1.2.2. Warm and cold contributions to the returning AMOC into the South Atlantic Ocean

While a portion of the South Atlantic upper waters is produced locally (Stramma & England, 1999), the eastern side of the South Atlantic basin also receives intermediate water from the Indian Ocean via the Agulhas Leakage. The Agulhas Current is one of the strongest western boundary currents and propagates warm and salty subtropical water poleward as a

narrow jet along the continental slope of Africa (Gründlingh, 1983; Peterson & Stramma, 1991; Lutjeharms, 2006). Near 36°S, the Agulhas Current leaves the continental shelf, developing meanders and oscillations of great amplitude (Harris & Bang, 1974), to retroflect back between 16°E and 20°E towards the Indian Ocean as the Agulhas Return Current (Figure 1.6; Lutjeharms & Van Ballegooyen, 1988). Its retroflexion area is highly variable, as well as the volume of its leakage (Phillips et al., 2021).

Gordon (1986) first proposed the global warm-salty route hypothesis, which postulates that the South Atlantic receives most of its upper waters from the Indian Ocean by the leakage of the ACR. Specifically, this route across the Indian Ocean would consist of North Pacific Central Water (from the thermocline) entering through the Indonesian Throughflow down to depths of 1000 m (Wyrtki, 1961) and flowing westwards in the 10°S - 15°S latitude belt, spread by the Indian SEC. The near-surface circulation is monsoon-dominated, with seasonally reversing currents north of around 10°S that can strongly influence the transport of the Indian SEC (Figure 1.6). Although its mean flow is weak, as it is largely obscured by eddies, it is estimated that it can reach about 20 Sv southward (Durgadoo et al., 2013), supplying a small fraction of the Agulhas Current transport.

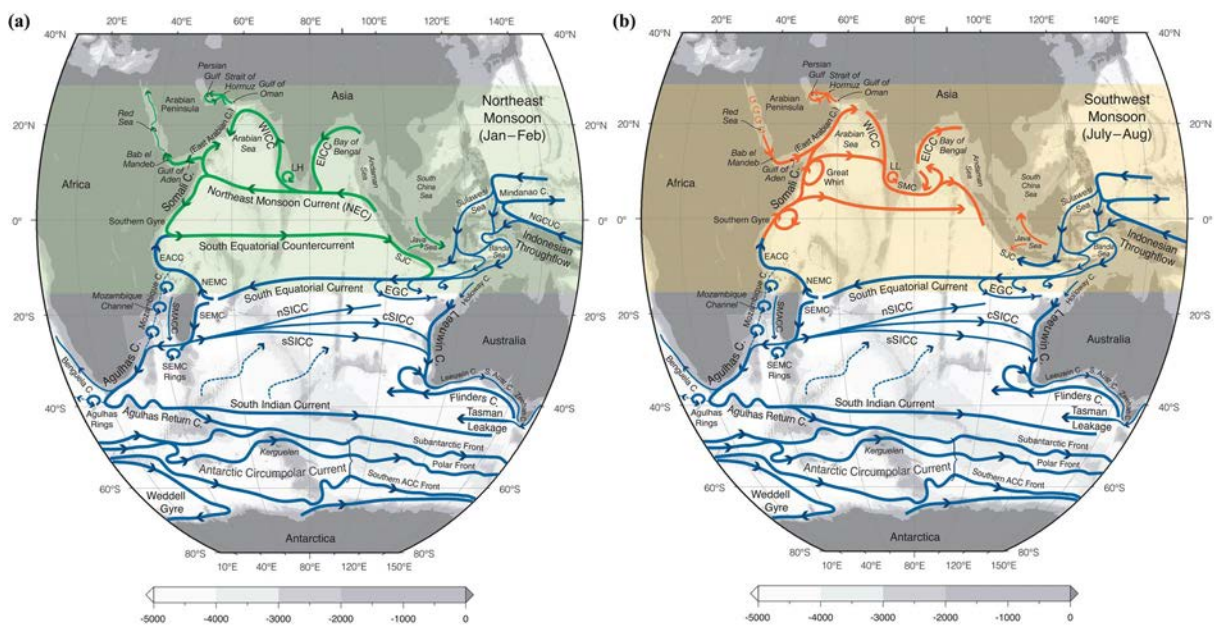


**Figure 1.6.** Schematic near-surface circulation within the Indian Ocean during the (a) northeast monsoon (January–February) and the (b) southwest monsoon (July–August). Blue arrows indicate year-round mean flows with no seasonal reversals and green/orange arrows represent the monsoonally reversing circulation. The ACC fronts are taken directly from Orsi et al. (1995). Acronyms are as follows: EACC, East African Coastal Current; NEMC, Northeast Madagascar Current; SEMC, Southeast Madagascar Current; SMACC, Southwest Madagascar Coastal Current; WICC, West Indian Coastal Current; EICC, East Indian Coastal Current; LH and LL, Lakshwadeep high and low; SJC, South Java

Current; EGC, Eastern Gyral Current; SICC, South Indian Countercurrent (south, central, and southern branches); NEC, Northeast Monsoon Current; SEC, Southwest Equatorial Current. The light grey shading shows seafloor bathymetry. Originally based on Schott & McCreary (2001). Source: Phillips et al. (2021).

The irregular contribution of the Agulhas Current to the South Atlantic Ocean occurs in the form of long filaments and large rings that leak westward at the ACR (Van Sebille et al., 2010; Casanova-Masjoan et al., 2017), with an average frequency of six rings per year (De Ruijter et al., 1999), in what is named the Agulhas Leakage. However, the entire Agulhas Leakage contribution to the Atlantic Ocean does not necessarily come from the Pacific Ocean. Indeed, the Agulhas Leakage is composed of waters originating from the Indonesian Throughflow, from the Tasman Leakage south of Australia, and waters originating indirectly from the Drake Passage through the ACC and its subsequent circulation in the Indian Ocean subtropical gyre (Gordon, 1986; Le Bars et al., 2013; Speich et al., 2001, 2002; Gordon et al., 1992; Rühls, 2018). Recent estimates point out an Agulhas Leakage mass transport that ranges roughly between 10 and 20 Sv (Van Sebille et al., 2010; Beron-Vera et al., 2013; Cheng et al., 2016; Holton et al., 2017; Daher et al., 2020).

Rintoul (1991) proposed the cold-water route, by which SAMW and AAIW – injected from the Pacific through the Drake Passage, the Malvinas Current and transported southeastward over the Mid-Atlantic Ridge – supply most of the South Atlantic upper waters that form part of the returning AMOC. However, part of these intermediate waters undergoes considerable air–sea transformations and interior diapycnal fluxes along its path to southern Africa and can be incorporated into the intense circulation in the southwest Indian Ocean before returning to the South Atlantic Ocean, in what is commonly identified as the indirect cold-water route. SAMW/AAIW waters may enter the South Indian subtropical gyre at 32°S via two main pathways: through the Crozet and Central Indian Basins (east South Africa), summing a total of about 27.1 Sv, and across the Perth Basin (southwest Australia), with about 10.6 Sv (see Figure 1.7 for a more accurate location of the basins). Mixing along this indirect cold route results in a warming and salinification of SAMW and AAIW before they move northward with the Benguela Current (Sloyan & Rintoul, 2001b). However, there is still no final agreement on the relative importance of the cold and warm routes (Garzoli & Matano, 2011). Diverse studies support both hypotheses, and discrepancies are mainly due to the definitions of both water routes and the methodological approaches used, which are very sensitive to the data's spatial-temporal resolution.

Finally, warm and cold routes meet at the Benguela Current to turn northwest into the SEC. According to Rodrigues et al. (2010), the mean total mass transports of both water routes are comparable in the upper 1000 dbar in Cape Basin: 19.1 Sv of water from the Pacific and

18.5 Sv from the Indian Ocean. However, only 12% of these water transports originated in the Pacific end up feeding directly the Benguela Current. In **Chapter 3.5**, we explore the cold and warm intermediate contributions that feed the eastern boundary current from its source, to identify their multiple direct and indirect pathways, the water mass transformations along their route and their temporal variability. Furthermore, we aim to distinguish and quantify the cold water transport that is transferred to the Indian Ocean to feed part of the warm-water route.

Nourished with both cold and warm route contributions, the SEC bifurcates near 25°S as it approaches the east coast of South America: at the south closing the subtropical gyre to join the Brazil Current and at the north to feed the North Brazil Current (NBC; Rodrigues et al., [2010](#); Cabré et al., [2019](#)). Most of the transport of the SEC flows north, mainly through the western boundary NBC, resulting in a weakened Brazil Current (Rodrigues et al., [2007](#)). After reaching the NBC, the returning limb of the AMOC enters the tropical gyre and continues north on its way to the high latitudes in the Northern Hemisphere.

### 1.3. Objectives and outline of this thesis

The main objective of this doctoral dissertation is to broaden our knowledge of the large-scale circulation, its variability and the water transfer from the Southern Ocean to the South Atlantic Ocean (Figure [1.7](#)). In particular, we aim to identify the diverse pathways, transit times, and water mass extension and transformations since their entry through the Drake Passage to their final incorporation into the South Atlantic subtropical gyre and partial outflow to the North Brazil Current.

In order to achieve this general objective, we divide this dissertation into five chapters covering the main results. These chapters are sorted following the path of the Antarctic waters, starting with their entry into the Scotia Sea, its circulation in the western part of the South Atlantic Ocean and then the entire South Atlantic Ocean to finally include part of the Indian Ocean. Each chapter considers a wider study area according to the extent of the Antarctic waters through the Drake Passage, following the direct and indirect paths in this cold route. The chapters follow the structure of scientific papers, which can result in some reiteration but allows reading them as independent pieces of research. We end with a General Discussion and Conclusions, discussing and summarising the principal results obtained.

### **CHAPTER 3.1. The transfer of Antarctic Circumpolar waters to the western South Atlantic Ocean**

The northern Scotia Sea boundaries are the only possible entrances for Southern Ocean waters into the western South Atlantic Ocean. In this chapter, we characterize the ACC through the Scotia Sea assessing the spatial pathways, the upper water mass transport, cross-frontal exchange and temporal variability of the water fluxes through the Drake Passage and Northern Passages, as inferred only with the vertical profiles and trajectories from Argo floats. Using these *in situ* measurements, we reconstruct the vertical hydrographic sections and estimate the reference velocities and transports associated with the different fronts and water masses in the Scotia Sea. Using data from one and a half decades, we estimate the water residence time in the Scotia Sea and analyze the seasonal and interannual changes.

### **CHAPTER 3.2. Mass and biogeochemical fluxes in the Scotia Sea**

A climatological inverse model is applied over the ridges of the Scotia Sea boundaries to balance heat, salt and mass properties in the upper neutral density layers of the Antarctic Circumpolar Current. The circulation model at the boundaries is reconstructed using Argo data with the addition of SODB, MEOP and ESASSI-08 datasets. The inverse model allows determining the reference velocity as well as the vertical advective and diffusive processes, which leads to the main circulation pattern and the water input/output transports per water mass. In addition, the distributions of dissolved oxygen, alkalinity, dissolved inorganic carbon and nitrate are combined with the calculated velocity fields to obtain their transports and balances, which allows estimating the consumption and production of biogeochemical processes that occur through the region. Furthermore, the inclusion of air-sea carbon exchange allows estimating the storage rate of anthropogenic carbon in the domain. The results have finally been compared with the SOSE and B-SOSE models.

### **CHAPTER 3.3. Spatial variability of horizontal diffusivity in the southwestern South Atlantic Ocean**

We present a model-dependent effective approach, the radial offset by diffusion (ROD) method, which allows calculating the horizontal diffusivity coefficients in the western South Atlantic Ocean, including their depth and latitudinal variability. In this chapter, we reproduce the trajectories of Argo, RAFOS, and GDP drifters with numerical simulations of Lagrangian virtual particles. The radial offsets between the drifters and the numerical particles show a Gaussian distribution, which changes with depth. These distributions are then simulated with a radial diffusive model by selecting the appropriate horizontal diffusivity coefficient.

### **CHAPTER 3.4. Direct pathways from the Drake Passage to the South Atlantic subtropical gyre**

The main aim of this chapter is to explore the pathways, transit times and seasonality of the Antarctic waters that remain in the ACC or are incorporated into the South Atlantic subtropical gyre, using the horizontal diffusivities previously estimated. Special attention is given to how long the water parcels recirculate in the subtropical gyre before escaping northward through the North Brazil Current as part of the returning limb of the AMOC. We use a reanalysis model to release Lagrangian virtual particles to assess the percentage of particles that follow each pathway, and further explore how the heat and salinity are modified, resulting in water mass transformations over the years.

### **CHAPTER 3.5. The cold and warm intermediate contributions to the South Atlantic subtropical gyre**

Most previous studies have suggested that the contribution of the cold-fresh waters to the subtropical gyre in the South Atlantic Ocean is minor as compared to the inflow of warm-salty waters from the Agulhas Current System. We compare the contributions of warm and cold routes by performing numerical simulations of Lagrangian trajectories with the main aim to identify the multiple direct and indirect cold and warm intermediate-water pathways reaching the eastern margin of the South Atlantic subtropical gyre. In particular, the predominant trajectories, transit times, water transformations, and spatiotemporal variability have been characterized by thousands of virtual particles released backwards and tracked for 75 years.

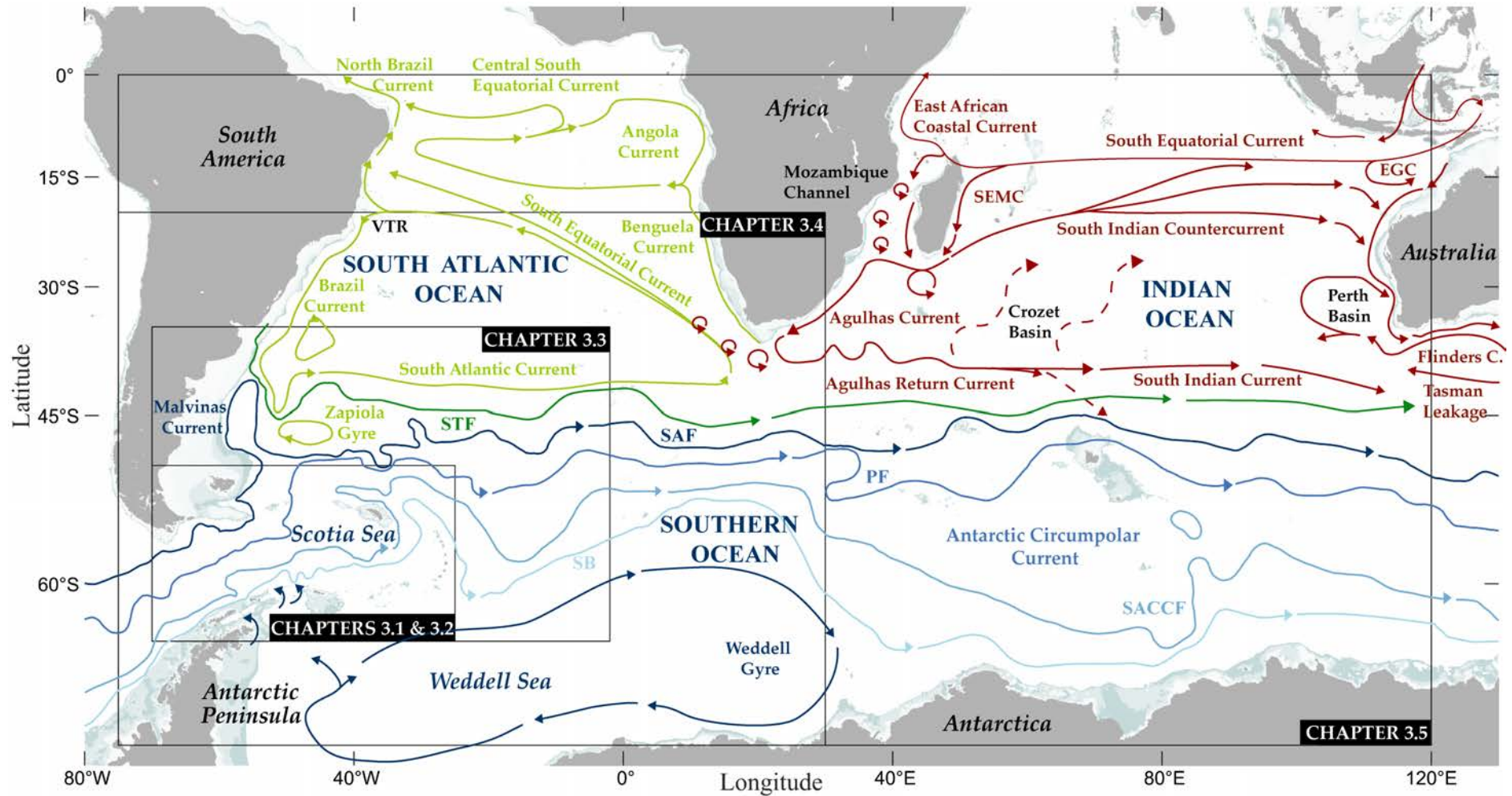


**Figure 1.7.** Geographic domains considered in each chapter of the thesis. The main surface currents that constitute the circulation of the Southern Ocean (blue), South Atlantic Ocean (green) and Indian Ocean (red) are shown schematically with the bathymetry/continents drawn in grey. Acronyms are: SEMC, Southeast Madagascar Current; VTR, Vitória-Trindade Ridge; EGC, Eastern Gyral Current; STF, Subtropical Front; SAF, Subantarctic Front; PF, Polar Front; SACCF, Southern Antarctic Circumpolar Front; and SB, Southern Boundary.

## **II. METHODOLOGY**



## 2.1. From Argo floats to model products

Unfortunately, in none of this thesis chapters has been possible to use *in situ* data collected by the author on an oceanographic cruise. On the one hand, this proves that sampling the remote Southern Ocean still remains as challenging as decades ago. But on the other hand, this also proves that it is possible to produce a thesis dissertation by combining several open datasets with the numerical models available. In the last decades, a massive effort has been made to monitor the whole global ocean, obtaining simultaneously thousands of *in situ* daily observations to improve the ocean-observing system for oceanographers. In this way, free access to scientific data boosts more scientific research and progress in marine research is made by sharing resources within the scientific community. The databases used, which provide *in situ* measurements and have made this thesis possible, are the following: Argo profiling floats, Global Drifter Program (GDP), Marine Mammal Exploring the Ocean Pole to Pole (MEOP), ESASSI-08 dataset, Southern Ocean Database (SODB), Biogeochemical Argo, GLODAPv2, NOCSv2.0 Surface Flux and Meteorological Dataset, AnIceFlux, SOCAT, RAFOS, SADCP from NOAA and Globcurrent data. Furthermore, several reanalysis products and global ocean models, which combine advanced modelling and data assimilation systems, have also been used to study our remote region. These products are the Southern Ocean State Estimate (SOSE), the Biogeochemical SOSE (B-SOSE), the European Centre for Medium-Range Weather Forecasts (ECMWF) and GLORYS12v1 (Table 2.1).

**Table 2.1.** Databases and model products used to develop this thesis dissertation.

| Name                | Provided or funded   | Variables   | Period                | Chapter          |
|---------------------|----------------------|---|-----------------------|------------------|
| Argo floats         | Coriolis and USGODAE | CTD and GPS positioning                                 | 2002-2018<br>200-2020 | 3.1, 3.2,<br>3.3 |
| Yomaha07            | ANDRO                | Velocity error estimations                              | 1997-2007             | 3.1              |
| MEOP database       | MEOP                 | CTD   | 2007-2010             | 3.2              |
| ESASSI-08           | ESASSI project       | CTD   | 2008                  | 3.2              |
| SODB                | TAMU / Chad Greene   | CTD, ACC fronts position                                | 2002-2013             | 3.1, 3.2,<br>3.3 |
| Biogeochemical Argo | SOCCOM               | Oxygen, nitrate, dissolved inorganic carbon, alkalinity | 2014-2019             | 3.2              |
| GLODAPv2            | GLODAP               | Oxygen, nitrate, dissolved inorganic carbon, alkalinity | 2002-2013             | 3.2              |

|   |                   |   |                        |                  |
|---|-------------------|---|------------------------|------------------|
| ERA5 and ERA-Interim<br>Surface Flux and Meteorological | ECMWF             | Evaporation, total precipitation, wind stress         | 2002-2018<br>2002-2013 | 3.2              |
|   | NOCS              | Air-sea net heat exchange                             | 2002-2014              | 3.2              |
| AnIceFlux   | ETH Zurich        | Sea-ice melting                                       | 2002-2008              | 3.2              |
| SOCAT   | NCEI              | pCO <sub>2</sub>                                      | 2002-2017              | 3.2              |
| SOSE  | SOCCOM            | CTD and velocity components                           | 2005-2010              | 3.2              |
| B-SOSE  | SOCCOM            | Dissolved oxygen, DIC, nitrate                        | 2008-2012              | 3.2              |
| GLORYS12v1  | Mercator<br>CMEMS | Three-dimensional velocity, temperature, and salinity | 2002-2020              | 3.3, 3.4,<br>3.5 |
|   |                   |   | 2015-2019              |                  |
| GDP   | NOAA              | GPS positioning                                       | 2005-2019              | 3.3              |
| SADCP   | NOAA              | Velocity components                                   | 1979-2013              | 3.1              |
| RAFOS   | WHOI              | GPS positioning                                       | 2002-2020              | 3.3              |
| GlobCurrent   | ESA               | Geostrophic and Ekman currents at the sea surface     | 2002-2016              | 3.2              |

### 2.1.1. *In situ* observations: floats, satellites, marine mammals and oceanographic cruises

The Argo program started in 1999 with the objective of real-time monitoring the upper-ocean waters. The goal was to set a global array of at least 3000 simultaneous profiling floats, implying a mean distance between floats of about 3°. This aim was achieved in November 2007, and the array has been maintained since then by deploying approximately 800 floats per year to replace the old ones. Furthermore, to improve the weather and climate forecast, the array provides a quantitative description of the changing state of the upper ocean and the patterns of ocean climate variability from months to decades, including heat, freshwater storage and transport, and seasonal to decadal climate variability. The Argo database provides an extensive array of conductivity-temperature-depth (CTD) profiles to monitor the current state of the ocean, and the trajectory data provides all the consecutive positions registered by the float during its lifetime (Argo, [2000](#)). This thesis uses this positioning data to reconstruct the trajectory, including the float velocity during the displacement from one point to another, and the temperature and salinity profiles to reconstruct the hydrographic vertical sections. From these data, the mean transports and the interannual and seasonal variability in Scotia Sea boundaries are obtained in **Chapter 3.1**. Additionally, the Argo dataset has delivered essential information on the main pathways along the 1000-m parking depth. **Chapter 3.1** can

confirm that Argo floats have collected enough measurements to develop a complete characterization of one region without more external data.

Because of the advantages and possibilities offered by Argo floats, the Southern Ocean Carbon and Climate Observations and Modeling project (SOCCOM) has deployed about 200 autonomous biogeochemical floats to provide nearly continuous temporal coverage over the entire Southern Ocean (Johnson et al., [2022](#)). The SOCCOM project is enhancing conventional Argo floats with biogeochemical sensors to measure carbon, nutrients, and oxygen, establishing the world's first large-scale biogeochemical Argo deployment. With this observational data, the program is focused on understanding the role of the vast Southern Ocean in climate change and biogeochemistry. Its future purpose is to analyze and improve a new generation of high-resolution earth system models and make better projections of the future trajectory of the Earth's climate and biogeochemistry. These SOCCOM floats – with over 100 still operating in the Southern Ocean – have made millions of biogeochemical measurements, many in regions and at seasons of the year never sampled before.

Both biogeochemical and classic floats drift, most of them with a parking depth of 1000 m, offer their position at the sea surface with a time resolution of 10 days. However, this is not the case for the satellite-tracked surface drifting buoys (Niiler, [2001](#)) that provide observations of near-surface circulation at unprecedented resolution through the GDP (Elipot et al., [2016](#)). The program's main objectives are to maintain a global array of about 1300 drifting buoys to provide an accurate and globally dense set of in-situ observations of the surface mixed layer currents, sea surface temperature and atmospheric pressure, among others, together with its data processing system. In September 2005, the array size achieved 1250 drifters. Each of these drifters is composed of a holey sock drogue, centred at 15 m depth, including a transmitter, a thermometer and a submergence sensor that detects if the drogue is lost. The drifter follows the flow integrated over the drogue depth, and the velocities and SST measurements are quality controlled and interpolated to intervals of 6 hours (Hansen & Herman, [1989](#); Hansen & Poulain, [1996](#)).

We have used additional 'data-collection platforms' that provide both higher temporal resolution and CTD data in the water column. Those platforms consist of the cost-effective marine mammals and the buoyancy-neutral RAFOS floats, which can monitor the remote and often inaccessible continental slopes and polar oceans covered by the sea-ice. The first dataset contributes to the MEOP database, which aims to obtain quality-controlled oceanographic data from instrumented marine animals (Treasure et al., [2017](#)). The project started in 2008, allowing to assess how animals respond to changes in oceanographic conditions through shallow temperature and salinity profiles. The MEOP, which nowadays includes 13 different nations, is the successor of the Sea Mammal Research Unitfirst (SMRU) and the Southern

Elephant seals as Oceanographic Samplers (SEaOS) projects. On the other hand, RAFOS floats are floating instruments designed to move with the water isopycnals, following density rather than pressure surfaces by adding a compressible element (Rossby et al., [1986](#); Rossby et al., [1993](#)). The RAFOS float triangulates its position based on the detected arrival times of signals from three sound sources and transmits the data back to the Argos satellite system after surfacing at the end of its mission. The use of satellites has allowed a nearly global coverage for float tracking, much wider than previously through the use of discrete listening stations.

We have been fortunate to count on the ESASSI-08 dataset, gathered during the ESASSI cruise carried out in January 2008 onboard the R.V. Hespérides over a sector of the South Scotia Ridge at the west of the South Orkney Islands (Palmer et al., [2012](#)). The region was surveyed with six hydrographic sections where direct current measurements from a ship-borne ADCP were collected with a spatial resolution of 1 – 2 nm.

Increasingly, attempts are being made to create databases that embrace all historical oceanographic cruises across the global ocean, making it easier to access data and hence, avoiding asking for cruise data individually. The SODB (Orsi & Whitworth III, [2005](#)) or the Southern Ocean Atlas, include WOCE data and over 122,000 hydrographic stations of high-quality historical data in the region south of 25°S mainly from the National Oceanographic Data Centre (<http://www.nodc.noaa.gov>), specifically their World Ocean Database (WOA98; WOA2001; Conkright et al., [2002](#)). Moreover, the Global Ocean Data Analysis Project (GLODAP) contains data from 989 cruises from all ocean areas of the globe in a synthesis activity for biogeochemical data collected through chemical analysis of water samples (Lauvset et al., [2021](#)). It provides data on salinity, oxygen, phosphate, nitrate, silicate, dissolved inorganic carbon, total alkalinity, pH, CFC-11, CFC-12, CFC-113 and CCl<sub>4</sub>. Hence, GLODAP enables the quantification of the ocean carbon sink and ocean acidification and evaluates ocean biogeochemical models in its second version, GLODAPv2, released in 2016 (Olsen et al., [2016](#)).

Other datasets provide the in-situ observations of hydrographic stations already time-averaged and space-gridded. The NOCSv2.0 Surface Flux and Meteorological Dataset (Berry & Kent, [2011](#)) is a monthly-mean gridded dataset of marine surface measurements and derived fluxes constructed using optimal interpolation. It covers from the 1973 to 2014 period, with a spatial resolution of 1 degree, and it contains variables such as heat fluxes (sensible, latent, shortwave radiation, longwave radiation), air temperature, sea surface temperature, wind speed, specific humidity, pressure and cloud cover. Additionally, the Surface Ocean CO<sub>2</sub> Atlas (SOCAT) is a synthesis activity for quality-controlled surface ocean fCO<sub>2</sub> (fugacity of carbon dioxide) observations by the international marine carbon research community. SOCAT enables quantification of the ocean carbon sink and ocean acidification, and its last version has observations from 1957 to 2020 for the global oceans and coastal seas (Bakker et al., [2016](#)).

Finally, the GlobCurrent is interpolated and collocated to a common grid with a daily spatial resolution of 25 km for the geostrophic surface and wind-induced currents at the surface and at 15 m depth. The data covers 23 years, from January 1993 to May 2016 (Johannessen et al., [2016](#)).

With the incorporation and combination of in-situ measurements with satellite data, it has been possible to estimate annual freshwater fluxes, perform sea-ice reconstructions and even produce global numerical weather predictions. The AnIceFlux dataset combines multiple products providing estimates related to the sea-ice formation from ocean freezing and snow-ice formation, sea-ice melting, lateral transport of sea ice in the Southern Ocean from 1982 to 2008 (Haumann et al., [2016](#), and all the references herein). The ERA5 (ECMWF Reanalysis v5) provides hourly estimates of a large number of atmospheric, land and oceanic climate variables (Hersbach et al., [2020](#)). The data cover the Earth on a 30 km grid and resolve the atmosphere using 137 levels from the surface up to a height of 80 km. It is produced by the Copernicus Climate Change Service at ECMWF, and it comprises atmospheric reanalysis of the global climate covering the period from January 1950 to the present.

### 2.1.2. Numerical model products

Regarding the model data, the regional eddy-permitting SOSE is a model generated from 2005 to 2010, which supplies a quantitatively useful climatology of the mean-state of the Southern Ocean (Mazloff et al., [2010](#)). These observations include Argo float profiles, shipboard CTD measurements, mooring data and satellite measurements of sea surface height and sea ice, among others. SOSE, with  $1/6^\circ$  of horizontal resolution, has advantages over other climatologies providing a self-consistent state estimate that satisfies momentum, volume, heat and freshwater conservation. The main purpose of SOSE is to provide a basic quantitative description of circulation and its variability in the early twenty-first century. In particular, it offers a quantitatively useful baseline for detecting past and future climate shifts and as a basis for analyzing the underlying physics controlling the circulation to understand if and how it might differ in other climates. The biogeochemical-sea ice-ocean state estimate version of SOSE, the B-SOSE, incorporates carbon, nitrogen and dissolved oxygen, among others, and constrains this output with biogeochemical Argo data, hydrographic cruises and satellites for the period 2008 - 2012 (Verdy & Mazloff, [2017](#)).

Finally, the GLORYS12v1 product (Lellouche et al., [2021](#)) is the CMEMS global ocean eddy-resolving reanalysis that aims to describe the mean and time-varying state of ocean circulation. It includes part of the mesoscale eddy field over recent decades, since satellite altimetry measurements of sea level provide reliable information on ocean eddies. The outputs of a numerical ocean general circulation model that simulates the evolution of the ocean's

physical properties are combined objectively with observations to generate a synthesized estimate of the state of the ocean. It considers the ECMWF atmospheric reanalysis ERAinterim, large-scale correction precipitations and climatological runoff (Berrisford et al., 2009), as well as freshwater fluxes from icebergs, and assimilates observations as *in situ* temperature and salinity profiles, satellite SST, sea-level anomalies and ice concentration obtained from satellite altimetry. The numerical model is based on the NEMO 3.1 version in the global 1/12° ORCA grid (2 - 9 km) configuration. In particular, GLORYS12v1 offers daily and monthly mean outputs for temperature, salinity, currents, sea level, mixed layer depth and ice from top to bottom. The global ocean outputs are displayed on a standard regular grid at 1/12° and on 50 standard levels.

## 2.2. Inverse model

### 2.2.1. Geostrophic velocity and transport

The circulation of the upper ocean is often divided conceptually into the wind-driven and the thermohaline components. Wind blowing over the ocean causes small capillary waves, which can become waves and swell. Regional wind variations drive the surface layers and the convergence or divergence of these surface transports sets into motion the thermocline layers (Wunsch, 1978). On the other hand, the deep ocean is largely driven by surface heating and cooling – thermal changes – and evaporation, precipitation, runoff, and sea ice formation processes – haline changes. The thermocline and deep layers are largely in near-geostrophic equilibrium (Talley, 2011).

The ocean is a stratified and turbulent fluid under the influence of the Earth's rotation. Its circulation is governed by Newton's laws of motion, mass, heat and salt conservation, and the equation of state that sets the thermodynamics of heat and salt. The set of equations that describe the physical state of the ocean include the momentum equations (2.1, 2.2, and 2.3, the last one in hydrostatic balance), the mass conservation equation (2.4), the equations of conservation for salt and heat (2.5, 2.6), and the equation of state (2.7):

$$\frac{\partial u}{\partial t} + u \frac{\partial u}{\partial x} + v \frac{\partial u}{\partial y} + w \frac{\partial u}{\partial z} - fv = -\frac{1}{\rho_0} \frac{\partial p}{\partial x} + \frac{1}{\rho_0} \left[ \frac{\partial}{\partial x} \left( A_h \frac{\partial u}{\partial x} \right) + \frac{\partial}{\partial y} \left( A_h \frac{\partial u}{\partial y} \right) + \frac{\partial}{\partial z} \left( A_v \frac{\partial u}{\partial z} \right) \right] \quad (2.1)$$

$$\frac{\partial v}{\partial t} + u \frac{\partial v}{\partial x} + v \frac{\partial v}{\partial y} + w \frac{\partial v}{\partial z} + fu = -\frac{1}{\rho_0} \frac{\partial p}{\partial y} + \frac{1}{\rho_0} \left[ \frac{\partial}{\partial x} \left( A_h \frac{\partial v}{\partial x} \right) + \frac{\partial}{\partial y} \left( A_h \frac{\partial v}{\partial y} \right) + \frac{\partial}{\partial z} \left( A_v \frac{\partial v}{\partial z} \right) \right] \quad (2.2)$$

$$0 = -\frac{\partial p}{\partial z} - \rho g \quad (2.3)$$

$$\frac{D\rho}{Dt} + \rho \left( \frac{\partial u}{\partial x} + \frac{\partial v}{\partial y} + \frac{\partial w}{\partial z} \right) = 0 \quad (2.4)$$

$$\frac{\partial S}{\partial t} + u \frac{\partial S}{\partial x} + v \frac{\partial S}{\partial y} + w \frac{\partial S}{\partial z} = Q_s + \frac{\partial}{\partial x} \left( K_H \frac{\partial S}{\partial x} \right) + \frac{\partial}{\partial y} \left( K_H \frac{\partial S}{\partial y} \right) + \frac{\partial}{\partial z} \left( K_V \frac{\partial S}{\partial z} \right) \quad (2.5)$$

$$\frac{\partial T}{\partial t} + u \frac{\partial T}{\partial x} + v \frac{\partial T}{\partial y} + w \frac{\partial T}{\partial z} = \frac{Q_H}{\rho c_p} + \frac{\partial}{\partial x} \left( K_H \frac{\partial T}{\partial x} \right) + \frac{\partial}{\partial y} \left( K_H \frac{\partial T}{\partial y} \right) + \frac{\partial}{\partial z} \left( K_V \frac{\partial T}{\partial z} \right) \quad (2.6)$$

$$\rho = \rho(S, T, p) \quad (2.7)$$

where  $\rho_0$  is the seawater mean density (about  $1027 \text{ kg m}^{-3}$ ), the  $D/Dt$  notation corresponds to the substantial derivative,  $g$  is the gravity acceleration,  $A_v$  and  $A_h$  are the kinematic vertical and horizontal turbulent viscosities,  $u, v$ , and  $w$  are the zonal, meridional and vertical velocity components,  $p$  corresponds to the sea pressure,  $K_H$  and  $K_V$  represent the horizontal and vertical eddy diffusivities,  $\rho$  is the seawater density,  $c_p$  is the specific heat of seawater and  $f$  is the Coriolis parameter defined as  $2\Omega \sin\varphi$ , being  $\Omega$  the angular velocity of Earth rotation ( $7.29 \times 10^{-5} \text{ s}^{-1}$ ), and  $\varphi$  corresponds to the latitude. In addition,  $Q_H$  is the heat source (positive/negative for heating/cooling term) and  $Q_s$  is the salinity source (positive for evaporation and brine rejection, negative for precipitation, sea-ice melting and runoff). The momentum balance is composed of the local acceleration, advection and Coriolis acceleration components resulting from the pressure gradient, gravity and friction forces.

Under the Boussinesq approximation (where  $\rho$  can be replaced by the constant  $\rho_0$  except for the hydrostatic balance equation) and removing the non-linear terms, the resulting momentum equations are:

$$\frac{\partial u}{\partial t} + u \frac{\partial u}{\partial x} + v \frac{\partial u}{\partial y} + w \frac{\partial u}{\partial z} - fv = -\frac{1}{\rho_0} \frac{\partial p}{\partial x} + A_v \frac{\partial^2 u}{\partial z^2} \quad (2.8)$$

$$\frac{\partial v}{\partial t} + u \frac{\partial v}{\partial x} + v \frac{\partial v}{\partial y} + w \frac{\partial v}{\partial z} + fu = -\frac{1}{\rho_0} \frac{\partial p}{\partial y} + A_v \frac{\partial^2 v}{\partial z^2} \quad (2.9)$$

$$0 = -\frac{\partial p}{\partial z} - \rho g \quad (2.10)$$

In the ocean interior, far from the sea surface, the sea bottom and the coast, the local and advective accelerations and the friction components can be neglected for the ocean at timescales longer than several days and at spatial scales longer than 10 - 100 km. Therefore, if we assume that the geophysical fluid is steady and in hydrostatic balance, the mathematical expressions above can be simplified to:

$$fv = \frac{1}{\rho_0} \frac{\partial p}{\partial x} \quad (2.11)$$

$$fu = -\frac{1}{\rho_0} \frac{\partial p}{\partial y} \quad (2.12)$$

$$\frac{\partial p}{\partial z} = -\rho g \quad (2.13)$$

These equations are known as geostrophic equations and define a balance between the Coriolis force and the force caused by the horizontal pressure gradient, where the flow moves perpendicular to the pressure gradient force (Talley, [2011](#)). The combination of these equations leads to the thermal wind equation, which relates the vertical shear of the geostrophic velocity in the ocean to the horizontal gradients of the density field:

$$\frac{\partial v}{\partial z} = -\frac{g}{\rho_0 f} \frac{\partial \rho}{\partial x} \quad (2.14)$$

$$\frac{\partial u}{\partial z} = \frac{g}{\rho_0 f} \frac{\partial \rho}{\partial y} \quad (2.15)$$

The geostrophic volume transports can be computed by multiplying the geostrophic velocities by the vertical area of the water column considering the distance between the sampling stations. Its unit is Sverdrups (Sv), equal to  $10^6 \text{ m}^3 \text{ s}^{-1}$  of water; multiplying volume transport by the density of the water parcel leads to mass transport ( $1 \text{ Sv} \cong 10^9 \text{ kg s}^{-1}$ ).

### 2.2.2. Inverse model formulation

According to the thermal wind expressions [2.14](#) and [2.15](#) defined above, we can estimate the variation of the horizontal velocity in the vertical (baroclinic component) but not the absolute values of geostrophic velocity directly. The inverse model is a technique which solves the physical oceanographic question of how to compute the geostrophic flow in the deep sea from observations by providing the reference velocity at the so called reference level (Wunsch, [1996](#)). Since then, inverse box models have been applied from a basin-scale up to global ocean circulation models (Fu, [1981](#); Rintoul & Wunsch, [1991](#); Vanicek & Siedler, [2002](#); Macdonald & Wunsch, [1996](#); Macdonald, [1998](#); Ganachaud & Wunsch, [2000](#); Ganachaud, [2003](#); Machín et al., [2006](#); Orúe-Echevarría et al., [2019](#); Burgoa et al., [2020](#), among others).

The geostrophic velocity is computed by the sum of two components: the relative geostrophic velocity, which varies with depth, also known as the baroclinic component, and the reference velocity, which is often referred to as the barotropic component. Baroclinicity refers to vertical shear associated with the sloping isopycnals, obtained after integrating the thermal wind equation for a vertical section using the *in situ* measured temperature and



salinity data, while solid-body type motions of the entire water column are often called barotropic (Talley, 2011). Most oceanic geostrophic flows have both barotropic and baroclinic contributions, being the absolute geostrophic velocity defined as:

$$v_{abs}(x, z) = v_{rel}(x, z) + b(x) = \frac{-g}{\rho_0 f} \int_{z_0}^z \frac{\partial \rho}{\partial x} dx + b(x) \quad (2.16)$$

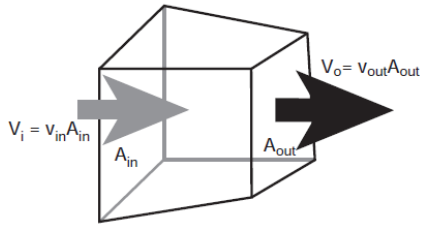
where  $x$  denotes the horizontal direction and  $z$  denotes the vertical direction;  $z_0$  is the depth of the reference level,  $\rho$  is the seawater density ( $\rho_0$  is a depth-mean density value),  $g$  is the gravitational acceleration,  $f$  is the Coriolis parameter, and  $b(x)$  corresponds to the reference velocity. The absolute velocity,  $v_{abs}(x, z)$ , is the sum of the velocity relative to the reference depth,  $v_{rel}(x, z)$  computed from the data, plus the reference velocity,  $b(x)$ , which is unknown and is provided by the inverse model. The surface formed by  $z_0$ , either a constant level or a constant property surface, is called the reference surface.

Finally, to obtain the net geostrophic transport of the entire water column between two consecutive stations pair, in this case from west to east, we would integrate along the section and the vertical:

$$T = \int_{west}^{east} dx \int_{z_0}^z \rho(x, z) v_{abs}(x, z) C(x, z) dz \quad (2.17)$$

being  $C$  the tracer concentration per unit mass ( $C=1$  for mass).  $T$  can also be the transport through an individual layer, with  $z$  and  $z_0$  then defining the upper and lower boundaries of the layer. Depending on the inverse model, this surface may be a constant depth (reference level), a neutral surface, or may be specified for each pair according to the surrounding water properties.

Wunsch (1977) was the first to apply inverse models in oceanography. According to the theory of the inverse models, to describe the ocean circulation property in a specific area, we assume that the region is in geostrophic and hydrostatic balance, which satisfies the conservation of mass, salt and heat in water parcels that are not in contact with the atmosphere, and further consider that the flow is steady. Hence, the inverse model provides the geostrophic velocities at the reference level, which allow balancing the geostrophic transports in a multilayered ocean. In a closed water volume, the net volume of fluid inflow must be equal to the volume outflow, according to:



$$\int \int_A \overrightarrow{v_{abs}} \cdot \overrightarrow{dA} = 0 \quad (2.18)$$

being  $\overrightarrow{v_{abs}}$  the absolute geostrophic velocity and  $\overrightarrow{dA}$  the element of area represented by its perpendicular unit vector. Considering mass conservation and that geostrophic velocity is the sum of the baroclinic ( $v_{rel}$ ) and the reference level ( $b$ ) components, the above expression can be rewritten as:

$$\int \int_A \rho(x, z) (\overrightarrow{v_{rel}}(x, y) + \vec{b}(x)) \cdot \overrightarrow{dA}(x, z) = 0 \quad (2.19)$$

which essentially means that we are considering solely the component of the velocity parallel to the vector  $\overrightarrow{dA}$ . By dividing the water column into neutral density layers (in our case, according to Table 3.1 in subsection 3.1.2.3), the previous equation can now be formulated as:

$$\sum_{j=1}^N \sum_{q=1}^Q \rho_{jq} (v_{rel_{jq}} + b_j) \Delta a_{jq} \cong 0 \quad (2.20)$$

where  $v_{rel_{jq}}$  is the relative velocity and  $\Delta a_{jq}$  is the vertical area of the layer, with the subindex  $j$  indicating the pair of stations and  $q$  indicating the layer. The result of that double summation is not exactly zero due to the noise caused by the presence of eddies, internal waves, etc. Therefore, setting  $E_{jq} = \rho_{jq} \Delta a_{jq}$ ,  $y_q = -\sum_{j=1}^N \rho_{jq} v_{rel_{jq}} \Delta a_{jq}$ , and  $n_q$  the term that represents the error of noise in each layer, the set of all such relations will have a matrix shape that can be written as:

$$Ex + n = y \quad (2.21)$$

where  $x$  is a vector  $N \times 1$  containing the unknown velocities at the reference level,  $E$  is the matrix of the coefficients with size  $Q \times N$ ,  $n$  is a vector  $Q \times 1$  that considers noise, and  $y$  accounts for the baroclinic component in each layer also with dimensions  $Q \times 1$ . The  $E$  matrix will also include the coefficients which correspond to the terms of the total mass conservation equation, as well as the total transport value entered in the  $y$  matrix. The matrices will take the following form:

$$\begin{pmatrix} e_{11} & e_{11} & \dots & e_{1n} \\ e_{21} & e_{22} & \dots & e_{2n} \\ \vdots & \vdots & \ddots & \vdots \\ e_{q1} & e_{q2} & \dots & e_{qn} \\ e_{t1} & e_{t2} & \dots & e_{tn} \end{pmatrix} \begin{pmatrix} b_1 \\ b_2 \\ \vdots \\ b_n \end{pmatrix} = \begin{pmatrix} y_1 \\ y_2 \\ \vdots \\ y_q \\ y_t \end{pmatrix}$$

**Matrix 2.1.** Schematic of the matrix system that sets the inverse model.

In this way, each time we implement the conservation of more properties, such as salt and heat (subsection [2.2.2.1](#)), to determine the oceanic circulation, the matrix system will gradually introduce new equations below the mass conservation equations, increasing the matrices' dimensions. Furthermore, the inverse model can use extra information from diapycnal fluxes (subsection [2.2.2.2](#)) and Ekman transport and freshwater fluxes (subsection [2.2.2.3](#)). However, the system of equations is undetermined since we will not be able to find as many equations as unknowns. Indeed, the matrix system will still have the same unknowns, although more information is available for its solution.

#### 2.2.2.1. Salt and heat conservation

As mentioned above, inverse models allow us to introduce the conservation of more properties as salt and heat conservation. Hidaka ([1940a](#), [1940b](#)) was the first to consider the conservation of salt equations and Riley ([1951](#)) added the conservation of oxygen and other common oceanographic tracers. Throughout the 1980s and 1990s, the inverse model technique was improved to allow the incorporation of freshwater flux (Fu, [1986](#)), tritium (Mémery & Wunsch, [1990](#)) and oxygen, heat and nutrients equations (Rintoul & Wunsch, [1991](#)). Then, Ganachaud & Wunsch ([2000](#)) applied a hydrographic inverse box model for the whole ocean, divided into neutral layers, combining mass, anomalies of salt, heat and conservative phosphate (or preformed phosphate, where phosphate is corrected using the apparent oxygen utilization).

Our inverse box model consists of a matrix system that includes the mass, heat and salt conservation equations plus two additional equations for the total mass and salt transports in the entire water column. Specifically, the heat and salinity conservative equations are introduced into the model as tracer anomalies because the noise inherent to the mass conservation tends to dominate most tracer conservation equations (Ganachaud, [2003](#)). To obtain the anomalies, we subtract the mass divergence times the average property concentration for each layer from each tracer conservation equation. For example, the salinity anomaly transport expression for each neutral density layer can be synthesized in:

$$T'_S = T_S - \bar{S}_C T_M \quad (2.22)$$

where  $T_M$  is mass transport,  $T_S$  is salt transport,  $T'_S$  the salt anomaly transport and the  $\bar{S}_C$  is the mean salinity of each neutral density layer. In this way, the salt anomaly gives the same information as salinity regarding the distribution of water masses in the study region, but using a variable that introduces independent information in the matrix system. As for the conservation of mass, we also introduce the conservation equation for the total salt anomaly.

The first layers of heat anomaly conservation equations are in contact with the atmosphere, continuously exchanging heat; hence, it is not conserved within those layers. Thus, an extra equation has been introduced for the first layers of the heat conservation equations, corresponding to ocean-atmosphere heat exchange (in our case, obtained from the Surface Flux and Meteorological Dataset, see Table 2.1). For the incorporation of the heat anomaly conservation equations, we repeated the same procedure as for the salinity anomaly, although in this case, the total heat anomaly equation is not introduced.

### 2.2.2.2. Diapycnal terms: advective and diffusive transfer

In the early formulations of the inverse models, mixing was considered negligible. In recent years, the diapycnal advection and diffusion terms have been included to take into account the possible exchange between the neutral density layers into which the water column is divided. These terms affect all the equations already introduced in the system matrix (mass, salt, heat, etc.).

After having applied Fick's law and Fourier's law for the conservation of a tracer in a closed volume as in the expression 2.18 and applying Gauss's theorem for each of the directions, the expression can be summarized as follows:

$$\iint_{A_x} \rho C u \, dy \, dz + \iint_{A_y} \rho C v \, dx \, dz = \iint_{A_z} \left( K_z \frac{\partial(\rho C)}{\partial z} - \rho C w \right) dx \, dy \quad (2.23)$$

where  $A_x$  and  $A_y$  are the vertical areas of the zonal and meridional sections, respectively, and  $A_z$  is the horizontal areas inside the volume,  $C$  represents the tracer concentration. The first member of the expression 2.23 accounts for the isopycnal advection of properties. The second member contains the diapycnal terms, the diffusion  $K_z \frac{\partial(\rho C)}{\partial z}$  and advection  $\rho C w$ . Making use of the Reynolds decomposition, we leave the first-order Reynolds correlation for diapycnal diffusion and set the mean terms for diapycnal advection, as follows (see subsection 2.2.4 in Machín, 2004):

$$\overline{K_z \frac{\partial(\rho C)}{\partial z}} - \bar{\rho} \bar{C} \bar{w} \quad (2.24)$$

Introducing the integrals again from the second member in the expression [2.23](#), we have

$$\iint_{A_z} \left( \overline{K_z} \frac{\partial(\overline{\rho C})}{\partial z} - \bar{\rho} \bar{C} \bar{w} \right) dx dy = A_z \left( \overline{K_z} \frac{\partial(\overline{\rho C})}{\partial z} - \bar{\rho} \bar{C} \bar{w} \right) \quad (2.25)$$

because the average terms do not depend on either  $x$  or  $y$ . Finally, from the [2.23](#) and [2.25](#) expressions, it can be concluded that:

$$\iint_{A_x} \rho C u dy dz + \iint_{A_y} \rho C v dx dz = A_z \left( \overline{K_z} \frac{\partial(\overline{\rho C})}{\partial z} - \bar{\rho} \bar{C} \bar{w} \right) \quad (2.26)$$

$A_z$  is the horizontal area covering each interface between the neutral density layers, which in our case is calculated considering all Argo measurements within the Scotia Sea through a DIVA optimal spatial interpolation (Troupin et al., [2012](#); Figure [3.30](#)). The variables  $\bar{\rho}$  and  $\bar{C}$  are the mean values of tracer density and concentration estimated at the interfaces. Therefore, the new unknowns introduced in the system are the diapycnal velocity,  $\bar{w}$ , and the diapycnal diffusion coefficient,  $\overline{K_z}$ , which are the average values of these variables over the entire  $A_z$  interface.

For the diapycnal advection, the salinity is again introduced as a salinity anomaly. However, now it is calculated as the difference between the mean salinity at an interface and at the overlaying layer. Considering the expression [2.22](#) and taking into account the diapycnal terms, we obtain:

$$T_S^i = \iint \rho S \overrightarrow{v}_{abs} \cdot \overrightarrow{dA} + A_z \left( \overline{K_z} \frac{\partial(\overline{\rho S})}{\partial z} - \bar{\rho} \bar{S}_i \bar{w} \right) - \bar{S}_c \left( \iint \rho \overrightarrow{v}_{abs} \cdot \overrightarrow{dA} + A_z \bar{\rho} \bar{w} \right) \quad (2.27)$$

where  $\bar{S}_i$  is the mean salinity over each interface. We introduce these new terms in the system of equations in the way that it fits the expression [2.21](#). All the above expressions, necessary for estimating the diapycnal fluxes, are explained in more detail in Wunsch ([1996](#)), Ganachaud ([2000](#)) and Machín ([2004](#)).

### 2.2.2.3. Ekman and freshwater fluxes

The first meters of the water column are affected by the Ekman transport due to the effect of wind on the ocean surface (Ekman, [1905](#)). From the ECMWF wind stress field, we calculate the meridional and zonal components of the Ekman transport across each section for one year by using the following expressions:

$$U = \frac{\tau_y}{\rho f}, \quad V = -\frac{\tau_x}{\rho f} \quad (2.28)$$

where  $\tau_x$  and  $\tau_y$  are the surface wind stress in the zonal and meridional directions, respectively, and  $\rho$  is the mean density of the ocean,  $1027 \text{ kg m}^{-3}$ . It also affects the rest of the equations as mass conservation and salt and heat anomalies. Then, to introduce the Ekman transport in the matrix system,  $T_{EK}$  is equal to the sum of the transport obtained with the annual average of the wind stress plus  $\Delta T_{EK}$ , a new unknown of the system.

$$T_{EK} = (T_{EK_{annual}} + \Delta T_{EK}) C \quad (2.29)$$

where  $C$  is the average property concentration in the upper layer(s) on each full section. In the sections where more than one layer outcrops, the Ekman transport was calculated according to the relative presence of the outcropping layer and attributing the corresponding part in the way that the sum of all layers corresponds to the total Ekman transport along the section. Furthermore, the Ekman transport varies from one transect to another, so the above expression must be entered for each transect separately:  $T_{EK_{DP}}, T_{EK_{NSR}}, T_{EK_{GP}}, T_{EK_{SSR}}, T_{EK_{PP}}$ .

The freshwater flux,  $F_W$ , corresponds to the difference between evaporation, precipitation and river contributions, affecting the salt anomaly equations. Thus, the freshwater term is multiplied by the mean salinity,  $T_S' = -\bar{S} \times F_W$ , in those anomaly salt equations of the outcropping layers and in the total salt anomaly conservation equation. Ekman transport and freshwater flux are introduced as unknowns.

#### 2.2.2.4. Gauss-Markov estimator

Once the matrix system is constructed, the inverse model will provide a solution,  $x$ , which includes the reference level velocity adjustment,  $b'$ , diapycnal velocities, diapycnal diffusion coefficients, Ekman transport adjustment and freshwater flux, using four expressions (Wunsch, 1996; Ganachaud, 2000):

$$\tilde{x} = R_{xx} E^T (E R_{xx} E^T + R_{nn})^{-1} y \quad (2.30)$$

$$n = y - E \tilde{x} \quad (2.31)$$

$$P = (R_{xx}^{-1} + E^T R_{nn}^{-1} E)^{-1} \quad (2.32)$$

$$P_{nn} = E P E^T \quad (2.33)$$

where  $P$  is an error covariance, and  $R_{nn}$  and  $R_{xx}$  correspond to the *a priori* information of the noise and the solution, respectively. Both  $R_{nn}$  and  $R_{xx}$  enable the Gauss-Markov theorem to be applied. The Gauss-Markov estimator allows obtaining the best solution,  $\tilde{x}$ , to the system of

undetermined equations by choosing from among all the possible solutions of the system the one that deviates least from the real solution,  $x$ . These expressions are extremely important because they permit the discussion of the solution from a set of linear algebraic equations in the presence of noise using information concerning the statistics of the noise and of the solution. In particular, the residuals and uncertainties of the inverse model solution are computed from expressions [2.31](#) and [2.33](#). However,  $\tilde{x}$  and  $P$  are estimators and, as with any statistical estimator, one must make *a posteriori* tests to check that the behavior of  $x$  and  $n$  is consistent with the assumed a priori statistics reflected in  $R_{nn}$  and  $R_{xx}$ .

The uncertainty in the solution,  $P$ , depends on the weight of the constraints (i.e., the *a priori* variance of  $n$ ) and the a priori variance of  $x$ , with this last variable formed from the a priori variances of  $b, w, K$  (see Table [3.13](#) in subsection [3.2.2.2](#)).

## 2.2.3. The full matrix system

$$\begin{pmatrix}
 e_{11} & \dots & e_{1n} & ad_{12} & 0 & 0 & \dots & 0 & 0 & 0 & 0 & 0 & \dots & 0 & 0 & -R_1 & -R_1 \\
 e_{21} & \dots & e_{2n} & -ad_{12} & ad_{23} & 0 & \dots & 0 & 0 & 0 & 0 & 0 & \dots & 0 & 0 & -R_2 & -R_2 \\
 e_{31} & \dots & e_{3n} & 0 & -ad_{23} & ad_{34} & \dots & 0 & 0 & 0 & 0 & 0 & \dots & 0 & 0 & -R_3 & -R_3 \\
 \vdots & \ddots & \vdots & \vdots & \vdots & \vdots & \ddots & \vdots & \vdots & \vdots & \vdots & \vdots & \ddots & \vdots & \vdots & \vdots & \vdots \\
 e_{q-1,1} & \dots & e_{q-1,n} & 0 & 0 & 0 & \dots & -ad_{q-2,q-1} & ad_{q-1,q} & 0 & 0 & 0 & \dots & 0 & 0 & 0 & 0 \\
 e_{q1} & \dots & e_{qn} & 0 & 0 & 0 & \dots & 0 & -ad_{q-1,q} & 0 & 0 & 0 & \dots & 0 & 0 & 0 & 0 \\
 e_{t1} & \dots & e_{tn} & 0 & 0 & 0 & \dots & 0 & 0 & 0 & 0 & 0 & \dots & 0 & 0 & -1 & -1 \\
 es'_{11} & \dots & es'_{1n} & ad_{s'_{12}} & 0 & 0 & \dots & 0 & 0 & dd_{s_{12}} & 0 & 0 & \dots & 0 & 0 & -S'R_1 & \bar{S}R_1 \\
 es'_{21} & \dots & es'_{2n} & -ad_{s'_{12}} & ad_{s'_{23}} & 0 & \dots & 0 & 0 & -dd_{s_{12}} & dd_{s_{23}} & 0 & \dots & 0 & 0 & -S'R_2 & \bar{S}R_2 \\
 es'_{31} & \dots & es'_{3n} & 0 & -ad_{s'_{23}} & ad_{s'_{34}} & \dots & 0 & 0 & 0 & -dd_{s_{23}} & dd_{s_{34}} & \dots & 0 & 0 & -S'R_3 & \bar{S}R_3 \\
 \vdots & \ddots & \vdots & \vdots & \vdots & \vdots & \ddots & \vdots & \vdots & \vdots & \vdots & \vdots & \ddots & \vdots & \vdots & \vdots & \vdots \\
 es'_{q-1,1} & \dots & es'_{q-1,n} & 0 & 0 & 0 & \dots & -ad_{s'_{q-2,q-1}} & ad_{s'_{q-1,q}} & 0 & 0 & 0 & \dots & -dd_{s_{q-2,q-1}} & dd_{s_{q-1,q}} & 0 & 0 \\
 es'_{q1} & \dots & es'_{qn} & 0 & 0 & 0 & \dots & 0 & -ad_{s'_{q-1,q}} & 0 & 0 & 0 & \dots & 0 & -dd_{s_{q-1,q}} & 0 & 0 \\
 es'_{t1} & \dots & es'_{tn} & 0 & 0 & 0 & \dots & 0 & 0 & 0 & 0 & 0 & \dots & 0 & 0 & -S' & \bar{S} \\
 ec'_{11} & \dots & ec'_{1n} & ad_{c'_{12}} & 0 & 0 & \dots & 0 & 0 & dd_{c_{12}} & 0 & 0 & \dots & 0 & 0 & -C'R_1 & 0 \\
 ec'_{21} & \dots & ec'_{2n} & -ad_{c'_{12}} & ad_{c'_{23}} & 0 & \dots & 0 & 0 & -dd_{c_{12}} & dd_{c_{23}} & 0 & \dots & 0 & 0 & -C'R_2 & 0 \\
 ec'_{31} & \dots & ec'_{3n} & 0 & -ad_{c'_{23}} & ad_{c'_{34}} & \dots & 0 & 0 & 0 & -dd_{c_{23}} & dd_{c_{34}} & \dots & 0 & 0 & -C'R_3 & 0 \\
 \vdots & \ddots & \vdots & \vdots & \vdots & \vdots & \ddots & \vdots & \vdots & \vdots & \vdots & \vdots & \ddots & \vdots & \vdots & \vdots & \vdots \\
 ec'_{q-1,1} & \dots & ec'_{q-1,n} & 0 & 0 & 0 & \dots & -ad_{c'_{q-2,q-1}} & ad_{c'_{q-1,q}} & 0 & 0 & 0 & \dots & -dd_{c_{q-2,q-1}} & dd_{c_{q-1,q}} & 0 & 0 \\
 ec'_{q1} & \dots & ec'_{qn} & 0 & 0 & 0 & \dots & 0 & -ad_{c'_{q-1,q}} & 0 & 0 & 0 & \dots & 0 & -dd_{c_{q-1,q}} & 0 & 0 \\
 ehe_{11} & \dots & ehe_{1n} & 0 & 0 & 0 & \dots & 0 & 0 & 0 & 0 & 0 & \dots & 0 & 0 & -C' & 0
 \end{pmatrix}
 \begin{pmatrix}
 b_1 \\
 b_2 \\
 \vdots \\
 b_n \\
 w_{12} \\
 \vdots \\
 k_{12} \\
 \vdots \\
 \Delta T_{EK} \\
 \vdots \\
 Fw
 \end{pmatrix}
 =
 \begin{pmatrix}
 y_1 + T_{EK} \\
 y_2 + T_{EK} \\
 \vdots \\
 y_q \\
 y_t + T_{EK} \\
 y_{s1} + S'T_{EK} \\
 \vdots \\
 y_{sq} \\
 y_{st} + S'T_{EK} \\
 y_{c1} + C'T_{EK} \\
 \vdots \\
 y_{cq} \\
 C'T_{EK}
 \end{pmatrix}$$

Isopycnal Advection
Diapycnal Advection
Diapycnal Diffusion
Ekman
Freshwater

**Matrix 2.2.** Matrix system for equations and unknowns in the inverse model, following the  $\mathbf{Ex} + \mathbf{n} = \mathbf{y}$  expression (subsection 2.2.2). The  $\mathbf{E}$  matrix includes the coefficients of mass ( $\mathbf{e}$ ), total mass ( $\mathbf{e}_t$ ), salinity anomaly ( $\mathbf{es}'$ ), total salinity anomaly ( $\mathbf{es}'_t$ ), and heat anomaly ( $\mathbf{ec}'$ ) in the conservation equations, and the air-sea heat exchange ( $\mathbf{ehe}$ ) as rows. Each station pair along the five sections is introduced as a column, followed by the diapycnal terms columns (advection,  $\mathbf{ad}$ , and diffusion,  $\mathbf{dd}$ ) between each layer interface. The subindex  $_{q-1,q}$  refers to the interface between the layers  $q - 1$  and  $q$ . The Ekman transport,  $\mathbf{T}_{EK}$ , is introduced in all transects but only appears once for space reasons (subsection 3.2.2.2).  $\mathbf{R}$  represents the relative presence of the neutral density layer at the surface, comprising values between 0 and 1. The last column corresponds to freshwater,  $\mathbf{Fw}$ , affecting only the mass and salinity anomaly transport equations.



The inverse box model implemented in **Chapter 3.2** over the Scotia Sea boundaries considers the upper 12 neutral-density layers comprised between 26.80 and 28.00 kg m<sup>-3</sup>. It includes mass, salt and heat conservation, considers diapycnal advection and diffusion processes, and implements Ekman transport and freshwater fluxes. Hence, the coefficients matrix,  $E$ , has a size of 39 × 1163. It has a total of 39 equations (rows): 13 for mass and total mass conservation, 13 for salt and total salt anomaly conservation, and 12+1 for heat anomaly conservation and air-sea heat exchange. Furthermore, it is composed of 1191 columns, of which 1163 correspond to hydrographic stations (every 3 km of the transect): 297 for the Drake Passage, 380 for the North Scotia Ridge, 132 for the Georgia Passage, 266 for the South Scotia Ridge, and 93 for the Philip Passage. Further, 11 columns correspond to the diapycnal advection terms and 11 more to the diapycnal diffusion terms, 5 to Ekman transports, and one to freshwater flux. The unknowns of the system,  $x$ , forms a vector with size 39 × 1 that contains the reference velocity, vertical velocity and diffusion, Ekman and freshwater unknowns (Table 3.13 in subsection 3.2.2.2). Finally,  $y$  has the same size as equations have in  $E$ , and it contains the sum of the total geostrophic transport, the total salt and heat anomaly transport per layer, plus the diapycnal transference and Ekman and freshwater contributions.

As mentioned above, the annual mean of Ekman transport at each Scotia Sea boundary or transect has been distributed equally between stations and added to the neutral density layer located at the surface according to their relative presence. In particular, at the Drake Passage, the first layer has a relative presence of 0.03, the second 0.08, 0.20, 0.39, 0.21 and 0.09 for the third, fourth, fifth and sixth, relatively. However, the freshwater fluxes have been determined for the whole horizontal area of the Scotia Sea and then introduced directly in  $E$  according to the relative presence of each neutral density layer at the surface (Figure 3.26). Regarding biogeochemistry, since the nutrients and components of the carbon budget are not conservative, they must be considered *a posteriori*. It means that their initial transports associated with the neutral density layers have been adjusted with the output solution offered by the inverse model. As with mass, salt and heat, they are modified by the reference velocity, vertical velocity and diffusion coefficient.

## 2.3. Lagrangian analysis

### 2.3.1. Evolution of the Lagrangian approach

The knowledge of oceanic basin interconnections in terms of pathways and associated timescales and transference of heat, salt and biogeochemical properties is of fundamental importance in physical oceanography. There are two general methods for estimating pathways

in the ocean. One approach consists of using tracers in Eulerian methods, based on describing fluid motion in a reference frame fixed in space. Most analytical and numerical models in fluid dynamics are made in the Eulerian framework since it is then straightforward to describe the motion as a function of position and time (Döös et al., [2011](#)). Instead, the second approach consists of the Lagrangian perspective, based on a description of the fluid in a reference frame that is moving with infinitesimal fluid particles.

Traditionally, the seawater pathways that define the global overturning circulation have been inferred observationally through Lagrangian observing programs using satellite-tracked surface drifting buoys from the Global Drifter Program (Elipot et al., [2016](#)) or the ARGO profiling floats (Argo, [2000](#)). However, such observational data becomes insufficient for a detailed and coherent spatio-temporal assessment of large-scale connectivity (Rühs, [2018](#)). In recent decades, large-scale connectivity studies have been performed through Lagrangian model simulations applied to ocean general circulation models (OGCMs). These numerical circulation models have evolved considerably, producing more accurate results with finer spatial and temporal resolutions (Prodhomme et al., [2016](#)). Performing Lagrangian numerical simulations on velocity fields from ocean general circulation models may reveal both major global transport pathways (Speich et al., [2001](#), [2007](#)) and details of individual pathways, for example, in the upper limb Indian-Atlantic connections (Donners & Drijfhout, [2004](#); Biastoch et al., [2008](#); Van Sebille et al., [2011](#); Rimaud et al., [2012](#); Durgadoo et al., [2013](#); Rühs et al., [2013](#)).

The Lagrangian analysis is a powerful technique to assess ocean interconnections and pathways by releasing an ensemble of virtual passive Lagrangian particles representing ocean fluid parcels, water masses, tracers such as temperature, salinity, nutrients, or even floating particles like seagrass, plastic, icebergs, etc. (Grech et al., [2016](#); Onink et al., [2019](#); Marsh et al., [2015](#)). The tridimensional OGCMs velocity field determines the Lagrangian off-line trajectories of water particles, computing them either forward or backwards in time. In order to address oceanic processes with longer time scales that exceed the numerical model timespan, one approach is to loop the original model output continually (Döös et al., [2008](#); Van Sebille et al., [2012](#)). A considerable number of model-independent tools for computing Lagrangian simulations is currently available, which include Ariane (Blanke & Raynaud, [1997](#)), TRACMASS (Döös et al., [2017](#)), the Connectivity Modelling System (Paris et al., [2013](#)), and recently the Parcels code (Lange & van Sebille, [2017](#); Delandmeter & van Sebille, [2019](#)), each of them with strengths and limitations.

### 2.3.2. Advection and diffusion algorithms

Through the Lagrangian analysis of the Eulerian velocity fields, the virtual fluid particles are simply advected with a simulated oceanic flow (Rühs, 2018). In other words, the Lagrangian method advances the particle coordinates in time by means of the Eulerian velocity flow and finds the particle position and properties through proper interpolation (Delandmeter & van Sebille, 2019). For an incompressible fluid (Boussinesq, non-divergent fluid), the Lagrangian fluid particle has constant volume along its trajectory (Van Sebille et al., 2018), and its velocity corresponds to the time derivative of the position. As the fluid parcel moves, it carries tracers such as salt, nutrients, heat, etc., being their concentration altered along their path in contact with adjacent seawater parcels. Computing the Lagrangian particle trajectory using a velocity field requires integrating the gridded velocity field to an arbitrary point in space and time. The updated zonal coordinate,  $x(t + \Delta t)$ , is determined as follows:

$$x(t + \Delta t) = x(t) + \int_t^{t+\Delta t} u(x(t), y(t), t) dt \quad (2.34)$$

where the integrand involves the Eulerian zonal velocity field  $u(x, y, t)$ , and similarly in the meridional coordinate. If the interval between consecutive velocity fields is generally longer than the time step,  $\Delta t$ , the temporal interpolation of the velocity fields is used to obtain the offline virtual particle trajectories. This temporal interpolation can be a large source of error, particularly when the time interval is longer than a few days (Da Costa & Blanke, 2004; Qin et al., 2014). On Arakawa C grids, where velocities are known on the edges of grid cells, the reconstruction of the continuous velocity field is often done using simple linear interpolation (Van Sebille et al., 2018).

In ocean models, the effect of unresolved small-scale motions on tracer mixing is parametrized as diffusive transport, often simulated as stochastic noise. There are different approaches to adding this stochastic noise to trajectories. The simplest option is to add the stochastic displacement to the particle positions, computed from a uniform lateral diffusion, by adding an extra term to the position in the previous expression 2.34:

$$x(t + \Delta t) = x(t) + \int_t^{t+\Delta t} u(x(t), y(t), t) dt + R\sqrt{2K\Delta t} \quad (2.35)$$

In this equation,  $R = N(-1, 1)$  is a random number taken from the normal distribution with zero mean and unit variance, and  $K$  is a constant tracer diffusivity coefficient. The presence of  $R$  is to avoid a unique solution and uniform distance added to the final particle

positions, simulating the stochastic fluctuations that usually represent unresolved motions like eddies, waves or small-scale turbulence (Van Sebille et al., [2018](#)).

### 2.3.3. Computing Lagrangian simulations

For all Lagrangian experiments of **Chapters 3.3, 3.4 and 3.5**, we use the Parcels code (Probably A Really Computationally Efficient Lagrangian Simulator), provided by [www.oceanparcels.org](http://www.oceanparcels.org), which allows tracking offline particles within a numerical circulation model simulating water parcels (Van Sebille et al., [2018](#)). It is formed by an efficient set of interpolation schemes according to each type of discretized field, from rectilinear to curvilinear grids. Also, it is based on built-in kernels, runs offline on stored velocity data, and provides extensive particle behaviour control (Delandmeter & van Sebille, [2019](#)). The kernels define particle dynamics, offering various options such as Runge–Kutta 4, Runge–Kutta–Fehlberg and explicit Euler integration schemes for advection (Lange & van Sebille, [2017](#)). Other physical processes influencing ocean circulation and parcels are density- and wind-driven currents, residual tidal currents, horizontal diffusivities, Brownian motions and Stokes drift.

The inputs for the Parcels code are the release section, the time-varying velocity components and tracer fields, and the uniform horizontal diffusivity,  $K$ , to simulate subscale dynamics not resolved by the model. We obtain the Parcels input from the GLORYS12v1 reanalysis product, which consists of daily three-dimensional velocity, temperature and salinity ( $u, v, w, T, S$ ) fields developed by the Mercator Ocean team on ORCA12 native grid (Arakawa C; Lellouche et al., [2021](#)). In a C grid discretization, the velocities are located on the cell edges and the tracers in the middle (Figure [2.1](#)).

This ocean reanalysis is characterized by having a horizontal resolution of  $1/12^\circ$  and 50 vertical levels (for further details, see subsection [2.1.2](#)). Using the three-dimensional fields on C grids, Parcels interpolates the horizontal velocities located at the edges of the cell  $u_{k,j+1,i}, u_{k,j+1,i+1}, v_{k,j,i+1}, v_{k,j+1,i+1}$  at the  $k$  vertical level. Further, the vertical velocity is interpolated as

$$w = \zeta w_0 + (1 - \zeta) w_1 \quad (2.36)$$

where  $\zeta$  is the vertical relative coordinate,  $w_0 = w_{k,j+1,i+1}$  and  $w_1 = w_{k+1,j+1,i+1}$ , which is consistent with the NEMO notation. For further detail on how the fluxes are linearly interpolated and divided by the Jacobian matrix and its validation and implementation into Parcels code, see Delandmeter & van Sebille ([2019](#)).

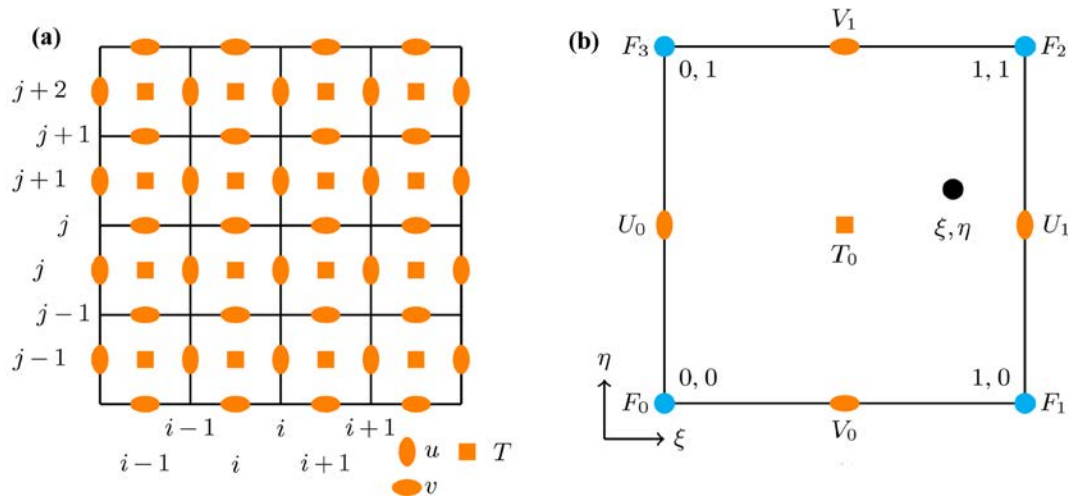


**Figure 2.1.** (a) Scheme of the position of the variables for a C grid or native grid (orange) and (b) compared with the positioning for an A grid (blue nodes). In the C grid,  $i$  and  $j$  respectively, represent the variable column and row indexing in arrays where the variables are stored. The indexing of the C grid follows the NEMO notations. Source: Delandmeter & van Sebille (2019).

The number of particles released,  $N$ , is set to be proportional to the volume transport,  $v A$  (where  $v$  is the zonal velocity and  $A$  is the vertical area of the pixel). However, there are two valid options depending on the initial transport and efficiency in interpreting: assign each particle the same transport (**Chapter 3.5**), so the number of particles released per cell is variable and changes as a function of the transport, or rather set a constant number of particles to be released per cell, with each particle representing a different transport (**Chapter 3.4**). The first option is easier and faster to read: just by counting the number of particles following each trajectory, one can know the transport they are carrying. However, the second case is computationally more efficient for large transports because the same transport can be simulated with a smaller number of particles. Nevertheless, this must be done with caution, as imposing a constant transport for each particle may result in low-velocity cells not releasing any particle, hence underestimating the total transport. Furthermore, to get a greater variety of trajectories within the same cell, it is not necessary to launch all the particles in the centre but at random points along its surface.

A wide range of temporal and spatial scales can be used according to the input files introduced into the Parcels code. Hence, while in **Chapters 3.3** and **3.5**, daily fields have been introduced in first place for the western South Atlantic Ocean and then for all the South Atlantic and Indian Oceans, for **Chapter 3.4** both annual and daily means obtained for the 2002 - 2019 period are used in order to obtain a climatological perspective, considering the whole South Atlantic domain up to  $20^\circ\text{S}$ . Each set of simulations presents a different scenario and their characteristics are summarized in Table 2.2.

**Table 2.2.** Comparison of the characteristics of the Lagrangian simulations in each chapter of this thesis.

|                                 | <b>Chapter 3.3</b>                      | <b>Chapter 3.4</b>                      | <b>Chapter 3.5</b>                     |
|---------------------------------|---|---|--|
| <b>Time-resolution fields</b>   | Daily                                   | Annual and daily means                  | Daily                                  |
| <b>Period input fields</b>      | 2002 to 2020                            | 2002 to 2019                            | 2015 to 2019                           |
| <b>Advection kernels</b>        | Runge–Kutta 4, 2D & 3D                  | Runge–Kutta 4, 3D                       | Runge–Kutta 4, 3D                      |
| <b>Diffusion kernels</b>        | No                                      | Horizontal uniform $K$                  | No                                     |
| <b>Output resolution</b>        | Daily                                   | Daily and every 4 days                  | Every 5 days                           |
| <b>Period running</b>           | 10 days                                 | 75 years                                | 75 years                               |
| <b>Domain</b>                   | 35°S - 64°S and 70°W - 10°W             | 20°S - 70°S and 70°W - 30°E             | 0°S - 70°S and 70°W - 120°E            |
| <b>Release section</b>          | Where Argo float sinks before the cycle | Drake Passage<br>55°S - 63°S at 63.75°W | Subtropical gyre<br>5°W - 18°E at 34°S |
| <b>Release depth or density</b> | Drifter depth                           | Surface to 28.00 kg m <sup>-3</sup>     | 26.8 - 27.5 kg m <sup>-3</sup>         |
| <b>Time evolution</b>           | Forward                                 | Forward                                 | Backwards                              |
| <b>Loop period</b>              | No                                      | Loop climatology                        | Loop five / one year                   |
| <b>Tracer</b>                   | No                                      | Salinity + pot. temp.                   | Salinity + pot. temp.                  |
| <b>Transport particle</b>       | No                                      | Cell transport / N                      | Always 0.01 Sv                         |

In **Chapter 3.3** (see subsection [3.3.3.1](#)), we released a numerical particle at the same position, depth and day of the year as a real 10-day cycle drifter crossing the South Atlantic Ocean and tracked its trajectory daily for ten days in an advection scenario. The horizontal diffusivities obtained are model-dependent, i.e., only valid for the GLORYS12v1 spatial resolution. In **Chapter 3.4** (see subsection [3.4.2.2](#)), the virtual particles are released forward in the Drake Passage and grouped into two sets of experiments. In both of them, particles are advected three-dimensionally and dispersed due to diffusion motions according to their current depth. Using the annual climatological mean, we tracked particles daily for 75 years to count the number of recirculations in the South Atlantic subtropical gyre. Then, we use the daily climatological mean to study the seasonal variability, also for 75 years. Finally, in **Chapter 3.5** (see subsection [3.5.2.1](#)), Lagrangian particles were released along the 34°S section, from 5°W to 18°E, corresponding to the intermediate waters found between the potential density surfaces of 26.8 and 27.5 kg m<sup>-3</sup> located approximately at 500 and 1500 m depth. In that particular case, particles are tracked backwards in time for 75 years with a 5-day resolution. The calculations are computed for two types of experiments: the first consisted of continually looping the velocity fields every five years, and the second consisted of calculating trajectories

looping for just one year to identify significant fluctuations attributable to interannual oscillation effects.

## 2.4. Horizontal diffusion coefficients

### 2.4.1. One major ocean dynamic challenge

Large-scale ocean circulation and the Earth's climate are sensitive to the presence and magnitude of mesoscale and submesoscale eddies. Eddies continually stir oceanic tracers along and across isopycnals surfaces, strongly influencing the dispersion of physical and biogeochemical tracers (Bracco et al., [2009](#)). At relatively short times and small scales, processes such as internal waves and other subinertial motions dominate mixing. When the dispersion patch becomes large enough to be effectively stretched by straining submesoscale motions, it finally extends around larger mesoscale structures. Baroclinic instabilities of oceanic currents also promote eddy mixing, locally enhancing the eddy kinetic energy and strengthening the meridional transport (Klocker et al., [2012](#); Roach et al., [2016](#)). Hence, diffusivities associated with turbulence and mixing processes at multiple scales have crucial consequences on large-scale circulation.

One of the major challenges in studying ocean dynamics lies in estimating the dispersion of particles by turbulent processes. The choice of realistic eddy horizontal diffusivity coefficients has meant an endless dilemma for oceanographers, being crucial for multiple applications such as assessing the distribution of heat and dispersion of tracers (Ollitrault & Colin de Verdière, [2002](#); Farneti et al., [2010](#)).

Technological advances during the last decade have largely increased the number of Lagrangian methods used to estimate the horizontal diffusion coefficients. Lagrangian estimates often use drifter tracks and statistical techniques to study the motion of single particles or the relative dispersion of groups of particles. Whereas GDP drifter's data have been widely used to estimate lateral diffusivity at the sea surface in different regions of the entire ocean (Abernathey & Marshall, [2013](#); Sallée et al., [2011](#); Chiswell, [2013](#); Zhurbas & Oh, [2003](#)), it has not been until last years that the increasing deployment of a large number of Argo floats has allowed determining diffusivities at depth (Ollitrault & Rannou, [2013](#); Rosell Fieschi, [2014](#); Roach et al., [2016](#)).

Due to its crucial impact on the overturning circulation, eddy lateral diffusivity is a key parameter that must be considered to improve the performance and accuracy in global and regional numerical models. While the advection processes are fairly well reproduced in many ocean numerical models, the subgrid motions are not properly sampled or modelled, leading

to their artificial introduction through different horizontal diffusion parameterizations (Döös et al., [2011](#)). Multiple horizontal diffusion schemes have been considered in global circulation models to assess the effect of subgrid motions on large-scale processes, such as the tropical Pacific Ocean circulation (Maes et al., [1997](#)), El Niño-Southern Oscillation variability (Raynaud et al., [2000](#)), the impact on the northern winter climatology (Stephenson, [1995](#)), and the effects of the damping mechanisms on atmospheric circulation studies (Laursen & Eliassen, [1989](#)). However, adding horizontal diffusion processes is not that simple because turbulent diffusion also depends on the grid resolution of the model (Okubo, [1971](#)), as these define the size and temporal memory of fluctuations around the mean advective values.

#### 2.4.2. Basic diffusive concepts

Tracer dispersal can be a combination of two different types of turbulent processes: mixing processes, which act to reduce tracer gradients, and stirring processes, which act to increase tracer gradients (Eckart, [1948](#)). Mixing processes represent those that can be modelled by diffusion as molecular or very small-scale advective processes, while stirring processes are events resolved by the numerical models (Sundermeyer & Price, [1998](#)). The distinction between these two types of processes is, in practice, one of small versus large scale or, in a modelling context, subgrid-scale parameterized motions versus resolved motions.

Diffusion is a fundamental characteristic of geophysical flows which determines the dispersion of tracers by turbulent processes. The one-dimensional diffusion equation:

$$\frac{\partial C}{\partial t} = K \frac{\partial^2 C}{\partial x^2} \quad (2.37)$$

where  $C$  represents the tracer concentration,  $x$  is the direction of diffusion,  $t$  the time and  $K$  is the horizontal diffusivity. Classic theoretical studies introduce the eddy diffusion coefficient,  $K$ , which introduces the concept of scale-dependent turbulence (Kersalé et al., [2016](#)). The  $K$  coefficient is analogous to the molecular diffusion coefficient in Fick's first law of diffusion but here it interprets mixing as induced by small turbulence rather than by molecular diffusion.

Dispersing properties depend on the spatiotemporal intermittence and turbulence of many processes, so diffusion is process-dependent. Its process dependency is reflected in the horizontal evolution of a patch of a passive tracer in three different phases (Garrett, [1983](#); Sundermeyer & Price, [1998](#)). For a small initial patch, during the first stage, the patch growth can be modelled as a diffusive process. For such times, the area  $A$  occupied by the tracer will grow linearly in time

$$A = 8 \pi K_s t \quad (2.38)$$



where  $K_s$  is an effective small-scale diffusivity and  $t$  is time. The magnitude of this small-scale diffusivity is  $(N^2/f^2) K_z$ , where  $N$  is the buoyancy frequency,  $f$  is the Coriolis parameter, and  $K_z$  is the vertical diffusivity (Young et al., 1982). As the patch grows, it will eventually reach a size where the mesoscale strain field begins to advect the tracer into long-thin streaks. For the second stage of dispersal, the tracer area grows exponentially in time, according to

$$A = 4 \pi \left( \frac{K_s}{\gamma_{rms}} \right) e^{\left( \alpha \gamma_{rms} \left( t - \frac{1}{2} \gamma_{rms}^{-1} \right) \right)} \quad (2.39)$$

where  $\gamma_{rms}$  is the mesoscale strain rate and  $\alpha$  is an order 1 coefficient to be determined (Garrett, 1983). Exponential growth will continue until the horizontal scale of the tracer patch exceeds that of the mesoscale eddies. At that time, the tracer dispersal enters a third stage in which continued stirring by eddies causes streaks to wrap around one another, eventually making the patch more homogeneous. Subsequently, for times much longer than ten days (Sundermeyer & Price, 1998), the rate of dispersal of the patch may again be modelled as a diffusive process, with its area increasing linearly in time,

$$A = 8 \pi K_e t \quad (2.40)$$

where  $K_e$  is the effective eddy diffusivity due to the mesoscale eddies. At later stages of the patch dispersion, its width can be hypothesized to be in a near-steady state.

#### 2.4.3. Radial offset by diffusion method

Direct estimates of the horizontal eddy diffusivity can be quantified through numerical simulations (described in the previous subsection 2.3.2) in combination with drifters' displacements. The simple and effective methodology developed in **Chapter 3.3**, named radial offset by diffusion (ROD), allows not only determining the diffusion coefficients but also studying their spatial variability. To use the ROD method, one must simulate the drifter's trajectory releasing Lagrangian particles over a numerical ocean model product, replicating as accurately as possible the initial trajectory conditions – the same date, depth and position – and obtaining the final position of the virtual particles. Since the resulting radial offsets (distance difference between an actual drifter and virtual particle positions) respond to diffusive processes, one can simulate the isotropic diffusive values that best reproduce the way floats evolve in time with the environmental flow.

To numerically simulate the experimental diffusive patch, we use a simple one-dimensional radial diffusive equation (same equation as 2.37 but written in polar coordinates

with angular symmetry), to be solved as one-dimensional parabolic and elliptic partial differential equations (Skeel & Berzins, 1990):

$$\frac{\partial c}{\partial t} = \frac{1}{r} \frac{\partial}{\partial r} \left( Kr \frac{\partial c}{\partial r} \right) \quad (2.41)$$

where  $c$  is the concentration of particles (number of particles per unit area) and  $K$  is the horizontal (effective) diffusion coefficient constant in time. The boundary conditions to solve the partial differential equations are  $\partial c / \partial r = 0$  both at the origin,  $r = 0$ , and for large radial values,  $r \rightarrow \infty$ . For the initial condition, one can set the concentration equal to 1 within a certain region close enough to the origin and zero elsewhere, implying an initial circular disk containing all diffusive particles. Hence, the initial disk area depends on the spatial resolution of the numerical circulation model used; as time increases, the isotropic diffusive cloud disperses more, decreasing the number of floats inside the original area. The disk area would have a radius  $R_n = (d_{lon}d_{lat}/\pi)^{1/2}$  where longitudinal ( $d_{lon}$ ) and latitudinal ( $d_{lat}$ ) sides are equal to the size of the numerical model grid cell and the initial simulated concentration of particles corresponds to  $N = \pi R_n^2$ .

The temporal spread of the particles follows a Gaussian distribution, which flattens as particles diffuse out of their original disk. The higher the horizontal diffusion coefficient, the flatter the distribution will be, although the total amount of particles remains constant in time and equal to  $N$ . Adjusting a Gaussian distribution to the drifter data and comparing it with a numerical solution of the radial diffusive equation, we can select the diffusivity coefficient that produces the best fit between the experimental and numerical distributions. However, to compare both Gaussian distributions, the first step is to produce a histogram of the concentration of particles or the number of particles for constant areas. The inner radius  $R_1$  must be large enough to ensure that the adjacent rings gather a significant number of particles but, at the same time, small enough to provide adequate resolution near the origin. The subsequent radius has to satisfy that the area of each subsequent ring always remains equal, which implies setting radial intervals that decrease from the origin, i.e., the areas must satisfy  $A = \pi R_j^2 - \pi R_{j-1}^2 = \pi R_1^2$ , where  $j$  identifies the subsequent rings.

After we calculate the concentration of the drifters, we multiply it by a ratio of the total number of numerical particles and the total number of drifters,  $N/n$ . We then fit this distribution with a Gaussian, ensuring that the correlation between the data and the Gaussian fit is high while the inner radius remains small. Finally, we find the coefficient of diffusion that produces a numerical solution of the radial equation that has the best agreement with the

numerical Gaussian distributions. Check subsection [3.3.3](#) to see how the methodology is applied in our study.

The ROD method allows studying the horizontal diffusion spatial variability in the global ocean. To quantify its vertical variability locally, as in **Chapter 3.3** for the western South Atlantic Ocean, the ROD method is computed for different depth ranges and an equation is obtained for the diffusion coefficient as a function of depth. In our case, the equation obtained for the coefficients is (units are  $\text{m}^2 \text{s}^{-1}$ ):

$$K = -2.16z + 4.52 \times 10^3 \quad (2.42)$$

where  $z$  represents the mean depth in each range. The meridional and zonal uniform horizontal diffusivities, which decrease in depth, are interpolated along the water column. This allows us to obtain the horizontal diffusion vertical distribution necessary to release particles in **Chapter 3.4**, adding a realistic radial distance appropriate for the GLORYS12v1 numerical model product and typical for the western South Atlantic Ocean.

The calculated horizontal diffusivities are introduced in the Lagrangian simulation code in order to track particles offline with a numerical circulation model. For this purpose, we use expression [2.34](#) and the extra term  $R\sqrt{2K\Delta t}$  as in equation [2.35](#), with  $K$  as the horizontal diffusion coefficients calculated in **Chapter 3.3** and  $R$  as random numbers from a normal distribution with zero mean; in this way, realistic radial distances are added to the final position of the advected particles. In summary, by adding these stochastic fluctuations to the numerical ocean products, we can better simulate unresolved submesoscale motions.

## **III. RESULTS**



## **CHAPTER 3.1**

---

# **The transfer of Antarctic Circumpolar waters to the western South Atlantic Ocean**

### 3.1.1. Context and objectives

The Antarctic Circumpolar Current (ACC) constitutes the skeleton of the global overturning circulation, as it exchanges heat, mass and freshwater between the Pacific, Atlantic and Indian Oceans (Rintoul & Naveira Garabato, [2013](#)). The persistent westerly wind field around Antarctica is the main forcing mechanism responsible for the eastward direction and predominantly barotropic structure of the ACC, although its path is largely constrained by bathymetric features. However, the ACC does not flow as a single barotropic jet; instead, it exhibits a complex structure of frontal systems that merge and diverge along the circumpolar path, as reflected from the three-dimensional distribution of temperature, salinity and dissolved oxygen (Orsi et al., [1995](#); Sokolov & Rintoul, [2007](#); Meredith, [2003](#); Kim & Orsi, [2014](#)).

A suitable location to measure the transport of the ACC is the latitudinally restricted Drake Passage. As part of the intensive measurements performed in the 1970s and 1980s during the International Southern Ocean Studies program, Whitworth & Peterson ([1985](#)) obtained the first ACC transport estimate, 134 Sv (1 Sv =  $10^6 \text{ m}^3 \text{ s}^{-1}$ ). Later estimates, ranging between 130 and 170 Sv, included those obtained by Orsi et al. ([1995](#)), Naveira Garabato et al. ([2002](#), [2003](#)), and Sokolov & Rintoul ([2009a](#), [2009b](#)). More recent studies have found transports to be as large as 173 Sv (Chidichimo et al., [2014](#); Donohue et al., [2016](#)) and 175 Sv (Colin de Verdière & Ollitrault, [2016](#)).

After crossing the Drake Passage, the ACC enters the Scotia Sea, a semi-enclosed basin bound by submarine ridge systems and island arcs (Figure [3.1](#)). The northern boundary is the North Scotia Ridge, a 2000-km submarine arc with several deep passages, which stretches between the southern tip of South America and the South Georgia Island, and the eastern boundary is the South Sandwich Arc, which has much shallower passages. To the south is the South Scotia Ridge, which is the tectonic extension of the Antarctic Peninsula. The bulk of the water transport into the Scotia Sea is carried out by the jets associated with the Subantarctic Front (SAF) and the Polar Front (PF) (Orsi et al., [1995](#)), which veer northward to exit through the passages in the North Scotia Ridge system (Smith et al., [2010](#)). The remaining ACC water flows eastward through the Scotia Sea associated with the Southern ACC Front (SACCF) and the Southern Boundary (SB) before exiting through the Georgia Passage, located east of South Georgia Island.

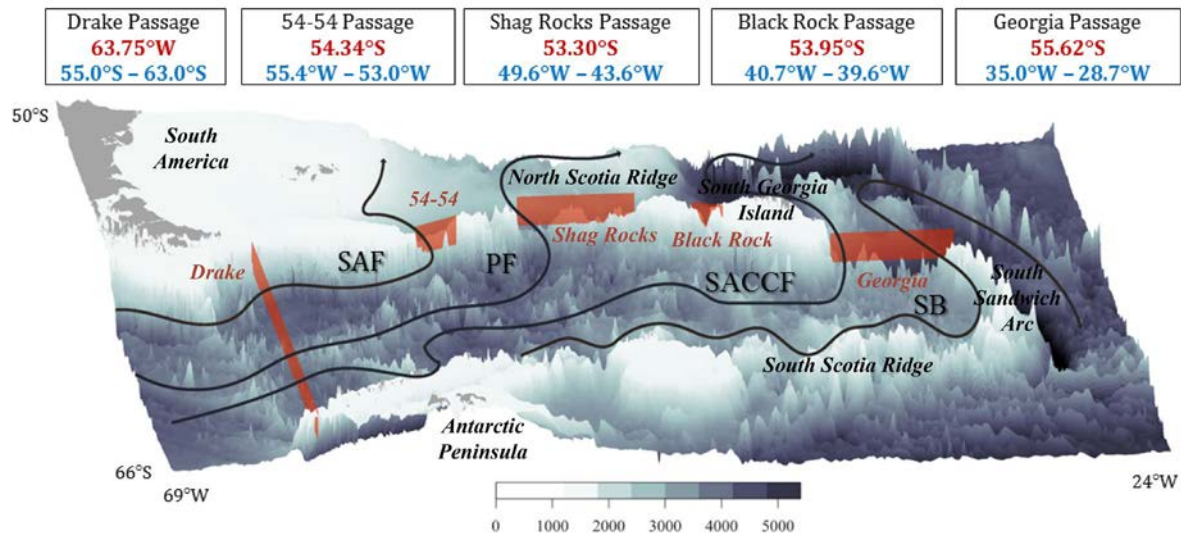


**Figure 3.1.** Bathymetry and main passages in the Scotia Sea, from west to east: Drake, 54-54, Shag Rocks, Black Rock and Georgia. The red bands indicate the location of the sections used in this study to characterize these passages. The surface position of the principal fronts is shown schematically: Subantarctic Front (SAF), Polar Front (PF), Southern Antarctic Circumpolar Current Front (SACCF) and the Southern Boundary (SB).

Several authors have explored how the ACC water masses leave the Scotia Sea through the topographic features along its boundary (e.g., Naveira Garabato et al., [2002](#), [2003](#); Thompson & Sallée, [2012](#)). Smith et al. ([2010](#)) determined that the total net volume transport associated with the SAF and PF systems over the North Scotia Ridge is  $117 \pm 10$  Sv. Thorpe et al. ([2002](#)) and Meredith ([2003](#)) explored the characteristics and temporal variability of the SACCF north of South Georgia Island. In contrast, along the South Scotia Ridge, the presence of the Weddell-Scotia Confluence acts as a barrier to water exchange between the Scotia Sea and the Weddell Gyre (Locarnini et al., [1993](#); Naveira Garabato et al., [2003](#)).

The spatial pathways and temporal variability of the water fluxes through the Scotia Sea remain open questions. In this study, we use the Argo float dataset to document these fluxes, with special attention to the role of the cross-frontal exchange. In subsection [3.1.2](#), we present the study area, the float dataset and the data processing details. In subsection [3.1.3](#), we show how we use the float data to develop hydrographic sections and reference velocities, which are used to obtain the transports. In subsection [3.1.4](#), we explore how these transports are associated with the different fronts, their interannual and seasonal variability and how they evolved during one and a half decades of the Argo dataset. We conclude in subsection [3.1.5](#) with some remarks about what we know and what yet remains unknown regarding the ACC structure across the passages bordering the Scotia Sea.



### 3.1.2. Material and methods

#### 3.1.2.1. Study area

There are three main deep passages along the North Scotia Ridge (Figure [3.1](#)), from west to east: the 54-54 Passage, the relatively deep and wide Shag Rocks Passage, and the narrow Black Rock Passage. Further east, between South Georgia Island (the easternmost landmass of the North Scotia Ridge) and the South Sandwich Arc (34.2°W to 28.9°W), the Georgia Passage is the deepest passage out of the Scotia Sea (3200 m). Hereafter, we will refer to these four passages (the three North Scotia Ridge Passages and the Georgia Passage) as the Northern Passages. There are some other significant passages in the South Sandwich Arc and the South Scotia Ridge, but we chose not to consider them in this study, as justified in the next subsection.

#### 3.1.2.2. Argo floats

The Argo program, which started in 1999 and became fully operational in 2007, provides a valuable set of observations to investigate the hydrography of the upper 2000 m of the water column, study the preferential pathways of intermediate waters, and explore the temporal variability of water transports and pathways. For our study, we have used all Argo float data (flagged as good) with a 1000 m parking depth, from January 2002 to December 2018.

In order to construct average hydrographic sections, from the sea surface down to 2000 m, we have used all float conductivity-temperature-depth (CTD) casts in a 50 km wide band, adjacent to the prescribed location of each passage's section (Figure [3.1](#)). The total number of CTD casts used within these 50 km wide passages is 527, distributed as follow: 221 profiles in Drake Passage, 211 profiles in the North Scotia Ridge passages (76, 116 and 19 profiles for the 54-54, Shag Rocks and Black Rock Passages, respectively), and 95 profiles in Georgia Passage. During the entire period, a few floats recirculated within the Drake and Northern Passages, no floats were found along the South Sandwich Arc, and only three floats crossed the South Scotia Ridge. Therefore, we cannot estimate the transports through the passages in these eastern and southern arcs. Instead, we assume that the amount of ACC water crossing the eastern and southern boundaries of the Scotia Sea is small and will use previous reports for these regions (Thorpe et al., [2002](#); Naveira Garabato et al., [2003](#); Palmer et al., [2012](#)) for drawing our final conclusions in subsection [3.1.5](#).

The number of floats that crossed the Drake Passage eastward is 198. However, in order to obtain the 1000-m reference velocities, we only used those floats (177) that had a 10-day cycle and a parking depth near 1000 m. Of these 1000 m floats, 130 exited the Scotia Sea through

the North Scotia Ridge passages (54, 66 and 10 through the 54-54, Shag Rocks and Black Rock Passages, respectively) and 40 through the Georgia Passage. The difference between the number of 1000 m parking-depth floats entering the Drake Passage and exiting the Northern Passages (177 vs 170) comes from 3 floats that exited through the South Scotia Ridge and 4 floats that either expired within the Scotia Sea or had not yet exited the region by December 2018. Finally, in order to track the number of floats associated with each front and to obtain a mean water residence time within the Scotia Sea, we used 187 floats that were parked at 1000 m, were released at least 30 days prior to reaching the Drake Passage and crossed the entire Scotia Sea.

### 3.1.2.3. Data processing

All float profiles measured near the sections (within the 50 km bands) are used to build the mean potential temperature and salinity vertical sections. These data are vertically interpolated at 10 dbar and horizontally gridded every 25 km, and further smoothed with a low-pass moving horizontal filter of 7 points, leading to an effective horizontal resolution of about 150 km. The neutral density and dynamic height anomaly (referenced to the 1000 dbar level, matching with the parking depth for the selected Argo floats) are calculated at each grid point, and the relative geostrophic velocities are calculated at the central position between grid points using the thermal wind equation.

The 1000 m reference velocities are calculated directly from the distance between the location of the first fix position after the float's arrival to the sea surface and the last surface fix position preceding the previous profile, divided by the time separation of about 10 days (Yoshinari et al., [2006](#); Lebedev et al., [2007](#); Ollitrault & Rannou, [2013](#); Rosell-Fieschi et al., [2015](#)). This is done for the fixings before and after crossing the nominal line defining each passage (Figure [3.1](#)). The velocity error depends on the vertical shear and the duration of the float's vertical excursion and time spent at the sea surface. At the beginning of the Argo program, a float had to spend several hours at the surface in order to transmit the positioning and CTD data, usually spending more than 18 h away from its parking depth. However, recent changes in the transmitting technology allow sending these data in much less time, about 20 min, which reduces the errors associated with the calculation of the reference velocity.

The float positions allow estimating the 1000 m velocity vectors through each passage, and the reference velocity is computed as the component of this velocity vector normal to the vertical section. The absolute geostrophic velocity is hence determined as the relative geostrophic velocity, referenced to the 1000 dbar level, plus the reference velocity at this level, as obtained from float displacements.

The absolute geostrophic velocities allow computing the total geostrophic transports through each passage down to 2000 m. These total transports are then decomposed into baroclinic and barotropic contributions, with the latter calculated as the fraction associated with the 2000 m velocity and the former as the portion linked to the geostrophic velocity relative to this deep level. Further, the transports are computed for the entire water column down to the common deepest neutral density in all sections ( $\gamma^n = 28.00 \text{ kg m}^{-3}$ ) as well as for individual neutral-density layers, selected as to represent the different water masses in the region (Table 3.1) (Reid et al., 1977; Sievers & Nowlin, 1984; Arhan et al., 1999; Naveira Garabato et al., 2002; Smith et al., 2010).

**Table 3.1.** Neutral density definitions for water masses in the Scotia Sea.

| Water Mass   | Acronym   | Neutral density layer ( $\text{kg m}^{-3}$ ) |
|--|-----------|--|
| Subantarctic Surface Water                             | SASW      | $\gamma^n < 26.90$                           |
| Subantarctic Mode Water                                | SAMW      | $26.90 < \gamma^n < 27.18$                   |
| Antarctic Surface Water / Antarctic Intermediate Water | AASW/AAIW | $27.18 < \gamma^n < 27.55$                   |
| Upper Circumpolar Deep Water                           | UCDW      | $27.55 < \gamma^n < 28.00$                   |
| Lower Circumpolar Deep Water                           | LCDW      | $28.00 < \gamma^n < 28.26$                   |
| Weddell Sea Deep Water                                 | WSDW      | $28.26 < \gamma^n < 28.40$                   |

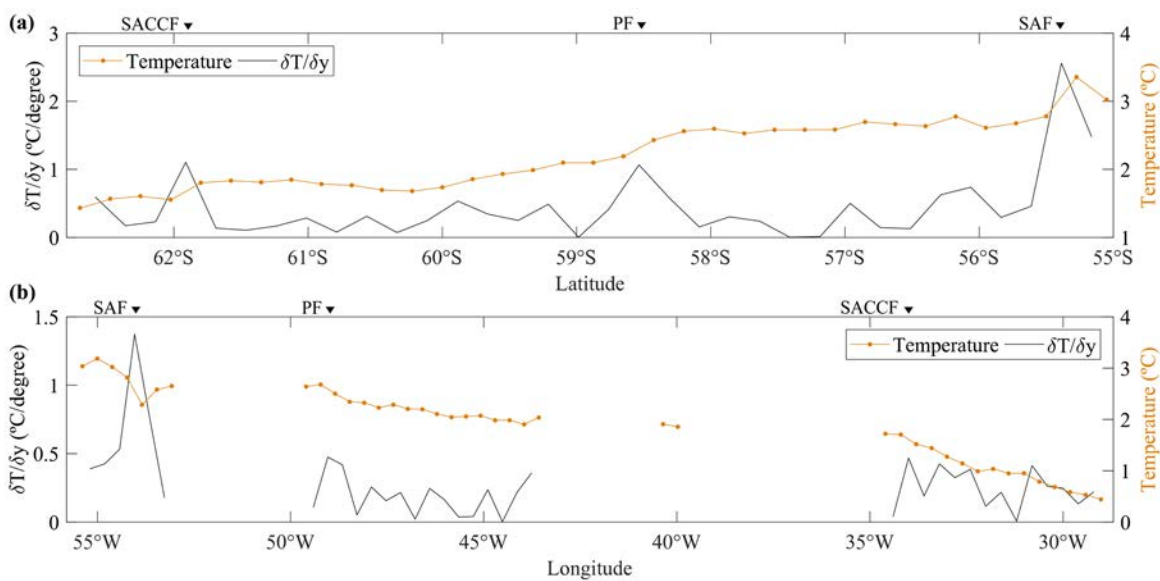


**Figure 3.2.** (a) Temperature (orange line) and temperature gradient (black line) at 1000 m across the Drake Passage and (b) the North Scotia Ridge and Georgia Passages. The locations of the Subantarctic Front (SAF), Polar Front (PF) and Southern Antarctic Circumpolar Current Front (SACCF) are shown.

The location of several fronts is obtained from the maximum temperature gradients at 1000 m (Figure 3.2). Once the fronts are located in all passages, we compute the water transports in those domains delimited by the fronts, both through the Drake and Northern Passages. For all our computations, we have used the frontal positions as obtained using the 2002 - 2018 average section, i.e., under the assumption that these positions are invariant. An analysis of its seasonal and interannual variability confirms that this is a reasonable assumption (Figure 3.3).

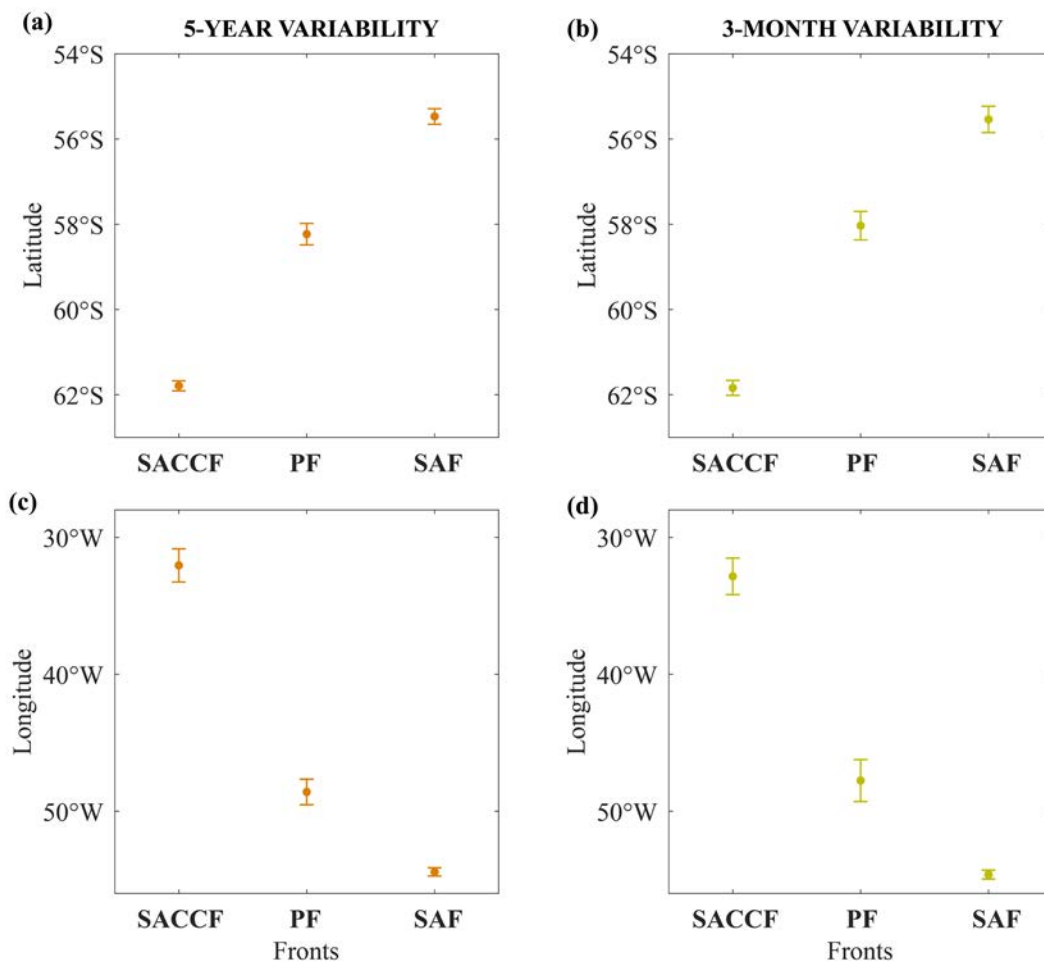


**Figure 3.3.** Mean position of the 1000-m temperature Antarctic fronts for the (left panels) 5-year and (right panels) 3-month periods. The variability is shown as the standard deviation of the eleven 5-year and twelve 3-month realizations, respectively. (a, b) Latitudinal position along the Drake Passage and (c, d) longitudinal position in the Northern Passages (SAF is located in the 54-54 Passage, PF in the Shag Rocks Passage and SACCF in the Georgia Passage).

The Argo floats drifting through the Scotia Sea can also be used to obtain the seasonal and interannual variability of the density fields, reference velocities and transports. The amount of data (number of floats crossing and sampling the reference sections) changes

throughout the year by as much as a factor of two (Table 3.2), but it is sufficient for calculating seasonal changes from 3-month datasets, centred from January through December. Over these 3-month periods, the maximum number of float crossings in the Drake Passage was 61 and the minimum was 29, while the maximum number of CTD casts within the 50 km wide strip was 66 and the minimum was 41. Considering that the Drake Passage section is about 860 km long, the latitudinal average resolutions (distance divided by number of floats) for calculating the reference velocities are between 16 and 30 km while, for building the hydrographic vertical sections, it is between 13 and 21 km.

**Table 3.2.** Number of float tracks and profiles crossing each passage, clustered over 3-month periods.

| PASSAGE |        |          |        |          |            |          |            |          |         |          |
|---------|--------|----------|--------|----------|------------|----------|------------|----------|---------|----------|
|         | Drake  |          | 54-54  |          | Shag Rocks |          | Black Rock |          | Georgia |          |
|         | Tracks | Profiles | Tracks | Profiles | Tracks     | Profiles | Tracks     | Profiles | Tracks  | Profiles |
| Dec-Feb | 54     | 63       | 6      | 11       | 23         | 40       | 13         | 4        | 20      | 36       |
| Jan-Mar | 55     | 54       | 8      | 8        | 25         | 41       | 14         | 4        | 20      | 33       |
| Feb-Apr | 55     | 66       | 9      | 5        | 26         | 38       | 15         | 3        | 13      | 27       |
| Mar-May | 61     | 60       | 14     | 28       | 32         | 33       | 15         | 2        | 10      | 18       |
| Apr-Jun | 55     | 57       | 17     | 43       | 32         | 35       | 15         | 2        | 7       | 16       |
| May-Jul | 45     | 44       | 23     | 47       | 26         | 24       | 16         | 3        | 5       | 26       |
| Jun-Aug | 36     | 41       | 22     | 28       | 15         | 25       | 16         | 5        | 4       | 26       |
| Jul-Sep | 29     | 66       | 18     | 12       | 9          | 18       | 16         | 7        | 5       | 25       |
| Aug-Oct | 29     | 62       | 14     | 11       | 10         | 15       | 15         | 7        | 11      | 16       |
| Sep-Nov | 40     | 58       | 12     | 9        | 14         | 18       | 15         | 8        | 9       | 15       |
| Oct-Dec | 51     | 45       | 12     | 13       | 15         | 22       | 15         | 6        | 14      | 21       |
| Nov-Jan | 59     | 50       | 9      | 13       | 21         | 39       | 15         | 6        | 15      | 26       |

In contrast, the distribution of data for different years is much less even. In order to avoid this intermittency, we have grouped the data in eleven 5-year periods centred on every year between 2006 and 2016 (Table 3.3). Because of the relatively small number of floats crossing the region during 2002 and 2003, we chose not to consider these two years (Table 3.4). Over these 5-year periods, the maximum and minimum number of floats crossing the Drake Passage was 112 and 65, while the maximum number of CTD casts within the 50 km wide strip

was 95 and the minimum was 55. Considering the width of the Drake Passage, this provides reasonably good latitudinal average resolutions of 8 - 13 km for calculating the reference velocities and 9 - 15 km for building the hydrographic vertical sections over the 5-year periods.

**Table 3.3.** Number of float tracks and profiles crossing each passage, clustered over 5-year periods.

|           | PASSAGE |          |        |          |            |          |            |          |         |          |
|-----------|---------|----------|--------|----------|------------|----------|------------|----------|---------|----------|
|           | Drake   |          | 54-54  |          | Shag Rocks |          | Black Rock |          | Georgia |          |
|           | Tracks  | Profiles | Tracks | Profiles | Tracks     | Profiles | Tracks     | Profiles | Tracks  | Profiles |
| 2004-2008 | 76      | 56       | 17     | 13       | 21         | 16       | 4          | 4        | 6       | 20       |
| 2005-2009 | 95      | 73       | 21     | 19       | 32         | 28       | 4          | 5        | 11      | 45       |
| 2006-2010 | 103     | 82       | 26     | 17       | 36         | 42       | 4          | 5        | 17      | 39       |
| 2007-2011 | 112     | 91       | 27     | 19       | 37         | 45       | 4          | 4        | 18      | 36       |
| 2008-2012 | 103     | 84       | 23     | 17       | 41         | 48       | 5          | 7        | 20      | 40       |
| 2009-2013 | 80      | 63       | 20     | 19       | 41         | 51       | 2          | 9        | 13      | 37       |
| 2010-2014 | 65      | 55       | 17     | 17       | 29         | 44       | 2          | 8        | 10      | 16       |
| 2011-2015 | 74      | 63       | 15     | 43       | 29         | 38       | 4          | 9        | 12      | 32       |
| 2012-2016 | 75      | 70       | 15     | 43       | 35         | 42       | 6          | 10       | 18      | 37       |
| 2013-2017 | 89      | 95       | 14     | 45       | 40         | 44       | 10         | 9        | 19      | 39       |
| 2014-2018 | 86      | 90       | 15     | 41       | 36         | 41       | 9          | 4        | 23      | 38       |

**Table 3.4.** Number of float tracks and profiles crossing each passage, clustered over 5-year periods, not used because of the relatively small number of floats crossing the region during 2002 and 2003.

|           | PASSAGE |          |        |          |            |          |            |          |         |          |
|-----------|---------|----------|--------|----------|------------|----------|------------|----------|---------|----------|
|           | Drake   |          | 54-54  |          | Shag Rocks |          | Black Rock |          | Georgia |          |
|           | Tracks  | Profiles | Tracks | Profiles | Tracks     | Profiles | Tracks     | Profiles | Tracks  | Profiles |
| 2002-2006 | 21      | 15       | 4      | 9        | 6          | 11       | 0          | 3        | 3       | 9        |
| 2003-2007 | 45      | 32       | 11     | 10       | 12         | 10       | 0          | 3        | 4       | 14       |

Finally, the procedure followed for each 3-month and 5-year interval is the same as the procedure used for the entire dataset. The seasonal variability is calculated as the standard deviation (SD) of the twelve 3-month calculations, while the interannual variability is calculated as the SD of the eleven 5-year realizations. Further, we use a simple procedure to assess the error bars associated with the reduction in the number of observations. The

procedure consists of randomly reducing the casts and reference velocities in the 2002 - 2018 mean section to the actual number of casts and reference velocities for each one of the 3-month and 5-year periods (Tables 3.2 and 3.3); this is done 100 times for each case and the SD is calculated.

### 3.1.3. Results

#### 3.1.3.1. Reference velocities

All Argo floats analyzed in this study entered the Scotia Sea via the Drake Passage and drifted east and north. In Figure 3.4, we show the positions of all floats as they crossed the nominal location of the western and northern sections enclosing the Scotia Sea, and in Figure 3.5, we show the inferred 1000 m velocity vectors.

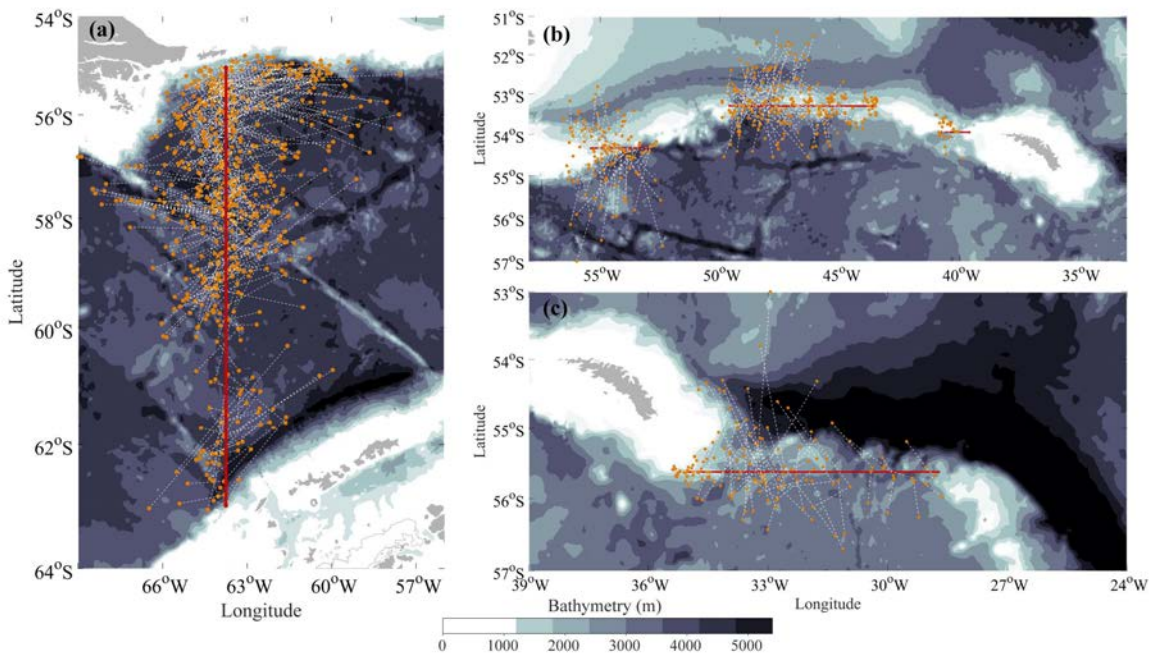


**Figure 3.4.** Argo floats crossing (a) the Drake Passage, (b) the North Scotia Ridge Passages (54-54, Shag Rocks and Black Rock), and (c) the Georgia Passage. A red line shows the location of the vertical sections across the passages. The orange dots show the surface float positions (last position before submerging and first position after surfacing), joined with a thin white dotted line. The white areas represent regions with water depth less than 1000 m.

The 1000 m Argo float velocities are validated using two sets of ship acoustic Doppler current profiler (SADCP) velocities. The first one comes from the Drake Passage section between 64°W and 62°W (1979 to 2013), while the second one comes from the Laurence Gould

Platform (2004 to 2018, with variable routes between the southern tip of South America and the Antarctic Peninsula), both included in the National Oceanic and Atmospheric Administration (NOAA) SADCP database (Caldwell et al., 2010). All datasets present velocities with similar patterns, with velocity maxima of  $0.2 - 0.3 \text{ m s}^{-1}$  between  $55^\circ\text{S}$  and  $56^\circ\text{S}$  (position of the SAF) and between  $58^\circ\text{S}$  and  $59^\circ\text{S}$  (PF location), and a more moderate increase (up to  $0.1 \text{ m s}^{-1}$ ) near  $62^\circ\text{S}$  (SACCF position) (Figure 3.6). We have also estimated the errors in the 1000 m reference velocities to be always well below  $0.01 \text{ m s}^{-1}$ , in good agreement with the velocity errors for these same passages according to the ANDRO database (Lebedev et al., 2007; Ollitrault & Rannou, 2013).

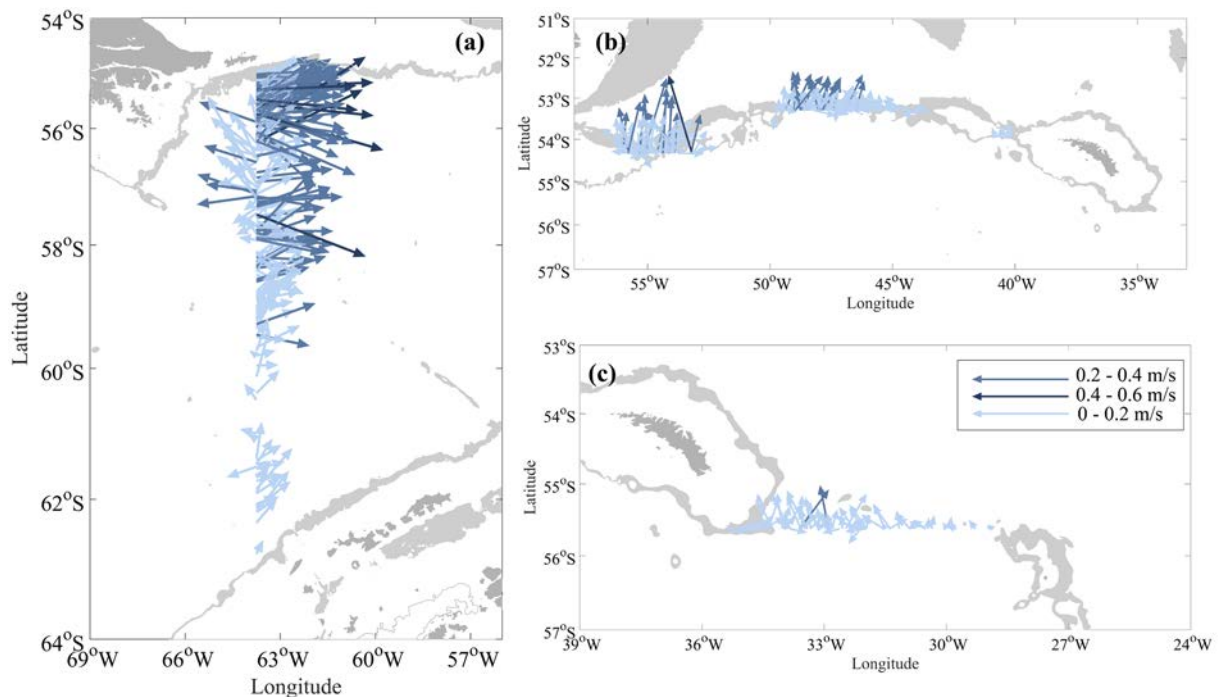


**Figure 3.5.** Velocity vectors at 1000 m along the vertical sections in (a) the Drake Passage, (b) the North Scotia Ridge Passages (54-54, Shag Rocks and Black Rock), and (c) the Georgia Passage. The arrows denote the velocity vectors associated with all floats crossing the passages, coloured according to their speed. The 1000 - 2000 m region is grey-shaded as to indicate the practical limits of our data.

We count the number of floats that cross the Drake and Northern Passages considering only those floats launched relatively far from the passages section, specifically at least three profiling cycles away (30 days). The comparison of the normal-to-section velocities and the number of floats crossing 25 km long transects shows a high (and significant,  $p < 0.01$ ) correlation between both variables: 0.85 for the Drake Passage and 0.75 for the Northern Passages (Figure 3.7). Both the peak zonal velocities and the largest number of floats entering the Scotia Sea correspond to the location of the SAF ( $55^\circ\text{S} - 56^\circ\text{S}$ ) and the PF ( $58^\circ\text{S} - 59^\circ\text{S}$ ), with fewer floats crossing east in between. South of  $59^\circ\text{S}$ , the number of floats is small yet non-



negligible. In the northern boundary of the Scotia Sea, the largest velocities and number of floats are found in the 54-54 Passage (associated with the SAF), the Shag Rocks Passage (associated with the PF) and the Georgia Passage (associated with the SACCF). These significant correlations indicate that floats tend to get caught in the frontal jets, hence reducing the velocity uncertainties in those regions with the swiftest flow.

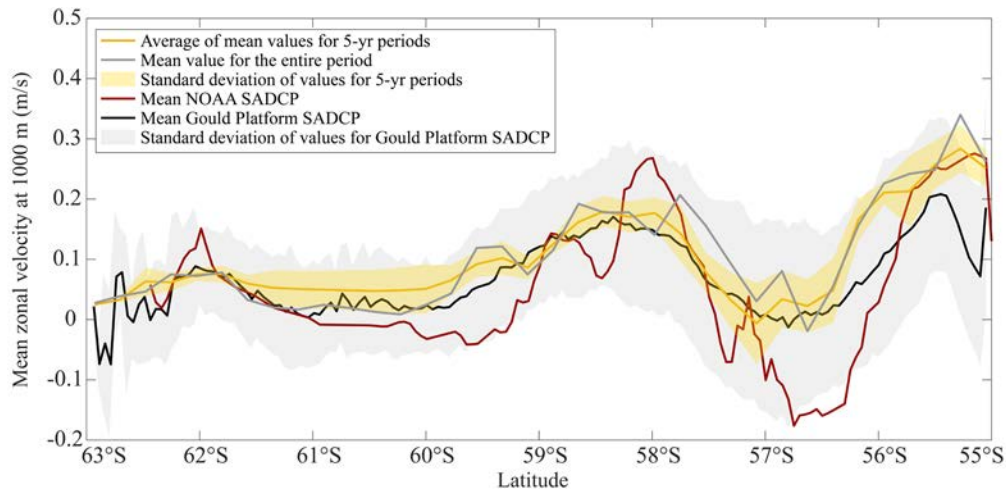


**Figure 3.6.** Mean 1000 m zonal velocities cross the Drake Passage, as inferred from Argo floats (mean values for the entire period and average of the 5-year period values), and as obtained with the NOAA SADCP dataset and with the Laurence M. Gould platform. The shaded areas represent the standard deviations of values from the Laurence M. Gould dataset.

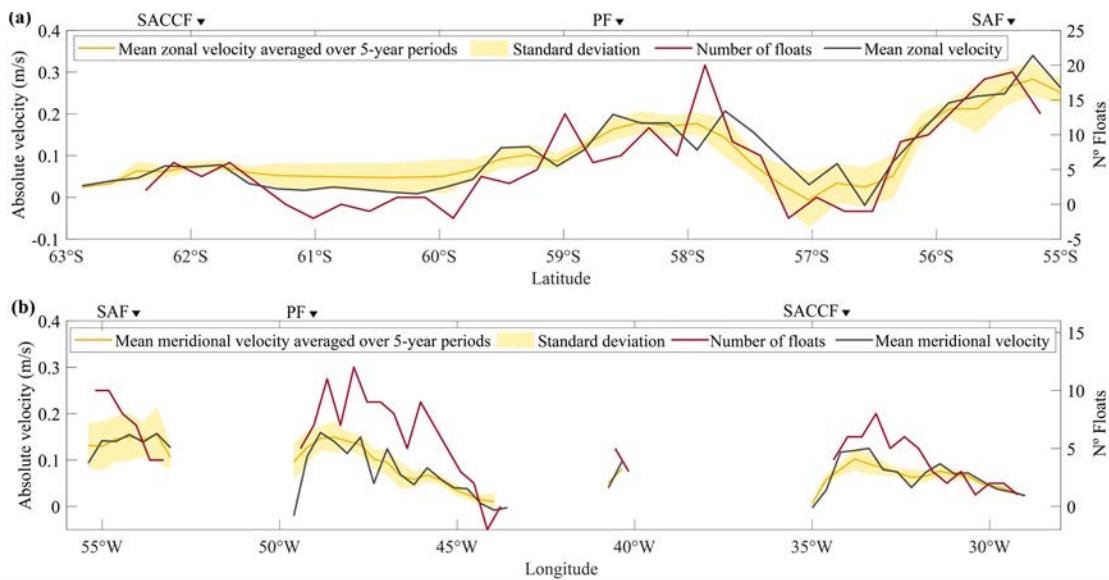


**Figure 3.7.** (Left axes) Normal-to-section 1000 m velocities and (right axes) number of floats for the entire period (purple line) crossing 25 km long transects, for (a) the Drake Passage and (b) the Northern Passages. The velocities are calculated as the mean for the entire period (2002 - 2018; black line) and as the average of the means for each 5-year periods (2006 - 2016; orange line); in the last case, the standard deviation is shown (yellow band).

### 3.1.3.2. Vertical sections

The Argo CTD casts, after gridding and low-pass filtering, can be used to represent the vertical distribution of temperature, salinity, neutral density and normal-to-section geostrophic velocity (Figure 3.8). The sloping temperature, salinity and density contours that characterize the SAF and PF show up clearly in the northern portion of the Drake Passage (Figure 3.8a). Relatively cold and salty waters are found at depth and south of the PF (58°S - 59°S). The temperature minima ( $\theta < 0$  °C) correspond to the near-surface southern waters (50 - 200 m), which are also relatively fresh, reflecting the relatively high precipitation (peak precipitation values in Antarctica, about 1000 – 1500 mm, take place in the western Antarctic Peninsula) and the summer melting of ice shelves and icebergs (Van Den Broeke & Van Lipzig, 2004; Liu & Curry, 2010). In contrast, the relatively warm surface waters in the South American side reveal the net annual-mean heat gain at these lower latitudes (Gille et al., 2016).

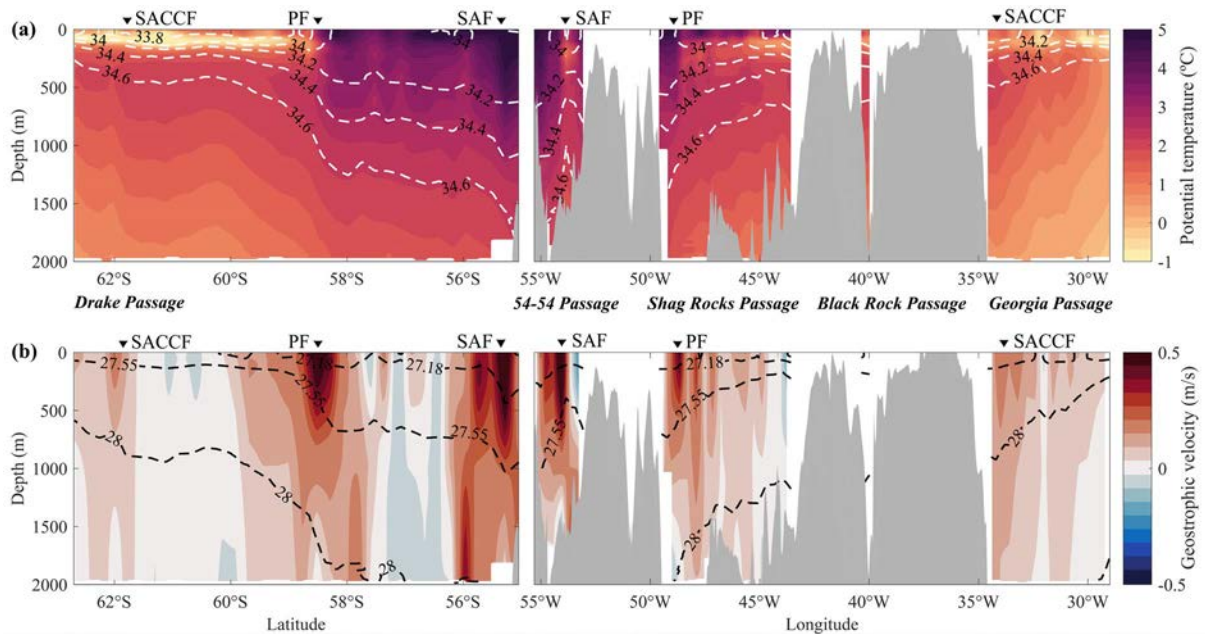


**Figure 3.8.** Vertical sections for (left) the Drake Passage and (right) the Northern Passages. (a) Potential temperature (coloured, °C) and practical salinity (dashed contours). (b) Geostrophic velocity (coloured, m/s; in Drake Passage the positive values correspond to eastward velocities, for the Northern Passages the positive velocities correspond to northward velocities) and neutral density (dashed contours,  $\text{kg m}^{-3}$ ; the selected isoneutrals denote the water mass boundaries in Table 3.1). The regional bathymetry is shaded in grey.

The north-south temperature and salinity distribution in the Drake Passage are reflected by analogous west-east changes in the Northern Passages (Figure 3.8a). The SAF is located within the 54-54 Passage and the PF is found in the western portion of the Shag Rocks Passage. The Georgia Passage also reveals steep isolines, probably reflecting the presence of

the two southernmost fronts (SACCF and SB). The relatively cold and fresh near-surface waters (50 - 200 m) – located south of the PF in the Drake Passage – are found east of the PF in the Northern Passages.

The density distributions confirm that the horizontal gradients in salinity and temperature drive a substantial density gradient, i.e., the thermohaline front turns into a density front (Figure 3.8b). This is true over most of the water column except in the near-surface region (50 - 200 m) south of the PF in the Drake Passage and east of the PF in the Northern Passages, where we find cold and fresh Antarctic surface waters. As a result, the density gradients are maximum at all depths in the SAF and deeper than 200 m in the PF.

The frontal systems show up clearly in the inferred velocity fields, with peak eastward velocities in excess or close to  $0.5 \text{ m s}^{-1}$  associated to the SAF ( $55^\circ\text{S} - 56^\circ\text{S}$  in the Drake Passage and  $54^\circ\text{W} - 55^\circ\text{W}$  in the 54-54 Passage) and PF ( $58^\circ\text{S} - 59^\circ\text{S}$  in the Drake Passage and  $48^\circ\text{W} - 49^\circ\text{W}$  in the Shag Rocks Passage) (Figure 3.8b). Further south in the Drake Passage ( $61.5^\circ\text{S} - 63^\circ\text{S}$ ) and east along the northern rim of the Scotia Sea ( $29^\circ\text{W} - 34^\circ\text{W}$  in the Georgia Passage), we find the shallower and weaker currents associated with the southern SACCF; the SB is hardly seen as it appears very close to the continental shelf of the Antarctic Peninsula.

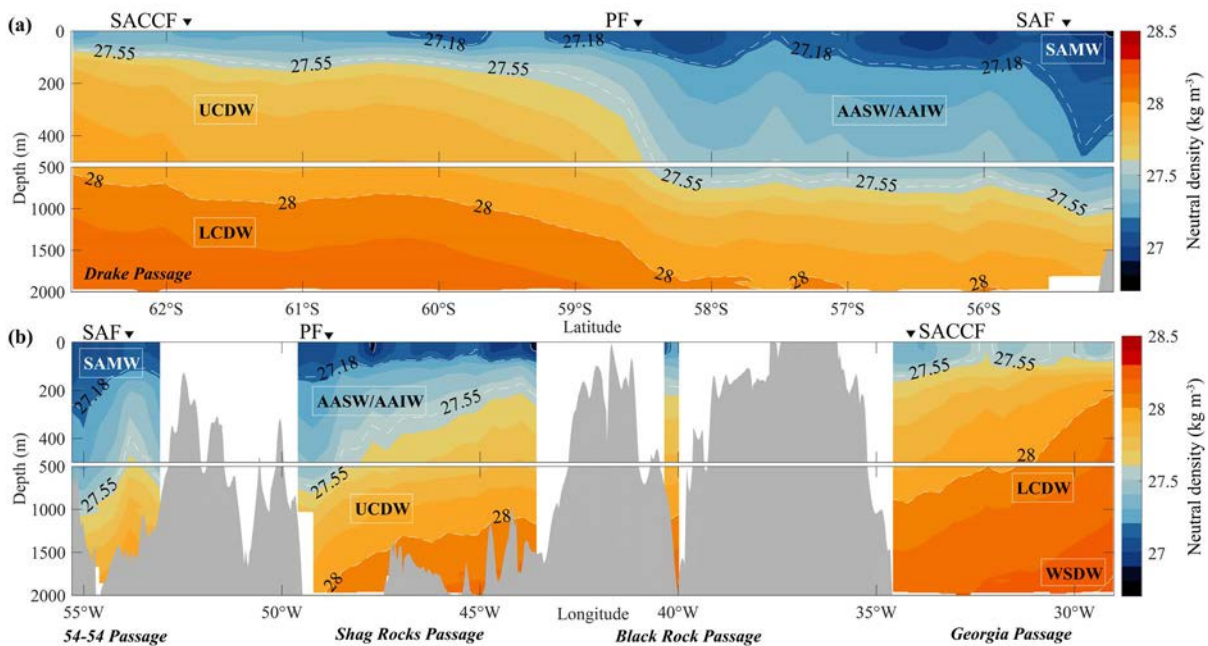


**Figure 3.9.** Density distribution across (a) the Drake Passage, and (b) the North Scotia Ridge (54-54, Shag Rocks and Black Rock) and Georgia Passages. The different water masses are labelled following the boundaries in Table 3.1.

Some light SASW appears occasionally in Argo floats crossing the northern end of the Drake Passage and crossing the middle and eastern end of the Shag Rocks Passage, but its presence is ephemeral, and SASW barely shows up in the mean density sections (Figure 3.9).

Further, only waters with neutral density less than  $28.00 \text{ kg m}^{-3}$  are fully sampled by the Argo floats (Figure 3.9). In the northern portion of the Drake Passage and the western part of the Shag Rocks Passage, the deepest waters have  $\gamma^n = 28.00 \text{ kg m}^{-3}$  (in the 54-54 Passage, because of its relatively shallow bathymetry, the deepest waters do not even reach this value). In contrast, in most of the Drake and Northern Passages, at 2000 m we find waters substantially denser than  $28.00 \text{ kg m}^{-3}$ . For this reason and under the assumption of zero diapycnal mixing, we will be able to close the water balances only down to  $\gamma^n = 28.00 \text{ kg m}^{-3}$ , i.e., for the surface, mode, surface-intermediate and upper-circumpolar deep waters (Table 3.1).

In the Drake Passage, the tilting isoneutrals are associated with the SAF near  $55.5^\circ\text{S}$  and with the PF near  $58.5^\circ\text{S}$  (Figure 3.9). In the northern half of the Drake Passage, the  $28.00 \text{ kg m}^{-3}$  isoneutral is fairly flat and close to 2000 m while, from the PF southwards, this isoneutral progressively rises some 1300 m, all the way to the Antarctic Peninsula. In the southern end of this section (near  $62^\circ\text{S}$ ), because of the near-surface intrusion of relatively fresh waters, we observe the sloping isoneutrals mainly at depths greater than 200 m.

The latitudinal density distribution in the Drake transect is largely mirrored by the zonal distribution along the northern boundary of the Scotia Sea. The deepest western waters again have neutral densities close to  $\gamma^n = 28.00 \text{ kg m}^{-3}$ . The SAF shows up in the middle of the 54-54 Passage and the PF is located in the western end of the Shag Rocks Passage. The  $28.00 \text{ kg m}^{-3}$  isoneutral and adjacent layers display large changes in depth in most of the Shag Rocks and Georgia Passages, in particular rising almost 700 m between the western and eastern ends of the Georgia Passage.

### 3.1.4. Discussion

#### 3.1.4.1. Water transports

The total water transports through the different passages down to 2000 m are presented in Table 3.5. The total input through the Drake Passage is  $164.2 \pm 10.8 \text{ Sv}$ , with a baroclinic contribution of  $55.6 \pm 12.6 \text{ Sv}$  and a barotropic part of  $108.6 \pm 12.8 \text{ Sv}$ . The total output through the Northern Passages is  $159.3 \pm 10.2 \text{ Sv}$ , with baroclinic and barotropic shares of  $64.6 \pm 19.6 \text{ Sv}$  and  $94.7 \pm 20.8 \text{ Sv}$ , respectively; overall, the outputs are roughly equally split among the 54-54, Shag Rocks and Georgia Passages ( $42.6$ ,  $59.6$  and  $53.8 \text{ Sv}$ , respectively). This apparently suggests a fairly good water balance, with a net convergence of only  $4.9 \text{ Sv}$  into the Scotia Sea; however, this may be misleading, as the water layers denser than  $\gamma^n > 28.00 \text{ kg m}^{-3}$  are only partly represented in some of our vertical sections.

**Table 3.5.** Total geostrophic transports through the passages down to 2000 m, with their baroclinic and barotropic contributions.

|         | Passage        | Total transport (Sv) | Baroclinic transport (Sv) | Barotropic transport (Sv) |
|---------|----------------|----------------------|---------------------------|---------------------------|
| Inflow  | Drake          | 164.2 ± 10.8         | 55.6 ± 12.6               | 108.6 ± 12.8              |
| Outflow | 54-54          | 42.6 ± 5.6           | 15.5 ± 11.0               | 27.1 ± 11.3               |
|         | Shag Rocks     | 59.6 ± 7.2           | 32.1 ± 10.4               | 27.5 ± 13.2               |
|         | Black Rock     | 3.3 ± 1.5            | 2.9 ± 1.4                 | 0.5 ± 0.7                 |
|         | Georgia        | 53.8 ± 2.6           | 14.2 ± 1.4                | 39.6 ± 3.2                |
|         | Total Northern | 159.3 ± 10.2         | 64.6 ± 19.6               | 94.7 ± 20.8               |

An alternative view would be to assess the water transports down to the 28.00 kg m<sup>-3</sup> isoneutral, which are layers fully sampled in all sections enclosing the Scotia Sea. Down to this level, and under the assumption of along-isoneutral flow, we would expect that the water transport would be balanced. As expected, the absolute transports are lower: 140.8 ± 7.4 Sv entering through the Drake Passage (baroclinic and barotropic contributions of 42.8 ± 8.9 Sv and 98.0 ± 7.4 Sv, respectively) and 115.9 ± 8.3 Sv exiting through the Northern Passages (baroclinic and barotropic parts of 45.8 ± 18.8 Sv and 70.1 ± 19.3 Sv, respectively). The imbalance is now much larger than down to 2000 m, with a total convergence of 24.9 Sv; most of this convergence corresponds to the AASW/AAIW (9.7 Sv) and UCDW (12.4 Sv) layers (Table 3.6). In the concluding section of this article, we will argue that this imbalance corresponds to water crossing the shallow regions in the Northern Passages.

**Table 3.6.** Total geostrophic transports (Sv) per layer through the Passages down to  $\gamma^n = 28.00$  kg m<sup>-3</sup>.

| Layer ( $\gamma^n$ , kg m <sup>-3</sup> ) | Drake (Sv) | Northern (Sv) | 54-54 (Sv) | Shag Rocks (Sv) | Black Rock (Sv) | Georgia (Sv) |
|---|------------|---------------|------------|-----------------|-----------------|--------------|
| SAMW (26.90 - 27.18)                      | 12.8       | 10.0          | 5.3        | 4.7             | -               | -            |
| AASW/AAIW (27.18 - 27.55)                 | 44.0       | 34.3          | 15.0       | 15.7            | 0.4             | 3.2          |
| UCDW (27.55 - 28.00)                      | 84.0       | 71.6          | 20.6       | 31.2            | 2.0             | 17.8         |
| All (< 28.00)                             | 140.8      | 115.9         | 40.9       | 51.6            | 2.4             | 21.0         |
| Barotropic (< 28.00)                      | 98.0       | 70.1          | 24.2       | 25.4            | 2.0             | 18.5         |
| Baroclinic (< 28.00)                      | 42.8       | 45.8          | 16.7       | 26.1            | 0.4             | 2.5          |

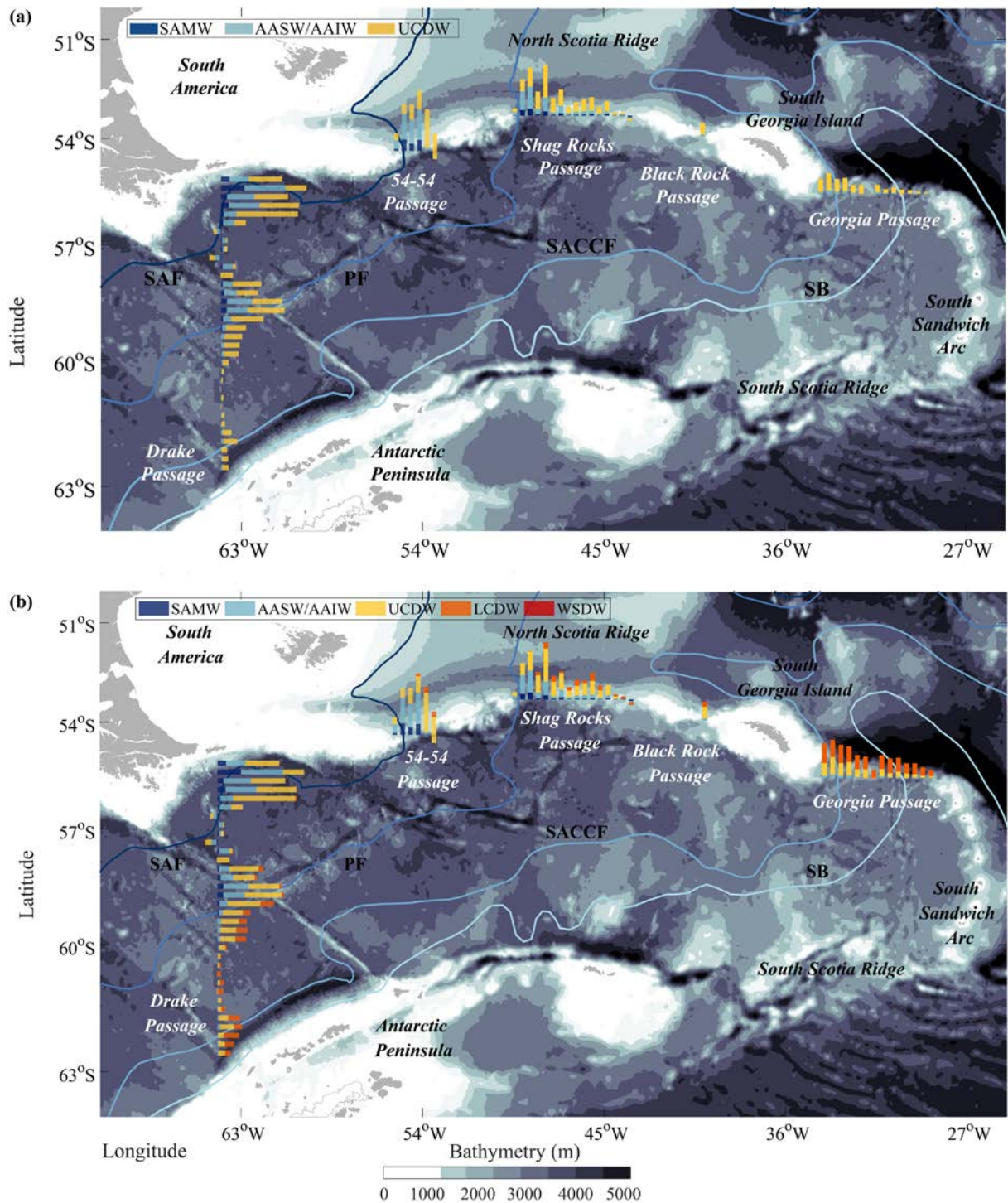


**Figure 3.10.** Transports per water mass (a) down to  $\gamma^n = 28.00 \text{ kg m}^{-3}$  and (b) down to 2000 m at 25 km intervals crossing each passage. The colour bars illustrate the partitioning of the transports among water masses (dark blue, SAMW; light blue, AASW/AAIW; yellow, UCDW; orange, LCDW; red, WSDW). The surface location of the different fronts comes from Greene (2020) through Orsi & Whitworth III (2005), using all historical hydrographic data available for the Southern Ocean and frontal definitions from Orsi et al. (1995).

The spatial distribution of water transports per layer is summarized in Figure [3.10](#). The zonal transports through the Drake Passage are clustered around the frontal systems: SAF (55°S - 56°S), PF (58°S - 59°S) and SACCF (52°S - 63°S). Similarly, the meridional transports through the Northern Passages are also dominated by the along frontal flow: SAF (54°W - 55°W), PF (48°W - 49°W) and SACCF (33°W - 34°W).

The relative contribution of mode and surface-intermediate waters vs UCDW changes in a similar fashion both latitudinally and zonally: the largest contribution of the mode and surface-intermediate waters is in the northern half of the Drake Passage and in the 54-54 and Shag Rocks Passages, while the largest fraction of UCDW is in the southern half of the Drake Passage and in the Georgia Passage (Figure [3.10a](#)). In particular, the SAMW outflow occurs entirely through the North Scotia Ridge discontinuities and is totally absent in the Georgia Passage; in contrast, we find AASW/AAIW, UCDW and LCDW in all passages. A small presence of WSDW in the eastern part of the Georgia Passage is also visible in the water transports down to 2000 m (Figure [3.10b](#)).

#### 3.1.4.2. Cross-frontal exchange

Frontal systems are often thought to act as barriers to different water masses but they are also the source of mesoscale and submesoscale instabilities that induce cross-frontal transfer. With this idea in mind, we wish to track the amount of water that enters through the Drake Passage between the frontal systems (as defined in subsection [3.1.2.3](#)) and how these waters are distributed between these same fronts when crossing the Northern Passages.

The three main frontal systems in the Drake Passage (from north to south: SAF, PF and SACCF) are also traceable in the Northern Passages: SAF reaches the 54-54 Passage, PF the Shag Rocks Passage and SACCF the Georgia Passage (Figures [3.2](#), [3.8](#) and [3.9](#)). Therefore, we are interested in exploring not only how the water entering through the Drake Passage exits through the Northern Passages (Tables [3.5](#) and [3.6](#)) but also to assess if there is some conservancy of the transports between the frontal systems that reflects some dynamical pathways. The results suggest that there are substantial mass transformations, with the region between the SAF and the PF losing as much as 62.8 Sv while all other regions gain water transport; north-west of the SAF gains 6.9 Sv, the region between PF and SACCF gains 19.6 Sv, and south-east of the SACCF gains 11.4 Sv (Table [3.7](#)).

**Table 3.7.** Geostrophic transports ( $S_v$ ) between fronts and through the different passages down to  $\gamma^n = 28.00 \text{ kg m}^{-3}$ : inflow through the Drake Passage and outflow through the Northern Passages. The longitudes roughly indicate the geographical boundaries (Figure 3.10). S.A. stands for South America, A.P. stands for Antarctic Peninsula and S.S.A. stands for the South Sandwich Arc.

| <b>Drake</b>    |                 |                   |                 |                   |                  |                     |
|-----------------|-----------------|-------------------|-----------------|-------------------|------------------|---------------------|
| <b>S.A.-SAF</b> | <b>SAF-PF</b>   |                   | <b>PF-SACCF</b> |                   |                  | <b>SACCF-A.P.</b>   |
| 18.1            | 83.2            |                   | 34.4            |                   |                  | 5.1                 |
| <b>54-54</b>    |                 | <b>Shag Rocks</b> |                 | <b>Black Rock</b> | <b>Georgia</b>   |                     |
| <b>S.A.-SAF</b> | <b>SAF-PF</b>   |                   | <b>PF-SACCF</b> |                   |                  | <b>SACCF-S.S.A.</b> |
| 25.0            | 20.4            |                   | 54.0            |                   |                  | 16.5                |
| <b>S.A.-SAF</b> | <b>SAF-53°W</b> | <b>49°W-PF</b>    | <b>PF-47°W</b>  | <b>41°W-40°W</b>  | <b>34°W-33°W</b> | <b>33°W-29°W</b>    |
| 25.0            | 15.9            | 4.5               | 47.1            | 2.4               | 4.5              | 16.5                |
| 40.9            |                 | 51.6              |                 | 2.4               | 21.0             |                     |

A complementary view of how water transport remains both blocked and mixed by the frontal systems is provided by the floats' trajectories. These trajectories will mostly resemble the motions at the 1000 m parking depth, modified by the relatively short period when the floats do their vertical cycle and remain at the sea surface. Nevertheless, because of the predominance of the barotropic contribution and since the geostrophic contribution is aligned with the frontal systems, we expect that the flow direction at all depths will remain similar to the 1000 m flow heading (Figure 3.8b).

The principal pathways for those floats crossing the Drake Passage on either side of a front (subsection 3.1.2.3) are shown in Figure 3.11. The results are consistent with the transports between fronts as reported in Table 3.8, with those floats entering between the SAF and the PF (Figure 3.11b) being most dispersed; only 29% of the floats remain between these fronts, with the losses split fairly equally between the adjacent domains. The floats north of the SAF and south of the SACCF also display substantial scattering. In contrast, those floats crossing the Drake Passage between the PF and the SACCF appear to experience the fewest losses (Table 3.8).



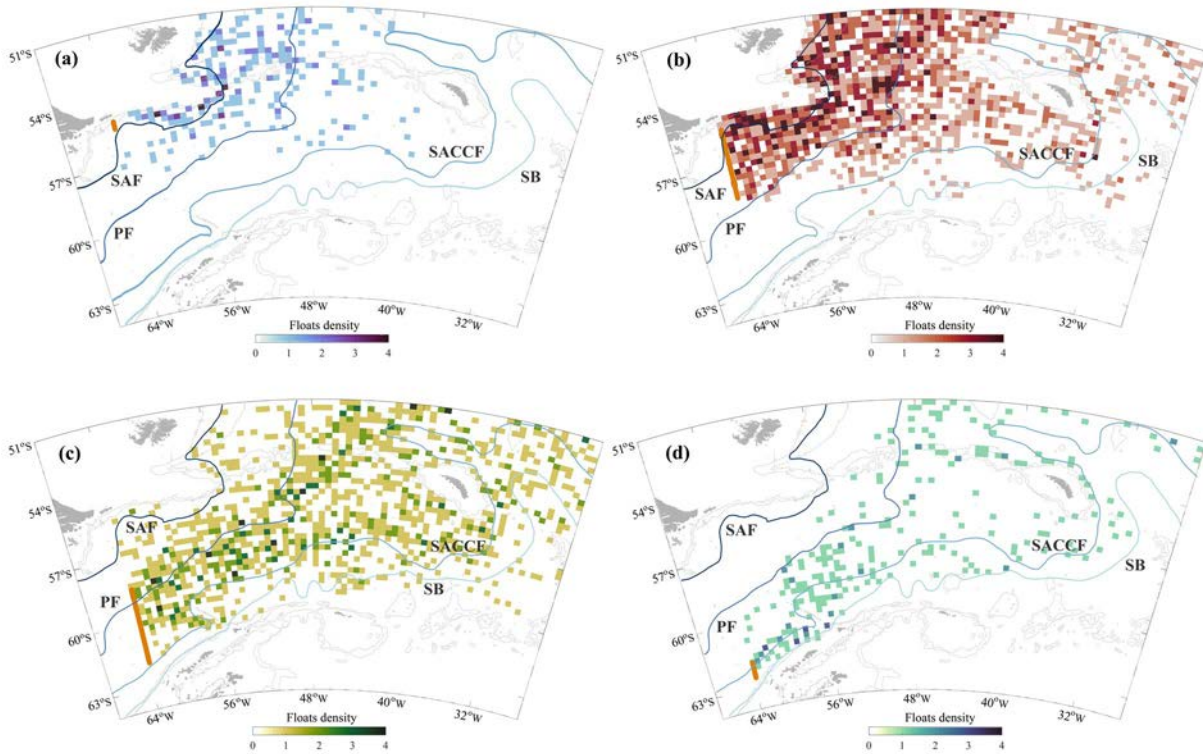


**Figure 3.11.** Number of floats that drift in the Scotia Sea after entering through the Drake Passage, counted over  $0.25^\circ \times 0.5^\circ$  latitude-longitude grid elements. The floats are identified and counted by their latitude of origin, represented by orange lines, in the Drake Passage: (a) South America to SAF, (b) SAF to PF, (c) PF to SACCF, and (d) SACCF to the Antarctic Peninsula. The surface location of the different fronts, as defined by Orsi et al. (1995), comes from Orsi & Whitworth III (2005) and available in Greene (2020) dataset.

**Table 3.8.** Number of Argo floats entering and departing the Scotia Sea between frontal systems; only those floats that exit the Scotia Sea are considered. The numbers in the first column indicate the floats entering through the Drake Passage and the numbers in the top row represent the floats exiting through the Northern Passages; the figures in each cell represent the number of floats entering and leaving through the corresponding frontal domain. Abbreviations: S.A. stands for South America, A.P. stands for Antarctic Peninsula and S.S.A. stands for the South Sandwich Arc.

| Output \ Input  | S.A.-SAF | SAF-PF | PF-SACCF | SACCF-S.S.A |
|-----------------|----------|--------|----------|-------------|
| Input           | 53       | 46     | 70       | 18          |
| S.A.-SAF<br>22  | 11       | 7      | 4        | 0           |
| SAF-PF<br>119   | 40       | 34     | 37       | 8           |
| PF-SACCF<br>40  | 2        | 5      | 25       | 8           |
| SACCF-A.P.<br>6 | 0        | 0      | 4        | 2           |

Finally, we can use the time taken by floats to cross from the Drake to the Northern sections to estimate the mean residence time of water masses near 1000 m in the Scotia Sea. The residence time for individual floats changes greatly, from as little as 20 days for those floats entering through the northern edge of the Drake Passage to as much as three years for those crossing through the southern end (Figure 3.12).

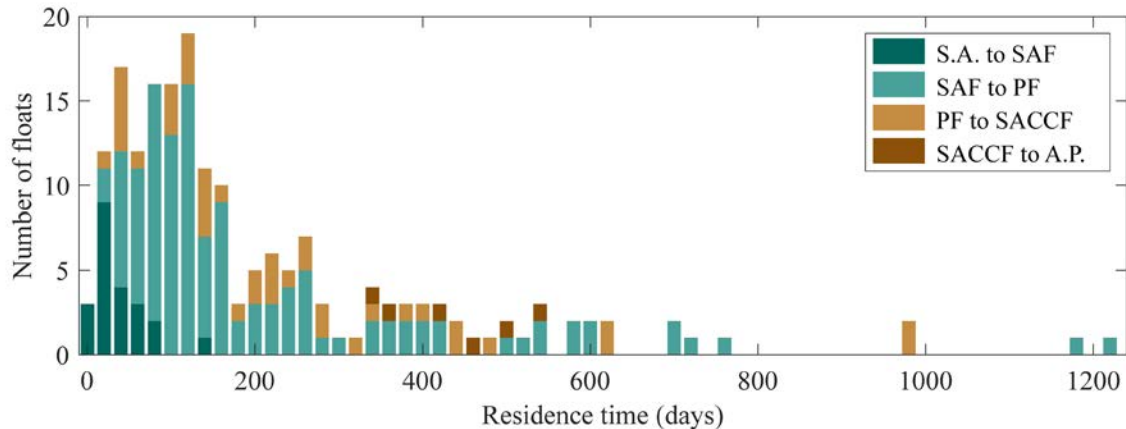


**Figure 3.12.** Number of floats as a function of residence time in the Scotia Sea, split according to their position between frontal systems as they enter the Drake Passage: South America (S.A.) to SAF, SAF to PF, PF to SACCF, and SACCF to the Antarctic Peninsula (A.P.). Each bar width corresponds to 20 days of residence time.

Considering only those floats that cross the Scotia Sea, the mean residence time is  $219 \pm 213$  days. According to the location of these floats as they cross the Drake Passage, the mean residence is  $45 \pm 30$  days for those floats entering between S.A. and the SAF,  $223 \pm 213$  days for floats entering between SAF and PF,  $266 \pm 226$  days for those entering between PF and SACCF, and  $443 \pm 77$  days for those crossing the Drake Passage between SACCF and A.P. The Scotia Sea has an area of about  $9 \times 10^5$  km<sup>2</sup>, and the corresponding volume down to 2000 m is about  $1.8 \times 10^{15}$  m<sup>3</sup>; therefore, a residence time of 219 days (7.3 months) would represent an average water transport of 95 Sv, which is not too far from our 2000 m barotropic transport through the Drake Passage (109 Sv).

#### 3.1.4.3. Interannual variability

Intense atmospheric forcing can modify the slope of isopycnals across the Southern Ocean and therefore influence the baroclinic transport of the ACC (Sokolov & Rintoul, 2009a, 2009b; Rintoul & Naveira Garabato, 2013; Kim & Orsi, 2014). Hence, we split the Argo data into 5-year overlapping periods in order to calculate the interannual variability. The mean density and normal-to-section velocity fields can be calculated by averaging the 5-year period

data, providing a total of 11 realizations centred from 2006 to 2016 (utilizing data spanning the 2004 - 2018 period). The resulting mean fields are nearly indistinguishable from the mean fields obtained using the full set of floats (Figures 3.8, 3.9 and 3.13). Additionally, the changes in the latitudinal and longitudinal positions of the 1000 m fronts are relatively small and are therefore ignored (Figure 3.3).

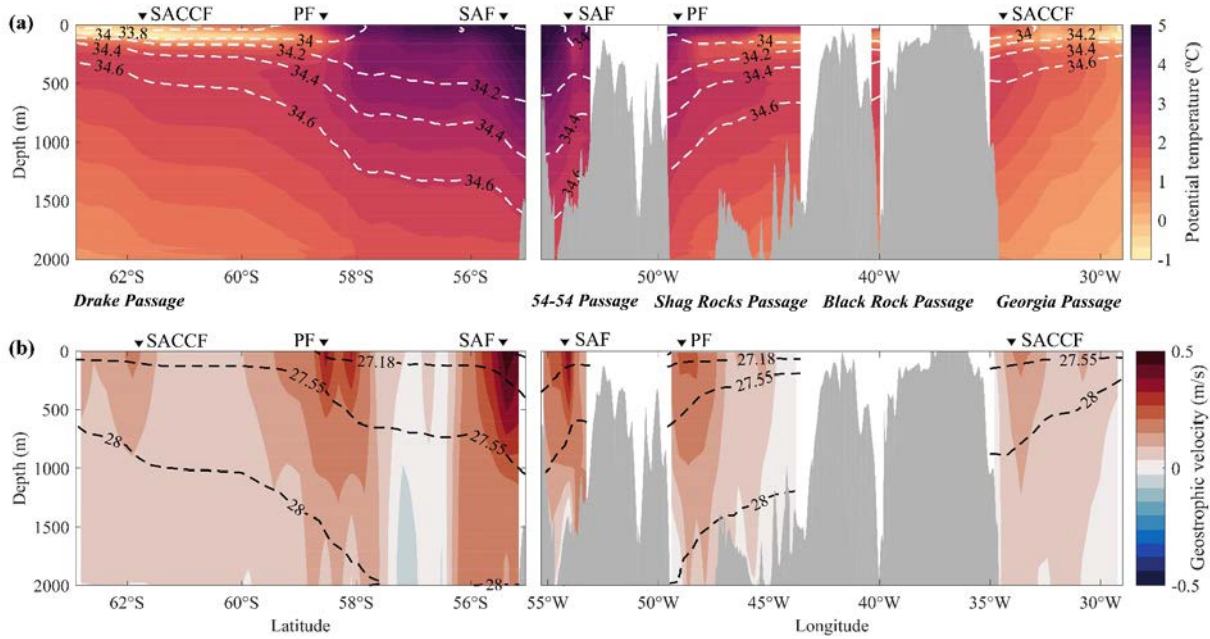


**Figure 3.13.** Vertical sections for (left) the Drake Passage and (right) the Northern Passages, calculated as the average of the eleven 5-year mean fields (2004-2016). (a) Potential temperature (coloured, °C) and practical salinity (dashed contours). (b) Geostrophic velocity (coloured, m/s; reddish-positive values represent eastward and northward velocities while bluish-negative values denote westward and southward velocities) and neutral density (dashed contours,  $\text{kg m}^{-3}$ ); the selected isoneutrals denote the water mass boundaries in Table 3.1. The regional bathymetry is shaded in grey.

The variability in the density and velocity fields is calculated as the SD of these 11 realizations (Figure 3.14). The SD in the density fields is largest in the surface layers and in the frontal regions, particularly in the PF for the Drake Passage and the SAF for the Shag Rocks Passage (Figure 3.14a). The SD in the 1000 m reference velocity is fairly constant everywhere, about  $0.05 \text{ m s}^{-1}$  (Figure 3.6). The SD in the geostrophic velocity fields is somewhat large in the upper 500 m of the SAF and PF regions (peak values up to  $0.15 \text{ m s}^{-1}$ ) both in the Drake and Northern Passages (Figure 3.14b); in particular, there is high latitudinal variability associated with the PF in the Drake Passage.

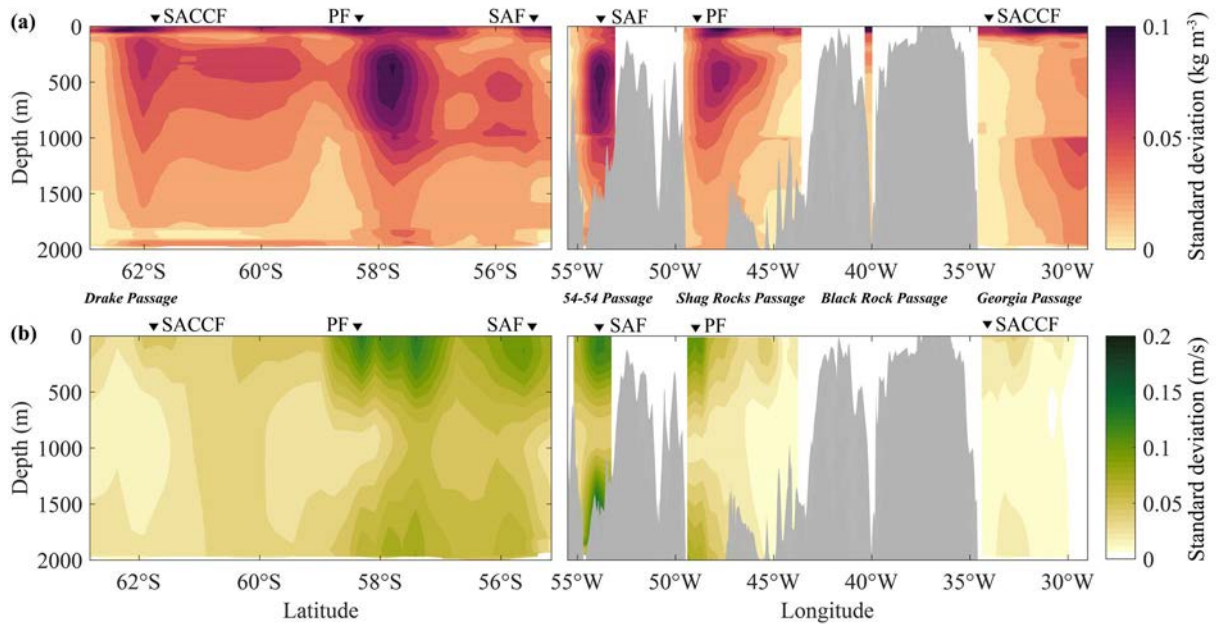


**Figure 3.14.** Standard deviation of the 5-year averaged fields of (a) density and (b) geostrophic velocity for (left panels) the Drake Passage and (right panels) the Northern Passages (Black Rock passage has been omitted in the geostrophic velocity).

The water transports through the Drake and Northern Passages, split among all three water masses, are shown in Figure 3.15; the Black Rock Passage is omitted because there are too few floats to calculate a trend. The error bars represent our best estimate of the variability associated with the reduction in the number of float casts and tracks for each 5-year period, as explained in subsection 3.1.2.3.

The transports through the Drake, Shag Rocks and Georgia Passages are fairly stable. The input through the Drake Passage ranges between 145.3 and 166.5 Sv, though the differences are not significant. The outflow through the Shag Rocks Passage is also fairly constant, always in the 55 - 60 Sv range except for a decrease between 2010 and 2012, which reaches as low as 44.9 Sv. In contrast, there is a negative overall trend in the output through the 54-54 Passage, from 52.8 down to 35.6 Sv, which shows steady between 2013 and 2016. Additionally, during these last years (2011 - 2016), the transport through the Georgia Passage increases between 17.3 and 21.9 Sv, although the variation is barely significant.

The transport variations in these passages may be attributable to differences in both the AASW/AAIW and UCDW masses. In particular, the decrease in transport through the 54-54 Passage is caused by a substantial decrease in both AASW/AAIW and UCDWs, while the increase in transport through Georgia Passage during the last years appears mostly associated with an increase in UCDW. A transfer of outflow waters from intermediate-west (54-54 Passage) to deep-east (Georgia Passage) appears plausible during the last 5-year periods.

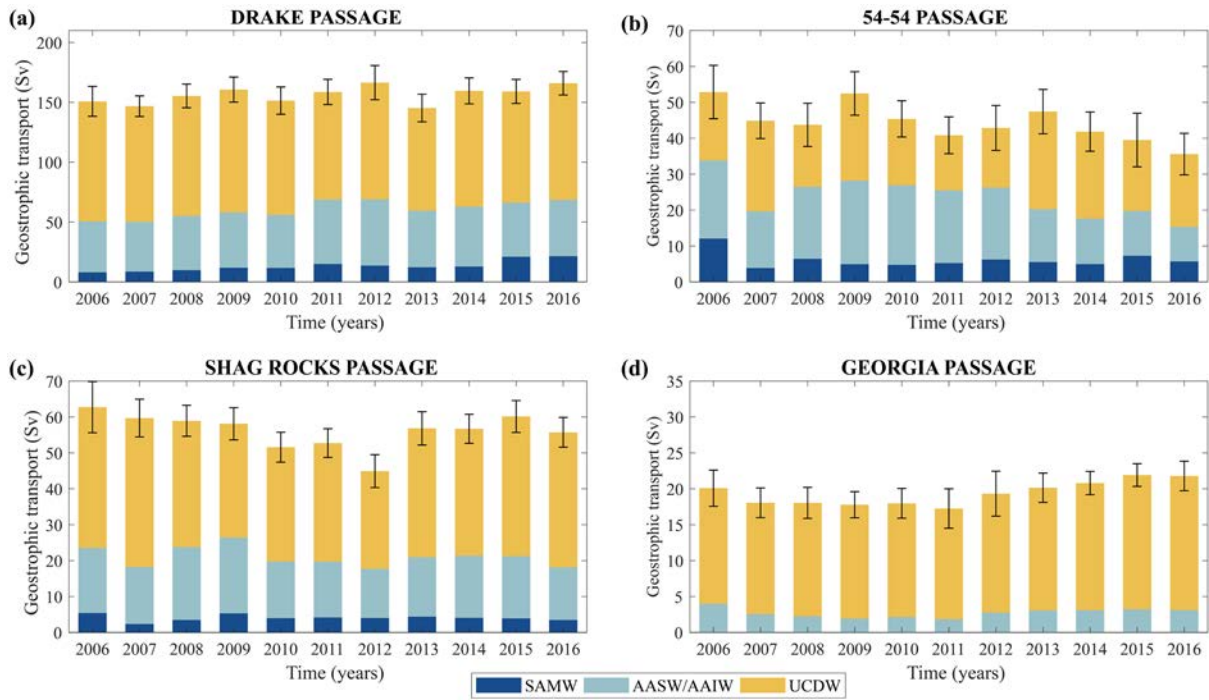


**Figure 3.15.** Total geostrophic transports through the passages down to  $\gamma^n = 28.00 \text{ kg m}^{-3}$ , averaged over 5-year periods, between 2006 and 2016: (a) Drake Passage, (b) 54-54 Passage, (c) Shag Rocks Passage, and (d) Georgia Passage. The contribution of each water mass and the error bars in the total transports are shown. Notice the change in the vertical scale from one panel to another.

#### 3.1.4.4. Seasonal variability

We also split the Argo data into 3-month intervals in order to obtain the seasonal variability. The mean density and normal-to-section velocity fields, per month, can be calculated by a running 3-month average of the data. The resulting mean fields are analogous to the mean fields obtained using the full set of floats (Figures 3.8 and 3.9, and Figure 3.16). As for the 5-year case, the latitudinal and longitudinal positions of the fronts are fairly stable and variations are therefore ignored (Figure 3.3).

The variability in the density and velocity fields is calculated as the SD of the twelve 3-month realizations. The SD in the density fields is analogous to the interannual values, yet smaller below 1000 m and larger in the seasonal mixed layer (Figure 3.17a); this high surface variability reaches deeper (as much as 100 m) between the PF and the SAF. The SD in the 1000 m reference velocity is fairly small, with peak values less than  $0.08 \text{ m s}^{-1}$  in the frontal regions. The SD in the geostrophic reference velocity again resembles the interannual fields, with maxima at the surface (Figure 3.17b). In the Drake Passage, the seasonal SD values are smaller than the interannual ones; further, the peak values stretch all the way between the two fronts rather than being located at the fronts themselves. In the Northern Passages, the peak SDs are associated with the SAF in the 54-54 Passage.

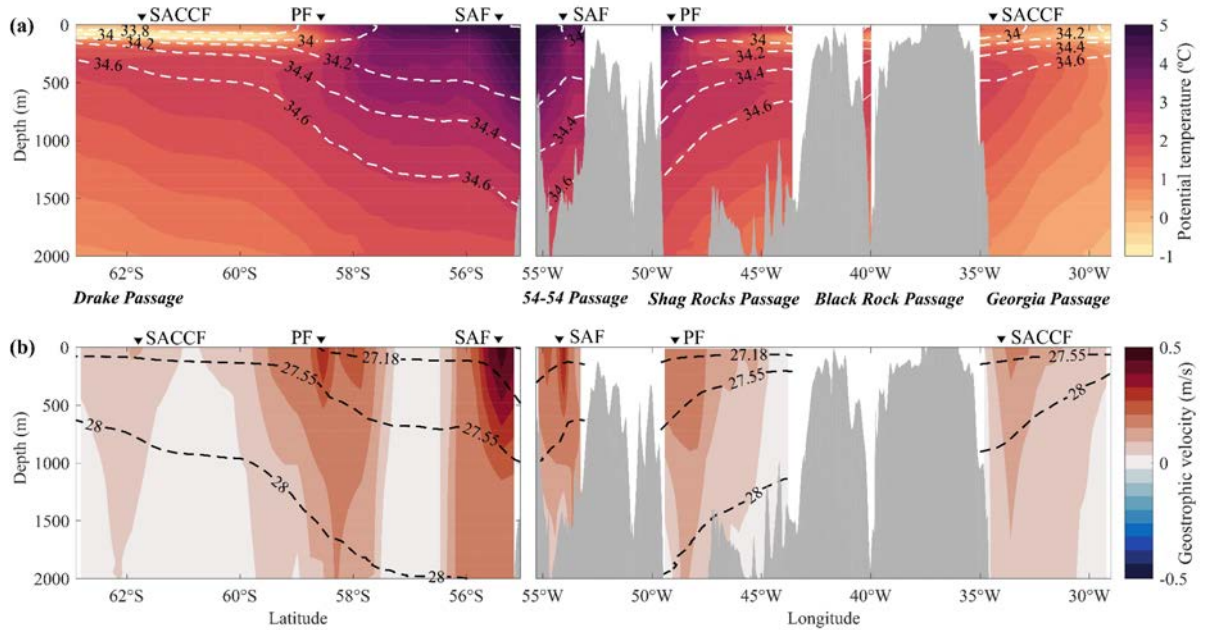


**Figure 3.16.** Vertical sections for (left) the Drake Passage and (right) the Northern Passages, calculated as the average of the twelve 3-month seasonal mean fields. (a) Potential temperature (coloured, °C) and practical salinity (dashed contours). (b) Geostrophic velocity (coloured, m/s; reddish-positive values represent eastward and northward velocities while bluish-negative values denote westward and southward velocities) and neutral density (dashed contours,  $\text{kg m}^{-3}$ ); the selected isoneutrals denote the water mass boundaries in Table 3.1. The regional bathymetry is shaded in grey.

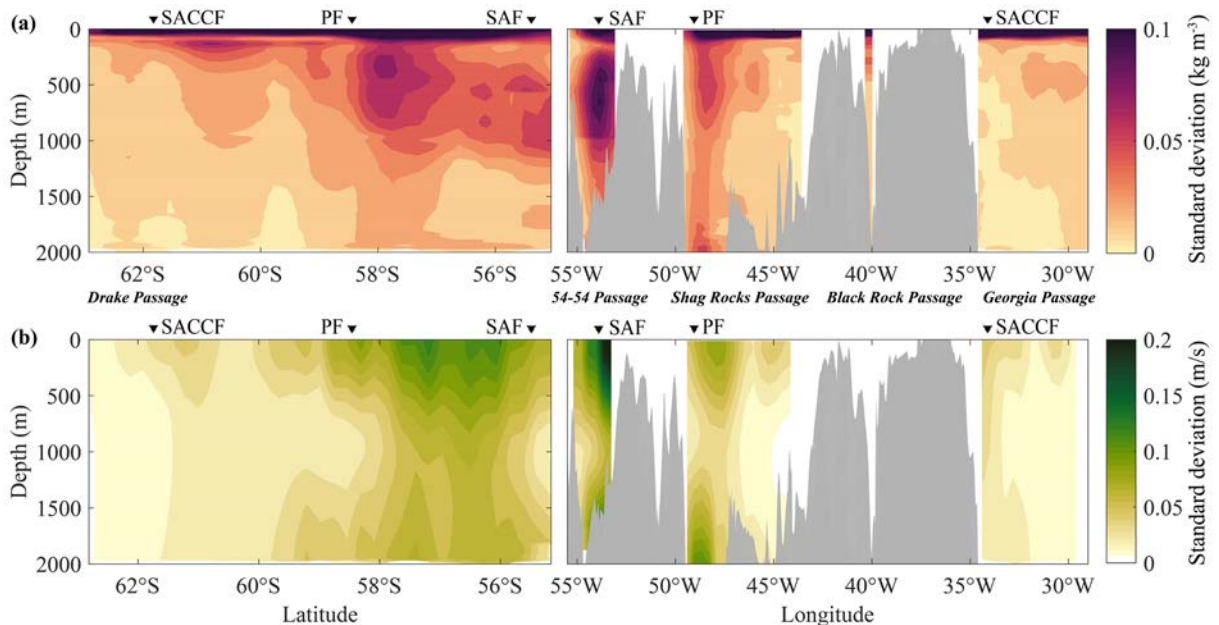


**Figure 3.17.** Standard deviation of the 3-month averaged fields. (a) Density and (b) geostrophic velocity for (left panels) the Drake Passage and (right panels) the Northern Passages (Black Rock passage has been omitted in the geostrophic velocity).

The seasonal variability of the water transports through the Drake and Northern Passages is substantial (Figure 3.18; again, the Black Rock Passage is omitted). The error bars show the potential effects of the reduced number of float casts and tracks for each realization, as explained in subsection 3.1.2.3.

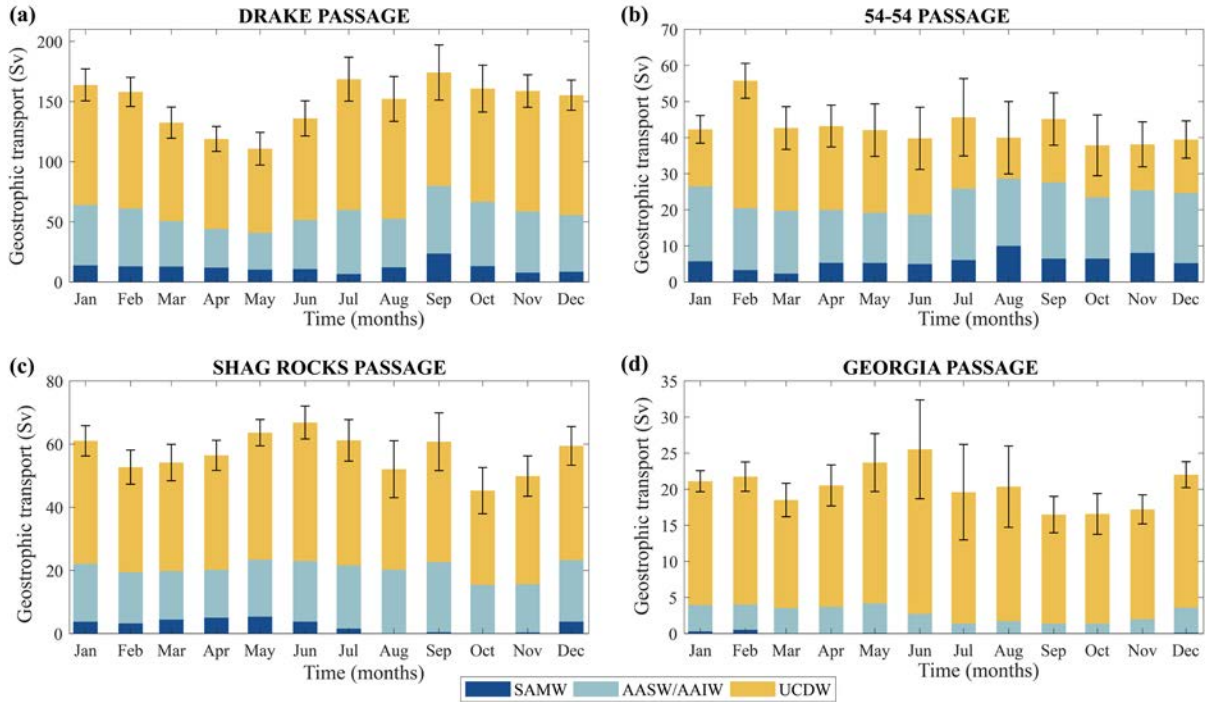


**Figure 3.18.** Total geostrophic transports through the passages down to  $\gamma^n = 28.00 \text{ kg m}^{-3}$ , averaged over 3-month intervals: (a) Drake Passage, (b) 54-54 Passage, (c) Shag Rocks Passage, and (d) Georgia Passage. The contribution of each water mass and the error bars in the total transports are shown. Notice the change in the vertical scale from one panel to another.

The water input through the Drake Passage ranges between 110.8 and 174.1 Sv, with a minimum in autumn and winter (March through June; we always refer to austral seasons). The seasonal change is mainly caused by fluctuations in both the AASW/AIW and UCDW transports. The transport in the Shag Rocks Passage is minimum in spring and maximum in winter (45.3 - 66.8 Sv range), while in the 54-54 Passage the transport is more stable, with a minimum in early summer (37.8 Sv). Finally, in the Georgia Passage again the minimum transport occurs in spring and the maximum in summer (16.5 - 25.6 Sv range). These seasonal variations are associated with changes in all water masses, with the winter disappearance of SAMW in the Shag Rocks Passage and AASW/AIW in the Georgia Passage.

#### 3.1.4.5. Comparison with previous estimates

Previous estimates of water transport through the Drake Passage range between 121 and 173 Sv (Table 3.9). When referenced to a deep-water level, these estimates remain very

large: 125 Sv (referenced to 2500 m, Whitworth & Peterson, [1985](#)) and 141 Sv (referenced to 3000 m, Koenig et al., [2014](#)). Using deep or near-bottom velocities, the barotropic contribution is relatively small (ranging between 5 and 41 Sv) as compared with the baroclinic one (from 98 to 136 Sv) (Gille, [2003](#); Chidichimo et al., [2014](#); Koenig et al., [2014](#); Donohue et al., [2016](#)). In contrast, there are only a few previous estimates of water transport through the North Scotia Ridge and Georgia Passages (Table [3.9](#)).

Naveira Garabato et al. ([2003](#)) estimated the output through these Northern Passages to be 119 and 30 Sv, respectively; this total output, 149 Sv, is only slightly above their estimate for the water input through the Drake Passage (143 Sv). More recently, Smith et al. ([2010](#)) have estimated that 117 Sv exit through the North Scotia Ridge Passages. Our results for the water transport through the Drake Passage are  $164.2 \pm 10.8$  Sv for the water column above 2000 m and  $140.8 \pm 7.4$  Sv for waters shallower than the  $28.00 \text{ kg m}^{-3}$  isoneutral surface (Table [3.9](#)). We have also found that the transports through the Northern Passages are  $159.3 \pm 10.2$  Sv down to 2000 m and  $115.9 \pm 8.3$  Sv down to the  $28.00 \text{ kg m}^{-3}$  isoneutral. The mean transports through the Northern Passages down to the  $28.00 \text{ kg m}^{-3}$  isoneutral surface are split into 40.9, 51.6, 2.4 and 21.0 Sv for the 54-54, Shag Rocks, Black Rock and Georgia passages, respectively. The 43.4 Sv that inflow through the Drake Passage between the  $28.00 \text{ kg m}^{-3}$  isoneutral and the 2000 m level outflows the Scotia Sea mostly through the Georgia Passage (32.8 Sv).

Our mean-transport estimates through the Drake Passage (140.8 Sv down to  $28.00 \text{ kg m}^{-3}$  and 164.2 Sv down to 2000 m) are in the high range of previous estimates. We may indirectly assess the robustness of these results by comparing these inputs with the outputs through the Northern Passages. Considering layers lighter than  $28.00 \text{ kg m}^{-3}$ , about two-thirds of the input and output transports correspond to UCDW and one-third to the surface-intermediate layers (AASW/AAIW), with the SAMW representing only about 5% - 10% of the total. Down to 2000 m, the input-output imbalance is small (input exceeds output by 4.7 Sv), although these numbers do not consider the water inflow through the South Scotia Ridge. In contrast, the imbalance increases to 24.9 Sv for isoneutrals lighter than  $28.00 \text{ kg m}^{-3}$ .

Previous studies indicate that there are  $19 \pm 7$  Sv of LCDW and WSDW entering the Scotia Sea through the South Scotia Ridge (Thorpe et al., [2002](#); Naveira Garabato et al., [2003](#)). Adding this transport to the 23.4 Sv that inflow through the Drake Passage between  $28.00 \text{ kg m}^{-3}$  and 2000 m, gives a total of 42.4 Sv, which fits very well the outflow of 43.4 Sv through the Northern Passages between  $28.00 \text{ kg m}^{-3}$  and 2000 m. Hence, we are left with about 25 Sv of unaccounted outflow through the northern and eastern Passages down to  $28.00 \text{ kg m}^{-3}$  (Figure [3.19](#)). We propose that these 25 Sv will flow out through areas of the North Scotia Ridge Passages that are unsampled by the Argo floats; considering that these shallow cross-sections



have an area of about  $250 \times 10^6 \text{ m}^2$  (Figure 3.9), this outflow would be accounted by a mean velocity of about  $0.1 \text{ m s}^{-1}$ .

**Table 3.9.** Comparison of barotropic, baroclinic and total transports (Sv) through the different Passages according to several authors and this study. The velocity reference level is indicated between parenthesis in the first column. For this study, the SD corresponds to the value obtained from the 5-year values between 2006 and 2016 (Table 3.6 shows, for this study, how the output splits among the 54-54, Shag Rocks and Black Rock Passages).

| Author  | Drake (Sv)       |                 |                  | North Scotia Ridge (Sv) |                 |                  | Georgia (Sv)   |                |                |
|---|------------------|-----------------|------------------|-------------------------|-----------------|------------------|----------------|----------------|----------------|
|   | Btropic          | Bclinic         | Total            | Btropic                 | Bclinic         | Total            | Btropic        | Bclinic        | Total          |
| Whitworth III et al. (1982)                     | -                | -               | 117 to 144       | -                       | -               | -                | -              | -              | -              |
| Whitworth & Peterson (1985)                     | -                | -               | $134 \pm 11$     | -                       | -               | -                | -              | -              | -              |
| Whitworth & Peterson (1985) (2500 m)            | -                | -               | $125 \pm 13$     | -                       | -               | -                | -              | -              | -              |
| Ganachaud & Wunsch (2000)                       | -                | -               | $140 \pm 6$      | -                       | -               | -                | -              | -              | -              |
| Sloyan & Rintoul (2001b)                        | -                | -               | $135 \pm 1$      | -                       | -               | -                | -              | -              | -              |
| Thorpe et al. (2002)                            | -                | -               | -                | -                       | -               | -                | -              | $14.5 \pm 1.5$ | -              |
| Meredith (2003)                                 | -                | -               | -                | -                       | -               | -                | 4.3            | 9.8            | 14.1           |
| Cunningham et al. (2003) (3000 m)               | -                | $107 \pm 10$    | -                | -                       | -               | -                | -              | -              | -              |
| Cunningham et al. (2003)                        | -                | -               | $137 \pm 8$      | -                       | -               | -                | -              | -              | -              |
| Gille (2003)                                    | $23 \pm 2$       | $98 \pm 5$      | $121 \pm 6$      | -                       | -               | -                | -              | -              | -              |
| Naveira Garabato et al. (2003)                  | -                | -               | $143 \pm 13$     | -                       | -               | $119 \pm 12$     | -              | -              | $30 \pm 10$    |
| Firing et al. (2011) (1000 m)                   | -                | -               | $95 \pm 2$       | -                       | -               | -                | -              | -              | -              |
| Firing et al. (2011)                            | -                | -               | $154 \pm 38$     | -                       | -               | -                | -              | -              | -              |
| Koenig et al. (2014) (3000 m)                   | $5 \pm 16$       | $136 \pm 11$    | $141 \pm 13$     | -                       | -               | -                | -              | -              | -              |
| Chidichimo et al. (2014), Donohue et al. (2016) | $46 \pm 9$       | $128 \pm 6$     | $173 \pm 11$     | -                       | -               | -                | -              | -              | -              |
| Colin de Verdière & Ollitrault (2016)           | -                | -               | 175              | -                       | -               | -                | -              | -              | -              |
| Smith et al. (2010)                             | -                | -               | -                | 73                      | 44              | $117 \pm 10$     | -              | -              | -              |
| This study (2000 m)                             | $108.6 \pm 12.8$ | $55.6 \pm 12.6$ | $164.2 \pm 10.8$ | $55.1 \pm 19.9$         | $50.4 \pm 19.1$ | $105.5 \pm 10.4$ | $39.6 \pm 3.2$ | $14.2 \pm 1.4$ | $53.8 \pm 2.6$ |
| This study (28.00 kg m <sup>-3</sup> )          | $98.0 \pm 7.4$   | $42.8 \pm 8.9$  | $140.8 \pm 7.4$  | $51.4 \pm 18.6$         | $43.5 \pm 18.9$ | $94.9 \pm 8.1$   | $18.5 \pm 1.3$ | $2.5 \pm 0.5$  | $21.0 \pm 1.7$ |

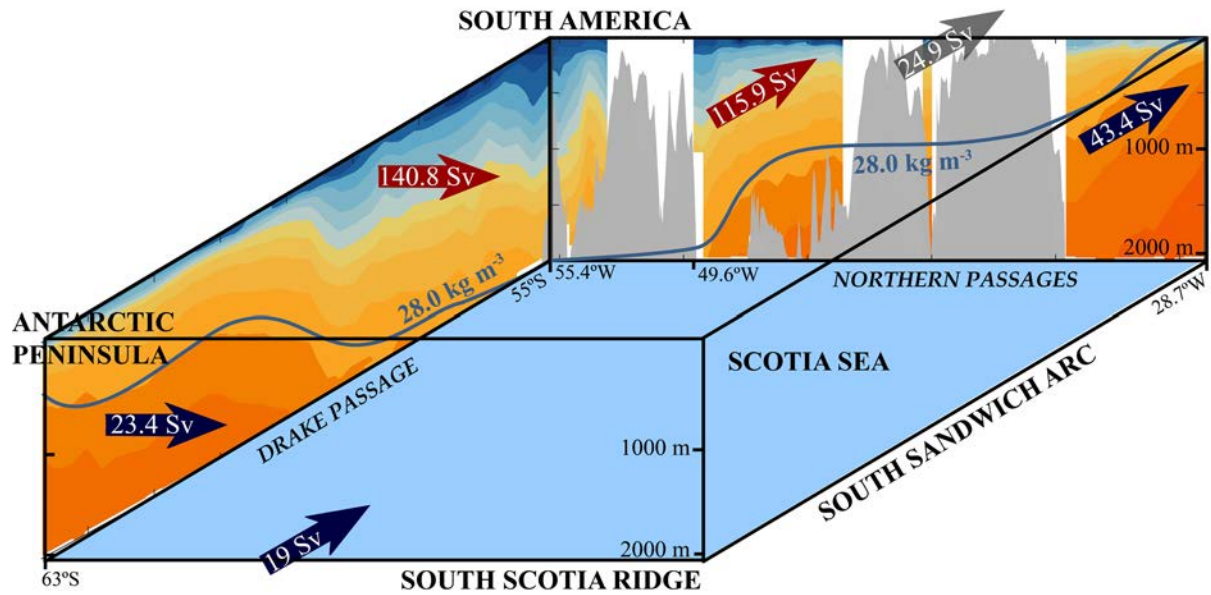


**Figure 3.19.** Schematics of input and output transports in the Scotia Sea. The solid red and blue arrows represent the calculated transports, and the solid gray arrow represent the estimated transports through the shallow Northern Passages.

The Argo dataset does not allow computing the water transports below 2000 m. If we compare our Drake Passage transports down to 2000 m,  $164.2 \pm 10.8$  Sv, with the upper range of all previously reported values, 173 - 175 Sv (Chidichimo et al., [2014](#); Donohue et al., [2016](#); Colin de Verdière & Ollitrault, [2016](#)), about 10 Sv would enter the Scotia Sea through the lower part of the water column. Considering the relatively shallow depths of the Northern Passages, this additional input could find its way out of the Scotia Sea more easily through the deepest point of the Shag Rocks Passage (Smith et al., [2010](#)) or veering eastward through the Georgia Passage.

### 3.1.5. Concluding remarks

We have used the Argo dataset to obtain the mean values and long-term variability of the vertical structure of the water column and the transports in and out of the Scotia Sea. In particular, we have provided estimates of the water balances for water masses that are fully sampled by the floats (SASW, SAMW, AASW/AAIW, UCDW), in our case down to the  $28.00 \text{ kg m}^{-3}$  isoneutral surface. Additionally, the Argo dataset has delivered information on the main pathways along the 1000 m parking depth.

The Argo floats data is already large enough to assess the interannual and seasonal variability of the water transports down to the  $28.00 \text{ kg m}^{-3}$  isoneutral in the Drake and

Northern Passages (Figures 3.15, 3.18 and 3.20). Regarding interannual variability, we have grouped the data over 5-year periods in order to have a robust result, although this discards the possibility of detecting any signal with shorter periods. With respect to seasonal variability, we have selected 3 months averaging as this is the longest possible interval to detect the seasonal cycle; the results over three months are somewhat noisy but do demonstrate the presence of substantial seasonality in the transports.

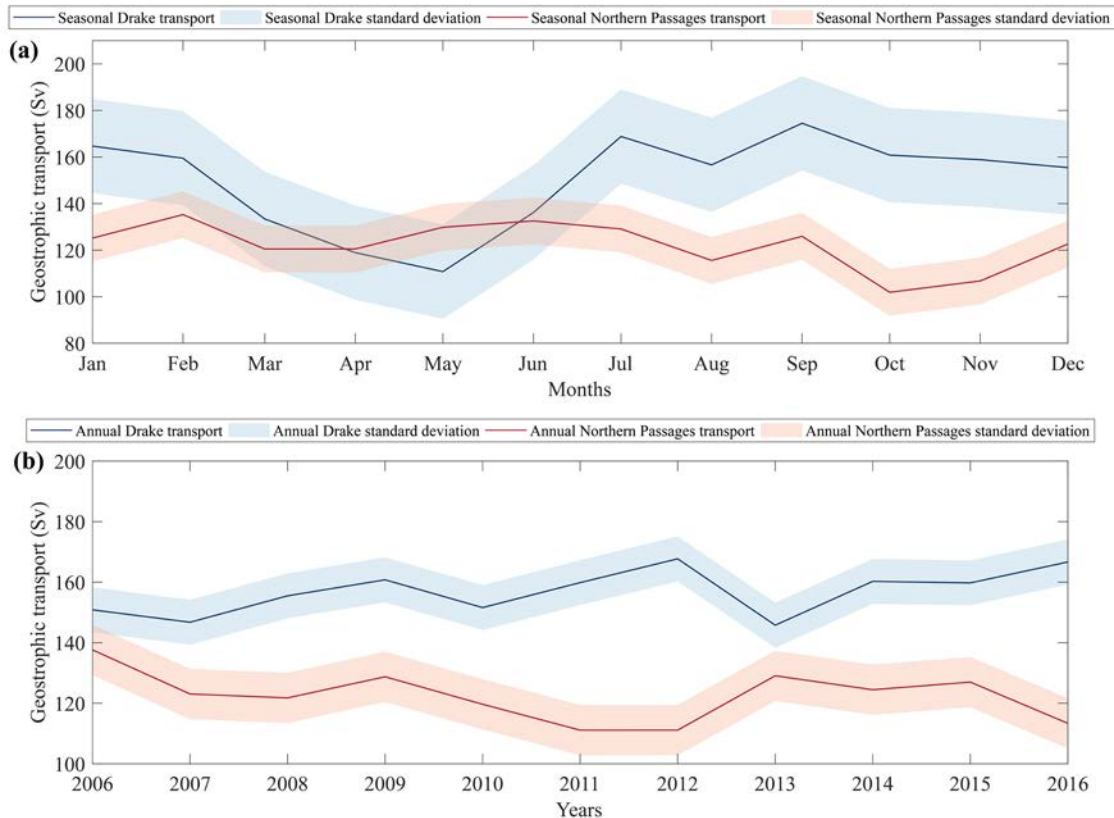


**Figure 3.20.** Water transports through the Drake (blue line) and Northern (red line) Passages, from the sea surface down to the  $28.00 \text{ kg m}^{-3}$  isoneutral. (a) Seasonal and (b) interannual variations; the SDs of the time series are represented as shaded coloured bands.

The 3-month averages show that the water transports (down to  $\gamma^n = 28.00 \text{ kg m}^{-3}$ ) range between 110.8 and 174.5 Sv for the Drake Passage and between 101.9 and 135.3 Sv for the Northern Passages (Figure 3.20a). The mean transport is  $149.9 \pm 20.2$  Sv through the Drake Passage and  $122.1 \pm 10.0$  Sv through the Northern Passages; the mean and SD of the imbalance is  $27.8 \pm 24.0$  Sv. The correlation between the Drake and Northern transports peaks at 0.79 for time lags of 6.4 months (significant at  $p < 0.01$ ). This time lag is one month shorter than the mean residence time of water masses in the Scotia Sea (219 days or 7.3 months), as deduced from the time that Argo floats take to cross it.

Considering the 5-year values, the water transports (down to  $\gamma^n = 28.00 \text{ kg m}^{-3}$ ) range between 145.8 and 167.7 Sv in the Drake Passage and between 111.1 and 137.6 Sv in the Northern Passages (Figure 3.20b). The surface-intermediate and upper-circumpolar water masses display similar large variability, with a remarkable decrease in the surface-intermediate layers and increase in the upper-circumpolar waters during the last years of the time series (2014 - 2016). The mean and SD transports are  $156.8 \pm 7.4 \text{ Sv}$  through the Drake Passage and  $122.4 \pm 8.3 \text{ Sv}$  through the Northern Passages; the mean and SD of the imbalance is  $34.4 \pm 13.9 \text{ Sv}$ .



**Figure 3.21.** Interannual variations of the (a) baroclinic and (b) barotropic contributions to the water transports through the Drake (blue line) and Northern (green line) Passages, from the sea surface down to the  $28.00 \text{ kg m}^{-3}$  isoneutral; the SDs of the time series are represented as shaded coloured bands.

Considering the transports down to  $28.00 \text{ kg m}^{-3}$ , the mean values obtained using the entire dataset (140.8 Sv through the Drake Passage and 115.9 Sv through the Northern Passages) are slightly below the mean values from either the 5-year ensembles ( $156.8 \text{ Sv}$  and  $122.4 \text{ Sv}$ , respectively) or the 3-month groups ( $149.9 \text{ Sv}$  and  $122.1 \text{ Sv}$ , respectively). These differences possibly arise because the seasonal and interannual oscillations are not sinusoidal and, further, because the 5-year averages give less relative weight to the initial and final years

of the time series (e.g., only one 5-year value uses the 2018 data while five values use the 2012 data). Hence, we consider that our best mean transport estimates come from the full dataset with the SD from the 5-year periods ( $140.8 \pm 7.4$  Sv for the Drake Passage and  $115.9 \pm 8.3$  Sv for the Northern Passages).

The SD of the total transports through the Drake and Northern Passages is generally smaller than the SD of either the baroclinic or barotropic contributions (Table 3.9). The 5-year averaged time series of the baroclinic and barotropic contributions display much greater variations than the joint transport (Figures 3.20 and 3.21). The two portions tend to compensate each other: for the Drake Passage, between 2011 and 2016, the baroclinic transport increased at the expense of the barotropic one, with a similar occurrence between 2010 and 2014 in the Northern Passages. This observation raises the possibility of interannual frontogenesis in the upper 2000 m accompanied by a weakening of the currents at depth; such an effect is also suggested by the observed interannual changes in the shares of the surface-intermediate vs upper circumpolar waters (Figure 3.15).

Smith et al. (2010) and Naveira Garabato et al. (2003) suggested that there is a substantial exchange of water masses across the PF and SAF in the North Scotia Ridge, leading to water transformations from deep to intermediate layers. Smith et al. (2010) determined that there is a total net transfer of 37 Sv from the PF to the SAF, with about 10 Sv corresponding to the AASW/AAIW masses. Our results, obtained following a different approach, are consistent with this view. Setting the fronts location at 1000 m as the boundaries between the water masses, we have explored the transports and number of floats that transit between adjacent fronts, down to the  $28.00 \text{ kg m}^{-3}$  isoneutral surface. The dominance of the relatively warm input (at the Drake Passage the transports north and south of the PF are 101.3 Sv and 39.6 Sv, respectively) contrasts with the preponderance of the relatively cold outputs (in the Northern Passages, we find 45.4 Sv and 70.5 Sv to the west and east of the PF, respectively). Similarly, the difference between floats entering north and south of the PF location at 1000 m (141 and 46) and exiting west and east of the PF (99 and 88) is remarkable.

We also observe some interannual variability in the intensity and position of both the SAF and, particularly, the PF across the Drake Passage (Figure 3.14). This is consistent with previous reports of a bimodal character of the PF (Cunningham et al., 2003; Sprintall, 2003; Lenn et al., 2007). Along the North Scotia Ridge, the SAF is always located in the 54-54 Passage, while the PF is found in the western margin of the Shag Rocks Passage. The jets associated with these fronts are rather localized, yet their intensity displays substantial interannual variability, which leads to the observed changes in transport (Figures 3.15 and 3.18).

There is low seasonal variability associated with the SAF and PF in the Drake Passage, which contrasts with the relatively high seasonal SD in the mode and surface-intermediate

waters between these fronts (Figure [3.17](#)). The mode waters experience seasonal changes in density and velocity that translate into a decrease in the transport of mode and surface-intermediate waters (Figure [3.18](#)). The large variations in the density structure and water transports in the Northern Passages support the idea of substantial seasonal changes in the transit time through the Scotia Sea (Figure [3.20](#)).

Note that the observed seasonal and interannual variability in the frontal structures takes place mostly in the surface-intermediate waters, typically much shallower than the 1000 m parking depth we have used to locate the frontal systems (Figure [3.3](#)). This is a source of uncertainty in the computed exchanges of water transports among frontal domains, which suggests that water transformations may be somewhat smaller than computed. Nevertheless, the observed high exchange of floats between frontal domains proves that most of the water changes are indeed real.

The Argo dataset proves to be a very useful resource to improve our knowledge of the hydrographic variables and reference velocities, both of the mean fields and their spatiotemporal variability, in remote regions such as the Scotia Sea. Further, the dataset complements the Eulerian averages with a Lagrangian view of those spatial connections that lie behind the variability. As the amount of available data increases, further analyses of the Argo dataset shall be able to improve this emerging image.



## **CHAPTER 3.2**

---

# **Mass and biogeochemical fluxes in the Scotia Sea**



### 3.2.1. Context and objectives

The wind-driven Antarctic Circumpolar Current (ACC) flows eastward around Antarctica, dominating the Southern Ocean circulation and promoting the exchange of heat, mass and freshwater between the Pacific, Atlantic and Indian Ocean basins (Rintoul & Naveira Garabato, [2013](#)). It consists of a complex frontal structure of multiple jets that merge and diverge along the circumpolar path, from north to south, mainly grouped in the Subantarctic Front (SAF), the Polar Front (PF) and the Southern ACC Front (SACCF). The southern limit of the ACC is the Southern Boundary (SB) Front, which is not always associated with a current core (Orsi et al., [1995](#); Sokolov & Rintoul, [2007](#); Meredith, [2003](#); Kim & Orsi, [2014](#)). Each frontal position coincides with a water mass boundary, displaying maximum density horizontal gradients and peak currents (Rintoul & Naveira Garabato, [2013](#)). On its pathway around the Antarctic continent, the ACC fronts are constrained latitudinally by the Drake Passage, between the Antarctic Peninsula and the southern tip of South America, before entering the Scotia Sea.

The Scotia Sea, in the southwestern Atlantic sector of the Southern Ocean, is surrounded by a shallow ridge system constituted to the north by the North Scotia Ridge (Smith et al., [2010](#); Artana et al., [2016](#)) and to the south and east by the South Scotia Ridge and the South Sandwich Island Arc (Thorpe et al., [2002](#)). After passing through the Drake Passage, the ACC flows downstream into the Scotia Sea and veers northward into the North Scotia Ridge and Georgia Passage (Figure [3.22](#); Ward et al., [2002](#); Naveira Garabato et al., [2003](#)). Inside the Scotia Sea, the ACC meets the denser waters from the Weddell Gyre, resulting in the Weddell–Scotia Confluence (Gordon, [1967](#)).

The water masses of the ACC experience intense modifications within the Scotia Sea (Naveira Garabato et al., [2003](#)). The most voluminous ACC water mass is the Circumpolar Deep Water (CDW, divided into upper, UCDW, and lower, LCDW), which experiences net poleward transport and upwelling. When the UCDW reaches the upper layers, it becomes the Antarctic Surface Water (AASW), which is transformed into Antarctic Intermediate Water (AAIW) as it flows north and is subducted near the Polar Front (PF). North of the SAF, the Subantarctic Mode Water (SAMW) is produced by the winter deepening of the upper-ocean mixed layer, where the Subantarctic Surface Water (SASW) can also be found from 150 to 450 m characterized by a shallow subsurface salinity maximum (Talley, [1996](#)). The remaining deep upwelled waters, LCDW, are transformed into the world's densest bottom waters, which are transported northward to fill the global abyssal ocean. Consequently, the Scotia Sea has a crucial role not only in the inter-basin exchange of ACC but also in the formation of the deep and intermediate waters in the global overturning circulation.

The Southern Ocean is characterized by persistent high nutrient and low chlorophyll (HNLC) concentrations, with moderate new primary production (Rubin, 2003; Ward et al., 2002). The deep upwelling waters are naturally depleted in dissolved oxygen (DO) and enriched in dissolved inorganic carbon (DIC) and macronutrients such as nitrate (NO<sub>3</sub>), and have negligible anthropogenic carbon concentrations (Gray et al., 2018). These outcropping waters may naturally outgas carbon into the atmosphere but can also uptake anthropogenic carbon (Gruber et al., 2009). The net uptake of total CO<sub>2</sub> (the sum of the natural and anthropogenic components) is determined by the resulting balance.

The Southern Ocean conditions the global carbon cycle and the sequestration rate of industrial CO<sub>2</sub> into the oceans (Sarmiento & Orr, 1991; Rubin, 2003). Several studies suggest that the Southern Ocean accounts for more than 40% of the global oceanic uptake of anthropogenic carbon dioxide (Sarmiento & Gruber, 2002; Sallée et al., 2012). Considering that nowadays, the anthropogenic carbon annual production is about 10 Pg C per year (Friedlingstein et al., 2019, 2020, 2022; Crisp et al., 2022), and that the ocean incorporates about 25% of these emissions (Canadell et al., 2007; Le Quéré et al., 2015), the net uptake of anthropogenic carbon in the Southern Ocean turns out to be about 1 Pg C yr<sup>-1</sup> (Bushinsky et al., 2019). This net uptake takes place between 35°S and 55°S, where surface waters sink as SAMW and AASW/AAIW, and contrasts with the outgassing of natural DIC south of 55°S as a result of the upwelling of old and highly-remineralized Upper Circumpolar Deep Waters (UCDW) (Mikaloff Fletcher et al., 2007; Lovenduski et al., 2019). Nevertheless, the Southern Ocean is one of the most poorly sampled global ocean regions – especially for variables such as nutrients, oxygen and carbon – hence there is an extensive lack of knowledge about its predominant biogeochemical processes.

There are different estimates of the ACC water mass transports through the Drake Passage and across the Scotia Sea boundaries (for a recent review, see **Chapter 3.1**). In particular, Naveira Garabato et al. (2003) applied an inverse model to the Scotia Sea and determined that the ACC volume transport is 143 ± 13 Sv at the Drake Passage and 149 ± 16 Sv on leaving the Scotia Sea, with the difference being supplied by Weddell Sea Deep Water (WSDW) over the South Scotia Ridge. Recent findings highlight that the ACC transports in the region could be as large as 173 Sv (Donohue et al., 2016) and 175 Sv (Colin de Verdière & Ollitrault, 2016). In **Chapter 3.1**, we used an extensive Argo dataset to conclude that 141 ± 7 Sv flow through the Drake Passage at layers shallower than 28.00 kg m<sup>-3</sup> and estimated an additional input of about 20 Sv of Weddell waters through the South Scotia Ridge passages.

In this study, we use several datasets to build climatological hydrographic and biogeochemical vertical sections enclosing the Scotia Sea, apply an inverse circulation model in order to estimate the fluxes and transports of water masses and biogeochemical properties,

and use the neutral-density layer and overall imbalances to draw conclusions in terms of vertical mixing and biogeochemical processes. The annual-mean hydrography extends along the Scotia Sea's natural boundaries: the Drake Passage, the North Scotia Ridge, the Georgia Passage, the South Scotia Ridge and the Philip Passage (Locarnini et al., 1993; Arhan et al., 1999). Our approach focuses on the isoneutral layers fully sampled in the upper 2000 m of the water column, which involves SASW, SAMW, AASW/AAIW and UCDW. The objective is to assess the intensity of the upper meridional overturning circulation in the Scotia Sea and its relevance in the balance of DO, DIC and inorganic nutrients.

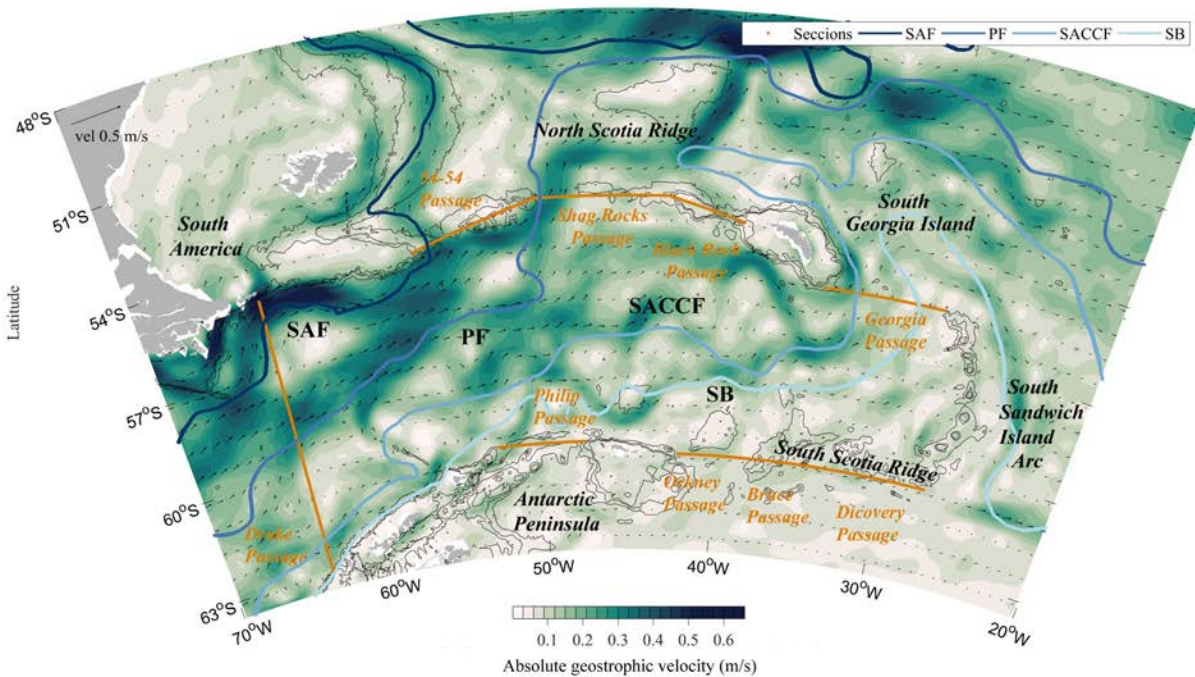


**Figure 3.22.** Climatological surface geostrophic velocities in the Scotia Sea (period 2002 - 2018) with the domain boundaries marked in orange, from west to east: the Drake Passage, the North Scotia Ridge, the Georgia Passage, the South Scotia Ridge and the Philip Passage. The blue lines represent the climatological location of the different Antarctic fronts as described by Orsi et al. (1995), from north to south: the Subantarctic Front (SAF), the Polar Front (PF), the Southern ACC Front (SACCF) and the Southern Boundary (SB) of the ACC.

The structure of this chapter is as follows. The area of study and datasets, the inverse model design, and the procedure to calculate the biogeochemical balances are described in subsection 3.2.2. Subsection 3.2.3 shows the climatological distribution of hydrographic and biogeochemical properties in vertical sections encompassing the Scotia Sea and presents the fields of velocity and biogeochemical fluxes as deduced with the inverse model. Subsection 3.2.4 presents the transports and imbalances of the physical and biogeochemical properties and leads to a value of anthropogenic DIC storage. Finally, we conclude in subsection 3.2.5

with some remarks about what we know and what yet remains unknown about the ACC as it crosses the Scotia Sea.

### 3.2.2. Materials and methods

#### 3.2.2.1. Domain and datasets

An inverse circulation model (Wunsch, [1996](#)) is applied to the entire Scotia Sea, encircled by five sections that join all the bathymetric passages deeper than 1000 meters: Drake Passage, North Scotia Ridge passages, Georgia Passage, South Scotia Ridge passages and Philip Passage (Figure [3.23](#)). The North Scotia Ridge passages are mainly composed, from west to east, by the 54-54, Shag Rocks and Black Rock Passages (Smith et al., [2010](#)), while the South Scotia Ridge comprises, from west to east, the Orkney, Bruce and Discovery Passages (Heywood et al., [2002](#)).

We use several datasets to reconstruct the average hydrographic sections from the surface down to 2000 m, comprising the conductivity-temperature-depth (CTD) casts recorded with Argo floats from 2002 to 2018, in almost all cases reaching only down to 2000 m (Argo, [2000](#)); the Marine Mammals Exploring the Oceans Pole to Pole (MEOP) measurements (Roquet et al., [2014](#); Treasure et al., [2017](#)); the ESASSI-08 dataset obtained west of the South Orkney Islands in January 2008 (Palmer et al., [2012](#)); and the Southern Ocean Data Base (SODB; Orsi & Whitworth III, [2005](#)).

Using these datasets, we have compiled all casts between 2002 and 2018 that were sampled within a 50-km wide band around the nominal location of each passage. Regarding the MEOP data, the profiles were previously checked with regional temperature-salinity diagrams as obtained from the Argo CTD casts flagged as good quality. Specifically, profiles that contain data that fall outside the full cloud of Argo data points are discarded. Further, because of the availability of the ESASSI-08 casts, we do not use shallow mammal dives in the Philip Passage as they often cause shallow biased and intermittency in the property distributions. Hence, the MEOP casts represent an important contribution mainly in poorly sampled edge sections, particularly in the upper slope regions in North Scotia Ridge. The number of casts for each passage is presented in Table [3.10](#), and the locations of each individual cast are presented in Figure [3.23](#). It is remarkable that 46% of the casts come from the Argo database, which implies that we can only ensure good horizontal resolution in the upper 2000 m of the water column.

**Table 3.10.** Number of casts recorded for each passage according to each database. The ESASSI-08 database only provides casts in the Philip passage, where MEOP profiles have been discarded in order to avoid shallow water column perturbations.

| PASSAGE            | DATABASE |      |      |           |
|--------------------|----------|------|------|-----------|
|                    | ARGO     | SODB | MEOP | ESASSI-08 |
| Drake              | 269      | 172  | 26   | 0         |
| North Scotia Ridge | 338      | 467  | 161  | 0         |
| Georgia            | 119      | 27   | 13   | 0         |
| South Scotia Ridge | 110      | 55   | 3    | 0         |
| Philip             | 48       | 67   | 0    | 31        |

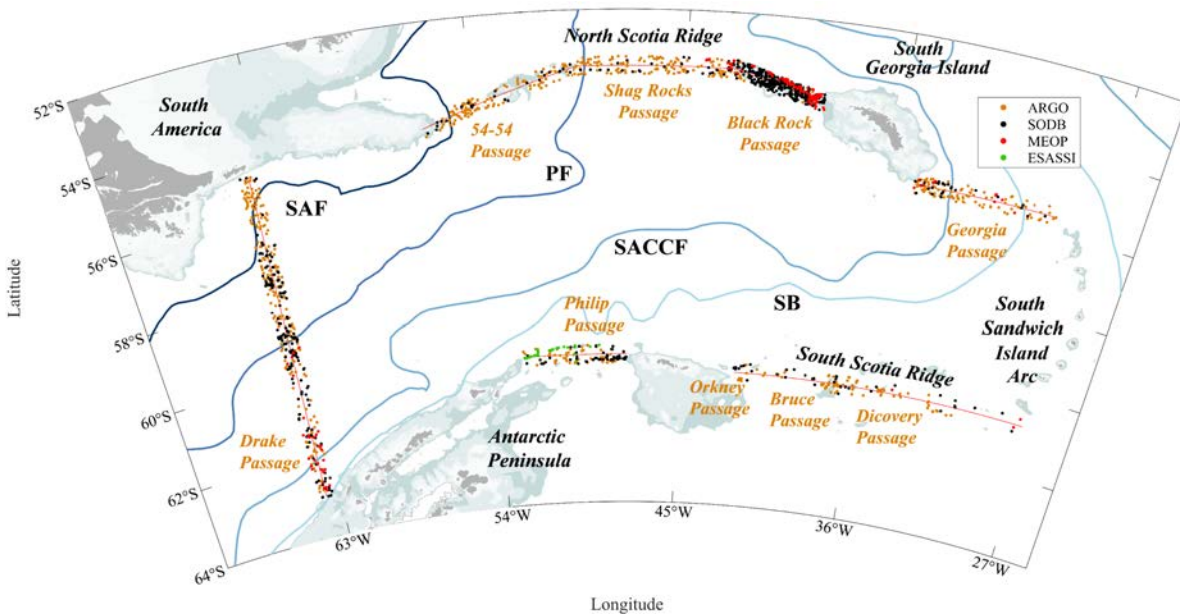


**Figure 3.23.** Location of the Argo, SODB, ESASSI-08 and MEOP profiles along the Scotia Sea boundaries. Blue lines represent the average location of the different Antarctic fronts (Orsi et al., 1995), from north to south: Subantarctic Front (SAF), Polar Front (PF), Southern ACC Front (SACCF) and Southern Boundary of the ACC (SB). Regions shallower than 1000 m are shown in grey.

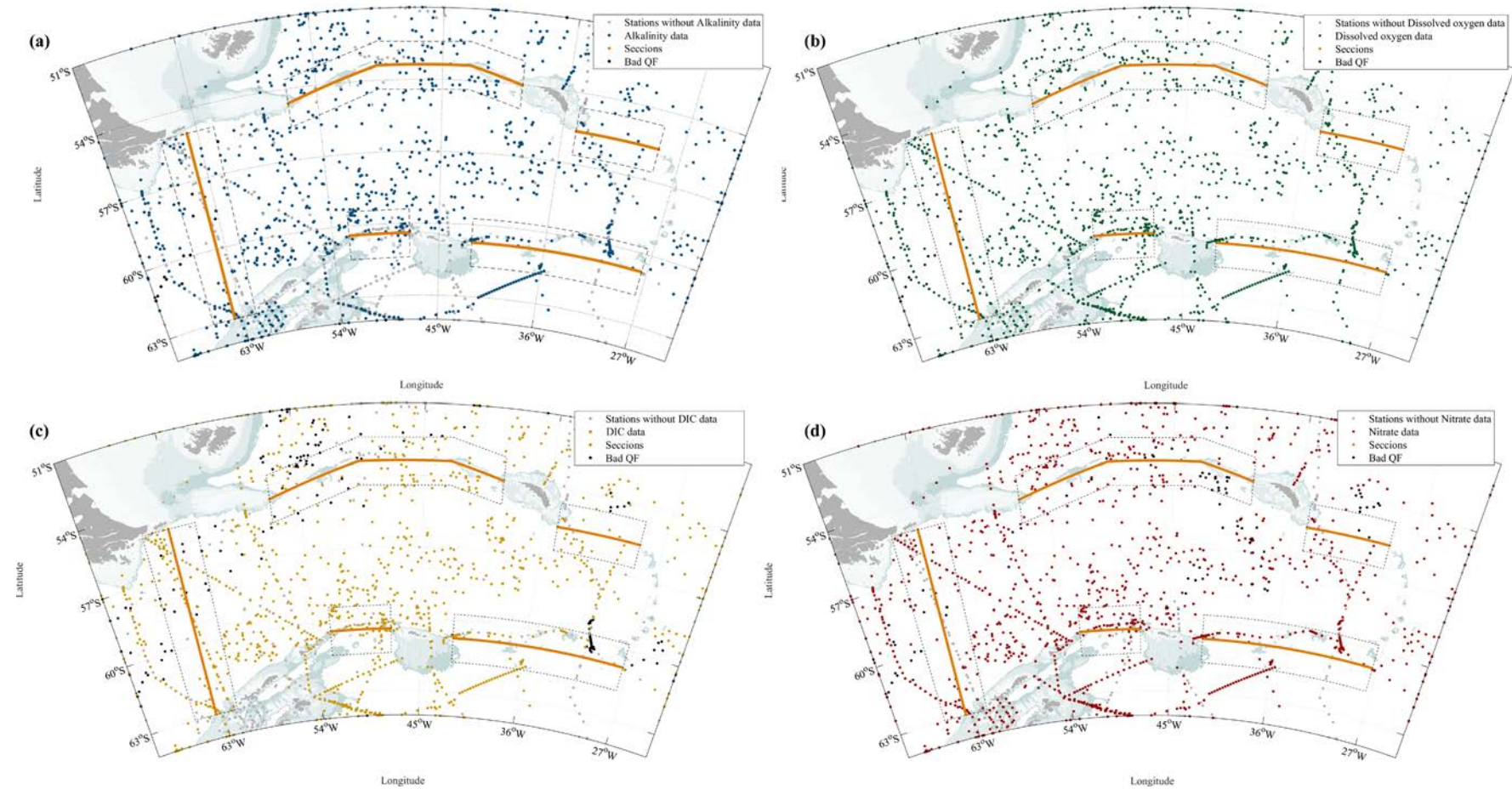
The hydrographic data is complemented with biogeochemical data (alkalinity, nitrate, DO and DIC) from two sources: the Southern Ocean Carbon and Climate Observations and Modeling (SOCCOM) large-scale biogeochemical Argo dataset, which again reaches down to only 2000 m (Russell et al., 2014), and the GLODAPv2 project, comprising data between 2002 and 2013 (Olsen et al., 2016). Using these datasets, we have compiled all casts that were done within a 111-km wide (equivalent to 1° of latitude) band around the nominal location of each passage. Despite the wider spatial and temporal range, these data are much less complete than

the hydrographic data (1005 biogeochemical stations as compared with 1906 hydrographic stations), so we search for simple linear relations between neutral density and these properties along the Scotia Sea boundaries (Table 3.11 and Figure 3.24). Specifically, we use the available data to establish linear relations between each biogeochemical property and neutral density as a function of latitude (in the western boundary) or longitude (along the southern and northern borders) (Figure 3.25). Using these relations, we get the vertical profiles of all biogeochemical properties at the same locations as the hydrographic casts.

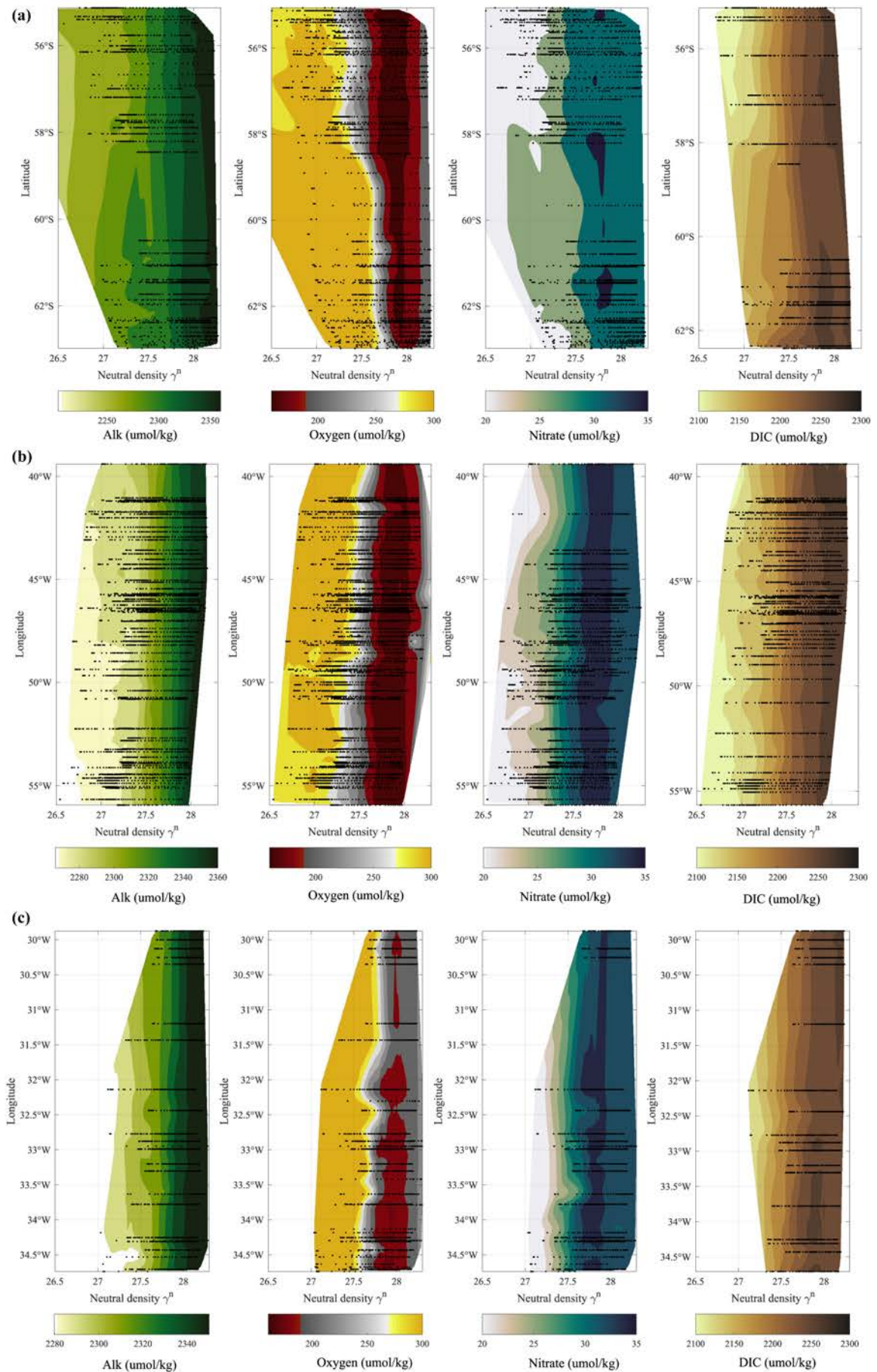
**Table 3.11.** Number of biogeochemical casts recorded in SOCCOM and GLODAPv2 databases for each passage within the dashed area 111.12 km at each side of the sections.

| PASSAGE            | BIOGEOCHEMICAL PROPERTY |                  |         |     |
|--------------------|-------------------------|------------------|---------|-----|
|                    | Alkalinity              | Dissolved oxygen | Nitrate | DIC |
| Drake              | 52                      | 83               | 70      | 55  |
| North Scotia Ridge | 68                      | 68               | 60      | 53  |
| Georgia            | 20                      | 28               | 17      | 20  |
| South Scotia Ridge | 57                      | 68               | 67      | 33  |
| Philip             | 34                      | 58               | 44      | 50  |

The annual-mean air-sea net heat exchange is obtained by adding the monthly-mean shortwave radiation, longwave radiation, latent heat flux and sensible heat flux, as available from the NOCSv2.0 Surface Flux and Meteorological Dataset, with  $1^\circ \times 1^\circ$  resolution and for the 2002 - 2014 period (Berry & Kent, 2011). Additionally, the annual-mean sea-ice melting is obtained from the AnIceFlux dataset (Haumann et al., 2016) from 2002 to 2008 with  $75 \times 75$  km resolution. We obtain the sea-surface wind stress and the evaporation-precipitation (E-P) data from the European Centre for Medium-Range Weather Forecasts (ECMWF) (Simmons et al., 1989). The E-P data and the zonal and meridional components of the sea-surface wind stress are available with a spatial resolution of  $0.75^\circ \times 0.75^\circ$  latitude-longitude grid. From the wind stress, we calculate the meridional and zonal components of the Ekman transport,  $T_{EK}$ , over the passages. The freshwater (evaporation minus precipitation and sea-ice melting), the air-sea  $p\text{CO}_2$ , and air-sea heat fluxes for the entire region are computed according to the percentage of each layer in contact with the atmosphere. The relative presence of each isoneutral layer at the sea surface is determined considering all Argo measurements within the Scotia Sea through a DIVA optimal spatial interpolation (Troupin et al., 2012), leading to fractional areas of 0.013, 0.089, 0.167, 0.174, 0.171, 0.15, 0.140, 0.068, 0.024 and 0.006 for layers 2 to 11, respectively (the presence of the first and last layer is almost negligible; Figure 3.26).



**Figure 3.24.** Distribution of (a) alkalinity, (b) dissolved oxygen, (c) DIC and (d) nitrate stations recorded in SOCCOM and GLODAPv2 databases. We only considered the stations comprised within the dashed area, 111.12 km at each side of the sections. In grey are represented the stations without these biogeochemical concentrations, and in black, where the data has been identified as bad quality flag.





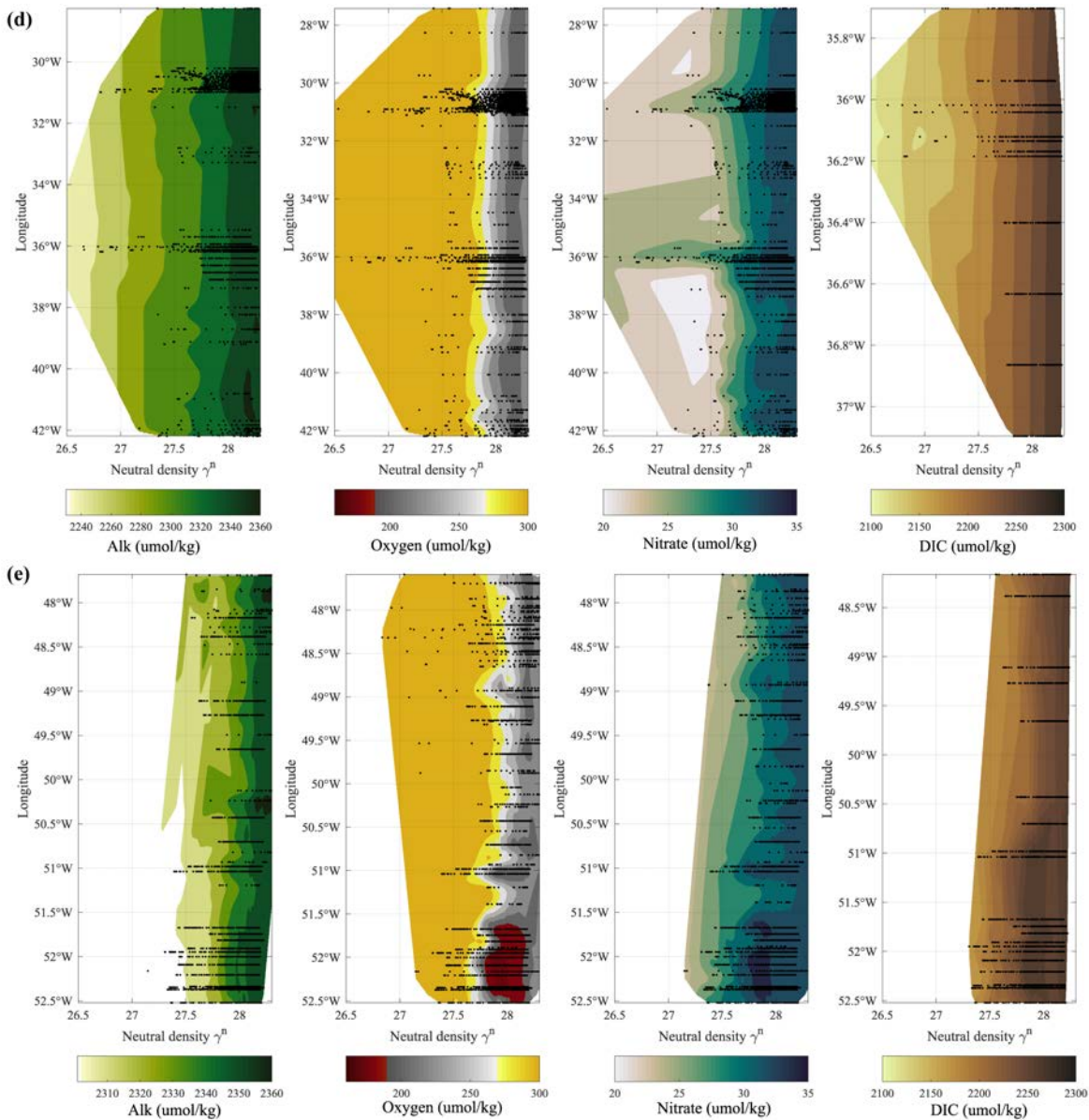


**Figure 3.25.** The linear relation of alkalinity, dissolved oxygen, nitrate and DIC concentrations ( $\mu\text{mol kg}^{-1}$ ; from left to right) with neutral density according to the SOCCOM and GLODAPv2 casts (represented in black) location in (a) Drake Passage, (b) North Scotia Ridge, (c) Georgia Passage, (d) South Scotia Ridge and (e) Philip Passage.

The annual-mean air-sea exchange of carbon dioxide ( $\text{CO}_2$ ) is estimated from the NCEI accession product, based on both the Surface Ocean  $\text{CO}_2$  Atlas Database (SOCAT) partial pressure of  $\text{CO}_2$  ( $p\text{CO}_2$ ) and on the  $p\text{CO}_2$  calculated from the SOCCOM biogeochemistry floats (Landschützer et al., 2019), available with  $1^\circ$  resolution and for the 2002 - 2017 period (Bushinsky et al., 2019); these data are spatially smoothed using a  $3 \times 3$  moving window. Finally, we use the velocity fields from the Southern Ocean State Estimate (SOSE), which is gridded at  $1/6^\circ$  horizontal resolution from 2005 to 2010 (Mazloff et al., 2010), to obtain water-transport estimates. Further, we combine these SOSE velocities with the Biogeochemical SOSE

(B-SOSE) biogeochemical property fields, with  $1/3^\circ$  resolution for the 2008 - 2012 period (Verdy & Mazloff, 2017), to determine the fluxes and transports of biogeochemical properties. The water-mass and biogeochemical property transports can then be compared with our estimates from the inverse model.

### 3.2.2.2. Inverse model setup

The inverse circulation model, which assumes that the ocean is in hydrostatic and geostrophic balance, splits the water column into isoneutral layers and imposes mass, salinity and heat conservation, within uncertainties, for each layer and the entire water column (Wunsch, 1996). In order to obtain the best possible solution, the model adjusts the horizontal reference velocity and permits water exchange between adjacent layers. Following Naveira Garabato et al. (2003), the water column is divided into 19 isoneutral layers that represent all different water masses (Table 3.12).

**Table 3.12.** Layers and approximate equivalent corresponding water mass definitions: Subantarctic Surface Water (SASW), Subantarctic Mode Water (SAMW), Antarctic Surface and Intermediate Waters (AASW/AAIW), the Upper Circumpolar Deep Water (UCDW), Lower Circumpolar Deep Water (LCDW) and Weddell Sea Deep Water (WSDW).

| Layer | Interfaces $\gamma^n$ (kg m <sup>-3</sup> ) | Water masses |
|-------|---|--------------|
| 1     | 26.80 – 26.90                               | SASW         |
| 2     | 26.90 – 27.00                               | SAMW         |
| 3     | 27.00 – 27.10                               |              |
| 4     | 27.10 – 27.20                               |              |
| 5     | 27.20 – 27.30                               | AASW/AAIW    |
| 6     | 27.30 – 27.40                               |              |
| 7     | 27.40 – 27.50                               |              |
| 8     | 27.50 – 27.60                               |              |
| 9     | 27.60 – 27.70                               | UCDW         |
| 10    | 27.70 – 27.80                               |              |
| 11    | 27.80 – 27.90                               |              |
| 12    | 27.90 – 28.00                               |              |
| 13    | 28.00 – 28.05                               | LCDW         |
| 14    | 28.05 – 28.10                               |              |
| 15    | 28.10 – 28.15                               |              |
| 16    | 28.15 – 28.20                               |              |
| 17    | 28.20 – 28.26                               |              |
| 18    | 28.26 – 28.31                               | WSDW         |
| 19    | 28.31 – 28.35                               |              |

The model assumes that the reconstructed hydrographic sections and associated transports are representative of the average climatological values. All hydrographic and biogeochemical properties are interpolated vertically over the hydrographic sections every 10 m with a second-order low pass-filter (wavenumber of  $0.5 \text{ m}^{-1}$ , or wavelength of  $4\pi \text{ m} = 12.6 \text{ m}$ ), and horizontally linearly-interpolated at 3 km and later smoothed with a 9-span moving-average filter (27 km). This interpolation is followed by the application of another two-dimensional mean filter (Reeves, [2022](#)) over a vertical-horizontal rectangle of size  $5 \times 9$  grid points, leading to an additional smoothing of 50 m in the vertical and 27 km in the horizontal, which preserves the main hydrographic signal. Finally, to fill the remaining empty gaps due to shorter profiles, we interpolate and extrapolate based on sparse linear algebra and partial differential equation (PDE) discretization (D'Errico, [2022](#)).

In the upper 2000 m of ACC in the Drake Passage section, we are only capable of quantifying the water dynamics entirely down to  $28.00 \text{ kg m}^{-3}$ . Hence, the inverse model is applied to the upper 12 neutral-density layers that are completely sampled down to this depth (i.e., neutral density  $\gamma^n$  comprised between 26.80 to  $28.00 \text{ kg m}^{-3}$ ), whereas the transport of the seven denser remaining layers as in Georgia and South Scotia Ridge passages, down to 2000 m, is calculated a posteriori considering geostrophic equilibrium.

In order to calculate the transports, the neutral density and dynamic height anomaly (referenced to the 1000-m level) are determined for each pair of stations, and the relative geostrophic velocities are calculated at the central position between the grid points using the thermal wind equation. The absolute geostrophic velocity is hence defined as the sum of two components: the geostrophic velocity relative to the reference level, which varies with horizontal position and depth, and the reference velocity  $b(x)$ , which is only a function of lateral position along the boundary vertical sections:

$$v_{abs}(x, z) = \frac{-g}{\rho_0 f} \int_{z_0}^z \frac{\partial \rho}{\partial x} dx + b(x) \quad (3.1)$$

where  $x$  denotes the horizontal direction and  $z$  denotes the vertical direction;  $z_0$  is the depth of the reference level,  $\rho$  is the water density ( $\rho_0$  is a depth-mean density value),  $g$  is the gravitational acceleration, and  $f$  is the Coriolis parameter.

The reference level is generally set at 1000 m, the parking depth for most Argo floats. The reference velocity,  $b(x)$ , is hence defined as the sum of the drifting speed of the Argo floats at the 1000-m parking depth and the adjustment provided by the inverse model,  $b'(x)$  (Ollitraul & Rannou, [2013](#); Rosell-Fieschi et al., [2015](#); **Chapter 3.1**). In the case of bottom depth less than 1000 m, we impose a no-motion layer at their deepest common level, while for absent Argo speed values, we set the 1000-m reference level as motionless. Furthermore, due to the

remarkable absence of Argo floats along the South Scotia Ridge and Philip Passage in the southern boundary of our domain, we impose a no-motion level at 2000 m. In all cases, this is an initial choice of reference velocity, which is adjusted by the inverse model in order to conserve the water properties. For each pair of stations and layer, we calculate the water transports in and out of the domain (negative values represent flow input, whereas positive values represent flow output).

Additionally, we incorporate the freshwater flux,  $F_w$ , to the upper Scotia Sea according to the relative presence of the model layers at the sea surface (Figure 3.26), and further incorporate the Ekman transports,  $T_{EK}$ , to the uppermost layer along the sections (Figure 3.27). Almost all the freshwater corresponds to ice-sea melting with  $0.01 \text{ Sv}$  ( $2.3 \times 10^{-4} \text{ Sv}$  correspond to evaporation and  $6.2 \times 10^{-4} \text{ Sv}$  to precipitation). Finally, the sum of Ekman transports through the boundaries of the domain are  $0.11 \text{ Sv}$  for the Drake Passage (zonal component) and  $0.26 \text{ Sv}$ ,  $0.39 \text{ Sv}$ ,  $0.55 \text{ Sv}$  and  $0.18 \text{ Sv}$  for the North Scotia Ridge, Georgia Passage, South Scotia Ridge and Philip Passage, respectively (meridional component).

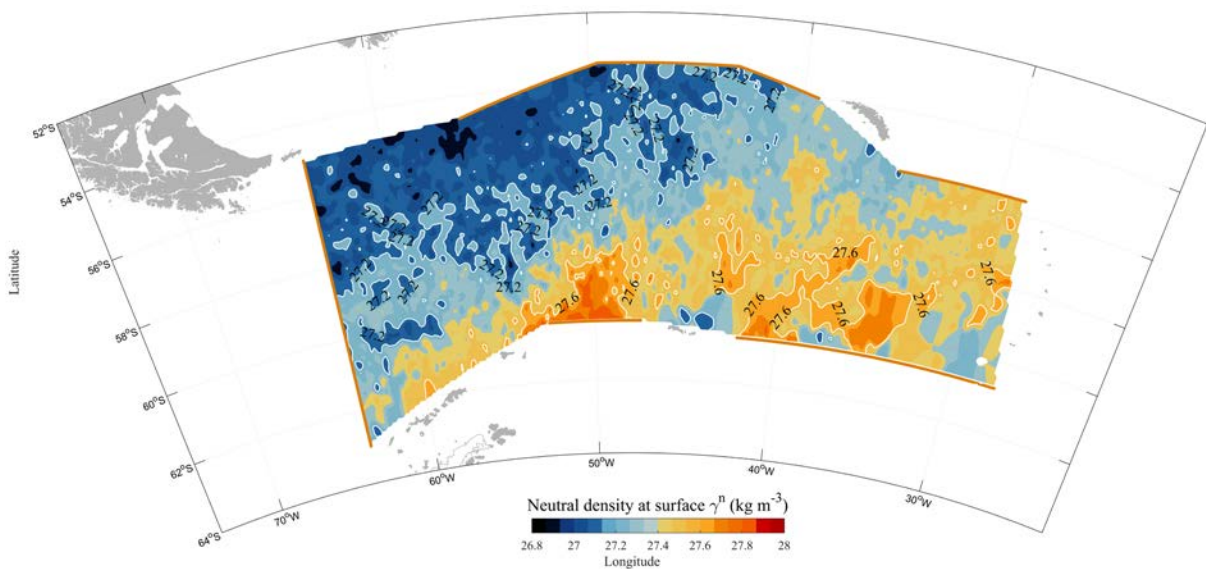


**Figure 3.26.** Neutral density layers ( $\text{kg m}^{-3}$ ) at the surface with white contours indicating the boundary of each water mass. The relative presence of each layer at the sea surface is 0.013 for layer number 2, 0.089 for layer 3, 0.167 for layer 4, 0.174 for layer 5, 0.171 for layer 6, 0.15 for layer 7, 0.140 for layer 8, 0.068 for layer 9, 0.024 for layer 10 and 0.006 for layer 11. For the first and last layers, their relative presence is almost negligible.

The inverse model has  $13 \times 3$  equations for mass, heat and salt conservation, one per isoneutral layer plus additional ones for the total mass and salt transports in the entire water column down to the reference isoneutral ( $28.00 \text{ kg m}^{-3}$ ) and one equation for the air-sea heat exchange,  $H_e$ , in the entire region (subsection 2.2.3). This last equation basically indicates that

the entire region gains  $4.2 \times 10^{13}$  Watts, which is distributed among layers proportional to their presence at the sea surface. The heat and salinity equations are set in terms of anomalies, defined as the difference between the actual value and the layer's temperature and salinity averages, respectively (Ganachaud, [2000](#), [2003](#)).

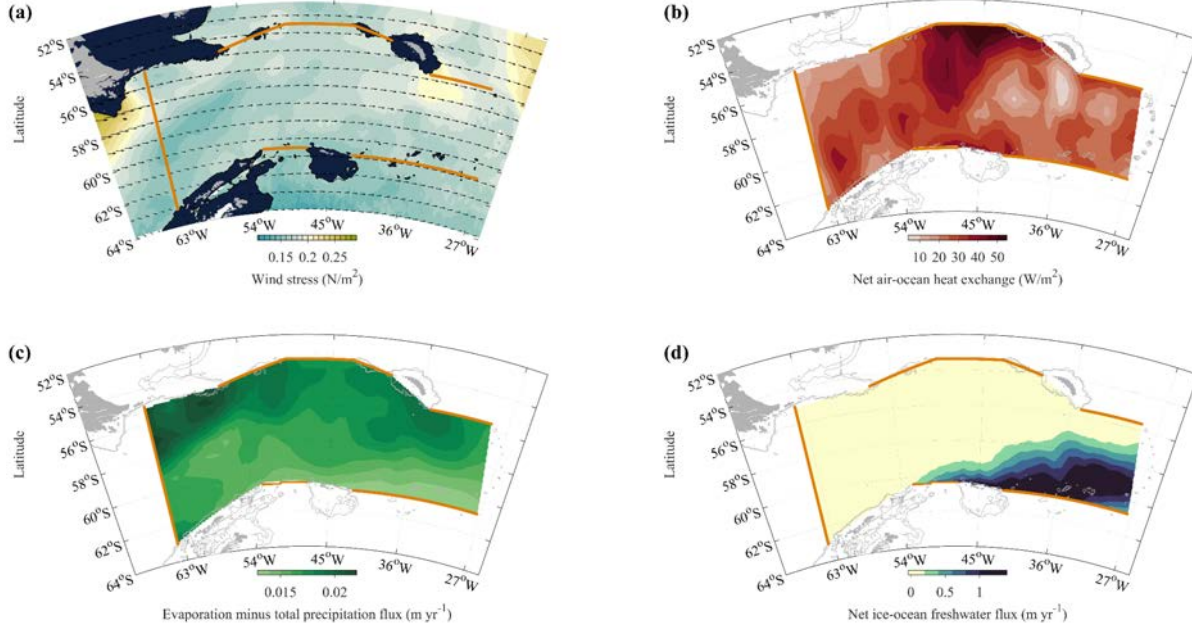


**Figure 3.27.** Annual-mean climatological distributions of (a) wind stress, (b) air-ocean heat exchange, (c) evaporation minus total precipitation and (d) ice-ocean water fluxes in the Scotia Sea. For the inverse model calculations, the freshwater fluxes are quantified within the region, while the Ekman transports are computed only along the boundaries.

As a result, our inverse model has a total of 39 equations (13 for mass and total mass conservation, 13 for salt and total salt anomaly conservation, and 13 for heat conservation). The unknowns in these equations are the adjustments of the reference velocities, the Ekman transports and the freshwater fluxes, and the mean vertical advection and diffusion terms over the entire domain (Table [3.13](#)). These vertical terms are included in the model in order to reflect the water mass transformation as a consequence of both two-way (mixing) and one-way (vertical velocity) between adjacent neutral density layers. While the vertical advection influences all the properties, the vertical diapycnal diffusion only alters the heat and salt equations, experiencing this latter a down-gradient transfer for the diapycnal diffusivities. The resulting matrix system for each property conservation equation and layer will take the following form:

$$\iint_{\gamma_n^2}^{\gamma_n^1} [\rho C (v_{rel} + b) + CT_{EK}] dz dx = \iint_{A_h} \left[ \left( K_z \frac{\partial(\rho C)}{\partial z} - w \rho C \right) + \delta_1(C) H_e + \delta_2(C) F_w \right] dx dy \quad (3.2)$$

where  $A_h$  represent the horizontal surface enclosing each isoneutral,  $C$  is the property concentration per unit mass ( $C = 1$  for mass),  $w$  corresponds to the diapycnal velocity,  $K_z$  to the vertical diffusion, and the last two terms represent the freshwater flux,  $F_w$ , and Ekman transport,  $T_{EK}$  (for the isopycnals layers in contact with the atmosphere);  $\delta_1(C)$  is a delta function equal to 1 when  $C$  is heat and zero otherwise, and  $\delta_2(C)$  is another delta function equal to 1 when  $C$  is salt and zero otherwise. Once we solve the inverse problem, the resulting velocity at the  $\gamma^n = 28.00 \text{ kg m}^{-3}$  isoneutral is used as the reference velocity to estimate the transports for the remaining seven layers down to 2000 m (LCDW and WSDW).

**Table 3.13.** *A priori* uncertainties for all unknowns and equations:  $b'$  corresponds to the velocity adjustment at the reference level;  $w'$  to the adjustment of the diapycnal velocity across the layer interfaces;  $K'$  to the adjustment of the diapycnal diffusion coefficients at the layer interfaces;  $\Delta T_{EK}$  to the annual-mean Ekman transport adjustment; and  $\Delta F_w$  to the annual-mean freshwater flux adjustment.

| Unknown         | <i>A priori</i> uncertainties in the unknowns                               |
|-----------------|---|
| $b'$            | 50% (SD Argo reference velocities) <sup>2</sup>                             |
| $w'$            | $2.05 \times 10^{-10}$ to $1.62 \times 10^{-13} \text{ m}^2 \text{ s}^{-2}$ |
| $K'$            | $1 \times 10^{-8} \text{ m}^4 \text{ s}^{-2}$                               |
| $\Delta T_{EK}$ | 50% annual average (Sv <sup>2</sup> )                                       |
| $\Delta F_w$    | 50% climatological value (Sv <sup>2</sup> )                                 |
| Equations       | <i>A priori</i> uncertainties in the equations                              |
| Mass            | $R_{mass} = 0.5 \text{ Sv}^2$   |
| Salt            | $0.01 R_{mass}$ (SD salt anomaly) <sup>2</sup>                              |
| Heat            | $R_{mass}$ (SD heat anomaly) <sup>2</sup>                                   |

The undetermined system of equations is solved with a Gauss-Markov estimator, a method that uses a priori variance information for each unknown (Table 3.13) to produce a minimum error-variance solution (Wunsch, 1996; Ganachaud, 2000; subsection 2.2.2.4). The model requires some prior estimates for the uncertainties of all variables, which essentially tells how reliable each variable is, i.e., the smaller the a priori uncertainty the more reliable is the variable, so the model will place more weight on producing a solution.

We set the standard deviation (SD) of the mass transport at  $0.7 \text{ Sv}$ , so that the *a priori* mass transport uncertainty  $R_{mass}$  becomes  $0.5 \text{ Sv}^2$ , and relate it to the *a priori* uncertainties of the heat ( $R_{heat}$ ) and salt ( $R_{salt}$ ) transports as follows:

$$R_{salt} = a R_{mass} SD_{salt}^2 \quad (3.3)$$

$$R_{heat} = b R_{mass} SD_{heat}^2 \quad (3.4)$$

where  $a$  and  $b$ , respectively, are the ratios (relative weights) of the salt and heat *a priori* uncertainties as compared with the mass uncertainty. The procedure followed consists of searching how the overall mass, heat and salt transports (down to the 28.00 kg m<sup>-3</sup> isoneutral) balance out as a function of these relative weights.

The ratios that best fit the three properties correspond to a heat/mass ratio  $b = 1$  and a salt/mass ratio  $a = 0.01$  (Figure 3.28). This implies that salt is highly conservative, which is consistent with the low exchange of water between the ocean and the atmosphere. Hence, the lowest value of uncertainty is assigned to the salt anomaly equations, and a much greater uncertainty (two orders of magnitudes larger) is allowed in the mass and heat anomaly equations.

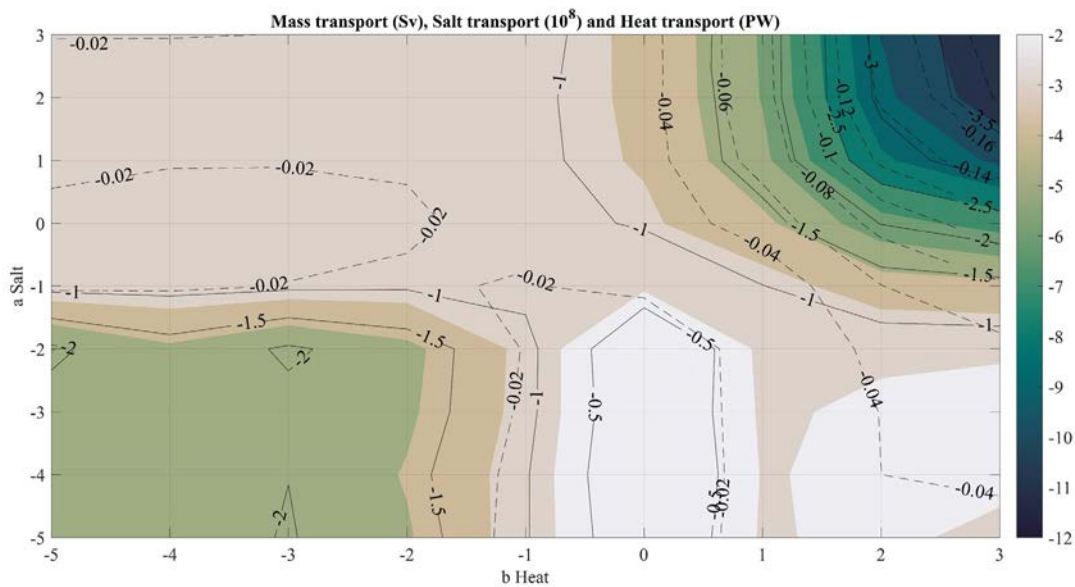


**Figure 3.28.** Imbalances in the total salt (solid contours), mass (background colours) and heat (dashed lines) as a function of the logarithm of the relative weight of the uncertainties of salt with respect to mass,  $a$ , and heat with respect to mass,  $b$ .

The *a priori* uncertainty of the reference level velocity is estimated from the SD of the speed of the Argo floats: Drake Passage, 0.085 m s<sup>-1</sup>; North Scotia Ridge passages, 0.059 m s<sup>-1</sup>; Georgia Passage, 0.042 m s<sup>-1</sup>; for the South Scotia Ridge passages and Philip Passage we set the average of the previous values, 0.062 m s<sup>-1</sup> (Table 3.13).

We introduce an initial adjustment to the vertical advection, the initial horizontal mass transport imbalances according to each neutral density layer up to 27.6 kg m<sup>-3</sup>, in the opposite sign. Down from this isoneutral interface, we only consider the inverse model adjustment. Their variances of the vertical velocities introduced *a priori* range from  $2.05 \times 10^{-10}$  to  $1.62 \times 10^{-13}$  m<sup>2</sup> s<sup>-2</sup> with the highest vertical velocity at the surface. Also, we introduce an initial vertical diffusion coefficient of 10<sup>-4</sup> m<sup>2</sup> s<sup>-1</sup> for all the layers based on its global ocean averaged value,

consistent with the values reported (coefficients between  $10^{-5} \text{ m}^2 \text{ s}^{-1}$  and  $10^{-2} \text{ m}^2 \text{ s}^{-1}$ , reaching the  $10^{-2} \text{ m}^2 \text{ s}^{-1}$  in contact with the seafloor) in the Scotia Sea and Drake Passage (Ledwell et al., 2011; Naveira Garabato et al., 2004). Therefore, it was decided to use a diffusion variance of  $10^{-8} \text{ m}^4 \text{ s}^{-2}$ .

### 3.2.2.3. Sensitivity study

In order to establish an objective criterion for selecting the optimal combination of percentages to apply to our uncertainties, especially to the diapycnal velocity and vertical diffusivity, we perform a sensitivity test. For that, the *a priori* uncertainties of the measured variables – Argo reference velocities, Ekman transport annual average and Freshwater climatological value – have been tested at 50% in front of the inferred variables – vertical velocities and diffusivities including the initial coefficient or adjustment introduced – with a wide range of percentages. These percentages span from 10% up to 400%, running the inverse model a total of 100 times. The parameters computed to determine the optimal combination are the total net transport imbalances of mass, heat, salt and DIC (Figure 3.29).

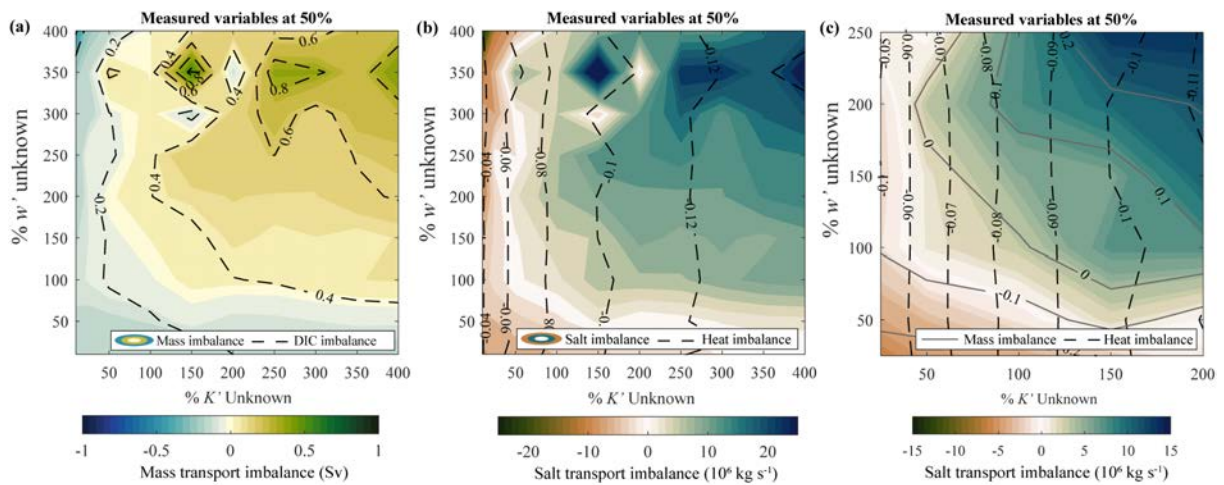


**Figure 3.29.** Net transport imbalances of (a) mass (Sv; coloured) and DIC (Pg of C year<sup>-1</sup>; dashed contours), and (b) salt ( $10^6 \text{ kg s}^{-1}$ ; coloured) and heat (PW; dashed contours) after applying the inverse model with different percentages to the uncertainties of  $w'$  and  $K'$  unknowns. Furthermore, (c) zoom of the mass (contours), heat (dashed contours) and salt (coloured) transport imbalances assessed together is shown applying from 25% to 200 - 250% of the uncertainties of both unknowns.

The mass, DIC and salt transport imbalances display a similar distribution for the same percentages applied to  $w'$  and  $K'$  unknowns. Instead, heat imbalances decrease with low percentages applied on  $K'$ . The minimum imbalance corresponds to mass and salt minimums of around 50% of  $K'$ , coinciding with small DIC and heat transport imbalance solutions of 0.28



Pg C year<sup>-1</sup> and -0.065 PW. Hence, the chosen percentages applied to the uncertainties of the diapycnal velocity and diffusion coefficients are 200% and 50%, respectively (Table 3.13).

#### 3.2.2.4. Biogeochemical approach

Once we have the velocity field in the Scotia Sea boundaries obtained from the inverse circulation model, we may compute the transports of the biogeochemical properties and assess their balances in the Scotia Sea. In particular, we explore the conservation of DIC with the objective of identifying the carbon budget components, including the input of anthropogenic carbon to the region. The procedure requires calculating the fluxes of biogeochemical properties through each pair of stations along the Scotia Sea boundaries as the product of velocity and the biogeochemical property concentration. Then, integrating them along the entire domain for each neutral density layer and down to the 28.00 kg m<sup>-3</sup> isoneutral surface.

The balances of nitrate and DIC within the study area may also be used to estimate the anthropogenic input of inorganic carbon, as follows:

$$\Delta T_{NO_3} \equiv T_{out,NO_3} - T_{in,NO_3} = I_{NO_3} \quad (3.5)$$

$$\Delta T_{DIC} \equiv T_{out,DIC} - T_{in,DIC} = E_{DIC} + A_{DIC} + I_{DIC} \quad (3.6)$$

where  $T_{in}$  and  $T_{out}$  stand for the amount of property entering and leaving the domain, respectively, and  $I$  stands for the net internal generation of the property as a result of biogeochemical processes.  $A$  and  $E$  affect only DIC, with  $A$  representing the accumulation of DIC within the domain due to the anthropogenic increase of carbon dioxide in the atmosphere and  $E$  accounting for the air-sea exchange of inorganic carbon. All exchanges outward of the domain are taken as positive, and positive  $I$ ,  $E$  and  $A$  values represent internal DIC gain within the basin.

Under the assumption that there is no long-term accumulation or loss of organic matter within the region, i.e., that carbon is a non-limiting nutrient so that the anthropogenic DIC input does not lead to a substantial change of productivity, equation 3.6 may be rewritten in terms of the changes (output minus input) of nitrate and DIC:

$$\Delta T_{DIC} = E_{DIC} + A_{DIC} + 7.3 \Delta T_{NO_3} \quad (3.7)$$

where we have considered a Redfield ratio of P:N:C:O = 1:16:117:170, with a carbon-nitrogen ratio of 16:117=7.3.

In order to estimate the DIC accumulation rate, we calculate the volume of the Scotia Sea down to 2000 m and the fraction volume occupied by each water mass. Their volumes are determined by multiplying their presence in the area according to the neutral density surfaces

at every 100-m depth. To obtain an optimal spatial interpolation of the neutral density surfaces for the whole Scotia Sea, we implemented a DIVA interpolation (Troupin et al., [2012](#)) from Argo measurements. Then, the total water-mass volume for each water mass is obtained by integrating all the water column. The surface of our study area is about  $1.5 \times 10^{12} \text{ m}^2$ , and the volume for each water mass turns out to be  $2.7 \times 10^{11} \text{ m}^3$  for SASW,  $7.0 \times 10^{13} \text{ m}^3$  for SAMW,  $3.6 \times 10^{14} \text{ m}^3$  for AASW/AAIW and  $10^{15} \text{ m}^3$  for UCDW. The volume associated with LCDW and WSDW is estimated to be about  $1.6 \times 10^{15} \text{ m}^3$  (Figure [3.30](#)).

In order to associate the biogeochemical imbalances to the main biological processes in the region, we have computed the transports in the warm (SASW/SAMW) and cold (AASW/AAIW and UCDW outcrop) sides of the Polar Front. The position of this front is identified from the maximum horizontal temperature gradients at 1000 meters depth as in **Chapter 3.1**; the front turns out to be approximately located at  $58^\circ\text{S}$  in the Drake Passage and  $49.5^\circ\text{W}$  in the North Scotia Ridge.

### 3.2.3. Results

#### 3.2.3.1. Vertical boundary sections

The hydrographic sections consist of 297, 380, 132, 266 and 93 stations in the Drake Passage, North Scotia Ridge, Georgia Passage, South Scotia Ridge and Philip Passage, respectively (Figure [3.31](#)). The hydrographic and biogeochemical data are available every 3 km in the horizontal and 10 m in the vertical, although, as explained before, they represent fields smoothed over about 27 km and 50 m, respectively. The frontal systems are clearly visible through the sloping temperature and salinity contours down to 2000 m, i.e., the saltiest and coldest waters (temperatures around  $0^\circ\text{C}$  and salinities above  $34.6 \text{ g kg}^{-1}$ ) are found over all the domain, except for the surface and intermediate layers in the northern portion of the Drake Passage and the western part of the North Scotia Ridge (Figure [3.31a](#)).

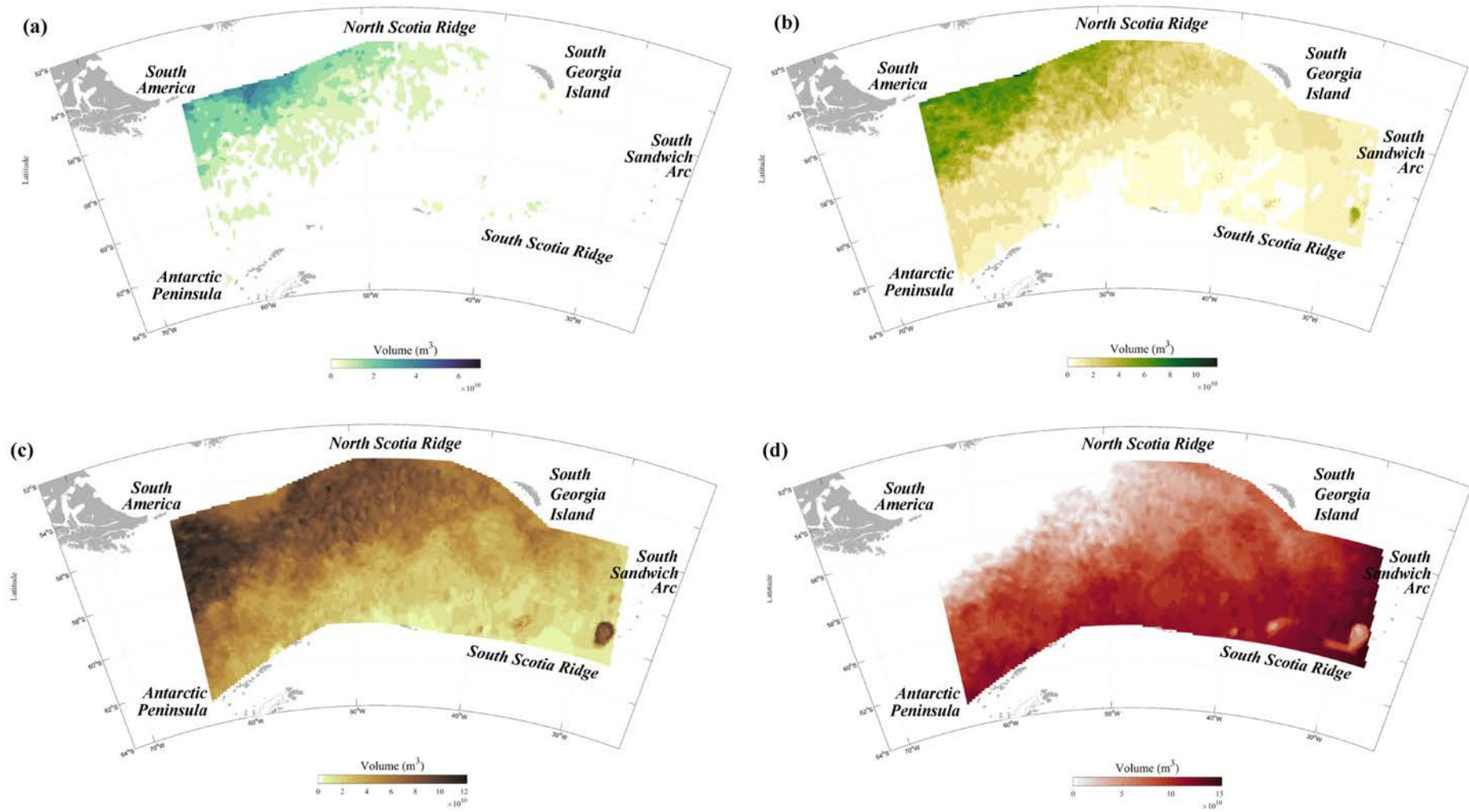


**Figure 3.30.** Volume estimation of (a) SASW/SAMW, (b) AASW/AAIW, (c) UCDW and (d) LCDW/WSDW within the Scotia Sea borders. Notice that lighter water accumulates at the Scotia Sea's upper margin while denser water accumulates at the lower margin.

In contrast, the relatively fresh and warm surface waters near South America reveal the positive heat and water exchange with the atmosphere (ocean net heat and freshwater gain, Figure 3.27).

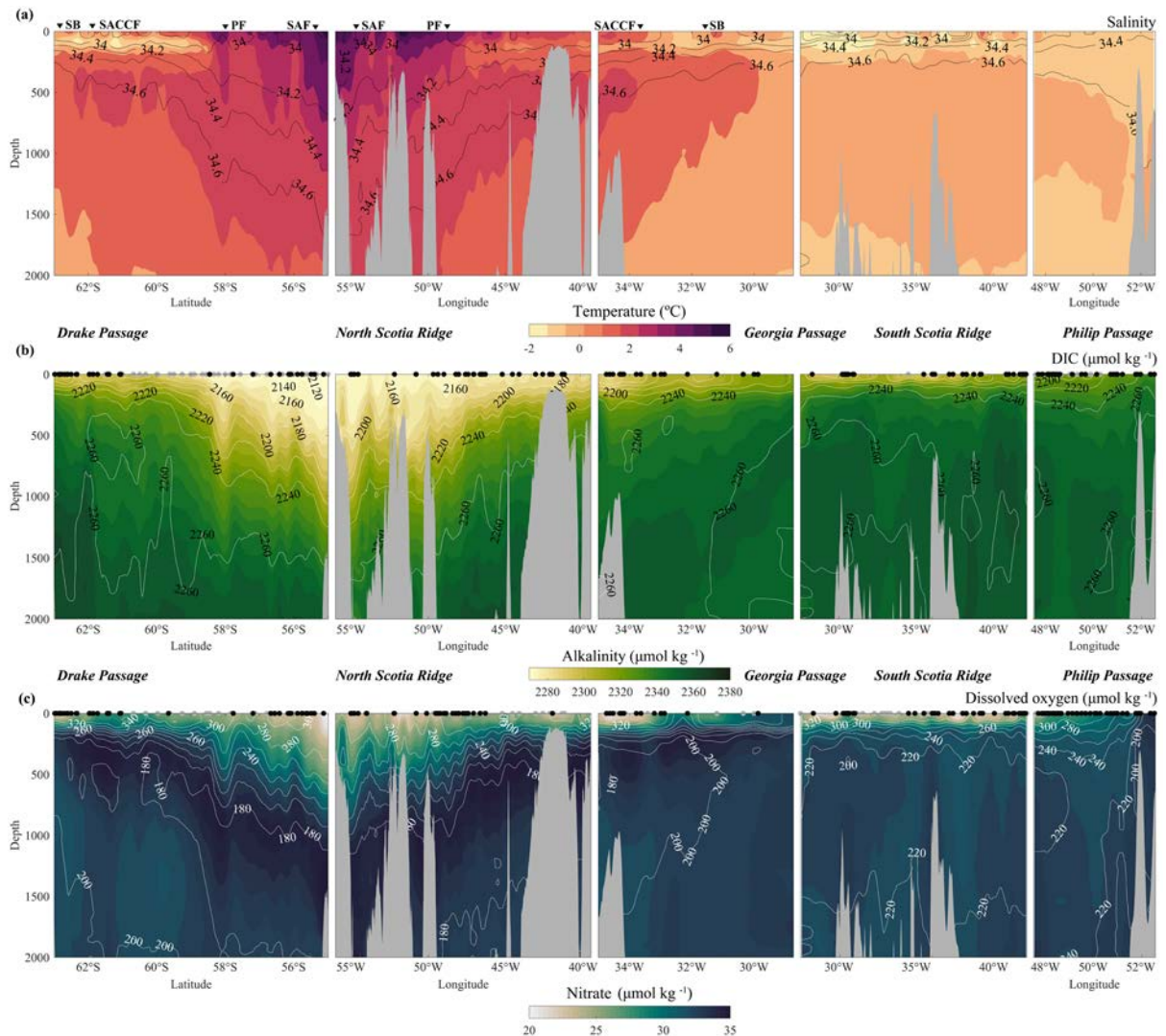


**Figure 3.31.** (a) Temperature (colour) and salinity (contours), (b) alkalinity (colour) and DIC (contours), and (c) nitrate (colour) and dissolved oxygen (contours) along the Scotia Sea boundaries. From left to right: Drake Passage, North Scotia Ridge, Georgia Passage, South Scotia Ridge and Philip Passage. In the upper horizontal axis, we represent the location of the fronts (upper panel) and the original position of the biogeochemical SOCCOM and GLODAPv2 casts (middle and lower panel); those SOCCOM and GLODAPv2 casts corresponding to the contour variable are represented in grey, whereas the black ones represent the coloured variable. Notice that positions may match, resulting in black dots overlapping the grey ones.

The vertical distribution of temperature, salinity and biogeochemical properties follow, to a large extent, the isoneutral layers. Thereby, the vertical biogeochemical sections have been completed using latitude- or longitude-dependent linear relations between each

biogeochemical property and neutral density (Figure 3.25). The location of the original biogeochemical casts and the resulting property distributions are represented in Figure 3.31b, c. We find the lowest nitrate, DIC and alkalinity concentrations and the highest DO concentrations in the warmer and saltier surface waters near the South American coast. DIC and alkalinity concentrations increase with density, with peak values in the deep Drake Passage of  $2260 \mu\text{mol kg}^{-1}$  and  $2360 \mu\text{mol kg}^{-1}$ , respectively. Instead, nitrate concentrations increase and dissolved oxygen decrease with depth up to  $\gamma^n = 27.9 \text{ kg m}^{-3}$ , reaching the highest concentrations of  $34 \mu\text{mol kg}^{-1}$  and the lowest of  $160 \mu\text{mol kg}^{-1}$ . Some intrusions of dense Weddell Sea waters, characterized by high DIC and alkalinity and low nitrate and dissolved oxygen, intrude into the basin through the South Scotia Ridge passages and Philip Passage at different depth levels.

Six water masses are distinguishable in the upper 2000 m of the ACC along the Scotia Sea boundaries (Figure 3.32), distributed in 19 neutral-density layers (although only the upper 12 layers, down to  $\gamma^n < 28.00 \text{ kg m}^{-3}$ , are fully sampled; Table 3.12). The DIC, dissolved oxygen and nitrate distribution according to the density layers along the Scotia Sea boundaries are represented in Figure 3.33. Due to the sharp tilting of the isoneutral layers in the region, the upper four water masses are in contact with the atmosphere at different latitudes or longitudes: the salty and warm SASW (one layer), fresh SAMW (three layers), fresh and cold AASW/AAIW (four layers) and the upper layers of low-oxygen UCDW (four layers). The two deeper water masses do not interact with the atmosphere: the LCDW and the WSDW, the latter detectable only in the eastern Georgia Passage, the South Scotia Ridge and the Philip Passage.

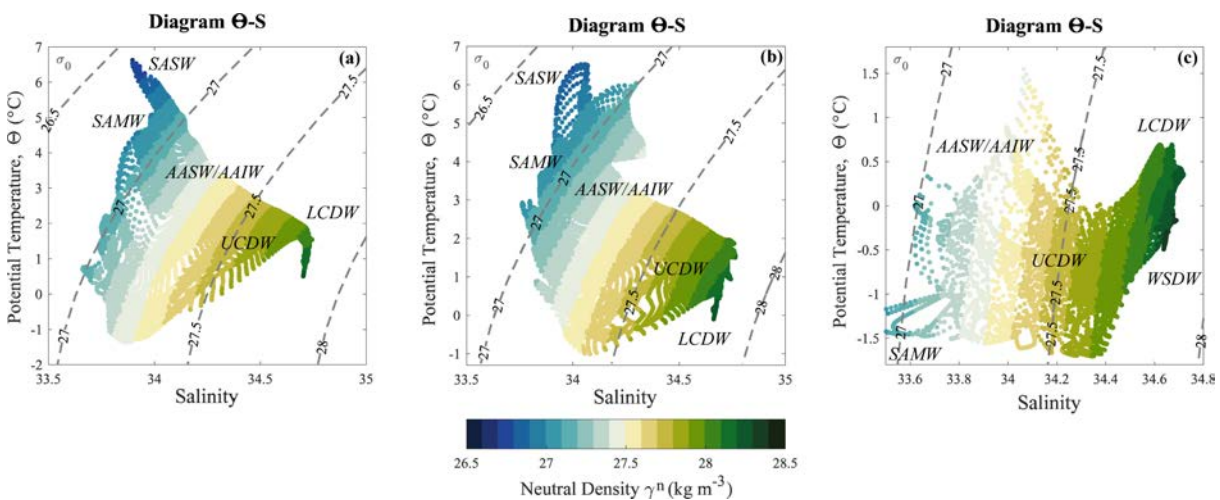


**Figure 3.32.**  $\theta$ - $S$  diagrams and neutral density distribution (colour) of the ACC down to 2000 m along the Scotia Sea boundaries: (a) Drake Passage, (b) North Scotia Ridge and Georgia Passage, and (c) South Scotia Ridge and Philip Passage. The dashed lines in grey correspond to the isopycnals. Also, the six main water masses have been identified: SASW, SAMW, AASW/AAIW, UCDW, LCDW and WSDW.

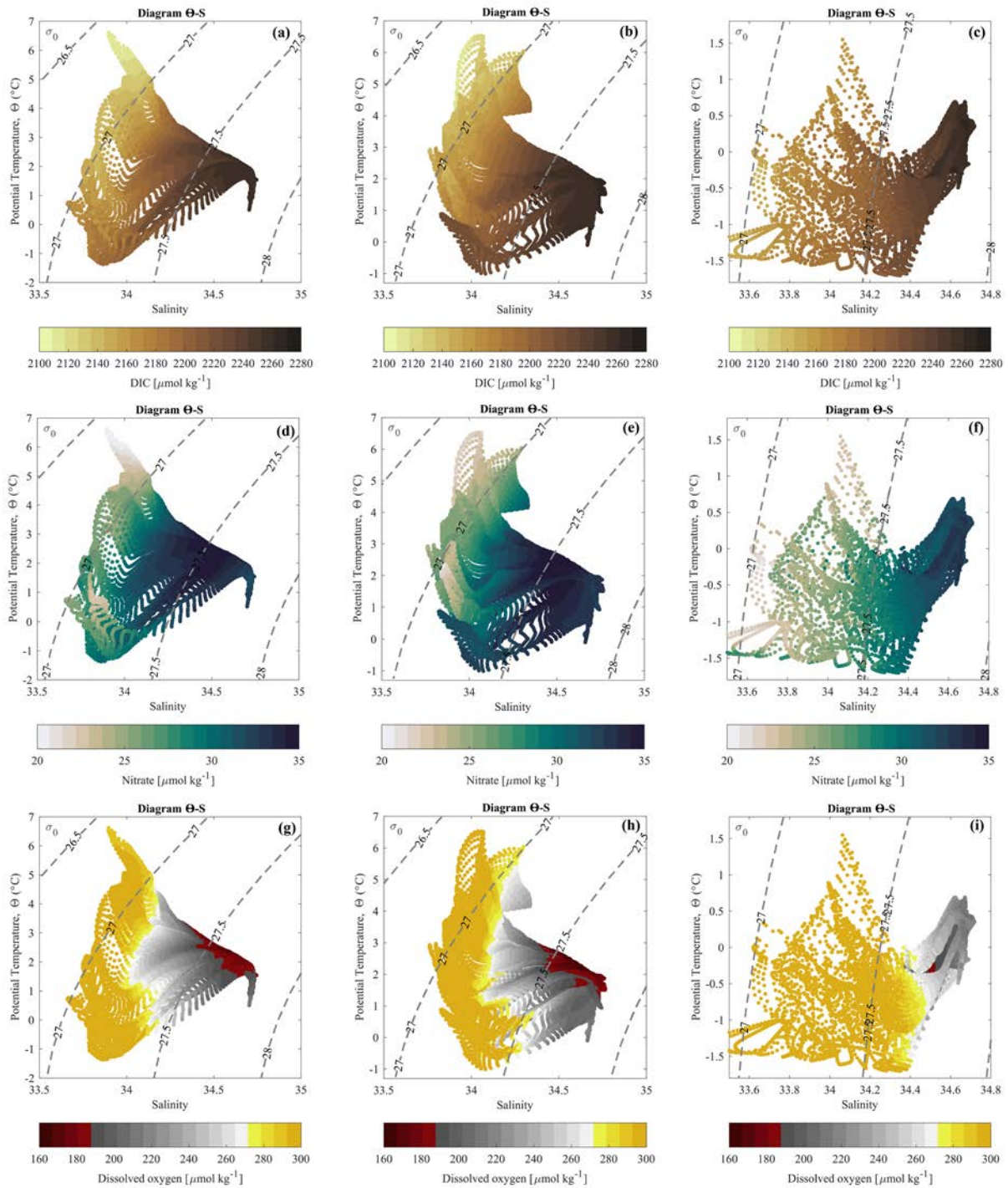


**Figure 3.33.** (a, b, c) DIC, (d, e, f) nitrate and (g, h, i) dissolved oxygen  $\theta$ -S diagrams up to 2000 m depth along the Scotia Sea boundaries: (a, d, g) Drake Passage, (b, e, h) North Scotia Ridge and Georgia Passage and (c, f, i) South Scotia Ridge and Philip Passage. The dashed lines in grey correspond to the isopycnals.

### 3.2.3.2. Water velocities and biogeochemical fluxes

The inverse model 1000-m reference velocities along the Scotia Sea boundaries are consistent with the initial Argo speeds (green and red lines in Figure 3.34a and 3.34b,

respectively). At this reference level, water enters the domain through the Drake Passage and leaves it mainly through the North Scotia Ridge and Georgia Passage. The maximum reference velocities, obtained by adding the inverse model adjustment to the Argo velocities, are  $0.28 \text{ m s}^{-1}$  in the Drake Passage,  $0.19 \text{ m s}^{-1}$  in the North Scotia Ridge,  $0.16 \text{ m s}^{-1}$  in the Georgia Passage,  $0.03 \text{ m s}^{-1}$  in the South Scotia Ridge, and  $0.02 \text{ m s}^{-1}$  in the Philip Passage. The high speeds in the Drake and Northern passages (the three North Scotia Ridge passages and the Georgia Passage as defined in **Chapter 3.1**) indicate that a large fraction of the transport is associated with the ACC fronts, with a substantial barotropic contribution in the upper 2000 m.

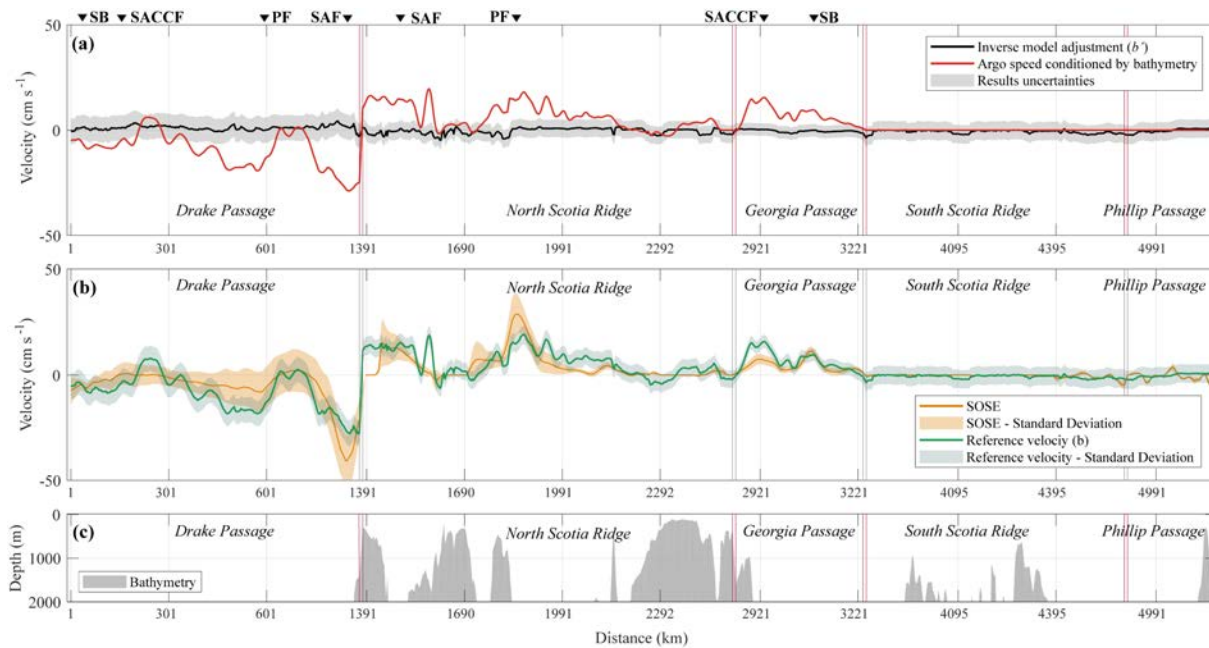


**Figure 3.34.** (a) Argo-float velocity ( $\text{cm s}^{-1}$ ) and inverse model adjustment at 1000 m, along the Scotia Sea boundaries. The inverse model is initialized using the Argo float velocities at 1000 m and zero velocities when the water depth is less than 1000 m and in the South Scotia Ridge and Philip Passage (because of the absence of Argo floats); the grey shading represents the *a priori* uncertainties. (b) Reference velocity at 1000 m (or the seafloor when shallower) as deduced from the inverse model (green line) and velocity at 1000 m from the SOSE model (orange line); the colour shading represents the respective standard deviation. (c) The bathymetry shallower than 2000 m along the Scotia Sea boundaries is shown in grey. Velocities are represented positive/negative to indicate water leaving/entering the domain, following the divergence/convergence sign criteria.

The inverse model incorporates vertical mixing between adjacent isopycnal layers through vertical advection and diffusion processes, which contributes to adjust the mass, salinity and heat balances in all the layers (Figure 3.35). Vertical advection represents one-way transfer of all physical (heat, salt and mass) and biogeochemical (DIC, alkalinity, nitrate and dissolved oxygen) properties. Vertical diffusion, on the other hand, represents two-way

exchange of all physical and biogeochemical properties, although the mass exchange is negligible (two-way volume exchange is zero, and the corresponding mass exchange is negligible because of the very small density differences between layers).

Vertical velocities obtained from the inverse model are  $10^{-6}$ -  $10^{-5}$   $\text{m s}^{-1}$ . For a region with an area of about  $1.5 \times 10^{12}$   $\text{m}^2$  this would represent a vertical transport adjustment of order 1 - 10 Sv. In terms of vertical diffusion, the inverse model applies up to  $3.5 \times 10^{-4}$   $\text{m}^2 \text{ s}^{-1}$  of divergence in the intermediate-deep neutral interface layer of  $27.6 \text{ kg m}^{-3}$  balancing the salt and heat transfer, being practically negligible its vertical contribution in salt transport. Instead, vertical advection causes convergence of all water properties for all interfaces with a negative vertical velocity involving a net downward mass, salt and heat transference of 0.9 Sv,  $32.5 \times 10^6 \text{ kg s}^{-1}$  and  $3.4 \times 10^{12}$  watts, respectively, to the deep layers beyond  $28.00 \text{ kg m}^{-3}$ . The maximum mass transference of 5.9 Sv corresponds to convergence and occurs through the  $27.2 \text{ kg m}^{-3}$  isoneutral interface from SAMW to AASW/AAIW. The diffusion brings about a negative transport of heat in the mode and surface-intermediate interfaces (SAMW and AASW/AAIW) and positive transport of salt mainly at deeper surface-intermediate and lighter deep waters (AASW/AAIW and UCDW).

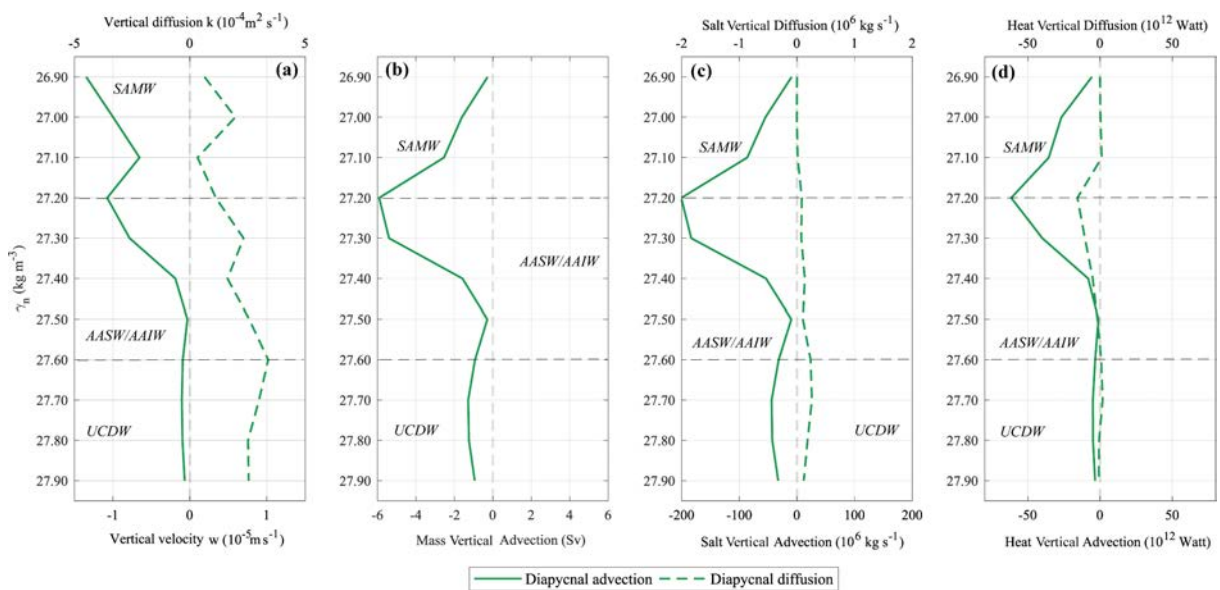


**Figure 3.35.** (a) Vertical velocity and diffusion after applying the inverse model, and vertical (b) mass advection, (c) salt advection and diffusion, and (d) heat advection and diffusion for the 11 neutral density interfaces. In green is represented the final diapycnal transference after adding the inverse model solution to the initial adjustment. Notice that the dashed lines correspond to the diapycnal diffusivities. Velocities are represented positive/negative to indicate water is diapycnal transferred up/down across the interfaces, following the divergence/convergence sign criteria.



The geostrophic velocity field that results after applying the inverse model is consistent with the neutral density field (Figure 3.36a). Peak surface velocities of  $0.68 \text{ m s}^{-1}$  and  $0.58 \text{ m s}^{-1}$  are associated with the SAF and PF, respectively. These two fronts coincide with the sloping isoneutrals in the northern and western half of the Drake Passage and the North Scotia Ridge. A weaker current core is linked to the SACCF in the southern portion of the Drake Passage and the western side of the Georgia Passage. The SB is barely noticeable in the Drake Passage but visible on the eastern side of the Georgia Passage. The relatively high positive velocities in Philip Passage indicate the existence of water inflow from the Weddell Sea.

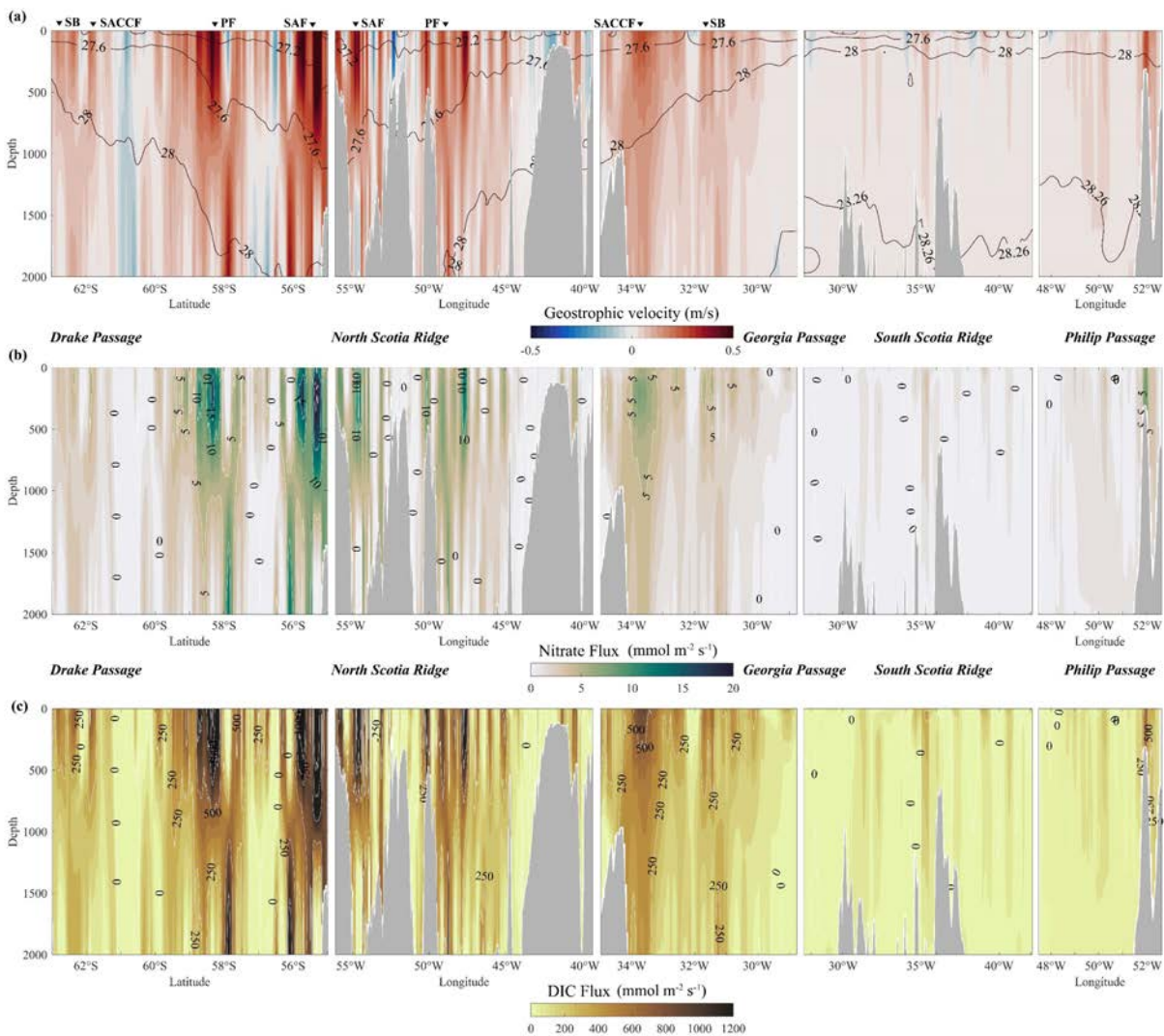


**Figure 3.36.** (a) Geostrophic velocity with neutral density contours ( $\text{kg m}^{-3}$ ), and (b) nitrate and (c) DIC fluxes along the Scotia Sea boundaries after applying the inverse model. From left to right: Drake Passage, North Scotia Ridge, Georgia Passage, South Scotia Ridge and Philip Passage. In the upper horizontal axis, we represent the location of the fronts (upper panel) and the vertical sections have a 3-km resolution. Positive/negative values in geostrophic velocity indicate north-east/south-west direction.

The distribution of the biogeochemical fluxes coincides largely with the geostrophic velocity fields associated with the SAF, PF and SACCF fronts (Figures 3.36b and 3.36c, see Figure 3.37 for dissolved oxygen and alkalinity fluxes). Since neither DIC nor nitrate are limiting in the upper ocean, the peak values occur in the upper ocean and decrease slowly with depth, although for nitrate, it can extend very deep because this property has subsurface maximum values (between about 27.5 and 27.7 kg m<sup>-3</sup>) that reach as deep as 1000 m near the northern portion of the Drake Passage. Intense cores characterize the northeastward fluxes at Drake Passage, with maximum values of 21.6 mmol m<sup>-2</sup> s<sup>-1</sup> centred around 200 m depth for the nitrate and 1493 mmol m<sup>-2</sup> s<sup>-1</sup> centred at the sea surface for DIC, that lose intensity as they cross the Scotia Sea and reach the Northern Passages. With the nutrient stream carried by the SACCF occurs the opposite, largely intensified in the western side of Georgia Passage.

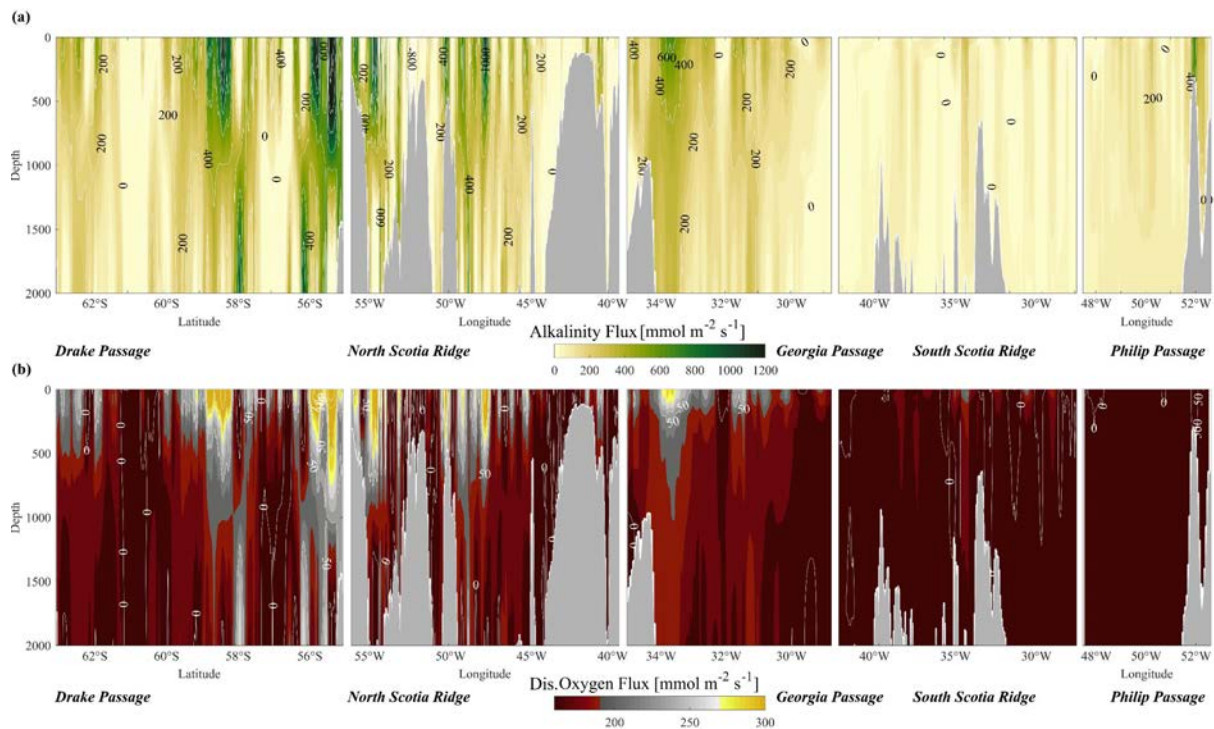


**Figure 3.37.** (a) Alkalinity flux and (b) dissolved oxygen flux along the Scotia Sea boundaries after applying the inverse model. From left to right: Drake Passage, North Scotia Ridge, Georgia Passage, South Scotia Ridge and Philip Passage.

## 3.2.4. Discussion

### 3.2.4.1. Water, salt and heat transports

In Figure 3.38, we present the individual and combined water transports and net imbalances in the top 12 neutral-density layers of our inverse model, i.e., down to  $\gamma^n = 28.00$

$\text{kg m}^{-3}$ , which represent those layers that are fully sampled in the upper 2000 m of the water column. Mass is largely conserved within all these layers, with a total imbalance of only 0.03 Sv, where 0.19 Sv of surface-mode waters (SASW and SAMW) plus 1.11 Sv of surface-intermediate (AASW and AAIW) waters outflow balance the 1.27 Sv of UCDW waters inflow. In these upper layers, the SAF and PF in the Drake Passage contribute almost equally with 62.1 Sv and 65.7 Sv, respectively; following into the northern boundary, the SAF loses strength (40.9 Sv), whereas the PF transport increases slightly (72.0 Sv). The remaining unbalanced layers ( $28.00 < \gamma^n < 28.35 \text{ kg m}^{-3}$ ) correspond to net inputs of 3.8 Sv of LCDW and 3.1 Sv of WSDW, which occur mainly over the South Scotia Ridge and Philip Passage (Figure 3.38a). Down to  $\gamma^n = 28.00 \text{ kg m}^{-3}$ , the accumulated transport through the Drake Passage peaks at 136.7 Sv, split in less than 0.2 Sv for SASW, 14.6 Sv for SAMW, 47.6 Sv for AASW/AAIW and 74.3 Sv for the UCDW. The mass transport imbalances represent only 0.14%, 0.81% and 0.93% of the SASW/SAMW, AASW/AAIW and UCDW mass transports into the Scotia Sea.

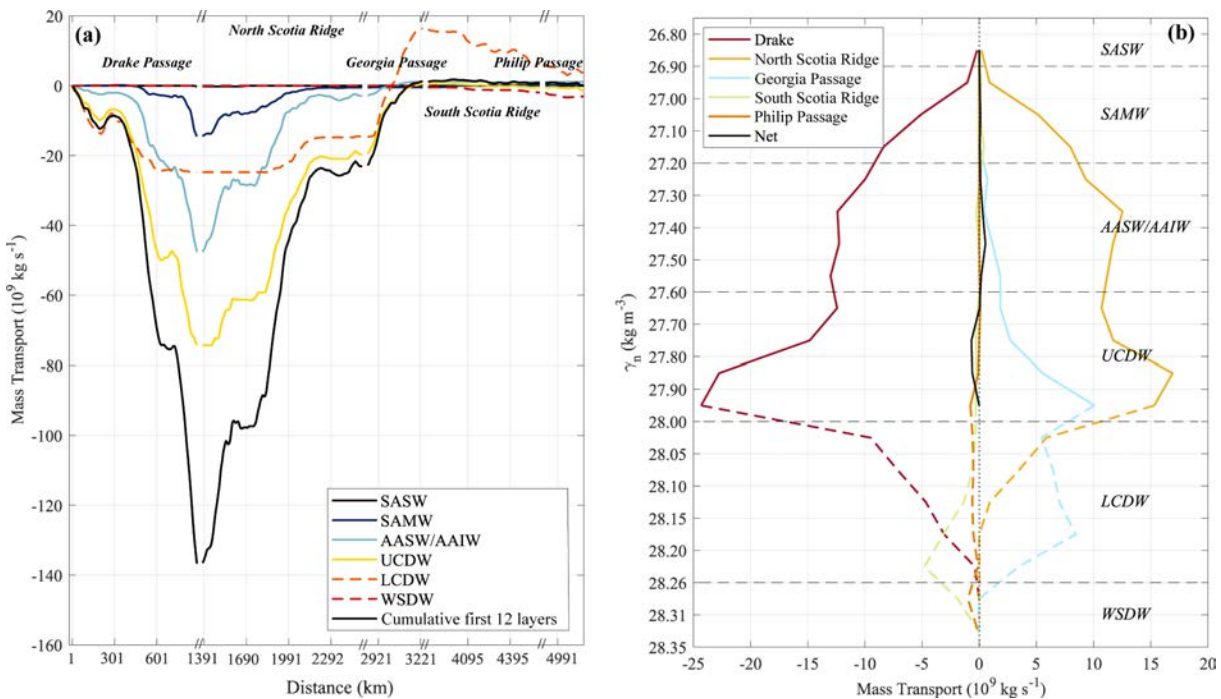


**Figure 3.38.** (a) Cumulative mass transports (per water mass and total down to  $\gamma^n = 28.00 \text{ kg m}^{-3}$ ), starting at the southern edge of the Drake Passage, and (b) mass transports through each main passage (Drake Passage, North Scotia Ridge, Georgia Passage, South Scotia Ridge and Philip Passage) and the net balance, distributed per isoneutral layers down to  $\gamma^n = 28.00 \text{ kg m}^{-3}$ . Positive (negative) values represent water leaving (entering) the domain; recall that those layers below  $\gamma^n = 28.00 \text{ kg m}^{-3}$  are not fully sampled, so the corresponding transports are shown as dashed lines in both panels.

The main circulation pattern consists of circumpolar water entering the Scotia Sea mainly via the Drake Passage, and to a much lesser extent through the South Scotia Ridge and

Philip Passage and emerging north through the North Scotia Ridge and Georgia Passages (Figures 3.39a and 3.40a). Considering the transports down to  $\gamma^n = 28.00 \text{ kg m}^{-3}$  (i.e., the densest UCDW layer), the main depth-integrated transports are  $136.7 \pm 1.0 \text{ Sv}$  input through the Drake Passage, and  $113.6 \pm 1.0 \text{ Sv}$  and  $24.3 \pm 0.3 \text{ Sv}$  outputs through the North Scotia Ridge and the Georgia Passage, respectively; through the South Scotia Ridge and Philip Passage, we observe an additional input of  $0.4 \pm 0.1 \text{ Sv}$  and  $0.8 \pm 0.1 \text{ Sv}$ . The highest transports coincide with the mean position of the surface ACC fronts (Orsi et al., 1995), separated by areas of more quiescent waters, often with opposite flows (Figure 3.34).

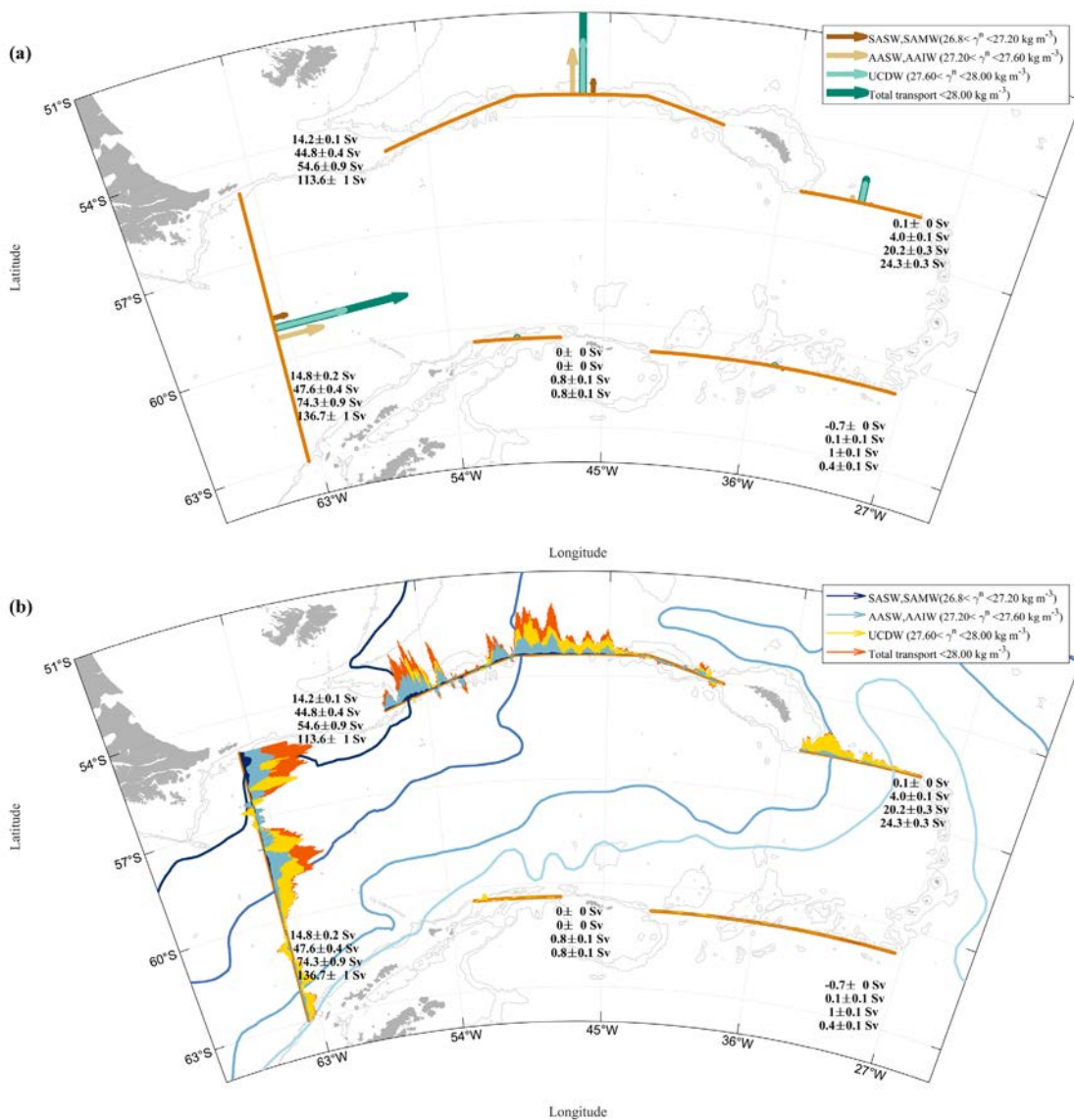


**Figure 3.39.** (a) Direction and magnitude of surface-mode (SASW, SAMW), surface-intermediate (AASW, AAIW), deep (UCDW) and total transports down to  $\gamma^n = 28.00 \text{ kg m}^{-3}$ . (b) Mass transport distribution along the Scotia Sea boundaries for each water mass and with a 3-km resolution. Positive/negative values in transports indicate north-east/south-west direction, transports through the Drake Passage, South Scotia Ridge and Philip Passage represent inflow and transports through the North Scotia Ridge and Georgia Passage represent outflow.

Northern Passages represent outflow. The blue lines represent the climatological location of the different ACC fronts obtained by Orsi et al. (1995).

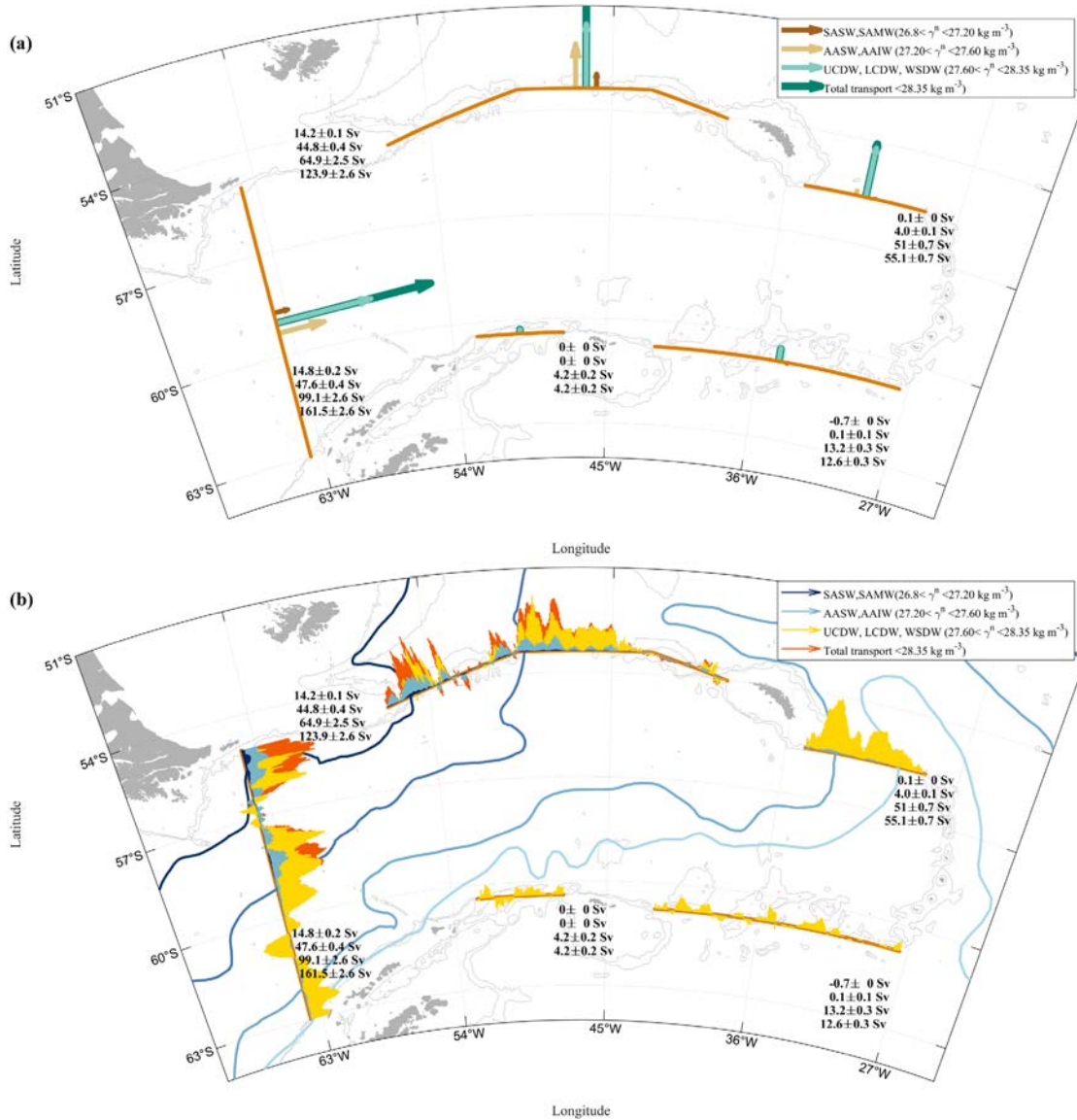


**Figure 3.40.** (a) Direction and magnitude of surface-mode, surface-intermediate, deep waters and total geostrophic transport, and (b) total mass transport distribution up to 2000 m along the different passages after applying the inverse model. Positive/negative values in transports indicate north-east/south-west direction, transports through the Drake Passage, South Scotia Ridge and Philip Passage represent inflow and transports through the Northern Passages represent outflow. The blue lines represent the climatological location of the different ACC fronts obtained by Orsi et al. (1995).

Considering also the 7 not-balanced layers down to 2000 m (which reach  $\gamma^n = 28.35 \text{ kg m}^{-3}$ ), the net ACC depth-integrated transports represent inflow across the Drake Passage ( $161.5 \pm 2.6 \text{ Sv}$ ), the South Scotia Ridge ( $12.6 \pm 0.3 \text{ Sv}$ ) and the Philip Passage ( $4.2 \pm 0.2 \text{ Sv}$ ), and outflow through the North Scotia Ridge ( $123.9 \pm 2.6 \text{ Sv}$ ), the Georgia Passage ( $55.1 \pm 0.7 \text{ Sv}$ ) (Figure

3.40). The mass transport contribution to the Scotia Sea through the Philip Passage and the South Scotia Ridge corresponds mainly to the deepest-water layers (LCDW and WSDW) leaving the Weddell Sea, reaching 3.5 Sv and 12.2 Sv, respectively. Whereas down to the densest layer, the total net transport for the South Scotia Ridge corresponds to water emerging from the Weddell Sea to the Scotia Sea, the surface-mode layers (between  $26.80 \text{ kg m}^{-3} < \gamma^n < 27.2 \text{ kg m}^{-3}$ ) display the opposite direction, with a dominant outflow of  $0.7 \pm 0 \text{ Sv}$  leaving the Scotia Sea. Hereafter, the not-balanced results obtained for the densest isoneutral layers up to 2000 m will not be shown.

The salt and heat transports carried by the ACC through the Drake Passage down to  $\gamma^n = 28.00 \text{ kg m}^{-3}$  are  $4.7 \times 10^9 \text{ kg s}^{-1}$  and 1.4 PW, respectively (Figure 3.41). The net salt transport imbalance shows a net gain of salt, about  $3.6 \times 10^6 \text{ kg s}^{-1}$ , which is 0.08% of the total net salt transport entering the region (Drake, South Scotia Ridge and Philip Passages). However, the net heat imbalance reveals a net heat loss of 0.065 PW, representing 4.6% of the total net heat transport entering the region. The net salt gain and heat loss reflect a net transfer of freshwater and heat from the ocean into the atmosphere (Figure 3.27).

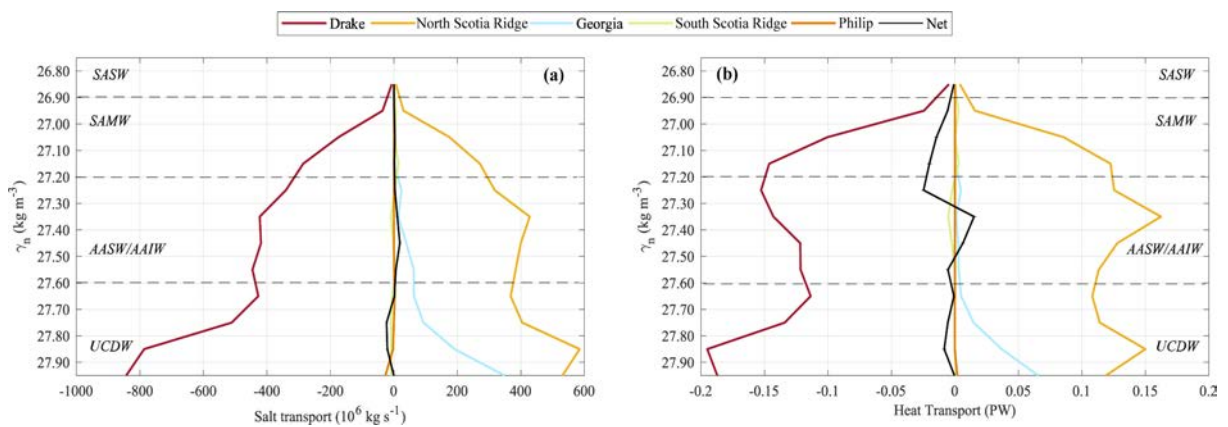


**Figure 3.41.** (a) Salt and (b) heat transports through each main passage (Drake Passage, North Scotia Ridge, Georgia Passage, South Scotia Ridge and Philip Passage) and the net balance, distributed in isoneutral layers down to  $\gamma^n = 28.00 \text{ kg m}^{-3}$ . Positive (negative) values represent heat and salt transports leaving (entering) the domain.

### 3.2.4.2. Transport of biogeochemical properties

The biogeochemical fluxes may be integrated over the boundary sections to obtain the corresponding transports for each water mass and the entire water column. The spatial distribution of biogeochemical transports, and its splitting between the different water masses, is shown in Figure 3.42. Peak values are associated with the maximum velocities and transports (Figures 3.34 and 3.36).

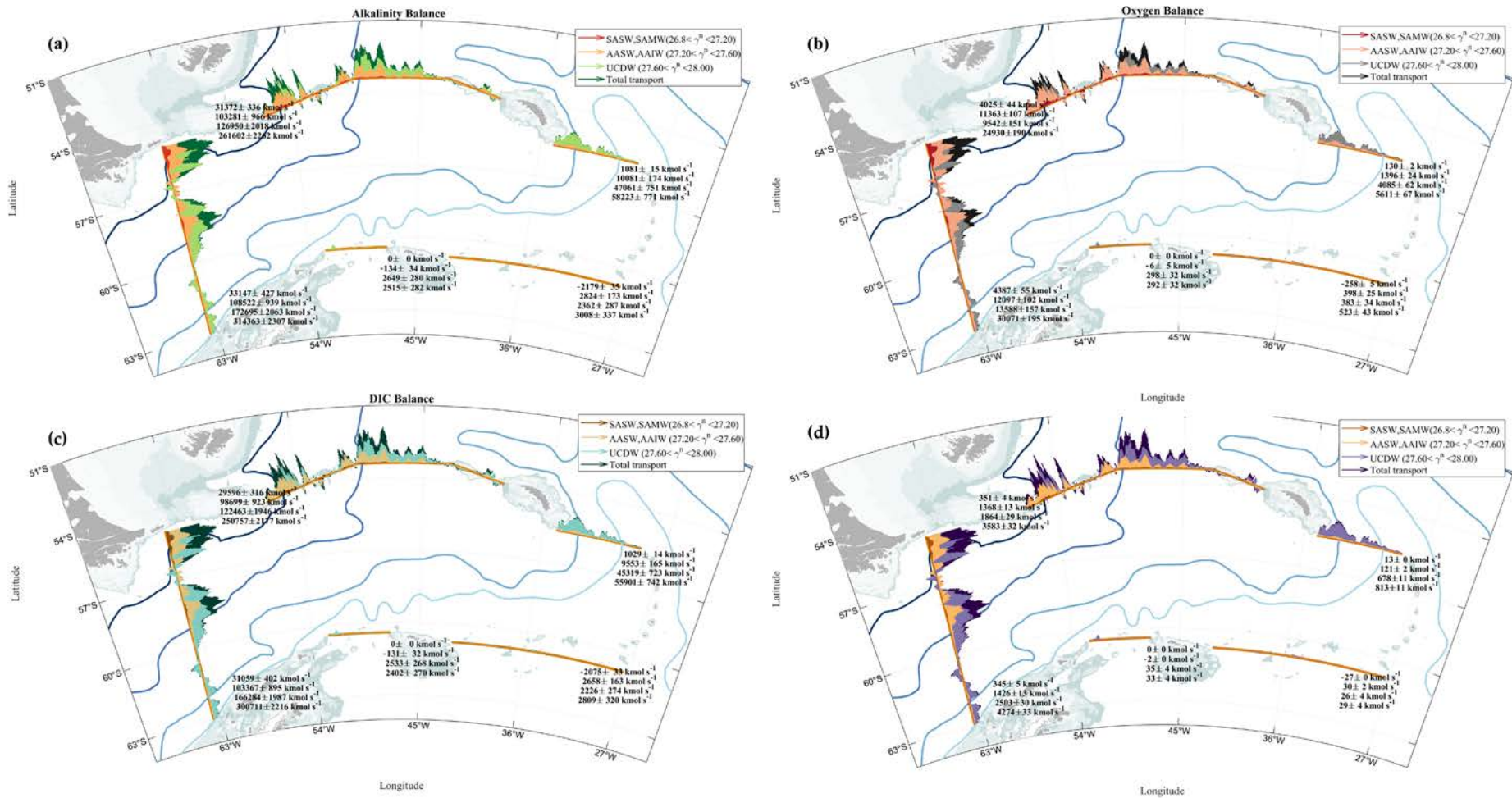


**Figure 3.42.** (a) Alkalinity, (b) DO, (c) DIC and (d) nitrate transports through the Scotia Sea boundaries, calculated every 3 km and split per water stratum as shown. Positive (negative) values represent north-east (south-west) biochemical properties transport in the domain. The blue lines represent the average location of the different ACC fronts (Orsi et al., 1995).

The major transports into and out of the Scotia Sea correspond to the surface-intermediate and upper circumpolar waters (Table 3.14). Down to  $\gamma^n = 28.00 \text{ kg m}^{-3}$ , there is a net inflow of 319886  $\text{kmol s}^{-1}$  of alkalinity, 30887  $\text{kmol s}^{-1}$  of DO, 4336  $\text{kmol s}^{-1}$  of nitrate and 305921  $\text{kmol s}^{-1}$  of DIC, and an outflow of 319826  $\text{kmol s}^{-1}$  of alkalinity, 30541  $\text{kmol s}^{-1}$  of DO, 4395  $\text{kmol s}^{-1}$  of nitrate and 306659  $\text{kmol s}^{-1}$  of DIC. In total, the upper-ocean layers up to  $\gamma^n = 28.00 \text{ kg m}^{-3}$  experience a production of DIC and nitrate and slight alkalinity and dissolved oxygen consumption.

**Table 3.14.** Alkalinity, dissolved oxygen, nitrate, and DIC transport imbalances obtained per water masses after applying the inverse model. Negative/positive values represent consumption/production.

| WATER MASSES<br>( $\gamma^n, \text{kg m}^{-3}$ ) | $T_{Atk}$   | $T_{O_2}$   | $T_{NO_3}$  | $T_{DIC}$   |
|--|---|---|---|---|
|  | Input, Output<br><i>Imbalance</i><br>( $\text{kmol s}^{-1}$ ) | Input, Output<br><i>Imbalance</i><br>( $\text{kmol s}^{-1}$ ) | Input, Output<br><i>Imbalance</i><br>( $\text{kmol s}^{-1}$ ) | Input, Output<br><i>Imbalance</i><br>( $\text{kmol s}^{-1}$ ) |
| SASW, SAMW<br>( $26.8 < \gamma^n < 27.2$ )       | 30968, 32453<br>1485  | 4129, 4155<br>26  | 318, 364<br>46  | 28984, 30625<br>1641  |
| AASW, AAIW<br>( $27.2 < \gamma^n < 27.6$ )       | 111212, 113362<br>2150  | 12489, 12759<br>270   | 1454, 1489<br>35  | 105894, 108252<br>2358  |
| UCDW<br>( $27.6 < \gamma^n < 28.00$ )            | 177706, 174011<br>-3695                                       | 14269, 13627<br>-642  | 2564, 2542<br>-22   | 171043, 167782<br>-3261                                       |
| TOTAL<br>( $26.8 < \gamma^n < 28.00$ )           | 319886, 319826<br>-60   | 30887, 30541<br>-346  | 4336, 4395<br>59  | 305921, 306659<br>738   |

The biogeochemical transports also consider vertical water exchange between adjacent isopycnals, which result from both vertical advection and diffusion of biogeochemical properties (Figure 3.43). The resulting diapycnal vertical advection presents the same pattern for all biogeochemical properties: causes maximum convergence to the surface-mode from surface-intermediate waters through 27.2  $\text{kg m}^{-3}$  isoneutral interface (of 1369  $\text{kmol s}^{-1}$ , 1304  $\text{kmol s}^{-1}$ , 1609  $\text{kmol s}^{-1}$  and 170  $\text{kmol s}^{-1}$  for alkalinity, DIC, DO and nitrate), almost divergence for the deep layers of surface-intermediate waters around the 27.5  $\text{kg m}^{-3}$  isoneutral interface (of 672  $\text{kmol s}^{-1}$ , 639  $\text{kmol s}^{-1}$ , 80  $\text{kmol s}^{-1}$  and 8  $\text{kmol s}^{-1}$  for alkalinity, DIC, DO and nitrate) and some downward transport transference into UCDW from the deepest layers below  $\gamma^n = 28.00 \text{ kg m}^{-3}$ . Instead, the diapycnal diffusion, which presents around one order less, brings divergence transport transference at 27.2 and 27.6  $\text{kg m}^{-3}$  for DIC, alkalinity and nitrate, while the dissolved oxygen presents the opposite scenario at the same interfaces. Between the surface-mode interfaces (SASW and SAMW), there are no barely diapycnal diffusion



transference for any of the biogeochemical properties. While the alkalinity, DIC and nitrate properties experience maximum divergence diffusive transports that range between 7 and 90  $\text{kmol s}^{-1}$ , the dissolved oxygen maximum convergence transport are of the order of 126  $\text{kmol s}^{-1}$ .

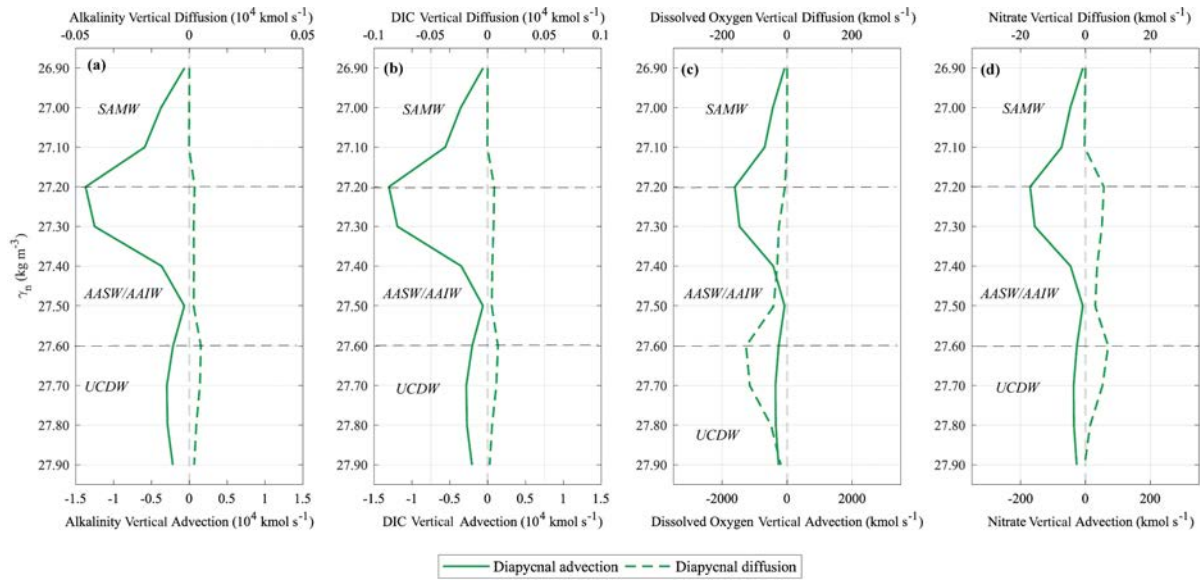


**Figure 3.43.** (a) Alkalinity, (b) DIC, (c) dissolved oxygen and (d) nitrate vertical advection (solid lines) and diffusion (dashed lines) after the inverse model for all neutral density interfaces. Positive/negative values indicate water transferred up/down across the interfaces.

### 3.2.4.3. Biogeochemical processes and anthropogenic DIC storage

Recall that the inverse model only requested that the conservative properties (mass, heat and salt) be balanced. Hence, the imbalances in the biogeochemical properties are calculated *a posteriori*, integrating the fluxes of biogeochemical properties to obtain the transports and calculating the input-output (horizontal and vertical) differences for each water stratum. These imbalances will respond to biological consumption and production, depletion or storage, and air-sea exchange.

Table 3.14 summarizes the biogeochemical imbalances in the different water layers. The surface-mode (SASW, SAMW) and surface-intermediate (AASW, AAIW) layers experience a production of nitrate, dissolved oxygen, alkalinity and DIC. In contrast, in the UCDW layers, we find a net consumption of all variables. Overall, always down to  $\gamma^n = 28.00 \text{ kg m}^{-3}$ , the Scotia Sea experiences a total net consumption of 60  $\text{kmol s}^{-1}$  of alkalinity and 346  $\text{kmol s}^{-1}$  of dissolved oxygen, and a total production of DIC and nitrate, all properties reflecting the same pattern: the dominance of surface-mode and surface-intermediate production and deep consumption.

The Scotia Sea has been reported to be a key site for the subduction of modal and intermediate waters of southern origin (SAMW and AAIW) into the ACC. These waters subduct at the SAF and PF to follow north into the Atlantic Ocean in order to balance the southward flow of North Atlantic Deep Water (Garzoli & Matano, 2011; Sloyan & Rintoul, 2001b). The PF represents a major boundary between the relatively warm and fresh waters close to South America – depleted in nitrate, DIC and enriched in dissolved oxygen – and the polar waters. Hence, it seems reasonable to explore whether the domains on both sides of the PF – the warm domain to the north and west of the PF and the cold domain to the south and east – display substantially different biogeochemical balances, e.g., with net primary production in the warm domain and remineralization in the cold domain.

**Table 3.15.** Inputs through the Drake Passage, the South Scotia Ridge and the Philip Passage, and outputs through the North Scotia Ridge and Georgia Passage, split into the warm (north and west of the PF) and cold (south and east of the PF) domains and water mass strata. The negative convergent (positive divergent) transport differences represent consumption (production).

| WARM SIDE (kmol s <sup>-1</sup> ) |           |        |       |           |        |       |       |        |        |
|-----------------------------------|-----------|--------|-------|-----------|--------|-------|-------|--------|--------|
|                                   | SASW/SAMW |        |       | AASW/AAIW |        |       | UCDW  |        |        |
|                                   | INPUT     | OUTPUT | DIFF. | INPUT     | OUTPUT | DIFF. | INPUT | OUTPUT | DIFF.  |
| Oxygen                            | 3764      | 2505   | -1259 | 7476      | 6842   | -634  | 6626  | 3315   | -3311  |
| Nitrate                           | 303       | 217    | -86   | 923       | 832    | -91   | 1269  | 658    | -611   |
| DIC                               | 27319     | 18664  | -8655 | 66966     | 60795  | -6171 | 84336 | 43155  | -41181 |
| Alkalinity                        | 29116     | 19807  | -9309 | 70277     | 63654  | -6623 | 87606 | 44745  | -42861 |
| Mass                              | 12.3      | 9.5    | -2.8  | 30.8      | 27.6   | -3.2  | 37.7  | 19.3   | -18.4  |

| COLD SIDE (kmol s <sup>-1</sup> ) |           |        |       |           |        |       |       |        |       |
|-----------------------------------|-----------|--------|-------|-----------|--------|-------|-------|--------|-------|
|                                   | SASW/SAMW |        |       | AASW/AAIW |        |       | UCDW  |        |       |
|                                   | INPUT     | OUTPUT | DIFF. | INPUT     | OUTPUT | DIFF. | INPUT | OUTPUT | DIFF. |
| Oxygen                            | 365       | 1650   | 1285  | 5013      | 5918   | 905   | 7644  | 10312  | 2668  |
| Nitrate                           | 15        | 148    | 133   | 531       | 657    | 126   | 1295  | 1884   | 589   |
| DIC                               | 1665      | 11960  | 10295 | 38929     | 47457  | 8528  | 86707 | 124627 | 37920 |
| Alkalinity                        | 7248      | 12646  | 5398  | 37192     | 49708  | 12516 | 88657 | 129265 | 40608 |
| Mass                              | 1.8       | 4.8    | 3.0   | 16.9      | 21.2   | 4.3   | 38.4  | 55.5   | 17.1  |

The inputs, outputs and net balances for each domain and water masses are presented in Table 3.15. We follow the convention that negative (positive) transport differences represent convergence (divergence), convergence meaning that the property is being lost (a sink) within the domain, while divergence implies that the property is produced (a source) within the domain. Remarkably, there is a net loss of all properties in the warm domain and a net production in the cold domain. This result does not support the initial notion that the two domains can be studied separately and rather sustains the idea of a net transfer of properties from the northern to the southern side of the PF supported by the high imbalance of UCDW waters.

Finally, we calculate the several non-advective terms that affect the DIC balance, with the objective of assessing the input of anthropogenic carbon to the region. These are the internal generation or consumption resulting from biogeochemical processes,  $I$ , the anthropogenic accumulation of DIC,  $A$ , and the air-sea exchange of inorganic carbon,  $E$ . First, the air-sea carbon dioxide exchange,  $E_{DIC}$ , is calculated to be  $-16.4 \text{ kmol s}^{-1}$  or  $-516 \times 10^6 \text{ kmol yr}^{-1}$ . Therefore, the region gains some little DIC through the air-sea exchange, at a rate of about  $0.01 \text{ Pg C yr}^{-1}$ , with most of it (79.6%) reaching the outcrop regions of the surface and intermediate layers (Figure 3.44).

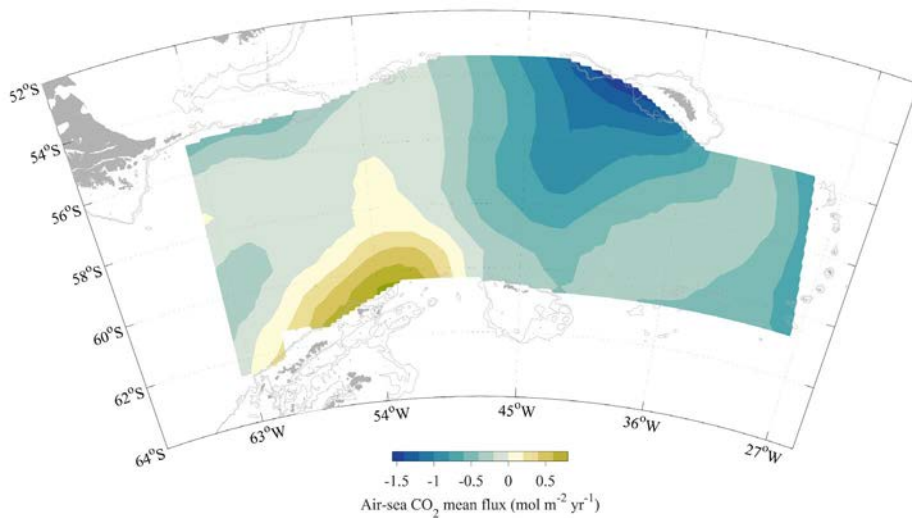


**Figure 3.44.** Spatial distribution of the annual-mean air-sea  $\text{CO}_2$  fluxes in the Scotia Sea as deduced from the NCEI product.

We set the generation or consumption of nitrate by biogeochemical processes to be equal to the nitrate imbalance,  $I_{\text{NO}_3} = \Delta T_{\text{NO}_3}$  (equation 3.5), and use the carbon-nitrogen ratio to estimate the internal DIC generation,  $I_{\text{DIC}} = 7.3 I_{\text{NO}_3} = 7.3 \Delta T_{\text{NO}_3}$ . It turns out that  $336 \text{ kmol s}^{-1}$  are produced in the surface-mode waters,  $256 \text{ kmol s}^{-1}$  are produced in the surface-

intermediate waters, and 161 kmol s<sup>-1</sup> are consumed in the deep waters, leading to a net biogeochemical DIC production imbalance of 431 kmol s<sup>-1</sup>.

Combining the DIC imbalances with the air-sea exchange and the production-consumption estimates, we assess the anthropogenic accumulation as  $A_{DIC} = \Delta T_{DIC} - E_{DIC} - 7.3 \Delta T_{NO_3}$  (equation 3.7). This term turns out to be the largest, with 1310 kmol s<sup>-1</sup> in the surface-mode layers, 2113 kmol s<sup>-1</sup> in the surface-intermediate layers and -3099 kmol s<sup>-1</sup> in the deep waters, summing up a total of 324 kmol s<sup>-1</sup> or 0.123 Pg C yr<sup>-1</sup> (Table 3.16).

**Table 3.16.** Contributions to the DIC balance,  $\Delta T_{DIC}$ , from the air-sea exchange,  $E_{DIC}$ , internal generation or consumption through biogeochemical processes,  $I_{DIC}$ , and anthropogenic accumulation,  $A_{DIC}$ . Values are shown for each water strata and the entire water column down to  $\gamma^n = 28.00$  kg m<sup>-3</sup>. The positive/negative values represent an ocean gain/loss.

| Neutral density (kg m <sup>-3</sup> ) | $\Delta T_{DIC}$ | $E_{DIC}$ | $I_{DIC}$ | $A_{DIC}$ |
|---------------------------------------|------------------|-----------|-----------|-----------|
| 26.8 < $\gamma^n$ < 27.2 (SASW, SAMW) | 1641             | -4.40     | 336       | 1310      |
| 27.2 < $\gamma^n$ < 27.6 (AASW, AAIW) | 2358             | -10.40    | 256       | 2113      |
| 27.6 < $\gamma^n$ < 28.00 (UCDW)      | -3261            | -1.59     | -161      | -3099     |
| TOTAL (kmol s <sup>-1</sup> )         | 738              | -16.4     | 431       | 324       |
| TOTAL (Pg C yr <sup>-1</sup> )        | 0.280            | -0.006    | 0.163     | 0.123     |

Finally, considering the total volume of the different water masses in the Scotia Sea (down to  $\gamma^n = 28.00$  kg m<sup>-3</sup>; see Figure 3.30) we may assess the corresponding temporal rates of anthropogenic DIC change. The total water volume is about  $1.4 \times 10^{15}$  m<sup>3</sup>, partitioned as  $0.7 \times 10^{14}$  m<sup>3</sup> of SASW/SAMW,  $3.6 \times 10^{14}$  m<sup>3</sup> of AASW/AAIW and  $1.0 \times 10^{15}$  m<sup>3</sup> of UCDW. Hence, the estimated dissolved inorganic carbon accumulation rate per water mass is maximum near the surface and negative at depth acting as a sink, as follows:  $1.3 \times 10^{-3}$  mol m<sup>-3</sup> yr<sup>-1</sup> for SASW/SAMW,  $1.9 \times 10^{-4}$  mol m<sup>-3</sup> yr<sup>-1</sup> corresponds to AASW/AAIW and  $-9.3 \times 10^{-5}$  mol m<sup>-3</sup> yr<sup>-1</sup> for UCDW.

#### 3.2.4.4. Comparison with SOSE and B-SOSE

We end up comparing the results of our model with the outputs from the Southern Ocean State Estimate (SOSE) model for the 2005 - 2010 period (subsection 3.3.2.1). A comparison of the reference velocities from our model – initialized with the velocities inferred from Argo floats drifting at 1000 m – shows good agreement of the mean and standard

deviation values (Figure 3.34). Regarding the distribution of the horizontal velocities along the boundary sections, the SOSE velocities are generally equal or higher except for the PF in the Drake Passage and the SACCF in the Georgia Passage (Mazloff et al., 2010). Figure 3.45 shows the difference in the cross-section velocities, showing that the inverse model at the Drake Passage underestimates the SAF velocities and slightly overestimates the PF velocities compared with the SOSE model.

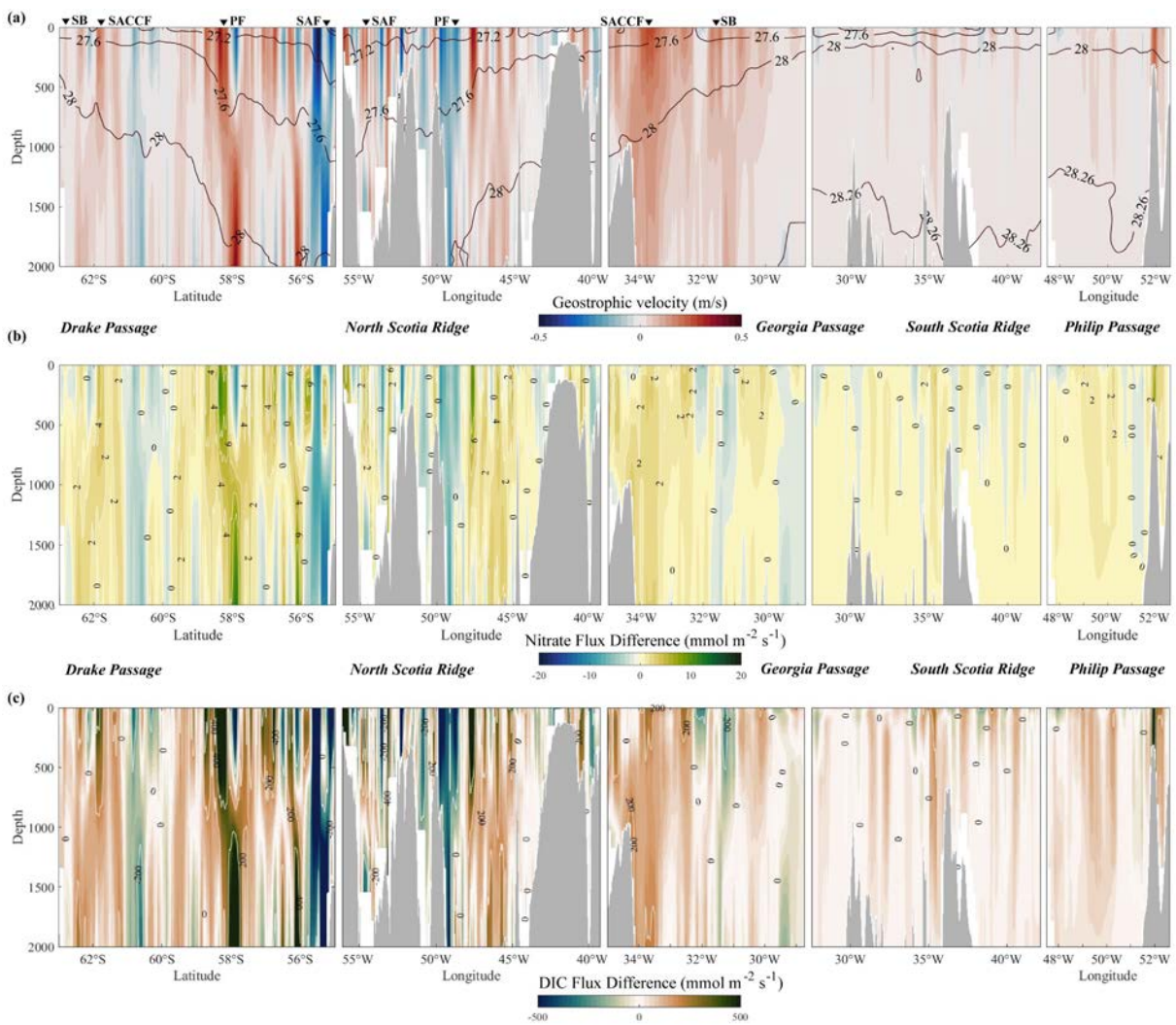


**Figure 3.45.** Inverse model and SOSE/B-SOSE differences in cross-section for (a) geostrophic velocity, (b) nitrate flux and (c) DIC flux along the Scotia Sea boundaries. From left to right: Drake Passage, North Scotia Ridge, Georgia Passage, South Scotia Ridge and Philip Passage. Positive/negative values indicate a dominance of the inverse model/SOSE properties fluxes.

Furthermore, in the Georgia Passage, the meridional geostrophic velocities are higher for the whole water column, especially in SACCF, where SOSE velocities are probably underestimated. Both nitrate and DIC fluxes differences present the same pattern and are similar to the inverse model/SOSE velocities difference, indicating that higher fluxes variations

are along the ACC fronts; for greater details about SOSE vertical sections of horizontal velocities, see Figure 3.46.

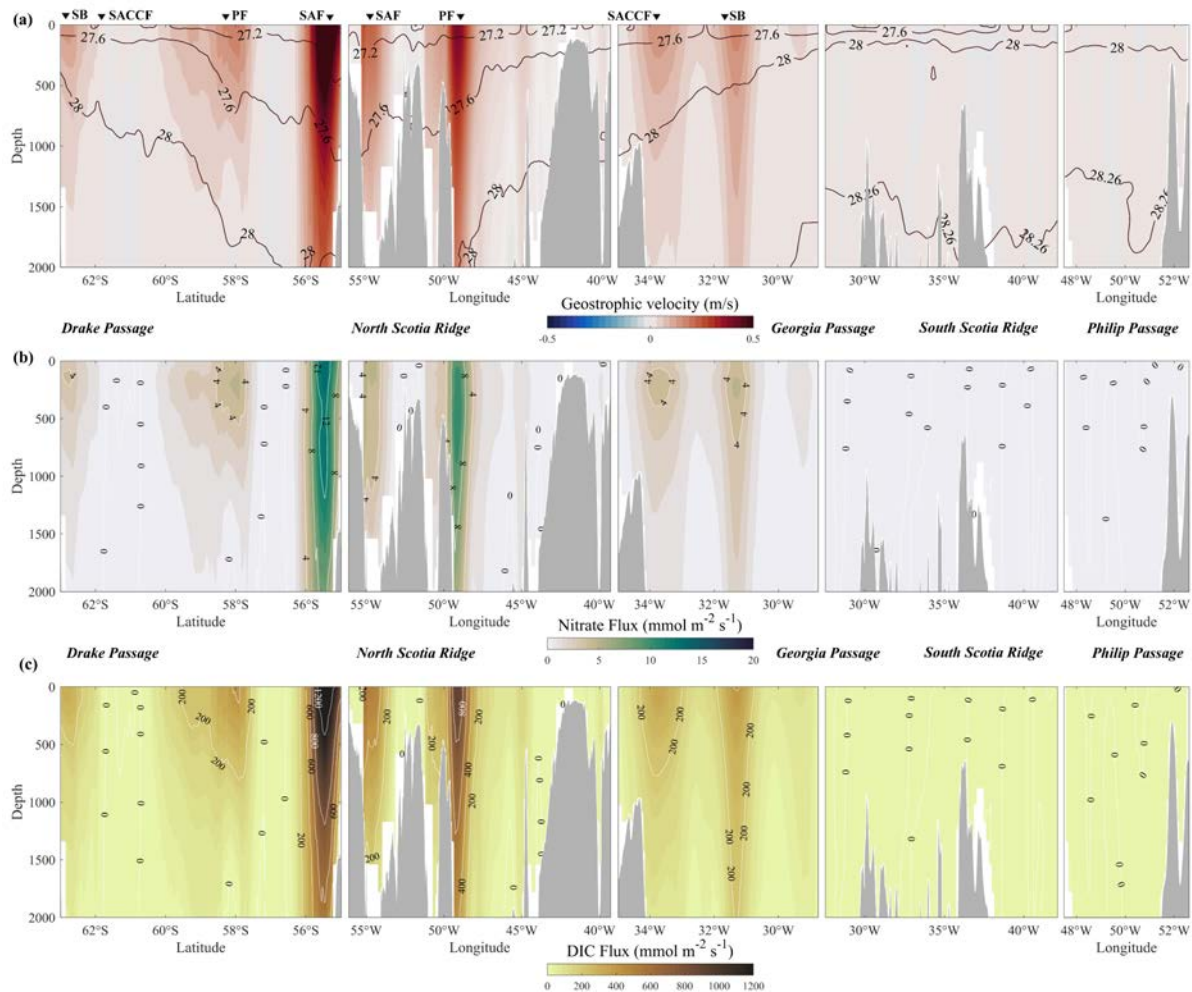


**Figure 3.46.** SOSE model distribution of (a) geostrophic velocity and neutral density layers (contours), (b) nitrate flux and (c) DIC flux along the Scotia Sea boundaries. From left to right, the sections are: the Drake Passage, North Scotia Ridge, Georgia Passage, South Scotia Ridge and Philip Passage. In the upper horizontal axis, we represent the location of the fronts (upper panel) and positive/negative values in geostrophic velocity and fluxes indicate north-east/south-west direction.

The water mass transports of the inverse model (IM) and SOSE also show fairly reasonable agreement, although the surface-mode and surface-intermediate transports produce substantially lesser than SOSE. In particular, the SOSE inflow through the Drake Passage is 105.2 Sv as compared with the 136.7 Sv calculated from our inverse model (Table 3.17 and Figure 3.47a). Estimates of full-depth water transports through the Drake Passage, as obtained with the SOSE model for our section, are  $153 \pm 5$  Sv (Mazloff et al., 2010) and  $164 \pm 23$  Sv (Firing et al., 2011).

**Table 3.17.** Mass, dissolved oxygen, nitrate and DIC transport imbalances per water masses comparison from B-SOSE model and our transports after applying the inverse model (BGC-IM). Negative/positive values represent consumption/production.

| Water masses | $\Delta\text{Mass}$ (Sv) |       | $\Delta T_{O_2}$ (kmol s <sup>-1</sup> ) |        | $\Delta T_{NO_3}$ (kmol s <sup>-1</sup> ) |        | $\Delta T_{DIC}$ (kmol s <sup>-1</sup> ) |        |
|--------------|--------------------------|-------|--|--------|---|--------|--|--------|
|              | IM                       | SOSE  | BGC-IM                                   | B-SOSE | BGC-IM                                    | B-SOSE | BGC-IM                                   | B-SOSE |
| SASW, SAMW   | 0.19                     | 2.09  | 26                                       | 663    | 46  | 78     | 1641                                     | 4657   |
| AASW, AAIW   | 1.11                     | 3.04  | 270                                      | 375    | 35  | 167    | 2358                                     | 7155   |
| UCDW         | -1.27                    | -1.03 | -642                                     | 53     | -22                                       | -43    | -3261                                    | -2361  |
| TOTAL        | 0.03                     | 4.10  | -346                                     | 1090   | 59  | 202    | 738                                      | 9452   |

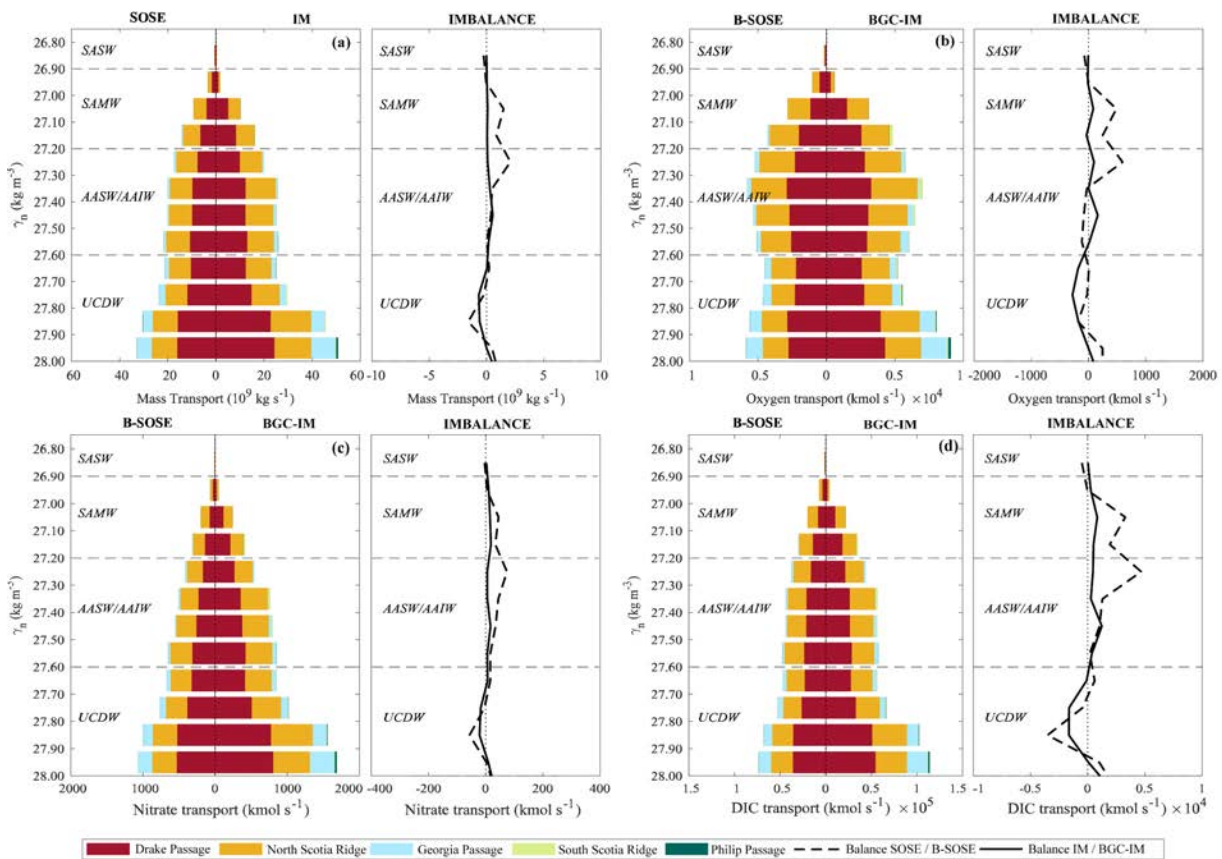


**Figure 3.47.** Comparison between (a) mass, (b) DO, (c) nitrate and (d) DIC transports per passages and their transport imbalances as obtained from the inverse (BGC-IM) and B-SOSE models. In the right panels, the solid and dashed lines correspond to the inverse and B-SOSE imbalances, respectively. For each neutral density and passage, the transports are drawn to the left for the B-SOSE model and to the right for the inverse model

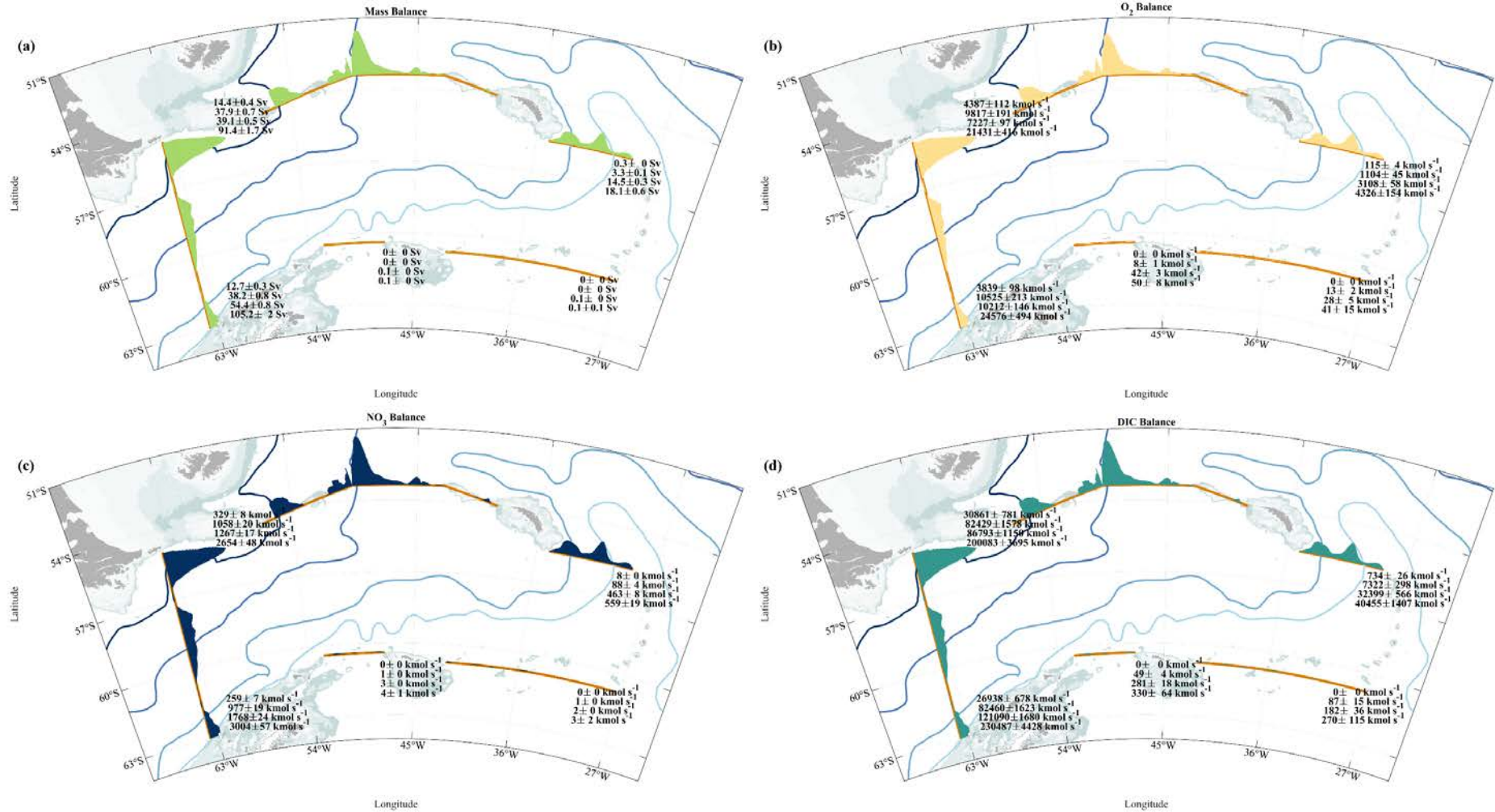


**Figure 3.48.** (a) SOSE mass balance and B-SOSE (b) dissolved oxygen, (c) nitrate and (d) DIC balances at the Scotia Sea boundaries. The first value for each passage corresponds to the surface-modal stratum transport (SASW, SAMW), the second corresponds to the surface-intermediate stratum transport (AASW, AAIW), the third to the bottom stratum (UCDW), and finally, the fourth corresponds to the total transport. Positive/negative values in transports indicate north-east/south-west direction.



The inverse model provides mass and biogeochemical transport imbalances that are substantially lower than those that arise from the B-SOSE model, except for the UCDW layers of all properties less for nitrate (Table 3.17). While mass, nitrate and DIC coincide in consumption/production processes for both models showing the same sign per all water masses, the dissolved oxygen from deep layers displays the opposite behaviour, increasing the total imbalance in the B-SOSE case (see Figure 3.48). Regarding DIC, both B-SOSE and the inverse model show production in the surface-mode and surface-intermediate waters and consumption in the UCDW, but the absolute differences in total balance are very large. These transport imbalances are consistent with the idea that deeper waters barely contact the surface and support remineralization (dissolved oxygen and DIC consumption).

The transports and resulting balances of biogeochemical properties in the upper 12 layers for the same pairs of stations along the sections have been calculated by combining the SOSE velocities with the property concentrations as available from the biogeochemical SOSE component (B-SOSE). As for the water transports, the imbalances are calculated as output minus input, hence implying that positive (negative) values represent production (consumption) within the domain. The inverse model and SOSE/B-SOSE vertical sections for nitrate, DO and DIC are qualitatively similar (see Figures 3.31 and 3.49) and share the same imbalance trend: production of all the properties for surface-mode and surface-intermediate waters and consumption for the deeper ones, except for the dissolved oxygen. Indeed, the sum of B-SOSE transports and *in situ* transports follow almost a symmetric pattern until the  $\gamma^n < 27.80 \text{ kg m}^{-3}$  isoneutral where a remarkable increase in the BCG-IM properties transport occurs for all passages. Also, all properties in the South Scotia Ridge and Philip Passage contribute with input transport, especially for the densest UCDW layers, while compared with B-SOSE transports, these are almost absent. These differences may partly be a consequence that the SOSE mass, heat and salt transports are not as well balanced as the inverse model (Table 3.17 and Figure 3.47), due to the low bathymetric resolution at depth with remarkably high gaps, the differences in the water column velocities, especially for the ACC fronts, or even is probably due to the fact that the B-SOSE is a much more restrained biogeochemical database, as it only uses observations between 2008 and 2012 years.

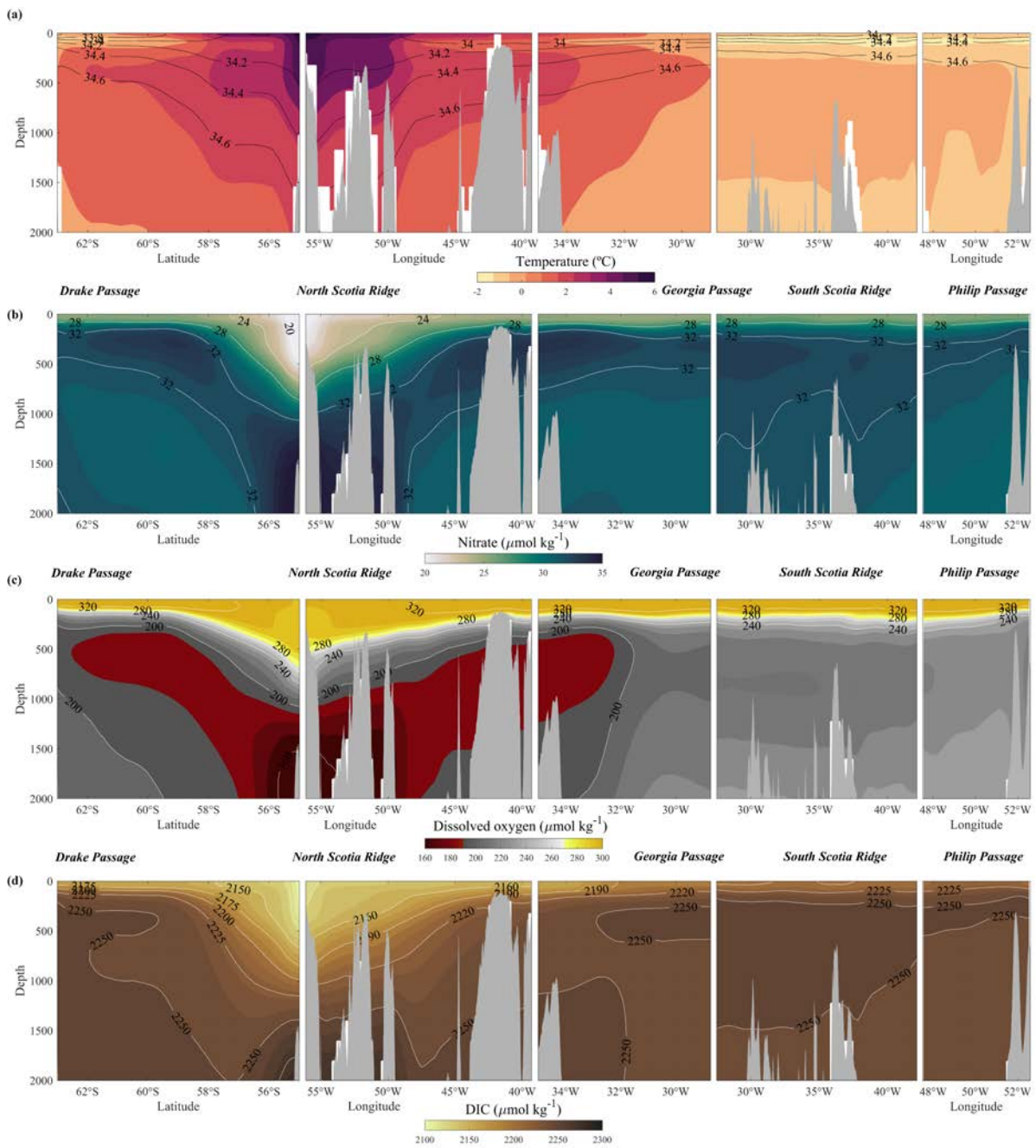


**Figure 3.49.** SOSE model distribution of (a) temperature and salinity (contours) and B-SOSE distribution of (b) nitrate, (c) dissolved oxygen and (d) DIC vertical sections along the Scotia Sea boundaries after the Argo profiles incorporation. The passages are Drake Passage, North Scotia Ridge, Georgia Passage, South Scotia Ridge, and Philip Passage from west to east.

### 3.2.5. Final remarks

We have combined hydrographic and velocity data collected along the Scotia Sea boundaries during the 2002 - 2018 period – from Argo floats, the SODB, the MEOP and the ESASSI-08 datasets – to construct an inverse box model of the ACC in the region. The

temperature and salinity, and hence neutral density, are interpolated along the vertical boundaries of the Scotia Sea with a resolution of 10 m in the vertical and 3 km in the horizontal, and the results are further smoothed over about 50 m in the vertical and 27 km in the horizontal in order to minimize the mesoscale intermittency. The model splits the domain into 12 isopycnal layers (down to  $\gamma^n = 28.00 \text{ kg m}^{-3}$ ) that are in geostrophic balance, have a non-zero reference velocity and may experience vertical exchange; further, it includes Ekman transports, freshwater fluxes and net air–sea heat exchange in the outcropping isopycnals layers. As a result, the model provides the velocity fields that cross the boundaries of the Scotia Sea, which allows calculating the water mass, heat and salt transports. Additionally, we use biogeochemical data from the SOCCOM floats and GLODAPv2 databases, together with empirical relationships between these variables and neutral density, to obtain the distribution of the biogeochemical properties with the same spatial resolution as the physical variables. These fields are combined with the inverse model velocities to produce the fluxes and transports of nitrate, DO and DIC. The property imbalances can hence be interpreted in terms of primary production, remineralization, and anthropogenic accumulation of DIC.

The main circulation patterns down to  $\gamma^n = 28.00 \text{ kg m}^{-3}$  reflect water input through the Drake Passage, South Scotia Ridge passages and Phillip Passage and water outputs through the North Scotia Ridge and Georgia Passage. The ACC enters  $136.7 \pm 1.0 \text{ Sv}$  through the Drake Passage and exits  $137.9 \pm 1.0 \text{ Sv}$  through the northern boundary ( $113.6 \text{ Sv}$  through the North Scotia Ridge and  $24.3 \text{ Sv}$  through the Georgia Passage), with the additional incorporation of waters through the South Scotia Ridge and Philip Passage and a net volume imbalance of only  $0.03 \text{ Sv}$ . Salt is highly conservative because of little exchange with the atmosphere. Instead, heat is conditioned by the interaction with the atmosphere, causing both heat and mass to have similar levels of uncertainty.

Considering only those layers down to the  $28.00 \text{ kg m}^{-3}$  isoneutral, our inverse circulation model reveals that the contribution of SASW/SAMW and AASW/AAIW through the southern edge (Philip Passage and South Scotia Ridge) is less than  $1.0 \text{ Sv}$ , practically negligible in the Philip Passage and contributing with opposite direction in the South Scotia Ridge. Furthermore, we estimate that the flow through the South Sandwich Arc is absent. These transports, which mainly consist of mode, surface-intermediate and upper circumpolar deep waters (SAMW, AASW/AAIW and UCDW), occupy the upper 2000 m of the water column to the northwest of the domain but only reach down several hundred meters in the southwest and northeast; in the southern margin they occupy even less, only the upper 200 m, so there is potentially a much greater inflow of the denser LCDW and WSDW.

The highest velocities are associated with high horizontal density gradients. Indeed, the largest horizontal transports are linked to the climatological frontal positions, as described

by Orsi et al. (1995). Particularly, the PF through the western North Scotia Ridge openings and to a lesser degree the SACCF through the Georgia Passage: the SAF crosses the 54-54 Passage in the western North Scotia Ridge (Naveira Garabato et al., 2002), the PF branches go through the western sills of Shag Rocks Passage in the central North Scotia Ridge (Smith et al., 2010), and the SACCF runs through the southern half of the Scotia Sea and loops anticyclonically around the shelf of Georgia Island before retroflecting to the east (Ward et al., 2002).

Our water mass transports through the Drake Passage and the northern boundary are substantially larger than those obtained by Naveira Garabato et al. (2003) with an inverse model for a similar domain. Down to  $\gamma^n = 28.00 \text{ kg m}^{-3}$ , they computed an inflow of  $107.0 \pm 4.3 \text{ Sv}$  from the Drake Passage and  $3.0 \pm 2.2 \text{ Sv}$  through the South Scotia Ridge, and an outflow of  $94.5 \pm 1 \text{ Sv}$  through the North Scotia Ridge and  $11.5 \pm 1.5 \text{ Sv}$  through the Georgia Passage. They also quantified the transports of denser waters, LCDW/WSDW, estimating a total inflow of  $46.5 \pm 9.2 \text{ Sv}$  through the Drake Passage and South Scotia Ridge, and outflows of  $41.5 \pm 8.8 \text{ Sv}$  through the northern outlets, North Scotia Ridge and Georgia Passage, and  $5.5 \pm 4.2 \text{ Sv}$  through the South Sandwich Arc. However, Naveira Garabato et al. (2003) found that diapycnal mixing was only significant in the deep layers associated with the rough topography. In our case, we obtain a diapycnal transport convergence at isoneutral  $27.2 \text{ kg m}^{-3}$  of almost  $6 \text{ Sv}$  but in the same line that the transference obtained by the authors between  $27.0 < \gamma^n < 27.2 \text{ kg m}^{-3}$  due to interior and air–sea interaction diapycnal volume fluxes. Palmer et al. (2012) also applied an inverse model, in this case to a domain south of the South Scotia Ridge, and found a net volume transport of  $7 \pm 5 \text{ Sv}$  of WDW from the Weddell Sea into the Scotia Sea.

We have also calculated a net heat transport loss of  $0.065 \pm 0.005 \text{ PW}$  and a freshwater flux gain of  $0.06 \pm 0.01 \text{ Sv}$ . These values are still far compared with the estimated transports out of the Southern Ocean across the  $30^\circ\text{S}$  from the SOSE model (Mazloff et al., 2010):  $0.3 \pm 0.5 \text{ PW}$  of heat and  $0.7 \pm 0.2 \text{ Sv}$  of freshwater. Instead, our heat transport estimate is a relatively high value as compared with the cross-ACC poleward heat flux,  $0.022 \pm 0.01 \text{ PW}$ , and the same occurs with the equatorward freshwater flux of  $0.02 \pm 0.01 \text{ Sv}$  inferred by Naveira Garabato et al. (2003).

Down to our reference level – the  $28.00 \text{ kg m}^{-3}$  isoneutral – we find that in the Scotia Sea, there is a total net production of  $59 \text{ kmol s}^{-1}$  of nitrate,  $738 \text{ kmol s}^{-1}$  of DIC and a net consumption of  $60 \text{ kmol s}^{-1}$  for alkalinity and  $346 \text{ kmol s}^{-1}$  of dissolved oxygen (Table 3.14). In terms of neutral density layers, it is possible to identify biological production and consumption processes. The surface-mode layers, mainly between  $27.0 < \gamma^n < 27.1 \text{ kg m}^{-3}$ , show a slight production of DO and DIC consistent with the idea of primary production (Table 3.17 and Figure 3.47). Regarding the surface-intermediate waters, especially the layer comprised between  $27.4 < \gamma^n < 27.5 \text{ kg m}^{-3}$ , the properties production is also consistent with primary

production processes. The deep waters ( $27.6 < \gamma^n < 28.00 \text{ kg m}^{-3}$ ) experience a clear consumption of all properties as expected from the remineralization of relatively young waters, except for the densest layer, which remains positive, suggesting that probably a fraction of UCDW emerges to the surface and occurs both processes.

Finally, we have estimated the main carbon budget components within the Scotia Sea boundaries: a carbon dioxide uptake from the air-sea exchange of  $0.006 \text{ Pg C yr}^{-1}$ , an internal production through biogeochemical processes of  $0.163 \text{ Pg C yr}^{-1}$ , and a net anthropogenic DIC accumulation of  $0.123 \text{ Pg C yr}^{-1}$ ; being this DIC accumulation rate maximum near the surface, and becoming negative, experiencing a consumption of DIC at depth. The Southern Ocean represents about 9% of the global ocean but accounts for between 30 and 40% of the global oceanic carbon anthropogenic uptake (Khatiwala et al., [2013](#); Sabine & Feely, [2007](#)). Verdy & Mazloff ([2017](#)) estimated a mean uptake of  $0.18 \text{ Pg C yr}^{-1}$  south of  $50^\circ\text{S}$ , resulting from the outgassing of natural DIC in the high-latitude upwelling waters and the uptake of anthropogenic DIC in the subducting SAMW and AASW/AAIW at lower latitudes (Mikaloff Fletcher et al., [2007](#); Lovenduski et al., [2019](#)). Further, large quantities of DIC are exported from the Weddell to the Scotia Sea, adding complexity to this area. Our results suggest that the Scotia Sea act as an anthropogenic DIC storage at surface-mode and surface-intermediate waters, although DIC is consumed at depth resulting in a net reservoir of the order of  $0.123 \text{ Pg C yr}^{-1}$ , which remarks the importance of this basin in the global carbon cycle.

## **CHAPTER 3.3**

---

# **Spatial variability of horizontal diffusivity in the southwestern South Atlantic Ocean**

### 3.3.1. Context and objectives

Diffusion is a fundamental characteristic of geophysical flows, yet its description and quantification remain elusive. It depends on the spatiotemporal intermittence and often associated turbulence of many processes acting at multiple scales, which are responsible for dispersing properties, so we may truly say that diffusion is process-dependent. Paradoxically, if we can sample or model a certain process, then we do not worry about diffusion, it naturally disappears and turns into advection. But the reality is that we are not capable of sampling or simulating all processes, there are many motions that we cannot model and become therefore enclosed under the wavy concept of turbulent diffusion.

The process-dependency of diffusion is reflected in the horizontal evolution of a patch of passive tracer through three different phases, as proposed by Garrett (1983) and Sundermeyer & Price (1998). At short subinertial time scales, small-scale processes such as internal waves and other subinertial motions dominate mixing, with local (small-scale) diffusivity coefficients of order 0.1 to 1 m<sup>2</sup> s<sup>-1</sup>. The slowly growing patch eventually becomes large enough to be effectively stretched by straining submesoscale motions, causing long and narrow streaks. These streaks finally turn larger than the mesoscale structures and extend around each other causing much faster homogenization, reaching (effective) diffusivity coefficients of the order of 1000 to 10,000 m<sup>2</sup> s<sup>-1</sup>.

Biogeochemical or physical anomalies can certainly be locally introduced into the ocean, but very often, as shown by satellite images, they appear as large regional patches. This is the case when we deal with large-scale or global circulation. Either because of large-scale atmospheric forcing or as a result of the long residence times of water masses, for many regions and applications, we can skip the small-scale and straining phases and turn directly to the high mesoscale diffusivity. From a practical perspective, this is also necessarily true because our large-scale or global circulation models still have a relatively coarse resolution (nowadays operational at 1/12° although likely improving to 1/36° in the coming years) that does not resolve most submesoscale or small-scale motions. Hence, if we wish to hindcast or forecast the temporal evolution of large-scale processes, such as the global overturning circulation, we must resort to expressing these unresolved spatiotemporal scales in terms of effective vertical and horizontal diffusivities.

Different Lagrangian and Eulerian methods have been used to estimate the horizontal diffusion coefficients. Lagrangian diffusivity studies gained momentum during the last decades thanks to the increased availability of drifter data. Most of these works rely on statistical techniques studying the motion of single particles or the relative dispersion of groups of particles (Davis, 1987, 1991a, 1991b; Babiano et al., 1990; Zhurbas & Oh, 2003;

LaCasce, [2008](#); Chiswell, [2013](#); LaCasce et al., [2014](#); Zhurbas et al., [2014](#); Balwada et al., [2021](#)), although other studies have assessed the rate of material transport across tracer contours (Nakamura, [1996](#); Abernathey & Marshall, [2013](#)) or have searched for diffusivities that bring the progress of numerical particles closest to the observed evolution of drifters (Döös et al., [2011](#); De Dominicis et al., [2012](#); Rühls, [2018](#)).

Eulerian diffusion studies have exploited the increasing amount of hydrographic data, particularly from Argo floats and altimetry data, obtaining estimates of velocity and length scales from the variance of properties and directly applying mixing length theory (Naveira Garabato et al., [2011](#); Abernathey & Marshall, [2013](#); Roach et al., [2016](#), [2018](#)). Other approaches have related eddy diffusivity with eddy kinetic energy (Naveira Garabato et al., [2011](#); Roach et al., [2018](#)) or have obtained the diffusion coefficients by adjusting the distribution of properties through inverse methods (Zika et al., [2010](#); Cole et al., [2015](#); Deng et al., [2014](#)). Remarkably, the mapping of the temporal evolution of artificial or natural tracers, as observed in major field experiments, has also provided direct estimates of the eddy diffusion coefficients (Ledwell et al., [1998](#); Sundermeyer & Price, [1998](#); Naveira Garabato et al., [2007](#); Tulloch et al., [2014](#); Boland et al., [2015](#)).

The horizontal diffusivity values that have arisen from all the above studies are extremely diverse, possibly not only reflecting spatial variability in fluid dynamics but also differences in the diffusive processes under consideration. For modelling purposes, turbulent diffusion depends on the spatiotemporal scales of the model, as these define the size and temporal memory of fluctuations around the mean advective values. A general rule of thumb is that the lower the spatiotemporal resolution of the model, the larger the diffusion coefficients. Hence, an alternative practical strategy could be to develop fit-to-model methods towards obtaining the horizontal diffusion coefficients, simple enough that they could be used as an easy initial step for choosing the most appropriate coefficients for each particular application.

Nowadays, the combination of the much improved operational numerical hindcasts, particularly thanks to the data assimilation of the last generation models, and the growing amount of accurate drifting data open the possibility of a simple Lagrangian approximation to obtain model-fit diffusion coefficients. Here we propose the radial offset by diffusion (ROD) method as a simple tool that calculates the difference in radial position between float positions and equivalent numerical particles, and whose Gaussian distribution is then adjusted with a simple radial diffusive model.

We first introduce the subantarctic South Atlantic case-study area and the field and numerical data to be used for our tests, subsection [3.3.2](#), and next describes the fundamentals of the ROD method, subsection [3.3.3](#). We then apply the method to the entire study area at



eight different depths and explore the spatial variability near the sea surface and at 1000-m depth for five regions, which are separated by the Antarctic Circumpolar Current (ACC) frontal systems, subsection 3.3.4. In subsection 3.3.5, we discuss the limitations and advantages of the method and compare our results with other observations for the case-study area. We end with some final thoughts in subsection 3.3.6.

### 3.3.2. Data

#### 3.3.2.1. Case-study area

With the objective of testing the method, we have used field and numerical data from the Drake Passage (64°W) until 10°W and between 36°S and 64°S (Figure 3.50). The case-study area is the southwestern South Atlantic and the corresponding sector of the Southern Ocean, including the Scotia Sea, covering the whole range of ACC waters. The dynamics of the area are largely controlled by the Southern Ocean frontal systems: Subantarctic Front (SAF), Polar Front (PF), Southern Antarctic Circumpolar Current Front (SACCF), and the Southern Boundary (SB) (Figure 3.50d). These frontal systems cross the Drake Passage and stretch first meridionally into the Scotia Sea and then northward and northeastward through the North Scotia Ridge, steering most of the circumpolar waters that enter the South Atlantic Ocean.

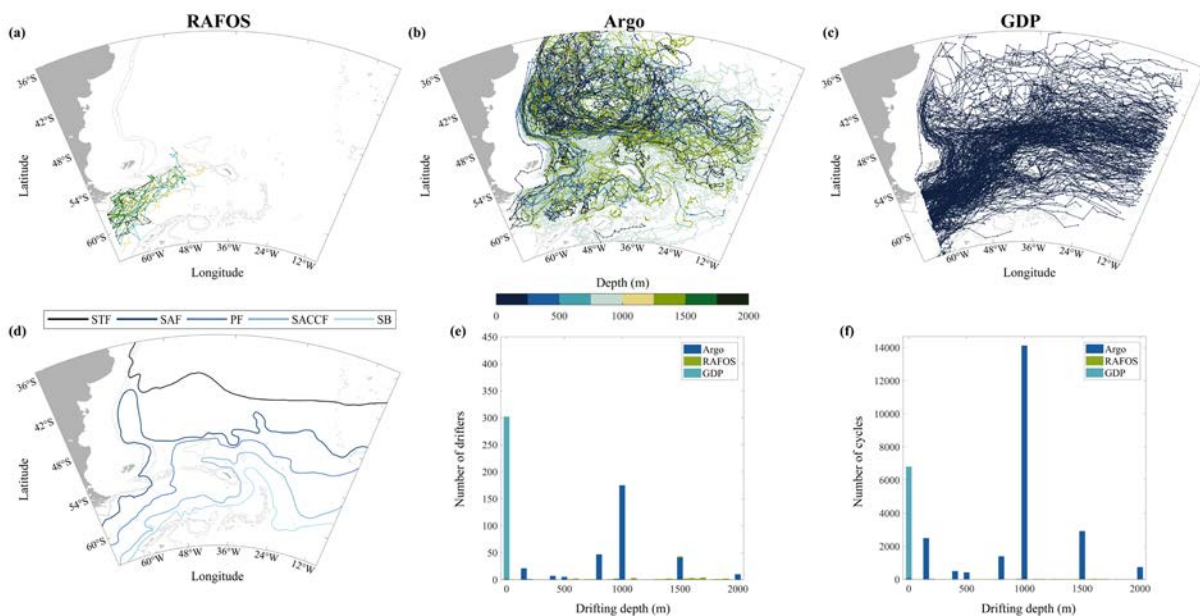


**Figure 3.50.** Trajectories of (a) RAFOS floats between 2009 and 2011, (b) Argo floats from 2002 to 2020, with positions shown every 10 days, and (c) GDP drifters from 2005 to 2020; the RAFOS and Argo floats are coloured according to their drifting depth. (d) Location of the Subtropical Front (STF), the Subantarctic Front (SAF), the Polar Front (PF), the Southern Antarctic Circumpolar Current Front

(SACCF) and the Southern Boundary (SB), as obtained by Orsi et al. (1995). (e) Number of drifters and (f) number of 10-day positions according to drifting depth and the type of drifter.

#### 3.3.2.2. Global Drifter Program data

The Global Drifter Program (GDP) started in 1995, although the oldest data records go back to 1979. The GDP maintains a fleet of about 1300 drifters with a holey-sock-type drogue centred at 15 m. All drifters sample surface temperature, although most drifters typically incorporate other sensors such as surface pressure and salinity. The drifters originally placed themselves using the ARGOS positioning system (CLS, 2011), with a typical 100-m resolution and several fixings per day. However, in recent years, they have progressively switched to the Global Positioning System (GPS), which provides hourly data with a resolution of order 1 m. The drifter database, which is available in near-real time through the GDP website (<https://www.aoml.noaa.gov/phod/gdp/>), consists of quality-controlled 6-hourly interpolated location, time, velocity and temperature with a position accuracy of about 100 m (Elipot et al., 2016).

We have used the trajectories from a total of 301 drifters that crossed the Drake Passage through 64°W and travelled the study area between 2005 and 2020 (Figures 3.50c, e). For our purposes, the 6-hourly positions are used to generate consecutive cycles of 10-day displacements (Figures 3.50c, f).

#### 3.3.2.3. RAFOS floats

The RAFOS floats are neutrally-buoyant instrumented drifters that receive acoustic signals emitted by several moored sound sources and hence calculate their position via triangulation; their position is provided daily with an estimated accuracy of about 1 km (Rossby et al., 1986; Baldawa et al., 2016). Here we have used a subset of 32 floats that were tracked between 2009 and 2011 as part of the Diapycnal and Isopycnal Mixing Experiment in the Southern Ocean (DIMES) (Baldawa et al., 2016, 2021). These represent all floats crossing the Drake Passage through 68°W and entering the Scotia Sea (Figures 3.50a, e).

The DIMES RAFOS floats drifted at varying depths, between 400 m and 2200 m. Most of the floats wandered at depths between 1200 m and 1600 m, although there were also a substantial number of displacements at other depths, particularly between 700 m and 800 m and between 1700 m and 1800 m (Figure 3.51). For our purposes, the daily positions are used to produce consecutive cycles of 10-day displacements (Figures 3.50a, f).

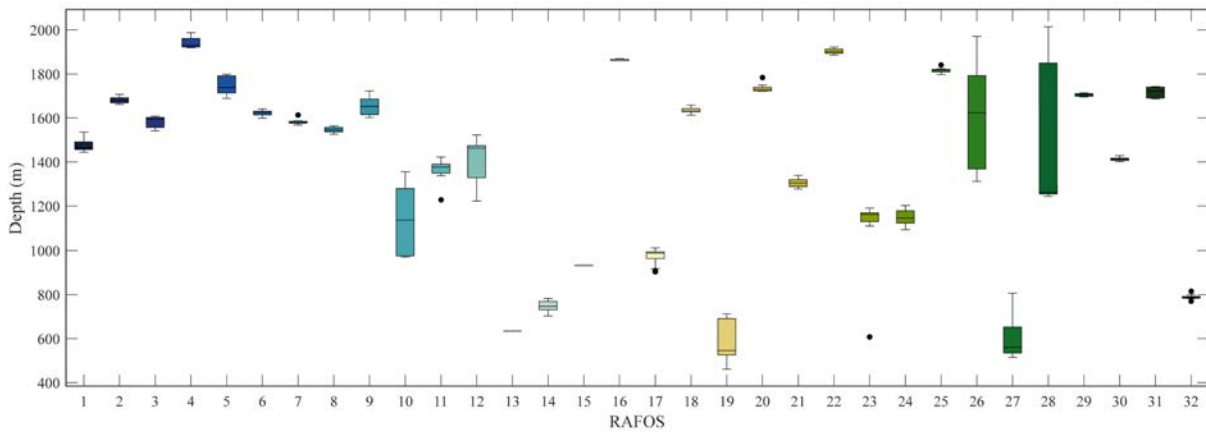


**Figure 3.51.** Vertical distribution of the 10-day cycles drifting depth along the 32 RAFOS trajectories. The 23<sup>rd</sup> RAFOS is the one most cycles performed inside the southwestern South Atlantic Ocean with a total of 29. The mean vertical displacement is about 149 m, being able to sink around 770 m along their trajectory as the 28<sup>th</sup> float from 1265 m to 2014 m depth.

#### 3.3.2.4. Argo floats

Since the first deployments in 1999, many Argo profiling floats have been launched as part of the International Argo Program (Argo, [2000](#)). The Argo array reached 3000 floats in 2007 and has been sustained at about 4000 for the last few years (Roemmich et al., [2022](#)). These floats provide not only an extremely valuable sampling of the hydrographic conditions in the upper 2000 m of the water column but also offer a unique description of the flow at their parking depths (Ollitrault et al., [2006](#); Lebedev et al., [2007](#); Rosell-Fieschi et al., [2015](#)). Every 10 days, the floats surface to transmit the collected hydrographic data, also providing an estimate of their 10-day average velocity. The 10-day displacement is calculated as a straight trajectory between the last position of the float before diving and the first position of the float as it returns to the sea surface. Rosell-Fieschi et al. (2015) estimated that the errors in the parking-depth velocities at 1000 m are less than 10% in 94% of the cases and less than 3% in 58% of the cases; for a displacement of about 50 km in 10 days, this last value represents an accuracy of 1.5 km.

We have considered all Argo floats that entered the study area through the Drake Passage between 2002 and 2020 (Figures [3.50b](#), e). The total number of floats was 310, with most of them (175) having the parking depth at 1000 m. For our analysis, we have removed all float cycles when the first or last surface positions were not flagged as good (Figures [3.50b](#), f).

#### 3.3.2.5. GLORYS12v1 reanalysis

We use daily three-dimensional velocity fields from the global physical reanalysis GLORYS12v1 (Garric et al., [2017](#); Lellouche et al., [2021](#)) developed by the Mercator Ocean team

and distributed by the Copernicus Marine Environment Monitoring Service (CMEMS; <http://marine.copernicus.eu>), which is eddy-resolving in our study area. This ocean reanalysis combines the NEMO ocean general circulation numerical model with observations to generate the best possible estimate of the state of the ocean. In particular, the GLORYS12v1 numerical data encompasses the entire period of all available drifter observations, allowing the comparison of numerical and field trajectories (subsection [3.3.3.1](#)).

GLORYS12v1 has a longitudinal resolution of  $1/12^\circ$  or 7.5 km at the equator and 4 km at  $64^\circ\text{S}$  of latitude, and 50 vertical levels, with maximum grid resolution at the surface and vertical spacing increasing gradually in depth. Reanalysis products such as GLORYS12v1 are significantly accurate and generally agreed with observations (Mignac et al., [2018](#); Orúe-Echeverría et al., [2021](#)).

### 3.3.3. Methods

#### 3.3.3.1. Comparing the field and numerical positions

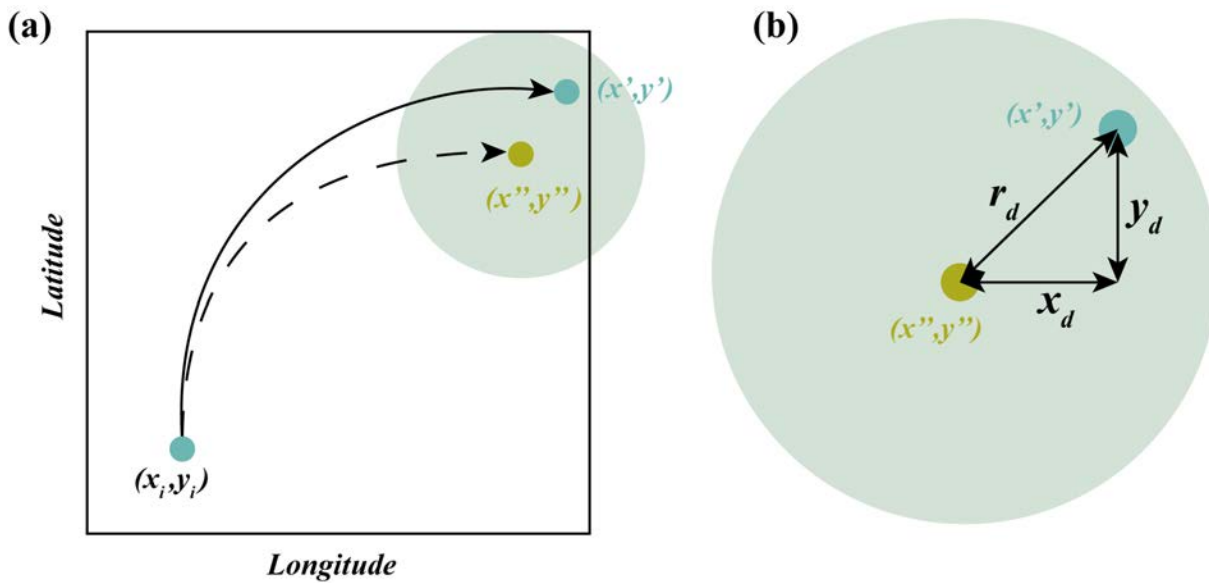
The numerical particles are released at the same position, depth and day of the year as the real drifter and tracked daily for 10 days using the GLORYS12v1 reanalysis daily velocity fields with the open-source Parcels software (Lange & van Sebille, [2017](#); Delandmeter & van Sebille, [2019](#)). Setting the time interval between positions as 10 days simply responds to the characteristic surfacing cycle of the Argo floats, which represent most of our available subsurface trajectories. Each drifter is modelled individually but for the overall numerical-field comparison (see below), the data are split into the GDP trajectories at 15 m and the trajectories in the following seven depth ranges: 150 - 200 m, 400 - 500 m, 700 - 800 m, 900 - 1100 m, 1200 - 1300 m, 1400 - 1600 m and 1800 - 2000 m.

The numerical trajectories that correspond to the GDP and Argo drifters are calculated using only the horizontal velocities. However, the RAFOS drifters also incorporate vertical velocities, because these drifters can display vertical motions as large as 200 m in response to the large tilting of isopycnals in frontal systems. Hence, in the case of the RAFOS drifters, it may happen that data from one drifter splits into several vertical ranges.

Hence, the resulting numerical trajectories do not include the subgrid horizontal motions, which have to be simulated through some additional random motion proportional to a selected horizontal diffusivity (e.g., Peña-Izquierdo et al., [2015](#); Vallès-Casanova et al., [2022](#)). In contrast, the drifters do have the full spatiotemporal range of horizontal motions – except those at spatial scales smaller than the size of the drifter – so they incorporate the principal subgrid motions that are not deterministically calculated by the numerical models.

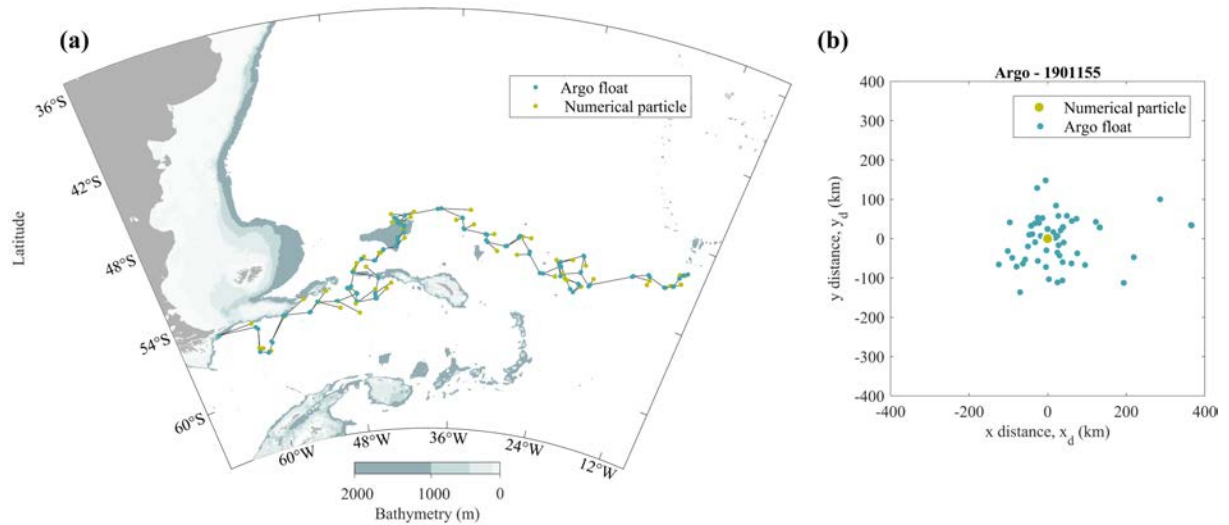
Hence, by releasing numerical particles at the same time and location as the actual drifter and tracking them during a certain time interval (in our case 10 days), we can find the distances associated with the subgrid motions.

The procedure to determine these diffusive (subgrid) motions is illustrated in Figure 3.52. Let us call  $(x_i, y_i)$  the initial location of both the drifter and the numerical particle, and  $(x', y')$  and  $(x'', y'')$  the position of the drifter and the numerical particle after 10 days, respectively. Naming  $x_d = x' - x''$  and  $y_d = y' - y''$  the longitudinal and latitudinal offsets, then the total or radial distance is given by  $r_d = (x_d^2 + y_d^2)^{\frac{1}{2}}$ .



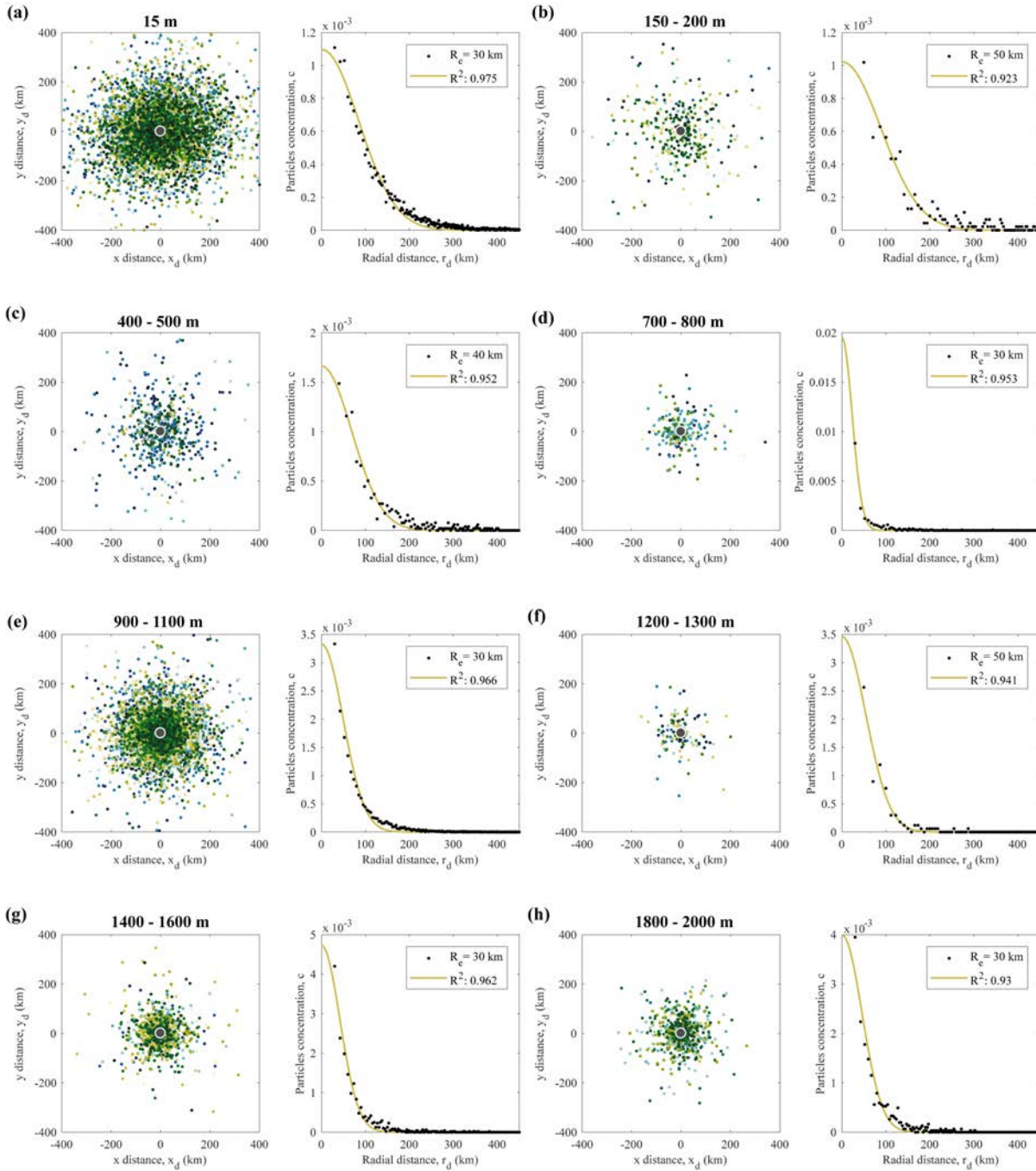
**Figure 3.52.** (a) Schematic trajectories of a drifter and the corresponding simulated numerical particle. The initial position of both drifter and numerical particle is  $(x_i, y_i)$ , and their final locations after 10 days are  $(x', y')$  and  $(x'', y'')$ , respectively. (b) Sketch of the final positions of both drifter and numerical particle: the longitudinal and latitudinal offsets are  $x_d = x' - x''$  and  $y_d = y' - y''$ , respectively, so that the offset (radial distance) is  $r_d = (x_d^2 + y_d^2)^{\frac{1}{2}}$ .

Figure 3.53 illustrates the procedure applied to one Argo float that crossed the study area, in this particular case, with a total of 53 cycles of 10 days each. We first calculate the float and numerical displacements for each cycle, leading to a scatterplot with 53 offsets (Figure 3.53b). This is then repeated for all floats drifting at similar depths, for example, for all RAFOS and Argo floats. These offsets are finally gathered together for similar drifting depth and geographical area; for example, the offsets for all GDP drifters (floating at 15 m) or the offsets for the Argo and RAFOS floats that drift at 1000 m, either over the entire area of study or for some specific region (Figures 3.54 and 3.55).



**Figure 3.53.** (a) Sample trajectory of an Argo float through the study area, with the colour convention following Figure 3.52. The blue dots, joined by black lines, represent the initial and final positions transmitted by the float during the 10-day cycle; note that there are pairs of blue dots very close to each other, which represent the first transmission of the float after arrival to the sea surface and the last transmission before immersion. The numerical trajectories are drawn as straight black lines that depart from the second blue dot and end in a green dot, which represents the final numerical positions. (b) Scattered plot showing the radial offsets between the Argo float and the corresponding numerical particles; the origin of coordinates, which is shown as a green dot, represents the position of the numerical particle at the end of each cycle.

It may happen that the centre of mass of the cloud of radial displacements does not coincide with the origin of coordinates for the scattered diagram – an origin that represents the positions reached by the numerical particles – meaning that there is some bias in the mean flow as predicted by the model in comparison to what is observed by the drifter. If this occurs, we simply shift the entire cloud to make the centre of mass fit to the origin of coordinates, recognizing that the bias is inherent to the model and not to the subgrid diffusive processes (Tables 3.18 and 3.19).



**Figure 3.54.** Scatter plot of radial distances (a-h, left columns) grouped per drifting depth range together with the normalized experimental concentration (dots) and the adjusted Gaussian distribution (green line) as in Figure 3.57c (a-h, right columns). In each scatter plot is represented the inner radius  $R_e$  and the correlation coefficient between the experimental points and the adjusted curve; the coloured dots identify data points from one same float.

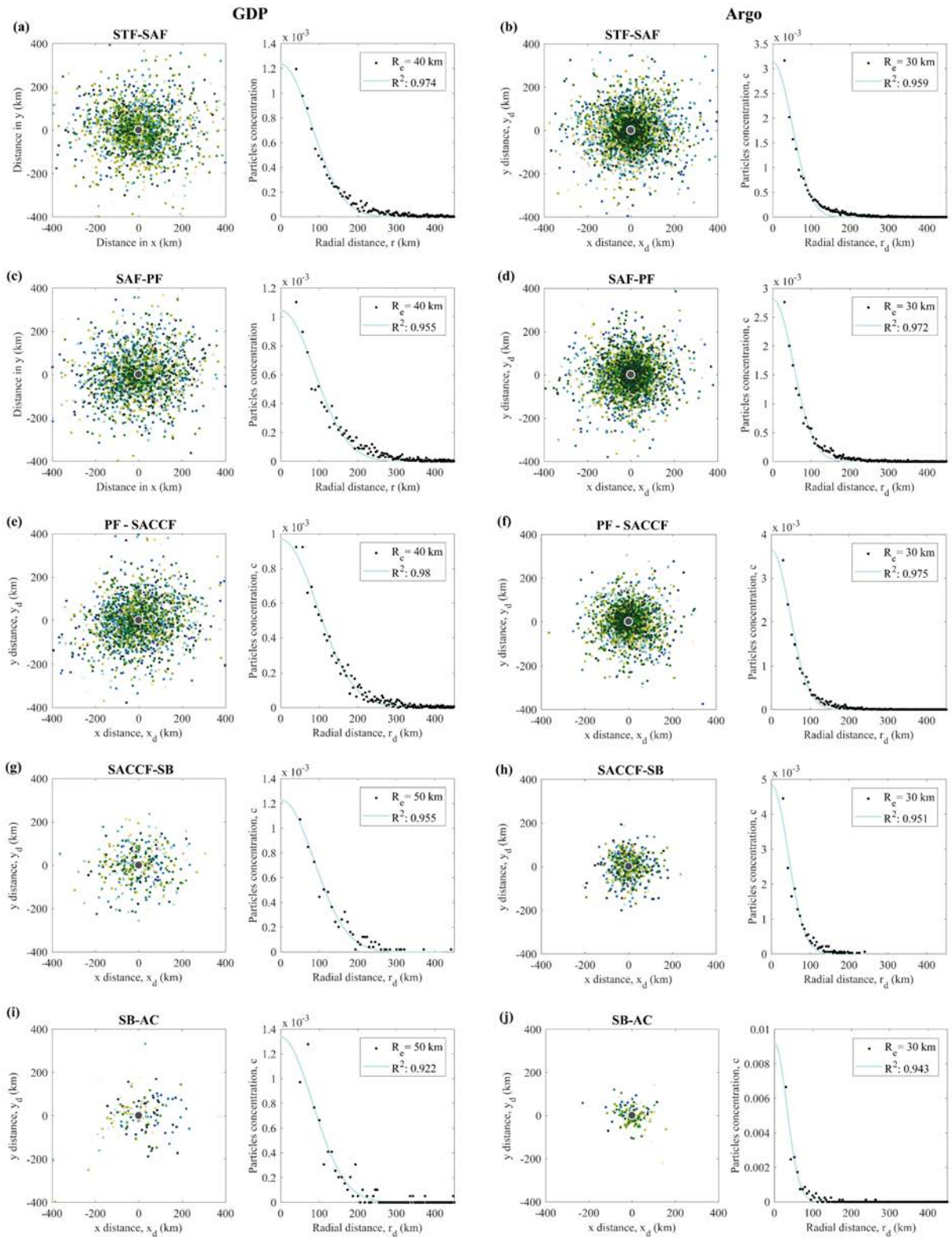


**Figure 3.55.** (Left columns; a, c, e, g, i) Scatter plot of radial offsets for the GDP 15-m drifters together with the normalized experimental concentration (dots) and the adjusted Gaussian distribution (blue line) as in Figure 3.57c. (Right columns; b, d, f, h, j) As before but for the Argo 1000-m floats. In each scatter plot is represented the inner radius  $R_e$  and the correlation coefficient between the experimental points and the adjusted curve; the coloured dots identify data points from one same float.



**Table 3.18.** Longitudinal ( $x_d$ ) and latitudinal ( $y_d$ ) separations between the centre of mass of the cloud of radial offsets and the origin of coordinates of the scattered diagram, grouped according to the depth range of the floats. The positive sign corresponds to east-north and the negative to west-south. For reference, a displacement of 10 km in 10 days represents a speed slightly less than 1 cm s<sup>-1</sup> (exactly  $8.64 \times 10^{-3}$  m s<sup>-1</sup>).

| Depth         | $x_d$ (km) | $y_d$ (km) |
|---------------|------------|------------|
| 15 m          | 51.95      | -3.77      |
| 150 - 200 m   | -30.22     | 9.73       |
| 400 - 500 m   | -1.89      | -2.26      |
| 700 - 800 m   | 7.14       | 4.31       |
| 900 - 1100 m  | 1.78       | -0.12      |
| 1200 - 1300 m | -2.08      | -4.29      |
| 1400 - 1600 m | -3.25      | -0.79      |
| 1800 - 2000 m | -4.08      | -4.84      |

**Table 3.19.** Longitudinal ( $x_d$ ) and latitudinal ( $y_d$ ) separations between the centre of mass of the cloud of radial offsets and the origin of coordinates of the scattered diagram, at 15 m (GDP) and near 1000 m (Argo floats), grouped per frontal region. The positive sign corresponds to east-north and the negative to west-south. For reference, a displacement of 10 km in 10 days represents a speed slightly less than 1 cm s<sup>-1</sup> (exactly  $8.64 \times 10^{-3}$  m s<sup>-1</sup>).

| Regions    | GDP (15 m) |            | Argo (1000 m) |            |
|------------|------------|------------|---------------|------------|
|            | $x_d$ (km) | $y_d$ (km) | $x_d$ (km)    | $y_d$ (km) |
| STF - SAF  | 57.80      | 6.01       | 0.59          | 1.39       |
| SAF - PF   | 40.13      | -4.51      | -3.54         | -4.02      |
| PF - SACCF | 54.26      | -12.97     | 5.26          | -4.12      |
| SACCF - SB | 71.66      | -19.12     | 3.38          | -6.76      |
| SB - A.C.  | 71.10      | -25.84     | -5.09         | 6.60       |

### 3.3.3.2. Radial diffusion model

The underlying premise of the radial offset by diffusion (ROD) approach is that the radial distances between the drifter and numerical positions respond to subgrid processes, i.e., to diffusive processes that are not considered by the numerical circulation model. With this idea in mind, we simulate the diffusive cloud (drifter minus numerical positions) through a simple one-dimensional radial diffusive equation

$$\frac{\partial c}{\partial t} = \frac{1}{r} \frac{\partial}{\partial r} \left( Kr \frac{\partial c}{\partial r} \right) = \frac{K}{r} \frac{\partial}{\partial r} \left( r \frac{\partial c}{\partial r} \right) \quad (3.8)$$

where  $c$  stands for a concentration of particles (number of particles per unit area) and  $K$  is the horizontal (effective) diffusion coefficient or (effective) diffusivity; in this expression  $r$  is the radial coordinate of the diffusive motions, which corresponds to the radial distance  $r_d$  between the correlative offsets of the drifter and numerical particle. In the last equality, we assume that the diffusivity is constant in space; for the numerical solution, we will further accept that  $K$  is constant in time.

The boundary conditions are  $\partial c / \partial r = 0$  both at the origin  $r = 0$  and for large radial values  $r \rightarrow \infty$ . For the initial condition, we set the concentration equal to one within a certain region close enough to the origin,  $c(r \leq R_n, t = 0) = 1$ , and zero elsewhere, which essentially implies that there is an initial circular disk that contains all diffusive particles (in our case the drifters). In the next subsection, we will explain how to normalize the actual number of drifters to reproduce this initial condition, but next, we explain how to determine  $R_n$ .

The initial disk is imagined as characterizing an area where we initially place all drifters and numerical particles; once released, these particles will evolve with the environmental flow, either with (the drifters) or without (the numerical particles) subgrid motions. Hence, we want this area to be representative of the horizontal velocity field experienced by the numerical particles. With this in mind, we choose a rectangular area with longitudinal ( $d_{lon}$ ) and latitudinal ( $d_{lat}$ ) sides equal to the size of the grid cell, which we imagine as centred at each node of the numerical model. The disk with the equivalent area would have a radius given by  $R_n = (d_{lon}d_{lat}/\pi)^{1/2}$ . Considering the  $1/12^\circ$  resolution of GLORYS12v1 and choosing  $50^\circ\text{S}$  as a latitude representative of the entire area of study, we obtain a radius  $R_n = 4.2$  km.

The diffusion equation is solved numerically using the Matlab *pdepe* function for one-dimensional parabolic and elliptic partial differential equations (Skeel & Berzins, 1990). It is solved in a domain of 420 km, with 100 elements of size  $\delta r = 420$  m and the radial coordinate given by  $r_i = i \delta r$ . The initial condition is expressed as:

$$c(r_i, t = 0) = \begin{cases} 1 & i < 10 \\ 0.5 & i = 10 \\ 0 & i > 10 \end{cases}$$

setting a concentration equal to one particle per square meter in a circle of radius  $R_n$  is equivalent to having initially  $N = \pi R_n^2 = 5.54 \times 10^7$  particles.

Figure 3.56 shows the numerical solution of the radial diffusive equation at different times, using the above boundary and initial conditions and a diffusion coefficient  $K = 1000 \text{ m}^2 \text{ s}^{-1}$ . The solution at any time is Gaussian, with the concentration near the origin decreasing and the distribution flattening as particles diffuse out of their original disk. The total amount of particles (concentration integrated over the entire horizontal domain) remains constant in time, equal to the initial value  $N$ .

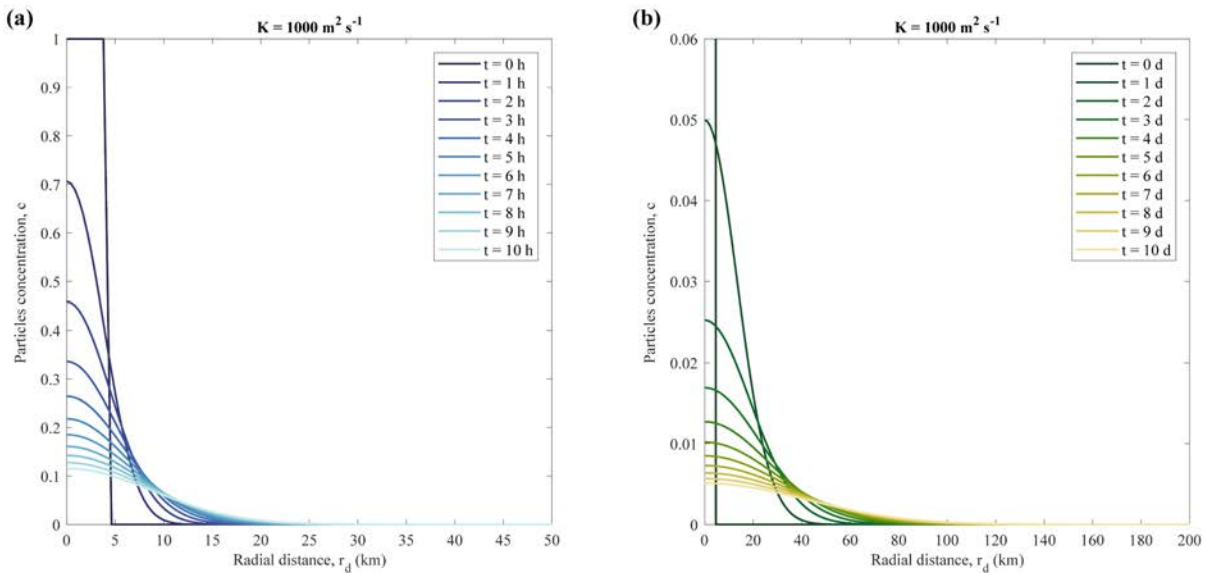


**Figure 3.56.** Numerical solution of the radial diffusive equation for  $K = 1000 \text{ m}^2 \text{ s}^{-1}$  at different times. (a) From  $t = 0$  to  $t = 10$  hours plotted every hour and (b) from  $t = 0$  to  $t = 10$  days plotted every day. Notice the differences in the horizontal and vertical axis between both panels.

### 3.3.3.3. Comparing the experimental and theoretical particle distributions

The comparison between the radial distribution of the drifters with respect to their centre of mass and the radial distribution of the concentration in the diffusion model is carried out in two steps: first, adjusting a Gaussian distribution to the drifter data, and second, selecting the diffusivity coefficient that produces the best fit between the experimental and numerical distributions.

The first step – the conversion of the cloud of radial displacements into a Gaussian distribution – requires initially producing a histogram of the number of particles for different radial coordinates. For this purpose, the number of particles has to be counted over equal

areas, which implies that the radial coordinates of the histogram ( $R_j$ ) have to be properly chosen, with the histogram radial intervals decreasing with distance from the origin (Figure 3.57a). Specifically, if the inner radius is  $R_1$  then its area is going to be  $A = \pi R_1^2$  and the area of any outer ring will have to be equal to the inner area,  $\pi R_j^2 - \pi R_{j-1}^2 = \pi R_1^2$ , which causes that the external border of the rings increases as  $R_j = j^{1/2} R_1$ .

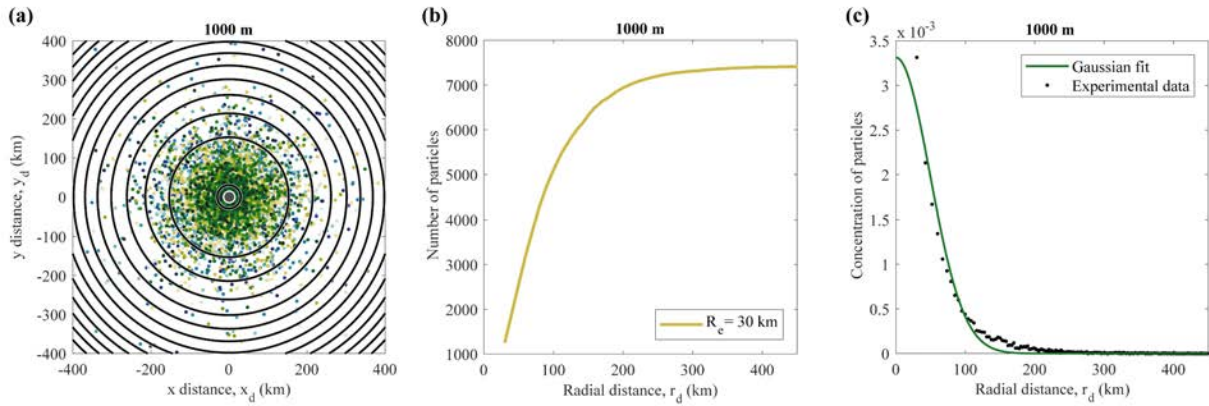


**Figure 3.57.** (a) Scatter plot of radial offsets for drifters at 1000 m, displaying rings of equal area; the coloured dots identify data points from one same float. In this subplot, we also draw the origin of coordinates (grey dot with a white border) and one ring every 25 rings computed (black circles), starting with the inner ring ( $R_e = 30$  km) and following with the relation  $R_j = j^{1/2} R_e$ . (b) Cumulative number of particles as a function of radial distance for  $R_e = 30$  km, disclosing the expected shape of the error function. (c) Normalized experimental concentration (dots) and the adjusted Gaussian distribution (green line).

The inner radius  $R_1$  has to be large enough to ensure that the adjacent rings gather a significant number of particles, but it has to be small enough to provide adequate resolution near the origin. We first calculate the histograms for different values of the inner radius, starting at  $R_1 = 10$  km and increasing at intervals of 10 km, and find the Gaussian that best fits the histogram data (Figure 3.58). For each case, it is computed the correlation between the data and the Gaussian fit, which increases with  $R_1$  until it approximately stabilizes, and select  $R_1$  as the minimum radius that has a high correlation value (Figure 3.59). Once we have the Gaussian fit, we can interpolate the number of drifters at those same radial coordinates as for the numerical model,  $r_i = i \delta r$  with  $\delta r = 420$  m. Hereafter we will use the nomenclature  $R_e = R_1$  to emphasize that it corresponds to the experimental inner radius, and in analogy with  $R_n$  as conforming to the inner radius of the numerical model; recall that  $R_n = 4.2$  km while a characteristic value of  $R_e$  is 30 km.

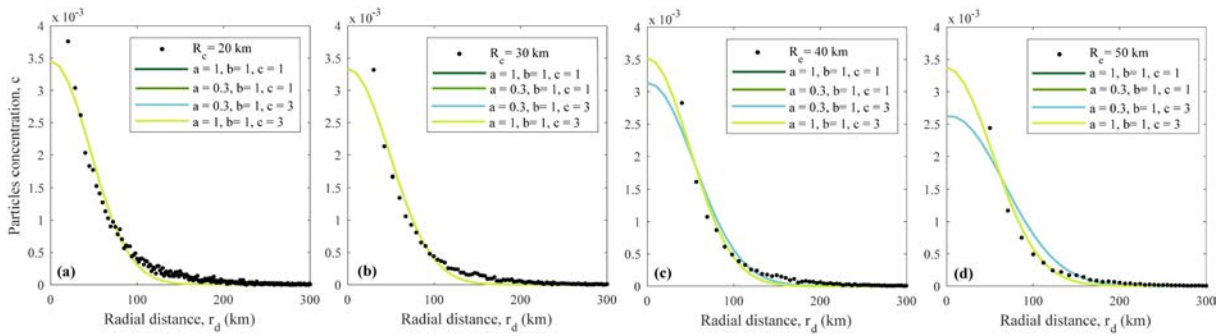


**Figure 3.58.** Gaussian adjustment that best fits the histogram data (black dots) according to the different weights given to the particles concentration for the radial distances at 1000 m depth comprised from 0 to 150 km, from 150 km to 300 km, and finally for radial distances higher than 300 km. The histograms for different values of the inner radius assed are (a)  $R_e = 20$  km, (b)  $R_e = 30$  km, (c)  $R_e = 40$  km and (d)  $R_e = 50$  km and increase at intervals of 10 km. Notice that some Gaussian adjustments are not visible because they are overlapped. The best and chosen fit for all histograms corresponds to  $a = 1, b = 1$  and  $c = 3$  (light green adjustment).

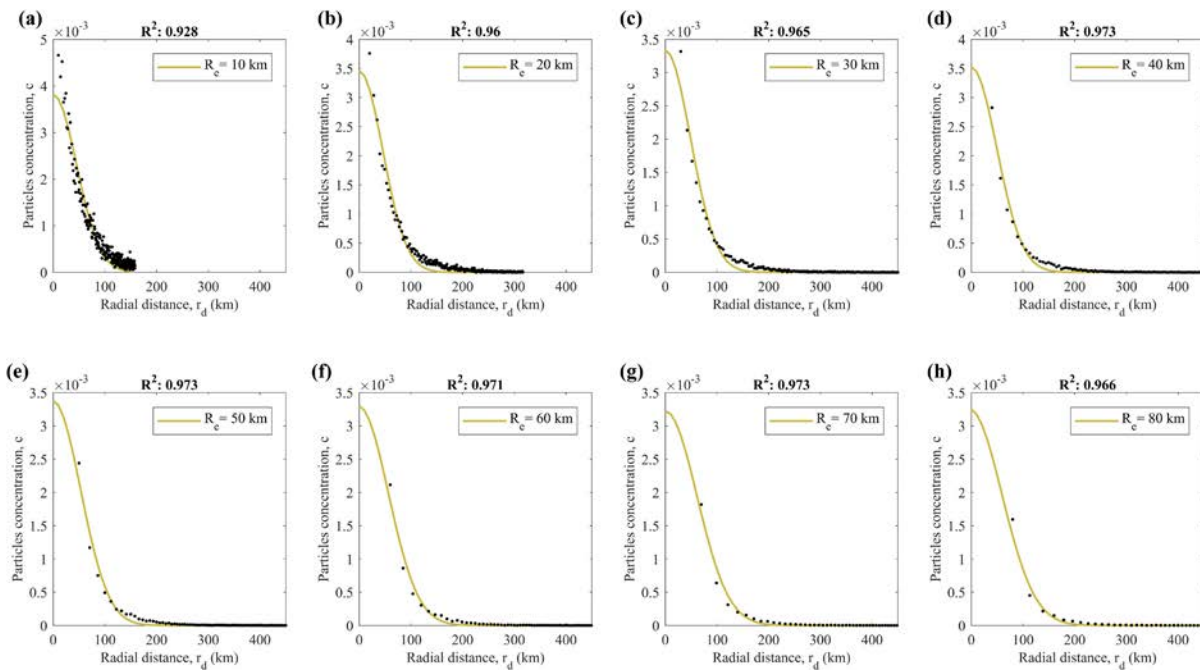


**Figure 3.59.** Degree of correlation ( $R^2$ ) between the histogram and the Gaussian fit as the inner radius increase from 10 km to 80 km at 1000 m depth. The  $R^2$  increase starting from (a) 0.928, (b) 0.960, (c) 0.963 and reach its maximum at (d, e, g) 0.973 to decrease again at (f) with 0.971 until (h) 0.966. When the  $R^2$  stabilizes, and the concentration of the particles (black dots) not show too much noise, the minimum radius that has a high correlation value ( $> 0.9$ ) is the one selected. The Gaussian fits are already adjusted with the  $a = 1, b = 1$  and  $c = 3$  weights.

The second step – finding the coefficient of diffusion that produces the best agreement between the experimental and numerical distributions – requires first converting the number of drifters into an experimental concentration of particles (simply dividing by  $A = \pi R_e^2$ ) and then normalizing this concentration by considering that the total number of numerical parcels is different to the total number of drifters. If the total number of numerical particles is  $N = \pi R_n^2 = 5.54 \times 10^7$  (which sets a concentration  $c = 1$  within the inner disk of radius  $R_n$ ) and the total number of drifters is  $n$  (which will change depending on the depth or region considered), then the experimental concentration of particles has to be normalized by the factor  $N/n$ .

Figure 3.57 illustrates some of the main aspects of the previous description. A distribution of the number of particles at different radial distances (as obtained for all pairs of numerical particles and drifters) is calculated using radial intervals of equal area (Figure 3.57a). The cumulative addition of the number of particles increases asymptotically until reaching the total number of observations, displaying the characteristic shape of the error function, which is the derivative of the Gaussian distribution (Figure 3.57b). A Gaussian curve is finally adjusted to the normalized experimental concentrations, that is, to the number of observations per unit area after applying the  $N/n$  factor for proper comparison with the numerical model (Figure 3.57c).

We are finally left to compare the values of the experimental Gaussian curve with the values of the numerical solution at  $t = 10$  days, in both cases using the data at the radial positions  $r_i = i \delta r$ . For this comparison, we compute the numerical solution for different horizontal diffusive coefficients  $K$ , increasing from 0 to 10,000  $\text{m}^2 \text{s}^{-1}$  at intervals of 10  $\text{m}^2 \text{s}^{-1}$ . The best fit is selected as the numerical curve that produces the minimum standard deviation between both distributions, as shown in the following subsection.

### 3.3.4. Results

#### 3.3.4.1. Variability with depth

The experimental and best-fit numerical concentrations for the GDP 15-m drifters and the subsurface Argo and RAFOS drifters are presented in Figure 3.60 (the corresponding scattered plots are available in Figures 3.54 and 3.55). The diffusion coefficient is maximum in the upper 200 m (4630 - 4980  $\text{m}^2 \text{s}^{-1}$ ) and decreases with depth, with minimum values in the 1400 - 2000 m depth range (1080 - 1270  $\text{m}^2 \text{s}^{-1}$ ). A discrepant much smaller value occurs at 700 - 800 m (260  $\text{m}^2 \text{s}^{-1}$ ), but these data correspond largely to waters south of the Southern Boundary front, where the flow is generally much weaker (Figure 3.61).

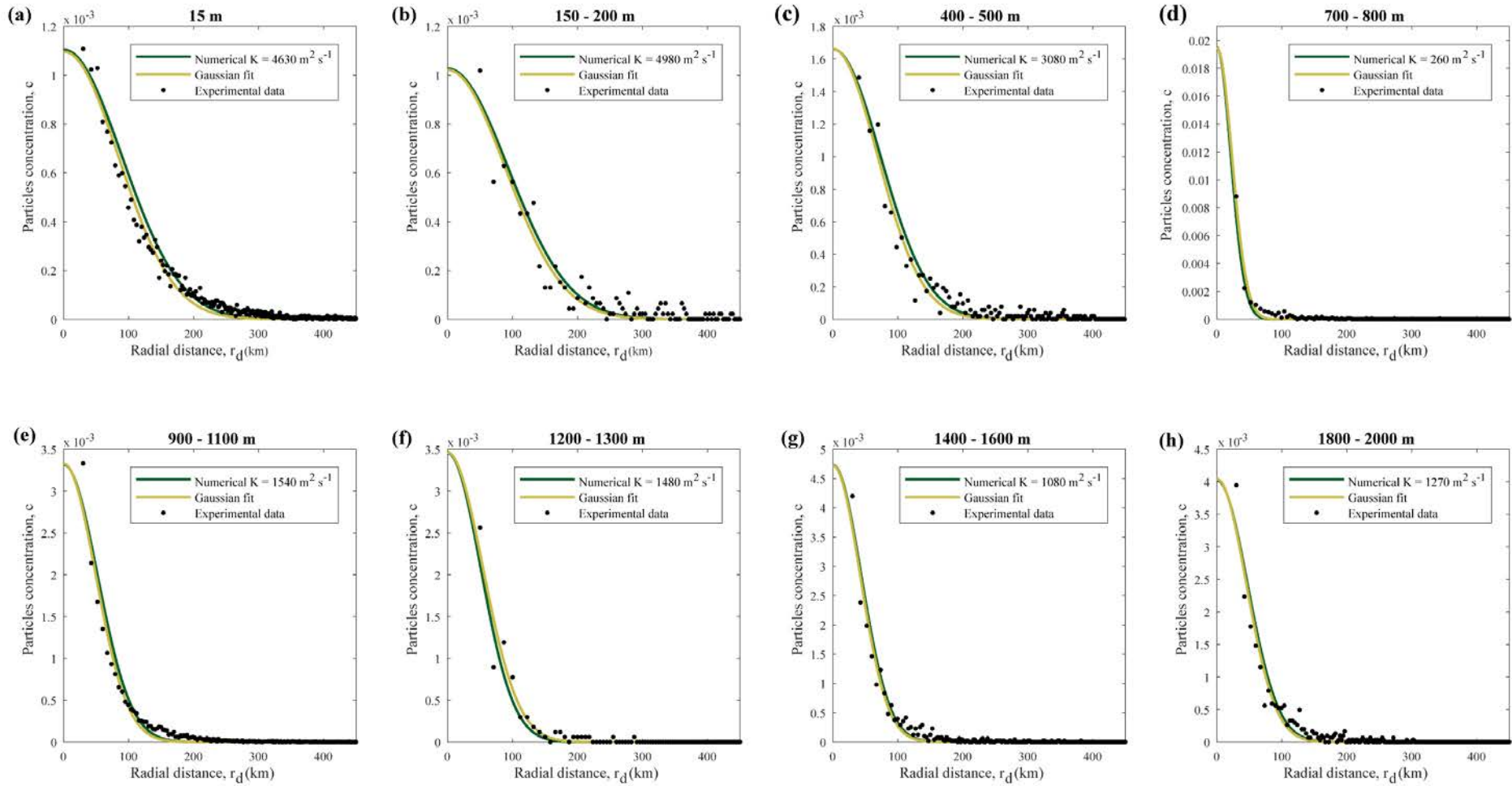


**Figure 3.60.** Gaussian adjustment (light green line) to the experimental particle concentrations (black dots) and the best-adjust numerical solution (dark green line) with the corresponding diffusion coefficient for each depth range as labelled. In all instances, the correlation ( $R^2$ ) between the experimental and numerical Gaussian curves, using data every 420 m, is greater than 0.95.

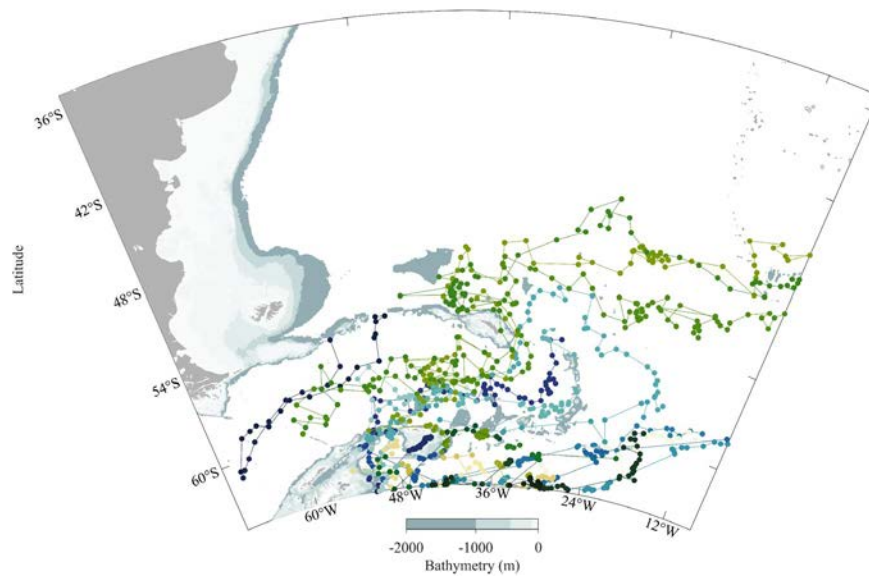


**Figure 3.61.** Distribution of the drifter trajectories along the southwestern South Atlantic Ocean at 700 - 800 m. The 10-day cycles are mainly constrained south of ACC and within the Weddell Sea, probably being the Argo and/or RAFOS floats carried by the SACCF and SB fronts. Each colour corresponds to one different float, and notice that large spacing between cycles in the Weddell Sea are due to the presence of sea-ice coverage, not to high velocities in the region

#### 3.3.4.2. Variability per frontal regions

The GDP and Argo programs provide sufficient drifting data to examine the spatial variability at 15 m and 1000 m. Hence, we use the frontal systems (Figure 3.50d) to separate the study area into five approximately zonal regions: Subtropical Front (STF) to SAF, SAF to PF, PF to SACCF, SACCF to SB, and south of SB (Figure 3.62). Each 10-day cycle is attributed to one single region.

The most dynamic regions of our study area are STF - SAF and SAF - PF. The STF - SAF region is characterized by the intense Malvinas Current and the mesoscalar features associated with the Brazil - Malvinas Confluence (Jullion et al., 2010; Mason et al., 2017; Artana et al., 2018; Orúe-Echevarría et al., 2019, 2021), and the SAF-PF region is distinguished by the intense currents associated with both frontal systems (Orsi et al., 1995; Naveira Garabato et al., 2003; Sokolov & Rintoul, 2007; Chapter 3.1). The flow in PF-SACCF and SACCF-SB decreases in intensity (Naveira Garabato et al., 2003; Chapter 3.1) and the region south of the SB, which includes the Powell Basin in the Weddell Sea, displays even lower velocities (Yamazaki et al., 2021; Reeve et al., 2019; Vernet et al., 2019).

The 15-m diffusivities are very large in all five regions, with values in the 4000 - 5000  $\text{m}^2 \text{s}^{-1}$  range, and only slightly less (3850  $\text{m}^2 \text{s}^{-1}$ ) in the domain south of SB, possibly reflecting the very intense winds in the whole area (Russell et al., 2016).



At 1000 m, the range of diffusivities is consistent with the intensity of the zonal jets and eddies, with peak values in the STF - SAF (1640  $\text{m}^2 \text{s}^{-1}$ ) and SAF - PF (1820  $\text{m}^2 \text{s}^{-1}$ ) regions and the minimum ones again south of the SB (530  $\text{m}^2 \text{s}^{-1}$ ).

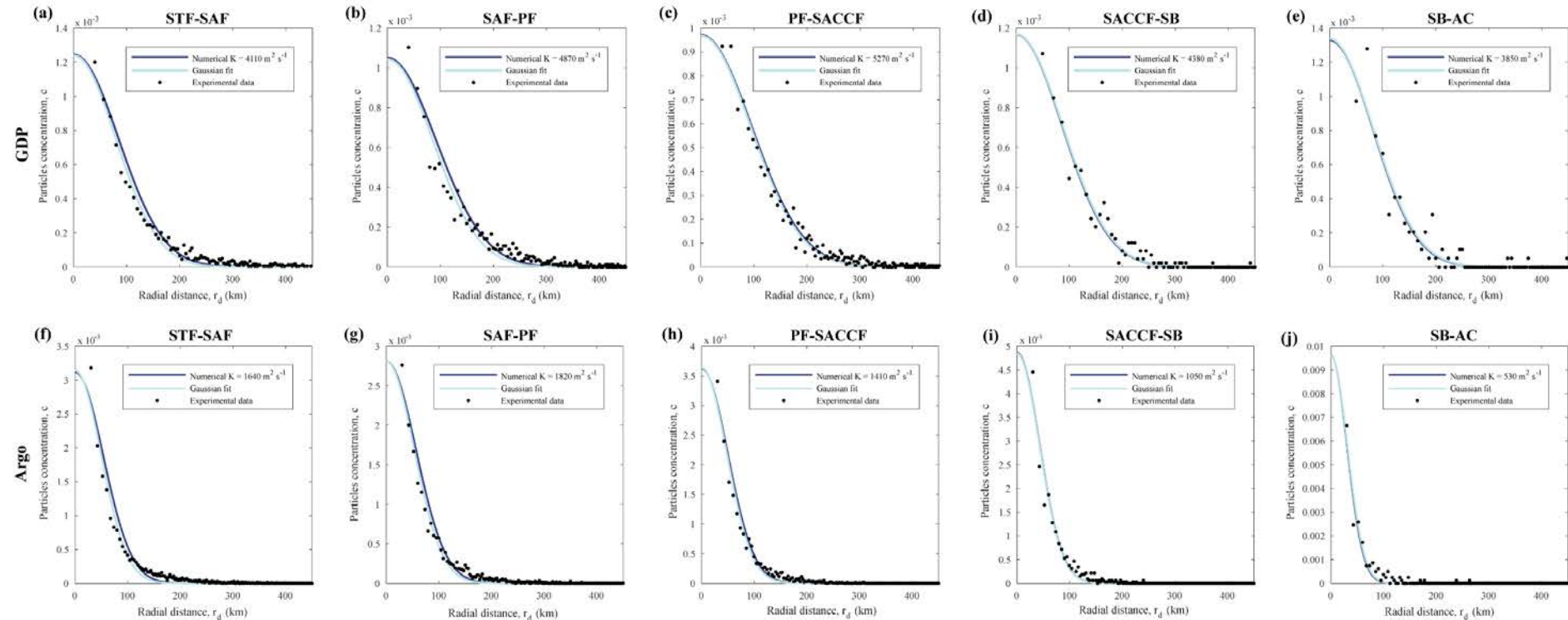


**Figure 3.62.** Gaussian adjustment (light blue line) to the experimental particle concentrations (black dots) and the best-adjusted numerical solution (dark blue line) with the corresponding diffusion coefficient for each region; the acronyms are Subtropical Front (STF), Subantarctic Front (SAF), Polar Front (PF), Southern Antarctic Circumpolar Current Front (SACCF), Southern Boundary (SB) and Antarctic continent (AC). The upper row corresponds to GDP data at 15 m and the lower row to Argo float data in the 900 - 1100 m depth range. In all instances, the correlation ( $R^2$ ) between the experimental and numerical Gaussian curves, using data every 420 m, is greater than 0.95.

### 3.3.5. Discussion

#### 3.3.5.1. Limitations and advantages of the method

The ROD method has limitations and advantages, both conceptual and experimental. From a conceptual perspective, the method has several constraints. First, both the data analysis and the diffusion model assume that motions are radial, ignoring the vertical motions that a float may experience during one cycle. Free motions in the ocean (those that do not experience the restoring gravitational force) take place along isentropic (approximately isopycnal) tilted surfaces, hence large subgrid motions during one single 10-day cycle could bring the float into neighbouring vertical zones, with different diffusive regimes, e.g., if a float experiences a displacement of 100 km across a frontal system with a 0.005 isopycnal slope then the depth change would be of 500 m. This indeed may be happening in some of our floats that drift close to frontal systems but our data shows that it is more an exception than a rule, with no substantial effect on the overall results (Figure 3.51). In any case, perhaps it is only a matter of thinking in terms of isopycnal rather than horizontal diffusivity, with changes occurring with potential density rather than depth.

A second conceptual limitation of the ROD method is the assumption that the coefficient of diffusion  $K$  does not depend on the polar coordinate, which essentially means that turbulence is isotropic. This may not be so in the ocean because of topographic and/or dynamic constraints, e.g., differences in one order of magnitude (from  $220 \text{ m}^2 \text{ s}^{-1}$  latitudinal to  $1500 \text{ m}^2 \text{ s}^{-1}$  zonal) have been estimated in the deep South Atlantic because of the presence of alternating zonal jets (Herbei et al., 2008). In particular, for our study area, geophysical turbulence is likely influenced by the frontal systems, with a preferential along-front (dominantly zonal) dispersive direction (Naveira Garabato et al., 2007; Roach et al., 2016). This is clear from the scattered plots in Figures 3.54 and 3.55, which illustrate clouds of points (radial offsets) that are slightly elongated in certain directions. Obviously, the entire method could be modified by replacing the polar coordinates with a Cartesian coordinate system, where the major axis would be aligned with the front and the minor axis would be in the cross-frontal direction. The observations could be adjusted with a two-dimensional Gaussian surface and the diffusion equation would be solved in Cartesian coordinates, with different along-front and cross-front diffusivities. This type of approximation would be important for studying large-scale meridional heat transport in regions such as the Southern Ocean.

The major conceptual and methodological advantage of the ROD method is precisely its simplicity, in accordance with its initial objective of providing model-suitable horizontal diffusivity. As it is, the ROD method can be easily implemented, either with model reanalysis

data or with forecast models. Actually, the ROD method was initially inspired by our desire to use a climatological daily output from GLORYS12v1 to explore the transfer of ACC waters all the way to the north of the South Atlantic Ocean (**Chapter 3.4**). Setting appropriate effective diffusivities is very important for daily velocity fields, as we have shown in this paper, but it is even more important for daily climatological velocity fields.

From an experimental view, the ROD method is limited by the accuracy of the position fixings. In this regard, the use of a time interval of 10 days brings several advantages. First, water parcels travelling with typical speeds in the range of  $0.05 \text{ m s}^{-1}$  to  $0.5 \text{ m s}^{-1}$  will travel distances between 43 km and 430 km in 10 days. These trajectories will certainly not be straight but represent net displacements of the order of 10 - 100 km, which is long enough to easily adjust a Gaussian curve to the data points. Further, these displacements range from the submesoscale to the mesoscale, so they should allow assessing the effective diffusivity associated with the third phase of diffusion (Garrett, 1983; Sundermeyer & Price, 1998). Finally, these distances are much larger than the accuracy in the drifters' positioning (1 - 100 m for the GDP and about 1 km for RAFOS and Argo floats), granting further confidence to the good performance and robustness of the method.

The one-dimensional radial diffusion equation appears as a sensible, simple yet realistic, option to simulate subgrid motions that are not resolved in numerical circulation models. It has also been used by other authors to explore the stirring properties of either floats or numerical particles, examining the temporal changes in the probability density functions (LaCasce, 2010; Graff et al., 2015; Bawalda et al., 2021). We may further explore the validity of this approximation by comparing the coefficients provided by the method with the expression that relates the diffusivity  $K$  with the variance of the parcel offsets  $\sigma^2$  during some relatively long time scale  $\tau$ , long-enough for the effective eddy diffusivity to develop (LaCasce et al., 2014; Roach et al., 2016).

$$K = \frac{\sigma^2}{2\tau} \quad (3.9)$$

We have used equation 3.9 for the eight depth ranges where we have applied the ROD method (Figure 3.60), with  $\sigma^2$  as obtained from the Gaussian distribution adjusted to the experimental particle concentrations and  $\tau = 10$  days (Figure 3.63). The data points show very good agreement, with a slope of the experimental  $\sigma^2/2\tau$  versus the method's  $K$  of 0.92 and a correlation coefficient of 0.99, hence granting further confidence for the ROD approach.

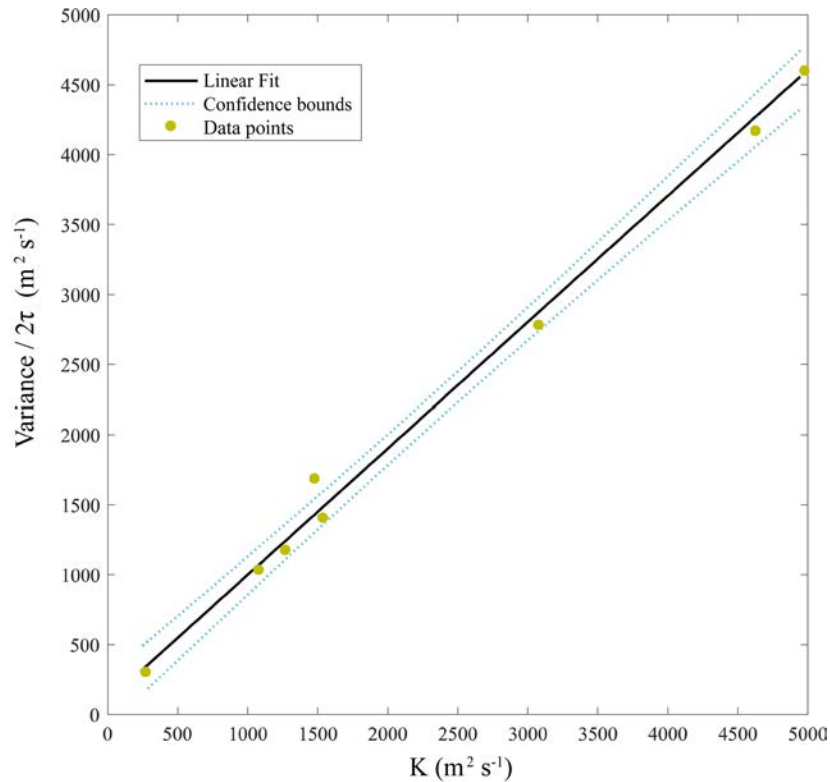


**Figure 3.63.** Scattered plot of the experimental  $\sigma^2/2\tau$  values as a function of the  $K$  values obtained through the ROD method. The linear regression is shown together with the 0.95 confidence bounds.

### 3.3.5.2. Comparison with other observations for the study area

We end up comparing our results for the study area with horizontal diffusivity estimates from other studies. A summary of our estimates for  $K$  as a function of depth and region is shown in Figure 3.64. In general, the horizontal diffusivity decreases with depth from values close to  $5000 \text{ m}^2 \text{ s}^{-1}$  in the near-surface waters to values about  $1100 - 1300 \text{ m}^2 \text{ s}^{-1}$  between  $1500$  and  $2000 \text{ m}$  (Figure 3.64a). The single exception is the mean value at  $750 \text{ m}$  ( $700 - 800 \text{ m}$  depth range), which shows a discrepant low value of  $260 \text{ m}^2 \text{ s}^{-1}$ . We have no answer for this dissimilarity, it could perhaps be related to a real decrease in the subgrid variability at these depths, but it seems more likely that it responds to the fact that a substantial fraction of the data at these depths correspond to Argo floats drifting south of the Southern Boundary, even within the Weddell Sea with the presence of substantial ice coverage (Figure 3.61). Therefore, it seems plausible that this low value responds to different dominant dynamical processes (Yamazaki et al., 2021; Reeve et al., 2019; Vernet et al., 2019).

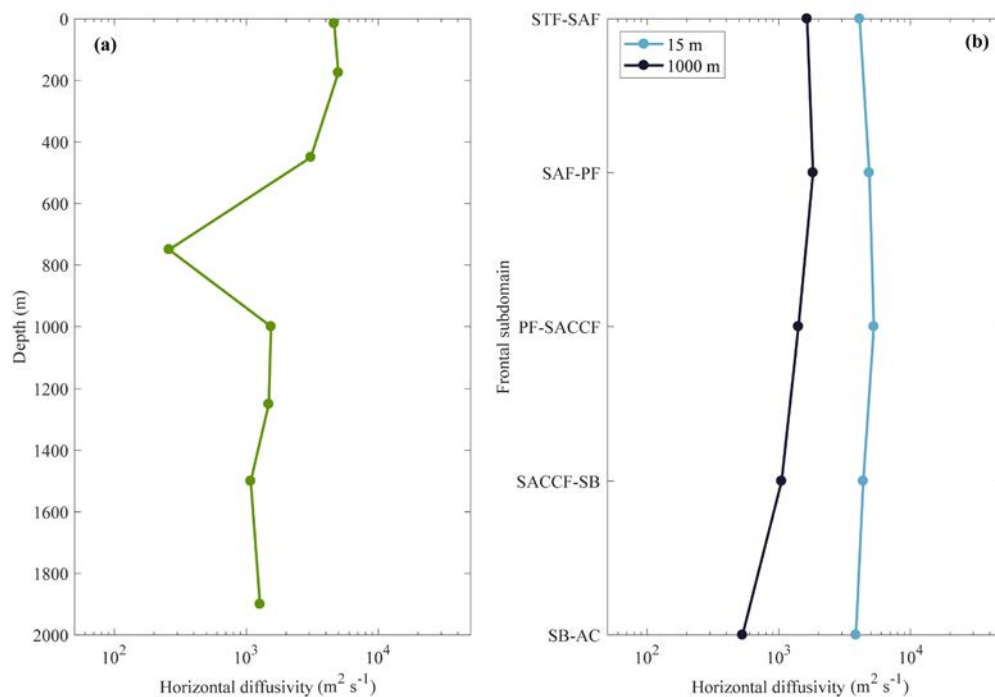


**Figure 3.64.** (a) Vertical distribution (green line) and (b) horizontal variability of the horizontal diffusion coefficients; the latter are shown only at 15 m (light blue line) and in the 900 - 1100 m depth range (dark blue line) for the five frontal regions as shown in Figure 3.50d (Orsi et al., 1995). The acronyms are Subtropical Front (STF), Subantarctic Front (SAF), Polar Front (PF), Southern Antarctic Circumpolar Current Front (SACCF), Southern Boundary (SB) and Antarctic continent (AC). Notice that the eddy-diffusion coefficients are in logarithmic scale.

The 15-m horizontal diffusion coefficients are fairly similar in all regions, probably reflecting that the surface layer is directly influenced by the intense westerly winds in the entire study area (Russell et al., 2016). In contrast, the 900 - 1100 m values do show a spatial pattern, with maximum values linked to the intense Subtropical, Subantarctic and Polar Fronts ( $1640 - 1820 m^2 s^{-1}$ ), intermediate values between the Polar Front and the Southern Boundary ( $1050 - 1410 m^2 s^{-1}$ ) and minimum values south of the Southern Boundary ( $530 m^2 s^{-1}$ ). Notice that the fast jet and high variability associated with the Polar Front takes place north of its surface location (see Figure 4 in Naveira Garabato et al., 2011, and Figures 3.8 and 3.14 in Chapter 3.1) within the SAF - PF region.

There is an extraordinary range of horizontal diffusion values reported in the literature. As explained in subsection 3.3.1, this is because the spreading of properties depends on the spatiotemporal scales that allow the dispersive processes to take place, with the last phase – which acts from the submesoscale to the mesoscale – producing the effective diffusion. Cole et al. (2015) and Roach et al. (2018) have provided global maps of this effective horizontal diffusivity.

Using  $3^\circ \times 3^\circ$  data from both the Argo program and a numerical circulation model, Cole et al. (2015) found values ranging between roughly  $200 \text{ m}^2 \text{ s}^{-1}$  and  $20,000 \text{ m}^2 \text{ s}^{-1}$  at the base of the winter mixed layer, with the largest values in western boundary currents and the equatorial jets. Zonally-averaged values for each ocean basin show peak surface values of about  $10,000 \text{ m}^2 \text{ s}^{-1}$  that decrease down to  $100 - 1000 \text{ m}^2 \text{ s}^{-1}$  near 2000 m depth. Roach et al. (2018) used GDP and Argo float data gridded at  $1^\circ \times 1^\circ$  to calculate the asymptotic eddy diffusivity, which they estimated take place at time scales of order 10 days near the sea surface and 100 days at 1000 m; in these calculations, the effect of the mean-flow in suppressing the eddy-related diffusion was considered (Ferrari & Nikurashin, 2010). They estimated the global mean eddy diffusivity to be  $2637 \pm 311 \text{ m}^2 \text{ s}^{-1}$  at the sea surface and  $543 \pm 155 \text{ m}^2 \text{ s}^{-1}$  at 1000 m, with maximum surface values in the western boundary currents and the equatorial jets, and maximum 1000-m values in the western boundary currents and along the ACC.

Several studies have explored the intensity of horizontal mixing in the yet poorly sampled Southern Ocean, which is of special relevance because of its key role in the global overturning circulation. Sallée et al. (2011) used sea surface height data ( $1/3^\circ$  daily) to estimate characteristic surface diffusivities ranging between  $1500 \text{ m}^2 \text{ s}^{-1}$  near the centre of the ACC and  $3000 \text{ m}^2 \text{ s}^{-1}$  in its northern flank. Naveira Garabato et al. (2011) used 22 hydrographic sections combined with sea surface height data ( $1/3^\circ$  weekly) and found that  $K$  is intensified in the inter-frontal regions, with values of about  $2000 \text{ m}^2 \text{ s}^{-1}$ , and is suppressed in the jet cores, with values of about  $200 \text{ m}^2 \text{ s}^{-1}$ , although with exceptions in some segments. These values are fairly uniform in the upper 1000 m of the water column, decreasing with depth in the underlying layers. Roach et al. (2016) explored the size of eddy diffusivity at 1000 m using several datasets: numerical at  $1/6^\circ$  and 5-day resolution, sea surface height at  $1/3^\circ$  and daily resolution, together with the 10-day Argo and daily RAFOS data. The datasets were analyzed with different methods, leading to several types of cross-flow effective diffusivities (named meridional, cross-contour and cross-stream) that take 10 to 50 days to reach asymptotic values between about  $300 \text{ m}^2 \text{ s}^{-1}$  and  $2500 \text{ m}^2 \text{ s}^{-1}$ . In a posterior study, Roach et al. (2018) calculated the Southern Ocean 1000-m effective diffusivity to be  $658 \pm 125 \text{ m}^2 \text{ s}^{-1}$ . Tulloch et al. (2014), from a tracer spreading experiment upstream of the Drake Passage, estimated a diffusivity of  $1200 \pm 500 \text{ m}^2 \text{ s}^{-1}$  at 1500 m.

In the Scotia Sea, tracking natural helium injected from hydrothermal vents near the Drake Passage into the ACC, Naveira Garabato et al. (2007) estimated a regional  $K$  average of  $1840 \pm 440 \text{ m}^2 \text{ s}^{-1}$  for the entire Upper Circumpolar Deep Waters (UCDW), spanning depths from a few hundred meters down to about 2000 m. Also, for the Scotia Sea, Roach et al. (2018) obtained a 1000-m effective diffusivity value of  $1019 \pm 158 \text{ m}^2 \text{ s}^{-1}$ .

All the above studies show that the horizontal diffusivity decreases with depth, with values of several thousand  $\text{m}^2 \text{s}^{-1}$  near the sea surface and between several hundred and a few thousand  $\text{m}^2 \text{s}^{-1}$  in the intermediate and deep layers. The large range of values is possibly not surprising considering the variety of datasets (with very different spatiotemporal resolution) and methodologies employed. In any case, the horizontal diffusion estimates we have obtained with the ROD method are consistent with the previously reported numbers.

### 3.3.6. Final remarks

The specification of horizontal diffusivity still remains a challenge. Oceanographers often wonder what horizontal diffusion coefficient is most appropriate for a certain study, whether it be a climatological basin-wide balance or a coastal application of a numerical circulation model. Motivated by this dilemma, we have developed the radial offset by diffusion (ROD) method as a simple yet robust approach that combines drifter and numerical trajectories to provide a first-order estimate of horizontal diffusivity  $K$ . Testing the ROD method in the ACC waters of the southwestern South Atlantic Ocean has shown that it is a simple and robust approach that provides realistic coefficients of horizontal diffusivity.

The ROD method is model-dependent, whether it be a numerical model or any directly or indirectly observed velocity field, in the sense that it provides  $K$  values that are only appropriate for that specific model. Using these coefficients with other models of similar spatiotemporal resolution is likely adequate but should be done with caution. Nevertheless, because of its simplicity, it could be employed for other applications. For example, we could easily increase the time interval of the studied trajectories in order to explore the asymptotic character of effective diffusivity, particularly in the deep waters (as extensively discussed by Roach et al., [2018](#)).

The ROD method also allows reducing the size of the domain under study, an important feature in order to investigate regional variations in mixing. For example, Naveira Garabato et al. ([2011](#)) argue that eddy mixing in the Southern Ocean is suppressed in frontal regions, where eddies propagate much slower than the mean flow. This leads to the counterintuitive idea that frontal jets, with increased eddy kinetic energy, may actually have relatively small cross-stream horizontal diffusion.

These authors further propose the existence of leaky sectors in jets, where cross-frontal mixing would not be inhibited. The ROD method appears as a potentially useful tool to explore this type of variability, e.g., focusing on the frontal systems or in regions with rough topography. In particular, we have found that the region between the Polar Front and the Subantarctic Front displays the maximum  $K$  value at 1000 m. These two fronts are by far the

most intense in the Scotia Sea (Naveira Garabato et al., [2011](#); **Chapter 3.1**), so it is plausible that the turbulent eddies generated in both neighbouring frontal systems could propagate into this relatively sluggish inter-frontal region, where eddies would not be suppressed.

The ROD method is a simple and cost-effective tool for assessing ocean lateral diffusivity, a key parameter for many applications, from the dispersion of properties in numerical circulation models to inverse-type regional balances. Thanks to the continuous increase in drifter data and the expanded availability of high-resolution numerical models and reanalysis, the ROD method could be applied basin-wide to quantify how mixing affects large-scale circulation, or used locally to investigate the relevance of different submesoscale and mesoscale processes in the distribution of water properties.





## **CHAPTER 3.4**

---

### **Direct pathways from the Drake Passage to the South Atlantic subtropical gyre**

### 3.4.1. Context and objectives

The returning limb of the Atlantic Meridional Overturning Circulation (AMOC) is largely sustained by Subantarctic and Antarctic waters crossing the Drake Passage, commonly referred to as the cold-water route (Rintoul, [1991](#)). This water enters the Scotia Sea and veers northward following the northern Antarctic Circumpolar Current (ACC) fronts and exiting through the narrow passages of the submarine North Scotia Ridge, the largest topographical obstacle of the ACC flow (Orsi et al., [1995](#); Cunningham et al., [2003](#); Smith et al., [2010](#); Donohue et al., [2016](#); **Chapter 3.1**). The Subantarctic Front (SAF), the northernmost front, follows the western slope of the Argentine Basin as the Malvinas Current (MC) (Vivier & Provost, [1999](#); Arhan et al., [2002](#); Saraceno et al., [2003](#)) before turning eastward at the Brazil-Malvinas Confluence (BMC), at about 40°S (Artana et al., [2016](#); Orúe-Echevarría, [2019](#)). Further south, the Polar Front (PF) follows an eastward path along the southern edge of the Argentine Basin before turning eastward near 50°S.

North of the SAF, we find the Subtropical Front (STF), which bounds the South Atlantic anticyclonic subtropical gyre. The STF and PF delimit the eastward flow of subantarctic mode and Antarctic intermediate waters in what is known as the South Atlantic Current (SAC), the southern limb of the subtropical gyre (Peterson & Stramma, [1991](#); Speich et al., [2001](#)). The SAC crosses the entire South Atlantic to eventually reach the eastern margin, where it is partly deflected northwards as the eastern boundary Benguela Current before turning westward into the northern portion of the subtropical gyre as the westward South Equatorial Current (SEC). However, how much of this cold water actually subducts along the SAF and STF and how much reaches the eastern boundary before being effectively incorporated into the subtropical gyre still remains largely unknown. This entire cold-water route is commonly called the direct cold-water route of the AMOC's returning limb, in contrast with the indirect pathways whereby the Drake Passage waters recirculate first through the Indian and Pacific Oceans.

Several studies have characterized the contribution of the cold-water route to the AMOC's upper limb. Early estimates using Lagrangian analyses concluded that only between 1 and 2 Sv of the cold waters going through the Drake Passage are directly incorporated into the subtropical gyre (Speich et al., [2001](#); Donners & Drijfhout, [2004](#); Friocourt et al., [2005](#)). Rühls et al. ([2019](#)) have estimated that depending on the strength of the Agulhas Leakage, the cold direct route contributes between 4.1 and 5.3 Sv to the North Brazil Current (6°S), occasionally exceeding the Agulhas contribution, which shows substantial seasonal and interannual variability. Indeed, several studies indicate that 4 to 6 Sv of Drake Passage inflow crosses the South Atlantic along the ACC and recirculates in the Indian Ocean before reaching the Agulhas Current and leaking into the South Atlantic subtropical gyre as part of Agulhas

Leakage (Friocourt et al., [2005](#); Speich et al., [2001](#), [2007](#)). However, most of the ocean model simulations used in various studies had a relatively coarse resolution, thus being non-eddy-resolving or eddy-permitting (Speich et al., [2001](#); Donners & Drijfhout, [2004](#)). Hence, the amount and characteristics of the cold-fresh waters contributing to the upper limb of the AMOC upper limb remain controversial (Garzoli & Matano, [2011](#); Bower et al., [2019](#)).

In this study, we use a Lagrangian numerical approach to explore the pathways, transport fractions, transit times and seasonality of the ACC waters that are incorporated into the South Atlantic Ocean. Specifically, we investigate the different partitioning of the Southern cold waters that cross the Drake Passage: how much enters directly to the South Atlantic subtropical gyre, how much recirculates in the subtropical gyre and how much actually escapes northward through the North Brazil Current (NBC) as part of the returning limb of the AMOC. With this objective, we assess the direct cold-fresh water route between the Drake Passage and two sections in the South Atlantic: one crossing the eastern edge of the subtropical gyre at 32°S and the other crossing the NBC at 21°S. The three-dimensional climatological velocity fields used are from a 1/12° horizontal resolution eddy-resolving ocean model product.

The structure of this chapter is as follows. Subsection [3.4.2](#) presents the study area, the reanalysis model products used, and the Lagrangian experiments carried out. Subsection [3.4.3](#) shows how the forward-tracked particles diverge, most remaining in the ACC and some turning north to be incorporated into the subtropical gyre. In subsection [3.4.4](#), we explore the seasonal variability of mass, heat and salinity transports at their final destinations. We conclude in subsection [3.4.5](#) with some remarks about what we know and what yet remains unknown regarding the incorporation of Antarctic waters into the South Atlantic Ocean as the returning limb of AMOC.

## **3.4.2. Materials and methods**

### **3.4.2.1. GLORYS12v1 reanalysis**

We carry out our study using the reanalysis model GLORYS12v1, an eddy-resolving model with a 1/12-degree resolution, provided by the Mercator Ocean team. The model output includes 18 years of daily salinity, potential temperature, and three-dimensional velocity fields, corresponding to the 2002 - 2019 period. The vertical discretization has 50 levels, with maximum grid resolution at the ocean surface and spacing increasing gradually to reach 5052 m depth. Our region of study includes the entire South Atlantic Ocean basin, between 20°S and 70°S in latitude and from 70°W to 30°E in longitude. This yields an effective latitudinal

resolution of 9.25 km and a longitudinal resolution ranging between 1.6 and 8.9 km, resolving all regional features and persistent mesoscale structures.

We divide the upper water column into different neutral density levels to discern the pathways and transports corresponding to the different ACC water masses. In the Drake Passage, the Subantarctic Surface Water (SASW) and Subantarctic Mode Water (SAMW) are found in the neutral density range  $26.80 < \gamma^n < 27.18 \text{ kg m}^{-3}$  (Naveira Garabato et al., 2002; Smith et al., 2010). The Antarctic Surface and Intermediate Waters (AASW/AAIW) are considered together and defined as water with neutral density between  $27.18 < \gamma^n < 27.55 \text{ kg m}^{-3}$ , and the Upper Circumpolar Deep Water (UCDW) lies between  $27.55 < \gamma^n < 28.00 \text{ kg m}^{-3}$  (see Table 3.1 in subsection 3.1.2.3).

### 3.4.2.2. Lagrangian experiments

The Lagrangian trajectories and transports are computed using the climatological annual-mean and the climatological daily-averaged velocity and thermohaline fields, as obtained from the 18 years of daily data. For the climatological annual-mean case, we release and track particles with a daily resolution and for the climatological daily-averaged case, we release and follow the particles every four days; this second case allows exploring the seasonal variability (subsection 3.5.4.2). No analysis of interannual variability has been done.

We track numerical particles with the OceanPacels v2.0 code, a computationally efficient offline Lagrangian simulator (Delandmeter & Van Sebille, 2019). The inputs for this code are the release section, the time-varying velocity component fields ( $u, v, w$ ) and the eddy diffusivities ( $K_H$ ) to simulate subscale dynamics not resolved by the model. The horizontal diffusion, which is set horizontally uniform but depth variable (Chapter 3.3), is included through a stochastic impulse ( $I$ ) every time that particles are advected. As in Peña-Izquierdo et al. (2015) and Döös et al. (2011), this impulse produces a random horizontal displacement of the numerical particle in both longitude and latitude according to  $I = R\sqrt{2K_H \Delta t}$ , where  $K_H$  is the horizontal eddy diffusivity coefficient,  $\Delta t$  is the time step, and  $R$  is a random number between -1 and 1 from a Gaussian distribution (as explained in subsection 2.3.2). To add a realistic depth variation of the horizontal diffusion coefficient, we use the results of the ROD method (Chapter 3.3), which establish an inverse dependence of  $K_H$  with depth  $z$ :

$$K_H = -2.16z + 4.52 \times 10^3 \quad (3.10)$$

The horizontal diffusivities are interpolated linearly along the entire water column and the domain. The number of particles released in each element of area of a vertical section,  $N$ , is set to be proportional to the water transport through that element of area,  $v A$ , where  $A$  is the cell

area and  $v$  is the velocity. The same water transport is assigned to each individual particle in one same vertical cell. Notice that particles coming from different cells may not have equivalent transports; thus, the percentages in relation to the transport volume may not match.

We release the particles at  $63.75^\circ\text{W}$ , in a meridional section along the Drake Passage, between the southern tip of South America and the Bransfield Peninsula. In order to obtain accurate estimations of the water masses transport, we release the particles up to the isoneutral of  $\gamma^n = 28.00 \text{ kg m}^{-3}$  with a vertical resolution of 20 m and a latitudinal resolution of 9.26 km (97 cells between  $55^\circ\text{S}$  and  $63^\circ\text{S}$ ). We then track the particles' trajectories forward over 75 years to define the most frequented pathways and to assess the water mass contributions and their percentage to each pathway.

Besides the Drake Passage release section, there are three other key sections for our calculations: a latitudinal section that crosses the ACC and two longitudinal that sample the boundary currents (Figure 3.65). The latitudinal section stretches south from the southern tip of Africa along  $25^\circ\text{E}$  and tracks those particles that leave the study domain carried out by the ACC. The second section samples the eastern boundary current at  $32^\circ\text{S}$ , from the African coast out to  $10^\circ\text{W}$ , tracking those particles incorporated into the subtropical gyre. The third section samples the South Atlantic western boundary current at  $21^\circ\text{S}$ , from the coast of South America out to  $0^\circ\text{W}$ , where the SEC bifurcates due to the quasi-zonal submarine Vitória-Trindade Ridge (VTR), following those particles that exit the subtropical gyre as part of the North Brazil UnderCurrent (NBUC) and the NBC (Stramma & England, 1999; Rodrigues et al., 2007). In each section, we compute the water, heat and salt transports and explore how the water particles change their depth, heat, salt and density.

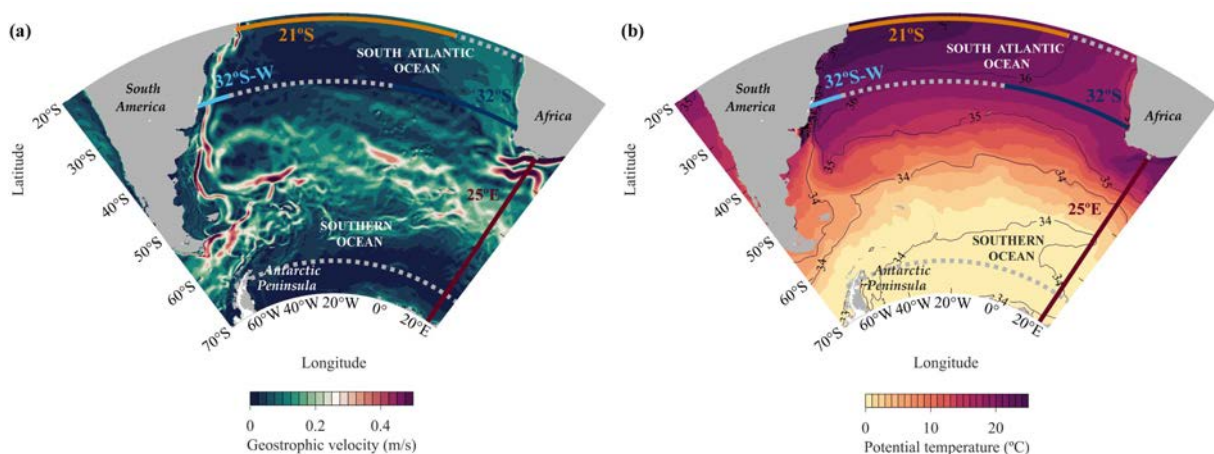


**Figure 3.65.** (a) Geostrophic velocities and (b) potential temperature (coloured) and salinity (contours) distributions in the surface of the South Atlantic Ocean with the positions of the four key sections: the  $25^\circ\text{E}$ ,  $32^\circ\text{S}$ ,  $21^\circ\text{S}$  and  $32^\circ\text{S-W}$  sections.

Moreover, we use an extra section along 32°S in the western margin (hereafter named 32°S-W) from the Brazil coastline to 45°W, hence tracking those particles that flow poleward with the western boundary Brazil Current (BC). This is a suitable zone for counting the particles that recirculate in the subtropical gyre, as its shape is reduced asymmetrically with depth (subsection [3.4.4.2](#)).

#### 3.4.2.3. Lagrangian streamfunctions

The Lagrangian streamfunctions reflect the pathways followed by the numerical particles that depart from some reference section (Blanke et al., [1999](#)). The calculation is straightforward if we assume conservation of volume transport, which holds true if all released particles leave the domain. The Lagrangian streamfunction is computed by adding to each grid cell the transports that are associated with each numerical particle, with the sign depending on the direction of the crossing particles. We take positive/negative transports for particles crossing eastward/westward and northward/southward. If more than one cell is crossed in a single time step, transport is added to each crossed intersection. Transports are typically integrated over all grid cells that lay between the isoneutral surfaces that characterize the different water masses. For those particles' trajectories that recirculate in the South Atlantic subtropical gyre, only the first recirculation is considered, disregarding particles that reach 32°S-W for the second time.

#### 3.4.2.4. Loss/gain of heat and salt transport

Because the South Atlantic Ocean plays a critical and distinctive role in the meridional heat and salt transports, we compute the total heat transport  $H$  (in watts) and salt transport  $S$  ( $\text{kg s}^{-1}$ ) through the reference sections as follows:

$$H = c_p \sum_{i=1}^N \rho_i V_i \Delta T \quad S = \sum_{i=1}^N \rho_i V_i \Delta S \quad (3.11)$$

in the left equation,  $\Delta T$  is the difference between the initial and final particle potential temperature, and  $c_p$  is the seawater heat capacity (in  $\text{J kg}^{-1} \text{C}^{-1}$ ),  $V_i$  is the particle volume transport (Sv) and  $\rho_i$  the water density at each specific location; in the right equation,  $\Delta S$  corresponds to the practical salinity difference (in units of gram salt per kilogram of water).

### 3.4.3. Results

#### 3.4.3.1. Transport contribution to the South Atlantic Ocean

For the climatological annual-mean Lagrangian simulation, we release in the Drake Passage section about 16537 particles from the sea surface down to  $28.00 \text{ kg m}^{-3}$ , which represents a net transport of 117.4 Sv (122.6 Sv of the total transport). These particles are then tracked daily for 75 years. At the end of this period, 91.4% of the particles have left the domain, and the remaining 8.6% (accounting for a net transport of 9.8 Sv, 10.5 Sv of the total transport) continue transiting within the South Atlantic Ocean.

The number of particles launched in the Drake Passage is proportional to the volume transport, and hence it is mainly associated with the ACC fronts, where the zonal velocity and transport are maximum (Figure 3.66). The total net transport entering through the Drake Passage is split into 15.0 Sv corresponding to the surface-mode waters (SASW and SAMW), 47.9 Sv to the surface-intermediate waters (AASW and AAIW) and 54.5 Sv to the deep waters (UCDW). Out of this total transport, 15.1 Sv reach the  $32^\circ\text{S}$  section to be incorporated into the eastern margin of the subtropical gyre and a total of 12.6 Sv end feeding the NBC at  $21^\circ\text{S}$ .

Figure 3.66 shows the potential temperature, salinity, neutral density and zonal velocity distributions in the Drake Passage down to 2500 m. In this figure, we also include the departing positions of the numerical particles up to  $\gamma^n < 28.00 \text{ kg m}^{-3}$ , coloured according to the key section they reach. The Lagrangian particles that enter the South Atlantic subtropical gyre cross the  $32^\circ\text{S}$  (blue) and reach the  $21^\circ\text{S}$  (orange), are found at all depths down to 2300 m, largely concentrated in the jets associated with the core of the three northernmost ACC fronts. In particular, most of them are found in the SAF and PF, and most of the water masses reaching  $21^\circ\text{S}$  are primarily surface-mode and surface-intermediate waters (SASW/SAMW and AASW/AAIW) lighter than  $27.6 \text{ kg m}^{-3}$ . These water masses travel northward near the sea surface to the eastern boundary off South Africa (in the Cape Basin), where they are incorporated into the subtropical gyre.

The maximum particle densities reaching  $32^\circ\text{S}$  and  $21^\circ\text{S}$  match the highest Eulerian meridional velocities (Figure 3.67a, b), concentrated at the surface and core of the ACC jets in the Drake Passage. Particles that reach the southern edge of the subtropical gyre and follow the SAC eastward join the  $32^\circ\text{S}$  section mainly between  $7^\circ\text{E}$  and  $12^\circ\text{E}$ , with the upper 65 m concentrating most of the transport, about 1.9 Sv (Figure 3.67c).



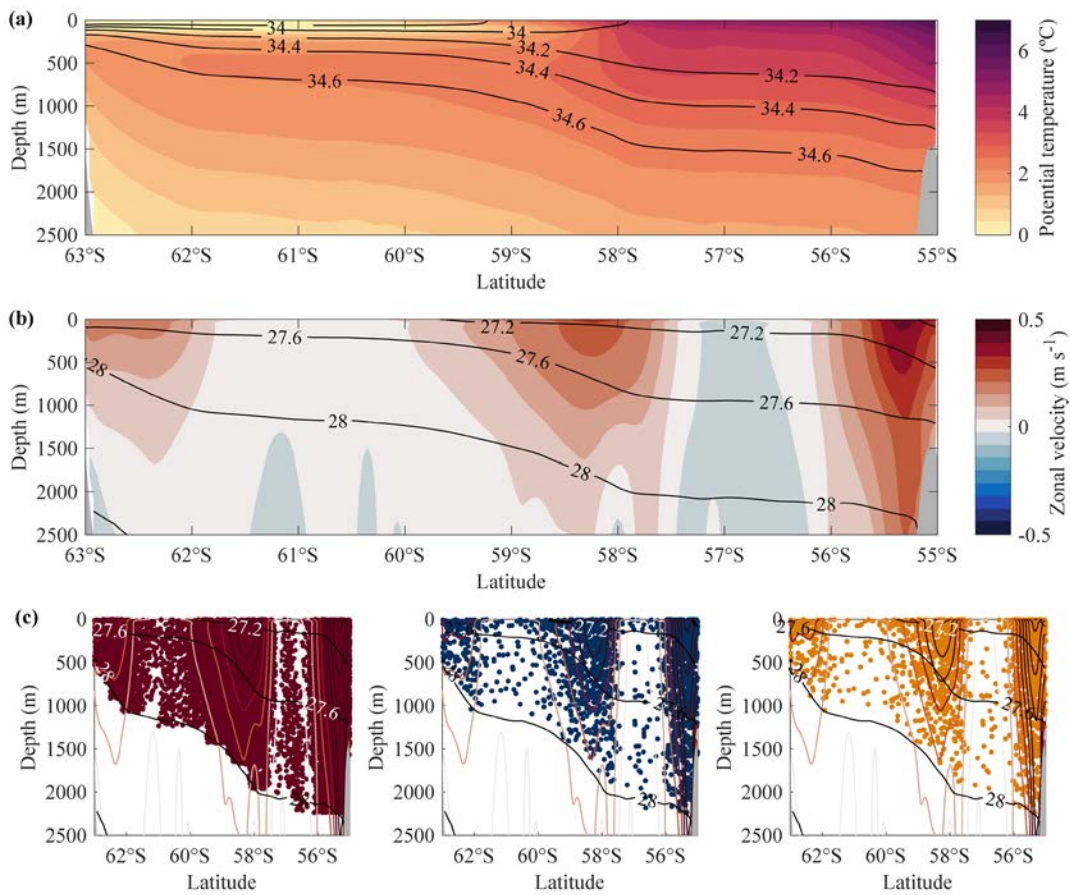


**Figure 3.66.** Distribution of (a) potential temperature (°C, coloured) and salinity (g kg<sup>-1</sup>, contours), (b) zonal velocity (m s<sup>-1</sup>, coloured) and neutral density (kg m<sup>-3</sup>, contours), and (c) particle release positions together with the zonal velocity and neutral density contours. The density of particles in (c) reflects the zonal speeds in the Drake Passage; the left panel shows those particles (coloured in red) remaining in the ACC (25°E), the central panel those that reach the 32°S section (coloured in blue), and the right panel those that reach the 21°S section (coloured in orange). The bathymetry is represented in grey.

About 68.5% of the northward transport at 32°S continues to 21°S, equivalent to 10.3 Sv. The particles that flow north to feed the NBC are vertically distributed in high meridional velocities and follow two dominant well-distinguished pathways (Figure 3.67d), probably bifurcated due to the proximity of the VTR seamount chain. The first pathway is concentrated close to the eastern Brazilian coast (around 40°W) at intermediate depths from 200 m to 1400 m. The second one, spread between 34°W and 0°W and between 50 m and 500 m, corresponds to a shallower branch of the SEC, with peak accumulated transport of 1.3 Sv near 130 m (right panel Figure 3.67d). Despite their separation, both branches probably exchange water parcels and experience similar thermohaline changes along their transit through the northern edge of the South Atlantic subtropical gyre.

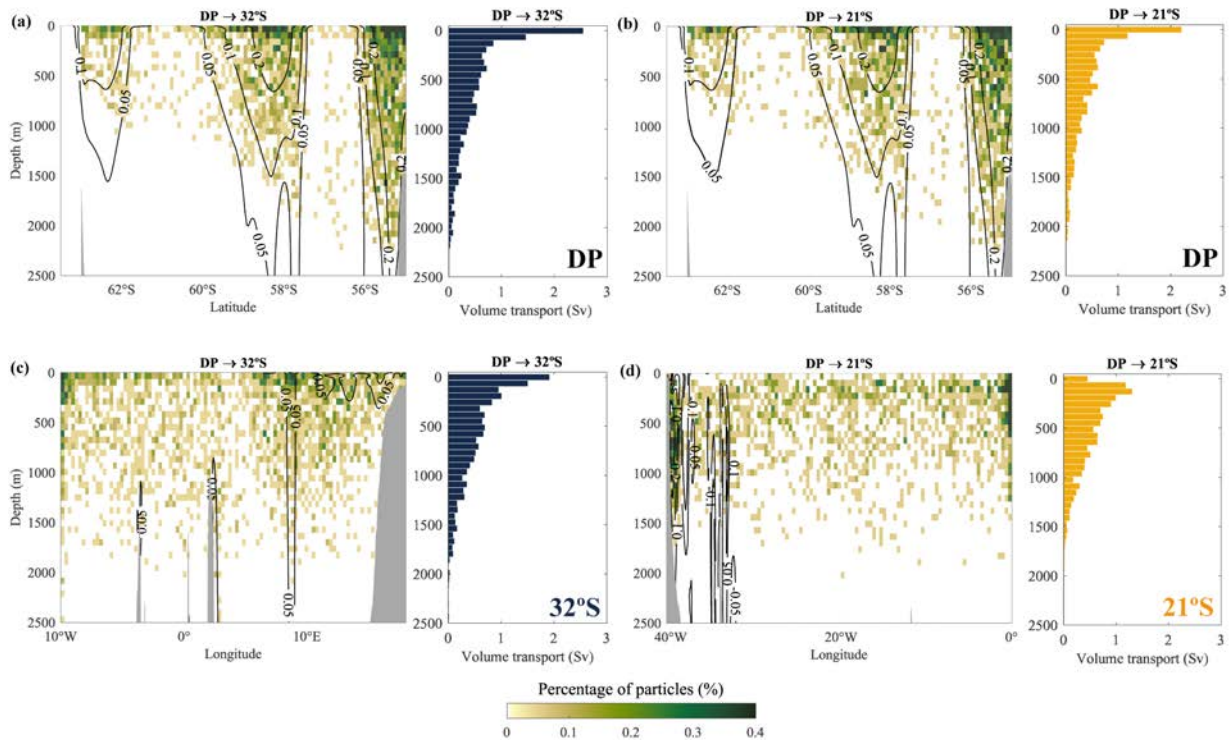


**Figure 3.67.** Distribution of particle percentages crossing the Drake Passage that reach (a) 32°S and (b) 21°S, and distribution of these same particles as they reach (c) 32°S and (d) 21°S. The black contours correspond to the zonal/meridional component of velocity ( $\text{m s}^{-1}$ ). The histograms show the total transports every 65 m.

Due to the added horizontal diffusivities, the trajectories have been remarkably diverse. Most particles (91.3%) cross 25°E, while 13.6% follow to 32°S and 11.3% reach 21°S, with particles crossing more than one section (Table 3.20a). These percentages correspond to 102.3 Sv, 14.9 Sv and 12.5 Sv for 25°E, the 32°S and 21°S, respectively (Table 3.20b). Considering the surface-mode waters (SASW, SAMW), only 66.0%, equal to 9.9 Sv, remain within the ACC and reach the 25°E section directly without entering the South Atlantic gyre. Of the remaining 34%, about 6.3% do not reach any section, and a total of 24.7% (3.8 Sv) is incorporated into the subtropical gyre through 32°S. Among the latter, 73.3% (2.8 Sv) veer northward and leave the domain through 21°S, representing most of the total SASW/SAMW transport (3.2 Sv) that crosses this section (Table 3.20b). The median times for the surface-mode water particles to reach 25°E, 32°S and 21°S are 3.4, 4.1 and 7.6 years, respectively (Figure 3.68a).

Regarding the surface-intermediate waters (AASW, AAIW), and ignoring particles that do not reach any section, 84.0% of these particles (39.0 Sv, Table 3.20) exclusively follow the ACC and cross the 25°E, while 14.0% (6.5 Sv) is incorporated into the subtropical gyre through 32°S. The median times for the AASW/AIW water particles to get to 25°E, 32°S and 21°S sections are 3.6, 5.8 and 10.2 years, respectively (Figure 3.68b). With respect to the UCDW and

ignoring particles that do not reach any section, 88.9% of these particles (45.7 Sv, Table 3.20) follow the ACC, and only 9.4% (4.8 Sv) cross 32°S and 5.7% (2.9 Sv) reach 21°S. The median times for the UCDW to reach 25°E, 32°S and 21°S are 4.9, 8.2 and 13.4 years, respectively (Figure 3.68c).

**Table 3.20.** Percentage of particles released at the Drake Passage and associated total transports that arrive at each key section (see Figure 3.65), distributed per water masses as defined in subsection 3.4.2.1. The percentages and transports do not consider the particles (8.6%) that remain in the domain without reaching any section.

| WATER MASS<br>Neutral density<br>(kg m <sup>-3</sup> ) | PERCENTAGES OF PARTICLES (%) |      |      |                |                |                |                       | TOTAL |
|--|------------------------------|------|------|----------------|----------------|----------------|-----------------------|-------|
|  | EXCLUSIVELY                  |      |      | BOTH           |                |                | ALL                   |       |
|  | 25°E                         | 32°S | 21°S | 32°S +<br>25°E | 32°S +<br>21°S | 25°E +<br>21°S | 25°E + 21°S<br>+ 32°S |       |
| <b>SASW/SAMW</b><br>26.80 < $\gamma^n$ < 27.18         | 8.9%                         | 0.0% | 0.3% | 0.9%           | 1.8%           | 0.2%           | 0.7%                  | 12.8% |
| <b>AASW/AAIW</b><br>27.18 < $\gamma^n$ < 27.55         | 34.7%                        | 0.2% | 0.7% | 1.5%           | 2.9%           | 0.1%           | 1.3%                  | 41.4% |
| <b>UCDW</b><br>27.55 < $\gamma^n$ < 28.00              | 40.8%                        | 0.4% | 0.5% | 1.3%           | 1.9%           | 0.2%           | 0.7%                  | 45.8% |
| <b>TOTAL</b><br>$\gamma^n$ < 28.00                     | 84.4%                        | 0.6% | 1.5% | 3.7%           | 6.6%           | 0.5%           | 2.7%                  | 100%  |

| WATER MASS<br>Neutral density<br>(kg m <sup>-3</sup> ) | TOTAL VOLUME TRANSPORT (Sv) |      |      |                |                |                |                       | TOTAL |
|--|-----------------------------|------|------|----------------|----------------|----------------|-----------------------|-------|
|  | EXCLUSIVELY                 |      |      | BOTH           |                |                | ALL                   |       |
|  | 25°E                        | 32°S | 21°S | 32°S +<br>25°E | 32°S +<br>21°S | 25°E +<br>21°S | 25°E + 21°S +<br>32°S |       |
| <b>SASW/SAMW</b><br>26.80 < $\gamma^n$ < 27.18         | 9.9                         | 0.0  | 0.2  | 1.0            | 2.0            | 0.2            | 0.8                   | 14.0  |
| <b>AASW/AAIW</b><br>27.18 < $\gamma^n$ < 27.55         | 39.0                        | 0.2  | 0.7  | 1.7            | 3.2            | 0.1            | 1.4                   | 46.3  |
| <b>UCDW</b><br>27.55 < $\gamma^n$ < 28.00              | 45.7                        | 0.5  | 0.8  | 1.4            | 2.1            | 0.3            | 0.8                   | 51.6  |
| <b>TOTAL</b><br>$\gamma^n$ < 28.00                     | 94.7                        | 0.7  | 1.7  | 4.1            | 7.3            | 0.6            | 3.0                   | 112.1 |

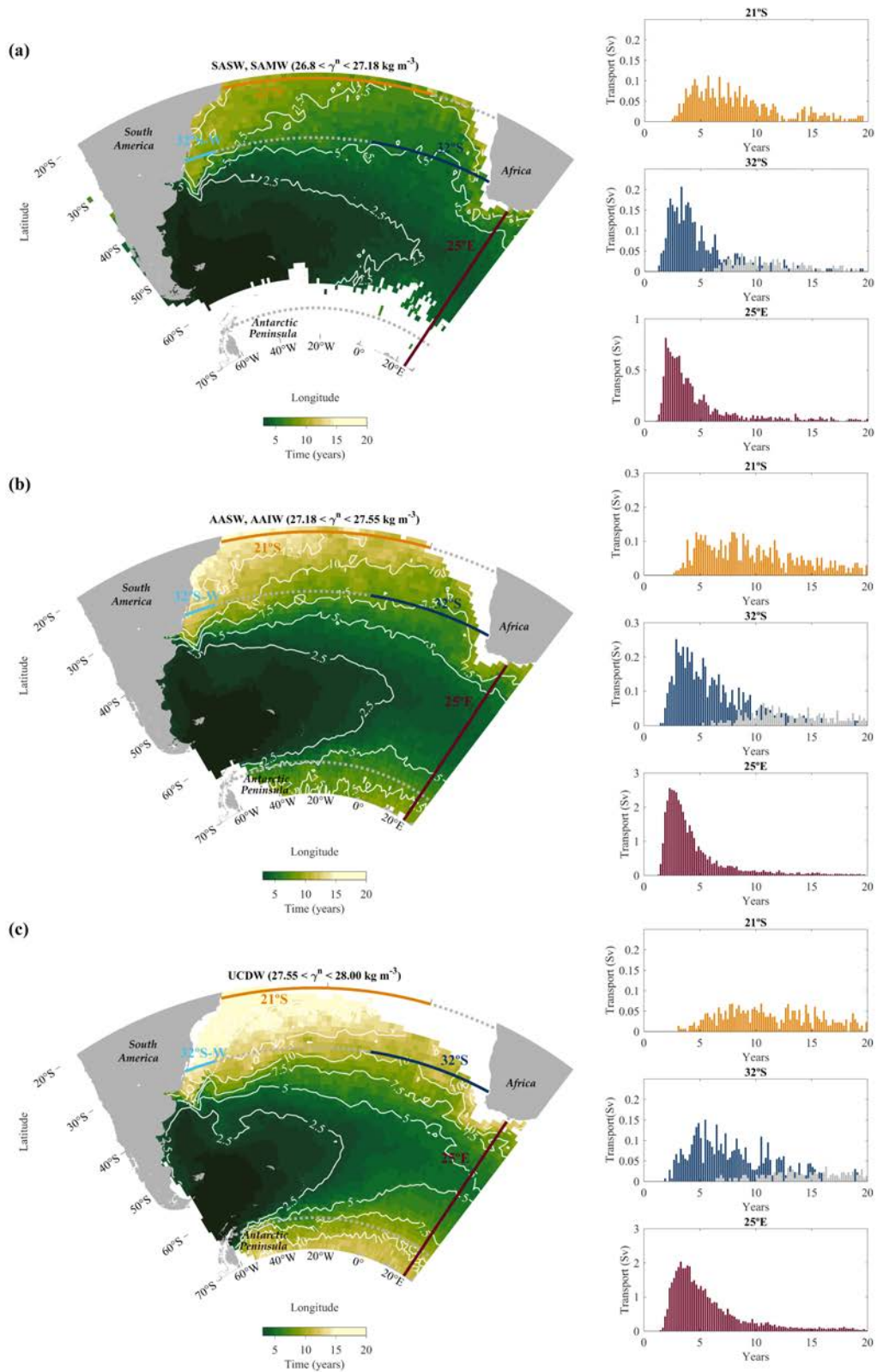


**Figure 3.68** (Left) Numerical trajectories tracked forward from the Drake Passage across the South Atlantic for (a) surface-mode waters, (b) surface-intermediate waters and (c) deep waters, coloured according to their median transit times. (Right) Transit-time histograms for the three routes: 25°E (red), 32°S (blue) and 21°S (orange). The grey bars in 32°S count particles that have crossed the 32°S-W section and recirculate the subtropical gyre completely to reach the 32°S section again. Only those routes with

a probability higher than 1.5% are considered, coinciding with the coloured distributions in Figure 3.69. Median times are higher because they consider the entire particle trajectory, including the subtropical gyre recirculations.

Long tails of the transit time distributions reflect the large number of particles that are trapped in mesoscale eddies or recirculate in gyres for years, such as in the Zapiola gyre, before crossing the section. Early Lagrangian model simulations (Boebel et al., 2003; Rimaud et al., 2012) have shown that the Cape Basin plays an important role in retaining particles. In the 32°S histogram, the median time for the particles to cross the section more than once after recirculating the entire subtropical gyre is about 10.9 years for surface-mode waters and 15.0 years for surface-intermediate waters (middle panels in Figure 3.68a, b).

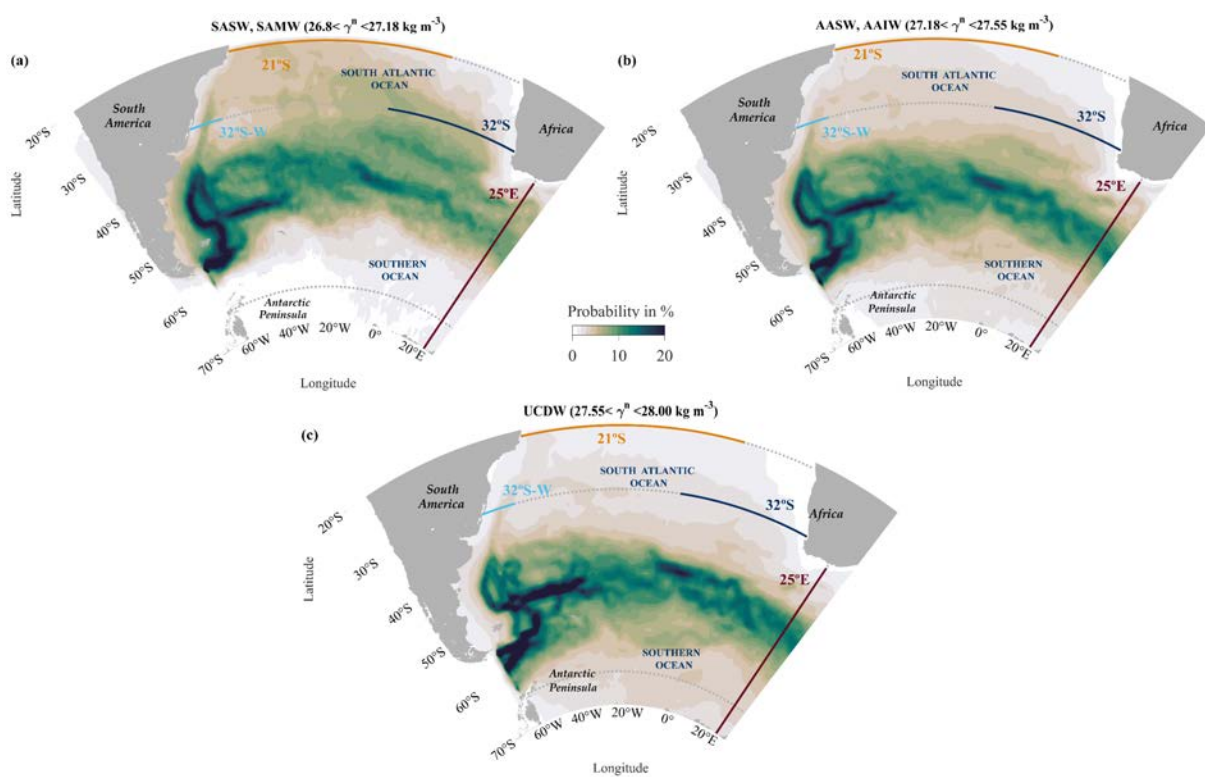


**Figure 3.69.** Climatological probability distributions of (a) surface and mode (SASW, SAMW), (b) surface and intermediate (AASW, AAIW) and (c) deep waters (UCDW). The grid used is 1° in longitude and latitude, each Lagrangian particle being only counted once per grid cell.

To visualize the main water mass pathways and contributions, we illustrate the probability that particles follow a particular route based on the normalized particle density distribution per bin, counting the presence of particles per bin only once (Figure 3.69). Surface-mode waters crossing the Drake Passage have an 80.5% probability of following the Subantarctic Front and be incorporated into the MC, and a nearly 20% of probability of crossing the basin via the SAC to finally be incorporated into the eastern boundary Benguela

Current. Figure [3.69a](#) reveals that particles leave the MC retroflexion and cross the SAC meridionally, between 15°W and 35°W, with large dispersion rather than a well-defined path to enter the subtropical gyre. Finally, surface particles recirculate inside the subtropical gyre to feed the BC with a frequency of around 7.5%, to then follow the SAC again.

Regarding the surface-intermediate waters (AASW, AAIW), the most probable spreading pathways are along the Subantarctic and Polar Fronts, following the ACC until crossing 25°E or eventually reaching 32°S and 21°S with probabilities of 3.5% and 2.5%, respectively. Finally, the UCDW transport is distributed between the three frontal jets more equally than the rest of the water masses, although mainly carried by the PF and practically converging into a single eastward ACC pathway between latitudes 46°S and 52°S with about 12% of probability (Figure [3.69c](#)).

The vertically integrated Lagrangian streamfunctions – from the sea surface down to the seafloor – illustrate the actual distribution of the ACC waters and their contribution to the subtropical gyre (Figure [3.70](#)). Most particles remain inside the ACC, especially between 50°S and 55°S, with more than 100 Sv reaching the Indian Ocean (Figure [3.70a](#)). The particles entering the western South Atlantic follow the MC in a narrow path (about 38 Sv) and are largely incorporated into the subtropical gyre (accumulating a maximum of 13.0 Sv); a maximum recirculation of 12.1 Sv takes place inside the Zapiola gyre.

Considering those trajectories that reach 32°S and/or 21°S, excluding those that only cross the 25°E, the Lagrangian streamfunction reveals that in the eastern subtropical gyre, which is characterized by a large presence of eddies, the accumulated transport exceeds 12 Sv (Figure [3.70b](#)). The western side of the gyre at 32°S-W, largely fed by BC, transports about 5 Sv. As previously indicated, some particles flow into the eastern part of the Agulhas basin and return via the Benguela Current system. The Lagrangian streamfunction (Figure [3.70b](#)) shows the existence of substantial recirculation in the South Atlantic subtropical gyre that crosses both sections at least once, although some may end up being incorporated into the ACC and entering the Indian Ocean.

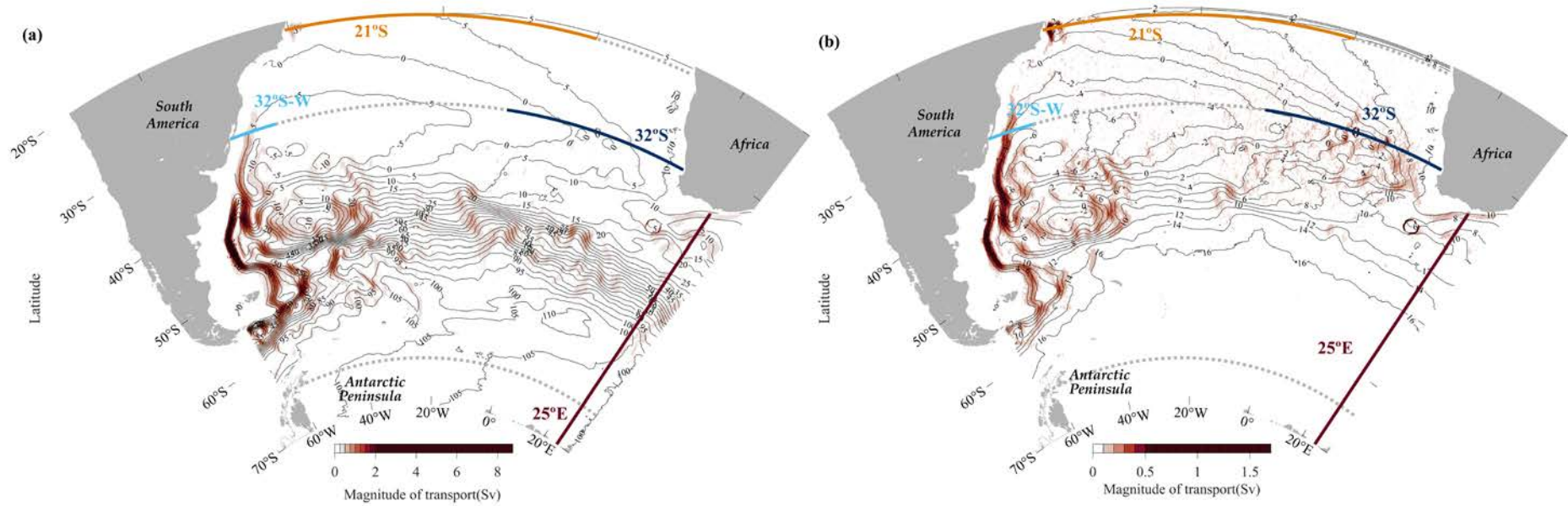


**Figure 3.70.** Climatological vertically-integrated mean Lagrangian streamfunction (contours) and the magnitude of the transport per cell in absolute values (colours) for numerical particles crossing the Drake Passage down to  $28.00 \text{ kg m}^{-3}$ . (a) Transports for all pathways and (b) transports considering only those trajectories incorporated to the subtropical gyre (crossing  $32^\circ\text{S}$  and/or  $21^\circ\text{S}$  sections). The contour intervals correspond to 5 Sv in the left panel and to 2 Sv in the right one. Only those particles that reach at least one section are considered; only the first subtropical gyre recirculation is considered, disregarding particles that reach  $32^\circ\text{S-W}$  for the second time.

### 3.4.3.2. Heat and freshwater transfer

Most cold-water route particles that join the subtropical gyre gradually increase their temperature and salinity along with a depth gain. The particle properties' gain or loss will depend on the path followed, modifying their initial thermohaline transports (Table 3.21). In the path towards 32°S, the surface-mode waters (SASW, SAMW) subduct a median of 24 m, gaining a median of 12.0 °C and 1.5 g kg<sup>-1</sup> of salinity (Figure 3.71a, d, g). When these particles reach 21°S, they sink a median of another 66 m, either because they lose buoyancy or because density surfaces are getting deeper or both, and gain a median of 0.3 g kg<sup>-1</sup> of salinity and 1.0 °C of temperature.

**Table 3.21.** Net mass, salt and heat initial transport per water mass and its sum at Drake Passage. Note that 10<sup>6</sup> kg s<sup>-1</sup> is approximately equivalent to 1 Sv.

| WATER MASS<br>Neutral density (kg m <sup>-3</sup> ) | Drake Passage   |   |                        |
|---|---|---|------------------------|
|   | Mass transport<br>(10 <sup>9</sup> kg s <sup>-1</sup> ) | Salt transport<br>(10 <sup>6</sup> kg s <sup>-1</sup> ) | Heat transport<br>(PW) |
| <b>SASW/SAMW</b><br>26.80 < $\gamma^n$ < 27.18      | 15.4  | 526   | 0.287                  |
| <b>AASW/AAIW</b><br>27.18 < $\gamma^n$ < 27.55      | 49.3  | 1685  | 0.571                  |
| <b>UCDW</b><br>27.55 < $\gamma^n$ < 28.00           | 56.3  | 1945  | 0.490                  |
| <b>TOTAL</b><br>$\gamma^n$ < 28.00                  | 121.0   | 4156  | 1.348                  |

Most of the AASW and AAIW waters that reach 32°S remain practically at the same depth, gaining less temperature and salt, a median of 0.8 g kg<sup>-1</sup> and 7.6 °C, probably due to the absence of ocean-atmosphere exchange. However, from 32°S to 21°S, particles generally maintain the same salinity and get slightly cooled. Regarding UCDW waters, they rise around 94 m and gain 2.4 °C of temperature in their path to 32°S. Hence, along its path to the subtropical gyre, the particles' properties change considerably, increasing their temperature and salinity, especially the surface-mode waters, leaving the Southern Ocean's characteristic properties behind. However, in the second part of their trajectory, particles crossing the gyre and reaching reach the east Brazilian coast, from 32°S to 21°S, experience minor sinking and cooling, with practically no salinity changes.



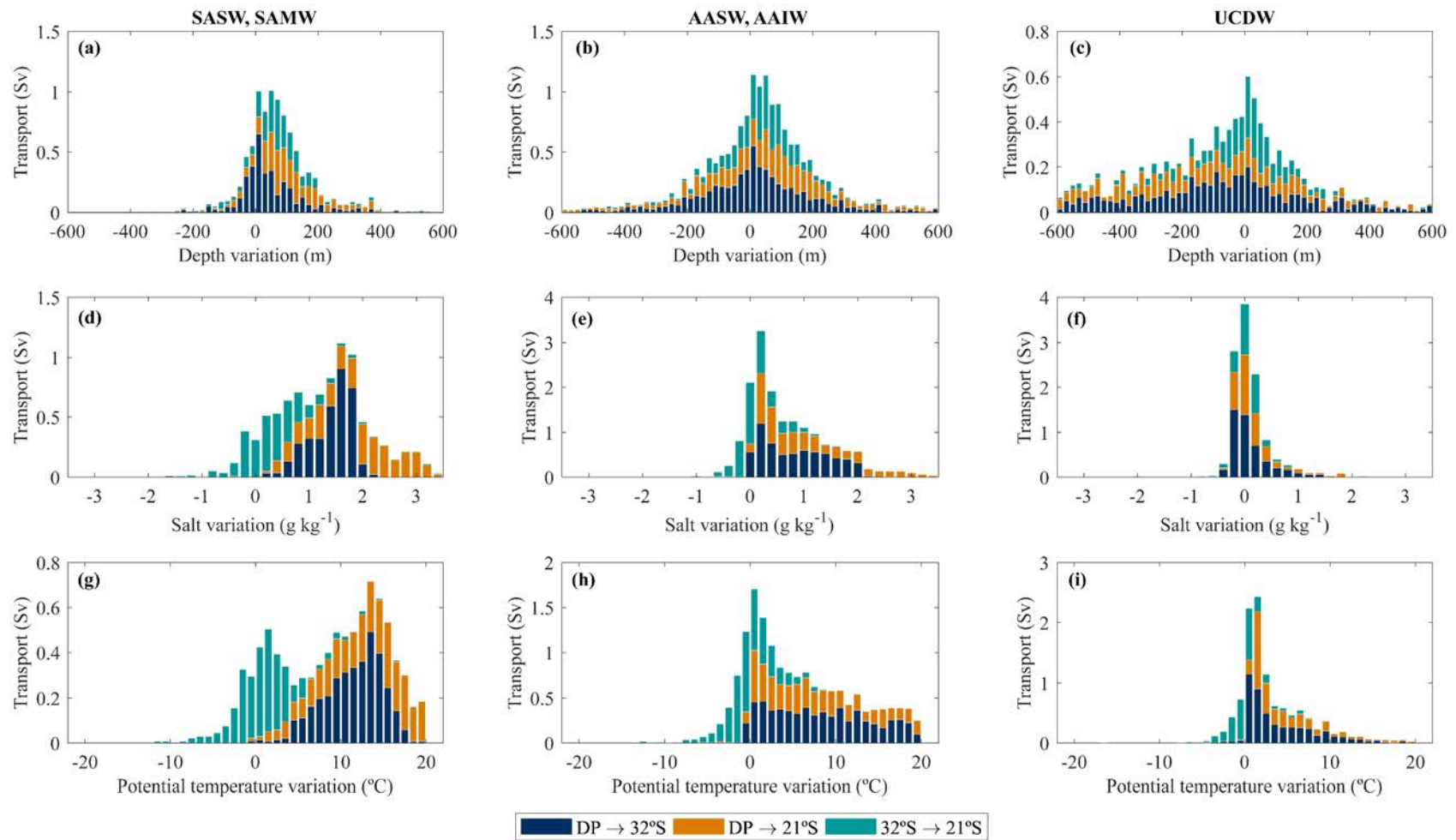


**Figure 3.71.** Histograms of water transport for particles that reach the 32°S section (blue) and 21°S section (orange) from the Drake Passage, plotted as a function of the change in (a, b, c) depth, (d, e, f) salt and (g, h, i) potential temperature along the trajectory, for surface-mode (a, d, g), surface-intermediate (b, e, h) and deep water masses (c, f, i). The property variations of particles between 32°S and 21°S are represented in turquoise. Positive/negative correspond to gain/loss.

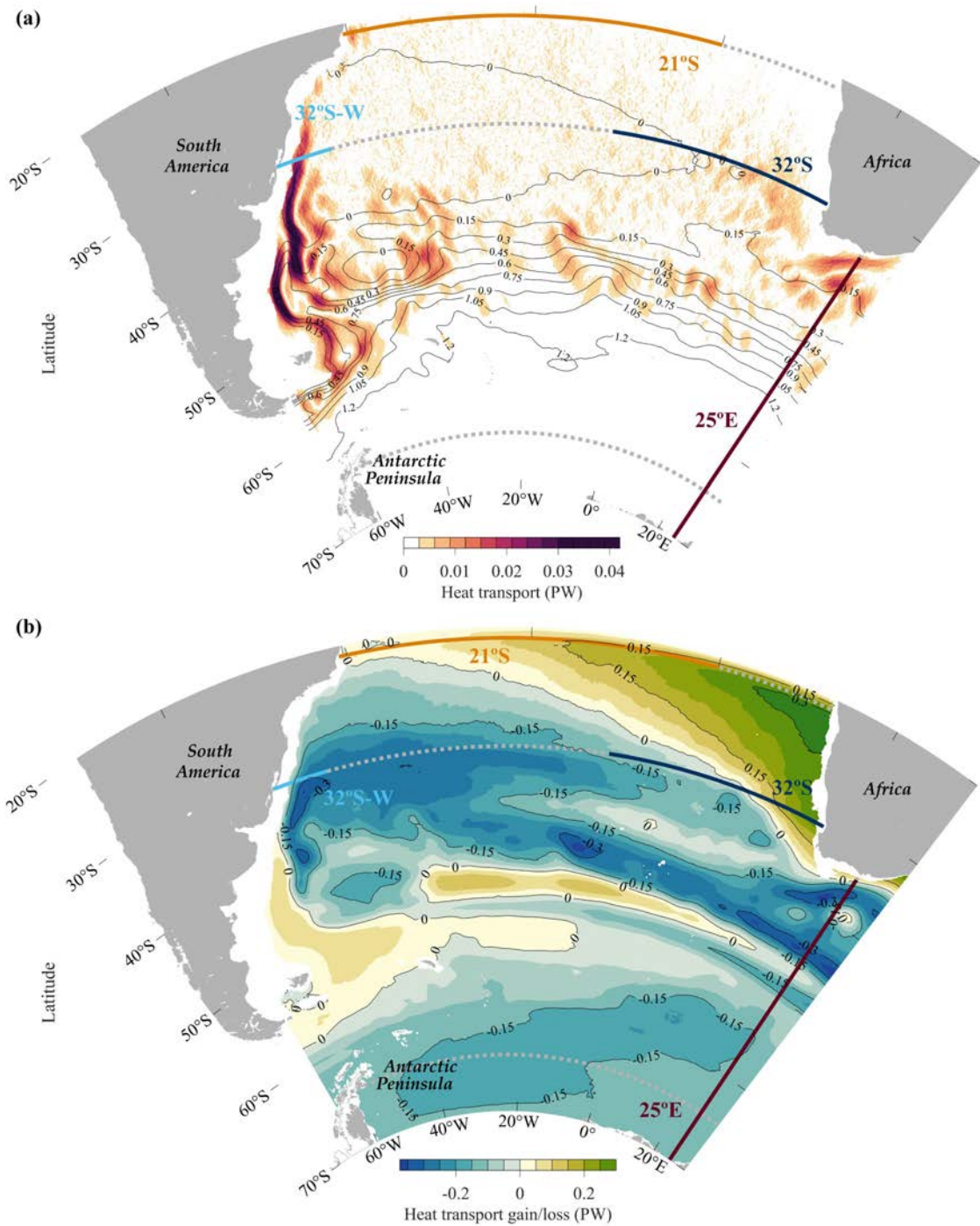


**Figure 3.72.** (a) Climatological vertically-integrated heat transport (PW) per cell in absolute values (colours) and conservative heat transport (contours) gradually accumulated from western and southern boundaries as particles increase their temperature. (b) Heat transport gain/loss in the domain. Only those particles that reach at least one section are considered, and the particle transport ( $v A$ ) is considered in absolute terms. Moreover, the particle trajectories are only included until they perform the second recirculation in the South Atlantic subtropical gyre, crossing the 32°S-W for the second time.

The total heat transport in the domain is the sum of the conserved heat transport—calculated considering that the water particles maintain their source temperature along their

trajectory—and the heat gain at any latitude as compared with at 63.75°W (Figure 3.72 and Table 3.23). Particles released in the Drake Passage carry a net heat transport of 1.35 PW. Water masses flowing east and leaving the domain through the 25°E section initially transport 1.03 PW of heat and gradually gain 0.36 PW and  $142.5 \times 10^6 \text{ kg s}^{-1}$  of salt along with the ACC (Tables 3.22 and 3.23). Water masses joining the eastern edge of the subtropical gyre transport 0.19 PW of heat and warm up to 0.65 PW, with the southwest coast of Africa standing as an area of high heat gain (Figure 3.72b).

**Table 3.22.** Total heat and salinity transport at the beginning and at the end of the different pathways according to the water masses. Whereas the DP → 32°S and DP → 21°S consider all the pathways until they cross the final section, the 32°S → 21°S and DP → 25°E only include those particles that follow these pathways. Note that  $10^6 \text{ kg s}^{-1}$  is approximately equivalent a 1 Sv.

| PATH        | BEGINNING and (END) |                  |                  |                  |   |                  |                    |                    |
|-------------|---------------------|------------------|------------------|------------------|---|------------------|--------------------|--------------------|
|             | Heat transport (PW) |                  |                  |                  | Salt transport ( $10^6 \text{ kg s}^{-1}$ ) |                  |                    |                    |
|             | Total               | SASW/<br>SAMW    | AASW/<br>AAIW    | UCDW             | Total                                       | SASW/<br>SAMW    | AASW/<br>AAIW      | UCDW               |
| DP → 25°E   | 1.034<br>(1.393)    | 0.191<br>(0.259) | 0.456<br>(0.649) | 0.387<br>(0.485) | 3218.7<br>(3361.2)                          | 350.0<br>(354.7) | 1334.7<br>(1378.3) | 1533.9<br>(1628.1) |
| DP → 32°S   | 0.186<br>(0.650)    | 0.069<br>(0.241) | 0.073<br>(0.287) | 0.044<br>(0.122) | 524.0<br>(532.5)                            | 129.1<br>(134.1) | 225.4<br>(230.0)   | 169.5<br>(168.4)   |
| DP → 21°S   | 0.158<br>(0.589)    | 0.060<br>(0.227) | 0.063<br>(0.254) | 0.035<br>(0.108) | 441.9<br>(451.0)                            | 111.9<br>(117.4) | 193.4<br>(197.2)   | 136.6<br>(136.4)   |
| 32°S → 21°S | 0.466<br>(0.478)    | 0.176<br>(0.186) | 0.210<br>(0.211) | 0.080<br>(0.081) | 365.1<br>(366.9)                            | 98.4<br>(99.3)   | 164.1<br>(164.4)   | 102.6<br>(103.2)   |

**Table 3.23.** Total heat gain and total salinity gain among different pathways and water masses. Note that  $10^6 \text{ kg s}^{-1}$  is equivalent a 1 Sv. Whereas the DP → 32°S and DP → 21°S consider all the pathways until they cross the final section, the 32°S → 21°S and DP → 25°E only include those particles that follow these pathways.

| PATHWAY     | Heat gain (PW) |           |           |       | Salt gain ( $10^6 \text{ kg s}^{-1}$ ) |           |           |      |
|-------------|----------------|-----------|-----------|-------|--|-----------|-----------|------|
|             | Total          | SASW/SAMW | AASW/AAIW | UCDW  | Total                                  | SASW/SAMW | AASW/AAIW | UCDW |
| DP → 25°E   | 0.359          | 0.068     | 0.193     | 0.098 | 142.5                                  | 4.7       | 43.6      | 94.2 |
| DP → 32°S   | 0.464          | 0.172     | 0.214     | 0.078 | 8.5                                    | 5.0       | 4.6       | -1.1 |
| DP → 21°S   | 0.431          | 0.167     | 0.191     | 0.073 | 9.1                                    | 5.5       | 3.8       | -0.2 |
| 32°S → 21°S | 0.012          | 0.010     | 0.001     | 0.001 | 1.8                                    | 0.9       | 0.3       | 0.6  |

Finally, part of these waters departs north of this latitude to reach the NBC in 21°S, gaining only 0.01 PW and  $1.8 \times 10^6 \text{ kg s}^{-1}$  of salt transport in this last stage. At their incorporation into the western boundary (21°S section), surface-intermediate and deep water masses hardly gain heat transport, although all of them gain substantial salt transport (Figure 3.72).

### 3.4.3.3. Water mass transformation

The water transport at each section comprises surface-mode, surface-intermediate and deep water masses, which can be characterized through the  $S_A - \theta$  diagrams (Figure 3.73). The diagrams at Drake Passage show that conservative temperatures range from -0.8 to 6.1 °C, regardless of their final section (Figure 3.73a, b, c).

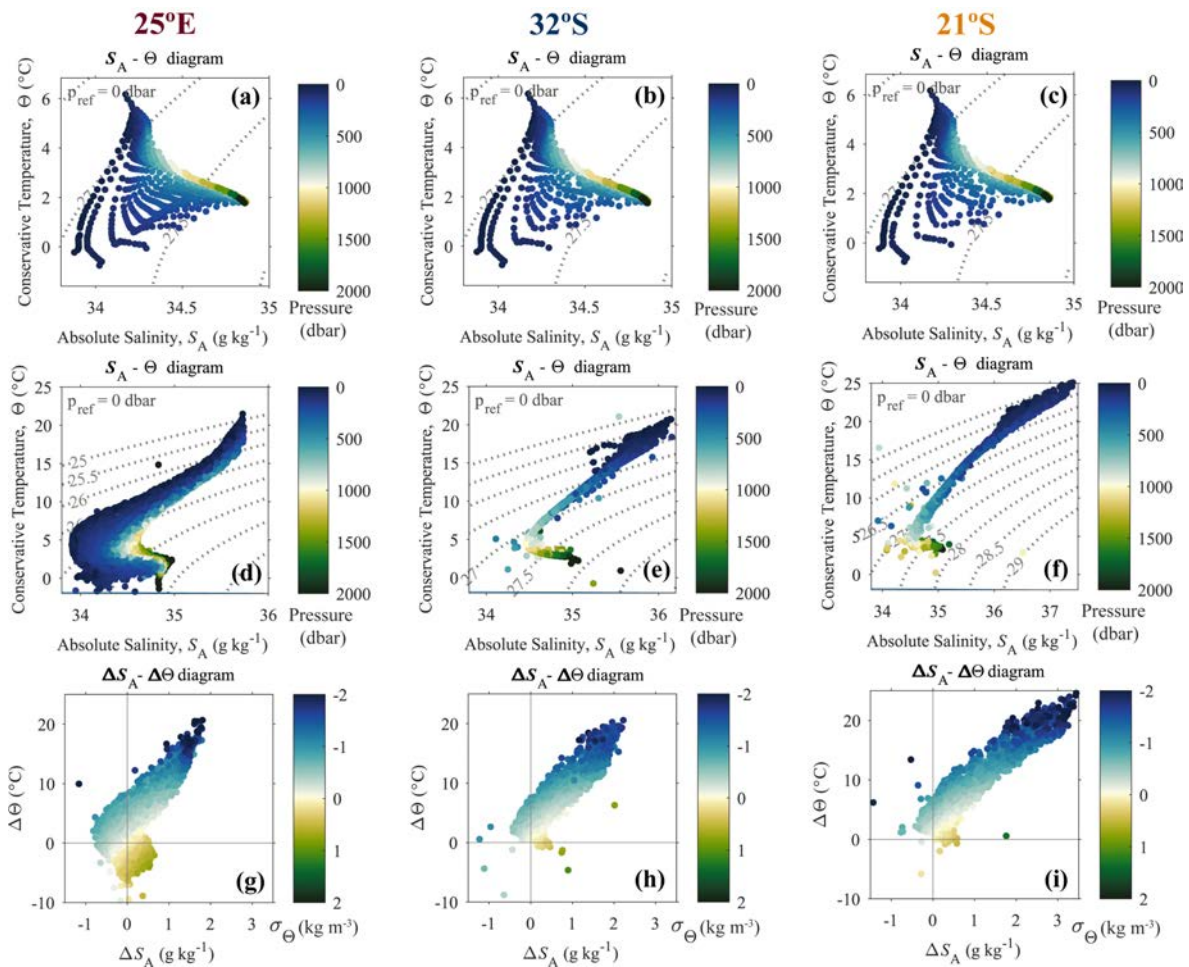


**Figure 3.73.** Conservative temperature and absolute salinity ( $S_A - \theta$  and  $\Delta S_A - \Delta \theta$  diagrams) diagrams of those particles that reach the (left) 25°E, (centre) 32°S and (right) 21°S sections, as they are: (a, b, c) in the Drake Passage and (d, e, f) in the respective final section; (g, h, i) property variations between both sections. Whereas the 32°S and 21°S consider all pathways until the section, the 25°E only includes those particles that follow this pathway.

The  $S_A - \theta$  diagram at 25°E reveals that cold waters after crossing the South Atlantic present a wide range of conservative temperatures from -1.9 to 21.4 °C, being not only much warmer at the surface but also substantially colder at depth (Figure 3.73d). Along its circumpolar path to the east, most of the water volume inflow remains in the ACC gaining temperature and salinity, and generally losing potential density as the  $\Delta S_A - \Delta \theta$  diagram shows (Figure 3.73g). Those water parcels that moved north and joined the subtropical gyre at 32°S present a similar  $S_A - \theta$  diagram in the Drake Passage than those particles that cross 25°E. In the 32°S and 21°S sections, the opposite occurs, increasing both variables linearly at the same time that depth decreases. Their  $\Delta S_A - \Delta \theta$  diagrams reflect a temperature and salinity increase up to 25.6 °C and 37.4 g kg<sup>-1</sup>, being more pronounced near the NBC. Indeed, as particles flow northward, the temperature increases, losing from the Drake Passage a median potential density of  $0.55 \pm 0.48$  kg m<sup>-3</sup> to 32°S and  $0.52 \pm 0.59$  kg m<sup>-3</sup> reaching 21°S (Figure 3.73h, i). This large conservative temperature changes and decrease in density may match with particles that enter the surface mixed layer and come in contact with the atmosphere. The net decrease in density results in a buoyancy gain and its corresponding shift towards upper waters.

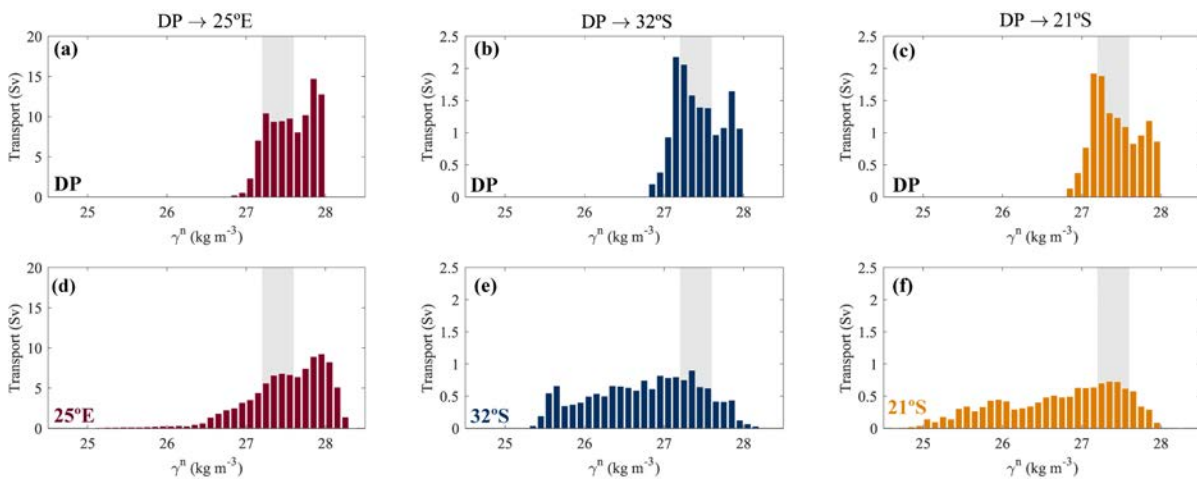


**Figure 3.74.** Water mass transports per neutral density as they depart from the (a, b, c) Drake Passage and as they reach (d) 25°E, (e) 32°S and (f) 21°S; the 25°E section only includes the particles that exclusively follow the ACC direct pathway. The shading illustrates the density range of surface-intermediate (AASW, AAIW) waters, separating the lighter surface-mode (SASW, SAMW) and denser deep (UCDW) waters.

The variations of thermohaline properties produce density changes that can be quantified as transformations in water masses (Figure 3.74). Particles following the ACC arrive at 25°E gaining 12.2 Sv of surface waters and 1.0 Sv of deep waters while losing 13.2 Sv of surface-intermediate waters. In the same way, particles that reach the subtropical gyre at 32°S also gain lighter water, 6.7 Sv exactly and lose 3.5 Sv and 3.2 Sv of surface-intermediate and

deep waters, respectively. Finally, those that are incorporated into the NBC gain 5.2 Sv of surface water and lose 2.7 Sv of surface-intermediate waters and 2.5 Sv of deep waters.

### 3.4.4. Discussion

#### 3.4.4.1. Net horizontal diffusion effect

Horizontal diffusion leads to additional displacements every time particles are advected. These resulting random radial motions follow a normal distribution and decrease with depth according to the expression 2.35. In that way, we compute the radial distances added daily to the advected particles for the first 20 years of the trajectories of the annual simulations to assess the magnitude of such distances (Figure 3.75).

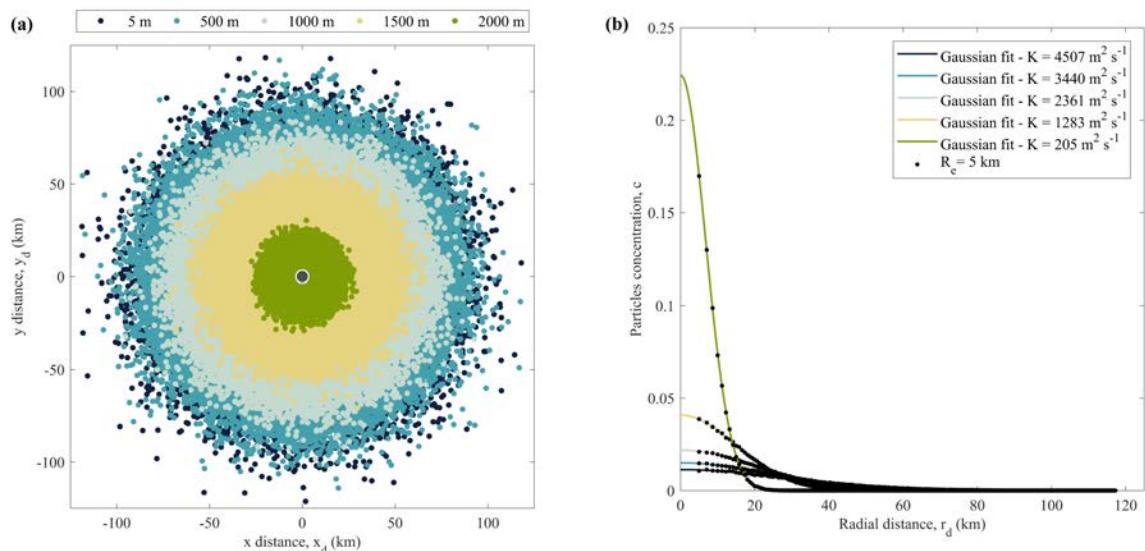


**Figure 3.75.** (a) Scatter plot of radial diffusive displacements added in the Lagrangian simulations every time a particle is advected at  $t = 1$  day, coloured according to their respective depth. (b) Gaussian distribution fitted for the particle's concentration as a function of radial distances for the different diffusion coefficients (see subsection 3.3.3 for further details); the Gaussian fits lead to a correlation of  $R^2 \cong 1$ , adjusted with the following weights:  $a = 1$  for radial distances lower than 50 km,  $b = 1$  between 50 km and 100 km, and  $c = 3$  for radial distances higher than 100 km.

We may appreciate that those deep particles (green) typically diffuse distances of the order of 10 km while the surface particles (dark blue) have characteristic values of 30 km and may even reach 100 km (Figure 3.75a). In order to assess the net effect and impact of horizontal diffusion on the water mass pathways, we have produced the probability distributions in the

absence of diffusion (Figure 3.76), which can be compared with the probability distributions in the presence of diffusion (Figure 3.69).

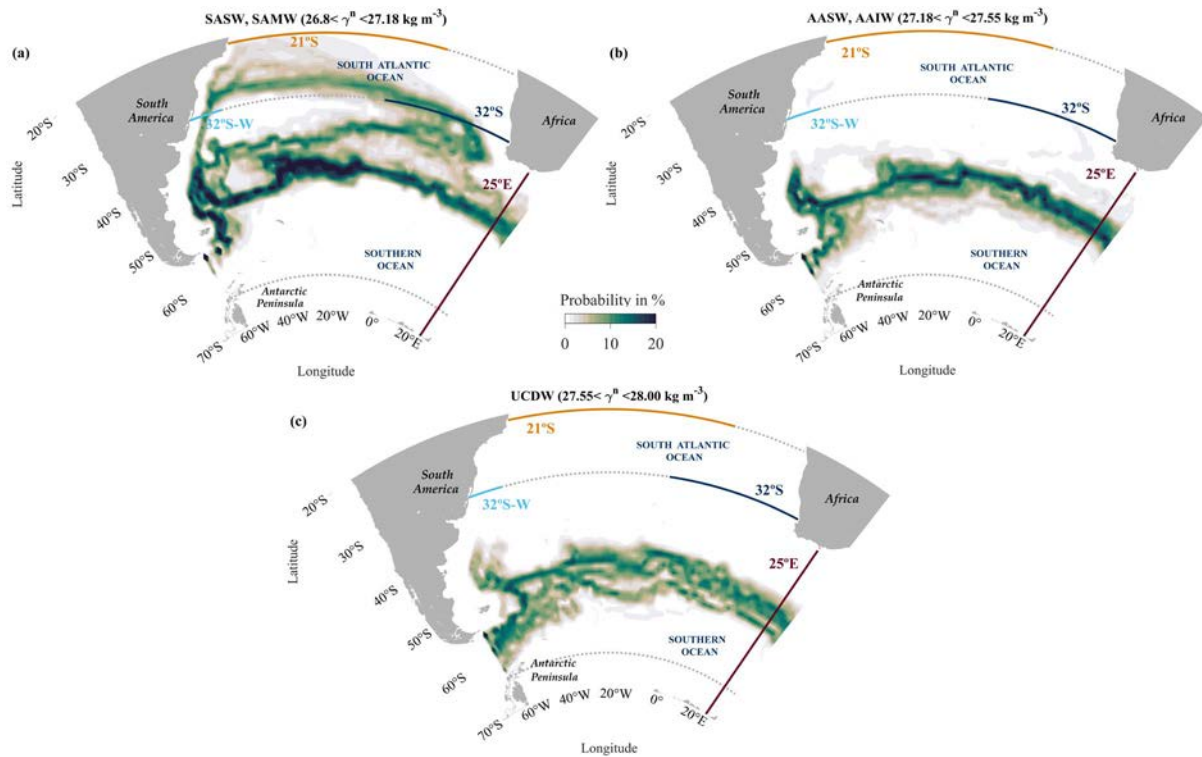


**Figure 3.76.** Climatological probability distributions of (a) surface-mode (SASW, SAMW), (b) surface-intermediate (AASW, AAIW) and (c) deep waters (UCDW) without diffusion processes. The grid used is  $1^\circ \times 1^\circ$  in longitude and latitude, each Lagrangian particle being only counted once per grid cell.

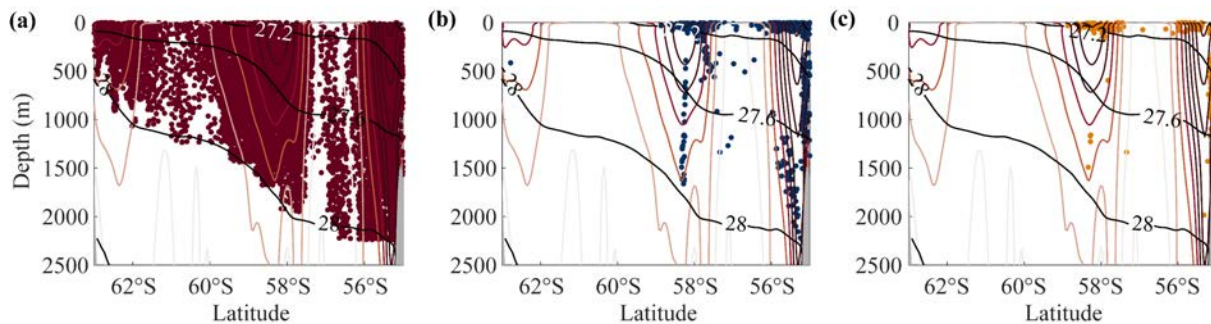


**Figure 3.77.** Distribution of particle release positions together with selected zonal velocity ( $\text{m s}^{-1}$ , coloured) and neutral density contours ( $\text{kg m}^{-3}$ , contours) coloured according to their section fate in the absence of diffusion processes. The density of particles reflect the zonal speeds in the Drake Passage; the left panel shows those particles (coloured in red) remaining in the (a) ACC ( $25^\circ\text{E}$ ), the central panel those that reach the (b)  $32^\circ\text{S}$  section (coloured in blue), and the right panel those that reach the (c)  $21^\circ\text{S}$  section (coloured in orange). The bathymetry is represented in grey; see Figure 3.66 for more details.

Without diffusion, the probability pathways are more clearly defined, with remarkably less dispersion. The surface particles follow two unique and well-defined routes, the path to the subtropical gyre and the one which follows the ACC, whereas for deep waters (Figure 3.76c) is possible to distinguish clearly up to 3 paths within the ACC route according to its frontal jets. Also, Figure 3.76 reveals that without diffusion, almost only surface-mode (SASW/SAMW) particles would enter the South Atlantic subtropical gyre, this scarce contribution following exclusively from the SAF and PF frontal systems (Figure 3.77). In particular, the total amount of transport incorporated into the 32°S only reaches 4.7 Sv without diffusion. Consequently, fewer particles get the NBC at the 21°S section, only a total of 1.3 Sv.

#### 3.4.4.2. Recirculation in the subtropical gyre

More than half of the Lagrangian particles that are incorporated into the South Atlantic subtropical gyre crossing 32°S, a total of 15.1 Sv, end diverging north and exiting through the 21°S section (68.5% of particles, which is equivalent to 10.3 Sv). The remaining particles (31.5%) together with the particles that end up crossing the 21°S section but before recirculate within the subtropical gyre even for decades, diverge south to feed the BC. The number of laps within the South Atlantic subtropical gyre and the average depth gained to escape or remain inside have been quantified with the help of the extra section along 32°S in the South Atlantic western margin (32°S-W). The procedure has been to count the number of instances and the transit times for particles departing and returning to 32°S-W, considering that a real subtropical gyre recirculation has to take a minimum of 3 years. (Figure 3.78).

After crossing the eastern boundary 32°S section, about 4.8 Sv follow southward along the South American coast feeding the BC, which is approximately half of the transport incorporated into the NBC. Those particles that only cross the 32°S-W section one time take a median of  $14.3 \pm 12.5$  years since they left the Drake Passage, and those that remain inside the gyre and cross it 2, 3, and 4 times take a median of  $25 \pm 14$  years,  $31 \pm 13$  years and  $48 \pm 8$  years since they were released, respectively. Whereas most of the particles only cross the 32°S western section once, not completing any lap, 1.3 Sv recirculate within the South Atlantic subtropical gyre performing up to three laps (Figure 3.78). Figure 3.78a reveals that the South Atlantic subtropical gyre has a median transit time of  $10.2 \pm 9.5$  years, performing the 78.1% of the recirculating particles only one lap. The 18.5% of the particles complete two laps and the 3.4% three of them.



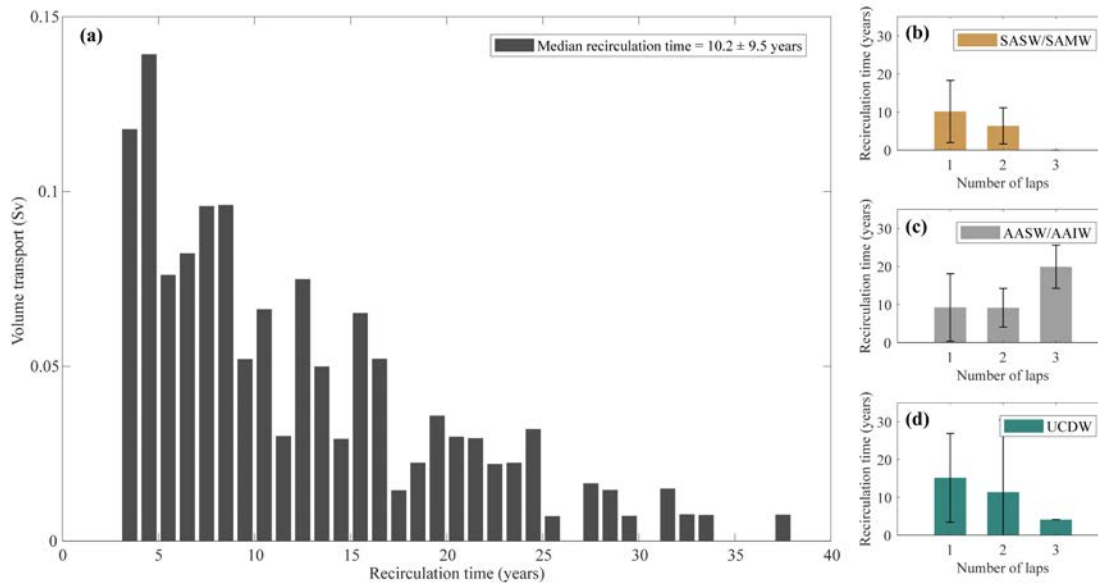


**Figure 3.78.** (a) Histogram of the years taken to recirculate the subtropical gyre, calculated as the time lap between two crossings of  $32^{\circ}\text{S-W}$ , plotted as a function of the associate volume transport. The number of laps completed within the subtropical gyre for the (b) surface-mode (SASW, SAMW), (c) surface-intermediate (AASW, AAIW) and (d) deep waters (UCDW).

**Table 3.24.** The median time taken and the median depth at which particles perform the South Atlantic subtropical gyre recirculations, according to its neutral density (water mass) at origin. The time represents the years passed until the particle returns to the  $32^{\circ}\text{S-W}$  section, and the depth is calculated as the average of the depths at the beginning and ending of the recirculation.

| Number of recirculation | Time (years)   |                |                 | Depth (m)     |               |                |
|-------------------------|----------------|----------------|-----------------|---------------|---------------|----------------|
|                         | SASW/SAMW      | AASW/AAIW      | UCDW            | SASW/SAMW     | AASW/AAIW     | UCDW           |
| 1                       | $10.1 \pm 8.2$ | $9.2 \pm 8.9$  | $15.2 \pm 11.7$ | $222 \pm 266$ | $606 \pm 414$ | $1234 \pm 413$ |
| 2                       | $6.4 \pm 4.8$  | $9.1 \pm 5.1$  | $11.4 \pm 19.1$ | $282 \pm 168$ | $741 \pm 478$ | $1002 \pm 284$ |
| 3                       | -              | $19.9 \pm 5.7$ | $4.1 \pm 0.0$   | -             | $440 \pm 183$ | $681 \pm 0$    |

Particles crossing  $32^{\circ}\text{S-W}$  for the first time flow at a median of  $199 \pm 148$  m depth, the subsequent times, depths and numbers of subtropical gyre recirculations per water masses are presented in Figure 3.78b, c, d and in Table 3.24. The SASW/SAMW waters get deeper at each lap, taking significantly less time until no particles remain inside for a third round. This result is consistent with the idea that particles that remain trapped within the subtropical gyre are those that sink with each recirculation, drawing a smaller gyre. In terms of AASW/AAIW, there is not much difference between the first and second lap, taking around 9 years and flowing at depths of 600 - 700 m, whereas the third turn takes significantly longer but flows

shallower, suggesting that these particles may have exited and re-entered within the gyre at some point along the path. Finally, the deep waters rise and take less time with each recirculation, from  $15.2 \pm 11.7$  years to  $4.1 \pm 0.0$  years.

#### 3.4.4.3. Seasonal variability

In order to analyze the seasonal variability, we have carried out the Lagrangian simulations with the climatological daily-mean fields, releasing particles every 4 days for the entire year and tracking them with a 4-day resolution. As in the climatological annual-mean simulation, the particles are tracked forward for 75 years, considering horizontal diffusivities. The transport of Antarctic waters from the Pacific Ocean through the Drake Passage and reaching the three key sections fluctuates throughout the year (Figure 3.79). At the Drake Passage, the net water transports display an annual mean of  $13.8 \pm 4.8$  Sv,  $44.5 \pm 4.8$  Sv and  $55.0 \pm 2.2$  Sv for the SASW/SAMW, AASW/AAIW and UCDW, which is less than using the climatological annual-mean fields. The corresponding water transports range from minima of 4.3 Sv, 35.5 Sv and 50.0 Sv to maxima of 22.1 Sv, 53.8 Sv and 59.4 Sv for the SASW/SAMW, AASW/AAIW and UCDW, respectively. The transport asymmetry throughout the year in the surface-mode and surface-intermediate waters is associated with the variability of the isoneutrals' depth at the release section. As a consequence of the cooling and freshening of the waters in late austral winter, the thickness of surface-intermediate waters increases as a result of the buoyancy loss in surface waters and the loss of stratification by convective processes.

**Table 3.25.** Water transports (left column) and transit times (right column) for the different pathways and water masses, as calculated from the climatological daily-mean fields. Whereas DP  $\rightarrow$  32°S and DP  $\rightarrow$  21°S consider all pathways until crossing the section, the DP  $\rightarrow$  25°E only includes those particles that follow this pathway.

| WATER MASS<br>$\gamma^n$ (kg m <sup>-3</sup> ) | Volume transports (Sv)   Transit times (years) |               |                       |               |                       |                |
|--|--|---------------|-----------------------|---------------|-----------------------|----------------|
|  | DP $\rightarrow$ 25°E                          |               | DP $\rightarrow$ 32°S |               | DP $\rightarrow$ 21°S |                |
| <b>SASW/SAMW</b><br>$26.80 < \gamma^n < 27.18$ | $12.2 \pm 3.2$                                 | $4.3 \pm 0.5$ | $1.6 \pm 0.5$         | $6.8 \pm 0.7$ | $1.2 \pm 0.4$         | $11.1 \pm 1.0$ |
| <b>AASW/AAIW</b><br>$27.18 < \gamma^n < 27.55$ | $37.9 \pm 3.4$                                 | $4.1 \pm 0.3$ | $5.5 \pm 0.5$         | $6.9 \pm 0.5$ | $4.4 \pm 0.4$         | $11.1 \pm 0.6$ |
| <b>UCDW</b><br>$27.55 < \gamma^n < 28.00$      | $44.8 \pm 2.1$                                 | $4.2 \pm 0.3$ | $7.0 \pm 0.4$         | $7.2 \pm 0.4$ | $5.6 \pm 0.4$         | $11.2 \pm 0.5$ |
| <b>TOTAL</b><br>$\gamma^n < 28.00$             | $94.9 \pm 5.1$                                 | -             | $14.1 \pm 0.8$        | -             | $11.2 \pm 0.7$        | -              |

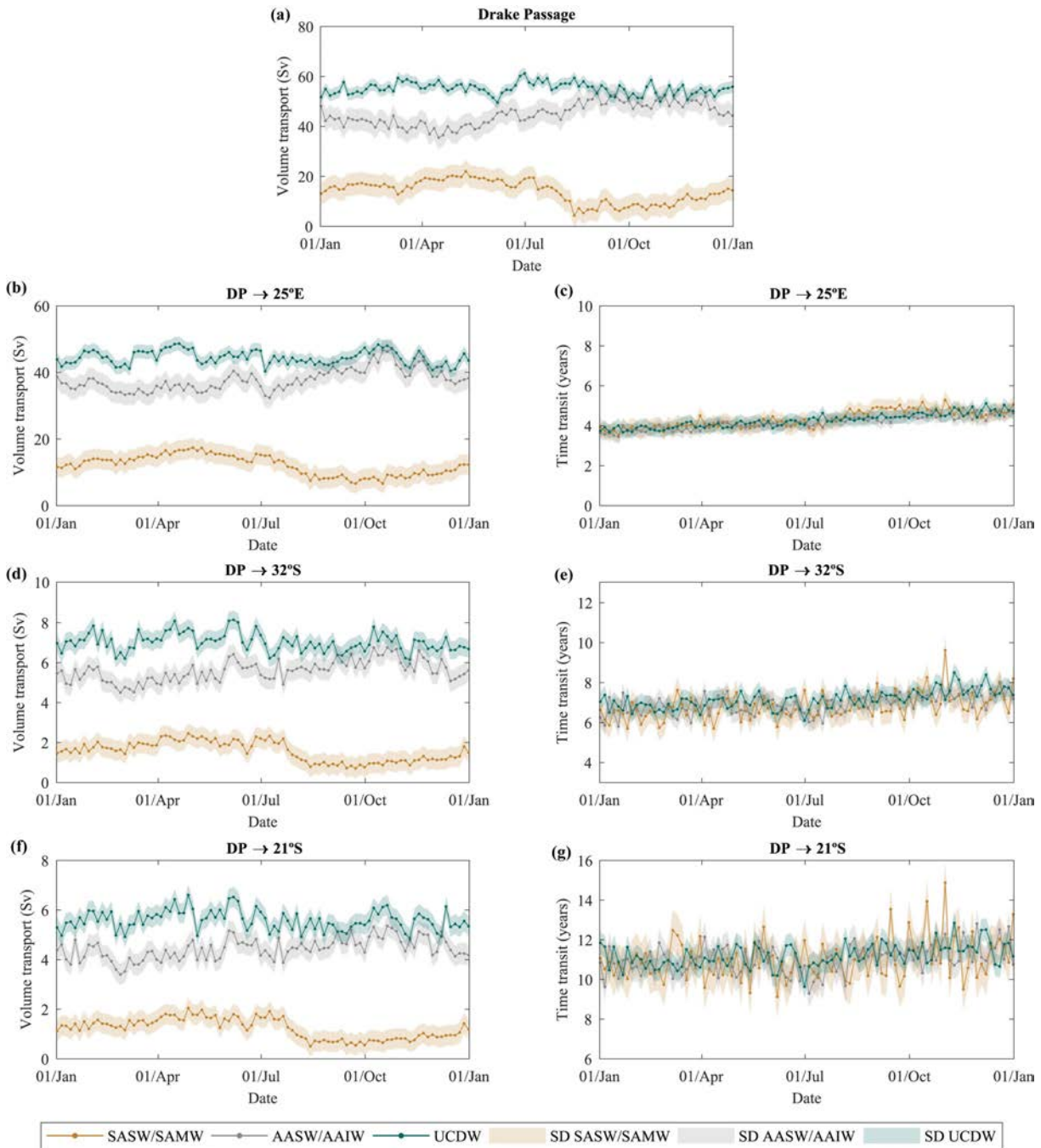


**Figure 3.79.** Seasonal variability of (a, b, d, f) volume transport and (c, e, g) transit times using the climatological daily-mean fields in (a) the Drake Passage and at (b, c) 25°E, (d, e) 32°S and (f, g) 21°S for the different water masses. Whereas the DP → 32°S and DP → 21°S consider all pathways until crossing the section, the DP → 25°E only includes those particles that follow this pathway.

The Lagrangian particles that arrive directly at 25°E carry a mean volume transport of  $12.2 \pm 3.2$  Sv for SASW/SAMW,  $37.9 \pm 3.4$  Sv for AASW/AAIW and  $44.8 \pm 2.1$  Sv for the UCDW (Table 3.25). The SASW/SAMW are the water masses that experience a higher seasonal variability, with SD ranging from 0.4 Sv to 3.2 Sv, regardless of the pathway followed, and the

path to 25°E has transit times with minimum variability (Figure 3.79c). Furthermore, a remarkable increase in AASW/AAIW transport stands out, with a proportional decrease of SASW/SAMW, during the austral spring in all sections. Regarding the transport incorporated to 32°S, the SASW/SAMW and AASW/AAIW transport averages are  $1.6 \pm 0.5$  Sv and  $5.5 \pm 0.5$  Sv with similar transit times of  $6.8 \pm 0.7$  years and  $6.9 \pm 0.5$  years (Table 3.25). A slight regular increase in transit times at the end of the year is noticeable for all routes exhibiting small time differences between water masses. At 21°S, the SASW/SAMW and AASW/AAIW display smaller volume transports (1.2 to 4.4 Sv) and longer transit times (11.1 years) than at 32°S section, as expected. In all transects, the UCDW transport is the dominant contribution, with mean transport of  $44.8 \pm 2.1$  Sv,  $7.0 \pm 0.4$  Sv and  $5.6 \pm 0.4$  Sv, not revealing any trend throughout the year.

#### 3.4.4.4. Comparison with other studies

The ACC is the dominant feature in the Southern Ocean in terms of mass, heat and freshwater transport, a truly interbasin connector that distributes cold-fresh waters around the globe. The Antarctic upper-ocean (up to  $\gamma^n = 28.00$  kg m<sup>-3</sup>) transports 117.4 Sv through the Drake Passage, with 102.4 Sv exiting the South Atlantic basin through 25°E, although just 94.8 Sv remain within the ACC being incorporated directly to the Indian Ocean in less than 5 years (Figure 3.80). A mean transport of 15.1 Sv arrives at the eastern margin of the South Atlantic subtropical gyre with a seasonal variability from 12.4 Sv to 15.7 Sv. About two-thirds of this input to the subtropical gyre, 10.3 Sv, will exit the subtropics at 21°S into the tropical region via the NBC.

The upper-ocean waters that remain in the ACC gain 0.36 PW of heat transport as they follow the direct path to 25°E; this gain increases further, to a total of 0.46 PW, if we also include those particles that recirculate in the South Atlantic Ocean before eventually exiting through 25°E. On the other hand, water masses joining the eastern edge of the subtropical gyre through 32°S warm up 0.46 PW, a heat gain that remains essentially invariable with only 0.01 PW as they reach the western boundary at 21°S. Regarding the salt fluxes, the waters remaining in the ACC gain  $142.5 \times 10^6$  kg s<sup>-1</sup>, increasing to  $155.6 \times 10^6$  kg s<sup>-1</sup> if we consider all particles that cross 25°E (Table 3.23 and Figure 3.80). Water masses that join the subtropical gyre have gained a considerable amount of  $8.5 \times 10^6$  kg s<sup>-1</sup> salt transport, increasing 68.5% of them with an additional  $1.8 \times 10^6$  kg s<sup>-1</sup> as they reach the Brazilian coast. As a result of the heat and salt exchanges, the water masses incorporated into the subtropical gyre at 32°S lose a mean potential density of  $0.6 \pm 0.5$  kg m<sup>-3</sup>, implying the transformation of 3.5 Sv of surface-intermediate waters and 3.2 Sv of deep waters into surface waters (subsection 3.4.3.3). As these waters reach the 21°S western boundary directly or not from the Drake Passage, the total

change will have decreased to an average of  $0.5 \pm 0.6 \text{ kg m}^{-3}$  of potential density, warming less and gaining more salt transport than waters incorporated to  $32^\circ\text{S}$  From Drake Passage (Figure 3.80).

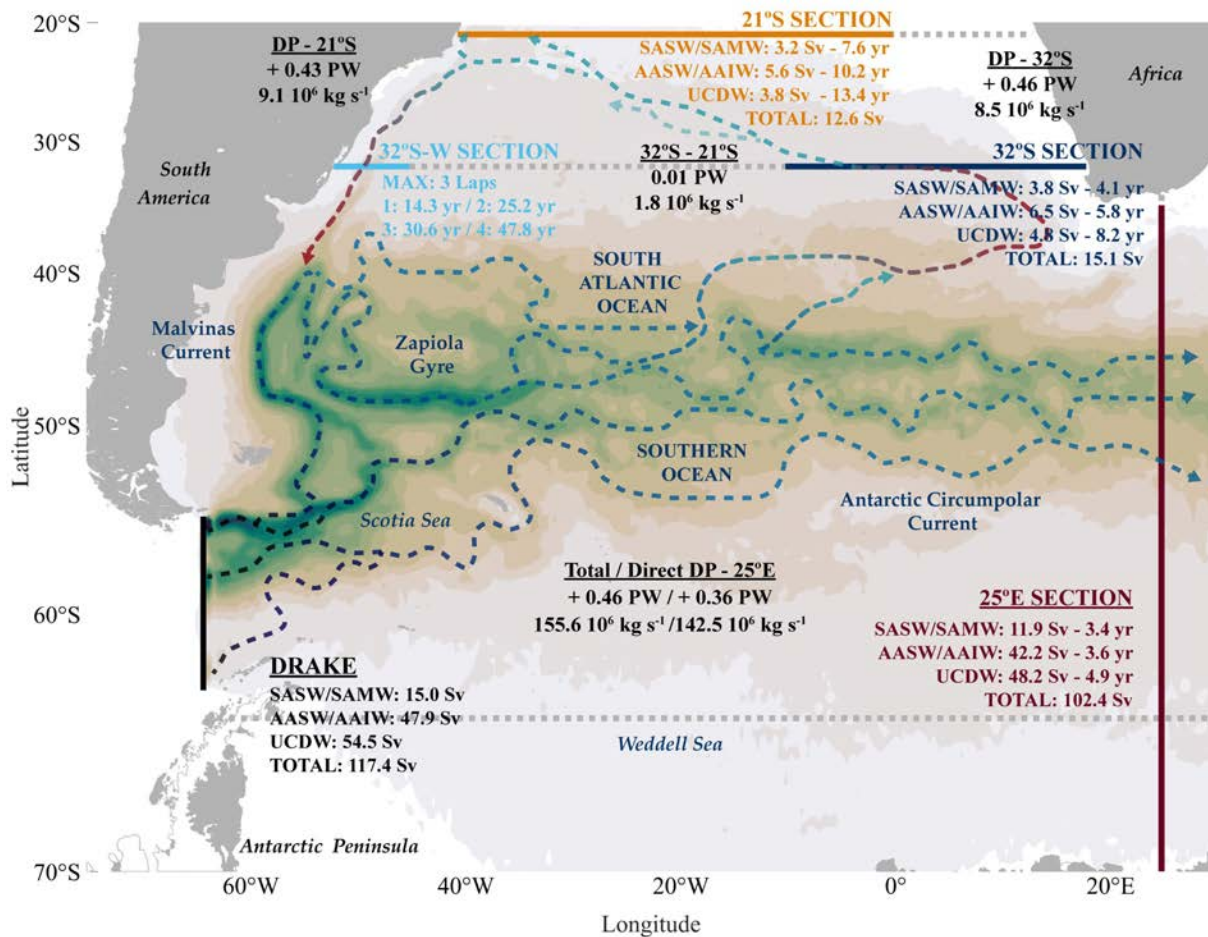


**Figure 3.80.** Scheme of the main could-route pathways up to  $\gamma^n < 28.00 \text{ kg m}^{-3}$ , over the climatological annual-mean probability distributions, with volume transports, transit times, and salt and heat transports at Drake Passage,  $25^\circ\text{E}$ ,  $32^\circ\text{S}$  and  $21^\circ\text{S}$  according to the different water masses. For the  $25^\circ\text{E}$  section, we show the direct (via ACC) and total (direct plus subtropical gyre recirculation) heat and salt transports. The grid used for the probability distribution includes all the trajectories with  $0.5^\circ$  in longitude and  $0.3^\circ$  latitude, coloured reaching the darkest green shade at 15% of probability. Each Lagrangian particle is only counted once per grid cell.

Previous Lagrangian studies concluded that after completing one circumpolar lap, the total ACC transport transferred to other basins ranges from 28.8 Sv to 35.9 Sv (Friocourt et al., 2005). Our results indicate that at least 9.7 Sv (all paths that not cross  $25^\circ\text{E}$ ; Table 3.20) of the ACC upper waters are transferred to the South Atlantic Ocean basin, leaving the circumpolar pathway. This transport is substantially larger than earlier estimates, which suggest that between 0.9 Sv and 3.9 Sv are exported to the South Atlantic subtropical gyre through the

direct cold-water route, with less than 2 Sv recirculating within the subtropical gyre before flowing equatorward (Speich et al., [2001](#); Donners & Drijfhout, [2004](#); Friocourt et al., [2005](#)). According to Rodrigues et al. ([2010](#)), only 8.7 Sv of the 39.7 Sv from the MC reach the eastern basin at 33°S latitude and among all this transport, only 4.7 Sv will be incorporated as the cold contribution in the South Atlantic subtropical gyre. However, other recent Lagrangian estimations (Rühs et al., [2019](#)) concluded that the Drake Passage contribution to the NBC at 6°S may vary from 5.5 to 13.1 Sv. Our climatological annual-mean results display that 15.1 Sv and 12.6 Sv reach the 32°S and 21°S sections (Figure [3.80](#)), respectively, so our transports are in line with Rühs et al. ([2019](#)).

Moreover, our findings support that the transport incorporated to the subtropical gyre occurs mostly through the three ACC fronts, mainly from the SAF and the PF (Figures [3.66](#) and [3.69](#)). This agrees with Cunningham et al. ([2003](#)) and Firing et al. ([2011](#)) but disagrees with Rühs et al. ([2019](#)), who argued that the major contribution to the South Atlantic branch of the AMOC's upper limb was the SAF. Even when we ignore diffusion processes, the contribution carried by the two northernmost fronts of the ACC is appreciated (Figures [3.76](#) and [3.77](#)).

In terms of transit times, our estimations from the Drake Passage to the eastern margin of the South Atlantic subtropical gyre agree with some previous studies. According to Speich et al. ([2001](#)), Drake Passage waters last a median transit time of 19 years for the direct incorporation to the North Atlantic (20°N) and 29 years if they have previously recirculated one time in the South Atlantic. Rühs et al. ([2019](#)) and Rousselet et al. ([2020](#)) have found that the most frequent transit time of the direct path to the western boundary at 6°S is around 12 years. These results are in fair agreement with our estimates, although slightly short for those initially defined as UCDW waters (13.4 years to arrive at 21°S; Figure [3.80](#)). Our results show that particles that recirculate within the South Atlantic subtropical gyre have a median recirculation time of  $10.2 \pm 9.5$  years; this time coincides grossly with the 10 more years that particles take to recirculate as indicated by Speich et al. ([2001](#)).

Regarding the thermohaline variations, Georgi & Toole ([1982](#)) determined that the ACC loses heat and gains fresh water in the Atlantic because of heat release to the atmosphere during the formation of deep and bottom waters in the high-latitude regions. In the same line, Rintoul ([1991](#)) pointed out that the ACC waters lose  $0.25 \pm 0.18$  PW of heat crossing the Atlantic Basin, largely as a result of the transformation of surface-intermediate into deep and bottom waters. Our estimates indicated the opposite result, with the upper-ocean waters, especially the surface-intermediate waters, gaining heat (Table [3.23](#)). Considering the northward transports, Cabré et al. ([2019](#)) found that surface and intermediate water masses gain 0.20 PW heat transport flowing from 30°S to 8°S, with a 0.15 PW gain occurring from 30°S to 18°S during the westward trip from east to west South Atlantic coasts. In this last stage, the 10.3 Sv of upper

waters that flow from 32°S to 21°S experience nearly zero warming (0.01 PW) and substantial salt gain ( $1.8 \times 10^6 \text{ kg s}^{-1}$ ); the latter as a result of mixing with the saline water masses from the Agulhas Current as indicated by Berglund et al. (2021).

### 3.4.5. Summary and conclusions

This study has launched Lagrangian simulations using 18 years of numerical data, between 2002 and 2019, from the GLORYS12v1 thermohaline and velocity fields. The calculations have allowed us to determine the fate and thermohaline changes of the upper-ocean ACC waters ( $\gamma^n < 28.00 \text{ kg m}^{-3}$ ) as they cross the Atlantic basin. In addition, part of the water transport that enters across the Drake Passage leaves the ACC and enters the South Atlantic subtropical gyre near its eastern boundary across 32°S. The number of subtropical recirculations of these upper waters and the fraction of water transport that finally veers northward to feed the NBC have been quantified, with this last fraction conforming the cold (and fresh) direct contribution to the AMOC returning limb.

Our climatological annual-mean estimates reveal that 84.4% (94.8 Sv) of the upper-ocean cold waters that cross the Drake Passage remain in the ACC after crossing the South Atlantic Ocean, feeding directly into the Indian Ocean (Table 3.20). Further, the contribution to the eastern margin of the subtropical gyre is sustained by 13.6 % (15.1 Sv) of these cold waters and 68.5% (10.3 Sv) of this transport eventually reaches the NBC. The incorporation into the subtropical gyre takes place mainly thanks the surface-intermediate waters (AASW/AAIW), which contribute with 6.5 Sv that are carried out by the three ACC fronts but primarily via the SAF and PF. The cold upper waters take as much a median of 8.2 years to reach the eastern edge of the subtropical gyre at 32°S, leaving the Southern Ocean completely.

The climatological daily-mean velocity fields allow assessing that the cold-water direct route varies seasonally between 12.4 Sv and 15.7 Sv, with an average transport ( $14.1 \pm 0.8 \text{ Sv}$ ) slightly below the value calculated with the annual climatology. These estimates suggest that seasonality does not play a significant role in the upper limb of the AMOC, being the SASW/SAMW which experience more variability. However, it defines the proportion of surface-mode and surface-intermediate waters formed, displaying a transport asymmetry pattern in the second half of the year with an increase in the AASW/AAIW at the expense of the SASW/SAMW.

In terms of heat transport, a significant increase of 0.46 PW takes place during the cold-water incorporation to the South Atlantic Ocean at 32°S, as the upper-ocean waters warm because of heat gain from the atmosphere and through mixing with the Agulhas Leakage waters. Instead, they hardly gain heat and only  $1.8 \times 10^6 \text{ kg s}^{-1}$  of salt transport on their

westward subtropical pathway to the western boundary at 21°S. This leads to a water mass transformation of 6.7 Sv of surface-intermediate and deep waters to surface waters along the path to 32°S. These thermohaline variations and water mass transformations point out that the South Atlantic Ocean is not only a passive conduit for remotely formed water masses, but it also represents an active source of thermohaline forcing and mixing, contributing to the returning branch of the AMOC.

From its Drake Passage source, upper waters take a median of  $14.3 \pm 12.5$  years to arrive at 32°S-W, in the southward western boundary Brazilian Current. Most of the water recirculating within the subtropical gyre (78.1% of 1.3 Sv) performs just one lap in the South Atlantic subtropical gyre, averaging  $25.2 \pm 14.3$  years to cross again the 32°S-W section from the source. Surface-mode and deep waters recirculate deeper and shallower, respectively, taking less time each lap, whereas the AASW/AAIW does not show much difference between the first two laps. About 8.6% (9.8 Sv) of the upper-ocean waters have a time residence in the South Atlantic Basin longer than 75 years, not reaching any edge/section of the domain in that period.

Our study confirms that numerical Lagrangian analysis is a very useful tool for assessing the mean values and temporal variability in the predominant pathways, volume transports, transit times and thermohaline transformations within key oceanic regions such as the South Atlantic subtropical gyre. In particular, our results have allowed assessing the potential role of horizontal diffusivities in modifying these pathways and transformations. Further advances would require considering the whole water column and including the cold indirect route, where Drake Passage waters recirculate within the Indian Ocean before flowing back into the South Atlantic Ocean as part of the Agulhas Leakage.





## **CHAPTER 3.5**

---

**The cold and warm intermediate  
contributions to the South Atlantic  
subtropical gyre**

### 3.5.1. Context and objectives

The returning limb of the Atlantic Meridional Overturning Circulation (AMOC), a key component of the Earth's climate system, is sustained by the northward transport of lighter upper-ocean waters from the South Atlantic Ocean back into high latitudes. The primary sources of this South Atlantic upper limb are two: the cold-fresh waters from the Pacific Ocean through the Drake Passage and the warm-salt waters from the Indian Ocean via the Agulhas Current System. Traditionally, these pathways have been referred to as the cold- (Rintoul, [1991](#)) and warm-water routes (Gordon, [1986](#)) due to their inherently different thermohaline properties. However, their relative contributions to the volume transport and properties of the AMOC upper limb remain controversial, prevailing the conception that the warm contribution is the major source of transport (Garzoli & Matano, [2011](#); R  hs et al., [2019](#)).

The Agulhas Current, the strong African western boundary current, retroflects back to the Indian Ocean leaking relatively warm and salty upper and intermediate waters into the South Atlantic Ocean, in what is known as the warm water route (Bower et al., [2019](#)). The global scale warm route originates in the Pacific, advecting the saltier water across the Indian Ocean in the 10° to 15°S latitude belt carried by the (Indian) South Equatorial Current (SEC). Hence, the SEC carries the Indonesian Throughflow Water (ITF) into the interior Indian Ocean, where it mixes with the Indian tropical waters, reaches the northern tip of eastern Madagascar and eventually flows southward within the Mozambique Channel to supply the Agulhas Current (Figure [3.81a](#); Gordon, [1986](#)). It is estimated that approximately a quarter of the Agulhas Current transport leaks to the South Atlantic Ocean in the form of Agulhas rings and filaments. Regardless, the Agulhas Leakage is subject to strong interannual variability and decadal variations, apparently having increased substantially in the last decades (Biaostoch et al., [2009](#)). In particular, an increase of 30% in the Agulhas Leakage between the 1960s and 2000s has been associated with changes in the Southern Hemisphere winds (Biaostoch et al., [2015](#); Durgadoo et al., [2013](#)). This resulting contribution does not completely flow directly into the AMOC, but about 50% recirculates within the South Atlantic subtropical gyre (R  hs et al., [2013](#)).

Regarding the cold route, a small fraction of the relatively cold and fresh upper waters that enter through the Drake Passage – with estimates ranging between 134 and 173 Sv (Cunningham et al., [2003](#); Donohue et al., [2016](#); **Chapter 3.1**) – diverts northward, following mainly the Subantarctic Front into the Malvinas Current. Then, it follows the South Atlantic Current and is incorporated into the South Atlantic subtropical gyre circulation, forming the direct cold-water route (Friocourt et al., [2005](#); Speich et al., [2001](#)). Early estimates of this direct cold-water contribution to the AMOC upper limb accounted for only 1 - 2 Sv (Donners &

Drijfhout, [2004](#); Friocourt et al., [2005](#); Speich et al., [2001](#)). An additional 4 - 6 Sv have been attributable to the indirect cold-water route. This is a relatively small fraction that follows the Antarctic Circumpolar Current into the Indian Ocean before flowing back to the Atlantic as part of the Agulhas Leakage (Friocourt et al., [2005](#); Speich et al., [2001](#), [2007](#)). Furthermore, there is estimated that exist a Southern Ocean contribution of 18 Sv of Subantarctic Mode and Antarctic Intermediate Waters (SAMW/AAIW) in the Indian Ocean sector that enter directly south to the African basin (Rintoul et al., [2001](#)).

Most authors consider the cold indirect contribution through the Indian Ocean as part of the warm water route. However, these studies were often based on the evaluation of relatively coarse resolution non-eddying, eddy-permitting ocean model simulations (Bjastoch et al., [2008](#); Durgadoo et al., [2013](#)) or even not considering the entire domain of the cold contribution through the Indian Ocean. As a result, the strength of the Agulhas Leakage is usually overestimated in relation to the Drake Passage contribution. Here, we aim to reproduce the Lagrangian analysis with higher spatiotemporal resolution eddy-resolving flow fields from ocean model simulations that include the entire South Atlantic and Indian basins. For this purpose, we carry out numerical simulations of Lagrangian trajectories with the main objective of assessing the multiple direct and indirect cold and warm intermediate-water pathways reaching the eastern margin of the South Atlantic subtropical gyre: predominant trajectories, transit times, water transformations, changes in thermohaline properties, and spatiotemporal interannual and seasonal variability. These different inflows have been characterized by thousands of particles released backwards in time from the eastern subtropical gyre where these two routes converge, still preserving part of their initial thermohaline properties.

Despite its importance in the AMOC, the pathways and inter-basin connections of the intermediate waters into the South Atlantic Ocean still remain relatively unexplored. In this study, we use the Lagrangian output from eddy-resolving ocean general circulation models to document these branches, with special attention to the incorporations into the subtropical gyre. In subsection [3.5.2](#), we present the release section, the intermediate water definition and the description of the Lagrangian experiments. In subsection [3.5.3](#), we present the probabilities for a particle to follow the different predominant pathways, indicating the transit times, the changes in thermohaline properties, and the spatiotemporal interannual and seasonal variability. In subsection [3.5.4](#), we explore in more detail the warm route and the indirect cold contribution within the Indian Ocean, and we propose a re-definition of the routes. We conclude in subsection [3.5.5](#) with some remarks about what we know and what yet remains unknown regarding the cold and warm contribution to the South Atlantic Ocean.

### 3.5.2. Methodology

#### 3.5.2.1. Area of study, reference sections and intermediate water masses

The Lagrangian numerical simulations focus on the pathways followed by the intermediate waters because of their importance as part of the returning limb of the AMOC. These intermediate water masses are usually documented to flow at layers located between about 500 and 2000 dbar as they transit through the Southern, South Atlantic and Indian Oceans. Beyond their formation regions at high southern latitudes, largely in the Pacific sector of the Southern Ocean (Talley, 2011), these intermediate waters have no interaction with the atmosphere, keeping their thermohaline characteristic properties largely during their path except for diffusion. The AAIW is commonly identified by a minimum salinity layer subducting near the Subantarctic Front (Hanawa & Talley, 2001; Rintoul et al., 2001). The potential density range settled by Roemmich (1983) and extended in R uhs et al. (2019) for the intermediate waters ( $26.8 < \sigma < 27.5 \text{ kg m}^{-3}$ ) coincides with the minimum of salinity in our reference section (34 S section; Figure 3.81b).

In this study, we aim to identify the main pathways and quantify the net water transformations of those intermediate waters that enter the South Atlantic Ocean from the Drake Passage and Agulhas Current, with potential densities between 26.8 and 27.5  $\text{kg m}^{-3}$ . For this purpose, we have established seven sections to study the percentage of particles and hence the transports incorporated into each potential path, with three main key sections (Figure 3.81a). First, the eastern boundary 34 S section (from 5 W to 18 E, hereafter the reference section), where the cold and warm water routes converge, is chosen to backtrack the intermediate waters proceeding from both routes. Second, the longitudinal section at 30 S from the African coast out to 40 E, fully sampling the Agulhas Current. Third, the Drake Passage section at 64 W between South America and the Antarctic Continent. The other four sections are as follows: Indonesian Throughflow (ITF), entrance to the Indian Ocean (IO), SEC bifurcation (21 S) and the Western Subtropical Gyre (WSG) (Figure 3.81a).

#### 3.5.2.2. Lagrangian simulations

The Lagrangian experiments consist of releasing between 2000 and 2500 particles every 10 days in the intermediate waters during the entire summer and winter seasons every year between 2015 and 2019. Particles are tracked backwards in time for 75 years with a 5-day resolution. The two release periods run between June 21 and September 22 for austral winter and from January 1 to March 20 for austral summer; notice that for the austral summer period we use a shorter period within the same year in order to avoid possible jumps in the velocity

time series. The number of particles released backwards in this study is proportional to the volume transport in the reference section, with each particle representing 0.01 Sv, so the velocity fields in this section define the number of particles launched. Hence, the total sum of their transport at the reference section reflects the current AAIW transport at the eastern margin of the South Atlantic subtropical gyre.

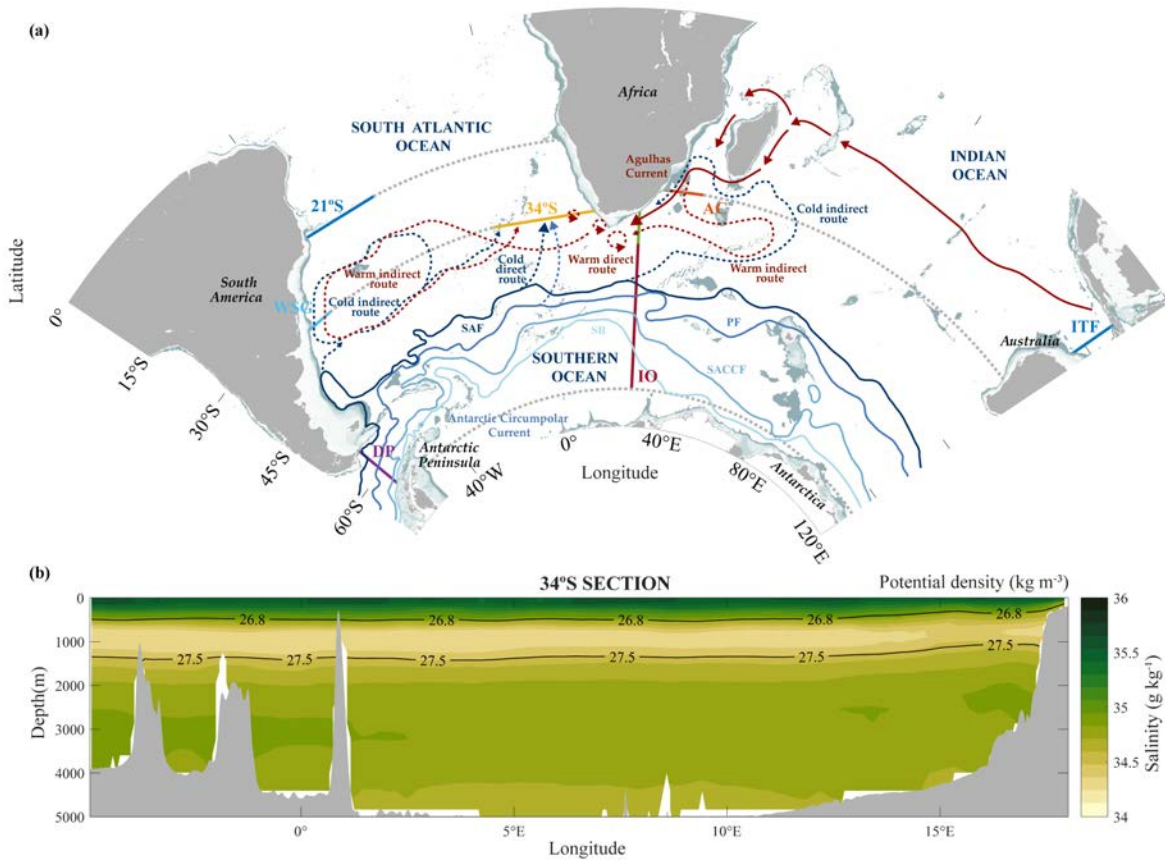


**Figure 3.81.** (a) Scheme of the direct and indirect pathways that form the cold and warm routes (dashed lines) of the intermediate waters to the South Atlantic Ocean: ACC fronts and circulation (in blue) and the Agulhas Current System with the main surface current that feeds it (in red). The vertical sections for tracking particles are shown: 34°S (reference section), DP (Drake Passage; 64°W), AC (Agulhas Current; 30°S), ITF (Indonesian Throughflow), IO (entrance to the Indian Ocean; 27°E), 21°S (SEC bifurcation) and WSG (Western Subtropical Gyre; 34°S). (b) Climatological mean salinity distribution along the reference section. The 2015 - 2019 average potential density contours that delimit the low-salinity intermediate waters are shown.

In order to identify the role of the seasonal and the interannual variability on the backwards trajectories, we extend our time series by means of a looping technique of the data. Even though the use of this looping technique is very extended (e.g., Döös et al., 2008; Rühls et al., 2013; Durgadoo et al., 2017), it may introduce unphysical jumps in the velocity and tracer fields (Rühls et al., 2019) so that the results have to be interpreted with caution. Fortunately,

these errors are small if a sufficiently high number of Lagrangian particles is considered and the (model) drift in the velocity fields is not too large (Döös et al., 2008; Thomas et al., 2015). We carry out two types of experiments: the first consists of backwards trajectories calculated looping the five years (2015 - 2019) continuously, and the second approach consists of calculating trajectories with data looping for one single year, the same year when particles are released. Hence, we have in total 20 sets of simulations: 10 looping the same year, hereafter the 1-year loop, and 10 of them looping after the full five years, hereafter the 5-year loop. In half of the simulations, the particles are released in austral summer, and in the other half, in austral winter (Figure 3.82). We use the 5-year looping simulations to assess the seasonal variability for both water routes on transport, time transit, thermohaline properties fluctuations and water mass transformations for both routes. The interannual variability, obtained by repeatedly looping the 1-year velocity fields for 75 years, is used and discussed only in subsection 3.5.4.2.

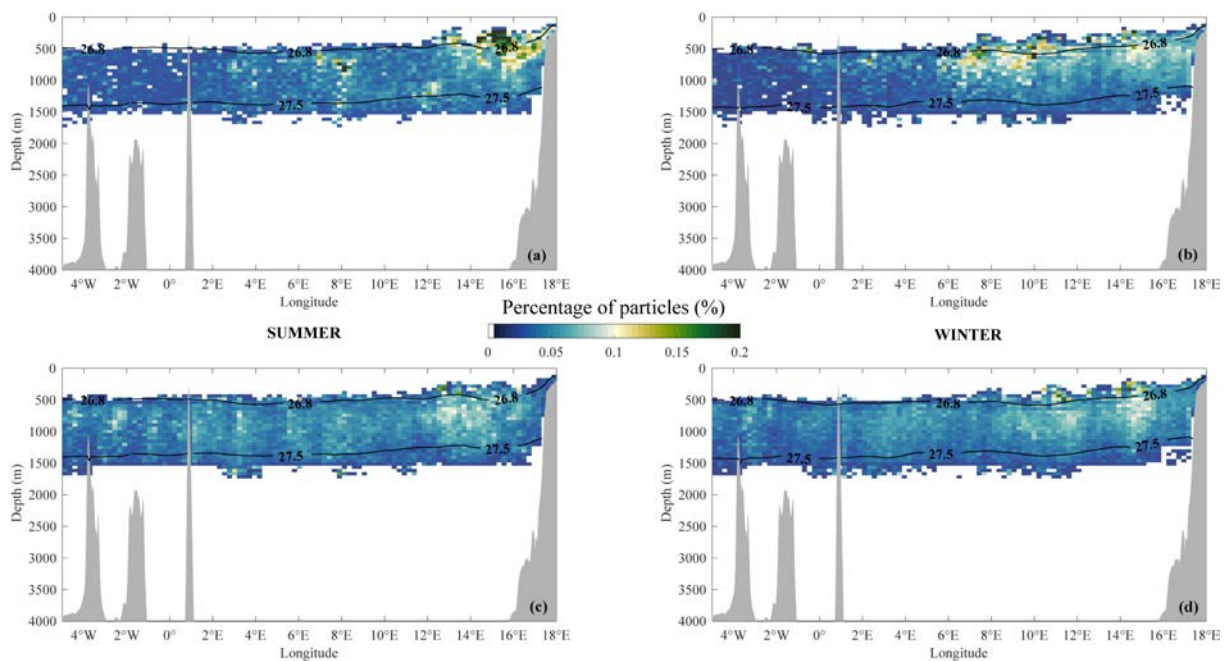


**Figure 3.82.** Distribution and percentage of Lagrangian particles released per bin along the 34°S vertical section that come from (a, b) the Agulhas Current and (c, d) the Drake Passage during summer (left panels) and winter (right panels) seasons. The number of particles released in the intermediate waters is proportional to the geostrophic transport. The time-averaged potential density contours of 26.8 and 27.5 kg m<sup>-3</sup> are plotted as a visual guide.

The backwards trajectories reveal the connectivity and transit times between far-separated branches of the AMOC. The Lagrangian trajectories are computed using the Parcels v2.0 code, a Lagrangian simulator that tracks offline particles within a numerical circulation model (Delandmeter & Van Sebille, 2019). The particles are advected backwards using the

daily three-dimensional velocity fields from the reanalysis numerical model GLORYS12v1 (Lellouche et al., [2021](#)), an eddy-permitting model with a  $1/12^\circ$  horizontal resolution, provided by the Mercator Ocean team. The model has 50 vertical levels, with maximum grid resolution at the surface. Our region of study includes all the South Atlantic and Indian Ocean basins, between  $0^\circ\text{S}$  -  $70^\circ\text{S}$  in latitude and  $70^\circ\text{W}$  -  $120^\circ\text{E}$  in longitude down to 5052 m, ensuring that we can follow the whole trajectories of the ocean water masses. The potential temperature and salinity fields from the model are linearly interpolated following the particles' positions. No additional Lagrangian diffusion parameterization was implemented, in contrast to **Chapter 3.4**.

### 3.5.3. Results

#### 3.5.3.1. Warm and cold pathways and transit times

During the austral winter, the mean cold route represents  $18.9 \pm 0.6\%$  of the total transport of intermediate waters in the reference section, more than the  $12.3 \pm 1.9\%$  fraction reaching this section via the warm route (through the AC section). Table [3.26](#) shows the net and total transports through the reference section ( $34^\circ\text{S}$ ), with the net transports representing the northward transfer through the section at any time and the total transport including the sum of individual particles crossing the section, regardless of the direction. Therefore, total transport that crosses this reference section may have originated at other locations, in particular the Drake Passage and Agulhas section, at many different times. These cold and warm mean contributions to the total transports decrease substantially in summer:  $17.9 \pm 2.3\%$  for the cold route and  $7.1 \pm 1.6\%$  for the warm route. The warm route contribution reaches the reference section mainly near the sea surface and the African continent, especially in summer, while the cold route particles are distributed more homogeneously along the reference section (Figure [3.82](#)). The predominant mean probability backwards trajectories are represented only for those particles that cross at any time the Drake Passage or Agulhas Current sampling sections (Figure [3.83](#)). Their water transport equivalences are 22.9 Sv and 9.1 Sv in austral summer and 25.1 Sv and 16.3 Sv for the cold and warm routes in austral winter, respectively (Table [3.26](#)).

Considering only those particles released back in austral summer, the bulk of the cold-fresh Southern waters takes between 4 and 6 years to reach the  $34^\circ\text{S}$  section (Figure [3.83f, h](#)), while most of the warm Agulhas waters last around 0.5 years (Figure [3.83b, d](#)).



In austral winter, the transit times are similar for water parcels coming from the Drake Passage. Regarding the warm waters, substantially more transport arrives from the Agulhas Current, taking a considerable part of them more than a year to be incorporated into the reference section. Both summer and winter particles follow the same pathways, with a slight change in the fraction of water, more visible in warm waters such as the subtropical gyre in winter (Figure 3.83c) and more likely to travel and disperse in the southern Indian Ocean in summer (Figure 3.83a). On average, there is higher variability in winter (SD of 0.07 Sv) as compared to summer (SD of 0.05 Sv) in both routes over the 75 years, reaching a maximum SD of 2.1 Sv for warm waters and 1.5 Sv for cold waters at the bulk of their contribution.

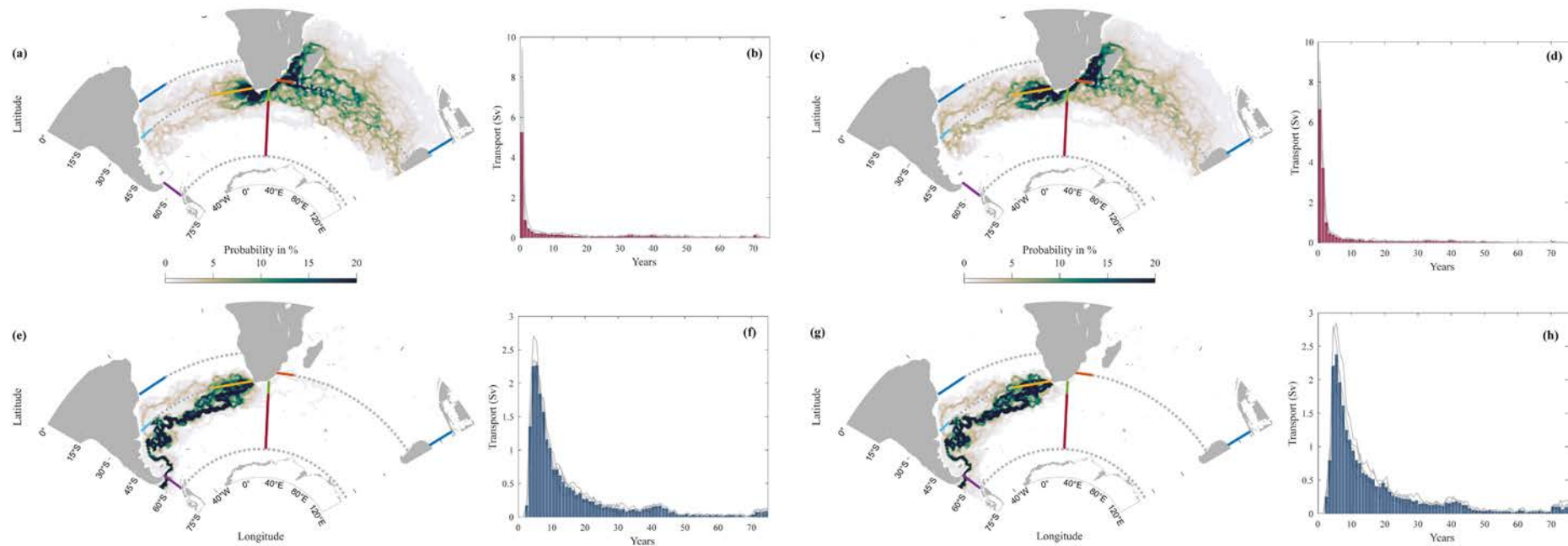


**Figure 3.83.** Mean probability distributions and time transits of (e, f, g, h) particles that follow the cold-water route and (a, b, c, d) particles that follow the warm route released in summer (a, b, e, f) and in winter (c, d, g, h). The grid used is  $0.5^\circ$  in latitude and  $1.3^\circ$  in longitude, having the same number of cells in both coordinates; each Lagrangian particle is only counted once per each grid cell.

The particle trajectories are very diverse, prevailing those that follow the SAC path in the cold-water route. Furthermore, the Mozambique Channel and Cape Basin regions stand out as a high probability area because of numerous mesoscale eddies where Lagrangian particles may get trapped for long periods, altering the mean transit times. Only about 30% of the released particles leave the domain completely after 75 years, and within this percentage, most of them reach the domain edge in less than 15 years independently of the route followed.

**Table 3.26.** Mean summer and winter AAIW transports at the reference section (eastern edge of subtropical gyre), the Drake Passage section and the Agulhas Current section, and the mode transit times to reach these last two sections from the reference section. The mode transit time corresponds to the most frequent time, coinciding with the peak of histograms in Figure 3.83b, d, f, h. Notice that the transport at the eastern margin of the subtropical gyre corresponds to the net (left) and total (right) sum of values, while for the Drake and Agulhas sections only the total transport.

|               | AAIW waters (26.8 - 27.5 kg m <sup>-3</sup> ) |                      |                        |                           |                        |
|---------------|---|----------------------|------------------------|---------------------------|------------------------|
|               | NET/TOTAL MEAN TRANSPORT (Sv)                 |                      |                        | MODE TRANSIT TIME (Years) |                        |
|               | Eastern margin of subtropical gyre (34°S)     | Drake Passage (64°W) | Agulhas Current (30°S) | Drake Passage (64°W)      | Agulhas Current (30°S) |
| <b>Winter</b> | 14.5 ± 4.4 / 132.6 ± 24.4                     | 25.1 ± 4.8           | 16.3 ± 4.2             | 5.3 ± 0.8                 | 0.8 ± 0.1              |
| <b>Summer</b> | 16.2 ± 4.1 / 127.6 ± 19.6                     | 22.9 ± 3.9           | 9.1 ± 2.4              | 5.6 ± 0.1                 | 0.3 ± 0.2              |

| YEARS       | AAIW waters (26.8 - 27.5 kg m <sup>-3</sup> ) |                        |                      |                        |
|-------------|---|------------------------|----------------------|------------------------|
|             | TOTAL MEAN TRANSPORT (Sv)                     |                        |                      |                        |
|             | Winter  |                        | Summer               |                        |
|             | Drake Passage (64°W)                          | Agulhas Current (30°S) | Drake Passage (64°W) | Agulhas Current (30°S) |
| <b>2015</b> | 23.5 ± 2.7                                    | 14.1 ± 1.1             | 22.7 ± 2.1           | 8.5 ± 2.9              |
| <b>2016</b> | 25.0 ± 3.7                                    | 19.2 ± 4.4             | 22.3 ± 5.1           | 10.9 ± 2.9             |
| <b>2017</b> | 27.9 ± 3.9                                    | 17.9 ± 2.3             | 21.5 ± 2.6           | 8.7 ± 1.6              |
| <b>2018</b> | 28.8 ± 5.7                                    | 18.1 ± 4.2             | 24.0 ± 4.4           | 8.2 ± 2.4              |
| <b>2019</b> | 20.3 ± 2.1                                    | 12.1 ± 3.4             | 24.3 ± 4.4           | 9.0 ± 1.4              |

The cold-water route can be divided into three main pathways (Figure 3.84d, e, f): the direct pathway, which represents 82.4 - 83.6% of the total particles that follow the cold route, equal to a mean transport of  $18.9 \pm 3.3$  Sv in summer and  $21.0 \pm 4.0$  Sv in winter, respectively, and two indirect pathways, which include the water parcels that recirculate in the western subtropical gyre before reaching the 34°S section and the waters that enter to the Indian Ocean and recirculate within the Agulhas basin before flowing back to the reference section via the Benguela Current (Figure 3.81a).

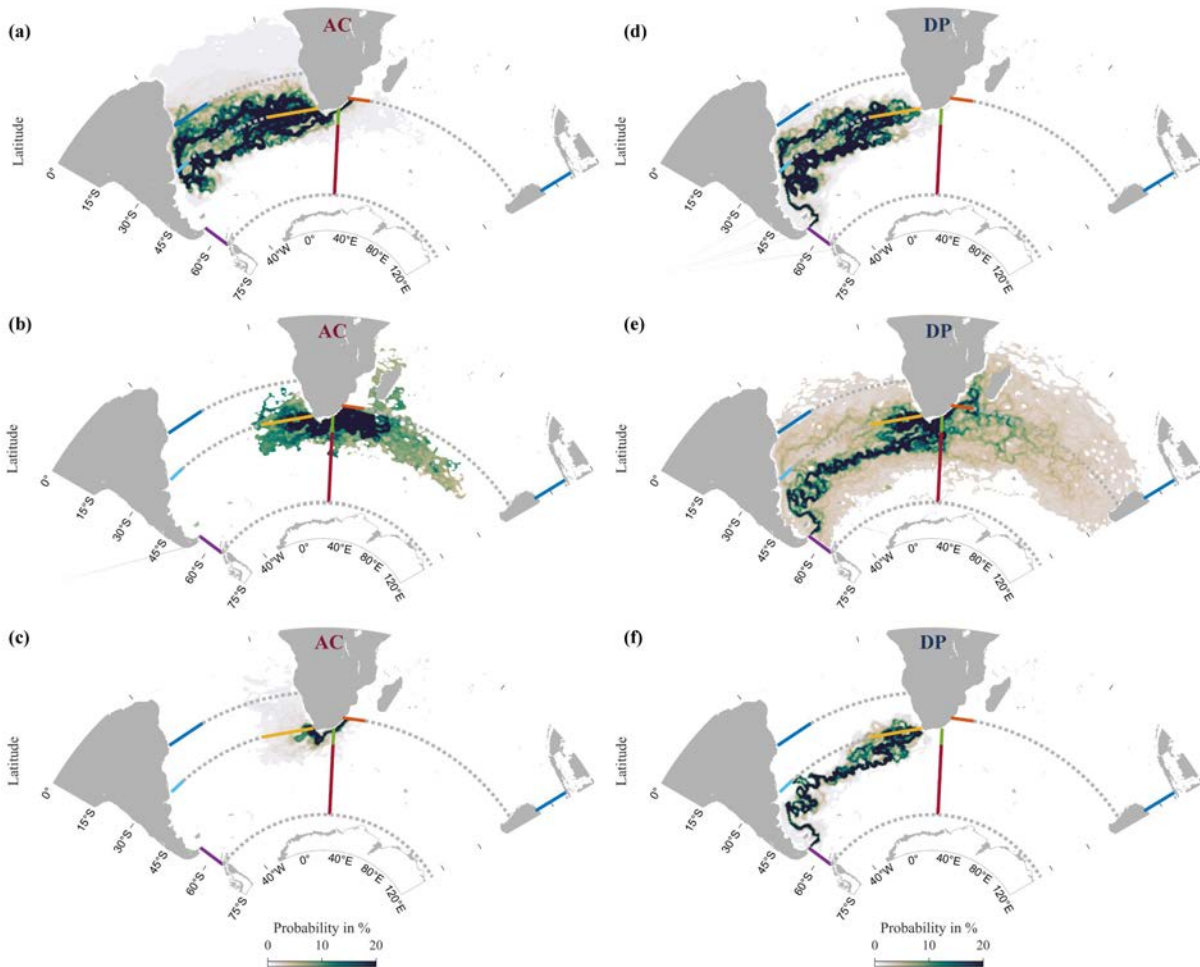


**Figure 3.84.** Mean probability distributions of (a, b, c) warm and (d, e, f) cold backwards trajectories until they reach the source section (AC or DP) of particles released in summer from the reference section: the indirect routes crossing (a, d) the western subtropical gyre, (b, e) the Indian Ocean, and (c, f) the direct route.

These two cold indirect pathways represent  $13.6 \pm 1.7\%$  and  $2.8 \pm 0.3\%$  in winter and  $15.9 \pm 1.4\%$  and  $1.7 \pm 0.2\%$ , in summer, respectively. Regarding the transit times, the direct incorporation constitutes the short pathway, taking a median of  $4.9 \pm 0.8$  and  $5.2 \pm 0.9$  years in winter and summer, respectively. The two cold indirect pathways constitute the tails of the histograms (Figure 3.83b, f, d, h), taking a median of  $9.1 \pm 12.1$  years when recirculating in the

western South Atlantic and a median of  $15.9 \pm 13.7$  years for those that recirculate in the Indian Ocean. The median of transit times provides estimates not skewed by a small proportion of extremely large or small times, together with the SDs from the mean illustrating the variability of these times. These large SDs of time depend on the presence of mesoscale eddies, the velocity difference between the ACC fronts and the South Atlantic currents, and the depth at which particles are flowing. Regardless of the season, both indirect cold routes can always be appreciated.

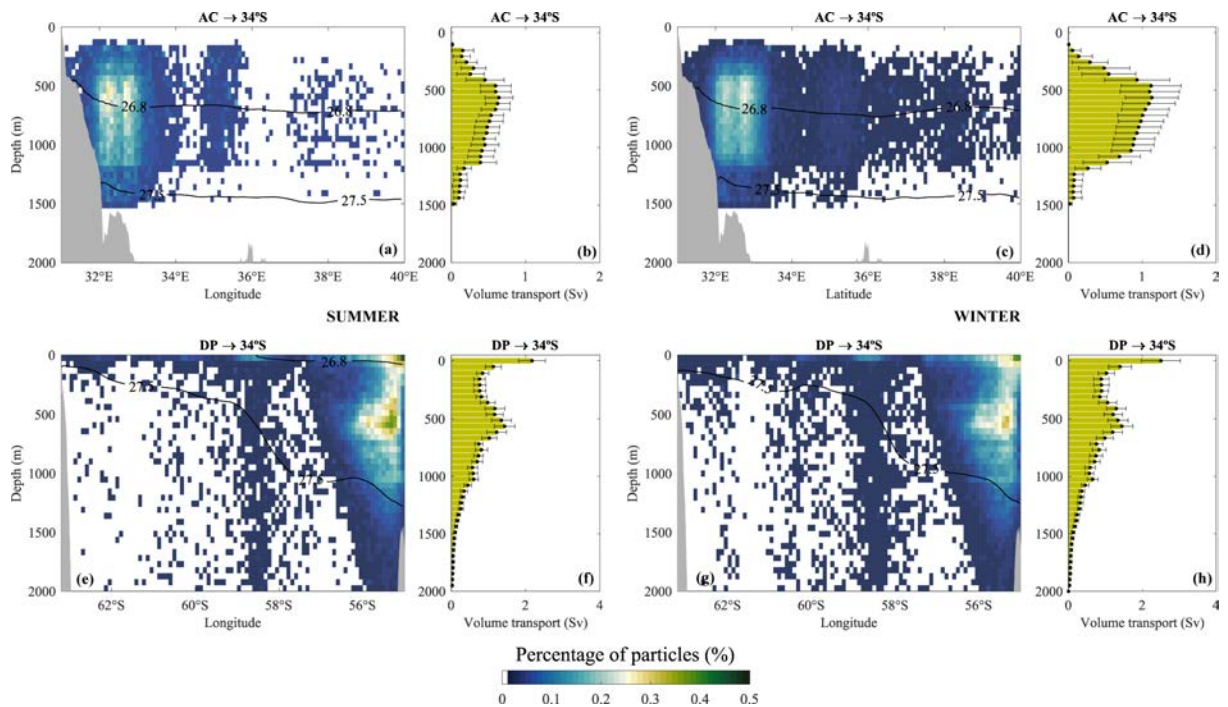


**Figure 3.85.** Percentage of particle distribution and the sum of their volume transport down to 2000 m at source sections: (a, b, c, d) Agulhas Current and (e, f, g, h) Drake Passage sections in summer and winter. The average potential density contours of  $26.8$  and  $27.5$   $\text{kg m}^{-3}$  for each season are plotted in solid lines. In grey is represented the bathymetry, the width of the green bars corresponds to 50 m and each bin is about  $0.1^\circ$  wide and 50 m depth.

Different routes can also be identified for the warm route into the reference section, largely dominated by the direct route from the Agulhas Current section (AC) but also with alternative pathways characterised by previous recirculations within the Atlantic and Indian Oceans (Figure 3.84a, b, c). In austral winter, the direct route feeds directly from the Agulhas Leakage, with 87.2% of the backtracked warm particles usually lasting less than one year (Figure 3.84c). On the one hand, the indirect trajectories that previously recirculate in the western subtropical gyre and cross the WSG section (Figure 3.81a) represent 7.6% of the particles and last between 8 and 21 years. On the other hand, 5.2% of the particles recirculate in the Indian Ocean crossing the IO section beyond  $40^\circ\text{E}$  (Figure 3.81b) before reaching the

34°S section, taking between 1 and 12 years. Both routes share trajectories crossing both the Drake and Agulhas sections (Figures 3.83a and 3.84e), indicating that cold waters proceeding from the Drake Passage also feed the Agulhas Current.

According to the source distribution (Figure 3.85), the warm-salty waters come mainly from the bulk of Agulhas Current, centred about 600 - 700 m (Figure 3.85a, c). In winter, the warm contribution is more spread throughout the entire section and its transport increases substantially. Regarding the cold-fresh route, the bulk of its transport is found between 0 - 50 m and 500 - 650 m, corresponding mainly to surface and intermediate waters. It comes from the Subantarctic Front, the most northern ACC front, usually found between 55°S and 56.5°S (Chapter 3.1). The seasonal variability of volume transport per depth is minimal, confirming a continuous cold and fresh water supply from the Drake Passage. Most particles that form the indirect cold route recirculating within the Indian Ocean arrive at the reference section close to the continent, together with the warm-water parcels (Figure 3.84e). The coinciding pathways suggest that both contributions probably mix before reaching the reference section.

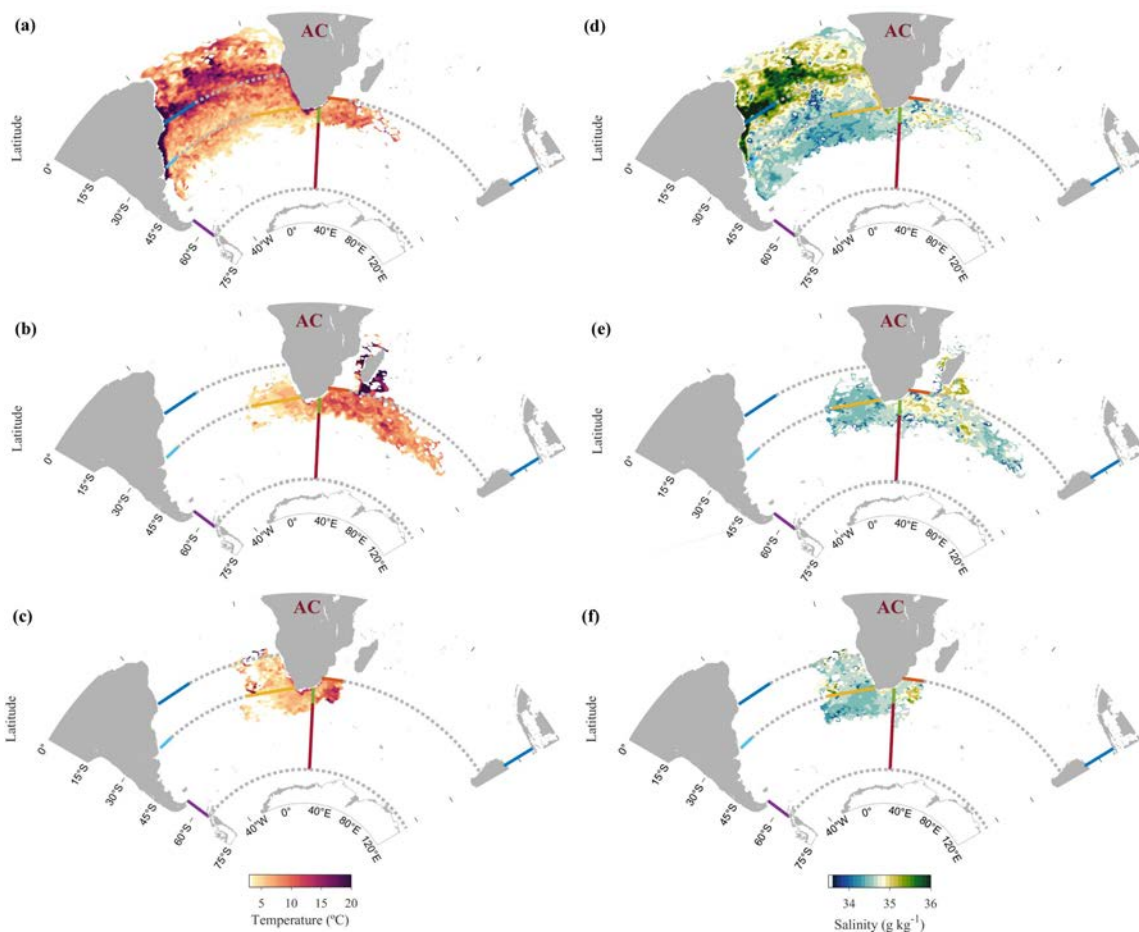


**Figure 3.86.** Thermohaline properties along the mean particle trajectories for the three main warm pathways for particles released on austral winter. (a, d) Indirect route across the western South Atlantic subtropical gyre; (b, e) indirect route after recirculating in the Indian Ocean; (c, f) direct route. Only pathways with a probability equal or higher than 0.5% are considered (Figure 3.84).

### 3.5.3.2. Thermohaline properties

During their transit through the South Atlantic Ocean, the AMOC intermediate waters experience significant thermohaline and density modifications (Figure 3.85). These changes in temperature and salinity along pathways are generally more pronounced when particles are close to the surface, as these waters are exposed to direct warming by solar heating, as well as to precipitation and evaporation processes.

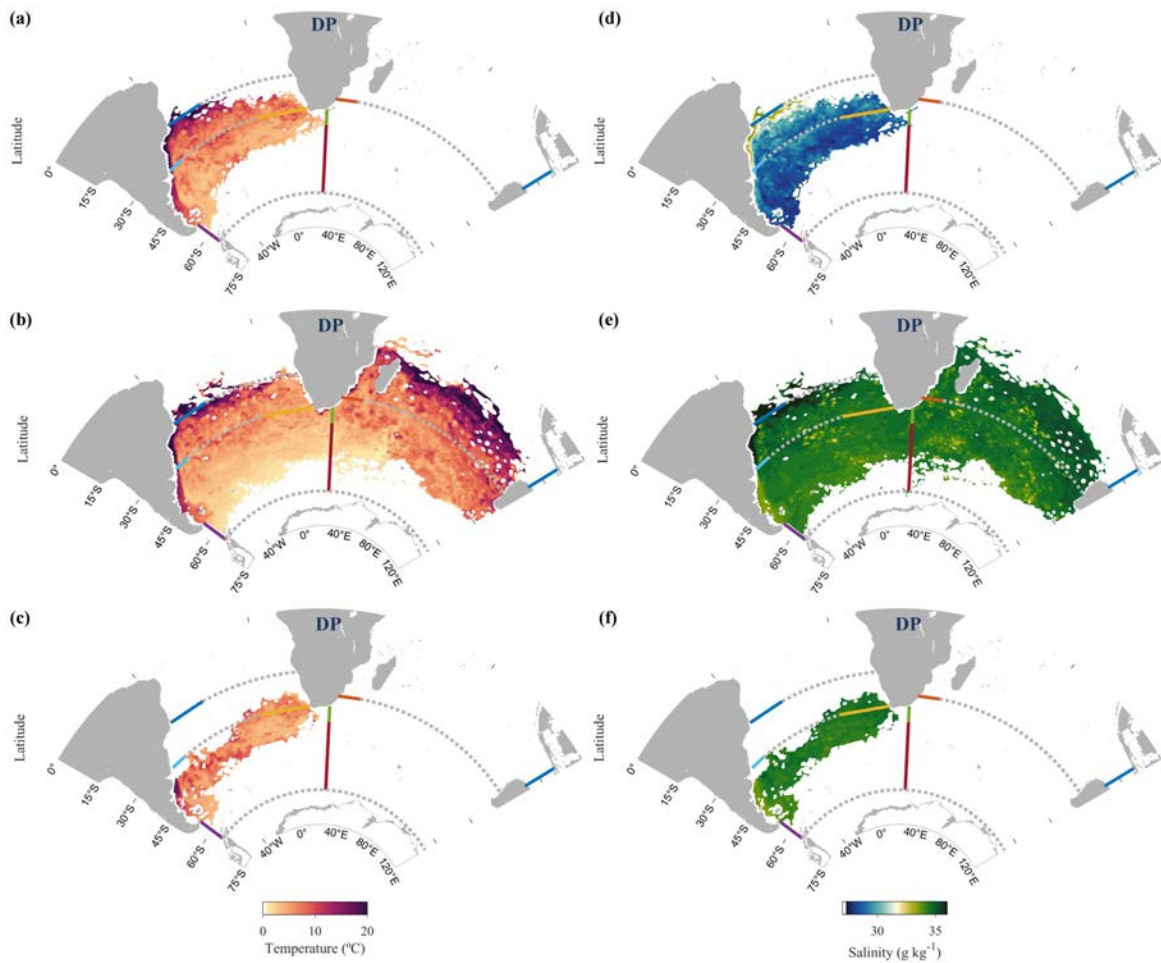


**Figure 3.87.** Thermohaline properties along the mean particle trajectories for the three main cold pathways for particles released in austral winter. (a, d) Indirect route across the western South Atlantic subtropical gyre; (b, e) indirect route after recirculating in the Indian Ocean; (c, f) direct route. Only pathways with a probability equal or higher than 0.5% are considered (Figure 3.84).

Figures 3.86 and 3.87 show the mean potential temperature and salinity along the three main warm and cold pathways, respectively, as computed from all particles released in austral winter. Regarding the warm route, those intermediate waters that upwell to the surface flowing across the Brazil Current, south Madagascar and along the Cape Basin regions reach warmer temperatures up to 27.6 °C while water parcels transiting at 40°S in the South Atlantic at greater depths remain cold with a fairly stable temperature around 5 °C.

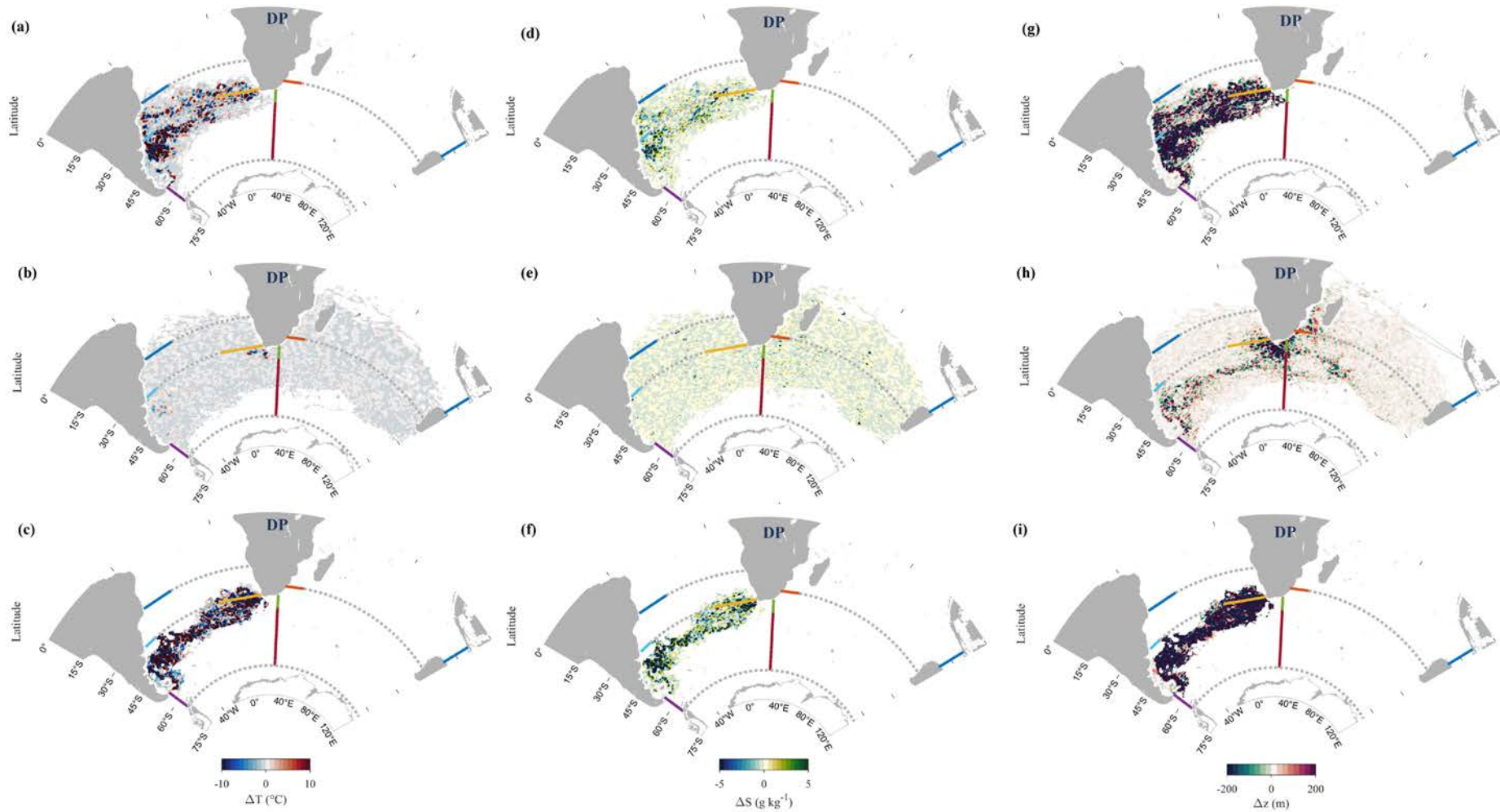


**Figure 3.88.** Thermohaline and depth variations along the mean particle trajectories for the three main cold pathways for particles released in austral winter. (a, d, g) Indirect route across the western South Atlantic subtropical gyre; (b, e, h) indirect route after recirculating in the Indian Ocean; (c, f, i) direct route. Only pathways with a probability equal or higher than 0.5% are considered, coinciding with the coloured distributions in Figure 3.84.

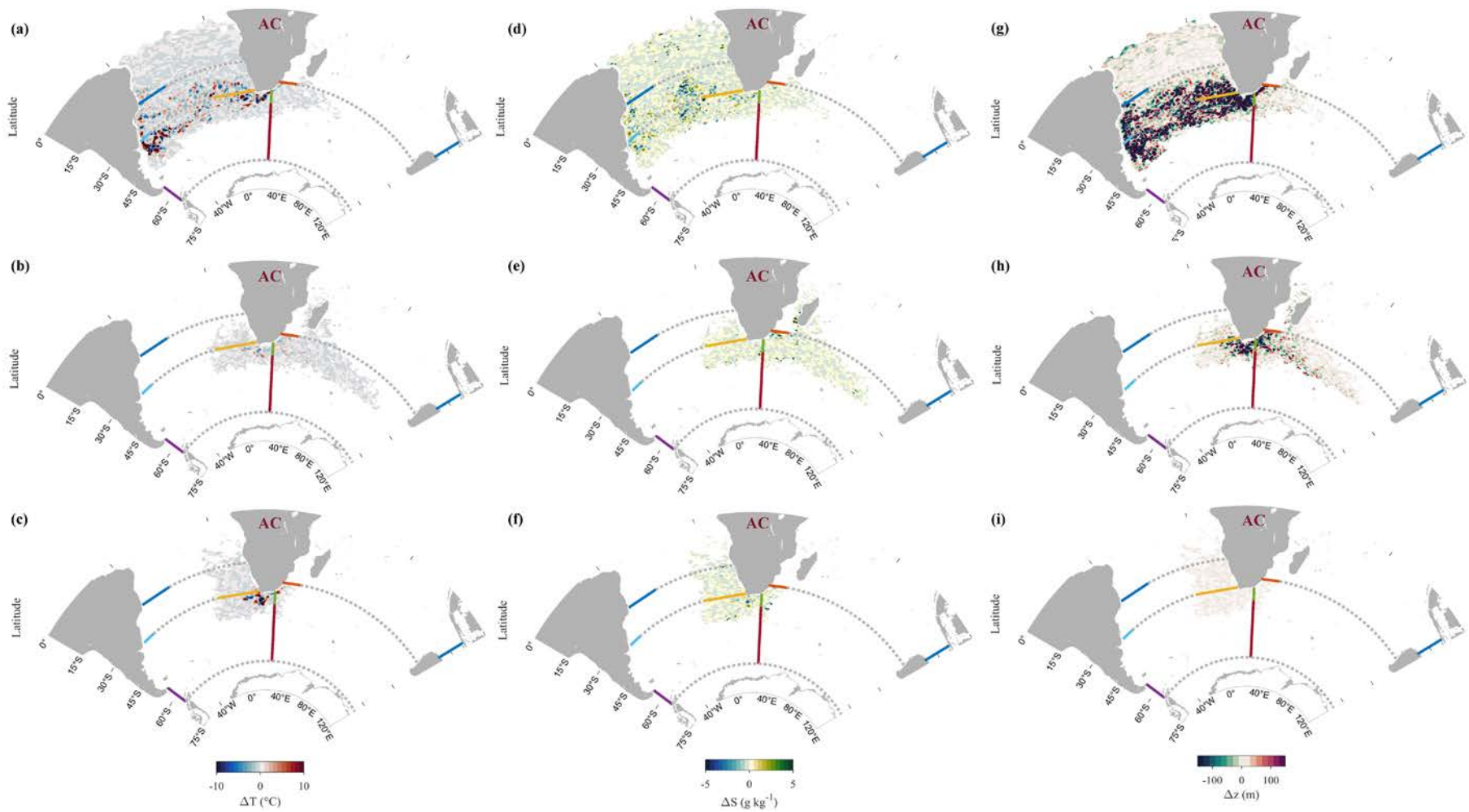


**Figure 3.89.** Thermohaline and depth variations along the mean particle trajectories for the three main warm pathways for particles released in austral winter. (a, d, g) Indirect route across the western South Atlantic subtropical gyre; (b, e, h) indirect route after recirculating in the Indian Ocean; (c, f, i) direct route. Only pathways with a probability equal or higher than 0.5% are considered, coinciding with the coloured distributions in Figure 3.84.



High salinities ( $> 35 \text{ g kg}^{-1}$ ) coincide with maximum temperatures, probably due to interaction and mixing with warmer and saltier waters. In terms of the cold route, the water parcels become warmer and saltier, becoming fresher those that previously recirculated in the western subtropical gyre. In particular, the fastest and highest changes in depth and thermohaline properties occur in the confluence zones of the Malvinas and Brazil Currents, and the Agulhas and South Atlantic Currents, influenced by mixing associated with mesoscale eddies (Figures 3.88 and 3.89)

**Table 3.27.** Potential temperature, salt and depth changes experienced by AAIW according to the individual warm and cold routes followed from either the Drake Passage section or the Agulhas Current section to the  $34^{\circ}\text{S}$  reference section for winter and summer. Negative/positive signs correspond to properties loss/gain.

| AAIW waters ( $26.8$ and $27.5 \text{ kg m}^{-3}$ ) |                    |                                       |                  |                             |                  |               |                |
|---|--------------------|---------------------------------------|------------------|-----------------------------|------------------|---------------|----------------|
| GAIN/LOSS   |                    | P. TEMPERATURE ( $^{\circ}\text{C}$ ) |                  | SALT ( $\text{g kg}^{-1}$ ) |                  | DEPTH (m)     |                |
|   |                    | Winter                                | Summer           | Winter                      | Summer           | Winter        | Summer         |
| Drake Passage ( $64^{\circ}\text{W}$ )              | Direct             | $-1.04 \pm 0.14$                      | $-0.98 \pm 0.29$ | $-0.27 \pm 0.02$            | $-0.29 \pm 0.06$ | $-374 \pm 26$ | $-460 \pm 160$ |
|   | Indirect West Gyre | $-1.36 \pm 0.19$                      | $-1.22 \pm 0.30$ | $-0.23 \pm 0.02$            | $-0.24 \pm 0.08$ | $-252 \pm 38$ | $-307 \pm 145$ |
|   | Indirect Indian    | $-1.09 \pm 0.15$                      | $-0.99 \pm 0.29$ | $-0.26 \pm 0.02$            | $-0.28 \pm 0.07$ | $-368 \pm 29$ | $-456 \pm 161$ |
| Agulhas Current ( $30^{\circ}\text{S}$ )            | Direct             | $2.19 \pm 0.51$                       | $2.29 \pm 0.97$  | $0.19 \pm 0.11$             | $0.22 \pm 0.11$  | $272 \pm 46$  | $265 \pm 108$  |
|   | Indirect West Gyre | $2.42 \pm 0.54$                       | $3.56 \pm 2.87$  | $0.18 \pm 0.20$             | $0.23 \pm 0.27$  | $112 \pm 60$  | $58 \pm 212$   |
|   | Indirect Indian    | $5.2 \pm 1.37$                        | $3.12 \pm 1.39$  | $0.37 \pm 0.12$             | $0.26 \pm 0.14$  | $108 \pm 86$  | $198 \pm 88$   |

Particles released in austral winter that follow the direct warm path from the reference section to the Agulhas Current gain a mean of  $2.2 \pm 0.5 \text{ }^{\circ}\text{C}$  in potential temperature and  $0.2 \pm 0.1 \text{ g kg}^{-1}$  in salt, sinking  $272 \pm 46 \text{ m}$ . Similarly, particles that follow the direct cold path from the reference section to the Drake Passage lose a mean of  $1.0 \pm 0.1 \text{ }^{\circ}\text{C}$  in potential temperature and  $0.3 \pm 0.0$  in salt and upwelling  $374 \pm 26 \text{ m}$  (Table 3.27). These variations are slightly higher during austral summer. Regarding the warm indirect routes, the pathway through the recirculation in the Indian Ocean experiences the largest thermohaline variations, followed by the recirculation in the western subtropical gyre, with smaller depth changes than in the direct warm route. On the other hand, the indirect cold routes do not experience changes

substantially different from those experienced by the direct route, probably because they have already freshened and cooled when reaching higher latitudes.

### 3.5.3.3. Density variations and water mass transformations

The changes in the thermohaline properties translate into potential density variations and, if density alterations are considerable, into water mass transformations. To quantify these changes, we analyse the conservative temperature and absolute salinity variations between the origin (the Drake Passage or the Agulhas Current) and the reference section for each contribution and season (Figures 3.90 and 3.91). Also, the potential density gained or lost has been quantified as well as the particle percentage distribution in the diagrams.

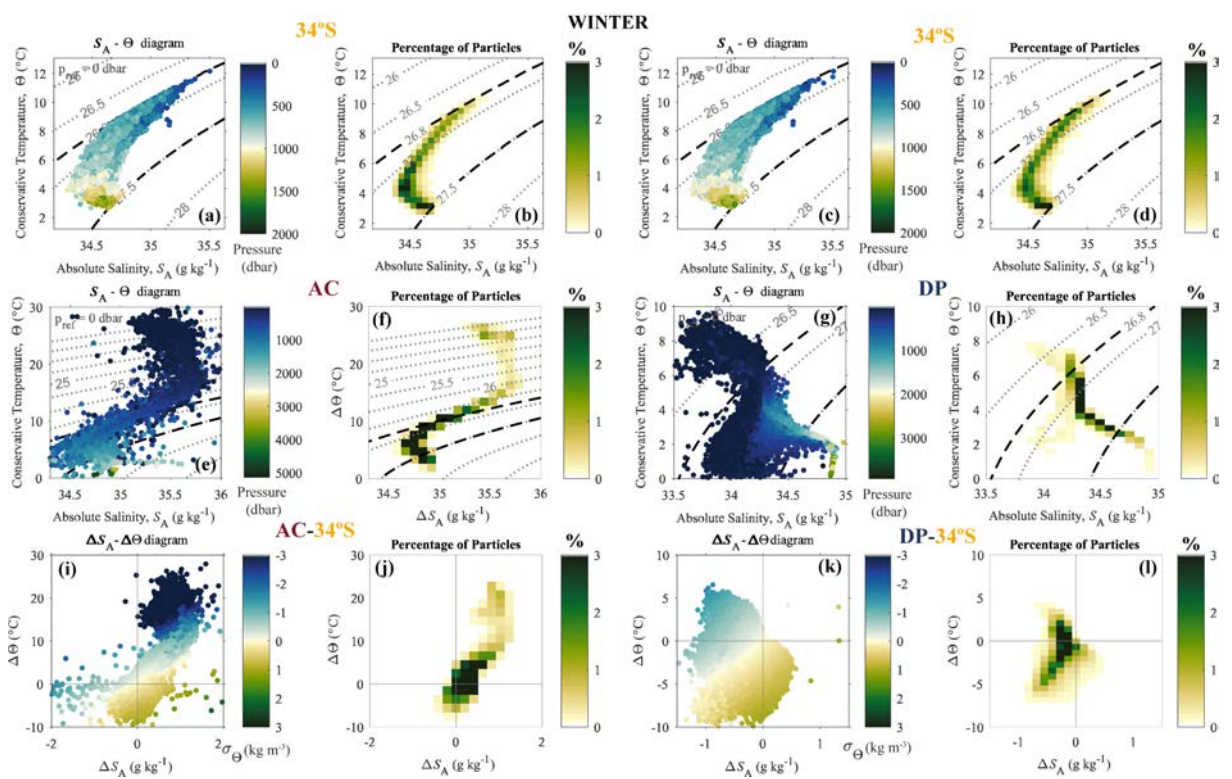


**Figure 3.90.** (a, e, c, g) Conservative temperature-absolute salinity diagrams,  $S_A - \theta$ , at the reference and source sections in the Drake Passage and the Agulhas Current for particles released in austral winter. (i, k) Diagrams of the variations of conservative temperature and absolute salinity ( $\Delta S_A - \Delta\theta$ ) of the intermediate water parcels between the reference section and at the source section in the Drake Passage or the Agulhas system, together with the resulting potential density gain or loss (colour; positive/negative for gain/loss). The particles percentage distribution in the diagrams is represented in the respective right panels (b, d, f, h, j, l).

In the reference section, both in summer and winter, the absolute salinity ranges from 34.3 to 35.5 g kg<sup>-1</sup> and the conservative temperature varies from 2.7 °C to 12.1 °C. However, in

the Agulhas Current and Drake Passage source regions, the maximum conservative temperatures reach 30.1 °C and 9.8 °C, respectively. In terms of potential density changes, the Agulhas water gains a mean of  $0.5 \pm 2.3 \text{ kg m}^{-3}$  in their transit, being less denser in their source. Net changes in potential density for the cold contribution are scarce, with a mean gain of  $0.08 \pm 0.4 \text{ kg m}^{-3}$  in their transit. The difference between the initial/final distributions allows quantifying the net transformation of water masses (Figure 3.92) according to the upper ( $\sigma < 26.8 \text{ kg m}^{-3}$ ), intermediate ( $26.8 < \sigma < 27.5 \text{ kg m}^{-3}$ ) and deep ( $\sigma > 27.5 \text{ kg m}^{-3}$ ) waters.

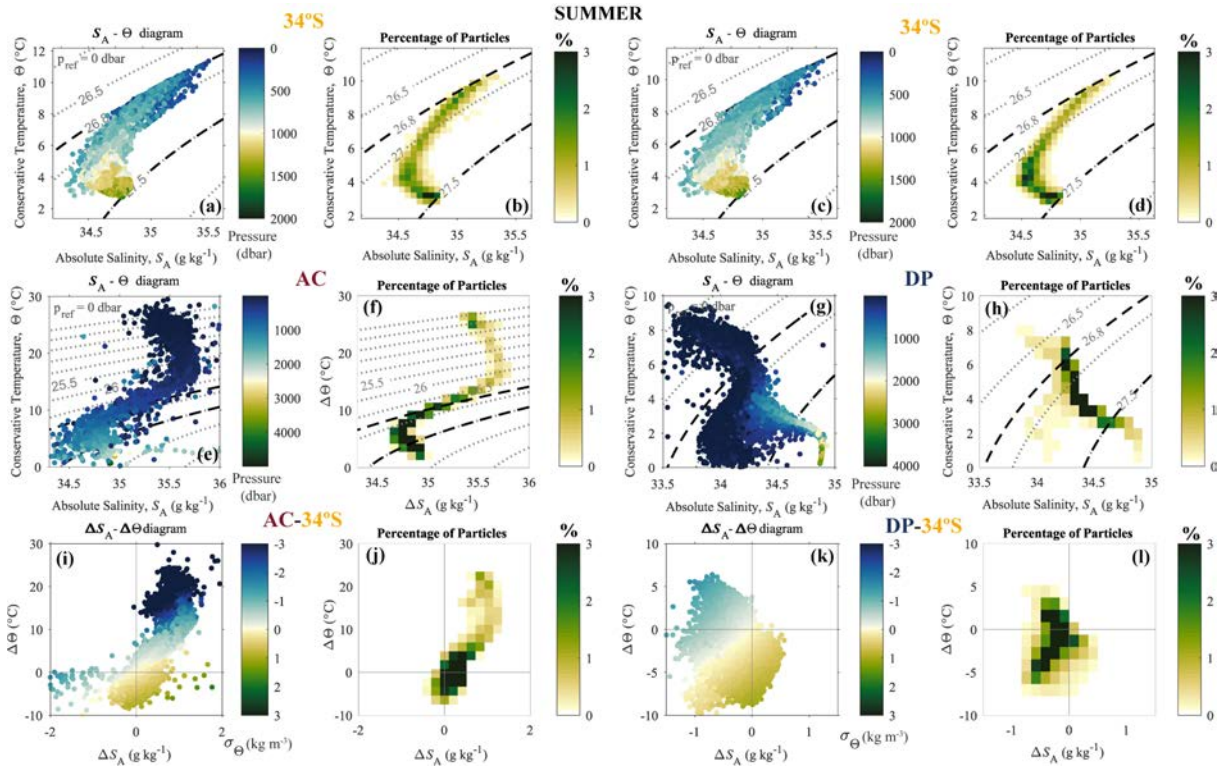


**Figure 3.91.** (a, e, c, g) Conservative temperature-absolute salinity diagrams,  $S_A - \theta$ , at the reference and source sections in the Drake Passage and the Agulhas Current for particles released in austral summer. (i, k) Diagrams of the variations of conservative temperature and absolute salinity ( $\Delta S_A - \Delta \theta$ ) of the intermediate water parcels between the reference section and at the source section in the Drake Passage or the Agulhas system, together with the resulting potential density gain or loss (colour; positive/negative for gain/loss). The particles percentage distribution in the diagrams is represented in the respective right panels (b, d, f, h, j, l).

For particles released in winter, most of the cold-water route transport (22.3 Sv out of 25.1 Sv) essentially maintains the potential density characteristics of the intermediate waters, especially for densities between  $27.0 \text{ kg m}^{-3}$  and  $27.1 \text{ kg m}^{-3}$ . Regarding the warm-water route, a mean of 16.3 Sv leaves the Agulhas Current to the reference section split into 3.7 Sv of upper waters, 10.6 Sv of intermediate waters and 2.0 Sv of deep waters (Figure 3.92e, f). Hence, most of the warm route contribution essentially maintains the original potential density (65.0% of

the total particles that cross through the AC section). In austral summer, the transport of upper and deep waters crossing this AC section that are transformed to intermediate waters are slightly less, with 2.2 Sv and 1.8 Sv, respectively, maintaining also most of the warm waters, 5.1 Sv, its original potential density. From the cold-water route to the reference section arrive 22.9 Sv, slightly less than in winter (Table 3.26). Among these, 20.4 Sv maintained their potential density characteristics while 1.5 Sv gained potential density and 1.0 became lighter flowing to the reference section. Furthermore, we observed that the warm water transformations present a large seasonal variability that can double in the winter as compared to summer (Figure 3.92f, h).

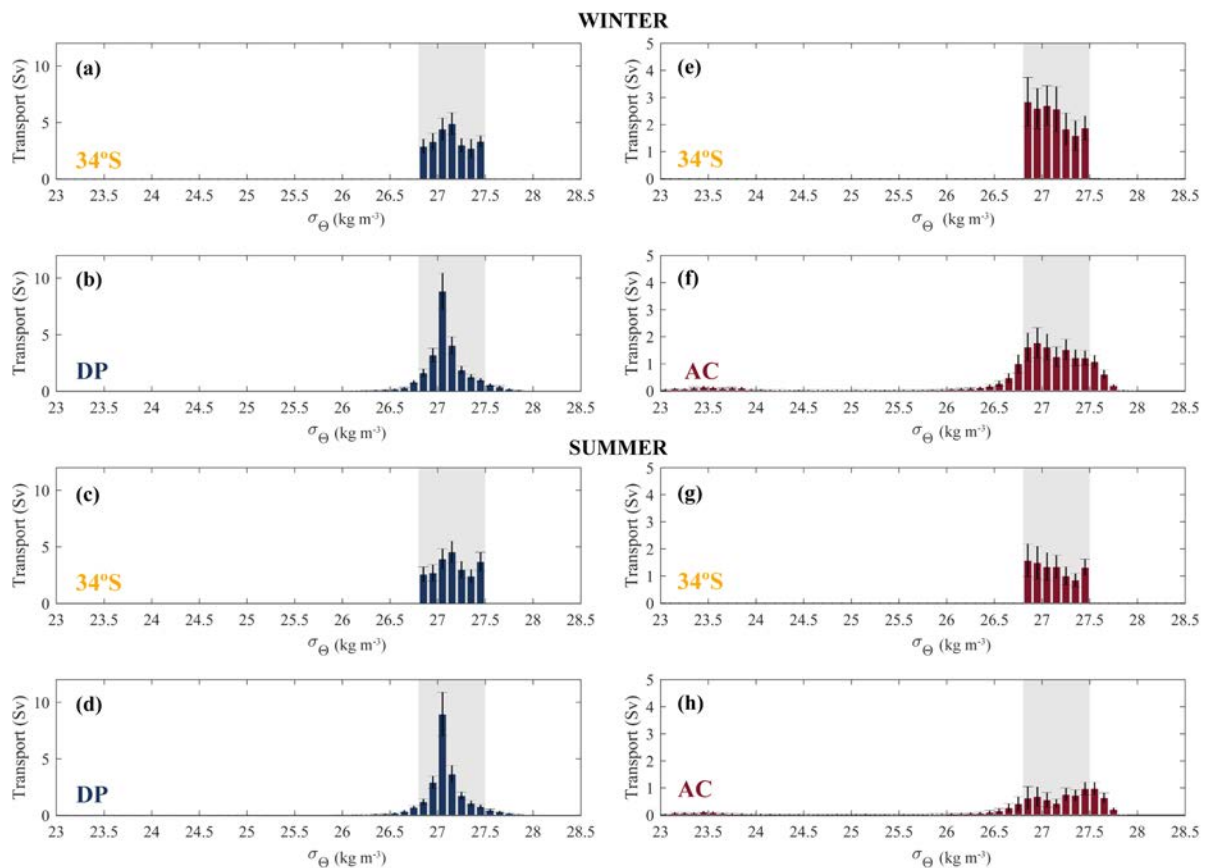


**Figure 3.92.** AAIW transport that experienced water mass transformations along the cold (left, in blue) or warm (right, in red) routes, according to their potential density, at Drake Passage (b, d) or Agulhas Current (f, h) and at the reference section (a, c, e, g). The smooth grey area divides the upper (left;  $\sigma < 26.8$  kg m<sup>-3</sup>), intermediate (grey shaded;  $26.8 < \sigma < 27.5$  kg m<sup>-3</sup>) and deep (right;  $\sigma > 27.5$  kg m<sup>-3</sup>) potential density ranges.

Regarding the water mass transformations experienced along each route, while the cold direct route dominates the intermediate water mass transformations,  $2.0 \pm 0.3$  Sv in summer and  $1.8 \pm 0.2$  Sv in winter, in the warm route more intermediate water changes its potential density when recirculates first in the western subtropical gyre,  $0.8 \pm 0.2$  Sv and  $0.5 \pm$

0.1 Sv, respectively (Table 3.28). For the cold direct route transformations, the 60 - 67% correspond to upper waters that gain density being transformed to AAIW. In the indirect cold pathways, the sum of transport transformed of upper and deep waters is similar for those that recirculate first in the western subtropical gyre, whereas in the indirect Indian Ocean pathway, deep waters getting lighter dominate the water mass transformations with transports of 0.1 - 0.2 Sv. For the AAIW waters originated in the Agulhas Current, the upper waters always undergo the largest potential density changes except for waters that first recirculate in the western edge of the subtropical gyre, displaying a more similar ratio of upper and deep transformed waters.

**Table 3.28.** Transport transformations suffered by AAIW according to the individual warm and cold routes followed from their source to the reference section depending on the release season. Negative/positive signs correspond to potential density loss/gain. The net transformation is quantified for upper ( $\sigma < 26.8 \text{ kg m}^{-3}$ ), intermediate ( $26.8 < \sigma < 27.5 \text{ kg m}^{-3}$ ), and deep ( $\sigma > 27.5 \text{ kg m}^{-3}$ ) waters.

| POTENTIAL DENSITY GAIN/LOSS ( $\text{kg m}^{-3}$ ) |                    | AAIW Transport (Sv) |                        |                 |                 |                        |                 |
|--|--------------------|---------------------|------------------------|-----------------|-----------------|------------------------|-----------------|
|  |                    | SUMMER              |                        |                 | WINTER          |                        |                 |
|  |                    | $\sigma < 26.8$     | $26.8 < \sigma < 27.5$ | $27.5 < \sigma$ | $\sigma < 26.8$ | $26.8 < \sigma < 27.5$ | $27.5 < \sigma$ |
| Drake Passage (64°W)                               | Direct             | 1.34 ± 0.22         | -2.00 ± 0.34           | 0.66 ± 0.13     | 1.06 ± 0.16     | -1.78 ± 0.19           | 0.72 ± 0.04     |
|  | Indirect West Gyre | 0.25 ± 0.05         | -0.50 ± 0.10           | 0.25 ± 0.06     | 0.20 ± 0.05     | -0.32 ± 0.07           | 0.12 ± 0.04     |
|  | Indirect Indian    | 0.02 ± 0.01         | -0.16 ± 0.04           | 0.14 ± 0.03     | 0.02 ± 0.01     | -0.25 ± 0.03           | 0.23 ± 0.03     |
| Agulhas Current (30°S)                             | Direct             | 0.48 ± 0.03         | -0.53 ± 0.05           | 0.05 ± 0.01     | 0.18 ± 0.08     | -0.22 ± 0.08           | 0.04 ± 0.02     |
|  | Indirect West Gyre | 0.36 ± 0.12         | -0.77 ± 0.20           | 0.39 ± 0.10     | 0.25 ± 0.04     | -0.50 ± 0.09           | 0.25 ± 0.05     |
|  | Indirect Indian    | 0.12 ± 0.06         | -0.16 ± 0.06           | 0.04 ± 0.01     | 0.45 ± 0.09     | -0.64 ± 0.09           | 0.09 ± 0.03     |

### 3.5.4. Discussion

#### 3.5.4.1. Cold and warm contribution through the Agulhas Current

The Agulhas Leakage contribution to the South Atlantic Ocean is composed of waters originated from the Indonesian Throughflow, from the Tasman Leakage, and from the ACC

waters after circulating in the Indian Ocean subtropical gyre (Gordon, 1986; Le Bars et al., 2013; Speich et al., 2001, 2002; Gordon et al., 1992; R  hs, 2018). Here, we are not able to differentiate if the Tasman leakage is also fed by the Southern Ocean waters, by the South Indian Current or by the Pacific waters that follow the East Australian Current to derive into the Flinders Current. However, particle trajectories present in both cold and warm individual pathways confirm that part of Drake Passage waters feeds the Agulhas Current before eventually being incorporated as intermediate waters at the 34 S section. To distinguish the original source of Agulhas waters, a new section has been included from 10 S to 20 S along 115 W that would cover all the water entering through the Indonesian Throughflow (ITF section in Figure 3.81a).

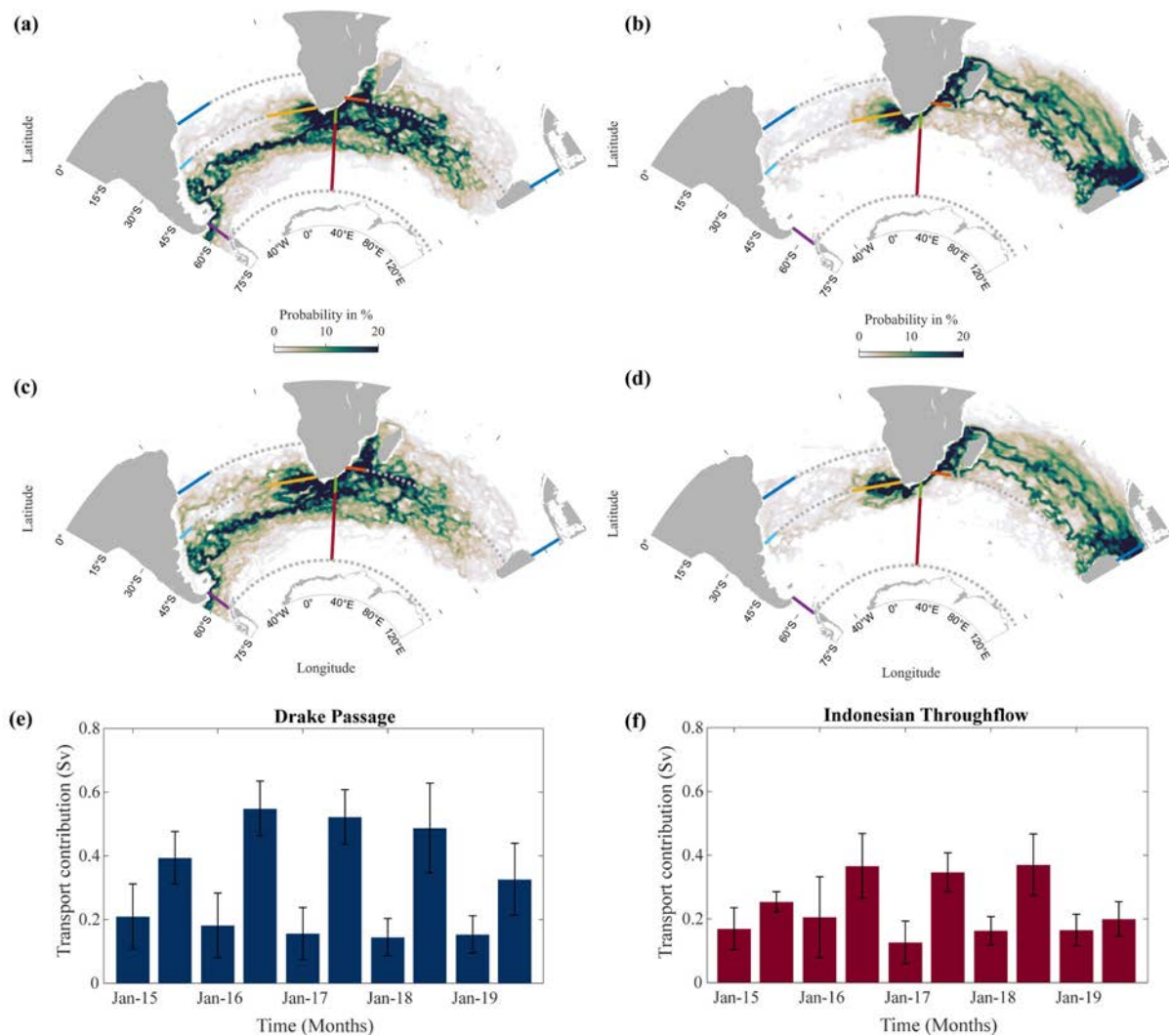


**Figure 3.93.** Mean probability distributions of particle trajectories that follow from the Agulhas Current section to the reference section in (a, b) winter and (c, d) summer, and their transport time evolution (e, f) from the Drake Passage and the Indonesian Throughflow.

Of the 22.9 - 25.1 Sv that conform the entire cold-water route in summer and winter, a total mean of  $0.3 \pm 0.2$  Sv feeds the Agulhas Current, whereas a total mean of  $0.2 \pm 0.1$  Sv come

from the ITF, contributing both sources in a similar amount after 75 years (Figure 3.93). These transports represent 1.9 - 2.8%, from the Drake Passage in summer and winter, and 1.8 - 1.9%, from the Indonesian Throughflow for the same seasons, of the total Agulhas Leakage contribution to the reference section at 34°S (Table 3.26).

Although the particles coming from the cold route have to cross entirely the South Atlantic and recirculate in the Indian Ocean, most of them take only twice the ITF waters transit times, between 12.5 and 15 years in front of 5 to 7.5 years. In addition, warm waters coming from the Pacific through the Indonesian Throughflow have an initial salinity and wide temperature ranges between 0.65 - 19.5 °C and 34.3 - 35.7 g kg<sup>-1</sup>, while those coming from the Drake Passage have mostly an initial temperature and salinity between 0.9 - 5.3 °C and 33.7 - 34.9 g kg<sup>-1</sup>. Their characteristic physical and biogeochemical properties, their proportion and the density alterations experienced along these two routes define the Agulhas Current water properties, each source contributing with its own water characteristics.

#### 3.5.4.2. Interannual variability

Until now, the cold- and warm-water routes have been compared thoroughly between two opposite seasons, summer and winter, looping the 5-year velocity fields repeatedly. However, the Lagrangian experiments looping the 1-year velocity fields for each year from 2015 to 2019, and their comparison may reveal large interannual variability strongly influenced by atmospheric oscillations or events (Figure 3.94).

First, this interannual variability is assessed in terms of volume transport, percentage of Lagrangian particles released, and transit time (Figure 3.95). The Agulhas Current contributes a mean of  $17.6 \pm 8.8$  Sv in front of  $17.5 \pm 6.2$  Sv, which contributes to the cold waters from the Drake Passage source. However, the warm waters not always exceed the cold contribution, the latter being higher at the beginning and at the end of the period, except for austral winter 2019, having a very strong seasonal variability, while the net transport at 34°S remains almost constant (Figure 3.95a). Regarding the individual paths, the direct cold and warm routes dominate with a mean of 83% and 86%, respectively; this proportion remains practically steady for the whole period even though the total transports increase in the winters of 2016 and 2017 for the warm and cold routes, respectively. The transit times for the total cold and water routes are practically constant, with an average of  $0.5 \pm 0.2$  years and  $4.9 \pm 0.6$  years, taking the cold route a maximum of 6.4 years in summer 2016 (Figure 3.95g).

The interannual variability is also present in the thermohaline and depth changes along the period (Figure 3.96). In the cases of the cold indirect that recirculate in the Indian Ocean and direct pathways, they experience potential temperature minimum and depth maximum differences around 0.9 °C and 200 m at the beginning and end of the 2015 - 2019 period.

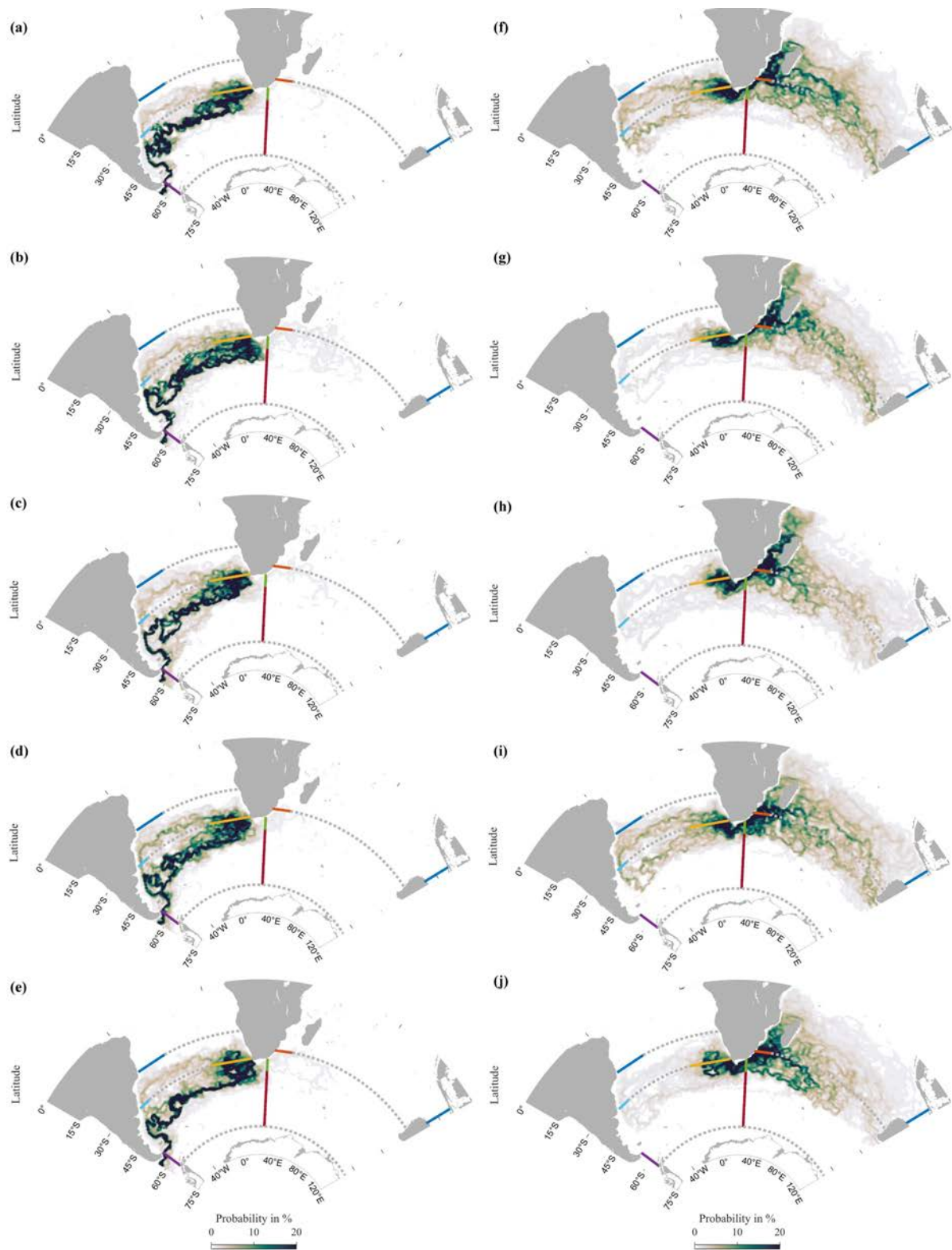


**Figure 3.94.** Probability distribution of particles released in austral winter looping 1-year velocity fields for 75 years. The left panels (a, b, c, d, e) correspond to the trajectories that cross the Drake Passage, while the right panels (f, g, h, i, j) to those that cross the Agulhas Current in (a, f) 2015, (b, g) 2016, (c, h) 2017, (d, i) 2018 and (e, j) 2019.



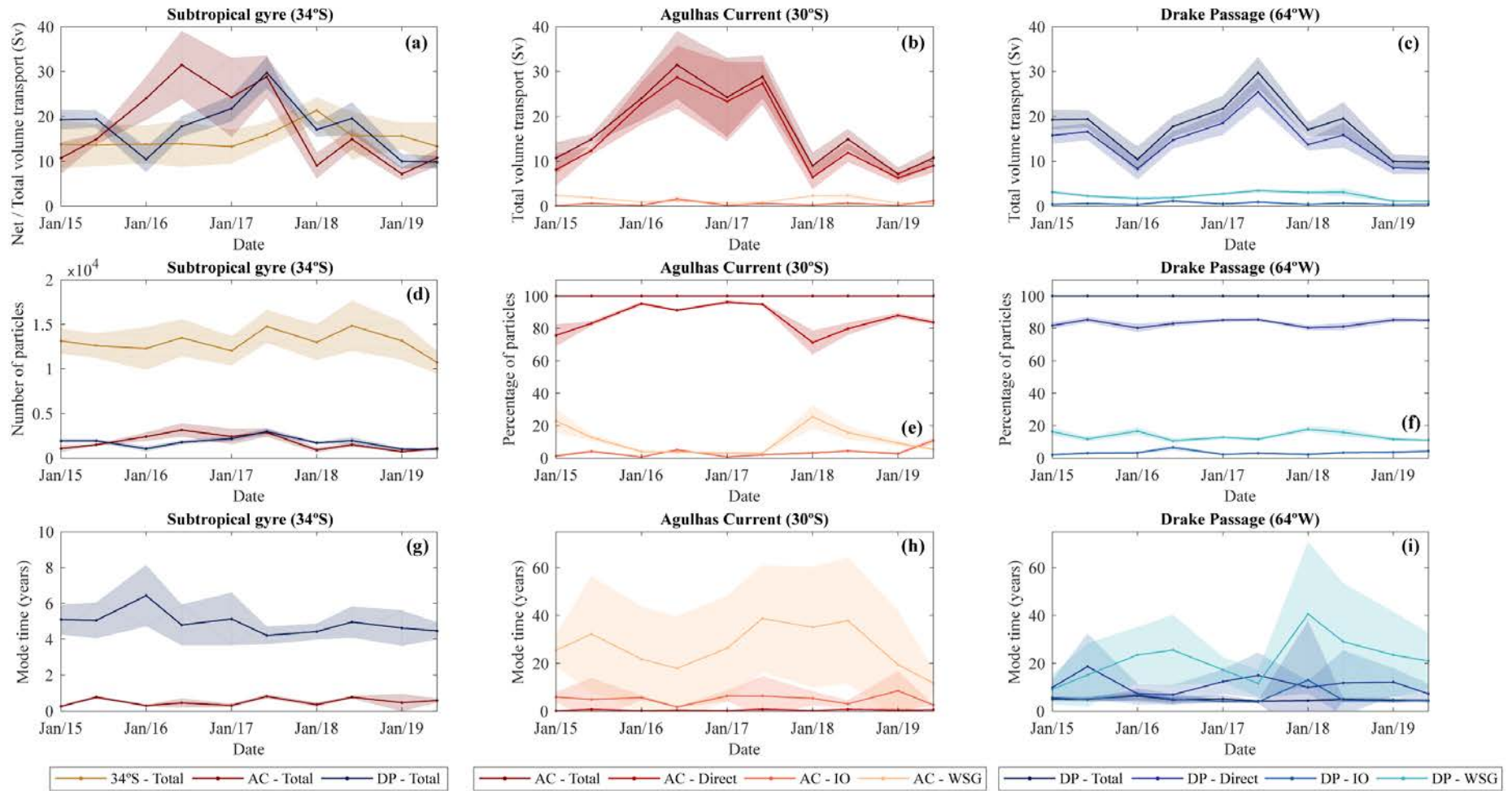


**Figure 3.95.** (a, b, c) Net/Total volume transport percentage, (d, e, f) number of Lagrangian particles (d, e, f), and (g, h, i) transit times for the total and individual cold (in blue) or warm (in red) routes at 34°S for one-year repeated loops (2015 to 2019 years) during 75 years. The abbreviations WSG and IO refer to the indirect pathways recirculating in the Indian Ocean and in the western subtropical gyre. The mode transit time corresponds to the most frequent time.

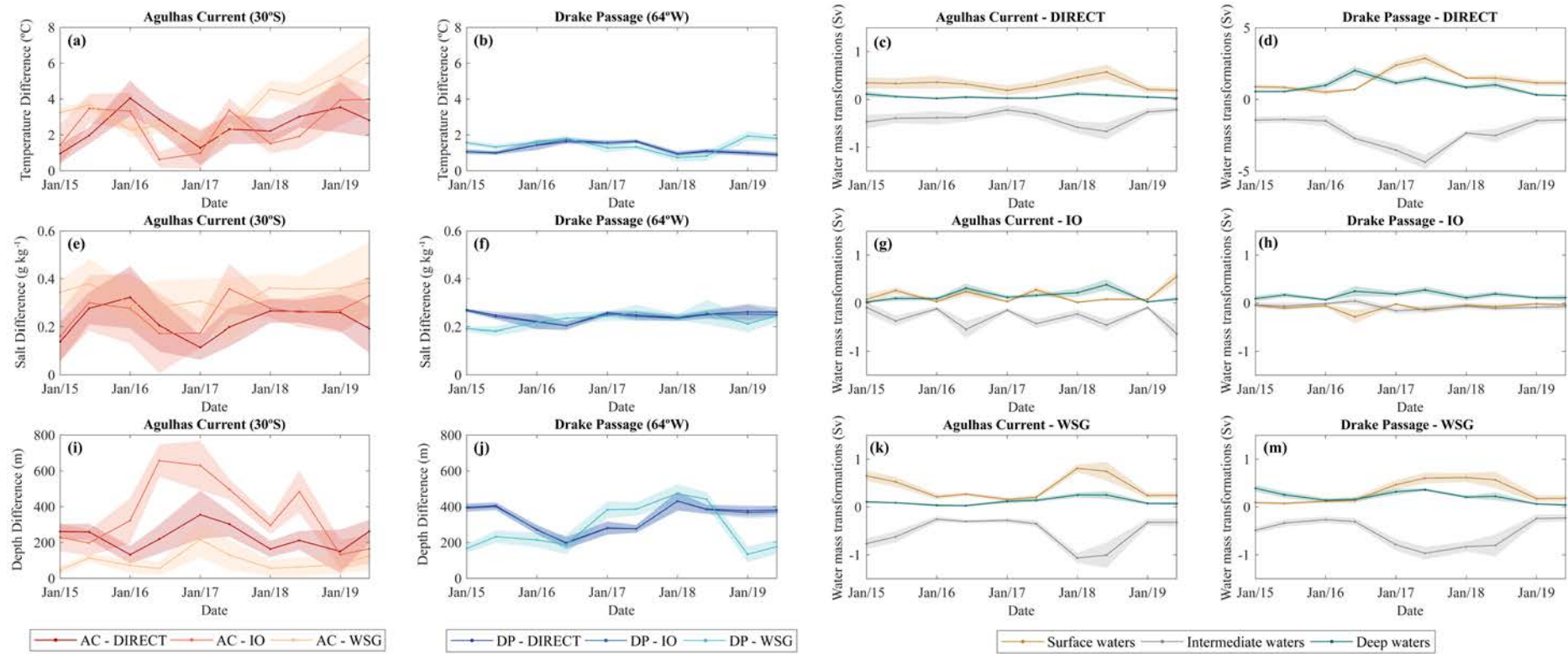


**Figure 3.96.** (a, b, e, f, i, j) Thermohaline and depth differences, and (c, d, g, h, k, m) water mass transformations along the individual pathways of the cold (in blue) and warm (in red) routes from their source at 34°S for one-year repeated loops (2015 to 2019 years) during 75 years. The abbreviations WSG and IO refer to the individual indirect pathways recirculating in the Indian Ocean or in the western edge of the subtropical gyre.

The indirect route that recirculates in the western subtropical gyre presents the opposite trend in the same properties. In general, the salinity remains almost constant for both routes, without any interannual salt variability higher than  $0.5 \text{ g kg}^{-1}$ . The depth difference in the cold waters displays a clear tendency, increasing for the direct path around 200 m in the last years, accompanied by a reduction of potential density changes and water mass transformations (Figure 3.96j, b, d). Regarding the warm route, the waters display a warming tendency for all the individual paths but with smaller density changes (Figure 3.96a, c). The individual warm indirect route that recirculates in the Indian Ocean has a very important seasonal component of around  $0.4 \text{ kg m}^{-3}$ , revealing that intermediate waters experience more potential density changes when particles are released in austral winter (Figure 3.96g).

Finally, this interannual variability also alters the volume of water mass transformations (Figure 3.96c, d, g, h, k, m). In general, the main contribution maintains their intermediate potential density, with the total amount of surface waters transformed into intermediate water always being less than 1.0 Sv, except for the cold direct pathway. Some years display large water mass transformations, such as along the direct cold route in the austral winter of 2017, when 4.4 Sv of surface waters are transformed into intermediate waters; this occurs simultaneously with the large transformations displayed by particles that recirculate in the western edge of the subtropical gyre (Figure 3.96d, m). In contrast, the indirect route that recirculates in the Indian Ocean appears to experience less interannual variations in the water mass transformations.

#### 3.5.4.3. Comparison with previous estimates

Our results show that looping 1-year the thermohaline and velocity fields, the cold and warm routes yielded comparable volumetric contributions to the upper limb of the AMOC for some years. Instead, when looping the 5-year fields, the cold-water contribution is substantially higher than the warm-water contribution and larger than previously inferred by other authors. Early calculations using coarse-resolution models identified a 6%–13% ratio between cold and warm transports (Speich et al., 2001, 2007; Donners & Drijfhout, 2004). Rodrigues et al. (2010) estimated from observations that the cold contribution might represent 36% of the total and R  hs et al. (2019) used a high-resolution circulation model to suggest that the cold contribution represents around 40% of the total. According to these authors, the AC transport contribution to the intermediate waters is always the largest, varying between 31% and 43%. However, considering only intermediate waters and the 2015 - 2019 period, we estimate that the cold contribution represents a mean ratio of 61% in winter and 72% in summer of the total routes transport.

Our results have shown that the direct pathway dominates in both water routes, but they have also shown that the indirect contributions cannot be neglected. Rühls et al. (2019) do not consider the indirect routes stating that most particles follow a relatively direct path to the Atlantic through the northern part of the Drake Passage, although pointing to the existence of other possible tracks.

In terms of transit times, Speich et al. (2001) found that waters coming from the Drake to the North Atlantic (20°N) through the circuit that includes a detour in the Indian Ocean lasts around 58 years. According to Rousselet et al. (2020) the indirect route to the tropical South Atlantic (6°S) has a typical transit time of around 30 years. Our transit times of the cold indirect path that recirculates in the Indian Ocean present a mean mode of  $15.9 \pm 13.7$  years from 34°S to the Drake Passage. Probably this mode time corresponds mostly to the particles that recirculate in the Indian Ocean, having probabilities around the 20% in Figure 3.84e; in this same figure, we may appreciate that some particles recirculate following a much longer path, reaching even the west coast of Australia.

The warm and salty waters from Agulhas Leakage contain a small fraction of Antarctic water that recirculates in the Indian Ocean, although this is often omitted, which contributes to underestimating the total cold contribution. Döös (1995) already noticed that some water in the warm path comes from the Drake Passage and recommended to be classified and considered as part of the cold-water path, or at least to some extent. In other early studies, Speich et al. (2001, 2002, 2007) emphasized that the warm-water route also contains waters originated at the Drake Passage and waters arriving via the Tasman Leakage, south of Australia. They estimated that the Drake and Indonesian Throughflow have almost equivalent contributions (6.5 and 5.3 Sv, respectively) to the North Atlantic Ocean. Of the 6.5 Sv coming from the Drake Passage, about 4.2 Sv is transported through the Indian Ocean subtropical gyre before coming back through Agulhas Current. Rousselet et al. (2020) affirmed that 80% of the particles that arrive to the tropical South Atlantic Ocean from the Drake Passage do so through the Agulhas Current. These authors sustain that the contribution that arrives to the tropical South Atlantic (6°S) is formed by the 15% of waters entering from the Drake Passage, 35% entering from the Indonesian Throughflow, and 49% coming from the Tasman Leakage.

Recent simulations point out an Agulhas Leakage of 10 - 20 Sv (Van Sebille et al., 2010; Beron-Vera et al., 2013; Cheng et al., 2016; Holton et al., 2017; Daher et al., 2020). Our estimates with the 5-year looping for the 2015 - 2019 period are consistent with these values and show substantial seasonal variability:  $16.3 \pm 4.2$  Sv in winter and  $9.1 \pm 2.4$  in summer. Although the 5-year loop simulations point to lower seasonal changes, when we analyze the results from the 1-year loop, we can confirm the Agulhas Leakage transport present a large interannual variability with a SD of 8.8 Sv (Figure 3.95).

Over the last decades, ocean-atmosphere simulations have pointed to a strengthening of the Agulhas Leakage in the South Atlantic Ocean (Biaostoch et al., 2009; Cheng, 2018). This increase in the Agulhas Leakage has been directly attributed to an increase in the Southern Hemisphere westerlies (Durgadoo et al., 2013; Biaostoch et al., 2015), and it is expected to continue under global warming conditions (Biaostoch & Böning, 2013). Looping the 1-year velocity fields for 75 years clearly reveals a substantial interannual variability, particularly showing that the Agulhas Leakage contribution dominated in 2016 and 2017, exceeding the contribution coming from the cold route. The high cold-water route contribution to the AMOC, similar or even above the warm-water contribution (which it partly feeds), suggests that transport changes at the Drake Passage could also affect the Agulhas Leakage contribution, reinforcing the idea of the critical role played by the cold-water route in the global ocean circulation (Purcell, 2014).

### 3.5.5. Preliminary conclusion

We have released Lagrangian particles during the summer and winter for the 2015 - 2019 period, looping the 5-year or the 1-year velocity fields, and have followed them for 75 years with the objective of backtracking the intermediate waters that arrive at the eastern edge of the South Atlantic subtropical gyre. The main results in terms of connecting pathways confirmed the existence of different pathways that form both the cold- and warm-water routes, with a contribution from the cold-water route larger than previously stated. In particular, the cold-route contribution to the intermediate waters at the eastern edge of the subtropical gyre represents between 17.3 - 18.9%, slightly more than 6.8 - 12.3% via the warm route. In both routes, there is a dominant direct pathway that is followed by 83.6 - 87.2% of the water parcels in austral winter.

With the backtrack trajectories, we have determined the transit times, the thermohaline properties changes and the water masses transformations between the two source regions and the eastern South Atlantic subtropical gyre. Depending on the release season, most of the warm waters last between 0.3 and 0.8 years to be incorporated into the reference section (34°S), while most of the cold waters last between 5.3 and 5.6 years, with the direct route representing the shortest and fastest pathway. When particles cross the Brazil Current, south Madagascar and Cape Basin regions, following the different paths, experience the highest thermohaline changes coinciding, generally, with sharp depth changes. These density alterations drive the water transformations during transiting the eastern subtropical South Atlantic, even though the bulk of both water routes remain within the intermediate waters' potential density range. In terms of water mass transformations, the direct cold route dominates with  $2.0 \pm 0.3$  Sv and

$1.8 \pm 0.2$  Sv in summer and winter mainly from intermediate to upper waters, while the indirect warm route that recirculates first in the western edge of the subtropical gyre experiences up to  $0.8 \pm 0.2$  Sv and  $0.5 \pm 0.1$  Sv in summer and winter, from intermediate waters transformed in equal proportion of shallow and deep waters.

Furthermore, by looping the 1-year velocity fields for 75 years, we have analysed the interannual variability along the pathways. Both routes contribute with a similar mean transport of around 17.5 Sv, exhibiting high interannual variability of 8.8 and 6.2 Sv for the warm- and cold-water routes, respectively. Analysing the individual pathways, the direct route is still dominant, maintaining their proportion almost constant even when the total transport increases. Regarding thermohaline properties, the cold direct and indirect routes that partly recirculate in the Indian Ocean experience potential temperature minimum and maximum depth differences at the beginning and end of the 2015 - 2019 period. Again, the intermediate waters dominate along the cold and warm routes with scarce density changes, standing out the huge water mass transformation of 4.4 Sv in the summer of 2017 from the surface into intermediate waters for the direct cold route.

Finally, considering the 75-year output from the 5-year looping simulations, we find a mean of  $0.3 \pm 0.2$  Sv from the cold route that feeds the Agulhas Current, similar to the contribution from the Indonesian Throughflow of  $0.2 \pm 0.1$  Sv. Each of these transports represents between 1.8 and 2.8% of the total Agulhas Leakage contribution to the reference section at 34°S. These water parcels from the Indonesian Throughflow take half the time of waters from the Drake Passage to be incorporated into the Agulhas Current.



## **IV. GENERAL DISCUSSION**



In this section, we initially introduce the advantages and limitations of combining the inverse box model, the ROD method and Lagrangian particle tracking techniques in order to characterize the transference of upper-ocean waters formed in the Southern Ocean to the South Atlantic subtropical gyre. Then, we present a summary of the results obtained in this thesis dissertation, discussing and comparing the different chapters and offering an integrated vision of the upper circulation in the region in terms of mass, heat and salt transports, diffusivities, transit times, water mass transformations, pathways, and spatiotemporal variability, among others.

#### 4.1. Advantages and limitations of the methodologies used

The combination of the Eulerian inverse box model with the Lagrangian particles tracking technique has proven to be very useful for establishing a consistent and solid scheme of the average oceanic circulation, helping identify how mass, heat and salt are transferred along the pathways. The Lagrangian approach, which consists of virtual fluid particles advected with the three-dimensional time-evolving velocity fields, allows tracking ocean interconnections at any time and location; in contrast, the inverse model offers an optimal solution of the characteristics and the size of the water masses transports, which is obtained after considering all available physical information – including heat air-sea exchange, freshwater flux and Ekman transports – and allowing for adjustments in the reference velocities and for non-zero diapycnal advection and diffusion. The resulting flow is then combined with the distribution of biogeochemical properties to infer the intensity of biological transformations as well as the rate of storage of inorganic carbon of anthropogenic origin.

With the application of the inverse box model in **Chapter 3.2**, we have obtained mass transports in line with the results obtained in **Chapter 3.1** up to the isoneutral of  $28.00 \text{ kg m}^{-3}$  ( $140.8 \pm 7.4 \text{ Sv}$  for the Drake Passage and  $115.9 \pm 8.3 \text{ Sv}$  for the Northern Passages). By adjusting the horizontal reference velocities and the diapycnal vertical velocities and diffusivities introduced, the inverse model transport estimates are well balanced, providing a robust result (Figure [4.1](#)). Moreover, the velocity fields in the Scotia Sea boundaries can serve as a reference for climatic and regional studies, in particular in regions with scarce data (ice cover limits oceanographic cruises to the austral summer months and also restrict the coverage by drifting buoys). Fortunately, every year more Argo, Deep-Argo and Biogeochemical-Argo floats are launched, getting a better coverage of these subpolar areas. These physical and biogeochemical water properties measurements complement hydrographic sections, improving the global inventory estimates (Johnson et al., [2015](#)). Indeed, the Argo floats dataset is already large enough to assess the interannual and seasonal variability of the water transports up to the

28.00 kg m<sup>-3</sup> isoneutral in the Drake and Northern Passages, as confirmed in **Chapter 3.1** (Figures 3.15 and 3.18). The three-month results are somewhat noisy but demonstrate that there is enough temporal float resolution to identify substantial seasonality in the transports.

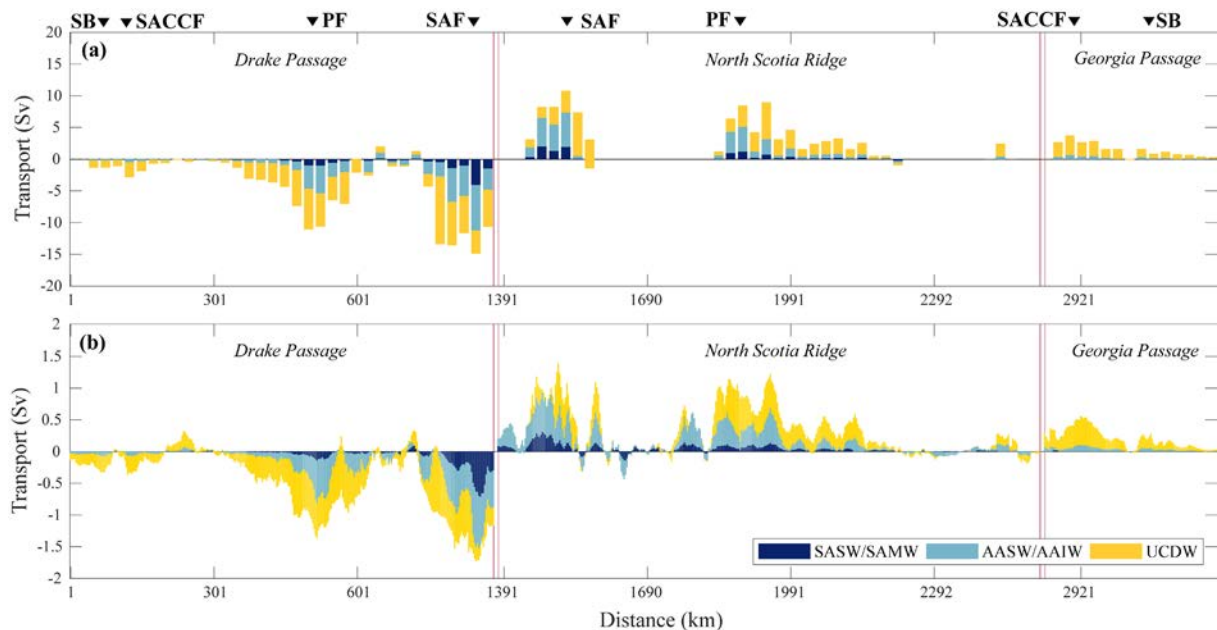


**Figure 4.1.** Comparison of the geostrophic transport distribution along the Drake Passage, North Scotia Ridge and Georgia Passage as calculated in (a) **Chapter 3.1** every 25 km and (b) **Chapter 3.2** for a 3-km resolution. Notice that transport bars are stacked and hence, slightly different from transports plotted in Figure 3.39b where they are overlapped. In **Chapter 3.1**, the main inflow/outflow is equal to  $140.8 \pm 7.4$  Sv for the Drake Passage and  $115.9 \pm 8.3$  Sv for the Northern Passages, while in **Chapter 3.2**, the sum corresponds to  $136.7 \pm 1.0$  Sv for the Drake Passage and  $137.9 \pm 1.0$  Sv for the Northern Passages.

Some conceptual weaknesses and limitations of the inverse box model method are summarized below. First, the observations ought to be as synoptic as possible, although this is not always achieved. Usually, the lack of synopticity is reflected in errors in the mass transports along the sections (Ganachaud, 2000). Second, as it is an undetermined system, where every equation provides very little information in relation to the other equations, it could result in an ill-posed system (i.e., bad conditioned; Wunsch, 1978) that requires additional transport constraints. Finally, it is fundamental to close the box edges in order to have a well-balanced result. In our study, we use the bathymetry to close the Scotia Sea boundary sections, causing a lack of data for the shallow regions because Argo floats are not capable of crossing them. We introduced the MEOP casts mainly in poorly sampled edge sections; however, the likely surface water leakage through the shallow bathymetry, mostly through the northern branch of the SAF, usually located east of the 54-54 passage (Artana et al., 2016), probably remains as our study's main weakness.

The inverse model requires some decisions that are always susceptible to modification or improvement, particularly regarding the reference velocities and the vertical fluxes (**Chapter 3.2**): the reference velocity solution would be more realistic by introducing *a priori in situ* measurements in the South Scotia Ridge and Philip Passage, and the constant vertical diffusion coefficient may be unrealistic. Also, an alternative parameterization would be to assign an independent transfer coefficient to each property (e.g., Sloyan & Rintoul, [2001a,b](#)), but it would require extra data to resolve them separately. Further, the *a priori* uncertainties introduced in the model may also be improved, and the weight of anomaly equations could be assessed through testing with a general circulation model (Ganachaud, [2000](#)) instead of applying the standard deviation estimate that was used here. Finally, we could incorporate additional equations for the conservative preformed nitrogen and phosphorous in the inverse model, hence implementing a quasi-extended OMP analysis approach (Llanillo et al., [2012](#)).

The release of Lagrangian virtual particles is a powerful tool to determine the source, fate, time scales and properties of water parcels advected in the global ocean, as seen in **Chapters 3.4** and **3.5**. In the last decades, Lagrangian analyses have become a preferential tool to estimate particle trajectories in numerical models, providing additional information on the water transports, transit times and basin interconnections between far-separated branches of the AMOC; otherwise, this information would be limited by the scarce numbers of surface drifters and float trajectories (Van Sebille et al., [2018](#)). However, the accuracy of this technique is conditioned by the resolution and amount of data assimilated by the numerical model. Furthermore, Lagrangian methods may experience mass conservation problems, as the spatial interpolation of velocities can introduce errors in the original flow field, particularly diverting from the model's boundary conditions (Pokrajac & Lazic, [2002](#)). Many studies have successfully compared the numerical model Mercator Ocean GLORYS12v1 reanalysis with independent observations from oceanographic cruises (e.g., Artana et al., [2018](#); Artana et al., [2019a](#); Poli et al., [2020](#); Verezemskaya et al., [2021](#); Lelleouche et al., [2021](#)).

Regarding the Parcels code, its major strengths consist of its ease to use, adaptation to all types of discretized fields, customizable extension interface and automated performance optimization (Van Sebille et al., [2018](#)). Its major limitations are high computationally cost, lack of subgrid parameterizations, time scales longer than the run time of simulations, and increasing positional errors for long time scales. Regarding these last two, there are oceanic processes that exceed the simulations' run times. A common solution to allow particles to be advected for longer time scales is to loop the velocity and tracer fields in time in such a way that they are returned to the first time step once the end has been reached (Döös et al., [2008](#); Van Sebille et al., [2012](#); Thomas et al., [2015](#)). With a time resolution higher than a week, the positional errors do not practically affect the particle trajectories (Qin et al., [2014](#)). However,

vertical velocities in upwelling areas are remarkably intermittent and do not show apparently well-defined vertical temporal structures. Moreover, some physical and dynamic processes, such as eddy lateral diffusion, often remain unresolved and have to be artificially introduced as a random motion to predict a more realistic water parcel distribution.

In **Chapter 3.3**, we propose the ROD method in order to quantify the coefficients of horizontal diffusivity in the western South Atlantic Ocean. Its major advantage is its robustness and simplicity, being easily implemented by combining the drifter positions with model reanalysis or forecast model data. These horizontal diffusion coefficients (horizontally uniform but changing with depth) are applied in **Chapter 3.4** to the climatological velocity fields from numerical ocean models in order to calculate more realistic particle trajectories. However, the ROD method has some experimental limitations. First, we assume that motions are one-dimensional in the horizontal plane. Even for the neutrally buoyant RAFOS floats, we have not considered the vertical motions of the drifters. Indeed, large subgrid along-isopycnal motions may bring the float into neighbouring vertical zones with different diffusive regimes. Moreover, the ROD method is limited by the accuracy of the position fixings and drifting depth. Although the accuracy of the position may diverge between 1-100 m for the GDP (Elipot et al., [2016](#)) and 1 km or less for RAFOS and Argo floats (Ollitrault & Rannou, [2013](#)), the distances derived by the floats in each 10-days cycle are much larger. Roach et al. ([2016](#)) concluded that the errors introduced by using an ARGOS-equipped profiling float in the Southern Ocean regime are comparable to the errors inherent in estimating diffusivity from RAFOS float or surface drifter trajectories. Nevertheless, the ROD method allows estimating the relatively large horizontal diffusivities that best match the actual drifters' displacements.

Regarding the drifting depth, we attribute the radial distances of a particular trajectory to a specific depth range; however, it is well-known that some floats are stuck in shallow bathymetry or continental shelf, so these distances would indeed correspond to a different depth range (e.g., Voet et al., [2010](#)). In addition, it is estimated that almost 10% of the drifting depths are erroneous either because of incorrect nominal parking depth or because floats did not stabilize properly at their programmed parking depth (Ollitrault & Rannou, [2013](#)). Fortunately, as mentioned in **Chapter 3.1**, the Argo improvements in technology have led to faster profiling and fewer hours spent at the sea surface, so we expect that the uncertainty on the radial distances will decrease in the future. Another limitation of the ROD method is the assumption that the turbulence is completely isotropic, displaying similar displacements zonally and meridionally. Also, the numerical model products may have their own limitations. In particular, surface particles released with the GLORYS12v1 velocity fields display a systematic rightward displacement as compared with the drifters; this displacement, which diminished with depth, is probably due to numerical model errors. These displacements have

been practically only noticeable in the top 150 meters of the water column; at depth where geostrophy dominates, these displacements are practically negligible.

Hamon et al. (2019) have emphasized the relative importance of considering multiple altimeters in the data assimilation and its effect on the accuracy of the mean dynamic topography measurements that are assimilated in Mercator Ocean global products. In particular, in the GLORYS12v1 product, there are also errors associated with sea ice concentration assimilation (Ivanova et al., 2015) and large-scale T/S biases above 100 m, among others (Lellouche et al., 2021). **Chapter 3.4** confirmed that combining the numerical Lagrangian tracking technique with drifter trajectories can improve water parcel predictions by adding effective horizontal diffusivities that make their trajectories become more realistic. In particular, without their implementation, the upper-ocean waters would exhibit faster transit times and a higher number of recirculations in the South Atlantic basin.

Finally, the time residence of the different water masses, quantified using both *in situ* measurements through Argo floats and numerical models through virtual particles, have shown consistent results. Indeed, **Chapter 3.3** confirms that the advected virtual particles predict reasonably well the final position of Argo floats, within a radius of less than 400 km for a time step of 10 days, the displacement being attributable to the effect of horizontal diffusion. This grants confidence to the residence times estimated through the particles simulations.

#### 4.2. Integrated vision of the Southern Ocean – South Atlantic Ocean connection

The Pacific waters enter the Atlantic Basin carried by the ACC through a large latitudinal topographic opening, the Drake Passage. As it crosses this Passage, the ACC carries  $164.2 \pm 10.8$  Sv down to 2000 m, with a predominant barotropic contribution that doubles the baroclinic one. In terms of isoneutral surfaces, in these upper-ocean waters, we only fully identify those layers down to UCDW ( $\gamma^n < 28.00$  kg m<sup>-3</sup>; Figure 3.9 and Tables 3.5, 3.6). As expected, the absolute geostrophic transports exiting northward the Scotia Sea are fairly similar and preserve the baroclinic and barotropic ratios:  $159.3 \pm 10.2$  Sv exit through the Northern Passages, which is equally split in 42.6, 59.6 and 53.8 Sv among the 54–54, Shag Rocks and Georgia Passages, respectively. Similarly to the zonal transports through the Drake Passage, these meridional transports through the Northern Passages are also dominated by the SAF (54°W – 55°W), the PF (48°W – 49°W), and the SACCF (33°W – 34°W) along-frontal flow. Along the Scotia Sea, the ACC experiences substantial mass transformations, with the domain comprised between the SAF and the PF losing 62.8 Sv while the remaining frontal regions gain water transports (Table 3.7). Furthermore, the ACC waters present a mean

residence time in the Scotia Sea of  $219 \pm 213$  days (7.3 months), with remarkable differences depending on the frontal subdomain followed. The interannual variability through the Drake, Shag Rocks and Georgia Passages is fairly stable, while the seasonal variability is notable, about 63.3 Sv, mainly caused by fluctuations in the AASW/AAIW and UCDW transports (Figures [3.15](#) and [3.18](#)).

In **Chapter 3.1**, we discuss that even early estimates suggested that the total amount of water transport entering through the Drake Passage was 134 Sv (Whitworth & Peterson, [1985](#)), more recent calculations point to values as large as 175 Sv (Chidichimo et al., [2014](#); Donohue et al., [2016](#); Colin de Verdière & Ollitrault, [2016](#)). Whereas the baroclinic geostrophic velocity can be completely determined from hydrographic data, a major problem has been to obtain the velocities at the reference level, a difficulty that has pervaded the oceanographic community for over a century. One possible approach would be to use surface altimetry in order to estimate the geostrophic surface velocities and use them as the reference values; however, this approach has the inconvenience that small relative errors in these fast velocity speeds can represent large transports. An alternative, which is used in **Chapter 3.1**, is to use Argo floats with a parking depth at 1000 m in such a way that their mean displacements turn out as an effective estimate of this reference velocity. A further improvement is made in **Chapter 3.2** by, first, combining the Argo vertical casts with other hydrographic data and, second, by processing all these data with inverse models in order to obtain reference velocities that provide an optimal solution that is consistent with the conservation hypothesis of mass, heat and salt in a multilayered geostrophic ocean (Machín et al., [2006](#)).

One important result that arises in **Chapter 3.1**, obtained using the extensive Argo dataset, is that the seasonal variability in the overall ACC transport dominates over the interannual variability, but the interannual variability has a greater effect on the intensity and position of SAF and PF (Figures [3.14](#) and [3.17](#)), led by the bimodal character of the PF (Cunningham et al., [2003](#); Lenn et al., [2007](#); Sprintall, [2003](#)). Indeed, in Artana et al. ([2016](#)), the spatial variability of the SAF and PF through the North Scotia Ridge, as inferred from ADT values, reveals occasional eastward migrations of the SAF to the Shag Rocks Passage and substantial changes in the PF position, even within the 54-54 Passage. In addition, this relatively high seasonal variability promotes the winter disappearance of the surface-mode and surface-intermediate water masses in the Northern Passages, which translates into a decrease in the total transport outflow (Figure [3.18](#)).

The role of Antarctic fronts, whether they act as barriers or blenders (Bower et al., [1985](#)), has also been widely discussed throughout this dissertation. Frontal systems are often thought to act as barriers for tracer exchange and water masses, as they display intense property gradients and the flow is predominant in the along-frontal direction, but fronts are also the

source of mesoscale and submesoscale instabilities that may induce cross-frontal transfer as well as of high vertical-shear that can promote a dynamically unstable water column. With this idea in mind, in **Chapter 3.1**, we differentiate the amount of water that enters through the Drake Passage between the frontal systems and how these waters are distributed between these same fronts when crossing the Northern Passages (Figure [3.11](#) and Table [3.8](#)). Our results suggest that there is a substantial exchange of water masses across the PF and SAF, with 101.3 Sv north of the PF and 39.6 Sv south of the PF at the Drake Passage in contrast with 45.4 Sv west of the PF and 70.5 Sv east of the PF at the Northern Passages. The trajectories of Argo floats carried mainly by the ACC fronts, in contrast to adjacent areas where there are few Argo floats (Figure [3.7](#)), point to the dynamic relevance of these frontal systems. Nevertheless, the observation that only 29% of the floats remain within their original frontal subdomain proves that there is water transfer between the different jets of the ACC frontal system (Table [3.8](#)). The cross-frontal instabilities enhance lateral mixing by increasing the lateral distances travelled by water parcels in mesoscale and submesoscale motions. In **Chapter 3.3**, we have used a simple and innovative method to quantify the variations of horizontal diffusivity from one frontal subdomain to another, as a reflection of changes in the intensity of mixing induced by mesoscale and submesoscale turbulence. It turns out that the northern ACC fronts, with a higher velocity and water transport, have the highest diffusion coefficients and promote higher cross-frontal exchange.

After characterizing the ACC along its path through the Scotia Sea and obtaining a remarkably good water transport balance up to isoneutral  $28.00 \text{ kg m}^{-3}$ , we applied an inverse box model within the Scotia Sea in order to improve the calculation of the climatological water-mass transports as well as to obtain the mean transports of biogeochemical properties (**Chapter 3.2**). The inferred main circulation pattern consists of water entering the Scotia Sea via the Drake Passage, South Scotia Ridge and Philip Passage, and emerging through the Northern Passages (North Scotia Ridge and Georgia Passages), with scarce water leaving over the shallower margins (Figure [3.39](#)). The absolute reference velocities in the Scotia Sea boundaries are calculated after adding the inverse model solution to the Argo's parking-depth speeds, concluding that the reference velocities maintain a similar pattern although with generally smaller values than previously obtained in **Chapter 3.1** (Figures [3.7](#) and [3.34](#)). This small overestimation could be due to either inaccuracies in the Argo drifting depth (Ollitraul & Rannou, [2013](#)) or to changes in the horizontal velocities experienced during the Argo's vertical displacements, rising or descending; the estimated errors in the 1000-m reference velocities are always below  $1 \text{ cm s}^{-1}$  (see subsection [3.1.3.1](#)). Velocities as large as  $28 \text{ cm s}^{-1}$  at the reference level suggest that a remarkable percentage of the transport associated with the ACC is barotropic, consistent with the results obtained in **Chapter 3.1** (Figure [4.2](#)).

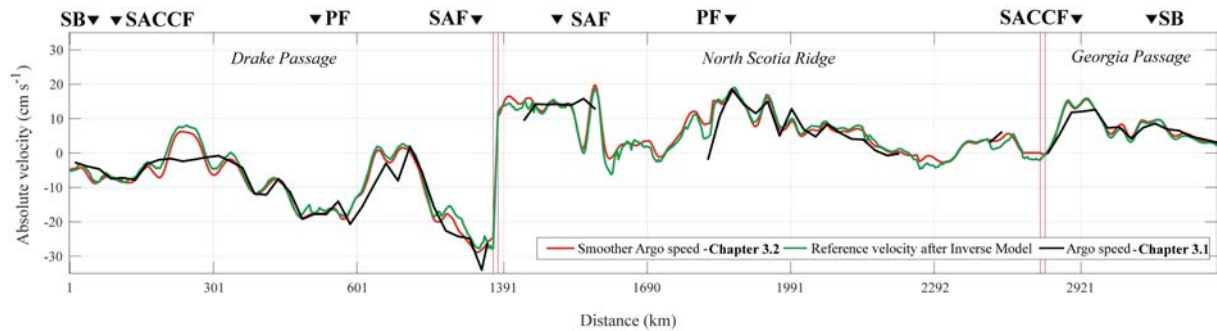


**Figure 4.2.** Comparison of the reference velocities at 1000 m along the Drake Passage, North Scotia Ridge and Georgia Passage, as obtained in **Chapter 3.1** (black line) and **Chapter 3.2** (red and green line). In **Chapter 3.2**, the absolute velocities are obtained from the mean Argo trajectories (red line) calculated with a horizontal resolution of 3 km and then adjusted with the inverse model solution (green line).

The maximum accumulated transport carried out by the ACC up to  $\gamma^n = 28.00 \text{ kg m}^{-3}$  in the Drake Passage is about 136.7 Sv, divided by 0.2 Sv for SASW, 14.6 Sv for SAMW, 47.6 Sv for AASW/AAIW and 74.3 Sv for the UCDW (Figure 3.38). The total water mass transport imbalance in the Scotia Sea is 0.03 Sv as a result of a net positive (outflow) imbalance of 1.3 Sv of SASW/SAMW and AASW/AAIW in front of a negative (inflow) imbalance of 1.27 Sv of UCDW. In this way, the mass transport imbalances represent only 0.14%, 0.81% and 0.93% of the SAMW, AASW/AAIW and UCDW mass transports in the Scotia Sea. Our inverse circulation model reveals that the flow of upper-ocean waters up to the isoneutral of  $28.00 \text{ kg m}^{-3}$  through the southern Scotia Sea sections, Philip Passage and South Scotia Ridge, contributes in total less than 3 Sv, regardless of the direction (Figure 3.39).

The southern cold and fresh inflow through the South Scotia Ridge and Philip Passages is mainly constituted by dense LCDW and WSDW (Figure 3.40). In **Chapter 3.1**, we expected that adding this LCDW/WSDW transport to the 23.4 Sv inflow through the Drake Passage between  $28.00 \text{ kg m}^{-3}$  and 2000 m would give a total of 42.4 Sv (Figure 3.19). The estimations obtained in **Chapter 3.2**, considering the southern Scotia Sea sections up to 2000 m, confirmed that this cold and fresh southern inflow of LCDW/WSDW represents 15.6 Sv and hence, summing a total of 39 Sv between  $28.00 \text{ kg m}^{-3}$  and 2000 m. Furthermore, in **Chapter 3.1**, the total transport imbalance up to  $28.00 \text{ kg m}^{-3}$  was substantially, around 24.9 Sv, in front of a mass transport imbalance of about 0.03 Sv after applying the inverse model (Figure 3.19).

In **Chapter 3.2**, we obtain that the flow associated with the SAF and PF in the Drake Passage contributes almost equally, with 62.1 Sv and 65.7 Sv, while in the Northern Passages, the SAF loses strength (40.9 Sv) and the PF transport increases slightly (72.0 Sv). This last transport ratio measured in the northern boundary is in line with the 40.9 Sv and 51.6 Sv obtained in North Scotia Ridge in **Chapter 3.1** (Table 3.7). However, in estimations for the



Drake Passage in **Chapter 3.1**, the SAF transport significantly dominates the section's contribution. Whereas the SAF/PF transport ratio of the inverse model (**Chapter 3.2**) agrees with Cunningham et al. (2003) transport estimates of 58 Sv and 53 Sv for the PF and SAF at the Drake Passage, the transport ratio obtained in **Chapter 3.1** is more in line with SOSE transports (Figures 3.8b and 3.46a) where the highest velocities of SAF dominate the water column. Moreover, according to Smith et al. (2010), the transport associated with SAF is less than PF, corresponding to  $31 \pm 7$  Sv in front of  $80 \pm 7$  Sv at Drake Passage, while at North Scotia Ridge contributes equally with  $52 \pm 4$  and  $58 \pm 5$  Sv, respectively. This variety of results suggests that the transports associated with the fronts display large variability, possibly as the result of the merging and dividing of both fronts and the associated water exchange throughout the Scotia Sea.

Regarding the net salt and heat transport imbalance, in average waters leave 0.08% saltier and 4.6% cooler than when they enter the region, leading to heat loss and salt gain in the Scotia Sea (Figure 3.41). In terms of diapycnal transference, the vertical velocities and diffusivities obtained after applying the inverse model reveal maximum values in the region of  $1.35 \times 10^{-5} \text{ m s}^{-1}$  and  $3.50 \times 10^{-4} \text{ m}^2 \text{ s}^{-1}$ , respectively (Figure 3.35).

The ACC biogeochemical properties imbalances reflect the presence of biological consumption or production of these properties as the water flows through the Scotia Sea. The comparison between the inverse model and SOSE/B-SOSE vertical sections for nitrate, DO and DIC reveal that fluxes are qualitatively similar (Figures 3.31 and 3.49) with relatively small differences in the absolute values. As mentioned before, this may partly be a consequence that SOSE velocities are equal or higher, especially in the SAF, except for the PF in the Drake Passage and the SACCF in Georgia Passage (Figure 3.46). Hence, the SOSE mass, heat and salt transports are not as well balanced as in the inverse model (Table 3.17 and Figure 3.47). Furthermore, B-SOSE is a much more restrained biogeochemical database, using only the observations done between 2008 and 2012. In addition, there are some gaps with no data in the vertical SOSE/B-SOSE sections, especially in the North Scotia Ridge, due to the irregular and sharp bathymetry (Figures 3.46 and 3.49). After the inverse model, we find a net production of DIC and nitrate, and a net consumption of alkalinity and dissolved oxygen in the Scotia Sea. Regarding the carbon budget components, the Scotia Sea uptakes  $0.006 \text{ Pg C yr}^{-1}$  through carbon dioxide air-sea exchange, produces  $0.163 \text{ Pg C yr}^{-1}$  through biogeochemical processes, and accumulates  $0.123 \text{ Pg C yr}^{-1}$  from anthropogenic origin hence acting as small atmospheric carbon storage (Table 3.16). Although it could seem a high value for anthropogenic accumulation in such a small region, large carbon quantities are exported from the Weddell Gyre across the South Scotia Ridge (Brown et al., 2015). As a result, the Scotia Sea

represents a region for anthropogenic DIC storage and sink at surface-intermediate and deep waters, respectively, which remarks the importance of this basin in the global carbon cycle.

In **Chapter 3.3**, we quantify realistic horizontal diffusivity coefficients in the western South Atlantic Ocean, which will be later used (**Chapter 3.4**) to produce more realistic water parcel distributions. For this purpose, we develop a simple method (radial offset by diffusion, ROD) that allows obtaining average diffusivity values for the entire domain as well as assessing their spatial variability across the ACC fronts and with depth. The isotropic dispersion offsets obtained between the final position of particles and floats after 10-day cycles follow a Gaussian fit, with maximum particle concentration around the initial position and decreasing uniformly away from the centre. The ROD method is model-dependent, meaning that it will provide diffusive coefficients for each model, depending on its configuration, particularly its spatial resolution. We used GLORYS12v1, a numerical model with  $1/12^\circ$  of horizontal resolution, obtaining that the surface radial distances cloud is not centred, rather experiencing a rightward displacement. We repeated these calculations using the velocity fields of GlobCurrent (Johannessen et al., [2016](#)) and observed that the surface particles reveal a similar bias (about 58 km on the x-axis and 16.3 km on the y-axis; not shown). These results point at some numerical model limitations in reproducing the Southern Ocean's mean velocities.

Maximum diffusion coefficients near the surface (15 m) correspond to the regions between the main ACC fronts (SAF - PF, PF - SACCF and SACCF - SB frontal subdomains) and decrease towards the ACC edges; in contrast, the diffusion coefficients at 1000 m generally decrease with increasing latitude (Figures [3.62](#) and [3.64](#)). One reason might be that the horizontal scale of these mesoscale eddies decreases to 5 – 10 km at those high latitudes, and their radial eddy velocities, which are directly proportional to the Rossby number, can reach up to  $0.5 \text{ m s}^{-1}$  (Manucharyan & Thompson, [2017](#)); when the horizontal size of an eddy is large as compared with its baroclinic deformation radius,  $R_d$ , the eddy may develop baroclinic instabilities that enhance mixing (Flierl, [1988](#); Sangrà et al., [2005](#)). Furthermore, Ferrari & Nikurashin ([2010](#)) suggested that eddy mixing is enhanced in the ACC flanks more than in its core because of the suppression of eddy mixing by the strong zonal current. Our estimates of 1000-m horizontal diffusivities across the ACC path range from 1050 to  $1820 \text{ m}^2 \text{ s}^{-1}$ , except south of the Southern Boundary, in line with the mean value of  $1840 \pm 440 \text{ m}^2 \text{ s}^{-1}$  for the entire UCDW obtained by Naveira Garabato et al. ([2007](#)) and also with the value of  $1019 \pm 158 \text{ m}^2 \text{ s}^{-1}$  calculated by Roach et al. ([2018](#)). Finally, it could be expected that RAFOS drifting buoys present a more accurate final position than Argo floats due to the absence of descending and ascending cycles. However, radial distances estimated at 1200 - 1300 m depth, where RAFOS

has a greater representation, agree with the other Argo distances obtained (Figures 3.50e, 3.54f and 3.60f).

We establish an inverse relation between horizontal diffusion and depth through the ROD method computed in Chapter 3.3. Using this linear equation (expression 2.42), we attribute a horizontal diffusion coefficient for each depth of the GLORYS12v1 numerical product. With the diffusivity's distribution at depth, we release particles in Chapter 3.4, adding random radial distances equal to  $R\sqrt{2K\Delta t}$ , as described in equation 2.35. The radial distances added to the simulated particles for a time resolution of 10 days agree with the radial offsets obtained in Chapter 3.3 for the same depth, fitting perfectly to a Gaussian distribution with a high correlation of  $R^2 \cong 1$  (Figure 4.3).

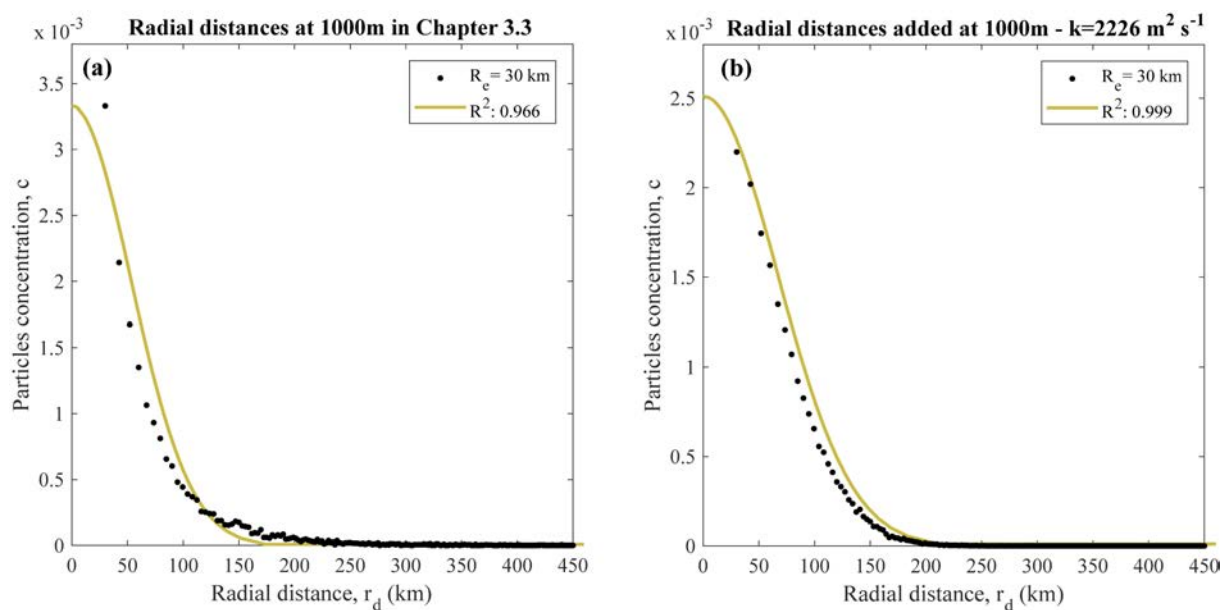


**Figure 4.3.** Comparison of the (a) radial distances at 1000 m obtained in Chapter 3.3, fit with a Gaussian distribution using  $K=1540 \text{ m}^2 \text{ s}^{-1}$ , with the (b) radial distances added to the 1000-m virtual particles advected by the GLORYS12v1 velocity fields, both with a 10-day time resolution. The coefficient introduced in the GLORYS12v1 Lagrangian simulations at 1000 m corresponds to  $K=2226 \text{ m}^2 \text{ s}^{-1}$ , according to the expression 2.42 in subsection 2.4.3.

In subsection 3.4.4.1, but for a daily time resolution, the added radial distances decrease with depth from maximum values around 110 km near the surface to 20 km at 2000 m, in accordance with the associated horizontal diffusion coefficient (Figure 3.75b). Without diffusion, our climatological particles simulations would be biased since the distribution and contribution of surface-intermediate and deep waters to the South Atlantic subtropical gyre would be scarce or practically negligible (Figure 3.76), in contrast with the observations from several authors (e.g., Stramma & England, 1999; Talley, 2011). In particular, the isoneutrals tilted at Drake Passage (e.g., Figures 3.8, 3.9a, 3.36 and 3.66) promote a larger northward

spread of the outcropped intermediate and deep waters due to the high horizontal diffusivities. Adding diffusivities, we can better simulate the diffusive effect of the submesoscale eddies on the numerical climatological velocity fields.

In **Chapter 3.4**, Lagrangian particles have been advected and horizontally diffused to determine what fraction of the upper-ocean transport ( $\gamma^n < 28.00 \text{ kg m}^{-3}$ ) remains in the ACC after crossing the South Atlantic Ocean and what fraction is incorporated into the South Atlantic subtropical gyre, in what constitutes the direct cold-water route. In addition, the time transits, thermohaline changes, water mass transformations and seasonal variability have been estimated for both pathways. In terms of annual climatological mean, out of 117.4 Sv of the upper-ocean transport entering through the Drake Passage, 102.4 Sv will end up crossing the entire South Atlantic basin to 25°E, although just 94.8 Sv remain within the ACC and are incorporated directly to the Indian Basin (Figure [3.80](#)). In turn, the total contribution to the eastern margin of the subtropical gyre is supported by 15.1 Sv, with a seasonal range from 12.4 Sv to 15.7 Sv, with 68.5% of its transport reaching the North Brazil Current (Figure [3.79](#)). This net transport inflow up to  $\gamma^n < 28.00 \text{ kg m}^{-3}$  across the Drake passage (63.75°W) is less than 144.4 Sv (**Chapter 3.1**) and 132.1 Sv (**Chapter 3.2**), displaying similar horizontal velocities and thermohaline properties distributions but smoother (Figure [4.4](#)). Specifically, 15.0 Sv correspond to the surface and mode waters, SASW/SAMW, 47.9 Sv to the surface-intermediate waters, AASW/AAIW, and 54.5 Sv to deep water masses, UCDW. Regarding our inverse model box solution (**Chapter 3.2**), the climatological annual-mean velocity fields slightly overestimate the SASW/SAMW and remarkably underestimate the UCDW contribution (12.7 Sv for SASW/SAMW, 46.2 Sv for AASW/AAIW and 73.2 Sv for the UCDW).

The eastern pathway to the South Atlantic subtropical gyre through 32°S is mainly followed by the surface-intermediate waters, AASW/AAIW, contributing up to 6.5 Sv carried out along the three ACC fronts (Figure [3.80](#)), mainly by the SAF and the PF as stated by Cunningham et al. ([2003](#)) and Firing et al. ([2011](#)). Moreover, our findings with backtrack trajectories (**Chapter 3.5**) from the eastern margin of subtropical gyre support that the cold-fresh water parcels come mainly from the SAF with a small contribution from the shallow surface PF waters. Seasonally, the cold contribution to the South Atlantic Ocean varies slightly from 12.4 Sv to 15.7 Sv, suggesting that seasonality plays a minor role (Figure [3.79](#); **Chapter 3.4**). The SASW/SAMW are the water masses that experience more transport variability in their incorporations to the 32°S and 21°S, whereas regarding the transit times, the waters that remain in the ACC path to 25°E show less variability with SDs from 0.3 to 0.5 years (Table [3.25](#)).

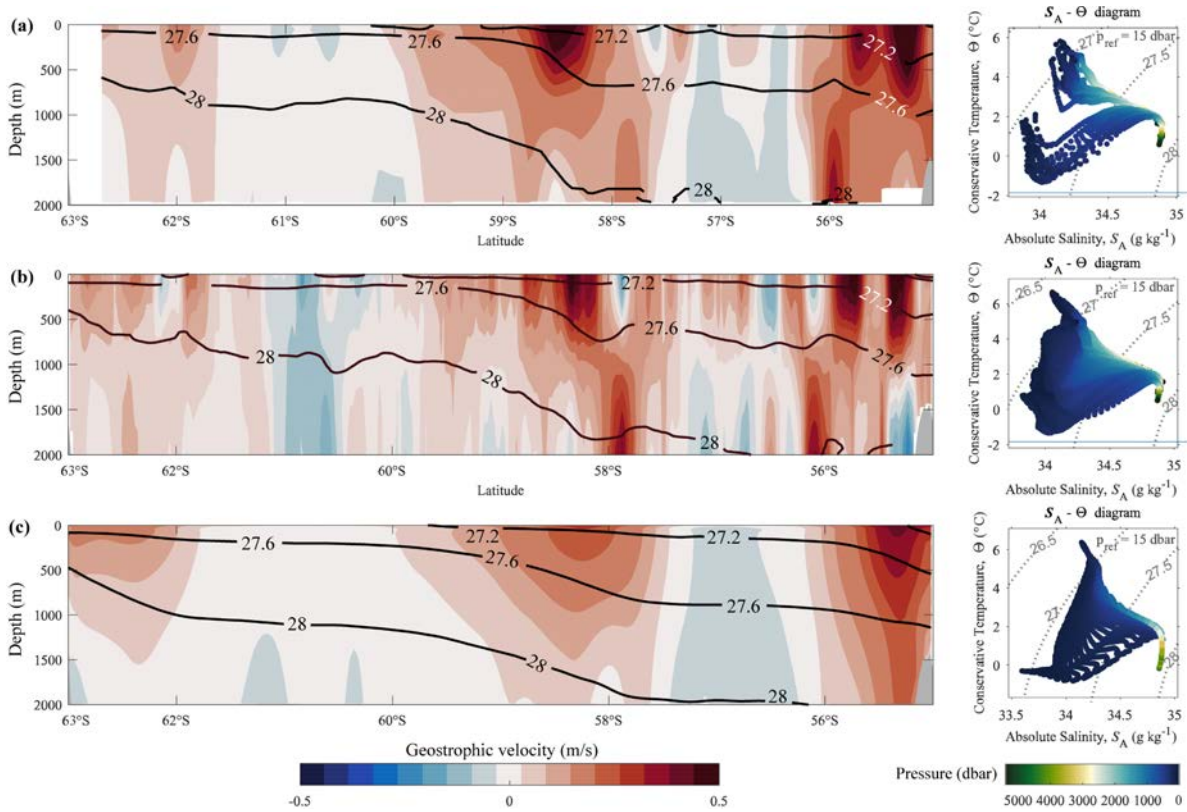


**Figure 4.4.** Comparison of the geostrophic velocities (coloured,  $\text{m s}^{-1}$ ) and neutral density (solid contours,  $\text{kg m}^{-3}$ ) vertical distributions of the ACC at the Drake Passage and their  $\theta - S_A$  diagram coloured according to pressure, inferred through (a) Argo casts with a 25-km resolution (**Chapter 3.1**), (b) after applying the inverse model with a 3-km resolution (**Chapter 3.2**) and (c) from the annual-average numerical model product GLORYS12v1 (**Chapter 3.4**). Positive values correspond to eastward velocities, and the selected isoneutrals denote the water mass boundaries in Table 3.1 in subsection 3.1.2.1. The regional bathymetry is shaded in grey.

In terms of heat transport, the cold and fresh upper-ocean water masses joining the eastern edge of the subtropical gyre warm up by 0.46 PW, starting from an initial heat transport in the Drake Passage of about 1.4 PW (**Chapters 3.2** and **3.4**). As obtained in **Chapter 3.2**, first, within the Scotia Sea boundaries, the upper-ocean waters do not experience warming; there is a net heat transport loss of  $0.065 \pm 0.005$  PW (Figure 3.41). After water masses reach the 32°S section, part of them barely warms up, gaining only 0.01 PW when they flow westward to the 21°S section. According to the salt fluxes, water masses incorporated into the subtropical gyre gain  $8.5 \times 10^6 \text{ kg s}^{-1}$  of salt transport, gaining  $1.8 \times 10^6 \text{ kg s}^{-1}$  more when they arrive at the Brazilian coast (Tables 3.22 and 3.23, and Figure 3.80). The water masses incorporated into the subtropical gyre at 32°S lose density, implying water transformations from surface-intermediate and deep layers, 3.5 Sv and 3.2 Sv, respectively, to surface waters (Figure 3.74). In **Chapter 3.5**, the intermediate waters along their direct path from the Drake Passage gain a mean of 0.98 - 1.04 °C of potential temperature, 0.27 - 0.29  $\text{g kg}^{-1}$  in salt, and

most of them sink a mean of 374 - 460 m in austral winter and summer, respectively (Table 3.27). These AAIW waters that follow the cold direct route also proceed from 1.06 - 1.34 Sv of upper waters and 0.66 - 0.72 Sv from deep waters (Table 3.28). Hence, when the surface-intermediate waters follow the cold direct path (Drake – South Atlantic subtropical gyre) forward in time, 3.5 Sv of a total of 6.5 Sv are transformed in surface waters, whereas backwards in time, only 1.8 - 2.0 Sv of 18.9 - 21.0 Sv are transformed, the vast majority preserving their original potential density range (Figures 3.74 and 3.92). All these transformations confirm that the South Atlantic Ocean is not a passive conduit but an active region of mixing, ventilating and subducting/upwelling of water masses.

According to previous studies, the cold-water contribution to the eastern margin of the South Atlantic subtropical gyre ranges from 0.9 Sv to 4.7 Sv (Speich et al., 2001; Donners & Drijfhout, 2004; Friocourt et al., 2005; Rodrigues et al., 2010). However, recent Lagrangian estimations by Rühls et al. (2019) concluded that the Drake Passage contribution to the North Brazil Current in the 6°S section varies from 5.5 to 13.1 Sv. These transport estimations are consistent with the total contribution of 12.6 Sv through the 21°S section, as calculated in Chapter 3.4 (Figure 3.80). According to Chapter 3.4, the cold contribution that reaches the western coast feeding the North Brazil Current is a little more than half of the transport in the eastern edge of the subtropical gyre. Hence, a cold contribution of 22.1 - 25.1 Sv at 34°S (Table 3.26; Chapter 3.5), although it may seem high, is less than twice 13.1 Sv and, therefore, consistent with the Rühls et al. (2019) estimates. One explanation of these recent large geostrophic transports could be that both studies, Rühls et al. (2019) and ours, have backtracked particles in key areas, with the use of daily velocity fields instead of climatologies and high-resolution (1/12° and 1/20°) numerical circulation model products.

In general terms, the climatological velocity and thermohaline fields, either annual or daily averages, smooth the large-scale structures ignoring the temporal variability and losing mesoscale and submesoscale structure. Even with the different initial conditions, different periods and being also forward vs backwards in time, the incorporation pathways to the South Atlantic Ocean of Chapter 3.4 and Chapter 3.5 are quite similar (Figure 4.5).

In Chapter 3.5, the main results confirmed that the cold-water route contributes to the intermediate waters at the eastern edge of the South Atlantic subtropical gyre more than previously stated, being essential for the upper limb transport of the AMOC. According to our estimations, the cold route transport represents 61% - 72% in front of 39 - 28% of the warm contribution, depending on the season (Table 3.26 and Figure 3.83). First, Gordon (1986) suggested that the volumetric capacity of the cold-water route is of secondary importance, no more than 25% of the warm-water route. Other early estimations indicated a 6% – 13% ratio between cold and warm transport using Lagrangian tools with coarser-resolution models

(Speich et al., 2001, 2007; Donners & Drijfhout, 2004). Rodrigues et al. (2010) estimated that the cold contribution reaches a 36% ratio, and R  hs et al. (2019) suggest that it is around 40%, always less than the warm contribution. However, the works by Schmitz (1995), Macdonald (1998) and Sloyan & Rintoul (2001a) supported the cold-water route hypothesis postulated in Rintoul (1991), which stated the dominance of the cold-water path over the warm-water path. For two decades, both hypotheses have been controversially discussed.

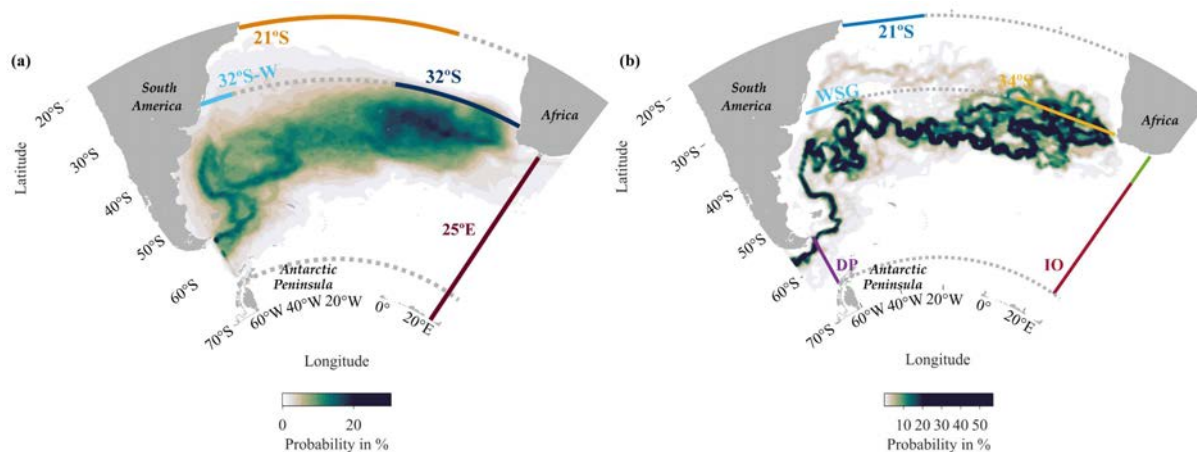


**Figure 4.5.** Comparison of the probability distributions for those particles that follow the direct cold-water route between Drake and the eastern side of the South Atlantic subtropical gyre: (a) averaged annually and tracked forward to 32°S for all the water masses (Chapter 3.4) and (b) seasonal-mean and tracked backwards from 34°S for intermediate waters (Chapter 3.5). The grid used in both cases is 0.5° in latitude and 1° in longitude, having the same number of cells in both coordinates, and each Lagrangian particle is only counted once per each grid cell. For the respective acronyms of the sections, see Figures 3.65 and 3.79. Particles have been tracked for 75 years in both Lagrangian simulations.

In terms of transit time distributions, in Chapter 3.1 through the analysis of the time-lag correlation between the Drake and Northern transports, we show that the average time that Argo floats take to cross the Scotia Sea last between 6.4 and 7.3 months. In Chapter 3.4 and using the climatological fields, the upper-ocean waters that cross the South Atlantic basin directly via the ACC reach the 25°E section after a median of 3.4, 3.6 and 4.9 years for SASW/SAMW, AASW/AAIW and UCDW, respectively. The same water masses take a little longer to be incorporated in the subtropical gyre at 32°S, 4.1, 5.8 and 8.2 years and spend a minimum of 7.6 years to reach 21°S section. Our results in Chapter 3.5, obtained through backtrack integration with the daily velocity fields, confirm that intermediate waters last 5.3 - 5.6 years to complete the cold-water route between the Drake Passage and the eastern margin of the South Atlantic subtropical gyre at 34°S.

Following with the intermediate waters, the transit times of the cold-water route estimated in **Chapter 3.5** closely match the transit times derived climatologically in **Chapter 3.4**. Indeed, the fact that the intermediate waters for the cold direct route last so similar in both chapters, 4.9 - 5.2 years and 5.8 years at 34°S and 32°S, respectively, even though the indistinct use of climatological annually-averaged and daily fields, suggests that adding diffusion to our climatological fields in order to simulate the mesoscale and submesoscale motions leads to results comparable to the daily fields trajectories and time transits (see Figures [3.68](#) and [3.83](#) and Table [3.26](#)). Furthermore, in **Chapter 3.5**, after identifying the three individual cold pathways, the first indirect pathway of recirculation in the western subtropical Atlantic Ocean presents a mode transit time of  $9.1 \pm 12.1$  years, whereas the second indirect path of recirculation in the Indian Ocean corresponds to a mean mode of  $15.9 \pm 13.7$  years (Figure [3.84](#)). Those indirect routes demonstrated that water parcels might recirculate in the western South Atlantic subtropical gyre or within the Indian Ocean before their incorporation into the subtropical gyre through its eastern margin, not only once the 32°S section is crossed. This leads us to suggest that this may also occur in **Chapter 3.4**, increasing the transit times to be incorporated into the subtropical gyre, indicating that a more exhaustive analysis should be made in the future. Furthermore, the fact that the transit time has increased from the direct route to the western part of the subtropical gyre indirect route but less than  $10.2 \pm 9.5$  years (as seen in Figure [3.78](#) in subsection [3.4.4.2](#)) suggests that these previous recirculations in the western South Atlantic subtropical gyre are smaller or/and faster. Hence, hereafter it would be appropriate to describe the cold route analysing the pathways separately; and although the recirculations are relatively low frequented, 31.5% of particles in **Chapter 3.4** and 13.6 - 15.9 % in **Chapter 3.5**, start to consider the recirculations in the South Atlantic subtropical gyre as part of the cold route.

Finally, the ACC water transports experience substantial interannual and seasonal changes. In the Scotia Sea, the seasonal variability is high, ranging between 110.8 and 174.5 Sv for the Drake Passage up to the isoneutral  $\gamma^n = 28.00 \text{ kg m}^{-3}$  (Figure [3.20a](#)), and it dominates over the interannual variability causing mainly fluctuations in the AASW/AAIW and UCDW transports and also controlling the SAF and PF intensity and position. Using the climatological daily-mean fields in **Chapter 3.4**, the ACC water mass transport fluctuates throughout the year, experiencing higher variability of SASW/SAMW and AASW/AAIW with SDs around 4.8 Sv at the Drake Passage, displaying both water masses a transport asymmetry pattern. In addition, the SASW/SAMW are the water masses that experience more seasonal variability in their incorporation to 32°S and 21°S, with SDs between 0.4 Sv and 1.0 Sv (Table [3.25](#)). In 32°S and 21°S, the UCDW transport is dominant, whereas using the climatological annual-mean fields, the AASW/AAIW contribution predominates (Figure [3.80](#)). Considering all the water



masses up to  $\gamma^n < 28.00 \text{ kg m}^{-3}$ , the cold direct contribution to the AMOC at  $32^\circ\text{S}$  varies from 12.4 Sv to 15.7 Sv with a transport average of  $14.1 \pm 0.8 \text{ Sv}$ . In **Chapter 3.5**, we have analysed the seasonal variability for the 2015 - 2019 period, estimating that the intermediate cold water contribution to the  $34^\circ\text{S}$  varies from  $22.9 \pm 3.9 \text{ Sv}$  to  $25.1 \pm 4.8 \text{ Sv}$  in austral summer and winter, respectively (Table [3.26](#)). In terms of interannual variability, the cold and warm routes contribute similarly, exhibiting a very strong interannual variability with high SDs of 8.8 and 6.2 Sv (Figure [3.95](#)). Hence, we can conclude that in the relatively small Scotia Sea the seasonal variability plays a crucial role in the ACC transports, whereas the interannual variability dominates on the larger South Atlantic scale, conditioning the proportion of water incorporated into the AMOC.

## **V. CONCLUSIONS**

The main transfer of Antarctic waters to the South Atlantic Ocean takes place when the Pacific waters carried by the wind-driven ACC cross eastward through the Drake Passage. The ACC upper-ocean waters, together with a minor exchange of Weddell waters through the South Scotia Ridge and Philip Passages, eventually flow northward into the South Atlantic through the North Scotia Ridge and Georgia Passages. The vertical ACC structure shows sloping isopycnals with remarkable horizontal density gradients coinciding with several frontal systems, where eastward velocities and hence geostrophic transports are maxima. The SAF and PF have fairly stable positions and are responsible for carrying most Antarctic waters, yet with considerable cross-frontal water exchange. These fronts and their associated transports eventually exit mainly through the Scotia Sea across 54-54 Passage and Shag Rocks Passage, respectively. The ACC experiences large seasonal and moderate interannual transport fluctuations as well as a slight gain of salt and loss of heat transport within the Scotia Sea. Further, it shows a total net production of nitrate and DIC and a net consumption of dissolved oxygen and alkalinity. The total carbon budget components within the Scotia Sea consist of low carbon dioxide uptake from the atmosphere, considerable internal production through biogeochemical processes and a net anthropogenic DIC accumulation of  $0.123 \text{ Pg C yr}^{-1}$ . The Scotia Sea acts as an anthropogenic DIC storage at the surface-mode and surface-intermediate waters, although it acts as a DIC sink at depth, resulting in a net carbon reservoir.

The horizontal diffusivities in the Scotia Sea and southwestern South Atlantic Ocean are subject to strong spatial variability. In particular, the lateral diffusion coefficient decreases with depth from maximum diffusivities of  $4630 - 4980 \text{ m}^2 \text{ s}^{-1}$  in the upper 200 m to minimum values of  $1080 - 1270 \text{ m}^2 \text{ s}^{-1}$  below 1400 m. The horizontal diffusivity near the sea surface is fairly constant in latitude varying from  $3850$  to  $5270 \text{ m}^2 \text{ s}^{-1}$ , whereas at 1000 m decreases in latitude reaching down to  $530 \text{ m}^2 \text{ s}^{-1}$  near the Antarctic continent.

Even though most water transport (84.4%) that crosses the Drake Passage remains in the circumpolar ACC path beyond the African continent, up to 15.1 Sv of cold and fresh waters are incorporated into the subtropical gyre through its eastern margin in what is known as the direct cold route. In this incorporation, water parcels gain heat and salt transport, and 3.5 Sv of surface-intermediate and 3.2 Sv of deep waters gain buoyancy, being transformed to surface waters. These waters incorporated in the subtropical gyre continue northwestward carried by the SEC to bifurcate when they eventually reach the east Brazil coast. About one-third (31.5%, representing 4.8 Sv) of these water parcels flow south with the Brazil Current, whereas the remaining particles (68.5%, or 10.3 Sv) escape northward feeding the North Brazil Current. Our climatological annual-mean estimations reveal that a total of 12.6 Sv, either having crossed the eastern margin to the subtropical gyre previously or not, reach the  $21^\circ\text{S}$  western section and are incorporated to the North Brazil Current as part of the returning limb of the AMOC.

It is estimated that 1.3 Sv from the cold route recirculate at least one time completely, counted from the western margin in the South Atlantic subtropical gyre.

Apart from the cold-fresh waters from the Pacific Ocean through the Drake Passage incorporated to the subtropical gyre, the upper returning branch of the AMOC is also fed by the warm-salty waters from the Indian Ocean via the Agulhas Current. The cold-water route contributes more than the warm-water route, and hence more than previously stated. At the same time, both routes can be divided into individual direct and indirect pathways; the indirect pathways are divided in those that recirculate in the western South Atlantic subtropical gyre and within the Indian Ocean before flowing north through the eastern margin of the South Atlantic subtropical gyre. Nevertheless, the direct pathways are predominant in both routes, with percentages of 83.6% and 87.2% in austral winter, being the shortest and taking less time. Whereas the entire warm contribution lasts a median between 0.3 and 0.8 years, the cold waters take from 5.3 to 5.6 years to be incorporated at 34°S. Although the cold direct route and the warm indirect pathway that recirculates in the western edge of the subtropical gyre are the pathways that experience the highest water mass transformations, the bulk of both water routes remain within the intermediate waters' potential density range. Finally, a total mean of  $0.3 \pm 0.2$  Sv of the cold route feeds the Agulhas Current, contributing to a similar amount of the waters coming from the Indonesian Throughflow.

### 5.1. Main scientific contributions

- Entering the Scotia Sea, the Antarctic Circumpolar Current carries  $164.2 \pm 10.8$  Sv down to 2000 m, losing 4.7 Sv when it exits through the Northern Passages. Its transport is equally split in 42.6, 59.6 and 53.8 Sv among the 54–54, Shag Rocks and Georgia Passages. Relative to the 2000 m, the mean barotropic contribution always represents over half the total transports. The ACC remains 6 to 8 months within the Scotia Sea and experiences a substantial water mass cross-frontal exchange of 62.8 Sv from the SAF - PF frontal subdomain to the adjacent subdomains. The ACC seasonal variability dominates over the interannual variability causing fluctuations mainly in the AASW/AAIW and UCDW transports.
- The Argo float dataset proves to be a very useful and effective resource to characterize climatologically the ACC up to the isoneutral  $28.00 \text{ kg m}^{-3}$ . In particular, it not only provides information of the water column hydrographic variables but also allows estimating the reference velocities at 1000 m, both of the mean fields and their spatiotemporal variability at seasonal and interannual scales.

- After balancing the mass transport between isoneutrals  $26.80$  and  $28.00 \text{ kg m}^{-3}$ , the maximum accumulated transport carried out by the ACC up to  $\gamma^n = 28.00 \text{ kg m}^{-3}$  is about  $136.7 \text{ Sv}$ , being the total water mass transport imbalance in the Scotia Sea about  $0.03 \text{ Sv}$ . In particular, the vertically integrated transports per section are as follows:  $136.7 \pm 1.0 \text{ Sv}$  for the Drake Passage,  $113.6 \pm 1.0 \text{ Sv}$  in North Scotia Ridge,  $24.3 \pm 0.3 \text{ Sv}$  through the Georgia Passage,  $0.4 \pm 0.1 \text{ Sv}$  for the South Scotia Ridge, and  $0.8 \pm 0.1 \text{ Sv}$  for the Philip Passage. Within the Scotia Sea boundaries, there is a net equator freshwater flux of  $0.06 \text{ Sv}$  and a heat transport loss of  $0.065 \text{ PW}$ .
- Up to  $28.00 \text{ kg m}^{-3}$  in the Scotia Sea, there is a total net production of  $59 \text{ kmol s}^{-1}$  of nitrate,  $738 \text{ kmol s}^{-1}$  of DIC and a net consumption of  $60 \text{ kmol s}^{-1}$  for alkalinity and  $346 \text{ kmol s}^{-1}$  of dissolved oxygen. Regarding the surface-mode and surface-intermediate waters, there is a production of all properties with the slight production of DO and DIC consistent with the idea of primary production, whereas in denser layers ( $27.6 < \gamma^n < 28.00 \text{ kg m}^{-3}$ ) occurs a remarkable consumption of all of them occurs, except for the densest layer, as expected from the remineralization of relatively young waters.
- The carbon budget components in the Scotia Sea consist of the absorption of  $16.4 \text{ kmol s}^{-1}$  of anthropogenic carbon dioxide through air-sea exchange, a net internal DIC generation due to biogeochemical and advective processes of  $431 \text{ kmol s}^{-1}$  and a net anthropogenic DIC accumulation of  $0.123 \text{ Pg C yr}^{-1}$ . Specifically, the Scotia Sea acts as an anthropogenic DIC storage at the surface-mode and surface-intermediate waters and as a DIC sink in the deeper layers, resulting in a net reservoir and confirming the importance of this basin in the global carbon cycle.
- We have developed the ROD method for estimating the horizontal eddy diffusivities based on the differences between the actual displacements of field drifters and the numerical trajectories of Lagrangian particles. Although it has been implemented in the western South Atlantic Ocean, the ROD method could be applied globally to explore the spatiotemporal distribution of horizontal diffusion. The method is simple and robust, potentially useful for many applications, from the dispersion of properties in numerical circulation models to inverse-type regional balances.
- The radial offset between a float position and the position of its equivalent numerical particle responds to diffusive processes that are not reproduced in numerical ocean models. The offsets produce an isotropic cloud of points which fits a Gaussian distribution

with high concentration near the origin and flattening as particles diffuse out of their origin area.

- The horizontal diffusion in the western South Atlantic Ocean descends with depth, reaching maximum values of  $4630 - 4980 \text{ m}^2 \text{ s}^{-1}$  in the upper 200 m and diminishing to  $1080 - 1270 \text{ m}^2 \text{ s}^{-1}$  between 1400 and 2000 m. The cross-frontal variability at 15 m is fairly constant in latitude ( $3850$  to  $5270 \text{ m}^2 \text{ s}^{-1}$ ), whereas at depths of 1000 m, the diffusivity changes from  $1640 - 1820 \text{ m}^2 \text{ s}^{-1}$  north of the Polar Front to  $530 \text{ m}^2 \text{ s}^{-1}$  south of the Southern Boundary, being lower at the southern frontal subdomains near the Antarctic continent.
- The application of Lagrangian tools to numerical ocean models helps to resolve the large-scale basin interconnections, determine the water's residence time, and decipher the water mass transformations, including changes in salt and heat transport. By identifying the water parcels' origin and pathways, these Lagrangian tools clarify a debate that has been ongoing for decades.
- The Lagrangian simulations reveal that  $94.8 \text{ Sv}$  entering from the Drake Passage up to  $28.00 \text{ kg m}^{-3}$  remains at the bulk of the Antarctic Circumpolar Current, directly reaching the Indian basin. An annual-mean total transport of  $15.1 \text{ Sv}$  arrives at the eastern margin of the South Atlantic subtropical gyre, with a slight seasonal variability ranging from  $12.4 \text{ Sv}$  to  $15.7 \text{ Sv}$ . About two-thirds of this transport,  $10.3 \text{ Sv}$ , flows northward, reaching the western boundary at  $21^\circ\text{S}$  to feed the North Brazil Current.
- The ACC water parcels that join the South Atlantic subtropical gyre as part of the AMOC's returning limb gain gradually  $0.46 \text{ PW}$  of heat and  $8.5 \times 10^6 \text{ kg s}^{-1}$  of salinity. About  $68.5\%$  ( $10.3 \text{ Sv}$ ) of these waters feed the North Brazil Current, gaining in this last stage only  $0.01 \text{ PW}$  of heat and  $1.8 \times 10^6 \text{ kg s}^{-1}$  of salt. At  $32^\circ\text{S}$ , these thermohaline changes result in a net decrease in potential density as well as in a net gain of buoyancy, leading to a water mass transformation of  $6.7 \text{ Sv}$  from surface-intermediate and deep waters to surface waters.
- From the Drake Passage, the upper-ocean waters take a median of  $14.3 \pm 12.5$  years to arrive at the Brazilian Current. The South Atlantic subtropical gyre has a median recirculation time of  $10.2 \pm 9.5$  years, recirculating  $1.3 \text{ Sv}$  up to three laps within the subtropical gyre. Whereas surface-mode waters, SASW/SAMW, get deeper at each lap, the deep waters, UCDW, rise and reduce their transit times. About  $8.6\%$  of the particles, accounting for a net transport of  $9.8 \text{ Sv}$ , have a residence time in the South Atlantic basin longer than 75 years, not reaching any section of the domain in that period.

- The ROD method has allowed adding realistic horizontal radial diffusive processes to the Lagrangian experiments, simulating the submesoscale of the climatological fields. Without diffusion, the water transport estimations would be biased with almost only the SASW/SAMW waters incorporated into the South Atlantic subtropical gyre, this contribution coming exclusively from the SAF and PF fronts.
- The backtrack trajectories have shown that the cold-route contribution to the intermediate waters represents between 17.9 - 18.9% of the total waters at the eastern edge of the South Atlantic subtropical gyre, slightly more than the 7.1 - 12.3% contribution via the warm route. Furthermore, in both routes, a dominant and direct pathway exists, which is followed by 83.6 - 87.2% of the water parcels in austral winter. Whereas the warm waters last between 0.3 and 0.8 years to be incorporated into the eastern edge of the subtropical gyre from the Agulhas Current, the cold waters last between 5.3 - 5.6 years, depending on the season.
- As the intermediate waters across the regions of the Brazil Current, south of Madagascar and Cape Basin, get warmer and saltier, experiencing the highest thermohaline and depth changes. The upper circumpolar cold waters experience density alterations through net warming and salinification in their northward pathway to lower latitudes, while a substantial proportion of the near-surface warm waters experience a net potential density gain through a net decrease in water temperature.
- Despite some changes in the potential density of intermediate waters during their transit to the eastern edge of the South Atlantic subtropical gyre, the bulk of both water routes remains within the intermediate water density range. These water mass transformations are more remarkable for the cold direct route and the warm indirect route that recirculates first in the western edge of the subtropical gyre. The first implies mainly a density gain from the surface to intermediate waters, and in the second path, an equal proportion of shallow and deep waters are transformed into intermediate waters.
- The interannual variability does not reveal any clear trend but looping the one-year velocity fields shows that the cold and warm mean transport contributions are similar, around 17.5 Sv, exhibiting both a very strong interannual variability with SDs of 8.8 Sv and 6.2 Sv. Despite eventual changes in the warm and cold total transports, proportions remain fairly constant with a preferential direct route.

- At the end of the 75-year simulations, the cold-water route feeds the Agulhas Current with a total mean of  $0.3 \pm 0.2$  Sv, a contribution similar to the  $0.2 \pm 0.1$  Sv proceeding from the Indonesian Throughflow.

## 5.2. Future lines of research

The results of this thesis have advanced our knowledge of the pathways and characteristics of the Antarctic circumpolar waters as they join the South Atlantic subtropical gyre and eventually reach the Brazilian coast to feed the North Brazil Current as part of the AMOC's returning limb.

- Two distinctive regimes are found in the Scotia Sea: the Pacific waters carried by the ACC and the denser Weddell waters from the Weddell Sea. Quantifying the volume, vertical structure and characteristics of the Weddell deep waters that feed the ACC across the South Scotia Ridge, carried by the Antarctic Slope Current, still remains as an outstanding task. The AABW and its precursors are mainly formed in the Weddell Sea through intense air-sea-ice interactions. Therefore, assessing these interactions, how they are controlled by the regional circulation patterns and sea-ice freezing, and their effect on deep-water formation as well as on the outcropping of relatively warm circumpolar waters is a necessary task. One potential line of research would be to explore the correlation between sea-ice formation or melting with deep-water mass formation, identifying the bottom-water pathways over the South Scotia Ridge and the role of the Weddell-Scotia Confluence.
- The inverse box model has shown that the Southern Ocean numerical model SOSE, despite it assimilates numerous observations, underestimates locally the water and property transports. One of the future contributions and lines of research could be to make a greater effort to validate such models with the observational data collected in this dissertation, hence contributing to their improvement.
- Another useful future contribution would be to reconstruct the spatial distribution of the horizontal diffusion for the whole Southern Ocean in different depths, using the cost-efficient ROD method described in this dissertation. It could include extending the method's applicability by adjusting the observations to a two-dimensional Gaussian surface and solving the diffusion equation in Cartesian coordinates, obtaining different zonal and meridional diffusivities. Estimating the relation of the horizontal diffusion



coefficients with the position of the ACC fronts taking into account their spatiotemporal variability, can also be a useful future contribution.

- A natural extension of the calculation of numerical trajectories would be the inclusion of the entire Southern Ocean to quantify the intensity and characteristics of the Antarctic waters' contribution to the different oceanic basins. In particular, it would be useful to assess how the heat and salt transfer are redistributed along the basin interconnections and whether they change over the years.
- Following some of the ideas in **Chapter 3.4**, it seems very relevant to further explore the recirculation of water parcels within the circumpolar path and the southern hemisphere subtropical gyres. The number of recirculations tells us how swift the exchange between adjacent gyres will be, with important implications on the strength of the GOC. It would be important to explore how the number of recirculations depends on the temporal resolution of the velocity fields as well as on the spatial variability of horizontal diffusion.
- The pathways and interactions of the NADW and the AABW within the South Atlantic have not been explored in this thesis. It would be important to quantify the total cold-fresh South Atlantic Ocean contribution considering also waters denser than  $28.00 \text{ kg m}^{-3}$  to better understand its scope and their interaction with the overlying NADW. At the same time, to find out how the AABW flows northward, filling and cooling the eastern South Atlantic abyssal basin, and to identify the main submarine passages in the Mid-Atlantic Ridge where its flow crosses into the western basin.
- The lateral mixing and convergence processes that occur in the subantarctic and subtropical fronts are key elements in the intensity of the AMOC. These fronts are often considered barriers delimiting different water masses but can also act as the source of instabilities that enhance the exchange of different water masses. Further, subantarctic waters penetrate beneath the frontal regions as the combined result of Ekman pumping and the deepening of the mixing layer depth during the austral winter. The current intensity of these processes and their evolution in different climatic scenarios due to the changing winds is another topic for possible future research.

## PUBLICATIONS

This thesis is based on the following manuscripts, which are listed below according to their order of appearance. **Chapters 3.2, 3.4 and 3.5** are works under progress, being this last chapter prepared in the frame of the international stays in the Laboratoire d'Océanographie et du Climat: Expérimentations et Approches Numériques (LOCEAN), Paris, under the supervision of Dra. Christine Provost, and the Commonwealth Scientific and Industrial Research Organisation (CSIRO), Tasmania, under the supervision of Dr. Steven Rintoul.

Olivé Abelló, A., Pelegrí, J. L., Machín, F. J., & Vallès-Casanova, I. (2021). The transfer of Antarctic circumpolar waters to the western South Atlantic Ocean. *Journal of Geophysical Research: Oceans*, 126, e2020JC017025. <https://doi.org/10.1029/2020JC017025>

Olivé Abelló, A., Pelegrí, J. L., Machín F, Haumann F.A., MacGilchrist G. A., Sarmiento, J.L., (2023). Biogeochemical and water balances in the Scotia Sea as inferred from an inverse circulation model. *To be submitted*.

Olivé Abelló, A., Pelegrí, J. L., Machín (2022). A simple method for estimating horizontal diffusivity. *Journal of Oceanic and Atmospheric Technology*. *In review*.

Related articles and book chapters, including candidate contributions:

Olivé Abelló A, Vinha B, Machín F, Zerbetto F, Bakalis E, Fraile-Nuez E (2021). Analysis of Volcanic Thermohaline Fluctuations of Tagoro Submarine Volcano (El Hierro Island, Canary Islands, Spain). *Geosciences* 11, 9: 374. <https://doi.org/10.3390/geosciences11090374>

Olivé Abelló A, Pelegrí JL, (2022). The impact of the Southern Ocean on climate. In "The ocean we want: inclusive and transformative ocean science", Pelegrí, J. L., Gili, J. M., Martínez de Albéniz, M. V. (eds.), pp. 44-46. <https://doi.org/10.20350/digitalCSIC/1405>

Pelegrí JL, Orúe-Echevarría D, Olivé Abelló A, Vallès-Casanova I (2022). Physical basis of ocean primary production. In "The ocean we want: inclusive and transformative ocean science", Pelegrí, J. L, Gili, J. M., Martínez de Albéniz, M. V. (eds.), pp. 96-98. <https://doi.org/10.20350/digitalCSIC/14076>

Vallès-Casanova, I., Fraile-Nuez, E., Martín-Rey, M., van Sebille, E., Cabré, A., Olivé-Abelló, A., & Pelegrí, J. L. Water mass transports and pathways in the North Brazil-Equatorial

Undercurrent retroflection. *Journal of Geophysical Research: Oceans*, e2021JC018150.  
<https://doi.org/10.1029/2021JC01815>

Morató, J. P., Pelegrí, J. L., Rey, M. M., Olivé Abelló, A., Vallès, X., Roca, J., ... & Casanova, I. V. (2022). Environmental predictors of SARS-CoV-2 infection incidence in Catalonia (northwestern Mediterranean). PREPRINT available at Research Square.  
<https://doi.org/10.21203/rs.3.rs-2206639/v1>

## LIST OF FIGURES

- Figure 1.1.** Simplified scheme of the Global Overturning Circulation and net transports (Sv) in different water strata across the selected hydrographic sections. Ribbons indicate flow direction and overturn locations schematically. Source: Talley (2008).....26
- Figure 1.2.** Overview of the upper (red) and lower (blue) limbs of the Atlantic Meridional Overturning Circulation in the South Atlantic Ocean. Bathymetry is shaded at 1000 m intervals. In alphabetical order: ACC, Antarctic Circumpolar Current; ACS, Agulhas Current System; ARs, Agulhas Rings; BC, Brazil Current; BCS, Benguela Current System; DWBC, Deep Western Boundary Current; EEs, Equatorial Excursions; EUC, Equatorial Undercurrent; FC, Florida Current; GS, Gulf Stream; IP, Interior Pathways; IRs, Irminger Rings; LC, Loop Current; MAR, mid-Atlantic Ridge; MC, Malvinas Current; NAC, North Atlantic Current; NBC, North Brazil Current; NBCr, North Brazil Current Rings; NBUC, North Brazil Undercurrent; NEC, North Equatorial Current; NECC, North Equatorial Counter Current; NRG, Northern Recirculation Gyre; R, Recirculation; SAC, South Atlantic Current; SEC, South Equatorial Current, TGBe, Tail of the Grand Bank Eddies. Source: Bower et al. (2019).....29
- Figure 1.3.** (a) Daily snapshot (30 May 2020) of the sea-surface eddy-rich structure in the Southern Ocean, as deduced from a 0.25° resolution dataset that combines satellite data with numerical model products. (b) Bathymetry and position of the ACC fronts as determined by Orsi et al. (1995), from north to south: Subtropical Front (STF), Subantarctic Front (SAF), Polar Front (PF), Southern ACC Front (SACCF), and Southern Boundary (SB) Front. ....31
- Figure 1.4.** Schematic meridional section in the Southern Ocean showing the water masses according to their neutral density ( $\text{kg m}^{-3}$ ), the meridional-vertical cells, and the main carbon dioxide and heat release/uptake zones relative to the circumpolar fronts. The water masses are Subantarctic Mode Water (SAMW), Subantarctic Surface Water (SASW), Antarctic Intermediate Water (AAIW), Upper Circumpolar Deep Water (UCDW), Lower Circumpolar Deep Water (LCDW), Antarctic Bottom Water (AABW) and North Atlantic Deep Water (NADW). Following Orsi et al. (1995) and Whitworth III et al. (1985).....33
- Figure 1.5.** Schematic illustration of the volume transports (Sv) down to 1000 dbar. The inputs to the Cape Basin are 19.1 Sv ( $4.7 + 4 + 10.4$  Sv) from the Pacific Ocean via the ACC

and 18.5 Sv (8.5 + 10 Sv) from the Indian Ocean. The arrows represent the transports, coloured according to the origin. The grey-shaded area represents the region where waters from both Pacific and Indian Oceans interact. Source: Rodrigues et al. (2010).

..... 40

**Figure 1.6.** Schematic near-surface circulation within the Indian Ocean during the (a) northeast monsoon (January–February) and the (b) southwest monsoon (July–August). Blue arrows indicate year-round mean flows with no seasonal reversals and green/orange arrows represent the monsoonally reversing circulation. The ACC fronts are taken directly from Orsi et al. (1995). Acronyms are as follows: EACC, East African Coastal Current; NEMC, Northeast Madagascar Current; SEMC, Southeast Madagascar Current; SMACC, Southwest Madagascar Coastal Current; WICC, West Indian Coastal Current; EICC, East Indian Coastal Current; LH and LL, Lakshwadeep high and low; SJC, South Java Current; EGC, Eastern Gyral Current; SICC, South Indian Countercurrent (south, central, and southern branches); NEC, Northeast Monsoon Current; SEC, Southwest Equatorial Current. The light grey shading shows seafloor bathymetry. Originally based on Schott & McCreary (2001). Source: Phillips et al. (2021). ..... 41

**Figure 1.7.** Geographic domains considered in each chapter of the thesis. The main surface currents that constitute the circulation of the Southern Ocean (blue), South Atlantic Ocean (green) and Indian Ocean (red) are shown schematically with the bathymetry/continents drawn in grey. Acronyms are: SEMC, Southeast Madagascar Current; VTR, Vitória-Trindade Ridge; EGC, Eastern Gyral Current; STF, Subtropical Front; SAF, Subantarctic Front; PF, Polar Front; SACCF, Southern Antarctic Circumpolar Front; and SB, Southern Boundary..... 46

**Figure 2.1.** (a) Scheme of the position of the variables for a C grid or native grid (orange) and (b) compared with the positioning for an A grid (blue nodes). In the C grid, *i* and *j* respectively, represent the variable column and row indexing in arrays where the variables are stored. The indexing of the C grid follows the NEMO notations. Source: Delandmeter & van Sebille (2019). ..... 68

**Figure 3.1.** Bathymetry and main passages in the Scotia Sea, from west to east: Drake, 54-54, Shag Rocks, Black Rock and Georgia. The red bands indicate the location of the sections used in this study to characterize these passages. The surface position of the principal fronts is shown schematically: Subantarctic Front (SAF), Polar Front (PF), Southern Antarctic Circumpolar Current Front (SACCF) and the Southern Boundary (SB)..... 79

- Figure 3.2.** (a) Temperature (orange line) and temperature gradient (black line) at 1000 m across the Drake Passage and (b) the North Scotia Ridge and Georgia Passages. The locations of the Subantarctic Front (SAF), Polar Front (PF) and Southern Antarctic Circumpolar Current Front (SACCF) are shown.....82
- Figure 3.3.** Mean position of the 1000-m temperature Antarctic fronts for the (left panels) 5-year and (right panels) 3-month periods. The variability is shown as the standard deviation of the eleven 5-year and twelve 3-month realizations, respectively. (a, b) Latitudinal position along the Drake Passage and (c, d) longitudinal position in the Northern Passages (SAF is located in the 54-54 Passage, PF in the Shag Rocks Passage and SACCF in the Georgia Passage).....83
- Figure 3.4.** Argo floats crossing (a) the Drake Passage, (b) the North Scotia Ridge Passages (54-54, Shag Rocks and Black Rock), and (c) the Georgia Passage. A red line shows the location of the vertical sections across the passages. The orange dots show the surface float positions (last position before submerging and first position after surfacing), joined with a thin white dotted line. The white areas represent regions with water depth less than 1000 m. ....86
- Figure 3.5.** Velocity vectors at 1000 m along the vertical sections in (a) the Drake Passage, (b) the North Scotia Ridge Passages (54-54, Shag Rocks and Black Rock), and (c) the Georgia Passage. The arrows denote the velocity vectors associated with all floats crossing the passages, coloured according to their speed. The 1000-2000 m region is gray-shaded as to indicate the practical limits of our data. ....87
- Figure 3.6.** Mean 1000 m zonal velocities cross the Drake Passage, as inferred from Argo floats (mean values for the entire period and average of the 5-year period values), and as obtained with the NOAA SADCP dataset and with the Laurence M. Gould platform. The shaded areas represent the standard deviations of values from the Laurence M. Gould dataset.....88
- Figure 3.7.** (Left axes) Normal-to-section 1000 m velocities and (right axes) number of floats for the entire period (purple line) crossing 25 km long transects, for (a) the Drake Passage and (b) the Northern Passages. The velocities are calculated as the mean for the entire period (2002 - 2018; black line) and as the average of the means for each 5-year periods (2006 - 2016; orange line); in the last case the standard deviation is shown (yellow band). ....88

- Figure 3.8.** Vertical sections for (left) the Drake Passage and (right) the Northern Passages. (a) Potential temperature (coloured, °C) and practical salinity (dashed contours). (b) Geostrophic velocity (coloured, m/s; in Drake Passage the positive values correspond to eastward velocities, for the Northern Passages the positive velocities correspond to northward velocities) and neutral density (dashed contours,  $\text{kg m}^{-3}$ ; the selected isoneutrals denote the water mass boundaries in Table 3.1). The regional bathymetry is shaded in grey..... 89
- Figure 3.9.** Density distribution across (a) the Drake Passage, and (b) the North Scotia Ridge (54-54, Shag Rocks and Black Rock) and Georgia Passages. The different water masses are labelled following the boundaries in Table 3.1..... 90
- Figure 3.10.** Transports per water mass (a) down to  $\gamma^n = 28.00 \text{ kg m}^{-3}$  and (b) down to 2000 m at 25 km intervals crossing each passage. The colour bars illustrate the partitioning of the transports among water masses (dark blue, SAMW; light blue, AASW/AAIW; yellow, UCDW; orange, LCDW; red, WSDW). The surface location of the different fronts comes from Greene (2020) through Orsi & Whitworth III (2005), using all historical hydrographic data available for the Southern Ocean and frontal definitions from Orsi et al. (1995)..... 93
- Figure 3.11.** Number of floats that drift in the Scotia Sea after entering through the Drake Passage, counted over  $0.25^\circ \times 0.5^\circ$  latitude-longitude grid elements. The floats are identified and counted by their latitude of origin, represented by orange lines, in the Drake Passage: (a) South America to SAF, (b) SAF to PF, (c) PF to SACCF, and (d) SACCF to the Antarctic Peninsula. The surface location of the different fronts, as defined by Orsi et al. (1995), comes from Orsi & Whitworth III (2005) and available in Greene (2020) dataset..... 96
- Figure 3.12.** Number of floats as a function of residence time in the Scotia Sea, split according to their position between frontal systems as they enter the Drake Passage: South America (S.A.) to SAF, SAF to PF, PF to SACCF, and SACCF to the Antarctic Peninsula (A.P.). Each bar width corresponds to 20 days of residence time. .... 97
- Figure 3.13.** Vertical sections for (left) the Drake Passage and (right) the Northern Passages, calculated as the average of the eleven 5-year mean fields (2004-2016). (a) Potential temperature (coloured, °C) and practical salinity (dashed contours). (b) Geostrophic velocity (coloured, m/s; reddish-positive values represent eastward and northward velocities while bluish-negative values denote westward and southward velocities)

- and neutral density (dashed contours,  $\text{kg m}^{-3}$ ); the selected isoneutrals denote the water mass boundaries in Table 3.1. The regional bathymetry is shaded in grey.....98
- Figure 3.14.** Standard deviation of the 5-year averaged fields of (a) density and (b) geostrophic velocity for (left panels) the Drake Passage and (right panels) the Northern Passages (Black Rock passage has been omitted in the geostrophic velocity).....99
- Figure 3.15.** Total geostrophic transports through the passages down to  $\gamma^n = 28.00 \text{ kg m}^{-3}$ , averaged over 5-year periods, between 2006 and 2016: (a) Drake Passage, (b) 54-54 Passage, (c) Shag Rocks Passage, and (d) Georgia Passage. The contribution of each water mass and the error bars in the total transports are shown. Notice the change in the vertical scale from one panel to another.....100
- Figure 3.16.** Vertical sections for (left) the Drake Passage and (right) the Northern Passages, calculated as the average of the twelve 3-month seasonal mean fields. (a) Potential temperature (coloured,  $^{\circ}\text{C}$ ) and practical salinity (dashed contours). (b) Geostrophic velocity (coloured,  $\text{m/s}$ ; reddish-positive values represent eastward and northward velocities while bluish-negative values denote westward and southward velocities) and neutral density (dashed contours,  $\text{kg m}^{-3}$ ); the selected isoneutrals denote the water mass boundaries in Table 3.1. The regional bathymetry is shaded in grey.....101
- Figure 3.17.** Standard deviation of the 3-month averaged fields. (a) Density and (b) geostrophic velocity for (left panels) the Drake Passage and (right panels) the Northern Passages (Black Rock passage has been omitted in the geostrophic velocity).....101
- Figure 3.18.** Total geostrophic transports through the passages down to  $\gamma^n = 28.00 \text{ kg m}^{-3}$ , averaged over 3-month intervals: (a) Drake Passage, (b) 54-54 Passage, (c) Shag Rocks Passage, and (d) Georgia Passage. The contribution of each water mass and the error bars in the total transports are shown. Notice the change in the vertical scale from one panel to another.....102
- Figure 3.19.** Schematics of input and output transports in the Scotia Sea. The solid red and blue arrows represent the calculated transports, and the solid gray arrow represent the estimated transports through the shallow Northern Passages.....105
- Figure 3.20.** Water transports through the Drake (blue line) and Northern (red line) Passages, from the sea surface down to the  $28.00 \text{ kg m}^{-3}$  isoneutral. (a) Seasonal and (b) interannual variations; the SDs of the time series are represented as shaded coloured bands.....106



- Figure 3.21.** Interannual variations of the (a) baroclinic and (b) barotropic contributions to the water transports through the Drake (blue line) and Northern (green line) Passages, from the sea surface down to the  $28.00 \text{ kg m}^{-3}$  isoneutral; the SDs of the time series are represented as shaded coloured bands. .... 107
- Figure 3.22.** Climatological surface geostrophic velocities in the Scotia Sea (period 2002 - 2018) with the domain boundaries marked in orange, from west to east: the Drake Passage, the North Scotia Ridge, the Georgia Passage, the South Scotia Ridge and the Philip Passage. The blue lines represent the climatological location of the different Antarctic fronts as described by Orsi et al. (1995), from north to south: the Subantarctic Front (SAF), the Polar Front (PF), the Southern ACC Front (SACCF) and the Southern Boundary (SB) of the ACC. .... 114
- Figure 3.23.** Location of the Argo, SODB, ESASSI-08 and MEOP profiles along the Scotia Sea boundaries. Blue lines represent the average location of the different Antarctic fronts (Orsi et al., 1995), from north to south: Subantarctic Front (SAF), Polar Front (PF), Southern ACC Front (SACCF) and Southern Boundary of the ACC (SB). Regions shallower than 1000 m are shown in grey..... 116
- Figure 3.24.** Distribution of (a) alkalinity, (b) dissolved oxygen, (c) DIC and (d) nitrate stations recorded in SOCCOM and GLODAPv2 databases. We only considered the stations comprised within the dashed area, 111.12 km at each side of the sections. In grey are represented the stations without these biogeochemical concentrations, and in black, where the data has been identified as bad quality flag..... 118
- Figure 3.25.** The linear relation of alkalinity, dissolved oxygen, nitrate and DIC concentrations ( $\mu\text{mol kg}^{-1}$ ; from left to right) with neutral density according to the SOCCOM and GLODAPv2 casts (represented in black) location in (a) Drake Passage, (b) North Scotia Ridge, (c) Georgia Passage, (d) South Scotia Ridge and (e) Philip Passage. .... 120
- Figure 3.26.** Neutral density layers ( $\text{kg m}^{-3}$ ) at the surface with white contours indicating the boundary of each water mass. The relative presence of each layer at the sea surface is 0.013 for layer number 2, 0.089 for layer 3, 0.167 for layer 4, 0.174 for layer 5, 0.171 for layer 6, 0.15 for layer 7, 0.140 for layer 8, 0.068 for layer 9, 0.024 for layer 10 and 0.006 for layer 11. For the first and last layers, their relative presence is almost negligible. .... 123

- Figure 3.27.** Annual-mean climatological distributions of (a) wind stress, (b) air-ocean heat exchange, (c) evaporation minus total precipitation and (d) ice-ocean water fluxes in the Scotia Sea. For the inverse model calculations, the freshwater fluxes are quantified within the region, while the Ekman transports are computed only along the boundaries.....124
- Figure 3.28.** Imbalances in the total salt (solid contours), mass (background colours) and heat (dashed lines) as a function of the logarithm of the relative weight of the uncertainties of salt with respect to mass, *a*, and heat with respect to mass, *b*. .....126
- Figure 3.29.** Net transport imbalances of (a) mass (Sv; coloured) and DIC (Pg of C year<sup>-1</sup>; dashed contours), and (b) salt (10<sup>6</sup> kg s<sup>-1</sup>; coloured) and heat (PW; dashed contours) after applying the inverse model with different percentages to the uncertainties of *w'* and *K'* unknowns. Furthermore, (c) zoom of the mass (contours), heat (dashed contours) and salt (coloured) transport imbalances assessed together is shown applying from 25% to 200 - 250% of the uncertainties of both unknowns.....127
- Figure 3.30.** Volume estimation of (a) SASW/SAMW, (b) AASW/AAIW, (c) UCDW and (d) LCDW/WSDW within the Scotia Sea borders. Notice that lighter water accumulates at the Scotia Sea's upper margin while denser water accumulates at the lower margin. ....130
- Figure 3.31.** (a) Temperature (colour) and salinity (contours), (b) alkalinity (colour) and DIC (contours), and (c) nitrate (colour) and dissolved oxygen (contours) along the Scotia Sea boundaries. From left to right: Drake Passage, North Scotia Ridge, Georgia Passage, South Scotia Ridge and Philip Passage. In the upper horizontal axis, we represent the location of the fronts (upper panel) and the original position of the biogeochemical SOCCOM and GLODAPv2 casts (middle and lower panel); those SOCCOM and GLODAPv2 casts corresponding to the contour variable are represented in grey, whereas the black ones represent the coloured variable. Notice that positions may match, resulting in black dots overlapping the grey ones.....131
- Figure 3.32.**  $\theta$ -S diagrams and neutral density distribution (colour) of the ACC down to 2000 m along the Scotia Sea boundaries: (a) Drake Passage, (b) North Scotia Ridge and Georgia Passage, and (c) South Scotia Ridge and Philip Passage. The dashed lines in grey correspond to the isopycnals. Also, the six main water masses have been identified: SASW, SAMW, AASW/AAIW, UCDW, LCDW and WSDW. ....132

- Figure 3.33.** (a, b, c) DIC, (d, e, f) nitrate and (g, h, i) dissolved oxygen  $\theta$ - $S$  diagrams up to 2000m depth along the Scotia Sea boundaries: (a, d, g) Drake Passage, (b, e, h) North Scotia Ridge and Georgia Passage and (c, f, i) South Scotia Ridge and Philip Passage. The dashed lines in grey correspond to the isopycnals. .... 133
- Figure 3.34.** (a) Argo-float velocity ( $\text{cm s}^{-1}$ ) and inverse model adjustment at 1000 m, along the Scotia Sea boundaries. The inverse model is initialized using the Argo float velocities at 1000 m and zero velocities when the water depth is less than 1000 m and in the South Scotia Ridge and Philip Passage (because of the absence of Argo floats); the grey shading represents the *a priori* uncertainties. (b) Reference velocity at 1000 m (or the seafloor when shallower) as deduced from the inverse model (green line) and velocity at 1000 m from the SOSE model (orange line); the colour shading represents the respective standard deviation. (c) The bathymetry shallower than 2000 m along the Scotia Sea boundaries is shown in grey. Velocities are represented positive/negative to indicate water leaving/entering the domain, following the divergence/convergence sign criteria. .... 134
- Figure 3.35.** (a) Vertical velocity and diffusion after applying the inverse model, and vertical (b) mass advection, (c) salt advection and diffusion, and (d) heat advection and diffusion for the 11 neutral density interfaces. In green is represented the final diapycnal transference after adding the inverse model solution to the initial adjustment. Notice that the dashed lines correspond to the diapycnal diffusivities. Velocities are represented positive/negative to indicate water is diapycnal transferred up/down across the interfaces, following the divergence/convergence sign criteria. 135
- Figure 3.36.** (a) Geostrophic velocity with neutral density contours ( $\text{kg m}^{-3}$ ), and (b) nitrate and (c) DIC fluxes along the Scotia Sea boundaries after applying the inverse model. From left to right: Drake Passage, North Scotia Ridge, Georgia Passage, South Scotia Ridge and Philip Passage. In the upper horizontal axis, we represent the location of the fronts (upper panel) and the vertical sections have a 3-km resolution. Positive/negative values in geostrophic velocity indicate north-east/south-west direction. .... 136
- Figure 3.37.** (a) Alkalinity flux and (b) dissolved oxygen flux along the Scotia Sea boundaries after applying the inverse model. From left to right: Drake Passage, North Scotia Ridge, Georgia Passage, South Scotia Ridge and Philip Passage..... 137
- Figure 3.38.** (a) Cumulative mass transports (per water mass and total down to  $\gamma^n = 28.00 \text{ kg m}^{-3}$ ), starting at the southern edge of the Drake Passage, and (b) mass transports

through each main passage (Drake Passage, North Scotia Ridge, Georgia Passage, South Scotia Ridge and Philip Passage) and the net balance, distributed per isoneutral layers down to  $\gamma^n = 28.00 \text{ kg m}^{-3}$ . Positive (negative) values represent water leaving (entering) the domain; recall that those layers below  $\gamma^n = 28.00 \text{ kg m}^{-3}$  are not fully sampled, so the corresponding transports are shown as dashed lines in both panels.

- .....138
- Figure 3.39.** (a) Direction and magnitude of surface-mode (SASW, SAMW), surface-intermediate (AASW, AAIW), deep (UCDW) and total transports down to  $\gamma^n = 28.00 \text{ kg m}^{-3}$ . (b) Mass transport distribution along the Scotia Sea boundaries for each water mass and with a 3-km resolution. Positive/negative values in transports indicate north-east/south-west direction, transports through the Drake Passage, South Scotia Ridge and Philip Passage represent inflow and transports through the Northern Passages represent outflow. The blue lines represent the climatological location of the different ACC fronts obtained by Orsi et al. (1995). .....139
- Figure 3.40.** (a) Direction and magnitude of surface-mode, surface-intermediate, deep and total geostrophic transport and (b) total mass transport distribution up to 2000 m along the different passages after applying the inverse model. Positive/negative values in transports indicate north-east/south-west direction, transports through the Drake Passage, South Scotia Ridge and Philip Passage represent inflow and transports through the Northern Passages represent outflow. The blue lines represent the climatological location of the different ACC fronts obtained by Orsi et al. (1995). ....140
- Figure 3.41.** (a) Salt and (b) heat transports through each main passage (Drake Passage, North Scotia Ridge, Georgia Passage, South Scotia Ridge and Philip Passage) and the net balance, distributed in isoneutral layers down to  $\gamma^n = 28.00 \text{ kg m}^{-3}$ . Positive (negative) values represent heat and salt transports leaving (entering) the domain. ....141
- Figure 3.42.** (a) Alkalinity, (b) DO, (c) DIC and (d) nitrate transports through the Scotia Sea boundaries, calculated every 3 km and split per water stratum as shown. Positive (negative) values represent north-east (south-west) biochemical properties transport in the domain. The blue lines represent the average location of the different ACC fronts (Orsi et al., 1995) .....142
- Figure 3.43.** (a) Alkalinity, (b) DIC, (c) dissolved oxygen and (d) nitrate vertical advection (solid lines) and diffusion (dashed lines) after the inverse model for all neutral density

interfaces. Positive/negative values indicate water transferred up/down across the interfaces..... 144

**Figure 3.44.** Spatial distribution of the annual-mean air-sea CO<sub>2</sub> fluxes in the Scotia Sea as deduced from the NCEI product..... 146

**Figure 3.45.** Inverse model and SOSE/B-SOSE differences in cross-section for (a) geostrophic velocity, (b) nitrate flux and (c) DIC flux along the Scotia Sea boundaries. From left to right: Drake Passage, North Scotia Ridge, Georgia Passage, South Scotia Ridge and Philip Passage. Positive/negative values indicate a dominance of the inverse model/SOSE properties fluxes. .... 148

**Figure 3.46.** SOSE model distribution of (a) geostrophic velocity and neutral density layers (contours), (b) nitrate flux and (c) DIC flux along the Scotia Sea boundaries. From left to right, the sections are: the Drake Passage, North Scotia Ridge, Georgia Passage, South Scotia Ridge and Philip Passage. In the upper horizontal axis, we represent the location of the fronts (upper panel) and positive/negative values in geostrophic velocity and fluxes indicate north-east/south-west direction. .... 149

**Figure 3.47.** Comparison between (a) mass, (b) DO, (c) nitrate and (d) DIC transports per passages and their transport imbalances as obtained from the inverse (BGC-IM) and B-SOSE models. In the right panels, the solid and dashed lines correspond to the inverse and B-SOSE imbalances, respectively. For each neutral density and passage, the transports are drawn to the left for the B-SOSE model and to the right for the inverse model..... 150

**Figure 3.48.** (a) SOSE mass balance and B-SOSE (b) dissolved oxygen, (c) nitrate and (d) DIC balances at the Scotia Sea boundaries. The first value for each passage corresponds to the surface-modal stratum transport (SASW, SAMW), the second corresponds to the surface-intermediate stratum transport (AASW, AAIW), the third to the bottom stratum (UCDW), and finally, the fourth corresponds to the total transport. Positive/negative values in transports indicate north-east/south-west direction. .... 151

**Figure 3.49.** SOSE model distribution of (a) temperature and salinity (contours) and B-SOSE distribution of (b) nitrate, (c) dissolved oxygen and (d) DIC vertical sections along the Scotia Sea boundaries after the Argo profiles incorporation. The passages are Drake Passage, North Scotia Ridge, Georgia Passage, South Scotia Ridge, and Philip Passage from west to east..... 153

- Figure 3.50.** Trajectories of (a) RAFOS floats between 2009 and 2011, (b) Argo floats from 2002 to 2020, with positions shown every 10 days, and (c) GDP drifters from 2005 to 2020; the RAFOS and Argo floats are coloured according to their drifting depth. (d) Location of the Subtropical Front (STF), the Subantarctic Front (SAF), the Polar Front (PF), the Southern Antarctic Circumpolar Current Front (SACCF) and the Southern Boundary (SB), as obtained by Orsi et al. (1995). (e) Number of drifters and (f) number of 10-day positions according to drifting depth and the type of drifter. ....160
- Figure 3.51.** Vertical distribution of the 10-day cycles drifting depth along the 32 RAFOS trajectories. The 23<sup>rd</sup> RAFOS is the one most cycles performed inside the southwestern South Atlantic Ocean with a total of 29. The mean vertical displacement is about 149 m, being able to sink around 770 m along their trajectory as the 28<sup>th</sup> float from 1265 m to 2014 m depth. ....162
- Figure 3.52.** (a) Schematic trajectories of a drifter and the corresponding simulated numerical particle. The initial position of both drifter and numerical particle is  $(x_i, y_i)$ , and their final locations after 10 days are  $(x', y')$  and  $(x'', y'')$ , respectively. (b) Sketch of the final positions of both drifter and numerical particle: the longitudinal and latitudinal offsets are  $x_d = x' - x''$  and  $y_d = y' - y''$ , respectively, so that the offset (radial distance) is  $r_d = (x_d^2 + y_d^2)^{\frac{1}{2}}$ . ....164
- Figure 3.53.** (a) Sample trajectory of an Argo float through the study area, with the colour convention following Figure 3.52. The blue dots, joined by black lines, represent the initial and final positions transmitted by the float during the 10-day cycle; note that there are pairs of blue dots very close to each other, which represent the first transmission of the float after arrival to the sea surface and the last transmission before immersion. The numerical trajectories are drawn as straight black lines that depart from the second blue dot and end in a green dot, which represents the final numerical positions. (b) Scattered plot showing the radial offsets between the Argo float and the corresponding numerical particles; the origin of coordinates, which is shown as a green dot, represents the position of the numerical particle at the end of each cycle. ....165
- Figure 3.54.** Scatter plot of radial distances (a-h, left columns) grouped per drifting depth range together with the normalized experimental concentration (dots) and the adjusted Gaussian distribution (green line) as in Figure 3.57c (a-h, right columns). In each scatter plot is represented the inner radius  $R_e$  and the correlation coefficient between the

experimental points and the adjusted curve; the coloured dots identify data points from one same float..... 166

**Figure 3.55.** (Left columns; a, c, e, g, i) Scatter plot of radial offsets for the GDP 15-m drifters together with the normalized experimental concentration (dots) and the adjusted Gaussian distribution (blue line) as in Figure 3.57c. (Right columns; b, d, f, h, j) As before but for the Argo 1000-m floats. In each scatter plot is represented the inner radius  $R_e$  and the correlation coefficient between the experimental points and the adjusted curve; the coloured dots identify data points from one same float..... 167

**Figure 3.56.** Numerical solution of the radial diffusive equation for  $K = 1000 \text{ m}^2 \text{ s}^{-1}$  at different times. (a) From  $t = 0$  to  $t = 10$  hours plotted every hour and (b) from  $t = 0$  to  $t = 10$  days plotted every day. Notice the differences in the horizontal and vertical axis between both panels..... 170

**Figure 3.57.** (a) Scatter plot of radial offsets for drifters at 1000 m, displaying rings of equal area; the coloured dots identify data points from one same float. In this subplot, we also draw the origin of coordinates (grey dot with a white border) and one ring every 25 rings computed (black circles), starting with the inner ring ( $R_e = 30 \text{ km}$ ) and following with the relation  $R_j = j^{1/2} R_e$ . (b) Cumulative number of particles as a function of radial distance for  $R_e = 30 \text{ km}$ , disclosing the expected shape of the error function. (c) Normalized experimental concentration (dots) and the adjusted Gaussian distribution (green line)..... 171

**Figure 3.58.** Gaussian adjustment that best fits the histogram data (black dots) according to the different weights given to the particles concentration for the radial distances at 1000 m depth comprised from 0 to 150 km, from 150 km to 300 km, and finally for radial distances higher than 300 km. The histograms for different values of the inner radius assed are (a)  $R_e = 20 \text{ km}$ , (b)  $R_e = 30 \text{ km}$ , (c)  $R_e = 40 \text{ km}$  and (d)  $R_e = 50 \text{ km}$  and increase at intervals of 10 km. Notice that some Gaussian adjustments are not visible because they are overlapped. The best and chosen fit for all histograms corresponds to  $a = 1$ ,  $b = 1$  and  $c = 3$  (light green adjustment)..... 172

**Figure 3.59.** Degree of correlation ( $R^2$ ) between the histogram and the Gaussian fit as the inner radius increase from 10 km to 80 km at 1000 m depth. The  $R^2$  increase starting from (a) 0.928, (b) 0.960, (c) 0.963 and reach its maximum at (d, e, g) 0.973 to decrease again at (f) with 0.971 until (h) 0.966. When the  $R^2$  stabilizes, and the concentration of the particles (black dots) not show too much noise, the minimum radius that has a high

- correlation value ( $> 0.9$ ) is the one selected. The Gaussian fits are already adjusted with the  $a = 1$ ,  $b = 1$  and  $c = 3$  weights.....172
- Figure 3.60.** Gaussian adjustment (light green line) to the experimental particle concentrations (black dots) and the best-adjust numerical solution (dark green line) with the corresponding diffusion coefficient for each depth range as labelled. In all instances, the correlation ( $R^2$ ) between the experimental and numerical Gaussian curves, using data every 420 m, is greater than 0.95. ....174
- Figure 3.61.** Distribution of the drifter trajectories along the southwestern South Atlantic Ocean at 700 - 800 m. The 10-day cycles are mainly constrained south of ACC and within the Weddell Sea, probably being the Argo and/or RAFOS floats carried by the SACCF and SB fronts. Each colour corresponds to one different float, and notice that large spacing between cycles in the Weddell Sea are due to the presence of sea-ice coverage, not to high velocities in the region.....175
- Figure 3.62.** Gaussian adjustment (light blue line) to the experimental particle concentrations (black dots) and the best-adjusted numerical solution (dark blue line) with the corresponding diffusion coefficient for each region; the acronyms are Subtropical Front (STF), Subantarctic Front (SAF), Polar Front (PF), Southern Antarctic Circumpolar Current Front (SACCF), Southern Boundary (SB) and Antarctic continent (AC). The upper row corresponds to GDP data at 15 m and the lower row to Argo float data in the 900 - 1100 m depth range. In all instances, the correlation ( $R^2$ ) between the experimental and numerical Gaussian curves, using data every 420 m, is greater than 0.95.....176
- Figure 3.63.** Scattered plot of the experimental  $\sigma^2/2\tau$  values as a function of the  $K$  values obtained through the ROD method. The linear regression is shown together with the 0.95 confidence bounds. ....179
- Figure 3.64.** (a) Vertical distribution (green line) and (b) horizontal variability of the horizontal diffusion coefficients; the latter are shown only at 15 m (light blue line) and in the 900 - 1100 m depth range (dark blue line) for the five frontal regions as shown in Figure 3.50d (Orsi et al., 1995). The acronyms are Subtropical Front (STF), Subantarctic Front (SAF), Polar Front (PF), Southern Antarctic Circumpolar Current Front (SACCF), Southern Boundary (SB) and Antarctic continent (AC). Notice that the eddy-diffusion coefficients are in logarithmic scale. ....180



- Figure 3.65.** (a) Geostrophic velocities and (b) potential temperature (coloured) and salinity (contours) distributions in the surface of the South Atlantic Ocean with the positions of the four key sections: the 25°E, 32°S, 21°S and 32°S-W sections..... 189
- Figure 3.66.** Distribution of (a) potential temperature (°C, coloured) and salinity (g kg<sup>-1</sup>, contours), (b) zonal velocity (m s<sup>-1</sup>, coloured) and neutral density (kg m<sup>-3</sup>, contours), and (c) particle release positions together with the zonal velocity and neutral density contours. The density of particles in (c) reflects the zonal speeds in the Drake Passage; the left panel shows those particles (coloured in red) remaining in the ACC (25°E), the central panel those that reach the 32°S section (coloured in blue), and the right panel those that reach the 21°S section (coloured in orange). The bathymetry is represented in grey..... 192
- Figure 3.67.** Distribution of particle percentages crossing the Drake Passage that reach (a) 32°S and (b) 21°S, and distribution of these same particles as they reach (c) 32°S and (d) 21°S. The black contours correspond to the zonal/meridional component of velocity (m s<sup>-1</sup>). The histograms show the total transports every 65 m. .... 193
- Figure 3.68** (Left) Numerical trajectories tracked forward from the Drake Passage across the South Atlantic for (a) surface-mode waters, (b) surface-intermediate waters and (c) deep waters, coloured according to their median transit times. (Right) Transit-time histograms for the three routes: 25°E (red), 32°S (blue) and 21°S (orange). The grey bars in 32°S count particles that have crossed the 32°S-W section and recirculate the subtropical gyre completely to reach the 32°S section again. Only those routes with a probability higher than 1.5% are considered, coinciding with the coloured distributions in Figure 3.69. Median times are higher because they consider the entire particle trajectory, including the subtropical gyre recirculations. .... 195
- Figure 3.69.** Climatological probability distributions of (a) surface and mode (SASW, SAMW), (b) surface and intermediate (AASW, AAIW) and (c) deep waters (UCDW). The grid used is 1° in longitude and latitude, each Lagrangian particle being only counted once per grid cell..... 196
- Figure 3.70.** Climatological vertically-integrated mean Lagrangian streamfunction (contours) and the magnitude of the transport per cell in absolute values (colours) for numerical particles crossing the Drake Passage down to 28.00 kg m<sup>-3</sup>. (a) Transports for all pathways and (b) transports considering only those trajectories incorporated to the subtropical gyre (crossing 32°S and/or 21°S sections). The contour intervals correspond

to 5 Sv in the left panel and to 2 Sv in the right one. Only those particles that reach at least one section are considered; only the first subtropical gyre recirculation is considered, disregarding particles that reach 32°S-W for the second time. ....198

**Figure 3.71.** Histograms of water transport for particles that reach the 32°S section (blue) and 21°S section (orange) from the Drake Passage, plotted as a function of the change in (a, b, c) depth, (d, e, f) salt and (g, h, i) potential temperature along the trajectory, for surface-mode (a, d, g), surface-intermediate (b, e, h) and deep water masses (c, f, i). The property variations of particles between 32°S and 21°S are represented in turquoise. Positive/negative values correspond to gain/loss.....200

**Figure 3.72.** (a) Climatological vertically-integrated heat transport (PW) per cell in absolute values (colours) and conservative heat transport (contours) gradually accumulated from western and southern boundaries as particles increase their temperature. (b) Heat transport gain/loss in the domain. Only those particles that reach at least one section are considered, and the particle transport ( $vA$ ) is considered in absolute terms. Moreover, the particle trajectories are only included until they perform the second recirculation in the South Atlantic subtropical gyre, crossing the 32°S-W for the second time.....201

**Figure 3.73.** Conservative temperature and absolute salinity ( $S_A - \theta$  and  $\Delta S_A - \Delta\theta$  diagrams) diagrams of those particles that reach the (left) 25°E, (centre) 32°S and (right) 21°S sections, as they are: (a, b, c) in the Drake Passage and (d, e, f) in the respective final section; (g, h, i) property variations between both sections. Whereas the 32°S and 21°S consider all pathways until the section, the 25°E only includes those particles that follow this pathway. ....203

**Figure 3.74.** Water mass transports per neutral density as they depart from the (a, b, c) Drake Passage and as they reach (d) 25°E, (e) 32°S and (f) 21°S; the 25°E section only includes the particles that exclusively follow the ACC direct pathway. The shading illustrates the density range of surface-intermediate (AASW, AAIW) waters, separating the lighter surface-mode (SASW, SAMW) and denser deep (UCDW) waters. ....204

**Figure 3.75.** (a) Scatter plot of radial diffusive displacements added in the Lagrangian simulations every time a particle is advected at  $t = 1$  day, coloured according to their respective depth. (b) Gaussian distribution fitted for the particle's concentration as a function of radial distances for the different diffusion coefficients (see subsection [3.3.3](#) for further details); the Gaussian fits lead to a correlation of  $R^2 \cong 1$ , adjusted with the

following weights:  $a = 1$  for radial distances lower than 50 km,  $b = 1$  between 50 km and 100 km, and  $c = 3$  for radial distances higher than 100 km..... 205

**Figure 3.76.** Climatological probability distributions of (a) surface-mode (SASW, SAMW), (b) surface-intermediate (AASW, AAIW) and (c) deep waters (UCDW) without diffusion processes. The grid used is  $1^\circ \times 1^\circ$  in longitude and latitude, each Lagrangian particle being only counted once per grid cell..... 206

**Figure 3.77.** Distribution of particle release positions together with selected zonal velocity ( $\text{m s}^{-1}$ , coloured) and neutral density contours ( $\text{kg m}^{-3}$ , contours) coloured according to their section fate in the absence of diffusion processes. The density of particles reflects the zonal speeds in the Drake Passage; the left panel shows those particles (coloured in red) remaining in the (a) ACC ( $25^\circ\text{E}$ ), the central panel those that reach the (b)  $32^\circ\text{S}$  section (coloured in blue), and the right panel those that reach the (c)  $21^\circ\text{S}$  section (coloured in orange). The bathymetry is represented in grey; see Figure 3.66 for more details. .... 206

**Figure 3.78.** (a) Histogram of the years taken to recirculate the subtropical gyre, calculated as the time lap between two crossings of  $32^\circ\text{S-W}$ , plotted as a function of the associate volume transport. The number of laps completed within the subtropical gyre for the (b) surface-mode (SASW, SAMW), (c) surface-intermediate (AASW, AAIW) and (d) deep waters (UCDW)..... 208

**Figure 3.79.** Seasonal variability of (a, b, d, f) volume transport and (c, e, g) transit times using the climatological daily-mean fields in (a) the Drake Passage and at (b, c)  $25^\circ\text{E}$ , (d, e)  $32^\circ\text{S}$  and (f, g)  $21^\circ\text{S}$  for the different water masses. Whereas the DP  $\rightarrow$   $32^\circ\text{S}$  and DP  $\rightarrow$   $21^\circ\text{S}$  consider all pathways until crossing the section, the DP  $\rightarrow$   $25^\circ\text{E}$  only includes those particles that follow this pathway..... 210

**Figure 3.80.** Scheme of the main could-route pathways up to  $\gamma^n < 28.00 \text{ kg m}^{-3}$ , over the climatological annual-mean probability distributions, with volume transports, transit times, and salt and heat transports at Drake Passage,  $25^\circ\text{E}$ ,  $32^\circ\text{S}$  and  $21^\circ\text{S}$  according to the different water masses. For the  $25^\circ\text{E}$  section, we show the direct (via ACC) and total (direct plus subtropical gyre recirculation) heat and salt transports. The grid used for the probability distribution includes all the trajectories with  $0.5^\circ$  in longitude and  $0.3^\circ$  latitude, coloured reaching the darkest green shade at 15% of probability. Each Lagrangian particle is only counted once per grid cell. .... 212

- Figure 3.81.** (a) Scheme of the direct and indirect pathways that form the cold and warm routes (dashed lines) of the intermediate waters to the South Atlantic Ocean: ACC fronts and circulation (in blue) and the Agulhas Current System with the main surface current that feeds it (in red). The vertical sections for tracking particles are shown: 34°S (reference section), DP (Drake Passage; 64°W), AC (Agulhas Current; 30°S), ITF (Indonesian Throughflow), IO (entrance to the Indian Ocean; 27°E), 21°S (SEC bifurcation) and WSG (Western Subtropical Gyre; 34°S). (b) Climatological mean salinity distribution along the reference section. The 2015 - 2019 average potential density contours that delimit the low-salinity intermediate waters are shown.....221
- Figure 3.82.** Distribution and percentage of Lagrangian particles released per bin along the 34°S vertical section that come from (a, b) the Agulhas Current and (c, d) the Drake Passage during summer (left panels) and winter (right panels) seasons. The number of particles released in the intermediate waters is proportional to the geostrophic transport. The time-averaged potential density contours of 26.8 and 27.5 kg m<sup>-3</sup> are plotted as a visual guide.....222
- Figure 3.83.** Mean probability distributions and time transits of (e, f, g, h) particles that follow the cold-water route and (a, b, c, d) particles that follow the warm route released in summer (a, b, e, f) and in winter (c, d, g, h). The grid used is 0.5° in latitude and 1.3° in longitude, having the same number of cells in both coordinates; each Lagrangian particle is only counted once per each grid cell. ....224
- Figure 3.84.** Mean probability distributions of (a, b, c) warm and (d, e, f) cold backwards trajectories until they reach the source section (AC or DP) of particles released in summer from the reference section: the indirect routes crossing (a, d) the western subtropical gyre, (b, e) the Indian Ocean, and (c, f) the direct route. ....226
- Figure 3.85.** Percentage of particle distribution and the sum of their volume transport down to 2000 m at source sections: (a, b, c, d) Agulhas Current and (e, f, g, h) Drake Passage sections in summer and winter. The average potential density contours of 26.8 and 27.5 kg m<sup>-3</sup> for each season are plotted in solid lines. In grey is represented the bathymetry, the width of the green bars corresponds to 50 m and each bin is about 0.1° wide and 50 m depth.....227
- Figure 3.86.** Thermohaline properties along the mean particle trajectories for the three main warm pathways for particles released on austral winter. (a, d) Indirect route across the western South Atlantic subtropical gyre; (b, e) indirect route after recirculating in the

- Indian Ocean; (c, f) direct route. Only pathways with a probability equal or higher than 0.5% are considered (Figure [3.84](#))..... 228
- Figure 3.87.** Thermohaline properties along the mean particle trajectories for the three main cold pathways for particles released in austral winter. (a, d) Indirect route across the western South Atlantic subtropical gyre; (b, e) indirect route after recirculating in the Indian Ocean; (c, f) direct route. Only pathways with a probability equal or higher than 0.5% are considered (Figure [3.84](#))..... 229
- Figure 3.88.** Thermohaline and depth variations along the mean particle trajectories for the three main cold pathways for particles released in austral winter. (a, d, g) Indirect route across the western South Atlantic subtropical gyre; (b, e, h) indirect route after recirculating in the Indian Ocean; (c, f, i) direct route. Only pathways with a probability equal or higher than 0.5% are considered, coinciding with the coloured distributions in Figure [3.84](#)..... 230
- Figure 3.89.** Thermohaline and depth variations along the mean particle trajectories for the three main warm pathways for particles released in austral winter. (a, d, g) Indirect route across the western South Atlantic subtropical gyre; (b, e, h) indirect route after recirculating in the Indian Ocean; (c, f, i) direct route. Only pathways with a probability equal or higher than 0.5% are considered, coinciding with the coloured distributions in Figure ..... 231
- Figure 3.90.** (a, e, c, g) Conservative temperature-absolute salinity diagrams,  $S_A-\theta$ , at the reference and source sections in the Drake Passage and the Agulhas Current for particles released in austral winter. (i, k) Diagrams of the variations of conservative temperature and absolute salinity ( $\Delta S_A - \Delta \theta$ ) of the intermediate water parcels between the reference section and at the source section in the Drake Passage or the Agulhas system, together with the resulting potential density gain or loss (colour; positive/negative for gain/loss). The particles percentage distribution in the diagrams is represented in the respective right panels (b, d, f, h, j, l). ..... 233
- Figure 3.91.** (a, e, c, g) Conservative temperature-absolute salinity diagrams,  $S_A - \theta$ , at the reference and source sections in the Drake Passage and the Agulhas Current for particles released in austral summer. (i, k) Diagrams of the variations of conservative temperature and absolute salinity ( $\Delta S_A - \Delta \theta$ ) of the intermediate water parcels between the reference section and at the source section in the Drake Passage or the Agulhas system, together with the resulting potential density gain or loss (colour;

- positive/negative for gain/loss). The particles percentage distribution in the diagrams is represented in the respective right panels (b, d, f, h, j, l). .....234
- Figure 3.92.** AAIW transport that experienced water mass transformations along the cold (left, in blue) or warm (right, in red) routes, according to their potential density, at Drake Passage (b, d) or Agulhas Current (f, h) and at the reference section (a, c, e, g). The smooth grey area divides the upper (left;  $\sigma < 26.8 \text{ kg m}^{-3}$ ), intermediate (grey shaded;  $26.8 < \sigma < 27.5 \text{ kg m}^{-3}$ ) and deep (right;  $\sigma > 27.5 \text{ kg m}^{-3}$ ) potential density ranges. ....235
- Figure 3.93.** Mean probability distributions of particle trajectories that follow from the Agulhas Current section to the reference section in (a, b) winter and (c, d) summer, and their transport time evolution (e, f) from the Drake Passage and the Indonesian Throughflow. ....237
- Figure 3.94.** Probability distribution of particles released in austral winter looping 1-year velocity fields for 75 years. The left panels (a, b, c, d, e) correspond to the trajectories that cross the Drake Passage, while the right panels (f, g, h, i, j) to those that cross the Agulhas Current in (a, f) 2015, (b, g) 2016, (c, h) 2017, (d, i) 2018 and (e, j) 2019. ....239
- Figure 3.95.** (a, b, c) Net/Total volume transport percentage, (d, e, f) number of Lagrangian particles (d, e, f), and (g, h, i) transit times for the total and individual cold (in blue) or warm (in red) routes at  $34^{\circ}\text{S}$  for one-year repeated loops (2015 to 2019 years) during 75 years. The abbreviations WSG and IO refer to the indirect pathways recirculating in the Indian Ocean and in the western subtropical gyre. The mode transit time corresponds to the most frequent time. ....240
- Figure 3.96.** (a, b, e, f, i, j) Thermohaline and depth differences, and (c, d, g, h, k, m) water mass transformations along the individual pathways of the cold (in blue) and warm (in red) routes from their source at  $34^{\circ}\text{S}$  for one-year repeated loops (2015 to 2019 years) during 75 years. The abbreviations WSG and IO refer to the individual indirect pathways recirculating in the Indian Ocean or in the western edge of the subtropical gyre. ....241
- Figure 4.1.** Comparison of the geostrophic transport distribution along the Drake Passage, North Scotia Ridge and Georgia Passage as calculated in (a) **Chapter 3.1** every 25 km and (b) **Chapter 3.2** for a 3-km resolution. Notice that transport bars are stacked and hence, slightly different from transports plotted in Figure 3.39b where they are overlapped. In **Chapter 3.1**, the main inflow/outflow is equal to  $140.8 \pm 7.4 \text{ Sv}$  for the Drake Passage and  $115.9 \pm 8.3 \text{ Sv}$  for the Northern Passages, while in **Chapter 3.2**, the

|  |     |
|--|-----|
| sum corresponds to $136.7 \pm 1.0$ Sv for the Drake Passage and $137.9 \pm 1.0$ Sv for the Northern Passages.....  | 249 |
| <b>Figure 4.2.</b> Comparison of the reference velocities at 1000 m along the Drake Passage, North Scotia Ridge and Georgia Passage, as obtained in <b>Chapter 3.1</b> (black line) and <b>Chapter 3.2</b> (red and green line). In <b>Chapter 3.2</b> , the absolute velocities are obtained from the mean Argo trajectories (red line) calculated with a horizontal resolution of 3 km and then adjusted with the inverse model solution (green line).....   | 255 |
| <b>Figure 4.3.</b> Comparison of the (a) radial distances at 1000 m obtained in <b>Chapter 3.3</b> , fit with a Gaussian distribution using $K=1540 \text{ m}^2 \text{ s}^{-1}$ , with the (b) radial distances added to the 1000-m virtual particles advected by the GLORYS12v1 velocity fields, both with a 10-day time resolution. The coefficient introduced in the GLORYS12v1 Lagrangian simulations at 1000 m corresponds to $K=2226 \text{ m}^2 \text{ s}^{-1}$ , according to the expression <a href="#">2.42</a> in subsection <a href="#">2.4.3</a> . .....  | 258 |
| <b>Figure 4.4.</b> Comparison of the geostrophic velocities (coloured, $\text{m s}^{-1}$ ) and neutral density (solid contours, $\text{kg m}^{-3}$ ) vertical distributions of the ACC at the Drake Passage and their $\theta$ - $S_A$ diagram coloured according to pressure, inferred through (a) Argo casts with a 25-km resolution ( <b>Chapter 3.1</b> ), (b) after applying the inverse model with a 3-km resolution ( <b>Chapter 3.2</b> ) and (c) from the annual-average numerical model product GLORYS12v1 ( <b>Chapter 3.4</b> ). Positive values correspond to eastward velocities, and the selected isoneutrals denote the water mass boundaries in Table <a href="#">3.1</a> in subsection <a href="#">3.1.2.1</a> . The regional bathymetry is shaded in grey. ....   | 260 |
| <b>Figure 4.5.</b> Comparison of the probability distributions for those particles that follow the direct cold-water route between Drake and the eastern side of the South Atlantic subtropical gyre: (a) averaged annually and tracked forward to $32^\circ\text{S}$ for all the water masses ( <b>Chapter 3.4</b> ) and (b) seasonal-mean and tracked backwards from $34^\circ\text{S}$ for intermediate waters ( <b>Chapter 3.5</b> ). The grid used in both cases is $0.5^\circ$ in latitude and $1^\circ$ in longitude, having the same number of cells in both coordinates, and each Lagrangian particle is only counted once per each grid cell. For the respective acronyms of the sections, see Figures <a href="#">3.65</a> and <a href="#">3.79</a> . Particles have been tracked for 75 years in both Lagrangian simulations. .... | 262 |

## LIST OF TABLES

|  |    |
|--|----|
| <b>Table 1.1</b> Principal water masses found/originated in the Southern Ocean. Adapted from Talley ( <a href="#">2011</a> ).  | 37 |
| <b>Table 2.1.</b> Databases and model products used to develop this thesis dissertation.   | 48 |
| <b>Table 2.2.</b> Comparison of the characteristics of the Lagrangian simulations in each chapter of this thesis.  | 69 |
| <b>Table 3.1.</b> Neutral density definitions for water masses in the Scotia Sea.  | 82 |
| <b>Table 3.2.</b> Number of float tracks and profiles crossing each passage, clustered over 3-month periods.   | 84 |
| <b>Table 3.3.</b> Number of float tracks and profiles crossing each passage, clustered over 5-year periods.  | 85 |
| <b>Table 3.4.</b> Number of float tracks and profiles crossing each passage, clustered over 5-year periods, not used because of the relatively small number of floats crossing the region during 2002 and 2003.  | 85 |
| <b>Table 3.5.</b> Total geostrophic transports through the passages down to 2000 m, with their baroclinic and barotropic contributions.  | 92 |
| <b>Table 3.6.</b> Total geostrophic transports (Sv) per layer through the Passages down to $\gamma^n = 28.00$ kg m <sup>-3</sup> .   | 92 |
| <b>Table 3.7.</b> Geostrophic transports (Sv) between fronts and through the different passages down to $\gamma^n = 28.00$ kg m <sup>-3</sup> : inflow through the Drake Passage and outflow through the Northern Passages. The longitudes roughly indicate the geographical boundaries (Figure <a href="#">3.10</a> ). S.A. stands for South America, A.P. stands for Antarctic Peninsula and S.S.A. stands for the South Sandwich Arc.     | 95 |
| <b>Table 3.8.</b> Number of Argo floats entering and departing the Scotia Sea between frontal systems; only those floats that exit the Scotia Sea are considered. The numbers in the first column indicate the floats entering through the Drake Passage and the numbers in the top row represent the floats exiting through the Northern Passages; the figures in each cell represent the number of floats entering and leaving through the |    |



corresponding frontal domain. Abbreviations: S.A. stands for South America, A.P. stands for Antarctic Peninsula and S.S.A. stands for the South Sandwich Arc..... 96

**Table 3.9.** Comparison of barotropic, baroclinic and total transports (Sv) through the different Passages according to several authors and this study. The velocity reference level is indicated between parenthesis in the first column. For this study, the SD corresponds to the value obtained from the 5-year values between 2006 and 2016 (Table 3.6 shows, for this study, how the output splits among the 54-54, Shag Rocks and Black Rock Passages)..... 104

**Table 3.10.** Number of casts recorded for each passage according to each database. The ESASSI-08 database only provides casts in the Philip passage, where MEOP profiles have been discarded in order to avoid shallow water column perturbations. .... 116

**Table 3.11.** Number of biogeochemical casts recorded in SOCCOM and GLODAPv2 databases for each passage within the dashed area 111.12 km at each side of the sections. .... 117

**Table 3.12.** Layers and approximate equivalent corresponding water mass definitions: Subantarctic Surface Water (SASW), Subantarctic Mode Water (SAMW), Antarctic Surface and Intermediate Waters (AASW/AAIW), the Upper Circumpolar Deep Water (UCDW), Lower Circumpolar Deep Water (LCDW) and Weddell Sea Deep Water (WSDW). .... 121

**Table 3.13.** *A priori* uncertainties for all unknowns and equations:  $b'$  corresponds to the velocity adjustment at the reference level;  $w'$  to the adjustment of the diapycnal velocity across the layer interfaces;  $K'$  to the adjustment of the diapycnal diffusion coefficients at the layer interfaces;  $\Delta T_{EK}$  to the annual-mean Ekman transport adjustment; and  $\Delta F_w$  to the annual-mean freshwater flux adjustment. .... 125

**Table 3.14.** Alkalinity, dissolved oxygen, nitrate, and DIC transport imbalances obtained per water masses after applying the inverse model. Negative/positive values represent consumption/production..... 143

**Table 3.15.** Inputs through the Drake Passage, the South Scotia Ridge and the Philip Passage, and outputs through the North Scotia Ridge and Georgia Passage, split into the warm (north and west of the PF) and cold (south and east of the PF) domains and water mass strata. The negative convergent (positive divergent) transport differences represent consumption (production). .... 145

- Table 3.16.** Contributions to the DIC balance,  $\Delta T_{DIC}$ , from the air-sea exchange,  $E_{DIC}$ , internal generation or consumption through biogeochemical processes,  $I_{DIC}$ , and anthropogenic accumulation,  $A_{DIC}$ . Values are shown for each water strata and the entire water column down to  $\gamma^n = 28.00 \text{ kg m}^{-3}$ . The positive/negative values represent an ocean gain/loss.....147
- Table 3.17.** Mass, dissolved oxygen, nitrate and DIC transport imbalances per water masses comparison from B-SOSE model and our transports after applying the inverse model (BGC-IM). Negative/positive values represent consumption/production.....150
- Table 3.18.** Longitudinal ( $x_d$ ) and latitudinal ( $y_d$ ) separations between the centre of mass of the cloud of radial offsets and the origin of coordinates of the scattered diagram, grouped according to the depth range of the floats. The positive sign corresponds to east-north and the negative to west-south. For reference, a displacement of 10 km in 10 days represents a speed slightly less than  $1 \text{ cm s}^{-1}$  (exactly  $8.64 \times 10^{-3} \text{ m s}^{-1}$ ).....168
- Table 3.19.** Longitudinal ( $x_d$ ) and latitudinal ( $y_d$ ) separations between the centre of mass of the cloud of radial offsets and the origin of coordinates of the scattered diagram, at 15 m (GDP) and near 1000 m (Argo floats), grouped per frontal region. The positive sign corresponds to east-north and the negative to west-south. For reference, a displacement of 10 km in 10 days represents a speed slightly less than  $1 \text{ cm s}^{-1}$  (exactly  $8.64 \times 10^{-3} \text{ m s}^{-1}$ ).....168
- Table 3.20.** Percentage of particles released at the Drake Passage and associated total transports that arrive at each key section (see Figure 3.65), distributed per water masses as defined in subsection 3.4.2.1. The percentages and transports do not consider the particles (8.6%) that remain in the domain without reaching any section.....194
- Table 3.21.** Net mass, salt and heat initial transport per water mass and its sum at Drake Passage. Note that  $10^6 \text{ kg s}^{-1}$  is approximately equivalent to 1 Sv.....199
- Table 3.22.** Total heat and salinity transport at the beginning and at the end of the different pathways according to the water masses. Whereas the DP  $\rightarrow$  32°S and DP  $\rightarrow$  21°S consider all the pathways until they cross the final section, the 32°S  $\rightarrow$  21°S and DP  $\rightarrow$  25°E only include those particles that follow these pathways. Note that  $10^6 \text{ kg s}^{-1}$  is approximately equivalent a 1 Sv.....202
- Table 3.23.** Total heat gain and total salinity gain among different pathways and water masses. Note that  $10^6 \text{ kg s}^{-1}$  is equivalent a 1 Sv. Whereas the DP  $\rightarrow$  32°S and DP  $\rightarrow$  21°S consider

all the pathways until they cross the final section, the  $32^{\circ}\text{S} \rightarrow 21^{\circ}\text{S}$  and  $\text{DP} \rightarrow 25^{\circ}\text{E}$  only include those particles that follow these pathways..... 202

**Table 3.24.** The median time taken and the median depth at which particles perform the South Atlantic subtropical gyre recirculations, according to its neutral density (water mass) at the origin. The time represents the years passed until the particle returns to the  $32^{\circ}\text{S}$ -W section, and the depth is calculated as the average of the depths at the beginning and ending of the recirculation..... 208

**Table 3.25.** Water transports (left column) and transit times (right column) for the different pathways and water masses, as calculated from the climatological daily-mean fields. Whereas  $\text{DP} \rightarrow 32^{\circ}\text{S}$  and  $\text{DP} \rightarrow 21^{\circ}\text{S}$  consider all pathways until crossing the section, the  $\text{DP} \rightarrow 25^{\circ}\text{E}$  only includes those particles that follow this pathway..... 209

**Table 3.26.** Mean summer and winter AAIW transports at the reference section (eastern edge of subtropical gyre), the Drake Passage section and the Agulhas Current section, and the mode transit times to reach these last two sections from the reference section. The mode transit time corresponds to the most frequent time, coinciding with the peak of histograms in Figure 3.83b, d, f, h. Notice that the transport at the eastern margin of the subtropical gyre corresponds to the net (left) and the total (right) sum of values, while for the Drake and Agulhas sections only the total transport. .... 225

**Table 3.27.** Potential temperature, salt and depth changes experienced by AAIW according to the individual warm and cold routes followed from either the Drake Passage section or the Agulhas Current section to the  $34^{\circ}\text{S}$  reference section for winter and summer. Negative/positive signs correspond to properties loss/gain. .... 232

**Table 3.28.** Transport transformations suffered by AAIW according to the individual warm and cold routes followed from their source to the reference section depending on the release season. Negative/positive signs correspond to potential density loss/gain. The net transformation is quantified for upper ( $\sigma < 26.8 \text{ kg m}^{-3}$ ), intermediate ( $26.8 < \sigma < 27.5 \text{ kg m}^{-3}$ ), and deep ( $\sigma > 27.5 \text{ kg m}^{-3}$ ) waters..... 236

## REFERENCES

- Aagaard, K., & Carmack, E. C. (1989). The role of sea ice and other fresh water in the Arctic circulation. *Journal of Geophysical Research: Oceans*, 94(C10), 14485-14498.
- Abernathy, R. P., & Marshall, J. (2013). Global surface eddy diffusivities derived from satellite altimetry. *Journal of Geophysical Research: Oceans*, 118(2), 901-916.
- Ansorge, I. J., & Lutjeharms, J. R. E. (2002). The hydrography and dynamics of the ocean environment of the Prince Edward Islands (Southern Ocean). *Journal of Marine Systems*, 37(1-3), 107-127.
- Argo (2000). Argo float data and metadata from Global Data Assembly Centre (Argo GDAC). SEANOE.
- Arhan, M., Heywood, K. J., & King, B. A. (1999). The deep waters from the Southern Ocean at the entry to the Argentine Basin. *Deep-Sea Research II*, 46, 475-499.
- Arhan, M., Naveira Garabato, A. C., Heywood, K. J., & Stevens, D. P. (2002). The antarctic circumpolar current between the Falkland Islands and South Georgia. *Journal of Physical Oceanography*, 32(6), 1914-1931.
- Artana, C., Ferrari, R., Koenig, Z., Saraceno, M., Piola, A. R., & Provost, C. (2016). Malvinas Current variability from Argo floats and satellite altimetry. *Journal of Geophysical Research: Oceans*, 121(7), 4854-4872.
- Artana, C., Lellouche, J. M., Park, Y. H., Garric, G., Koenig, Z., Sennéchaël, N., ... & Provost, C. (2018). Fronts of the Malvinas Current System: surface and subsurface expressions revealed by satellite altimetry, Argo floats, and Mercator operational model outputs. *Journal of Geophysical Research: Oceans*, 123(8), 5261-5285.
- Artana, C., Provost, C., Lellouche, J. M., Rio, M. H., Ferrari, R., & Sennéchaël, N. (2019a). The Malvinas current at the confluence with the Brazil current: Inferences from 25 years of Mercator ocean reanalysis. *Journal of Geophysical Research: Oceans*, 124(10), 7178-7200.
- Babiano, A., Basdevant, C., Le Roy, P., & Sadourny, R. (1990). Relative dispersion in two-dimensional turbulence. *Journal of Fluid Mechanics*, 214, 535-557.
- Bakker, D. C., Pfeil, B., Landa, C. S., Metzl, N., O'Brien, K. M., Olsen, A., ... & Xu, S. (2016). A multi-decade record of high-quality fCO<sub>2</sub> data in version 3 of the Surface Ocean CO<sub>2</sub> Atlas (SOCAT). *Earth System Science Data*, 8(2), 383-413.

- Baldawa, D., K. G. Speer, J. H. LaCasce, W. B. Owens, J. Marshall, and R. Ferrari. (2016). Circulation and stirring in the southeast Pacific Ocean and the Scotia Sea sectors of the Antarctic Circumpolar Current. *Journal of Physical Oceanography*, 46, 2005–2027.
- Baldawa, D., LaCasce, J. H., Speer, K. G., & Ferrari, R. (2021). Relative dispersion in the Antarctic circumpolar current. *Journal of Physical Oceanography*, 51(2), 553-574.
- Belkin, I. M., & Gordon, A. L. (1996). Southern Ocean fronts from the Greenwich meridian to Tasmania. *Journal of Geophysical Research: Oceans*, 101(C2), 3675-3696.
- Berglund, S., Döös, K., Campino, A. A., & Nycander, J. (2021). The Water Mass Transformation in the Upper Limb of the Overturning Circulation in the Southern Hemisphere. *Journal of Geophysical Research: Oceans*, 126(8), 1–13.
- Beron-Vera, F. J., Wang, Y., Olascoaga, M. J., Goni, G. J., & Haller, G. (2013). Objective detection of oceanic eddies and the Agulhas leakage. *Journal of Physical Oceanography*, 43(7), 1426-1438.
- Berrisford, P., Dee, D. P. K. F., Fielding, K., Fuentes, M., Kallberg, P., Kobayashi, S., & Uppala, S. (2009). The ERA-interim archive. *ERA report series*, (1), 1-16.
- Berry, D. I., & Kent, E. C. (2011). Air–sea fluxes from ICOADS: The construction of a new gridded dataset with uncertainty estimates. *International Journal of Climatology*, 31(7), 987-1001.
- Bianchi, A. A., Giulivi, C. F., & Piola, A. R. (1993). Mixing in the Brazil-Malvinas confluence. *Deep Sea Research Part I: Oceanographic Research Papers*, 40(7), 1345-1358.
- Biastoch, A., & Böning, C. W. (2013). Anthropogenic impact on Agulhas leakage. *Geophysical Research Letters*, 40(6), 1138-1143.
- Biastoch, A., Böning, C. W., & Lutjeharms, J. R. E. (2008). Agulhas leakage dynamics affects decadal variability in Atlantic overturning circulation. *Nature*, 456(7221), 489-492.
- Biastoch, A., Böning, C. W., Schwarzkopf, F. U., & Lutjeharms, J. R. E. (2009). Increase in Agulhas leakage due to poleward shift of Southern Hemisphere westerlies. *Nature*, 462(7272), 495-498.
- Biastoch, A., Durgadoo, J. V., Morrison, A. K., Van Sebille, E., Weijer, W., & Griffies, S. M. (2015). Atlantic multi-decadal oscillation covaries with Agulhas leakage. *Nature communications*, 6(1), 1-7.

- Blanke, B., & Raynaud, S. (1997). Kinematics of the Pacific equatorial undercurrent: An Eulerian and Lagrangian approach from GCM results. *Journal of Physical Oceanography*, 27(6), 1038-1053.
- Blanke, B., Arhan, M., Madec, G., & Roche, S. (1999). Warm water paths in the equatorial Atlantic as diagnosed with a general circulation model. *Journal of Physical Oceanography*, 29(11), 2753-2768.
- Boebel, O., Lutjeharms, J., Schmid, C., Zenk, W., Rossby, T., & Barron, C. (2003). The Cape Cauldron: a regime of turbulent inter-ocean exchange. *Deep Sea Research Part II: Topical Studies in Oceanography*, 50(1), 57-86.
- Boland, E. J. D., E. Shuckburgh, P. H. Haynes, J. R. Ledwell, M.-J. Messias, and A. J. Watson (2015). Estimating a submesoscale diffusivity using a roughness measure applied to a tracer release experiment in the Southern Ocean. *Journal of Physical Oceanography*, 45, 1610–1631.
- Botnikov, V. N. (1963). Geographical position of the Antarctic Convergence Zone in the Antarctic Ocean. *Soviet Antarctic Exped. Inform. Bull.*, 41, 324-327.
- Bower, A. S., Rossby, H. T., & Lillibridge, J. L. (1985). The Gulf Stream—barrier or blender?. *Journal of Physical Oceanography*, 15(1), 24-32.
- Bower, A., Lozier, S., Biastoch, A., Drouin, K., Foukal, N., Furey, H., ... & Zou, S. (2019). Lagrangian views of the pathways of the Atlantic Meridional Overturning Circulation. *Journal of Geophysical Research: Oceans*, 124(8), 5313-5335.
- Bracco, A., Clayton, S., & Pasquero, C. (2009). Horizontal advection, diffusion, and plankton spectra at the sea surface. *Journal of Geophysical Research: Oceans*, 114(C2).
- Broecker, W. (2010). The great ocean conveyor. In *The Great Ocean Conveyor*. Princeton University Press.
- Broecker, W. S. (1987). The biggest chill. *Natural History Magazine*, 74-82.
- Brown, P. J., Jullion, L., Landschützer, P., Bakker, D. C., Naveira Garabato, A. C., Meredith, M. P., ... & Wanninkhof, R. (2015). Carbon dynamics of the Weddell Gyre, Southern Ocean. *Global Biogeochemical Cycles*, 29(3), 288-306.
- Bryden, H. L., Longworth, H. R., & Cunningham, S. A. (2005). Slowing of the Atlantic meridional overturning circulation at 25 N. *Nature*, 438(7068), 655-657.
- Buckley, M. W., & Marshall, J. (2016). Observations, inferences, and mechanisms of the Atlantic Meridional Overturning Circulation: A review. *Reviews of Geophysics*, 54(1), 5-63.

- Burgoa, N., Machín, F., Marrero-Díaz, Á., Rodríguez-Santana, Á., Martínez-Marrero, A., Arístegui, J., & Duarte, C. M. (2020). Mass, nutrients and dissolved organic carbon (DOC) lateral transports off northwest Africa during fall 2002 and spring 2003. *Ocean Science*, 16(2), 483-511.
- Bushinsky, S. M., Landschützer, P., Rödenbeck, C., Gray, A. R., Baker, D., Mazloff, M. R., ... & Sarmiento, J. L. (2019). Reassessing Southern Ocean air-sea CO<sub>2</sub> flux estimates with the addition of biogeochemical float observations. *Global biogeochemical cycles*, 33(11), 1370-1388.
- Cabré, A., Pelegrí, J. L., & Vallès-Casanova, I. (2019). Subtropical-tropical transfer in the South Atlantic Ocean. *Journal of Geophysical Research: Oceans*, 124(7), 4820-4837.
- Caldwell, P. C., Firing, E., & Hummon, J. M. (2010). Ocean currents measured by Shipboard Acoustic Doppler Current Profilers (SADCP) from global oceans as part of the Joint Archive (JASADCP) since 1985. Southern Ocean, Scotia Sea, Ross Sea Data set. NOAA National Centers for Environmental Information. Accessed December 2020.
- Campos, M. L. A. M., Sanders, R., & Jickells, T. (1999). The dissolved iodate and iodide distribution in the South Atlantic from the Weddell Sea to Brazil. *Marine Chemistry*, 65(3-4), 167-175.
- Canadell, J. G., Le Quéré, C., Raupach, M. R., Field, C. B., Buitenhuis, E. T., Ciais, P., ... & Marland, G. (2007). Contributions to accelerating atmospheric CO<sub>2</sub> growth from economic activity, carbon intensity, and efficiency of natural sinks. *Proceedings of the national academy of sciences*, 104(47), 18866-18870.
- Carter, L., McCave, I. N., & Williams, M. J. (2008). Circulation and water masses of the Southern Ocean: a review. *Developments in earth and environmental sciences*, 8, 85-114.
- Casanova-Masjoan, M., Pelegrí, J. L., Sangrà, P., Martínez, A., Grisolia-Santos, D., Pérez-Hernández, M. D., & Hernández-Guerra, A. (2017). Characteristics and evolution of an Agulhas ring. *Journal of Geophysical Research: Oceans*, 122(9), 7049-7065.
- Cerovečki, I., Meijers, A. J., Mazloff, M. R., Gille, S. T., Tamsitt, V. M., & Holland, P. R. (2019). The effects of enhanced sea ice export from the Ross Sea on recent cooling and freshening of the Southeast Pacific. *Journal of Climate*, 32(7), 2013-2035.
- Cheng, Y. (2018). *Agulhas Leakage Variability and Its Climate Implications in a Coupled System*. [Doctoral dissertation]. University of Miami.
- Cheng, Y., Putrasahan, D., Beal, L., & Kirtman, B. (2016). Quantifying Agulhas leakage in a high-resolution climate model. *Journal of climate*, 29(19), 6881-6892.

- Chidichimo, M. P., Donohue, K. A., Watts, D. R., & Tracey, K. L. (2014). Baroclinic transport time series of the Antarctic Circumpolar Current measured in Drake Passage. *Journal of Physical Oceanography*, 44(7), 1829–1853.
- Chiswell, S. M. (2013). Lagrangian Time Scales and Eddy Diffusivity at 1000m Compared to the Surface in the South Pacific and Indian Oceans. *Journal of Physical Oceanography*, 43(12), 2718–2732.
- CLS. (2011). Argos User's Manual. [Available at <http://www.argos-system.org/manual/>.]
- Cole, S. T., Wortham, C., Kunze, E., & Owens, W. B. (2015). Eddy stirring and horizontal diffusivity from Argo float observations: Geographic and depth variability. *Geophysical Research Letters*, 42(10), 3989–3997.
- Colin de Verdière, A., & Ollitrault, M. (2016). A direct determination of the World Ocean Barotropic circulation. *Journal of Physical Oceanography*, 46(1), 255–273.
- Conkright, M. E., Locarnini, R. A., Garcia, H. E., O'Brien, T. D., Boyer, T. P., Stephens, C., & Antonov, J. I. (2002). World Ocean Atlas 2001: Objective analyses, data statistics, and figures: CD-ROM documentation.
- Crisp, D., Dolman, H., Tanhua, T., McKinley, G. A., Hauck, J., Bastos, A., ... & Aich, V. (2022). How Well Do We Understand the Land-Ocean-Atmosphere Carbon Cycle?. *Reviews of Geophysics*, 60(2), e2021RG000736.
- Cunningham, S. A., Alderson, S. G., King, B. A., & Brandon, M. A. (2003). Transport and variability of the Antarctic Circumpolar Current in Drake Passage. *Journal of Geophysical Research: Oceans*, 108(C5), 8084.
- Da Costa, M. V., & Blanke, B. (2004). Lagrangian methods for flow climatologies and trajectory error assessment. *Ocean Modelling*, 6(3-4), 335–358.
- Daher, H., Beal, L. M., & Schwarzkopf, F. U. (2020). A new improved estimation of Agulhas leakage using observations and simulations of Lagrangian floats and drifters. *Journal of Geophysical Research: Oceans*, 125(4), e2019JC015753.
- Davis, R.E. (1987). Modeling eddy transport of passive tracers, *J. Mar. Res.* 45 (3), 635–666.
- Davis, R.E. (1991a). Lagrangian ocean studies, *Annu. Rev. Fluid Mech.*, 23(1), 43–64.
- Davis, R.E. (1991b). Observing the general circulation with floats, *Deep\_Sea Res.* 38 (S1), S531–S571.



- De Dominicis, M., Leuzzi, G., Monti, P., Pinardi, N., & Poulain, P. M. (2012). Eddy diffusivity derived from drifter data for dispersion model applications. *Ocean Dynamics*, 62(9), 1381-1398.
- De Ruijter, W. D., Biastoch, A., Drijfhout, S. S., Lutjeharms, J. R. E., Matano, R. P., Pichevin, T., ... & Weijer, W. (1999). Indian-Atlantic interocean exchange: Dynamics, estimation and impact. *Journal of Geophysical Research: Oceans*, 104(C9), 20885-20910.
- Deacon, G. E. R. (1982). Physical and biological zonation in the Southern Ocean. *Deep Sea Research Part A. Oceanographic Research Papers*, 29(1), 1-15.
- Delandmeter, P., & Van Sebille, E. (2019). The Parcels v2.0 Lagrangian framework: New field interpolation schemes. *Geoscientific Model Development*, 12(8), 3571–3584. <https://doi.org/10.5194/gmd-12-3571-2019>
- Deng, Z. C., Hon, Y. C., & Yang, L. (2014). An optimal control method for nonlinear inverse diffusion coefficient problem. *Journal of Optimization Theory and Applications*, 160(3), 890-910.
- D'Errico, J. (2022). inpaint\_nans ([https://www.mathworks.com/matlabcentral/fileexchange/4551-inpaint\\_nans](https://www.mathworks.com/matlabcentral/fileexchange/4551-inpaint_nans)), MATLAB Central File Exchange. December 11, 2022.
- Donners, J., & Drijfhout, S. S. (2004). The Lagrangian view of South Atlantic interocean exchange in a global ocean model compared with inverse model results. *Journal of physical oceanography*, 34(5), 1019-1035.
- Donohue, K. A., Tracey, K. L., Watts, D. R., Chidichimo, M. P., & Chereskin, T. K. (2016). Mean Antarctic Circumpolar Current transport measured in Drake Passage. *Geophysical Research Letters*, 43(22), 11760–11767.
- Döös, K. (1995). Interocean exchange of water masses. *Journal of Geophysical Research: Oceans*, 100(C7), 13499-13514.
- Döös, K., Jönsson, B., & Kjellsson, J. (2017). Evaluation of oceanic and atmospheric trajectory schemes in the TRACMASS trajectory model v6. 0. *Geoscientific Model Development*, 10(4), 1733-1749.
- Döös, K., Nycander, J., & Coward, A. C. (2008). Lagrangian decomposition of the Deacon Cell. *Journal of Geophysical Research: Oceans*, 113(C7).
- Döös, K., Rupolo, V., & Brodeau, L. (2011). Dispersion of surface drifters and model-simulated trajectories. *Ocean Modelling*, 39(3–4), 301–310.

- Durgadoo, J. V., Loveday, B. R., Reason, C. J., Penven, P., & Biastoch, A. (2013). Agulhas leakage predominantly responds to the Southern Hemisphere westerlies. *Journal of Physical Oceanography*, 43(10), 2113-2131.
- Durgadoo, J. V., Rühls, S., Biastoch, A., & Böning, C. W. (2017). Indian Ocean sources of Agulhas leakage. *Journal of Geophysical Research: Oceans*, 122(4), 3481-3499.
- Eckart, C. (1948). An analysis of the stirring and mixing processes in incompressible fluids. *Journal of Marine Research*.
- Ekman, V. W. (1905). On the influence of the earth's rotation on ocean-currents.
- Elipot, S., Lumpkin, R., Perez, R. C., Lilly, J. M., Early, J. J., & Sykulski, A. M. (2016). A global surface drifter data set at hourly resolution. *Journal of Geophysical Research: Oceans*, 121(5), 2937-2966.
- Fahrbach, E., Rohardt, G., Scheele, N., Schröder, M., Strass, V., & Wisotzki, A. (1995). Formation and discharge of deep and bottom water in the northwestern Weddell Sea. *Journal of Marine Research*, 53(4), 515-538.
- Farneti, R., Delworth, T. L., Rosati, A. J., Griffies, S. M., & Zeng, F. (2010). The role of mesoscale eddies in the rectification of the Southern Ocean response to climate change. *Journal of Physical Oceanography*, 40(7), 1539-1557.
- Ferrari, R., & Nikurashin, M. (2010). Suppression of eddy diffusivity across jets in the Southern Ocean. *Journal of Physical Oceanography*, 40(7), 1501-1519.
- Firing, Y. L., Chereskin, T. K., & Mazloff, M. R. (2011). Vertical structure and transport of the Antarctic Circumpolar Current in Drake Passage from direct velocity observations. *Journal of Geophysical Research: Oceans*, 116(C8).
- Flierl, G. R. (1988). On the instability of geostrophic vortices. *Journal of fluid mechanics*, 197, 349-388.
- Foster, T. D., & Carmack, E. C. (1976). Frontal zone mixing and Antarctic Bottom Water formation in the southern Weddell Sea. In *Deep Sea Research and Oceanographic Abstracts* (Vol. 23, No. 4, pp. 301-317). Elsevier.
- Franco, B. C., Piola, A. R., Rivas, A. L., Baldoni, A., & Pisoni, J. P. (2008). Multiple thermal fronts near the Patagonian shelf break. *Geophysical Research Letters*, 35(2).
- Friedlingstein, P., Jones, M. W., O'Sullivan, M., Andrew, R. M., Bakker, D. C., Hauck, J., ... & Zeng, J. (2022). Global carbon budget 2021. *Earth System Science Data*, 14(4), 1917-2005.

- Friedlingstein, P., Jones, M. W., O'sullivan, M., Andrew, R. M., Hauck, J., Peters, G. P., ... & Zaehle, S. (2019). Global carbon budget 2019. *Earth System Science Data*, 11(4), 1783-1838.
- Friedlingstein, P., O'sullivan, M., Jones, M. W., Andrew, R. M., Hauck, J., Olsen, A., ... & Zaehle, S. (2020). Global carbon budget 2020. *Earth System Science Data*, 12(4), 3269-3340.
- Friocourt, Y., Drijfhout, S., Blanke, B., & Speich, S. (2005). Water mass export from Drake Passage to the Atlantic, Indian, and Pacific oceans: a Lagrangian model analysis. *Journal of physical oceanography*, 35(7), 1206-1222.
- Frölicher, T. L., Sarmiento, J. L., Paynter, D. J., Dunne, J. P., Krasting, J. P., & Winton, M. (2015). Dominance of the Southern Ocean in anthropogenic carbon and heat uptake in CMIP5 models. *Journal of Climate*, 28(2), 862-886.
- Fu, L. L. (1981). The general circulation and meridional heat transport of the subtropical South Atlantic determined by inverse methods. *Journal of Physical Oceanography*, 11(9), 1171-1193.
- Fu, L. L. (1986). Mass, heat and freshwater fluxes in the South Indian Ocean. *Journal of Physical Oceanography*, 16(10), 1683-1693.
- Ganachaud, A. (2000). *Large scale oceanic circulation and fluxes of freshwater, heat, nutrients and oxygen*. MASSACHUSETTS INST OF TECH CAMBRIDGE. [Doctoral Dissertation].
- Ganachaud, A. (2003). Large-scale mass transports, water mass formation, and diffusivities estimated from World Ocean Circulation Experiment (WOCE) hydrographic data. *Journal of Geophysical Research: Oceans*, 108(C7).
- Ganachaud, A., & Wunsch, C. (2000). Improved estimates of global ocean circulation, heat transport and mixing from hydrographic data. *Nature*, 408, 453-457,
- Garrett, C. (1983). On the initial streakiness of a dispersing tracer in two- and three-dimensional turbulence. *Dynamics of Atmospheres and Oceans*, 7(4), 265-277.
- Garric, G., Parent, L., Greiner, E., Drévillon, M., Hamon, M., Lellouche, J. M., ... & Le Traon, P. Y. (2017). Performance and quality assessment of the global ocean eddy-permitting physical reanalysis GLORYS2V4. In *EGU General Assembly Conference Abstracts* (p. 18776).
- Garzoli, S. L., & Matano, R. (2011). The South Atlantic and the Atlantic meridional overturning circulation. *Deep Sea Research Part II: Topical Studies in Oceanography*, 58(17-18), 1837-1847.

- Georgi, D. T., & Toole, J.M. (1982). The Antarctic Circumpolar Current and the oceanic heat and freshwater budgets. *Journal of Marine Research*, 40 (supplement), 183-197.
- Gille, S. (2003). Float observations of the Southern Ocean. Part I: Estimating mean fields, bottom velocities, and topographic steering. *Journal of Physical Oceanography*, 33, 1167–1181.
- Gille, S., Josey, S., & Swart, S. (2016). New approaches for air-sea fluxes in the Southern Ocean. *Eos*, 97.
- Gordon, A. L. (1967). Geostrophic Transport Through the Drake Passage. *Science*, 156(3783), 1732–1734.
- Gordon, A. L. (1975). General ocean circulation. *Numerical models of ocean circulation*, 39-53.
- Gordon, A. L. (1986). Inter-ocean exchange of thermocline water. *Journal of Geophysical Research: Oceans*, 91(C4), 5037-5046.
- Gordon, A. L. (1991). Two stable modes of Southern Ocean winter stratification. In *Elsevier Oceanography Series* (Vol. 57, pp. 17-35). Elsevier.
- Gordon, A. L., Huber, B. A., Hellmer, H. H., & Field, A. (1993). Deep and bottom water of the Weddell Sea's western rim. *Science*, 262(5130), 95-97.
- Gordon, A. L., Visbeck, M., & Huber, B. (2001). Export of Weddell Sea deep and bottom water. *Journal of Geophysical Research: Oceans*, 106(C5), 9005-9017.
- Gordon, A. L., Weiss, R. F., Smethie Jr, W. M., & Warner, M. J. (1992). Thermocline and intermediate water communication between the South Atlantic and Indian Oceans. *Journal of Geophysical Research: Oceans*, 97(C5), 7223-7240.
- Gordon, A. L., Zambianchi, E., Orsi, A., Visbeck, M., Giulivi, C. F., Whitworth III, T., & Spezie, G. (2004). Energetic plumes over the western Ross Sea continental slope. *Geophysical Research Letters*, 31(21).
- Graff, L. S., Guttu, S., & LaCasce, J. H. (2015). Relative dispersion in the atmosphere from reanalysis winds. *Journal of the Atmospheric Sciences*, 72(7), 2769-2785.
- Gray, A. R., Johnson, K. S., Bushinsky, S. M., Riser, S. C., Russell, J. L., Talley, L. D., ... & Sarmiento, J. L. (2018). Autonomous biogeochemical floats detect significant carbon dioxide outgassing in the high-latitude Southern Ocean. *Geophysical Research Letters*, 45(17), 9049-9057.

- Grech, A., Wolter, J., Coles, R., McKenzie, L., Rasheed, M., Thomas, C., ... & Hanert, E. (2016). Spatial patterns of seagrass dispersal and settlement. *Diversity and Distributions*, 22(11), 1150-1162.
- Greene, C. (2020). *SODB Southern Ocean Database Toolbox*. MATLAB Central File Exchange Retrieved from <https://www.mathworks.com/matlabcentral/fileexchange/52347-sodb-southern-ocean-database-toolbox>
- Gruber, N., Gloor, M., Mikaloff Fletcher, S. E., Doney, S. C., Dutkiewicz, S., Follows, M. J., ... Takahashi, T. (2009). Oceanic sources, sinks, and transport of atmospheric CO<sub>2</sub>. *Global Biogeochemical Cycles*, 23(1), 1–21.
- Gründlingh, M. L. (1983). On the course of the Agulhas Current. *South African Geographical Journal*, 65(1), 49-57.
- Häkkinen, S., & Rhines, P. B. (2004). Decline of subpolar North Atlantic circulation during the 1990s. *Science*, 304(5670), 555-559.
- Hamon, M., Greiner, E., Le Traon, P. Y., & Remy, E. (2019). Impact of multiple altimeter data and mean dynamic topography in a global analysis and forecasting system. *Journal of Atmospheric and Oceanic Technology*, 36(7), 1255-1266.
- Hanawa, K., & Talley, L. D. (2001). Mode waters. In *International Geophysics* (Vol. 77, pp. 373-386). Academic Press.
- Hansen, D. V., & Herman, A. (1989). Temporal sampling requirements for surface drifting buoys in the tropical Pacific. *Journal of Atmospheric and Oceanic Technology*, 6(4), 599-607.
- Hansen, D. V., & Poulain, P. M. (1996). Processing of WOCE/TOGA drifter data. *J. Atmos. Oceanic Technol*, 13(4), 900-909.
- Harris, T.F.W. & Bang, N.D. (1974). Topographic Rossby waves in the Agulhas Current. *South African Journal of Science*, 70, pp. 212-214
- Haumann, F. A., Gruber, N., Münnich, M., Frenger, I., & Kern, S. (2016). Antarctic sea-ice freshwater fluxes associated with freezing, transport, and melting (AnIceFlux).
- Herbei, R., McKeague, I. W., & Speer, K. G. (2008). Gyres and jets: Inversion of tracer data for ocean circulation structure. *Journal of Physical Oceanography*, 38(6), 1180-1202.
- Hersbach, H., Bell, B., Berrisford, P., Hirahara, S., Horányi, A., Muñoz-Sabater, J., ... & Thépaut, J. N. (2020). The ERA5 global reanalysis. *Quarterly Journal of the Royal Meteorological Society*, 146(730), 1999-2049.

- Heywood, K. J., Naveira Garabato, A. C., & Stevens, D. P. (2002). High mixing rates in the abyssal Southern Ocean. *Nature*, *415*(6875), 1011-1014.
- Hidaka, K. (1940a). Absolute evaluation of ocean currents in dynamical calculations. *Proceedings of the Imperial Academy*, *16*(8), 391-393.
- Hidaka, K. (1940b). Practical evaluation of ocean currents. *Proceedings of the Imperial Academy*, *16*(8), 394-397.
- Holton, L., Deshayes, J., Backeberg, B. C., Loveday, B. R., Hermes, J. C., & Reason, C. J. C. (2017). Spatio-temporal characteristics of Agulhas leakage: a model inter-comparison study. *Climate Dynamics*, *48*(7), 2107-2121.
- Ivanova, N., Pedersen, L. T., Tonboe, R. T., Kern, S., Heygster, G., Lavergne, T., ... & Shokr, M. (2015). Inter-comparison and evaluation of sea ice algorithms: towards further identification of challenges and optimal approach using passive microwave observations. *The Cryosphere*, *9*(5), 1797-1817.
- Jackett, D. R., & McDougall, T. J. (1997). A neutral density variable for the world's oceans. *Journal of Physical Oceanography*, *27*(2), 237-263.
- Jacobs, S. (1986). Temperature vs. depth from expendable bathythermograph casts taken from the US Coast Guard icebreaker Northwind. Modified after Burckle, Jacobs, and McLaughlin (in press). *Antarctic Journal of the United States*, *21*(5), 123.
- Jacobs, S. S., Amos, A. F., & Bruchhausen, P. M. (1970). Ross Sea oceanography and Antarctic bottom water formation. In *Deep Sea Research and Oceanographic Abstracts* (Vol. 17, No. 6, pp. 935-962). Elsevier.
- Jacobs, S. S., Fairbanks, R. G., & Horibe, Y. (1985). Origin and evolution of water masses near the Antarctic continental margin: Evidence from H<sub>2</sub>18O/H<sub>2</sub>16O ratios in seawater. *Oceanology of the Antarctic continental shelf*, *43*, 59-85.
- Jeffreys, H. (1925). On the formation of water waves by wind. *Proceedings of the royal society of London. Series A, containing papers of a mathematical and physical character*, *107*(742), 189-206.
- Johannessen, J. A., Chapron, B., Collard, F., Rio, M. H., Piollé, J. F., Gaultier, L., ... & Hansen, M. (2016). GlobCurrent: Multisensor synergy for surface current estimation. ESA.
- Johnson, G. C., Lyman, J. M., & Purkey, S. G. (2015). Informing deep Argo array design using Argo and full-depth hydrographic section data. *Journal of Atmospheric and Oceanic Technology*, *32*(11), 2187-2198.

- Johnson, K. S., Mazloff, M. R., Bif, M. B., Takeshita, Y., Jannasch, H. W., Maurer, T. L., ... & Talley, L. D. (2022). Carbon to nitrogen uptake ratios observed across the Southern Ocean by the SOCCOM profiling float array. *Journal of Geophysical Research: Oceans*, e2022JC018859.
- Joyce, T. M., Zenk, W., & Toole, J. M. (1978). The anatomy of the Antarctic polar front in the Drake Passage. *Journal of Geophysical Research: Oceans*, 83(C12), 6093-6113.
- Jullion, L., Heywood, K. J., Naveira Garabato, A. C., & Stevens, D. P. (2010). Circulation and water mass modification in the Brazil–Malvinas Confluence. *Journal of Physical Oceanography*, 40(5), 845-864.
- Kersalé, M., Marie, L., Le Cann, B., Serpette, A., Lathuilière, C., Le Boyer, A., ... & Lazure, P. (2016). Poleward along-shore current pulses on the inner shelf of the Bay of Biscay. *Estuarine, Coastal and Shelf Science*, 179, 155-171.
- Khatiwala, S., Tanhua, T., Mikaloff Fletcher, S., Gerber, M., Doney, S. C., Graven, H. D., ... & Sabine, C. L. (2013). Global ocean storage of anthropogenic carbon. *Biogeosciences*, 10(4), 2169-2191.
- Kim, Y. S., & Orsi, A. H. (2014). On the variability of Antarctic Circumpolar Current fronts inferred from 1992–2011 Altimetry. *Journal of Physical Oceanography*, 44(12), 3054–3071.
- Klocker, A., Ferrari, R., & LaCasce, J. H. (2012). Estimating suppression of eddy mixing by mean flows. *Journal of Physical Oceanography*, 42(9), 1566-1576.
- Koenig, Z., Provost, C., Ferrari, R., Sennechael, N., & Rio, M. H. (2014). Volume transport of the Antarctic Circumpolar Current: Production and validation of a 20 year long time series obtained from in situ and satellite observations. *Journal of Geophysical Research: Oceans*, 119(8), 5407–5433.
- Kuhlbrodt, T., Griesel, A., Montoya, M., Levermann, A., Hofmann, M., & Rahmstorf, S. (2007). On the driving processes of the Atlantic meridional overturning circulation. *Reviews of Geophysics*, 45(2).
- LaCasce, J. (2008). Statistics from Lagrangian observations. *Progress in Oceanography*, 77(1), 1-29.
- LaCasce, J. H. (2010). Relative displacement probability distribution functions from balloons and drifters. *Journal of Marine Research*, 68(3-4), 433-457.
- LaCasce, J. H., Ferrari, R., Marshall, J., Tulloch, R., Balwada, D., & Speer, K. (2014). Float-derived isopycnal diffusivities in the DIMES experiment. *Journal of Physical Oceanography*, 44(2), 764–780.

- Landschützer, P., Bushinsky, S. M., & Gray, A. R. (2019). A combined globally mapped carbon dioxide (CO<sub>2</sub>) flux estimate based on the Surface Ocean CO<sub>2</sub> Atlas Database (SOCAT) and Southern Ocean Carbon and Climate Observations and Modeling (SOCCOM) biogeochemistry floats from 1982 to 2017 (NCEI Accession 0191304). *NOAA National Centers for Environmental Information*.
- Lange, M., & van Sebille, E. (2017). Parcels v0. 9: prototyping a Lagrangian ocean analysis framework for the petascale age. *Geoscientific Model Development*, 10(11), 4175-4186.
- Laursen, L., & Eliassen, E. (1989). On the effects of the damping mechanisms in an atmospheric general circulation model. *Tellus A: Dynamic Meteorology and Oceanography*, 41(5), 385-400.
- Lauvset, S. K., Lange, N., Tanhua, T., Bittig, H. C., Olsen, A., Kozyr, A., ... & Key, R. M. (2021). An updated version of the global interior ocean biogeochemical data product, GLODAPv2. 2021. *Earth System Science Data*, 13(12), 5565-5589.
- Le Bars, D., Dijkstra, H. A., & De Ruijter, W. P. M. (2013). Impact of the Indonesian Throughflow on Agulhas leakage. *Ocean Science*, 9(5), 773-785.
- Le Quéré, C., Moriarty, R., Andrew, R. M., Peters, G. P., Ciais, P., Friedlingstein, P., ... & Zeng, N. (2015). Global carbon budget 2014. *Earth System Science Data*, 7(1), 47-85.
- Lebedev, K. V., Yoshinari, H., Maximenko, N. A., & Hacker, P. W. (2007). YoMaHa'07: Velocity data assessed from trajectories of Argo floats at parking level and at the sea surface. *IAPRC Technical Note*, 4(2), 1-16.
- Ledwell, J. R., St. Laurent, L. C., Girton, J. B., & Toole, J. M. (2011). Diapycnal mixing in the Antarctic circumpolar current. *Journal of Physical Oceanography*, 41(1), 241-246.
- Ledwell, J., Watson, A., & Law, C. (1998). Mixing of a tracer in the pycnocline. *Journal of Geophysical Research*, 103(21), 499-21.
- Lellouche, J. M., Greiner, E., Bourdallé-Badie, R., Garric, G., Mellet, A., Drévillion, M., et al. (2021). The Copernicus global 1/12° oceanic and sea ice GLORYS12 reanalysis. *Frontiers of Earth Science*, 9, 698876.
- Lenn, Y.-D., Chereskin, T. K., Sprintall, J., & Firing, E. (2007). Mean jets, mesoscale variability and eddy momentum fluxes in the surface layer of the Antarctic Circumpolar Current in Drake Passage. *Journal of Marine Research*, 65(1), 27-58.



- Li, Z., England, M. H., Groeskamp, S., Cerovečki, I., & Luo, Y. (2021). The origin and fate of subantarctic mode water in the Southern Ocean. *Journal of Physical Oceanography*, 51(9), 2951-2972.
- Liu, J., & Curry, J. A. (2010). Accelerated warming of the Southern Ocean and its impacts on the hydrological cycle and sea ice. *Proceedings of the National Academy of Sciences*, 107(34), 14987-14992.
- Llanillo, P. J., Pelegrí, J. L., Gasser, M., Emelianov, M., Gourrion, J., Rodríguez-Santana, A., & Duarte, C. M. (2012). Meridional and zonal changes in water properties along the continental slope off central and northern Chile. *Ciencias Marinas*, 38(1B), 307-332.
- Locarnini, R. A., Whitworth, T., & Nowlin, W. D. (1993). The importance of the Scotia Sea on the outflow of Weddell Sea Deep Water. *Journal of Marine Research*, 51(1), 135-153.
- Lovenduski, N. S., Bonan, G. B., Yeager, S. G., Lindsay, K., & Lombardozzi, D. L. (2019). High predictability of terrestrial carbon fluxes from an initialized decadal prediction system. *Environmental Research Letters*, 14(12).
- Lozier, M. S. (2010). Deconstructing the conveyor belt. *Science*, 328(5985), 1507-1511.
- Lozier, M. S., Bacon, S., Bower, A. S., Cunningham, S. A., De Jong, M. F., De Steur, L., ... & Zika, J. D. (2017). Overturning in the Subpolar North Atlantic Program: A new international ocean observing system. *Bulletin of the American Meteorological Society*, 98(4), 737-752.
- Lumpkin, R., & Johnson, G. C. (2013). Global ocean surface velocities from drifters: Mean, variance, El Niño–Southern Oscillation response, and seasonal cycle. *Journal of Geophysical Research: Oceans*, 118(6), 2992-3006.
- Lumpkin, R., & Speer, K. (2007). Global ocean meridional overturning. *Journal of Physical Oceanography*, 37(10), 2550-2562.
- Lutjeharms, J. R. (2006). *The Agulhas current retroflexion* (pp. 151-207). Springer Berlin Heidelberg.
- Lutjeharms, J. R. E., & Van Ballegooyen, R. C. (1988). The retroflexion of the Agulhas Current. *Journal of Physical Oceanography*, 18(11), 1570-1583.
- Macdonald, A. M. (1998). The global ocean circulation: A hydrographic estimate and regional analysis. *Progress in Oceanography*, 41(3), 281-382.
- Macdonald, A. M., & Wunsch, C. (1996). An estimate of global ocean circulation and heat fluxes. *Nature*, 382(6590), 436-439.

- Machín, F. (2004). Variabilidad espacio temporal de la Corriente de Canarias, del afloramiento costero al noroeste de África y de los intercambios atmósfera-oceano de calor y agua dulce. [Doctoral Dissertation].
- Machín, F., & Pelegrí, J. L. (2009). Northward penetration of Antarctic intermediate water off Northwest Africa. *Journal of Physical Oceanography*, 39(3), 512-535.
- Machín, F., Hernández-Guerra, A., & Pelegrí, J. L. (2006). Mass fluxes in the Canary Basin. *Progress in Oceanography*, 70(2-4), 416-447.
- Maes, C., Madec, G., & Delecluse, P. (1997). Sensitivity of an equatorial Pacific OGCM to the lateral diffusion. *Monthly weather review*, 125(5), 958-971.
- Manucharyan, G. E., & Thompson, A. F. (2017). Submesoscale sea ice-ocean interactions in marginal ice zones. *Journal of Geophysical Research: Oceans*, 122(12), 9455-9475.
- Marsh, R., Ivchenko, V. O., Skliris, N., Alderson, S., Bigg, G. R., Madec, G., ... & Zalesny, V. B. (2015). NEMO-ICB (v1. 0): interactive icebergs in the NEMO ocean model globally configured at eddy-permitting resolution. *Geoscientific Model Development*, 8(5), 1547-1562.
- Mason, E., Pascual, A., Gaube, P., Ruiz, S., Pelegrí, J. L., & Delepouille, A. (2017). Subregional characterization of mesoscale eddies across the Brazil-Malvinas Confluence. *Journal of Geophysical Research: Oceans*, 122(4), 3329-3357.
- Mazloff, M. R., Heimbach, P., & Wunsch, C. (2010). An eddy-permitting Southern Ocean state estimate. *Journal of Physical Oceanography*, 40(5), 880-899.
- McCartney, M. S. (1977). Subantarctic Mode Water. A Voyage of Discovery: George Deacon 70th Anniversary Volume, MV Angel, Ed. *Deep-Sea Research*, 103-119.
- McCartney, M. S., & Talley, L. D. (1982). The subpolar mode water of the North Atlantic Ocean. *Journal of Physical Oceanography*, 12(11), 1169-1188.
- Mémery, L., & Wunsch, C. (1990). Constraining the North Atlantic circulation with tritium data. *Journal of Geophysical Research: Oceans*, 95(C4), 5239-5256.
- Meredith, M. P. (2003). Southern ACC front to the northeast of South Georgia: Pathways, characteristics, and fluxes. *Journal of Geophysical Research*, 108(C5), 3162.
- Mignac, D., Ferreira, D., & Haines, K. (2018). South Atlantic meridional transports from NEMO based simulations and reanalyses. *Ocean Science*, 14(1), 53-68.

- Mikaloff Fletcher, S. E., Gruber, N., Jacobson, A. R., Gloor, M., Doney, S. C., Dutkiewicz, S., ... Sarmiento, J. L. (2007). Inverse estimates of the oceanic sources and sinks of natural CO<sub>2</sub> and the implied oceanic carbon transport. *Global Biogeochemical Cycles*, 21(1), 1–19.
- Morris, M., Stanton, B., & Neil, H. (2001). Subantarctic oceanography around New Zealand: preliminary results from an ongoing survey. *New Zealand Journal of Marine and Freshwater Research*, 35(3), 499-519.
- Munk, W., & Wunsch, C. (1998). Abyssal recipes II: Energetics of tidal and wind mixing. *Deep Sea Research Part I: Oceanographic Research Papers*, 45(12), 1977-2010.
- Nakamura, N. (1996). Two-dimensional mixing, edge formation, and permeability diagnosed in an area coordinate. *Journal of Atmospheric Sciences*, 53(11), 1524-1537.
- Naveira Garabato, A. C., Ferrari, R., & Polzin, K. L. (2011). Eddy stirring in the Southern Ocean. *Journal of Geophysical Research: Oceans*, 116(C9).
- Naveira Garabato, A. C., Heywood, K. J., & Stevens, D. P. (2002). Modification and pathways of Southern Ocean Deep Waters in the Scotia Sea. *Deep-Sea Research Part I Oceanographic Research Papers*, 49(4), 681–705.
- Naveira Garabato, A. C., Polzin, K. L., King, B. A., Heywood, K. J., & Visbeck, M. (2004). Widespread intense turbulent mixing in the Southern Ocean. *Science*, 303(5655), 210-213.
- Naveira Garabato, A. C., Stevens, D. P., & Heywood, K. J. (2003). Water mass conversion, fluxes and mixing in the Scotia Sea diagnosed by an inverse model. *Journal of Physical Oceanography*, 33, 2565–2587.
- Naveira Garabato, A. C., Stevens, D. P., Watson, A. J., & Roether, W. (2007). Short-circuiting of the overturning circulation in the Antarctic Circumpolar Current. *Nature*, 447(7141), 194-197.
- Niiler, P. (2001). The world ocean surface circulation. In *International geophysics* (Vol. 77, pp. 193-204). Academic Press.
- Nikurashin, M., & Vallis, G. (2011). A theory of deep stratification and overturning circulation in the ocean. *Journal of Physical Oceanography*, 41(3), 485-502.
- Okubo, A. (1971). Oceanic diffusion diagrams. In *Deep sea research and oceanographic abstracts* (Vol. 18, No. 8, pp. 789-802). Elsevier.

- Ollitrault, M., & Colin de Verdière, A. (2002). SOFAR floats reveal midlatitude intermediate North Atlantic general circulation. Part II: An Eulerian statistical view. *Journal of physical oceanography*, 32(7), 2034-2053.
- Ollitrault, M., & Rannou, J. P. (2013). ANDRO: An Argo-based deep displacement dataset. *Journal of Atmospheric and Oceanic Technology*, 30(4), 759-788.
- Ollitrault, M., Lankhorst, M., Fratantoni, D., Richardson, P., & Zenk, W. (2006). Zonal intermediate currents in the equatorial Atlantic Ocean. *Geophysical Research Letters*, 33(5).
- Olsen, A., Key, R. M., van Heuven, S., Lauvset, S. K., Velo, A., Lin, X., Schirnack, C., Kozyr, A., Tanhua, T., Hoppema, M., Jutterström, S., Steinfeldt, R., Jeansson, E., Ishii, M., Pérez, F. F. and Suzuki, T. (2016). The Global Ocean Data Analysis Project version 2 (GLODAPv2) – an internally consistent data product for the world ocean. *Earth System Science Data*, 8(2), 297-323.
- Onink, V., Wichmann, D., Delandmeter, P., & van Sebille, E. (2019). The role of Ekman currents, geostrophy, and stokes drift in the accumulation of floating microplastic. *Journal of Geophysical Research: Oceans*, 124(3), 1474-1490.
- Orsi, A. H., & Whitworth, T., III. (2005). In M. Sparrow, P. Chapman, & J. Gould (Eds.), *Hydrographic Atlas of the World Ocean Circulation. Experiment (WOCE). Volume 1: Southern Ocean*. International WOCE Project Office.
- Orsi, A. H., Johnson, G. C., & Bullister, J. L. (1999). Circulation, mixing, and production of Antarctic Bottom Water. *Progress in Oceanography*, 43(1), 55-109.
- Orsi, A. H., Whitworth III, T., & Nowlin Jr, W. D. (1995). On the meridional extent and fronts of the Antarctic Circumpolar Current. *Deep Sea Research Part I: Oceanographic Research Papers*, 42(5), 641-673.
- Orúe-Echevarría, D. (2019). The Brazil-Malvinas Confluence: from local to global scales. [Doctoral dissertation].
- Orúe-Echevarría, D., Pelegrí, J. L., Alonso-González, I. J., Benítez-Barrios, V. M., Emelianov, M., García-Olivares, A., ... & Vidal, M. (2021). A view of the Brazil-Malvinas confluence, March 2015. *Deep Sea Research Part I: Oceanographic Research Papers*, 172, 103533.
- Orúe-Echevarría, D., Pelegrí, J. L., Machín, F., Hernández-Guerra, A., & Emelianov, M. (2019). Inverse modeling the Brazil-Malvinas Confluence. *Journal of Geophysical Research: Oceans*, 124(1), 527-554.

- Palmer, M., Gomis, D., Flexas, M. del M., Jordà, G., Jullion, L., Tsubouchi, T., & Naveira Garabato, A. C. (2012). Water mass pathways and transports over the South Scotia Ridge west of 50°W. *Deep-Sea Research Part I: Oceanographic Research Papers*, 59, 8–24.
- Paris, C. B., Helgers, J., Van Sebille, E., & Srinivasan, A. (2013). Connectivity Modeling System: A probabilistic modeling tool for the multi-scale tracking of biotic and abiotic variability in the ocean. *Environmental Modelling & Software*, 42, 47-54.
- Park, Y. H., Charriaud, E., & Fieux, M. (1998). Thermohaline structure of the Antarctic surface water/winter water in the Indian sector of the Southern Ocean. *Journal of Marine Systems*, 17(1-4), 5-23.
- Peña-Izquierdo, J., van Sebille, E., Pelegrí, J. L., Sprintall, J., Mason, E., Llanillo, P. J., & Machín, F. (2015). Water mass pathways to the North Atlantic oxygen minimum zone. *Journal of Geophysical Research: Oceans*, 120(5), 3350-3372.
- Peterson, R. G., & Stramma, L. (1991). Upper-level circulation in the South Atlantic Ocean. *Progress in oceanography*, 26(1), 1-73.
- Peterson, R. G., & Whitworth III, T. (1989). The Subantarctic and Polar Fronts in relation to deep water masses through the southwestern Atlantic. *Journal of Geophysical Research: Oceans*, 94(C8), 10817-10838.
- Phillips, H. E., Tandon, A., Furue, R., Hood, R., Ummenhofer, C. C., Benthuisen, J. A., ... & Wiggert, J. (2021). Progress in understanding of Indian Ocean circulation, variability, air–sea exchange, and impacts on biogeochemistry. *Ocean Science*, 17(6), 1677-1751.
- Piola, A. R., & Gordon, A. L. (1984). Pacific and Indian Ocean upper-layer salinity budget. *Journal of Physical Oceanography*, 14(4), 747-753.
- Piola, A. R., Franco, B. C., Palma, E. D., & Saraceno, M. (2013). Multiple jets in the Malvinas Current. *Journal of Geophysical Research: Oceans*, 118(4), 2107-2117.
- Pokrajac, D., & Lazic, R. (2002). An efficient algorithm for high accuracy particle tracking in finite elements. *Advances in Water Resources*, 25(4), 353-369.
- Poli, L., Artana, C., Provost, C., Sirven, J., Sennéchaël, N., Cuypers, Y., & Lellouche, J. M. (2020). Anatomy of subinertial waves along the Patagonian shelf break in a 1/12 global operational model. *Journal of Geophysical Research: Oceans*, 125(12), e2020JC016641.
- Prodhomme, C., Batté, L., Massonnet, F., Davini, P., Bellprat, O., Guemas, V., & Doblas-Reyes, F. J. (2016). Benefits of increasing the model resolution for the seasonal forecast quality in EC-Earth. *Journal of Climate*, 29(24), 9141-9162.

- Provost, C., Escoffier, C., Maamaatuaiahutapu, K., Kartavtseff, A., & Garçon, V. (1999). Subtropical mode waters in the South Atlantic Ocean. *Journal of Geophysical Research: Oceans*, 104(C9), 21033-21049.
- Provost, C., Gana, S., Garçon, V., Maamaatuaiahutapu, K., & England, M. (1995). Hydrographic conditions in the Brazil-Malvinas Confluence during austral summer 1990. *Journal of Geophysical Research: Oceans*, 100(C6), 10655-10678.
- Purcell, C. (2014). *Investigations of the warm and cold water route ocean gateways on glacial-interglacial and millennial timescales*. [Doctoral dissertation]. Cardiff University.
- Qin, X., van Sebille, E., & Gupta, A. S. (2014). Quantification of errors induced by temporal resolution on Lagrangian particles in an eddy-resolving model. *Ocean Modelling*, 76, 20-30.
- Raynaud, S., Speich, S., Guilyardi, E., & Madec, G. (2000). Impacts of the ocean lateral diffusion on the El Niño/Southern Oscillation-like variability of a global coupled general circulation model. *Geophysical Research Letters*, 27(19), 3041-3044.
- Reeve, K. A., Boebel, O., Strass, V., Kanzow, T., & Gerdes, R. (2019). Horizontal circulation and volume transports in the Weddell Gyre derived from Argo float data. *Progress in Oceanography*, 175, 263-283.
- Reeves, G. (2022). smooth2a (<https://www.mathworks.com/matlabcentral/fileexchange/23287-smooth2a>), MATLAB Central File Exchange. December 11, 2022.
- Reid, J. L. (1994). On the total geostrophic circulation of the North Atlantic Ocean: Flow patterns, tracers, and transports. *Progress in Oceanography*, 33(1), 1-92.
- Reid, J. L., & Lynn, R. J. (1971). On the influence of the Norwegian-Greenland and Weddell seas upon the bottom waters of the Indian and Pacific oceans. In *Deep Sea Research and Oceanographic Abstracts* (Vol. 18, No. 11, pp. 1063-1088). Elsevier.
- Reid, J. L., Nowlin, W. D., Jr, & Patzert, W. C. (1977). On the characteristics and circulation of the southwestern Atlantic Ocean. *Journal of Physical Oceanography*(7), 62-91.
- Richardson, P. L. (2008). On the history of meridional overturning circulation schematic diagrams. *Progress in Oceanography*, 76(4), 466-486.
- Ridgway, K. R., & Dunn, J. R. (2007). Observational evidence for a Southern Hemisphere oceanic supergyre. *Geophysical Research Letters*, 34(13).
- Riley, G. A. (1951). Oxygen, phosphate, and nitrate in the Atlantic Ocean. *Bull. Bingham Oceanogr. Coll.*, 13(1), 1-124.

- Rimaud, J., Speich, S., Blanke, B., & Grima, N. (2012). The exchange of Intermediate Water in the southeast Atlantic: Water mass transformations diagnosed from the Lagrangian analysis of a regional ocean model. *Journal of Geophysical Research: Oceans*, 117(C8).
- Rintoul, S. R. (1985). On the origin and influence of Adélie Land Bottom Water. *Ocean, ice, and atmosphere: Interactions at the Antarctic continental margin*, 75, 151-171.
- Rintoul, S. R. (1991). South Atlantic interbasin exchange. *Journal of Geophysical Research: Oceans*, 96(C2), 2675-2692.
- Rintoul, S. R., & Naveira Garabato, A. C. (2013). Dynamics of the Southern Ocean circulation. *International Geophysics*, 103, 471-492.
- Rintoul, S. R., & Wunsch, C. (1991). Mass, heat, oxygen and nutrient fluxes and budgets in the North Atlantic Ocean. *Deep Sea Research Part A. Oceanographic Research Papers*, 38, S355-S377.
- Rintoul, S. R., Hughes, C. W., & Olbers, D. (2001). The Antarctic circumpolar current system. In *International Geophysics* (Vol. 77, pp. 271-XXXVI). Academic Press.
- Rintoul, S. R., Speer, K., Sparrow, M., Meredith, M., Hofmann, E., Fahrbach, E., ... & Gladyshev, S. (2010). Southern Ocean Observing System (SOOS): Rationale and strategy for sustained observations of the Southern Ocean. *Proceedings of OceanObs '09: Sustained Ocean Observations and Information for Society*.
- Roach, C. J., Balwada, D., & Speer, K. (2016). Horizontal mixing in the Southern Ocean from Argo float trajectories. *Journal of Geophysical Research: Oceans*, 121(8), 5570-5586.
- Roach, C. J., Balwada, D., & Speer, K. (2018). Global observations of horizontal mixing from Argo float and surface drifter trajectories. *Journal of Geophysical Research: Oceans*, 123(7), 4560-4575.
- Rödenbeck, C., Keeling, R. F., Bakker, D. C. E., Metzl, N., Olsen, A., Sabine, C., & Heimann, M. (2013). Global surface-ocean pCO<sub>2</sub> and sea-Air CO<sub>2</sub> flux variability from an observation-driven ocean mixed-layer scheme. *Ocean Science*, 9(2), 193-216.
- Rodrigues, R. R., Rothstein, L. M., & Wimbush, M. (2007). Seasonal variability of the South Equatorial Current bifurcation in the Atlantic Ocean: A numerical study. *Journal of Physical Oceanography*, 37(1), 16-30.
- Rodrigues, R. R., Wimbush, M., Watts, D. R., Rothstein, L. M., & Ollitrault, M. (2010). South Atlantic mass transports obtained from subsurface float and hydrographic data. *Journal of Marine Research*, 68(6), 819-850.

- Roemmich, D. (1983). The balance of geostrophic and Ekman transports in the tropical Atlantic Ocean. *Journal of Physical Oceanography*, 13(8), 1534-1539.
- Roemmich, D., Wilson, W. S., Gould, W. J., Owens, W. B., Le Traon, P. Y., Freeland, H. J., ... & Zilberman, N. (2022). The Argo Program. In *Partnerships in Marine Research* (pp. 53-69). Elsevier.
- Roemmich, D., Wilson, W. S., Gould, W. J., Owens, W. B., Le Traon, P. Y., Freeland, H. J., ... & Zilberman, N. (2022). The Argo Program. In *Partnerships in Marine Research* (pp. 53-69). Elsevier.
- Roquet, F., Williams, G., Hindell, M. A., Harcourt, R., McMahon, C., Guinet, C., ... & Fedak, M. (2014). A Southern Indian Ocean database of hydrographic profiles obtained with instrumented elephant seals. *Scientific data*, 1(1), 1-10.
- Rosell Fieschi, M. (2014). Ocean velocities as inferred from Argo floats: methodology and applications. [Doctoral dissertation].
- Rosell-Fieschi, M., Pelegri, J. L., & Gourrion, J. (2015). Zonal jets in the equatorial Atlantic Ocean. *Progress in Oceanography*, 130, 1–18. <https://doi.org/10.1016/j.pocean.2014.08.008>
- Rossby, T., Dorson, D., & Fontaine, J. (1986). The RAFOS system. *Journal of atmospheric and oceanic technology*, 3(4), 672-679.
- Rossby, T., Ellis, J., & Webb, D. C. (1993). An efficient sound source for wide-area RAFOS navigation. *Journal of Atmospheric and Oceanic Technology*, 10(3), 397-403.
- Rousselet, L., Cessi, P., & Forget, G. (2020). Routes of the upper branch of the Atlantic Meridional Overturning Circulation according to an ocean state estimate. *Geophysical research letters*, 47(18), e2020GL089137.
- Rubin, S. I. (2003). Carbon and nutrient cycling in the upper water column across the polar Frontal Zone and Antarctic circumpolar current along 170°W. *Global Biogeochemical Cycles*, 17(3). <https://doi.org/10.1029/2002gb001900>
- Rühs, S. (2018). Lagrangian connectivity of the upper limb of the overturning circulation studied with high-resolution ocean models. [Doctoral dissertation].
- Rühs, S., Durgadoo, J. V., Behrens, E., & Biastoch, A. (2013). Advective timescales and pathways of Agulhas leakage. *Geophysical Research Letters*, 40(15), 3997-4000.
- Rühs, S., Schwarzkopf, F. U., Speich, S., & Biastoch, A. (2019). Cold vs. warm water route-sources for the upper limb of the Atlantic Meridional Overturning Circulation revisited in a high-resolution ocean model. *Ocean Science*, 15(3), 489-512.



- Russell, J. L., Dixon, K. W., Gnanadesikan, A., Stouffer, R. J., & Toggweiler, J. R. (2016). The Southern Hemisphere westerlies in a warming world: Propping open the door to the deep ocean. *Journal of Climate*, 19(24), 6382-6390.
- Russell, J., Sarmiento, J., Cullen, H., Hotinski, R., Johnson, K., Riser, S., & Talley, L. (2014). The southern ocean carbon and climate observations and modeling program (soccom). *Ocean Carbon Biogeochem. Newsl*, 7, 1-5.
- Sabine, C. L., & Feely, R. A. (2007). The oceanic sink for carbon dioxide. *Greenhouse gas sinks*, 31.
- Sallée, J. B., Matear, R. J., Rintoul, S. R., & Lenton, A. (2012). Localized subduction of anthropogenic carbon dioxide in the Southern Hemisphere oceans. *Nature Geoscience*, 5(8), 579-584.
- Sallée, J. B., Speer, K., & Rintoul, S. R. (2011). Mean-flow and topographic control on surface eddy-mixing in the Southern Ocean. *Journal of Marine Research*, 69(4-5), 753-777.
- Sangrà, P., Pelegrí, J. L., Hernández-Guerra, A., Arregui, I., Martín, J. M., Marrero-Díaz, A., ... & Rodríguez-Santana, A. (2005). Life history of an anticyclonic eddy. *Journal of Geophysical Research: Oceans*, 110(C3).
- Saraceno, M., Provost, C., Piola, A., Bava, J., Gagliardini, A., & y Naturales, E. (2003). The Brazil Malvinas Frontal System as seen from nine years of AVHRR data. *Journal of Geophysical Research*, 109, C5.
- Sarmiento, J. L., & Gruber, N. (2002). Sinks for anthropogenic carbon. *Physics today*, 55(8), 30-36.
- Sarmiento, J. L., & Orr, J. C. (1991). Three-dimensional simulations of the impact of Southern Ocean nutrient depletion on atmospheric CO<sub>2</sub> and ocean chemistry. *Limnology and Oceanography*, 36(8), 1928-1950.
- Schmitz Jr, W. J. (1995). On the interbasin-scale thermohaline circulation. *Reviews of Geophysics*, 33(2), 151-173.
- Schott, F. A., & McCreary Jr, J. P. (2001). The monsoon circulation of the Indian Ocean. *Progress in Oceanography*, 51(1), 1-123.
- Sievers, H. A., & Emery, W. J. (1978). Variability of the Antarctic Polar frontal Zone in the Drake Passage—summer 1976–1977. *Journal of Geophysical Research: Oceans*, 83(C6), 3010-3022.
- Sievers, H. A., & Nowlin, W. D., Jr. (1984). The stratification and water masses at Drake Passage. *Journal of Geophysical Research*, 89, 10489–10514.

- Simmons, A. J., Burridge, D. M., Jarraud, M., Girard, C., & Wergen, W. (1989). The ECMWF medium-range prediction models development of the numerical formulations and the impact of increased resolution. *Meteorology and atmospheric physics*, 40(1), 28-60.
- Skeel, R. D., & Berzins, M. (1990). A method for the spatial discretization of parabolic equations in one space variable. *SIAM journal on scientific and statistical computing*, 11(1), 1-32.
- Sloyan, B. M. (2006). Antarctic bottom and lower circumpolar deep water circulation in the eastern Indian Ocean. *Journal of Geophysical Research: Oceans*, 111(C2).
- Sloyan, B. M., & Rintoul, S. R. (2001a). The Southern Ocean limb of the global deep overturning circulation. *Journal of Physical Oceanography*, 31(1), 143-173.
- Sloyan, B. M., & Rintoul, S. R. (2001b). Circulation, renewal, and modification of Antarctic Mode and Intermediate Water. *Journal of physical oceanography*, 31(4), 1005-1030.
- Smith, I. J., Stevens, D. P., Heywood, K. J., & Meredith, M. P. (2010). The flow of the Antarctic Circumpolar Current over the North Scotia Ridge. *Deep-Sea Research Part I: Oceanographic Research Papers*, 57(1), 14-28.
- Sokolov, S., & Rintoul, S. R. (2007). Multiple jets of the Antarctic Circumpolar Current south of Australia. *Journal of Physical Oceanography*, 37(5), 1394-1412.
- Sokolov, S., & Rintoul, S. R. (2009a). Circumpolar structure and distribution of the Antarctic Circumpolar Current fronts: 1. Mean circumpolar paths. *Journal of Geophysical Research*, 114, C11018.
- Sokolov, S., & Rintoul, S. R. (2009b). Circumpolar structure and distribution of the Antarctic Circumpolar Current fronts: 2. Variability and relationship to sea surface height. *Journal of Geophysical Research: Oceans*, 114(C11).
- Speich, S., Blanke, B., & Cai, W. (2007). Atlantic meridional overturning circulation and the Southern Hemisphere supergyre. *Geophysical Research Letters*, 34(23).
- Speich, S., Blanke, B., & Madec, G. (2001). Warm and cold water routes of an OGCM thermohaline conveyor belt. *Geophysical research letters*, 28(2), 311-314.
- Speich, S., Blanke, B., de Vries, P., Drijfhout, S., Döös, K., Ganachaud, A., & Marsh, R. (2002). Tasman leakage: A new route in the global ocean conveyor belt. *Geophysical Research Letters*, 29(10), 55-1.
- Sprintall, J. (2003). Seasonal to interannual upper-ocean variability in the Drake Passage. *Journal of Marine Research*, 61(1), 27-57.

- Stephenson, D. B. (1995). The impact of changing the horizontal diffusion scheme on the northern winter climatology of a general circulation model. *Quarterly Journal of the Royal Meteorological Society*, 121(521), 211-226.
- Stommel, H. (1958). The abyssal circulation. *Deep-Sea Research*, 5, 80-82.
- Stommel, H. (1961). Thermohaline convection with two stable regimes of flow. *Tellus*, 13(2), 224-230.
- Stramma, L., & England, M. (1999). On the water masses and mean circulation of the South Atlantic Ocean. *Journal of Geophysical Research: Oceans*, 104(C9), 20863-20883.
- Stramma, L., & Peterson, R. G. (1990). The south atlantic current. *Journal of Physical Oceanography*, 20(6), 846-859.
- Suga, T., & Talley, L. D. (1995). Antarctic Intermediate Water circulation in the tropical and subtropical South Atlantic. *Journal of Geophysical Research: Oceans*, 100(C7), 13441-13453.
- Sundermeyer, M. A., & Price, J. F. (1998). Lateral mixing and the North Atlantic Tracer Release Experiment: Observations and numerical simulations of Lagrangian particles and a passive tracer. *Journal of Geophysical Research: Oceans*, 103(C10), 21481-21497.
- Talley, L. D. (1996). Antarctic intermediate water in the South Atlantic. In *The South Atlantic* (pp. 219-238). Springer, Berlin, Heidelberg.
- Talley, L. D. (2003). Shallow, intermediate, and deep overturning components of the global heat budget. *Journal of Physical oceanography*, 33(3), 530-560.
- Talley, L. D. (2008). Freshwater transport estimates and the global overturning circulation: Shallow, deep and throughflow components. *Progress in Oceanography*, 78(4), 257-303.
- Talley, L. D. (2011). *Descriptive physical oceanography: an introduction*. Academic press.
- Talley, L. D. (2013). Closure of the global overturning circulation through the Indian, Pacific, and Southern Oceans: Schematics and transports. *Oceanography*, 26(1), 80-97.
- Thomas, M. D., Tréguier, A. M., Blanke, B., Deshayes, J., & Voldoire, A. (2015). A Lagrangian method to isolate the impacts of mixed layer subduction on the meridional overturning circulation in a numerical model. *Journal of Climate*, 28(19), 7503-7517.
- Thompson, A. F., & Sallee, J. B. (2012). Jets and topography: Jet transitions and the impact on transport in the Antarctic Circumpolar Current. *Journal of Physical Oceanography*, 42(6), 956-972.

- Thorpe, S. E., Heywood, K. J., Brandon, M. A., & Stevens, D. P. (2002). Variability of the southern Antarctic Circumpolar Current front north of South Georgia. *Journal of Marine Systems*, 37(1–3), 87–105.
- Tomczak, M. and Godfrey, J. S. (1994). *Regional Oceanography: An Introduction*. Pergamon, United Kingdom. 422 pp.
- Treasure, A. M., Roquet, F., Ansorge, I. J., Bester, M. N., Boehme, L., Bornemann, H., ... & De Bruyn, P. N. (2017). Marine mammals exploring the oceans pole to pole: a review of the MEOP consortium. *Oceanography*, 30(2), 132-138.
- Trenberth, K. E., & Caron, J. M. (2001). Estimates of meridional atmosphere and ocean heat transports. *Journal of Climate*, 14(16), 3433-3443.
- Troupin, C., Barth, A., Sirjacobs, D., Ouberdous, M., Brankart, J. M., Brasseur, P., ... & Beckers, J. M. (2012). Generation of analysis and consistent error fields using the Data Interpolating Variational Analysis (DIVA). *Ocean Modelling*, 52, 90-101.
- Tsuchiya, M., Talley, L. D., & McCartney, M. S. (1994). Water-mass distributions in the western South Atlantic; A section from South Georgia Island (54S) northward across the equator. *Journal of Marine Research*, 52(1), 55-81.
- Tulloch, R., Ferrari, R., Jahn, O., Klocker, A., LaCasce, J., Ledwell, J. R., ... & Watson, A. (2014). Direct estimate of lateral eddy diffusivity upstream of Drake Passage. *Journal of Physical Oceanography*, 44(10), 2593-2616.
- Vallès-Casanova I, Fraile-Nuez E, Martín-Rey M, van Sebille E, Cabré A, Olivé-Abelló A, Pelegrí JL. (2022). Water mass transports and pathways in the North Brazil - Equatorial Undercurrent retroflexion. *Journal of Geophysical Research: Oceans*, 127, e2021JC018150.
- Van Den Broeke, M. R., & Van Lipzig, N. P. (2004). Changes in Antarctic temperature, wind, and precipitation in response to the Antarctic Oscillation. *Annals of Glaciology*, 39, 119–126.
- Van Sebille, E., Beal, L. M., & Johns, W. E. (2011). Advective time scales of Agulhas leakage to the North Atlantic in surface drifter observations and the 3D OFES model. *Journal of Physical Oceanography*, 41(5), 1026-1034.
- Van Sebille, E., Griffies, S. M., Abernathey, R., Adams, T. P., Berloff, P., Biastoch, A., ... & Zika, J. D. (2018). Lagrangian ocean analysis: Fundamentals and practices. *Ocean Modelling*, 121, 49-75.

- Van Sebille, E., Johns, W. E., & Beal, L. M. (2012). Does the vorticity flux from Agulhas rings control the zonal pathway of NADW across the South Atlantic?. *Journal of Geophysical Research: Oceans*, 117(C5).
- Van Sebille, E., Van Leeuwen, P. J., Biastoch, A., & de Ruijter, W. P. (2010). Flux comparison of Eulerian and Lagrangian estimates of Agulhas leakage: A case study using a numerical model. *Deep Sea Research Part I: Oceanographic Research Papers*, 57(3), 319-327.
- Vanicek, M., & Siedler, G. (2002). Zonal fluxes in the deep water layers of the western South Atlantic Ocean. *Journal of physical oceanography*, 32(8), 2205-2235.
- Verdy, A., & Mazloff, M. R. (2017). A data assimilating model for estimating Southern Ocean biogeochemistry. *Journal of Geophysical Research: Oceans*, 122(9), 6968-6988.
- Verezemskaya, P., Barnier, B., Gulev, S. K., Gladyshev, S., Molines, J. M., Gladyshev, V., ... & Gavrikov, A. (2021). Assessing Eddying (1/12°) Ocean Reanalysis GLORYS12 Using the 14-yr Instrumental Record From 59.5° N Section in the Atlantic. *Journal of Geophysical Research: Oceans*, 126(6), e2020JC016317.
- Vernet, M., Geibert, W., Hoppema, M., Brown, P. J., Haas, C., Hellmer, H. H., ... & Verdy, A. (2019). The Weddell Gyre, Southern Ocean: present knowledge and future challenges. *Reviews of Geophysics*, 57(3), 623-708.
- Vivier, F., & Provost, C. (1999). Direct velocity measurements in the Malvinas Current. *Journal of Geophysical Research: Oceans*, 104(C9), 21083-21103.
- Voet, G., Quadfasel, D., Mork, K. A., & Søiland, H. (2010). The mid-depth circulation of the Nordic Seas derived from profiling float observations. *Tellus A: Dynamic Meteorology and Oceanography*, 62(4), 516-529.
- Ward, P., Whitehouse, M., Meredith, M., Murphy, E., Shreeve, R., Korb, R., ... Bone, D. (2002). The Southern Antarctic Circumpolar Current Front: Physical and biological coupling at South Georgia. *Deep-Sea Research Part I: Oceanographic Research Papers*, 49(12), 2183-2202.
- Wefer, G., Berger, W. H., Siedler, G., Webb, D. J., & Talley, L. D. (1996). Antarctic Intermediate Water in the South Atlantic. *The South Atlantic*, (1922), 219-238. [https://doi.org/10.1007/978-3-642-80353-6\\_11](https://doi.org/10.1007/978-3-642-80353-6_11)
- Whitworth III, T., Nowlin, W. D., Jr., & Worley, S. J. (1982). The net transport of the Antarctic Circumpolar Current through Drake Passage. *Journal of Physical Oceanography*, 12(9), 960-971.

- Whitworth III, T., Orsi, A. H., Kim, S. J., Nowlin Jr, W. D., & Locarnini, R. A. (1985). Water masses and mixing near the Antarctic Slope Front. *Ocean, ice, and atmosphere: interactions at the Antarctic continental margin*, 75, 1-27.
- Whitworth, T., & Peterson, R. G. (1985). Volume transport of the Antarctic Circumpolar Current from bottom pressure measurements. *Journal of Physical Oceanography*, 15, 810–816.
- Wunsch, C. (1977). Determining the general circulation of the oceans: a preliminary discussion. *Science*, 196(4292), 871-875.
- Wunsch, C. (1978). The North Atlantic general circulation west of 50 W determined by inverse methods. *Reviews of Geophysics*, 16(4), 583-620.
- Wunsch, C. (1996). *The ocean circulation inverse problem*. Cambridge University Press.
- Wunsch, C. (2002). What is the thermohaline circulation?. *Science*, 298(5596), 1179-1181.
- Wunsch, C., & Ferrari, R. (2004). Vertical mixing, energy, and the general circulation of the oceans. *Annual Review of Fluid Mechanics*, 36(1), 281-314.
- Wunsch, C., Hu, D., & Grant, B. (1983). Mass, heat, salt and nutrient fluxes in the South Pacific Ocean. *Journal of Physical Oceanography*, 13(5), 725-753.
- Wyrtki, K. (1961). *Physical oceanography of the Southeast Asian waters* (Vol. 2). University of California, Scripps Institution of Oceanography.
- Yamazaki, K., Aoki, S., Katsumata, K., Hirano, D., Nakayama, Y. (2021). Multidecadal poleward shift of the southern boundary of the Antarctic Circumpolar Current off East Antarctica. *Science Advances*, 7, eabf8755.
- Yoshinari, H., Maximenko, N. A., & Hacker, P. W. (2006). YoMaHa'05: Velocity data assessed from trajectories of Argo floats at parking level and at the sea surface. *IPRC Technical Note*, 4, 20.
- Young, W. R., Rhines, P. B., & Garrett, C. J. R. (1982). Shear-flow dispersion, internal waves and horizontal mixing in the ocean. *Journal of Physical Oceanography*, 12(6), 515-527.
- Zhurbas, V. M., Lyzhkov, D. A., & Kuzmina, N. P. (2014). Estimates of the lateral eddy diffusivity in the Indian Ocean as derived from drifter data. *Oceanology*, 54(3), 281-288.
- Zhurbas, V., & Oh, I. S. (2003). Lateral diffusivity and Lagrangian scales in the Pacific Ocean as derived from drifter data. *Journal of Geophysical Research: Oceans*, 108(C5).
- Zika, J. D., McDougall, T. J., & Sloyan, B. M. (2010). A tracer-contour inverse method for estimating ocean circulation and mixing. *Journal of Physical Oceanography*, 40(1), 26– 47.



